Nano-Optics and Nanophotonics

Ana Predojević
Morgan W. Mitchell *Editors*

Engineering the Atom-Photon Interaction

Controlling Fundamental Processes with Photons, Atoms and Solids

Springer

Nano-Optics and Nanophotonics

The Springer Series in Nano-Optics and Nanophotonics provides an expanding selection of research monographs in the area of nano-optics and nanophotonics, science- and technology-based on optical interactions of matter in the nanoscale and related topics of contemporary interest. With this broad coverage of topics, the series is of use to all research scientists, engineers and graduate students who need up-to-date reference books. The editors encourage prospective authors to correspond with them in advance of submitting a manuscript. Submission of manuscripts should be made to the editor-in-chief, one of the editors or to Springer.

More information about this series at http://www.springer.com/series/8765

Ana Predojević · Morgan W. Mitchell
Editors

Engineering the Atom-Photon Interaction

Controlling Fundamental Processes with Photons, Atoms and Solids

Springer

Editors
Ana Predojević
Experimental Physics
University of Innsbruck
Innsbruck
Austria

Morgan W. Mitchell
ICFO – Institut de Ciències Fotòniques
Barcelona
Spain

and

ICREA – Institució Catalana de Recerca i Estudis Avançats
Barcelona
Spain

ISSN 2192-1970 ISSN 2192-1989 (electronic)
Nano-Optics and Nanophotonics
ISBN 978-3-319-19230-7 ISBN 978-3-319-19231-4 (eBook)
DOI 10.1007/978-3-319-19231-4

Library of Congress Control Number: 2015942751

Springer Cham Heidelberg New York Dordrecht London

Printed on acid-free paper

Springer International Publishing AG Switzerland is part of Springer Science+Business Media (www.springer.com)

Preface

Controlled manipulation of individual quantum systems is one of the most striking achievements of early twenty-first century experimental science. Today, individual atoms and photons can be guided through complex coherent evolutions with exquisite control, performing quantum information tasks previously seen only on theoreticians' notepads. One of the most critical capabilities, also one of the most challenging, is the controlled interaction of material quantum systems—atoms—with optical quantum systems—photons. This capability lies at the heart of both quantum networking, the distribution of quantum information among separated nodes, and quantum sensing, in which atoms acting as sensors are "read out" by a photonic quantum system.

Achieving control in this area requires rethinking fundamental processes such as absorption and emission of single photons. Breaking from the traditional view that these processes are immutable and unpredictable, recent experiments explore how such fundamental interactions can be shaped and controlled, an *engineering* of the atom-photon interaction. Progress has been swift, both in established methods such as cavity QED, and in wholly new methods such as heralded single-photon absorption and on-demand photon generation by parametric down-conversion. The techniques are finding application in a broad range of material systems, including trapped ions, neutral atoms, molecules, impurities in crystals, and semiconductor quantum dots.

This book aims to provide an accessible overview of the diverse but closely interconnected activities at this new frontier of quantum optics. The topics addressed include generation of indistinguishable photons, methods to make these photons compatible with the narrow transitions of atomic systems, and their interaction with solid state and atomic media. Free-space interaction between single photons and single trapped ions plays a prominent role, as does modification of emission properties and shaping of the photon wave function using cavity QED. Leaders of the field, in most cases the originators of the techniques being described,

contributed the individual chapters, each of which presents the principles, state of the art, and envisioned future of a method to engineer the atom-photon interaction.

We thank all the authors for their generous contributions of time, effort, and expertise, without which this volume would not have been possible.

Innsbruck — Ana Predojević
Barcelona — Morgan W. Mitchell

Contents

Part I Cavity QED

1 Cavity Induced Interfacing of Atoms and Light 3
Axel Kuhn
1.1 Introduction 3
1.2 Cavities for Interfacing Light and Matter 4
1.2.1 Atom-Photon Interaction in Resonators 5
1.2.2 Single-Photon Emission 9
1.3 Cavity-Enhanced Atom-Photon Entanglement 18
1.4 Photon Coherence, Amplitude and Phase Control 21
1.4.1 Indistinguishability of Photons 21
1.4.2 Arbitrary Shaping of Amplitude and Phase 23
1.5 Cavity-Based Quantum Memories 28
1.6 Future Directions 34
References 35

2 A Highly Efficient Single Photon-Single Quantum Dot Interface 39
Loic Lanco and Pascale Senellart
2.1 Motivations 39
2.2 Efficient Quantum Dot-Photon Interfacing 41
2.2.1 Basics of Cavity-QED in a Quantum Dot-Micropillar Device 41
2.2.2 Deterministic QD-Cavity Coupling Through In Situ Lithography 43
2.2.3 Critical Parameters: Beyond the Purcell Factor 45
2.3 Ultrabright Single Photon Sources 46
2.3.1 Why Are Bright Single Photon Sources Desirable? . . . 46
2.3.2 Demonstration of Single Photon Sources with Record Brightness 47
2.3.3 Purity of the Single Photon Emission 49

2.3.4 High Indistinguishability Through a Control of the QD Environment 51
2.3.5 Electrically Controlled Sources 54
2.3.6 Implementation of an Entangling CNOT Gate. 56
2.4 Nonlinear Optics with Few-Photon Pulses 59
2.4.1 Motivations: Photon Blockade and Photon Routing . . . 59
2.4.2 Observation of Nonlinearities at the Few-Photon Scale. 61
2.4.3 Device Optimization: Towards a Single-Photon Router? 63
2.4.4 Resonant Excitation: Application to Fast Optical Nanosensing 64
2.5 Future Challenges 65
References. 67

Part II Light Meets a Single Atom

3 Photon-Atom Coupling with Parabolic Mirrors 75
Markus Sondermann and Gerd Leuchs
3.1 Coupling to an Atom: The Role of Dipole Radiation. 75
3.1.1 General Considerations 75
3.1.2 Defining a Coupling Efficiency. 77
3.2 Dipole-Mode Generation with a Parabolic Mirror 78
3.2.1 Finding the Optimum Field Mode 78
3.2.2 Generation and Characterization of Field Modes Tailored for Efficient Free-Space Coupling. 81
3.3 Overview of Experiments on Photon-Atom Coupling in Free Space 82
3.3.1 Shifting the Phase of a Coherent Beam 83
3.3.2 Extinction of a Weak Coherent Beam 84
3.3.3 Absorption of Single Photons 85
3.4 Absorbing a Single Photon: Temporal Mode Shaping 87
3.4.1 Choosing the Right Mode 87
3.4.2 Generation of Exponentially Increasing Pulses 88
3.4.3 An Analogous Experiment: Coupling to a Resonator 89
3.5 Trapping Ions in Parabolic Mirrors 90
3.5.1 Parabolic Mirror Ion Trap 90
3.5.2 Fluorescence Collection 92
3.6 Experimental Determination of the Coupling Efficiency 92
3.7 Outlook 95
References. 95

4 Free Space Interference Experiments with Single Photons and Single Ions 99
Lukáš Slodička, Gabriel Hétet, Markus Hennrich and Rainer Blatt
4.1 Coupling to a Single Ion in Free Space 100
4.1.1 Electromagnetically Induced Transparency from a Single Atom in Free Space 101
4.1.2 Single Ion as a Mirror of an Optical Cavity 108
4.2 Probabilistic Entanglement Between Distant Ions 111
4.2.1 Single-Photon and Two-Photon Protocols 111
4.2.2 Generation of Entanglement by a Single Photon Detection 114
4.2.3 Experimental Realization 115
4.2.4 Summary 120
References 121

5 Single Photon Absorption by a Single Atom: From Heralded Absorption to Polarization State Mapping 125
Nicolas Piro and Jürgen Eschner
5.1 Introduction 126
5.2 Single Photon-Single Atom Interaction and Entanglement Schemes 127
5.2.1 Single Photon Absorption Schemes 127
5.2.2 Photon-Atom State Transfer and Entanglement Swapping Schemes 129
5.3 Experimental Setup 130
5.4 Experimental Progress 132
5.4.1 Single Photon Absorption by a Single Ion 132
5.4.2 Polarization Control in the Absorption Event 134
5.4.3 Photon-to-Ion State Transfer by Heralded Absorption 138
5.5 Conclusions and Outlook 138
References 140

Part III Light Meets Many Atoms

6 Narrowband Biphotons: Generation, Manipulation, and Applications 145
Chih-Sung Chuu and Shengwang Du
6.1 Introduction 145
6.2 Monolithic Resonant Parametric Down-Conversion with Cluster Effect 146
6.2.1 Single-Mode Output 147
6.2.2 Experimental Realization 148

6.3 Backward-Wave Biphoton Generation 149
6.3.1 General Formulism: Free Space 150
6.3.2 General Formalism: Resonant SPDC 153
6.3.3 Single-Mode Output 155
6.3.4 Experimental Challenge 156
6.4 Spontaneous Four-Wave Mixing with Electromagnetically Induced Transparency 157
6.4.1 Damped Rabi Oscillation Regime 160
6.4.2 Group Delay Regime 162
6.5 Manipulation of Narrowband Single Photons 165
6.6 Applications 173
6.7 Summary 179
References 179

7 Generation, Characterization and Use of Atom-Resonant Indistinguishable Photon Pairs 183
Morgan W. Mitchell
7.1 Introduction 183
7.1.1 CESPDC Sources 184
7.1.2 Atomic Frequency Filters 185
7.2 Atom-Resonant Indistinguishable Photon Pairs in a Single Mode 186
7.2.1 Type-I CESPDC Source 186
7.2.2 A FADOF at the Rb D_1 Line 187
7.2.3 Spectral Purification of Degenerate Photon Pairs from Type-I CESPDC 190
7.2.4 Interference of Biphoton Amplitudes from Distinct Sources 193
7.2.5 Full Reconstruction of the Biphoton Wave-function . . . 196
7.3 Generation of Spectrally-Pure, Atom-Resonant NooN States . . . 197
7.3.1 NooN States 197
7.3.2 Type-II CESPDC Source 198
7.3.3 Induced Dichroism Atomic Filter 202
7.3.4 Spectral Purity Measurement 203
7.3.5 Quantum-Enhanced Sensing of Atoms Using Atom-Tuned NooN States 204
7.4 Conclusions 208
References 211

Part IV Storage and Retrieval of Non-classical States

8 On-Demand Release of a Heralded Quantum State from Concatenated Optical Cavities 217
Jun-ichi Yoshikawa, Kenzo Makino and Akira Furusawa
8.1 Introduction 217
8.2 Working Principle 220
8.3 Experimental Demonstration for a Heralded Single-Photon State 222
8.3.1 Experimental Methods 223
8.3.2 Experimental Results 228
8.4 Summary 229
References 239

9 Quantum Light Storage in Solid State Atomic Ensembles 241
Hugues de Riedmatten and Mikael Afzelius
9.1 Introduction 241
9.2 Rare-Earth-Ion Doped Crystals 243
9.3 Quantum Memory Protocols 245
9.4 State of the Art 249
9.5 Quantum Light Sources Compatible with Solid State Quantum Memories 251
9.5.1 Characterizing Photon Pair Sources 253
9.5.2 A Quantum Light Source Compatible with Nd Doped Crystals 255
9.5.3 A Quantum Light Source Compatible with Pr Doped Crystals 257
9.6 Quantum Light Storage Experiments 259
9.6.1 Quantum Entanglement Storage in Nd:YSO Crystals 259
9.6.2 Quantum Storage of Heralded Single Photon in a Pr^{3+}:Y_2SiO_5Crystal 263
9.7 Prospects for Spin-Wave Storage with Quantum Light 266
9.8 Outlook 268
References 268

Part V New Sources of Entangled Photon Pairs

10 Engineering of Quantum Dot Photon Sources via Electro-elastic Fields 277
Rinaldo Trotta and Armando Rastelli
10.1 Engineering of Quantum Dot Photon Sources via Electro-elastic Fields 277

10.2 Hybrid Semiconductor-Piezoelectric Quantum Dot Devices: The First High-Speed, Wavelength-Tunable, and All-Electrically-Controlled Source of Single Photons 280
10.3 Independent Control of Different Quantum Dot Parameters via Electro-elastic Fields 284
10.3.1 Independent Control of Charge State and Emission Energy 284
10.3.2 Independent Control of Exciton and Biexciton Energy 286
10.4 Controlling and Erasing the Fine Structure Splitting for the Generation of Highly Entangled Photon Pairs 288
10.4.1 Controlling and Erasing the Exciton Fine Structure Splitting via Electro-elastic Fields 289
10.4.2 Generation of Highly Entangled Photon Pairs via Electro-elastic Tuning of Single Semiconductor QDs 293
10.5 Conclusions and Outlook 298
References 299

11 Resonant Excitation and Photon Entanglement from Semiconductor Quantum Dots 303
Ana Predojević
11.1 Introduction 303
11.2 On-Demand Generation of Photon Pairs Using Single Semiconductor Quantum Dots 304
11.2.1 Quantum Dots and Polarization Entanglement 305
11.2.2 Resonant Excitation 307
11.2.3 Theoretical Description of the Two-Photon Excitation Process 309
11.3 Measurements Under Resonant Excitation 313
11.3.1 Coherent Control 313
11.3.2 Photon Statistics Under Resonant Excitation 314
11.3.3 Time-Bin Entanglement 316
11.4 Future Directions 321
References 321

Part VI Distinguishability of Photons

12 Generation and Application of Frequency-Uncorrelated Photon Pairs 327
Tian-Ming Zhao, Xiao-Hui Bao, Bo Zhao and Jian-Wei Pan
12.1 Introduction 327
12.2 Single Photon Wavepacket Generation by SPDC 329

12.3 Group Velocity Mismatching 330
12.4 Narrowband Entanglement Sources 334
12.5 Applications 338
12.6 Conclusions 341
References 341

13 Single Semiconductor Quantum Dots in Microcavities: Bright Sources of Indistinguishable Photons 343
C. Schneider, P. Gold, C.-Y. Lu, S. Höfling, J.-W. Pan and M. Kamp
13.1 Introduction 343
13.2 A Pedestrian's Guide to Two Photon Interference 344
13.2.1 Quantum Dot Single Photon Source 344
13.2.2 Photon Interference with Quantum Light 345
13.3 A Bright Quasi-planar Single Photon Source 347
13.4 Emission of Single and Indistinguishable Photons from Single Quantum Dots 349
13.4.1 Single Photon Emission from Single QDs 349
13.4.2 Two Photon Interference with Single Photons 353
13.5 Two Photon Interference from Remote, Single Quantum Dots 356
13.5.1 Conclusion 359
References 360

Part VII Beyond Photons

14 Towards Quantum Repeaters with Solid-State Qubits: Spin-Photon Entanglement Generation Using Self-assembled Quantum Dots 365
Peter L. McMahon and Kristiaan De Greve
14.1 Introduction 365
14.2 Quantum Repeaters 366
14.2.1 Motivation for Quantum Repeaters 367
14.2.2 Design of Quantum Repeaters 373
14.3 Quantum Dots as Building Blocks for Quantum Repeaters 380
14.3.1 Quantum Dots as Quantum Memories 381
14.3.2 Quantum Dots as Photon Sources 387
14.3.3 Entanglement Between a Spin in a Quantum Dot and an Emitted Photon 388
14.4 Conclusion 396
References 398

Index 403

Contributors

Mikael Afzelius Group of Applied Physics, University of Geneva, Geneva, Switzerland

Xiao-Hui Bao Hefei National Laboratory for Physical Sciences at Microscale, Department of Modern Physics, Anhui, China

Rainer Blatt University of Innsbruck, Innsbruck, Austria; Institute for Quantum Optics and Quantum Information, Austrian Academy of Sciences, Innsbruck, Austria

Chih-Sung Chuu Department of Physics and Frontier Research Center on Fundamental and Applied Sciences of Matters, National Tsing Hua University, Hsinchu, Taiwan

Kristiaan De Greve Department of Physics, Harvard University, Cambridge, MA, USA

Hugues de Riedmatten ICFO-The Institute of Photonic Sciences, Barcelona, Spain; ICREA-Institució Catalana de Recerca i Estudis Avançats, Barcelona, Spain

Shengwang Du Department of Physics, The Hong Kong University of Science and Technology, Clear Water Bay, Kowloon, Hong Kong, People's Republic of China

Jürgen Eschner Universität des Saarlandes, Saarland, Germany

Akira Furusawa Department of Applied Physics, School of Engineering, The University of Tokyo, Bunkyo-ku, Tokyo, Japan

P. Gold University of Würzburg, Würzburg, Germany

Markus Hennrich University of Innsbruck, Innsbruck, Austria; Department of Physics, Stockholm University, Stockholm, Sweden

Gabriel Hétet Laboratoire Pierre Aigrain, Ecole Normale Supérieure-PSL Research University, CNRS, Université Pierre et Marie Curie-Sorbonne Universités, Université Paris Diderot-Sorbonne Paris Cité, Paris Cedex 05, France

S. Höfling University of Würzburg, Würzburg, Germany; SUPA, School of Physics and Astronomy, University of St Andrews, St Andrews, UK

M. Kamp University of Würzburg, Würzburg, Germany

Axel Kuhn Clarendon Laboratory, University of Oxford, Oxford, UK

Loic Lanco CNRS-LPN Laboratoire de Photonique Et de Nanostructures, Route de Nozay, Marcoussis, France; Université Paris Diderot, Paris Cedex 13, France

Gerd Leuchs Department of Physics, University of Erlangen-Nuremberg, Erlangen, Germany; Max Planck Institute for the Science of Light, Erlangen, Germany; Department of Physics, University of Ottawa, Ottawa, ON, Canada

C.-Y. Lu University of Würzburg, Würzburg, Germany; University of Science and Technology of China, Hefei, Anhui, P.R. China

Kenzo Makino Department of Applied Physics, School of Engineering, The University of Tokyo, Bunkyo-ku, Tokyo, Japan

Peter L. McMahon E.L. Ginzton Laboratory and Department of Applied Physics, Stanford University, Stanford, CA, USA

Morgan W. Mitchell ICFO – Institut de Ciències Fotòniques, Castelldefels, Barcelona, Spain; ICREA – Institució Catalana de Recerca i Estudis Avançats, Barcelona, Spain

Jian-Wei Pan University of Würzburg, Würzburg, Germany; University of Science and Technology of China, Hefei, Anhui, P.R. China; Hefei National Laboratory for Physical Sciences at Microscale, Department of Modern Physics, Anhui, China

Nicolas Piro École Polytechnique Fédérale de Lausanne, Lausanne, Switzerland

Ana Predojević Experimental Physics, University of Innsbruck, Innsbruck, Austria

Armando Rastelli Institute of Semiconductor and Solid State Physics, Johannes Kepler University Linz, Linz, Austria

C. Schneider University of Würzburg, Würzburg, Germany

Pascale Senellart CNRS-LPN Laboratoire de Photonique Et de Nanostructures, Route de Nozay, Marcoussis, France; Physics Department, Ecole Polytechnique-RD128, Palaiseau Cedex, France

Lukáš Slodička Department of Optics, Palacký University, Olomouc, Czech Republic

Markus Sondermann Department of Physics, University of Erlangen-Nuremberg, Erlangen, Germany

Rinaldo Trotta Institute of Semiconductor and Solid State Physics, Johannes Kepler University Linz, Linz, Austria

Jun-ichi Yoshikawa Department of Applied Physics, School of Engineering, The University of Tokyo, Bunkyo-ku, Tokyo, Japan

Bo Zhao Hefei National Laboratory for Physical Sciences at Microscale, Department of Modern Physics, Anhui, China

Tian-Ming Zhao Hefei National Laboratory for Physical Sciences at Microscale, Department of Modern Physics, Anhui, China

Part I
Cavity QED

Chapter 1
Cavity Induced Interfacing of Atoms and Light

Axel Kuhn

Abstract This chapter introduces cavity-based light-matter quantum interfaces, with a single atom or ion in strong coupling to a high-finesse optical cavity. We discuss the deterministic generation of indistinguishable single photons from these systems; the atom-photon entanglement inextricably linked to this process; and the information encoding using spatio-temporal modes within these photons. Furthermore, we show how to establish a time-reversal of the aforementioned emission process to use a coupled atom-cavity system as a quantum memory. Along the line, we also discuss the performance and characterisation of cavity photons in elementary linear-optics arrangements with single beam splitters for quantum-homodyne measurements.

1.1 Introduction

The interfacing of discrete matter states and photons, the storage and retrieval of single photons, and the entanglement and mapping of quantum states between distant entities are key elements of quantum networks for distributed quantum information processing [1]. Ideally, such systems are composed of individual nodes acting as quantum gates or memories, with optical interlinks that allow for the entanglement or teleportation of their quantum states, or for optical quantum information processing using linear optics acting on the light traveling between the nodes [2, 3]. With individual photons carrying the information, substantial efforts have been made that focus on their production and characterisation. Applications that rely on single photons and on their indistinguishability include quantum cryptography, optical quantum computing, light-matter entanglement, and atom-photon state mapping, which all have successfully been demonstrated. For these purposes, sources of single photons that are based on single isolated quantum systems like a single atom or ion are ideal, given their capability of emitting streams of indistinguishable photons on demand.

A. Kuhn (✉)
Clarendon Laboratory, University of Oxford, Parks Road, Oxford UX1 3PU, UK
e-mail: axel.kuhn@physics.ox.ac.uk

A. Predojević and M.W. Mitchell (eds.), *Engineering the Atom-Photon Interaction*,
Nano-Optics and Nanophotonics, DOI 10.1007/978-3-319-19231-4_1

This approach is inherently simple and robust because a single quantum system can only emit one single photon in a de-excitation process. With all atoms or ions of the same isotope being identical, different photon sources based on one-and-the-same species are able of producing indistinguishable photons without further measures, provided the same transitions are used and the electromagnetic environment is identical for all atoms. This makes them ideal candidates for the implementation of large-scale quantum computing networks.

In the present chapter, we primarily discuss the quantum-state control of an atom strongly coupled to an optical cavity, with particular focus on the deterministic generation of single photons in arbitrary spatio-temporal modes. Important fundamental properties of on-demand single photon sources are analyzed, including single photon purity and indistinguishability. In this context, understanding and controlling the fundamental processes that govern the interaction of atoms with optical cavities is important for the development of improved single-photon emitters. These interactions are examined in the context of cavity-quantum electrodynamic (cavity-QED) effects. We show how to apply these to channel the photon emission into a single mode of the radiation field, with the vacuum field inside the cavity stimulating the process. Furthermore we elucidate how to determine and control the coherence properties of these photons in the time domain and use that degree of control for information encoding, and for information or photon-storage in single atoms by means of a time-reversal of the photon emission processes.

1.2 Cavities for Interfacing Light and Matter

In this section, we closely follow, summarize and extend our recently published review articles [4, 5] in order to introduce the concepts, characteristic properties, and major implementations of state-of-the-art single-photon sources based on single atoms or ions in cavities. These have all the potential to meet the requirements of optical quantum computing and quantum networking schemes, namely deterministic single-photon emission with unit efficiency, directed emission into a single spatial mode of the radiation field, indistinguishable photons with immaculate temporal and spatial coherence, and reversible quantum state mapping and entanglement between atoms and photons.

Starting from the elementary principles of cavity quantum electrodynamics, we discuss the coupling of a single quantum system to the quantised radiation field within optical resonators. Then we show how to exploit these effects to generate single photons on demand in the strong coupling regime and the bad cavity limit, using either an adiabatic driving technique or a sudden excitation of the emitter. To conclude, we discuss a couple of prominent experimental achievements and examine the different approaches for obtaining single photons from cavities using either atoms or ions as photon emitters.

1.2.1 Atom-Photon Interaction in Resonators

Any single quantum system that shows discrete energy levels, like an individual atom or ion, can be coupled to the quantised modes of the radiation field in a cavity. Here we introduce the relevant features of cavity-QED and the Jaynes-Cummings model [6, 7], and then extend these to three-level atoms with two dipole transitions driven by two radiation fields. One of the fields is from a laser, the other is the cavity field coupled to the atom. We furthermore explain how the behaviour of a coupled-atom system depends on the most relevant cavity parameters, such as the cavity's mode volume and its finesse.

Field quantisation: We consider a Fabry-Perot cavity with mirror separation l and reflectivity $\mathscr{R}$. The cavity has a free spectral range $\Delta\omega_{\mathrm{FSR}} = 2\pi \times c/(2l)$, and its finesse is defined as $\mathscr{F} = \pi\sqrt{\mathscr{R}}/(1-\mathscr{R})$. In the vicinity of a resonance, the transmission profile is Lorentzian with a linewidth (FWHM) of $2\kappa = \Delta\omega_{\mathrm{FSR}}/\mathscr{F}$, which is twice the decay rate, κ, of the cavity field. Curved mirrors are normally used to restrict the cavity eigenmodes to geometrically stable Laguerre-Gaussian or Hermite-Gaussian modes. In most cases, just one of these modes is of interest, characterised by its mode function $\psi_{\mathrm{cav}}(\mathbf{r})$ and its resonance frequency ω_{cav}. The state vector can therefore be expressed as a superposition of photon-number states, $|n\rangle$, and for n photons in the mode the energy is $\hbar\omega_{\mathrm{cav}}(n+\frac{1}{2})$. The equidistant energy spacing imposes an analogous treatment of the cavity as a harmonic oscillator. Creation and annihilation operators for a photon, $\hat{a}^\dagger$ and $\hat{a}$, are then used to express the Hamiltonian of the cavity,

$$H_{\mathrm{cav}} = \hbar\omega_{\mathrm{cav}}\left(\hat{a}^\dagger\hat{a} + \frac{1}{2}\right). \tag{1.1}$$

We emphasize that this does not take account of any losses, whereas in a real cavity, all photon number states decay until thermal equilibrium with the environment is reached. In the optical domain, the latter corresponds to the vacuum state, $|0\rangle$, with no photons remaining in the cavity.

Two-level atom: We now analyse how the cavity field interacts with a two-level atom with ground state $|g\rangle$ and excited state $|x\rangle$ of energies $\hbar\omega_{\mathrm{g}}$ and $\hbar\omega_{\mathrm{x}}$, respectively, and transition dipole moment μ_{xg}. The Hamiltonian of the atom reads

$$H_{\mathrm{A}} = \hbar\omega_{\mathrm{g}}|g\rangle\langle g| + \hbar\omega_{\mathrm{x}}|x\rangle\langle x|. \tag{1.2}$$

The coupling to the field mode of the cavity is expressed by the atom-cavity coupling constant,

$$g(\mathbf{r}) = g_0\,\psi_{\mathrm{cav}}(\mathbf{r}),\ \text{with}\ g_0 = \sqrt{(\mu_{\mathrm{xg}}^2\omega_{\mathrm{cav}})/(2\hbar\varepsilon_0 V)}, \tag{1.3}$$

where V is the mode volume of the cavity. As the atom is barely moving during the interaction, we can safely disregard its external degrees of freedom. Furthermore we assume maximum coupling, i.e. $\psi_{\mathrm{cav}}(\mathbf{r}_{\mathrm{atom}}) = 1$, so that one obtains $g(\mathbf{r}) = g_0$. In a closed system, any change of the atomic state would go hand-in-hand with a corresponding change of the photon number, n. Hence the interaction Hamiltonian of the atom-cavity system reads

$$H_{\mathrm{int}} = -\hbar g_0 \left[|x\rangle\langle g|\hat{a} + \hat{a}^{\dagger}|g\rangle\langle x| \right]. \tag{1.4}$$

For a given excitation number n, the cavity only couples $|g, n\rangle$ and $|x, n-1\rangle$. If the cavity mode is resonant with the atomic transition, i.e. if $\omega_{cav} = \omega_x - \omega_g$, the population oscillates with the Rabi frequency $\Omega_{\mathrm{cav}} = 2g_0\sqrt{n}$ between these states.

The eigenfrequencies of the total Hamiltonian, $H = H_{\mathrm{cav}} + H_{\mathrm{A}} + H_{\mathrm{int}}$, can be found easily. In the rotating wave approximation, they read

$$\omega_{\mathrm{n}}^{\pm} = \omega_{\mathrm{cav}}\left(n + \frac{1}{2}\right) + \frac{1}{2}\left(\Delta_{\mathrm{cav}} \pm \sqrt{4ng_0^2 + \Delta_{\mathrm{cav}}^2}\right), \tag{1.5}$$

where $\Delta_{\mathrm{cav}} = \omega_{\mathrm{x}} - \omega_{\mathrm{g}} - \omega_{\mathrm{cav}}$ is the detuning between atom and cavity. Figure 1.1 illustrates this level splitting. Within each n manifold, the two eigenstates are split by $\Omega_{\mathrm{eff,n}} = \sqrt{4ng_0^2 + \Delta_{\mathrm{cav}}^2}$, which is the effective Rabi frequency at which the population oscillates between states $|g, n\rangle$ and $|x, n-1\rangle$. This means that the cavity field stimulates the emission of an excited atom into the cavity, thus de-exciting the atom and increasing the photon number by one. Subsequently, the atom is re-excited by absorbing a photon from the cavity field, and so forth. In particular, an excited atom and a cavity containing no photon are sufficient to start the oscillation between $|x, 0\rangle$ and $|g, 1\rangle$ at frequency $\sqrt{4g_0^2 + \Delta_{\mathrm{cav}}^2}$. This phenomenon is known as vacuum

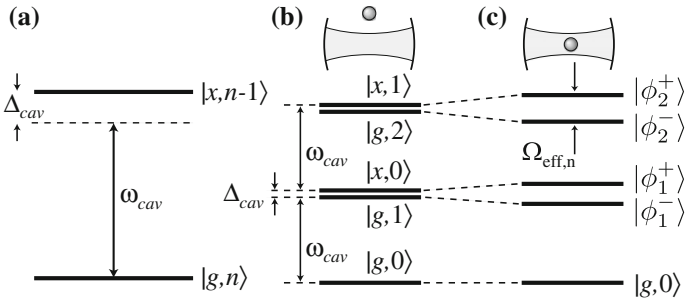

Fig. 1.1 Atom-cavity coupling (from [4]): **a** a two-level atom with ground state $|g\rangle$ and excited state $|x\rangle$ coupled to a cavity containing n photons. In the dressed-level scheme of the combined atom-cavity system with the atom outside (**b**) or inside (**c**) the cavity, the state doublets are either split by Δ_{cav} or by the effective Rabi frequency, $\Omega_{\mathrm{eff,n}}$, respectively

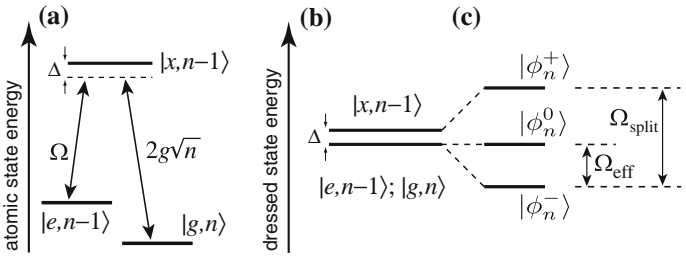

Fig. 1.2 Three-level atom in cavity coupling (from [4]): **a** a three-level atom driven by a classical laser field of Rabi frequency Ω, coupled to a cavity containing n photons. **b** Dressed-level scheme of the combined system without coupling, and **c** for an atom interacting with laser and cavity. The triplet is split by $\Omega_{\text{split}} = \sqrt{4ng_0^2 + \Omega^2 + \Delta^2}$. In the limit of a large detuning Δ, the Raman transition $|e, n-1\rangle \leftrightarrow |g, n\rangle$ is driven at the effective Rabi frequency $\Omega_{\text{eff}} = \frac{1}{2}\left(\Omega_{\text{split}} - |\Delta|\right) \approx (4ng_0^2 + \Omega^2)/|4\Delta|$

Rabi oscillation. On resonance, i.e. for $\Delta_{\text{cav}} = 0$, the oscillation frequency is $2g_0$, also known as vacuum Rabi frequency.

To summarise, the atom-cavity interaction splits the photon number states into doublets of non-degenerate dressed states, which are named after Jaynes and Cummings [6, 7]. Only the ground state $|g, 0\rangle$ is not coupled to other states and is not subject to any energy shift or splitting.

Three-level atom: We now consider an atom with a $\Lambda-$type three-level scheme providing transition frequencies $\omega_{\text{xe}} = \omega_{\text{x}} - \omega_{\text{e}}$ and $\omega_{\text{xg}} = \omega_{\text{x}} - \omega_{\text{g}}$ as depicted in Fig. 1.2. The $|e\rangle \leftrightarrow |x\rangle$ transition is driven by a classical light field of frequency ω_{L} with Rabi frequency Ω, while a cavity mode with frequency ω_{cav} couples to the $|g\rangle \leftrightarrow |x\rangle$ transition. The respective detunings are defined as $\Delta_{\text{L}} = \omega_{\text{xe}} - \omega_{\text{L}}$ and $\Delta_{\text{cav}} = \omega_{\text{xg}} - \omega_{\text{cav}}$. Provided the driving laser and the cavity only couple to their respective transitions, the interaction Hamiltonian

$$\begin{aligned} H_{\text{int}} = \hbar[&\Delta_{\text{L}}|e\rangle\langle e| + \Delta_{\text{cav}}|g\rangle\langle g| - \frac{\Omega}{2}(|x\rangle\langle e| + |e\rangle\langle x|) \\ &- g_0(|x\rangle\langle g|a + a^\dagger|g\rangle\langle x|)] \end{aligned} \tag{1.6}$$

determines the behaviour of the system. Given an arbitrary excitation number n, this Hamiltonian couples only the three states $|e, n-1\rangle$, $|x, n-1\rangle$, $|g, n\rangle$. For this triplet and a Raman-resonant interaction with $\Delta_{\text{L}} = \Delta_{\text{cav}} \equiv \Delta$, the eigenfrequencies of the coupled system read

$$\begin{aligned} \omega_{\text{n}}^0 &= \omega_{\text{cav}}\left(n + \frac{1}{2}\right) \quad \text{and} \\ \omega_{\text{n}}^\pm &= \omega_{\text{cav}}\left(n + \frac{1}{2}\right) + \frac{1}{2}\left(\Delta \pm \sqrt{4ng_0^2 + \Omega^2 + \Delta^2}\right). \end{aligned} \tag{1.7}$$

The previously-discussed Jaynes-Cummings doublets are now replaced by dressed-state triplets,

$$
\begin{aligned}
|\phi_{\mathrm{n}}^{0}\rangle &= \cos\Theta|e,n-1\rangle - \sin\Theta|g,n\rangle, \\
|\phi_{\mathrm{n}}^{+}\rangle &= \cos\Phi\sin\Theta|e,n-1\rangle - \sin\Phi|x,n-1\rangle + \cos\Phi\cos\Theta|g,n\rangle, \\
|\phi_{\mathrm{n}}^{-}\rangle &= \sin\Phi\sin\Theta|e,n-1\rangle + \cos\Phi|x,n-1\rangle + \sin\Phi\cos\Theta|g,n\rangle,
\end{aligned}
\tag{1.8}
$$

where the mixing angles Θ and Φ are given by

$$
\tan\Theta = \frac{\Omega}{2g_0\sqrt{n}}, \quad \tan\Phi = \frac{\sqrt{4ng_0^2+\Omega^2}}{\sqrt{4ng_0^2+\Omega^2+\Delta^2}-\Delta}. \tag{1.9}
$$

The interaction with the light lifts the degeneracy of the eigenstates. However, $|\phi_{\mathrm{n}}^{0}\rangle$ is neither subject to an energy shift, nor does the excited atomic state contribute to it. Therefore it is a 'dark state' which cannot decay by spontaneous emission.

In the limit of vanishing Ω, the states $|\phi_{\mathrm{n}}^{\pm}\rangle$ correspond to the Jaynes-Cummings doublet and the third eigenstate, $|\phi_{\mathrm{n}}^{0}\rangle$, coincides with $|e,n-1\rangle$. Also the eigenfrequency ω_{n}^{0} is not affected by Ω or g_0. Therefore transitions between the dark states $|\phi_{\mathrm{n+1}}^{0}\rangle$ and $|\phi_{\mathrm{n}}^{0}\rangle$ are always in resonance with the cavity. This holds, in particular, for the transition from $|\phi_{1}^{0}\rangle$ to $|\phi_{0}^{0}\rangle \equiv |g,0\rangle$ as the $n=0$ state never splits.

Cavity-coupling regimes: So far, we have been considering the interaction Hamiltonian and the associated eigenvalues and dressed eigenstates that one obtains whenever a two- or three-level atom is coupled to a cavity. We have been neglecting the atomic polarisation decay rate, γ, and also the field-decay rate of the cavity, κ (Note that we have chosen a definition where the population decay rate of the atom reads 2γ, and the photon loss rate from the cavity is 2κ). It is evident that both relaxation rates result in a damping of a possible vacuum-Rabi oscillation between states $|x,0\rangle$ and $|g,1\rangle$. Only in the regime of *strong atom-cavity coupling*, with $g_0 \gg \{\kappa,\gamma\}$, the damping is weak enough so that vacuum-Rabi oscillations do occur. The other extreme is the *bad-cavity regime*, with $\kappa \gg g_0^2/\kappa \gg \gamma$, which results in strong damping and quasi-stationary quantum states of the coupled system if it is continuously driven.

Two properties of the cavity can be used to distinguish between these regimes: First the strength of the atom-cavity coupling, $g_0 \propto 1/\sqrt{V}$ (dependant upon the mode volume of the cavity), and second the finesse $\mathscr{F} = \pi\sqrt{R}/(1-R)$ of the resonator, which depends on the mirror reflectivity R. The finesse gives the mean number of round trips in the cavity before a photon is lost by transmission through one of the cavity mirrors, and it is also identical to the ratio of free spectral range $\Delta\omega_{\mathrm{FSR}}$ to cavity linewidth 2κ. To reach strong coupling, a high value of g_0 and therefore a short cavity of small mode volume are normally required. Keeping κ small enough at the same time then calls for a high finesse and a mirror reflectivity $R \geq 99.999\,\%$.

1.2.2 Single-Photon Emission

For the deterministic generation of single photons from coupled atom-cavity systems, all schemes implemented to date rely on the Purcell effect [8]. The spatial mode density in the cavity and the coupling to the relevant modes is substantially different from free space [9], such that the spontaneous photon emission into a resonant cavity gets either enhanced ($f > 1$) or inhibited ($f < 1$) by the Purcell factor

$$f = \frac{3Q\lambda^3}{4\pi^2 V},$$

depending on the cavity's mode volume, V, and quality factor, Q. More importantly, the probability of spontaneous emission placing a photon into the cavity is given by $\beta = f/(f+1)$. If the mode volume of the cavity is sufficiently small, the emitter and cavity couple so strongly that $\beta \approx 1$, i.e. emissions into the cavity outweigh spontaneous emissions into free space. A deterministic photon emission into a single field mode is therefore possible with an efficiency close to unity. These effects have first been observed by Carmichael et al. [10] and De Martini et al. [11]. Moreover, with the coherence properties uniquely determined by the parameters of the cavity and the driving process, one should be able to obtain indistinguishable photons from different cavities. Furthermore the reversibility of the photon generation process, and quantum networking between different cavities has been predicted [12–14], and demonstrated [15–17]. We now introduce different ways of producing single photons from such a system. These include cavity-enhanced spontaneous emission and Raman transitions stimulated by the vacuum field while driven by classical laser pulses. In particular, we discuss a scheme for adiabatic coupling between a single atom and an optical cavity, which is based on a unitary evolution of the coupled atom-cavity system [18, 19], and is therefore intrinsically reversible.

For a photon emission from the cavity to take place, it is evident that a finite value of κ is mandatory, otherwise any light would remain trapped between the mirrors. Moreover, as κ is the decay rate of the cavity field, the associated duration of an emitted photon is typically κ^{-1} or more. We also emphasise that γ plays a crucial role in most experimental settings, since it accounts for the spontaneous emission into non-cavity modes, and therefore leads to a reduction of efficiency. The relation of the atom-cavity coupling constant and the Rabi frequency of the driving field to the two decay rates can be used for marking the difference between three basic classes of single-photon emission schemes from cavity-QED systems.

Cavity-enhanced spontaneous emission: We assume that a sudden excitation process (e.g. a short π pulse with $\Omega \gg \{g_0, \kappa, \gamma\}$, or some internal relaxation cascade from energetically higher states) prepares the atom in its excited state $|x, 0\rangle$. From there, a photon gets spontaneously emitted either into the cavity or into free space. To analyse the process, we simply consider an excited two-level atom coupled to an empty cavity. This particular situation is the textbook example of cavity-QED

that has been thoroughly analysed in the past. In fact, it has been proposed by Purcell [8] and demonstrated by Heinzen et al. [20] and Morin et al. [21] that the spontaneous emission properties of an atom coupled to a cavity are significantly different from those in free space. For an analysis of the atom's behaviour, it suffices to look at the evolution of the $n = 1$ Jaynes-Cummings doublet under the influence of the atomic polarisation decay rate γ and the cavity-field decay rate κ. Non-cavity spontaneous decay of the atom and photon emission through one of the cavity mirrors both lead the system into state $|g, 0\rangle$, which does not belong to the $n = 1$ doublet. Therefore we can deal with these decay processes phenomenologically by introducing non-hermitian damping terms into the interaction Hamiltonian,

$$H'_{\text{int}} = -\hbar g_0 \left(|x\rangle\langle g|\hat{a} + \hat{a}^\dagger |g\rangle\langle x| \right) - i\hbar\gamma |x\rangle\langle x| - i\hbar\kappa \hat{a}^\dagger \hat{a}. \tag{1.10}$$

Figure 1.3a shows the time evolution of the atom-cavity system when $\kappa > g_0$. The strong damping of the cavity inhibits any vacuum-Rabi oscillation, since the photon is emitted from the cavity before it can be reabsorbed by the atom. Therefore the transient population in state $|g, 1\rangle$ is negligible and the adiabatic approximation $\dot{c}_{\text{g}} \approx 0$ can be applied, which gives

$$\frac{d}{dt} c_{\text{x}} = -\gamma c_{\text{x}} - \frac{g_0^2}{\kappa} c_{\text{x}}, \tag{1.11}$$

with the solution

$$c_{\text{x}}(t) = \exp\left(-\left[\gamma + \frac{g_0^2}{\kappa} \right] t \right). \tag{1.12}$$

It is straightforward to see that the ratio of the emission rate into the cavity, g_0^2/κ, to the spontaneous emission probability into free space becomes $g_0^2/(\kappa\gamma) \equiv f$, i.e. the Purcell factor. It equals twice the one-atom cooperativity parameter, C, originally introduced in the context of optical bistability [22]. Hence the photon-emission probability from the cavity reads $P_{\text{Emit}} = 2C/(2C + 1)$. Note that the atom radiates mainly into the cavity if $g_0^2/\kappa \gg \gamma$. Together with $\kappa \gg g_0$, this condition constitutes the bad-cavity regime.

The other extreme is strong coupling, with $g_0 \gg (\kappa, \gamma)$. In this case vacuum Rabi oscillations between $|x, 0\rangle$ and $|g, 1\rangle$ occur, with both states decaying at the respective rates γ and κ. Figure 1.3b shows a situation where the atom-cavity coupling, g_0, saturates the $|x, 0\rangle \leftrightarrow |g, 1\rangle$ transition. On average, the probabilities to find the system in either one of these two states are equal, and therefore the average ratio of the emission probability into the cavity to the spontaneous emission probability into free space is given by κ/γ. The vacuum-Rabi oscillation gives rise to an amplitude modulation of the photons emitted from the cavity here.

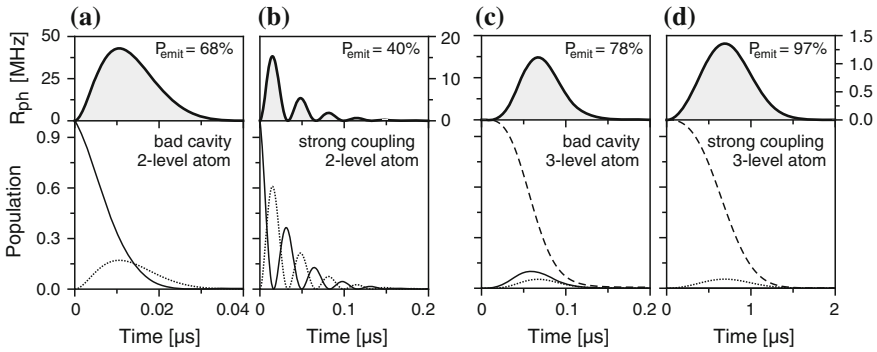

Fig. 1.3 Evolution of the atomic states and photon emission rate $R_{\rm ph} = 2\kappa\rho_{\rm gg}$ in different coupling cases (adapted from [5]): **a** and **b** are for an excited two-level atom coupled to the cavity, showing populations $\rho_{\rm xx}$ (*solid*) and $\rho_{\rm gg}$ (*dotted*) of the product states $|x, 0\rangle$ and $|g, 1\rangle$. **c** and **d** are for a three-level atom-cavity system prepared in $|e, 0\rangle$ and exposed to a pump pulse driving $|e\rangle - |x\rangle$ while the cavity couples $|x\rangle$ and $|g\rangle$. The initial-state population $\rho_{\rm ee}$ is dashed. **a** and **c** display the bad-cavity regime with $(g_0, \gamma, \kappa) = 2\pi \times (15, 3, 20)$ MHz, while **b** and **d** depict the strong-coupling case with $(g_0, \gamma, \kappa) = 2\pi \times (15, 3, 2)$ MHz. The pump pulses read $\Omega(t) = g_0 \sin(\pi t/200\,ns)$ in (**c**), and $\Omega(t) = g_0 \times t/(1\,\mu s)$ in (**d**). No transient population is found in $\rho_{\rm xx}$ in the latter case. The overall photon-emission probability reads always $P_{\rm Emit} = \int R_{\rm ph} dt$

Bad-cavity regime: To take the effect of a slow excitation process into account, we consider a Λ-type three-level atom coupled to a cavity. In the bad-cavity regime, $\kappa \gg g_0^2/\kappa \gg \gamma$, the loss of excitation into unwanted modes of the radiation field is small and we may follow Law et al. [23, 24]. We assume that the atom's $|e\rangle - |x\rangle$ transition is excited by a pump laser pulse while the atom emits a photon into the cavity by enhanced spontaneous emission. The cavity-field decay rate κ sets the fastest time scale, while the spontaneous emission rate into the cavity, g_0^2/κ, dominates the incoherent decay of the polarisation from the excited atomic state. Provided any decay leads to a loss from the three-level system, the evolution of the wave vector is governed by the non-Hermitian Hamiltonian

$$H'_{\rm int} = H_{\rm int} - i\hbar\kappa\hat{a}^\dagger\hat{a} - i\hbar\gamma|x\rangle\langle x|, \tag{1.13}$$

with $H_{\rm int}$ from (1.6). To simplify the analysis, we take only the vacuum state, $|0\rangle$, and the one-photon state, $|1\rangle$, into account, thus that the state vector reads

$$|\Psi(t)\rangle = c_{\rm e}(t)|e, 0\rangle + c_{\rm x}(t)|x, 0\rangle + c_{\rm g}(t)|g, 1\rangle, \tag{1.14}$$

where $c_{\rm e}$, $c_{\rm x}$ and $c_{\rm g}$ are complex amplitudes. Their time evolution is given by the Schrödinger equation, $i\hbar\frac{d}{dt}|\Psi\rangle = H'_{\rm int}|\Psi\rangle$, which yields

$$\begin{aligned} i\dot{c}_{\mathrm{e}} &= \frac{1}{2}\Omega(t)c_{\mathrm{x}} \\ i\dot{c}_{\mathrm{x}} &= \frac{1}{2}\Omega(t)c_{\mathrm{e}} + g_0 c_{\mathrm{g}} - i\gamma c_{\mathrm{x}} \\ i\dot{c}_{\mathrm{g}} &= g_0 c_{\mathrm{x}} - i\kappa c_{\mathrm{g}}, \end{aligned} \tag{1.15}$$

with the initial condition $c_{\mathrm{e}}(0) = 1$, $c_{\mathrm{x}}(0) = c_{\mathrm{g}}(0) = 0$ and $\Omega(0) = 0$. An adiabatic solution of (1.15) is found if the decay is so fast that c_{x} and c_{g} are nearly time independent. This allows one to make the approximations $\dot{c}_{\mathrm{x}} = 0$ and $\dot{c}_{\mathrm{g}} = 0$, with the result

$$\begin{aligned} c_{\mathrm{e}}(t) &\approx \exp\left(-\frac{\alpha}{4}\int_0^t \Omega^2(t')dt'\right) \\ c_{\mathrm{x}}(t) &\approx -\frac{i}{2}\alpha\Omega(t)c_{\mathrm{e}}(t) \\ c_{\mathrm{g}}(t) &\approx -\frac{i}{\kappa}g_0 c_{\mathrm{x}}(t), \end{aligned} \tag{1.16}$$

where $\alpha = 2/(2\gamma + 2g_0^2/\kappa)$. Photon emissions from the cavity occur if the system is in $|g, 1\rangle$, at the photon-emission rate $R_{\mathrm{ph}}(t) = 2\kappa|c_{\mathrm{g}}(t)|^2$. This yields a photon-emission probability of

$$\begin{aligned} P_{\mathrm{Emit}} &= \int R_{\mathrm{ph}}(t)dt \\ &= \frac{g_0^2\alpha}{\kappa}\left[1 - \exp\left(-\frac{\alpha}{2}\int \Omega^2(t)dt\right)\right] \longrightarrow \frac{g_0^2\alpha}{\kappa}. \end{aligned} \tag{1.17}$$

Note that the exponential in (1.17) vanishes if the area $\int \Omega(t)dt$ of the exciting pump pulse is large enough. In this limit, the overall photon-emission probability does not depend on the shape and amplitude of the pump pulse. With a suitable choice of g_0, α, and κ, high photon-emission probabilities can be reached [24]. Furthermore, as the stationary state of the coupled system depends on $\Omega(t)$, the time envelope of the photon can be controlled to a large extent.

Strong-coupling regime: To study the effect of the exciting laser pulse in the strong-coupling regime, we again consider a Λ-type three-level atom coupled to a cavity. We assume that the strong-coupling condition also applies to the Rabi frequency of the driving field, i.e. $\{g_0, \Omega\} \gg \{\kappa, \gamma\}$. In this case, we can safely neglect the effect of the two damping rates on the time scale of the excitation. We then seek a method to effectively stimulate a Raman transition between the two ground states that also places a photon into the cavity. For instance, the driving process can be implemented in form of an adiabatic passage (STIRAP process [18, 19]) or a far-off resonant Raman process to avoid any transient population of the excited state, thus reducing losses due to spontaneous emission into free space. An efficiency for photon

generation close to unity can be reached this way. Once a photon is placed into the cavity, it gets emitted due to the finite cavity lifetime.

The most promising approach is to implement an adiabatic passage in the optical domain between the two ground states [25, 26]. In fact, adiabatic passage methods have been used for coherent population transfer in atoms or molecules for many years. For instance, if a Raman transition is driven by two distinct pulses of variable amplitudes, effects like electromagnetically induced transparency (EIT) [27, 28], slow light [29, 30], and stimulated Raman scattering by adiabatic passage (STIRAP) [19] are observed. These effects have been demonstrated with classical light fields and have in common that the system's state vector, $|\Psi\rangle$, follows a dark eigenstate, e.g. $|\phi_{\mathrm{n}}^{0}\rangle$, of the time-dependent interaction Hamiltonian. In principle, the time evolution of the system is completely controlled by the variation of this eigenstate. However, a more detailed analysis [25, 31] reveals that the eigenstates must change slowly enough to allow adiabatic following. Only if this condition is met, a three-level atom-cavity system, once prepared in $|\phi_{\mathrm{n}}^{0}\rangle$, stays there forever, thus allowing one to control the relative population of $|e, n-1\rangle$ and $|g, n\rangle$ by adjusting the pump Rabi frequency Ω. This is obvious for a system initially prepared in $|e, n-1\rangle$. As can be seen from (1.8), that state coincides with $|\phi_{\mathrm{n}}^{0}\rangle$ if the condition $2g_0\sqrt{n} \gg \Omega$ is initially met. Once the system has been prepared in the dark state, the ratio between the populations of the contributing states reads

$$\frac{|\langle e, n-1|\Psi\rangle|^2}{|\langle g, n|\Psi\rangle|^2} = \frac{4ng_0^2}{\Omega^2}. \tag{1.18}$$

As proposed in [18], we assume that an atom in state $|e\rangle$ is placed into an empty cavity, which nonetheless drives the $|g, 1\rangle \leftrightarrow |x, 0\rangle$ transition with the Vacuum Rabi frequency $2g_0$. The initial state $|e, 0\rangle$ therefore coincides with $|\phi_{1}^{0}\rangle$ as long as no pump laser is applied. The atom then gets exposed to a laser pulse coupling the $|e\rangle \leftrightarrow |x\rangle$ transition with a slowly rising amplitude that leads to $\Omega \gg 2g_0$. In turn, the atom-cavity system evolves from $|e, 0\rangle$ to $|g, 1\rangle$, thus increasing the photon number by one. This scheme can be seen as vacuum-stimulated Raman scattering by adiabatic passage, also known as V-STIRAP. If we assume a cavity decay time, κ^{-1} much longer than the interaction time, a photon is emitted from the cavity with a probability close to unity and with properties uniquely defined by κ, after the system has been excited to $|g, 1\rangle$.

In contrast to such an idealised scenario, Fig. 1.3d shows a more realistic situation where a photon is generated and already emitted from the cavity during the excitation process. This is due to the cavity decay time being comparable or shorter than the duration of the exciting laser pulse. Even in this case, no secondary excitations or photon emissions can take place. The system eventually reaches the decoupled state $|g, 0\rangle$ when the photon escapes. However, the photon-emission probability is slightly reduced as the non-Hermitian contribution of κ to the interaction Hamiltonian is affecting the dark eigenstate $|\phi_{1}^{0}\rangle$ of the Jaynes-Cummings triplet (1.8). It now has a small admixture of $|x, 0\rangle$ and hence is weakly affected by spontaneous emission losses [25].

1.2.2.1 Single-Photon Emission from Atoms or Ions in Cavities

Many revolutionary photon generation schemes have recently been demonstrated, such as a single-photon turnstile device based on the Coulomb blockade mechanism in a quantum dot [32], the fluorescence of a single molecule [33, 34], or a single colour centre (Nitrogen vacancy) in diamond [35, 36], or the photon emission of a single quantum dot into free space [37–39]. All these schemes emit photons upon an external trigger event. The photons are spontaneously emitted into various modes of the radiation field, e.g. into all directions, and often show a broad energy distribution. Nonetheless these photons are excellent for quantum cryptography and communication, and also a reversal of the free-space spontaneous emission has been demonstrated, see chapters by Leuchs and Sondermann, Chuu and Du, and Piro and Eschner. Cavity QED has the potential of performing this bi-directional state mapping between atoms and photons very effectively, and thus is expected to levy many fundamental limitations to scalability in quantum computing or quantum networking. We therefore focus here on cavity-enhanced emission techniques into well-defined modes of the radiation field.

Neutral atoms: A straightforward implementation of a cavity-based single-photon source consists of a single atom placed between two cavity mirrors, with a stream of laser pulses travelling perpendicular to the cavity axis to trigger photon emissions. The most simplistic approach to achieve this is by sending a dilute atomic beam through the cavity, with an average number of atoms in the mode far below one. However, for a thermal beam, the obvious drawback would be an interaction time between atom and cavity far too short to achieve any control of the exact photon emission time. Hence cold (and therefore slow) atoms are required to overcome this limitation. The author followed this route [40, 41], using a magneto-optical trap to cool a cloud of rubidium atoms below 100 μK at a distance close to the cavity. Atoms released from the trap eventually travel through the cavity, either falling from above or being injected from below in an atomic fountain. Atoms enter the cavity randomly, but interact with its mode for 20–200 μs. Within this limited interaction time, between 20 and 200 single-photon emissions can be triggered. Figure 1.4 illustrates this setup, together with the excitation scheme between hyperfine states in ^{87}Rb used to generate single photons by the adiabatic passage technique discussed on page 10.

Bursts of single photons are emitted from the cavity whenever a single atom passes its mode, and strong antibunching is found in the photon statistics, as shown in Fig. 1.4a. A sub-Poissonian photon statistics is found when conditioning the experiment on the actual presence of an atom in the cavity [42]. In many cases, this is automatically granted—a good example is the characterisation of the photons by two-photon interference. For such experiments, pairs of photons are needed that meet simultaneously at a beamsplitter. With just one source under investigation, this is achieved with a long optical fibre delaying the first photon of a pair of successively emitted ones. With the occurrence of such photon pairs being the precondition to observe any correlation and the probability for successive photon emissions being

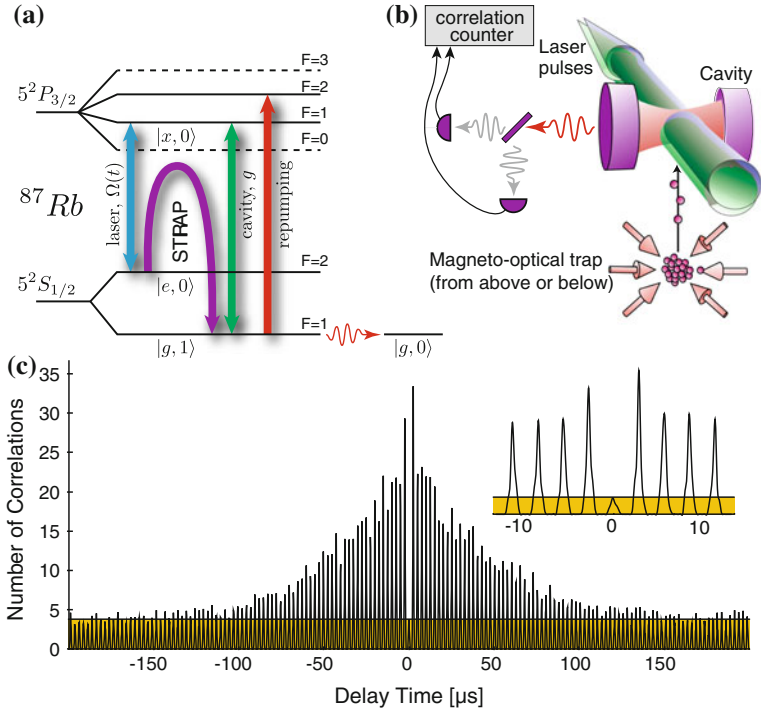

Fig. 1.4 Single-photon source based on atoms travelling through an optical cavity. **a** Excitation scheme realised in ^{87}Rb for the pulsed single-photon generation. The atomic states labeled $|e\rangle$, $|x\rangle$ and $|g\rangle$ are involved in the Raman process, and the states $|0\rangle$ and $|1\rangle$ denote the photon number in the cavity. **b** A cloud of laser-cooled atoms moves through an optical cavity either from above [40], or from below using an atomic fountain [41]. Laser pulses travel perpendicular to the cavity axis to control the emission process. The light is analysed using a Hanbury-Brown and Twiss (HBT) setup with a pair of avalanche photodiodes. **c** Intensity correlation of the emitted light measured with the HBT setup, with atoms injected using an atomic fountain [41]. The contribution of correlations between real photons and detector dark counts is shown in yellow

vanishingly small without atoms, the presence of an atom is actually assured whenever data is recorded.

Only lately, refined versions of this type of photon emitter have been realised, with a single atom held in the cavity using a dipole-force trap. McKeever et al. [43] managed to hold a single Cs atom in the cavity with a dipole-trapping beam running along the cavity axis, while Hijlkema et al. [44] are using a combination of dipole trapping beams running perpendicular and along the cavity to catch and hold a single Rb atom in the cavity mode. As illustrated in Fig. 1.5, the trapped atom is in both cases exposed to a sequence of laser pulses alternating between triggering the photon emission, cooling and repumping the atom to its initial state to repeat the sequence. The atom is trapped, so that the photon statistics is not affected by fluctuations in the atom number and therefore is sub-Poissonian, see Fig. 1.5c. Moreover, with trapping

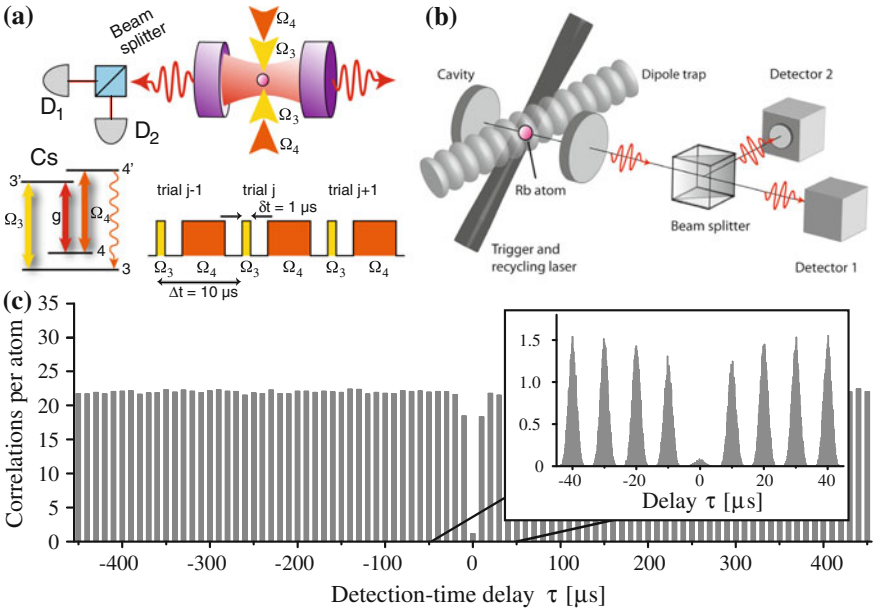

Fig. 1.5 Atom-cavity systems with a single atom at rest in the cavity mode. **a** The setup by McKeever et al. [43] is using a dipole trap running along the cavity axis to hold a single caesium atom in the cavity. The cavity is symmetric, so that half the photons are directed towards a pair of detectors for analysing the photon statistics. **b** The author has been using a dipole trap running perpendicular to the cavity axis, The trap is holding a single rubidium atom in the cavity [44]. The cavity is asymmetric, and photons emitted through its output coupler are directed to a pair of photon counters to record the second-order correlation function of the photon stream. In both cases, the trapped atom is exposed to a sequence of laser pulses that trigger the photon emission, cool the atom, and re-establish the initial condition by optical pumping. **c** Intensity correlation function of the light emitted form a trapped-atom-cavity system, as found by the author [44]

times for single atoms up to a minute, a quasi-continuous bit-stream of photons is obtained.

The major advantage of using neutral atoms as photon emitters in Fabry-Perot type cavities is that a relatively short cavity (some 100 μm) of high finesse (between 10^5 and 10^6) can be used. One thus obtains strong atom-cavity coupling, and the photon generation can be driven either in the steady-state regime or dynamically by V-STIRAP. This allows one to control the coherence properties and the shape of the photons to a large extent, as discussed in Sect. 1.4.2. Photon generation efficiencies as high as 65 % have been reported with these systems. Furthermore, based on the excellent coherence properties, first applications such as atom-photon entanglement and atom-photon state mapping [45–48] have recently been demonstrated.

Apart from the above Fabry-Perot type cavities, many other micro-structured cavities have been explored during the last years. These often provide a much smaller mode volume and hence boost the atom-cavity coupling strength by about an order of

magnitude. However, this goes hand-in-hand with increased cavity losses and thus a much larger cavity linewidth, which might be in conflict with the desired addressing of individual atomic transitions. Among the most relevant new developments are fibre-tip cavities, which use dielectric Bragg stacks at the tip of an optical fibre as cavity mirrors [49, 50]. Due to the small diameter of the fibre, either two fibre tips can be brought very close together, or a single fibre tip can be complemented by a micro-structured mirror on a chip to form a high-finesse optical cavity. A slightly different approach is the use of ring-cavities realised in solid state, guiding the light in a whispering gallery mode. An atom can be easily coupled to the evanescent field of the cavity mode, provided it can be brought close to the surface of the substrate. Nice examples are microtoroidal cavities realised at the California Institute of Technology [51, 52], and bottle-neck cavities in optical fibres [53]. These cavities have no well-defined mirrors and therefore no output coupler, so one usually arranges for emission into well-defined spatio-temporal modes via evanescent-field coupling to the core of an optical fibre.

We would like to remind the reader at this point that a large variety of other exciting cavity-QED experiments have been performed that were not aiming at a single-photon emission in the optical regime. Most important amongst those are the coupling of Rydberg atoms [54] or superconductive SQUIDs [55] to microwave cavities, which is also a well-established way of placing single photons into a cavity using either π pulses [56] or dark resonances [57]. Also the coupling of ultracold quantum gases to optical cavities has been studied extensively [49, 58], and has proven to be a useful method to acquire information on the atom statistics. Last but not least, large efforts have been made to study cavity-mediated forces on either single atoms or atomic ensembles [59–64], which lead to the development of cavity-mediated cooling techniques.

Trapped ions: Although neutral-atom systems have their advantages for the generation of single photons, such experiments are sometimes subject to undesired variations in the atom-cavity coupling strength and multi-atom effects. Also trapping times are still limited in the intra-cavity dipole-trapping of single atoms. A possible solution is to use a strongly localised single ion in an optical cavity, as has first been demonstrated by Keller et al. [65]. In their experiment, an ion is optimally coupled to a well-defined field mode, resulting in the reproducible generation of single-photon pulses with precisely defined timing. The stream of emitted photons is uninterrupted over the storage time of the ion, which, in principle, could last for several days.

The major difficulty in combining an ion trap with a high-finesse optical cavity comes from the dielectric cavity mirrors, which influence the trapping potential if they get too close to the ion. This effect might be detrimental in case the mirrors get electrically charged during loading of the ion trap, e.g. by the electron beam used to ionise the atoms. Figure 1.6a shows how this problem has been solved in [65] by shuttling the trapped ion from a spatially separate loading region into the cavity. Nonetheless, the cavity in these experiments is typically more than 10–20 mm long to avoid distortion of the trap. Thus the coupling to the cavity is weak, and although optimised pump pulses were used, the single-photon efficiency in [65] did not exceed

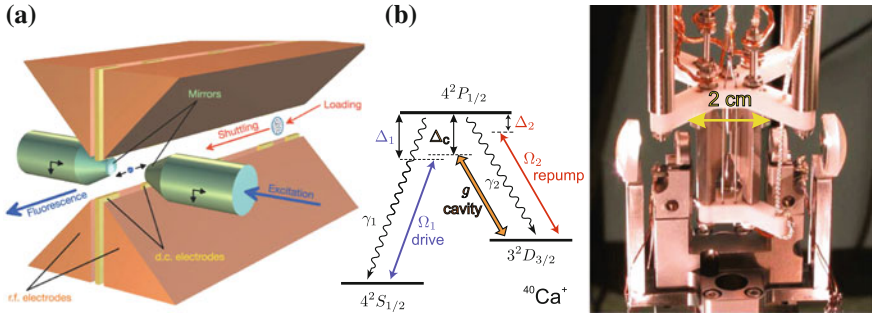

Fig. 1.6 Arrangement of ion-trap electrodes and cavity in **a** the experiment by Keller et al. [65]. The ion is shuttled to the cavity region after loading. Upon excitation of the ion from the side of the cavity, a single photon gets emitted into the cavity mode (Reprinted by permission from Nature Publishing Group: Nature, Guthöhrlein et al. [66], Copyright 2001). The ion-cavity arrangement and excitation scheme in $^{40}Ca^+$ studied by Russo and Barros et al. [67, 68] in Innsbruck **(b)** is using a near-concentric cavity which leads to an increased density of otherwise non-degenerate transverse modes (Panel **b** adapted with permission from Springer: Applied Physics B, Russo et al. [67], Copyright 2009)

$(8.0 \pm 1.3)\%$. This is in good accordance with theoretical calculations, which also show that the efficiency can be substantially increased in future experiments by reducing the cavity length. It is important to point out that the low efficiency does not interfere with the singleness of the photons. Hence the $g^{(2)}$ correlation function of the emitted photon stream corresponds to the one depicted in Fig. 1.5c, with $g^{(2)}(0) \rightarrow 0$. With an improved ion-cavity setup, Barros et al. [68] were able to reach a single-photon emission efficiency of $(88 \pm 17)\%$ in a cavity of comparable length, using a more favourable mode structure in the near-confocal cavity depicted in Fig. 1.6b and far-off resonant Raman transitions between magnetic sublevels of the ion.

1.3 Cavity-Enhanced Atom-Photon Entanglement

In their groundbreaking experiments, Monroe [69] and Weinfurter [70] successfully demonstrated the entanglement of the polarisation of a single photon with the spin of a single ion or atom, respectively. To do so, they drove a free-space excitation and emission scheme in a single trapped ion or atom that lead to two possible final spin states of the atom, $|\downarrow\rangle$ and $|\uparrow\rangle$ upon emission of either a σ^+ or σ^- polarised photon, thus projecting the whole system into the entangled atom-photon state

$$(|\sigma^+, \downarrow\rangle - |\sigma^-, \uparrow\rangle)/\sqrt{2}. \tag{1.19}$$

Projective measurements on pairs of photons emitted from two distant atoms or ions were then used for entanglement swapping, thus resulting in the entanglement and teleportation of quantum states [71]. Such photon-matter entanglement has a potential advantage of adding memory capabilities to quantum information protocols. In addition, this provides a quantum matter-light interface, thereby using different physical media for different purposes in a quantum information application. However, the spontaneous emission of photons into all directions is an inherent limitation of this approach. Even the best collection optics captures at most 25 % of the photons [72], with actual experiments reaching overall photon-detection efficiencies of about 5×10^{-4} [70]. Combined with the spontaneous character of the emission, efficiencies are very low and scaling is a serious issue.

We shall see in the following that the coupling of atoms or ions to optical cavities is one effective solution to this problem, with quantum state mapping and entanglement between atomic spin and photon polarisation recently achieved in cavity-based single-photon emitters [45–48]. Very much like what was discussed in the preceding sections, this is achieved using an intrinsically deterministic single-photon emission from a single ^{87}Rb atom in strong coupling to an optical cavity [45]. The triggered emission of a first photon entangles the internal state of the atom and the polarization state of the photon. To probe the degree of entanglement, the atomic state is then mapped onto the state of a second single photon. As a result of the state mapping a pair of entangled photons is produced, one emitted after the other into the same spatial mode. The polarization state of the two photons is analyzed by tomography, which also probes the prior entanglement between the atom and the first photon.

All the relevant steps of entanglement preparation and detection are shown schematically in Fig. 1.7. The rubidium atom is prepared in the $|F = 2, m_F = 0\rangle$ state of the $5S_{1/2}$ ground level. Then a π-polarized laser pulse (polarised linearly along the cavity axis and resonant with the transition from $F = 2$ to $F' = 1$ in the excited $5P_{3/2}$ level) together with the cavity (coupling levels $F = 1$ and $F' = 1$)

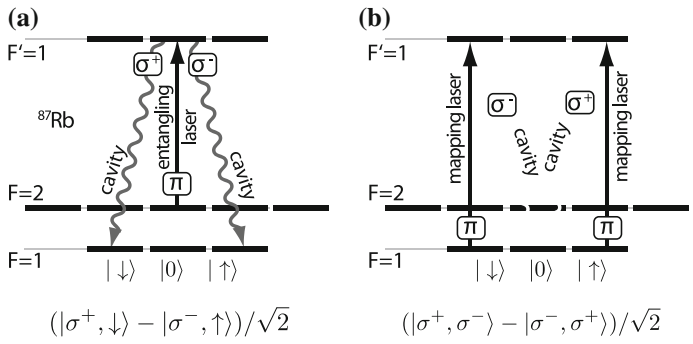

Fig. 1.7 Entanglement and state mapping (from [45]): laser pulses drive vacuum-stimulated Raman transitions, first **a** creating an entanglement between the atom and the emitted photon, and then **b** mapping the atomic state onto the polarization of a second photon. Entanglement is then shared between two flying photons, with the atom disentangled

drives a Raman transition to the $|F = 1, m_F = \pm 1\rangle$ magnetic substates of the ground level. No other cavity-enhanced transitions are possible because the cavity only supports left- and right-handed circularly polarized σ^+ and σ^- polarisation along its axis. Therefore the two different paths to $|\downarrow\rangle \equiv |F = 1, m_F = -1\rangle$ and $|\uparrow\rangle \equiv |F = 1, m_F = +1\rangle$ result in the generation of a σ^+ and σ^- photon, respectively. Thus the atom becomes entangled with the photon and the resulting overall quantum state is identical to the one obtained in the free-space experiments, outlined above in (1.19). However, the substantial difference is that the photon gets deterministically emitted into a single spatial mode, well defined by the geometry of the surrounding cavity. Hence the success probability is close to unity, and a scalable arrangement of atom-cavity arrays is therefore in reach.

To probe the atom-photon entanglement established this way, the atomic state is mapped onto another photon in a second step. This photon can be easily analysed outside the cavity. To do so, a π-polarized laser pulse resonant with the transition from $F = 1$ to $F' = 1$ drives a second Raman transition in the cavity. This is transferring any atom from state $|\downarrow\rangle$ to $|0\rangle \equiv |F = 1, m_F = 0\rangle$ upon emission of a σ^+ photon, whereas $|\uparrow\rangle$ atoms are equally transferred to $|0\rangle$, but upon a σ^- emission. Hence the atom eventually gets disentangled, and a polarization entanglement

$$(|\sigma^+, \sigma^-\rangle - |\sigma^-, \sigma^+\rangle)/\sqrt{2} \tag{1.20}$$

is established between the two successively emitted photons. Because the photons are created in the same spatial mode, a non-polarizing beam splitter (NPBS) is used to direct the photons randomly to one of two measurement setups. This allows each photon to be detected in either the H/V, circular right/left (R/L), or linear diagonal/antidiagonal (D/A) basis. Thus a full quantum state tomography is performed by measuring correlations between the photons in several different bases, selected by using different settings of half- and quarter-wave plates [73, 74]. These measurements lead to the reconstructed density matrix shown in Fig. 1.8. It has only positive

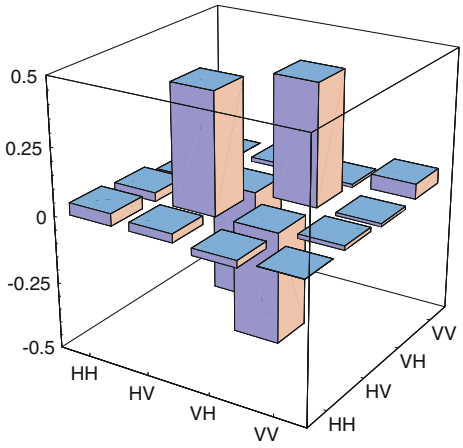

Fig. 1.8 Real part of the density matrix reconstructed from quantum state tomography of successively emitted photon pairs (from [45]): all imaginary parts (not shown) have a magnitude smaller than 0.03. Fidelity with the expected Bell state is 86.0(4)%. About 2200 entanglement events were collected for each of nine measurement settings

eigenvalues, and its fidelity with respect to the expected Bell state is $F = 86.0(4)\%$, with $0.5 < F \leq 1$ proving entanglement.

Based on this successful atom-photon entanglement scheme, elementary quantum-network links implementing teleportation protocols between remote trapped atoms and atom-photon quantum gate operations have recently been demonstrated [46–48, 75]. These achievements represent a big step towards a feasible quantum-computing system because they show how to overcome most scalability issues to quantum networking in a large distributed light-matter based approach.

1.4 Photon Coherence, Amplitude and Phase Control

The vast majority of single-photon applications not only rely on the deterministic emission of single photons, but also require them to be indistinguishable from one another. In other words, their mutual coherence is a key element whenever two or more photons are required simultaneously. The most prominent example to that respect is linear optics quantum computing (LOQC) as initially proposed by Knill et al. [2], with its feasibility demonstrated using spontaneously emitted photon pairs from parametric down conversion [76]. Scaling LOQC to useful dimensions calls for deterministically emitted indistinguishable photons. Furthermore, with photons used as information carriers, it is common practice to use their polarization, spatio-temporal mode structure or frequency for encoding classical or quantum state superpositions. To do so, the capability of shaping photonic modes is essential. Several of these aspects are going to be discussed here.

1.4.1 Indistinguishability of Photons

At first glance, one would expect any single-photon emitter that is based on a single quantum system of well-defined level structure to deliver indistinguishable photons of well-defined energy. However, this is often not the case for a large number of reasons. For instance, multiple pathways leading to the desired single-photon emission or the degeneracy of spin states might lead to broadening of the spectral mode or to photons in different polarisation states, entangled with the atomic spin [45]. Also spontaneous relaxation cascades within the emitter result in a timing jitter of the last step of the cascade, which is linked to the desired photon emission. Nevertheless, atoms coupled to cavities have been shown to emit nearly indistinguishable photons with well defined timing. Their coherence properties are normally governed by the dynamics of the Raman process controlling the generation of photons, and-surprisingly-not substantially limited by the properties and lifetime of the cavity mode or the atoms [77].

Probing photons for indistinguishability is often accomplished with a two-photon interference experiment of the Hong-Ou-Mandel (HOM) type. For two identical

photons that arrive simultaneously at different inputs of a 50:50 beam splitter, they bunch and then leave as a photon pair into either one or the other output port. Hence no correlations are found between two detectors that monitor the two outputs. This technique has been well established in connection with photons emitted from spontaneous parametric-down conversion (SPDC) sources, with the correlations between the outputs measured as a function of the *arrival*-time delay between photons.

For the cavity-based emitters discussed here, the situation is substantially different. The bandwidth of these photons is very narrow, and therefore their coherence time (or length) might be extremely long, i.e. several μs (some 100 m). The time resolution of the detectors is normally 3–4 orders of magnitude faster than this photon length, so that the two-photon correlation signal is now determined as a function of the detection-time delay, with the arrival-time delay of the long photons deliberately set to zero [78, 79]. This can be seen as a quantum-homodyne measurement at the single-photon level, with a single local-oscillator photon arriving at one port of a beam splitter, and a single signal photon arriving at the other port. To develop an understanding how the probability for photon coincidences between the two output ports of the beam splitter depends on the detection-time difference and the mutual phase coherence of the two photons, a step-by-step analysis of the associated quantum jumps and quantum state evolution is most instructive.

Prior to the first photodetection, two photons arrive simultaneously in the input modes A and B at the beam splitter and the overall state of the system reads $|1_A 1_B\rangle$. The first photo detection at time t_1 in either output C or D could have been of either photon, thus the remaining quantum state reduces to

$$|\psi(t_1)\rangle = (|1_A 0_B\rangle \pm |0_A 1_B\rangle)/\sqrt{2}, \tag{1.21}$$

where "+"and "−" correspond to the photodetection in port C and D, respectively. We now assume that the second photodetection takes place $\Delta\tau$ later, at time $t_2 = t_1 + \Delta\tau$, with the input modes A and B having acquired a phase difference $\Delta\phi$ (for whatever reason) during that time interval. Hence prior to the second detection, the reduced quantum state has evolved to

$$|\psi(t_2)\rangle = (|1_A 0_B\rangle \pm e^{i\Delta\phi}|0_A 1_B\rangle)/\sqrt{2}. \tag{1.22}$$

By consequence, the probability for the second photon being detected in the same port as the first photon is $P_{\text{same}} = \cos^2(\Delta\phi/2)$, while the probability for the second photon being detected in the respective other beam-splitter port reads

$$P_{\text{other}} = \sin^2(\Delta\phi/2). \tag{1.23}$$

The probability P_{CD} for coincidence counts between the two detectors in the beam splitter's output ports C and D is therefore proportional to $\sin^2(\Delta\phi/2)$. This implies that any systematic variation of the phase difference $\Delta\phi$ between the two input modes A and B with time $\Delta\tau$ leads to a characteristic modulation of the coincidence function

$$g^{(2)}_{\mathrm{CD}}(\Delta\tau) = \frac{\langle P_C(t) P_D(t+\Delta\tau)\rangle_t}{\langle P_C\rangle\langle P_D\rangle} \propto \sin^2(\Delta\phi(\Delta\tau)/2). \tag{1.24}$$

A good example is the analysis of two photons of different frequency. We consider one photon of well-defined frequency ω_0 acting as *local oscillator* arriving at port A at the beam splitter, and another one of frequency $\omega_0 + \Delta\omega$ which we regard as *signal photon* arriving simultaneously at port B. Their mutual phase is undefined until the first photodetection at t_1, and thereafter evolves according to $\Delta\phi(\Delta\tau) = \Delta\omega \times \Delta\tau$. In this case, the probability for coincidence counts between the beam splitter outputs,

$$P_{\mathrm{CD}}(\Delta\tau) \propto \sin^2(\Delta\omega \times \Delta\tau/2), \tag{1.25}$$

oscillates at the difference frequency between local oscillator and signal photon. This phenomenon has been extensively discussed in [77, 78] and is also illustrated in Fig. 1.9. Furthermore, the figure shows the effect of random dephasing on the time-resolved correlation function. For photons of 1 µs duration, a 470 ns wide dip has been found around $\Delta\tau = 0$. Thereafter, the coincidence probability reached the same mean value that is found with non-interfering photons of, e.g., different polarisation. In this case, we conclude that the dip-width in the coincidence function is identical to the mutual coherence time between the two photons. It is remarkable that it exceeds the decay time of both cavity and atom by one order of magnitude in that particular experiment. This proves that the photon's coherence is to a large extent controlled by the Raman process driving the photon generation, without being limited by the decay channels within the system.

1.4.2 Arbitrary Shaping of Amplitude and Phase

From the discussion in Sect. 1.2.2 we have seen that the dynamic evolution of the atomic quantum states determines the photon emission probability, and thereby also the photon's waveform. This raises the question as to what extent one can arbitrarily shape the photons in time by controlling the envelope of the driving field. This is important for applications such as quantum state mapping, where photon wave packets symmetric in space and time should allow for a time-reversal of the emission process [12]. Employing photons of soliton-shape for dispersion-free propagation could also help boost quantum communication protocols.

Photon shaping can be addressed by solving the master equation of the atom-photon system, which yields the time-dependent probability amplitudes, and by consequence also the wave function of the photon emitted from the cavity [40, 65]. Only recently, we have shown [14, 41, 80] that this analysis can be reversed, giving a unambiguous analytic expression for the time evolution of the driving field in dependence of the desired shape of the photon. This model is valid in the strong-coupling and bad-cavity regime, and it generally allows one to fully control the coherence and population flow in any Raman process. Designing the driving pulse to obtain

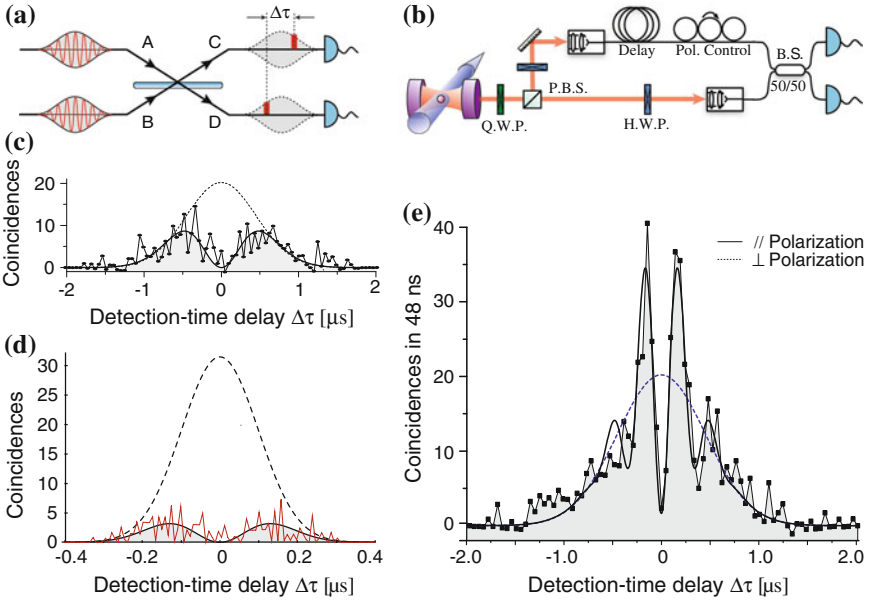

Fig. 1.9 Time-resolved two-photon interference of photons arriving simultaneously at a beam splitter (**a**). With photons emitted successively from one atom-cavity system, this has been achieved using an optical delay line (**b**). Panel **c** shows the correlation function from [77] for photons of 1.0 μs duration as a function of detection-time delay $\Delta\tau$. A pronounced dip at the origin is found, with the dip-width indicating the photon coherence time. The *dotted line* shows correlations found if distinguishable photons of perpendicular polarisation are used, while the *solid line* depicts the correlations found if the photon polarisation is parallel. Panel **d** shows data from a more recent experiment [41] with photons of 0.3 μs duration. The photons are nearly indistinguishable and the integral two-photon coincidence probability drops to 20 % of the reference value found with non-interfering photons. Panel **e** shows data from [77, 78] with interfering photons of different frequency. This gives rise to a pronounced oscillation of the coincidence signal as a function of $\Delta\tau$ with the difference frequency $\Delta\omega$

photonic wave packets of any possible desired shape $\psi_{\rm ph}(t)$ is straight forward [14, 80]. Starting from the three-level atom discussed in Sect. sec:atomspsphotoninteraction, we consider only the states $|e,0\rangle$, $|x,0\rangle$, and $|g,1\rangle$ of the $n = 1$ triplet and their corresponding probability amplitudes $\mathbf{c}(t) = \left[c_{\rm e}(t), c_{\rm x}(t), c_{\rm g}(t)\right]^T$, with the atom-cavity system initially prepared in $|e,0\rangle$. The Hamiltonian (1.6) and the decay of atomic spin and cavity field at rates γ and κ, respectively, define the master equation of the system,

$$i\hbar\frac{d}{dt}\mathbf{c}(t) = -\frac{\hbar}{2}\begin{pmatrix} 0 & \Omega(t) & 0 \\ \Omega(t) & 2i\gamma & 2g \\ 0 & 2g & 2i\kappa \end{pmatrix}\mathbf{c}(t). \tag{1.26}$$

The cavity-field decay at rate κ unambiguously links the probability amplitude of $|g,1\rangle$ to the desired wave function $\psi_{\rm ph}(t)$ of the photon. Furthermore, $|g,1\rangle$ only couples to $|x,0\rangle$ with the well-defined atom-cavity coupling g, while the Rabi frequency Ω of the driving laser is linking $|x,0\rangle$ to $|e,0\rangle$. Hence the time evolution of the probability amplitudes and $\Omega(t)$ read

$$c_{\rm g}(t) = \psi_{\rm ph}(t)/\sqrt{2\kappa}, \tag{1.27}$$

$$c_{\rm x}(t) = -\frac{i}{g}\left[\dot{c}_{\rm g}(t) + \kappa c_{\rm g}(t)\right] \tag{1.28}$$

$$\Omega(t)c_e(t) = 2\left[i\dot{c}_x(t) + i\gamma c_x(t) - g c_g(t)\right]. \tag{1.29}$$

We can use the continuity of the system, taking into account the decay of atom polarisation and cavity field at rates γ and κ, respectively, to get to an independent expression for

$$|c_e(t)|^2 = 1 - |c_x(t)|^2 - |c_g(t)|^2 - \int_0^t dt\left[2\gamma|c_x(t)|^2 + 2\kappa|c_g(t)|^2\right]. \tag{1.30}$$

With the Hamiltonian not comprising any detuning and assuming $\psi_{\rm ph}$ to be real, one can easily verify that the probability amplitude $c_x(t)$ is purely imaginary, while $c_e(t)$ and $c_g(t)$ are both real. Hence with the desired photon shape as a starting point, we have obtained analytic expressions for all probability amplitudes. These then yield the Rabi frequency

$$\Omega(t) = \frac{2\left[i\dot{c}_x(t) + i\gamma c_x(t) - g c_g(t)\right]}{\sqrt{1 - |c_x(t)|^2 - |c_g(t)|^2 - \int_0^t dt\left[2\gamma|c_x(t)|^2 + 2\kappa|c_g(t)|^2\right]}}, \tag{1.31}$$

which is a real function defining the driving pulse required to obtain the desired photon shape.

Figure 1.10 compares some of the results obtained in producing photons of arbitrary shape. For instance, the driving laser pulse shown in Fig. 1.10g has been calculated according to (1.31) to produce the photon shape from Fig. 1.10h. From all data and calculation, it is obvious that stronger driving is required to counterbalance the depletion of the atom-cavity system towards the end of the pulse. Therefore a very asymmetric driving pulse leads to the emission of photons symmetric in time, and vice versa, as can be seen from comparing Fig. 1.10c, e.

Amongst the large variety of shapes that have been produced, their possible subdivision into various peaks within separate time-bins is a distinctive feature, seen that it allows for time-bin encoding of quantum information. For instance, we recently have been imprinting different mutual phases on various time bins of multi-peak photons [81], and then successfully retrieved this phase information in a time-resolved

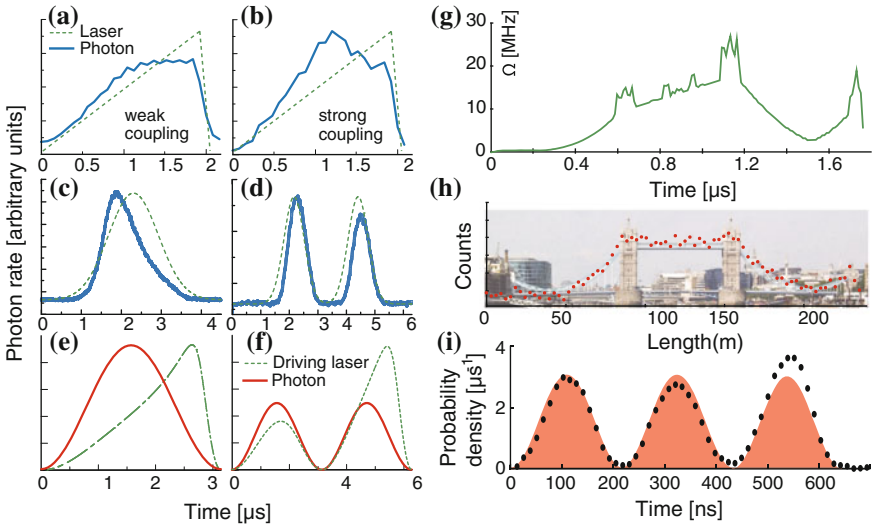

Fig. 1.10 Photons made to measure: **a**–**d** show photon shapes realised in several experiments and their driving laser pulses. The histogram of the photon-detection time has been recorded for several hundred single-photon emissions. The data shown in **a**, **b** is taken from [40], with neutral atoms falling through a high-finesse cavity acting as photon emitters. The linear increase in Rabi frequency is the same in both cases, and the difference in photon shape is caused by variations in the coupling strength to the cavity. The data shown in **c**, **d** is taken from [65], with a single ion trapped between the cavity mirrors. It shows that the photon shape depends strongly on the driving laser pulse (Panels **c**, **d** adapted with permission from Nature Publishing Group: Nature, Keller et al. [65], Copyright 2004). **e**, **f** show the Rabi frequency one needs to apply to achieve symmetric single or twin-peak photon pulses with an efficiency close to unity. This is a result from an analytical solution of the problem discussed in [80]. The latter scheme has been applied successfully for generating photons of various arbitrary shapes [41], with examples shown in (**g**–**i**)

quantum-homodyne experiment based on two-photon interference. The latter is illustrated in Fig. 1.11. Subsequently emitted triple-peak photons from the atom-cavity system are sent into optical-fibre made delay lines to arrive simultaneously at a beam splitter. While the mechanism described above is used to sub-divide the photons into three peaks of equal amplitude, i.e. three well-separate time bins or temporal modes, we also impose phase changes from one time bin to the next. The latter is accomplished by phase-shifting the driving laser with an acousto-optic modulator. Therefore the signal photons emitted from the cavity are prepared in a W-state with arbitrary relative phases between their constituent temporal modes,

$$|\Psi_{\text{photon}}\rangle = (e^{i\phi_1}|1,0,0\rangle + e^{i\phi_2}|0,1,0\rangle + e^{i\phi_3}|0,0,1\rangle)/\sqrt{3}. \tag{1.32}$$

We may safely assume that $\phi_1 = 0$ as only relative phases are of any relevance. The atom-cavity system is driven in a way that an alternating sequence of signal photons and local-oscillator photons gets emitted, with the local-oscillator photons

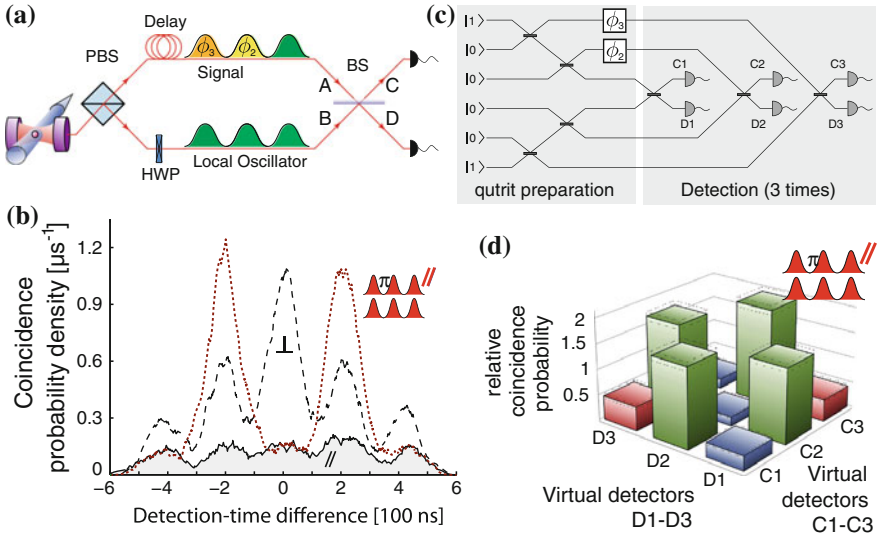

Fig. 1.11 Qutrits, from [81]: **a** pairs of triple-peak photons subsequently emitted are delayed such they arrive simultaneously at a beam splitter. Time-resolved coincidences are then registered between output ports C and D. The signal photon carries mutual phases ϕ_1 and ϕ_2 between peaks, the local oscillator does not. **b** Time-resolved homodyne signal for photons of perpendicular (*black*) and parallel (*blue*) polarization, with the signal photon having a phase shift in the central time bin of $\phi_1 = \pi$ (*red*). The solid traces result from summing all coincidences found within a 60 ns wide interval around each point of the trace. For some of these data points, the statistical error is shown. **c** Corresponding virtual circuit if the same experiment was done in the spatial domain. The actual physical system, consisting of one beam splitter and two detectors, would then correspond to a six-detector setup. All time-resolved photodetections in the real system can be easily associated with corresponding virtual detectors firing. **d** Relative coincidence probabilities between virtual detectors (*blue* detections within the same time bin; *green* detections in successive time bins; *red* detections two time-bins apart)

not being subject to any phase shifts between its constituents, but otherwise identical to the signal photons. This ensures that a signal photon (including phase jumps) and a local-oscillator photon (without phase jumps) always arrive simultaneously at the beam splitter behind the delay lines whenever two successively emitted photons enter the correct delay paths. Two detectors, labeled C and D, are monitoring the output ports of this beam splitter. Their time resolution is good enough to discriminate whether photons are detected during the first, second or third peak. The probability for photon-photon correlations across different time bins and detectors therefore reflects the phase change within the photons—i.e. the probability for correlations between the two detectors monitoring the beam-splitter output depends strongly on the timing of the photo detections. For instance, the coincidence probability $P(C_\mathrm{i}, D_\mathrm{j})$ for detector C clicking in time bin i and detector D in time bin j is then

$$P(C_\mathrm{i}, D_\mathrm{j}) \propto \sin^2\left((\phi_\mathrm{i} - \phi_\mathrm{j})/2\right). \tag{1.33}$$

We have been exploring these phenomena [81] with the experiment illustrated in Fig. 1.11, using two types different signal photons. One with no mutual phase shifts, i.e. $\phi_1 = \phi_2 = \phi_3 = 0$, and the other with $\phi_1 = 0,\ \phi_2 = \pi,\ \phi_3 = 0$. In the first case, signal and local oscillator photons are identical. By consequence, no correlations between the two detectors arise (apart from a constant background level due to detector noise). In the second case the adjacent time bins within the signal photon are π out of phase. Therefore the probability for correlations between the two detectors increases dramatically if the detectors fire in adjacent time bins, but it stays zero for detections within the same time bin, and for detections occurring in the first and third time bin. These new findings demonstrate nicely that atom-cavity systems give us the capability of fully controlling the temporal evolution of amplitude and phase within single deterministically generated photons. Their characterisation with time-resolved Hong-Ou-Mandel interference used for quantum homodyning the photons then reveals these phases again in the photon-photon correlations.

The availability of time bins as an additional degree of freedom to LOQC in an essentially deterministic photon-generation scheme is a big step towards large-scale quantum computing in photonic networks [82]. Arbitrary single-qubit operations on time-bin encoded qubits seem straightforward to implement with phase-coherent optical delay lines and active optical routing to either switch between temporal and spatial modes, or to swap the two time bins. Controlling the atom-photon coupling might also allow the mapping of atomic superposition states to time-binned photons [14, 47]; and the long coherence time, combined with fast detectors, makes real-time feedback possible during photon generation.

1.5 Cavity-Based Quantum Memories

Up to this point, we have been discussing cavity-based single-photon emission, atom-photon state mapping, entanglement and basic linear optical phenomena using these photons. All these processes rely on a unitary time evolution of the atom-cavity system upon photon emission, in a process which intrinsically is fully reversible. Due to this property, it should be possible to use atoms in strong cavity coupling as universal nodes within a large quantum optical network. The latter is a very promising route towards hybrid quantum computing, which has the potential to overcome many scalability issues because it combines stationary atomic quantum bits with fast photonic links and linear optical information processing in a so-called ‘quantum internet’ [83], which is based on photon-mediated state mapping between two distant atoms placed in spatially separated optical cavities [12]. Here, we basically summarize our model from [14] and discuss how to expand our previous Raman scheme to capture a single photon of arbitrary temporal shape with one atom coupled to an optical cavity, using a control pulse of suitable temporal shape to ensure impedance matching throughout the photon arrival, which is necessary for complete state mapping from photon to atom. We also note that quantum networking between two cavities has recently been

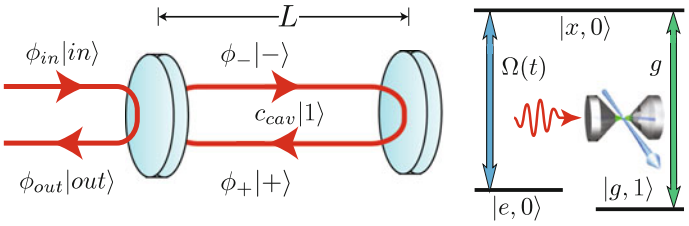

Fig. 1.12 Cavity coupling (from [14]): a photon arrives from the left and either gets reflected off the cavity or couples to its internal modes. The three levels of the atom inside the cavity are labeled $|e\rangle$, $|x\rangle$ and $|g\rangle$, with photon number states $|0\rangle$ and $|1\rangle$. The couplings of the control pulse and cavity are given by $\Omega(t)$ and g respectively, and the atom is initially prepared in state $|g\rangle$

experimentally demonstrated with atomic ensembles [84, 85] and single atoms in strong cavity coupling [17, 47].

In addition to the single-photon emission and the associated quantum state mapping in emission, the newly declared goal is now to find a control pulse that achieves complete absorption of single incoming photons of arbitrary temporal shape, given by the running-wave probability amplitude $\phi_{in}(t)$, which arrives at one cavity mirror.[1] This relates most obviously to mapping Fock-state encoded qubits to atomic states [12, 15], but also extends to other possible superposition states, e.g. photonic time bin or polarisation encoded qubits [17, 45, 86].

Prior to investigating the effect of the atom-cavity and atom-laser coupling, we briefly revisit the input-output coupling of an optical cavity in the time domain (Fig. 1.12). Inside the cavity, we assume that the mode spacing is so large that only one single mode of frequency ω_{cav} contributes, with the dimension-less probability amplitude $c_{cav}(t)$ determining the occupation of the one-photon Fock state $|1\rangle$. Furthermore, we assume that coupling to the outside field is fully controlled by the field reflection and transmission coefficients, r and τ, of the coupling mirror, while the other has a reflectivity of 100 %. We decompose the cavity mode into submodes $|+\rangle$ and $|-\rangle$, travelling towards and away from the coupling mirror, so that the spatio-temporal representation of the cavity field reads

$$\phi_+(t)|+\rangle + \phi_-(t)|-\rangle, \tag{1.34}$$

where $\Delta\phi = \phi_-(t) - \phi_+(t)$ is the change of the running-wave probability amplitude at the coupling mirror. The latter is small for mirrors of high reflectivity, such that $c_{cav}(t) \simeq \phi_+(t)\sqrt{t_r} \simeq \phi_-(t)\sqrt{t_r}$, with $t_r = 2L/c$ the cavity's round-trip time. We also decompose the field outside the cavity into incoming and outgoing spatio-temporal field modes, with running-wave probability amplitudes $\phi_{in}(t + z/c)$ and $\phi_{out}(t - z/c)$ for finding the photon in the $|in\rangle$ and $|out\rangle$ states at time t and position

[1] $\phi_{in}(t)$ is the probability amplitude of the running photon, with $\int_{-\infty}^{+\infty} |\phi_{in}(t)|^2 dt = 1$ and $|\phi_{in}(t)|^2 dt$ the probability of the photon arriving at the mirror within $[t, t + dt]$.

z, respectively. The coupling mirror at $z = 0$ acts as a beam splitter with the operator $a_-^\dagger(ra_+ + \tau a_{in}) + a_{out}^\dagger(\tau a_+ - ra_{in})$ coupling the four running-wave modes inside and outside the cavity. In matrix form, this coupling equation reads

$$\begin{pmatrix} \phi_+ + \Delta\phi \\ \phi_{out} \end{pmatrix} = \begin{pmatrix} \phi_- \\ \phi_{out} \end{pmatrix} = \begin{pmatrix} r & \tau \\ \tau & -r \end{pmatrix} \begin{pmatrix} \phi_+ \\ \phi_{in} \end{pmatrix} \tag{1.35}$$

To relate $c_{cav}(t)$ to the running-wave probability amplitudes, we take $r \approx 1 - \kappa t_r$ and $\tau = \sqrt{2\kappa t_r}$, where κ is the field decay rate of the cavity. Furthermore, we make use of

$$\frac{dc_{cav}}{dt} \simeq \frac{c_{cav}(t + t_r) - c_{cav}(t)}{t_r} = \frac{(\phi_- - \phi_+)\sqrt{t_r}}{t_r} = \frac{\Delta\phi}{\sqrt{t_r}}. \tag{1.36}$$

With these relations, the first line of (1.35) can be written as $c_{cav}/t_r + \dot{c}_{cav} = (1-\kappa t_r)c_{cav}/t_r + \sqrt{2\kappa}\phi_{in}$. Therefore (1.35) takes the form of a differential equation

$$\begin{pmatrix} \dot{c}_{cav} \\ \phi_{out} \end{pmatrix} = \begin{pmatrix} -\kappa & \sqrt{2\kappa} \\ \sqrt{2\kappa} & -r \end{pmatrix} \begin{pmatrix} c_{cav} \\ \phi_{in} \end{pmatrix}. \tag{1.37}$$

This describes the coupling of a resonant photon into and out of the cavity mode. The reader might note that the result obtained from our simplified input-output model is fully equivalent to the conclusions drawn from the more sophisticated standard approach that involves a decomposition of the continuum into a large number of frequency modes [87]. No such decomposition is applied here as we study the problem uniquely in the time domain.

Next, we examine the coupling of a single atom to the cavity, as discussed in the preceding sections. We again consider a three level Λ-type atom with two electronically stable ground states $|e\rangle$ and $|g\rangle$, coupled by either the cavity field mode or the control laser field to one-and-the-same electronically excited state $|x\rangle$. For the one-photon multiplet of the generalised Jaynes-Cummings ladder, the cavity-mediated coupling between $|g, 1\rangle$ and $|x, 0\rangle$ is given by the atom-cavity coupling strength g, while the control laser couples $|e, 0\rangle$ with $|x, 0\rangle$ with Rabi frequency $\Omega(t)$. The probability amplitudes of these particular three product states read $c_e(t)$, $c_g(t)$, and $c_x(t)$, respectively, with their time evolution given by

$$\begin{pmatrix} \dot{c}_e \\ \dot{c}_x \\ \dot{c}_g \\ \phi_{out} \end{pmatrix} = \begin{pmatrix} 0 & -i\Omega(t)^*/2 & 0 & 0 \\ -i\Omega(t)/2 & -\gamma & -ig & 0 \\ 0 & -ig^* & -\kappa & \sqrt{2\kappa} \\ 0 & 0 & \sqrt{2\kappa} & -r \end{pmatrix} \begin{pmatrix} c_e \\ c_x \\ c_g \\ \phi_{in} \end{pmatrix}, \tag{1.38}$$

which is formally equivalent to the Schrödinger equation (1.26) which we've been considering for single-photon shaping, but now includes the input-output relation from (1.37). This new master equation is modelling the atom coupled to the cavity

as an open quantum system, driven by the incoming photon, with its probability amplitude $\phi_{in}(t)$ to be taken at $z = 0$, and possibly coupling or directly reflecting light into the outgoing field with amplitude $\phi_{out}(t)$. We also note that $c_g(t) \equiv c_{cav}(t)$ because the state $|g, 1\rangle$ is the only atom-field product state in which there is one photon in the cavity. On resonance, g and $\phi_{in}(t)$ are both real, and by consequence $c_g(t)$ and $c_e(t)$ are real while $c_x(t)$ is purely imaginary. Because we are considering only one photon, the probability of occupying $|g, 0\rangle$ is given by the overall probability of having a photon outside the cavity, either in state $|in\rangle$ or in $|out\rangle$. These states couple only via the cavity mirror to $|g, 1\rangle$.

The realisation of a cavity-based single-atom quantum memory is based on the complete absorption of the incoming photon, which is described by its time-dependent probability amplitude $\phi_{in}(t)$. This calls for perfect impedance matching, i.e. no reflection and $\phi_{out}(t) = 0$ at all times. This condition yields

$$c_g(t) = \phi_{in}(t)/\sqrt{2\kappa} \tag{1.39}$$

$$c_x(t) = i\left[\dot{c}_g(t) - \kappa c_g(t)\right]/g^* = i\left[\dot{\phi}_{in}(t) - \kappa\phi_{in}(t)\right]/g^*\sqrt{2\kappa} \tag{1.40}$$

$$\Omega(t)c_e(t) = 2\left[i\dot{c}_x(t) + i\gamma c_x(t) - g c_g(t)\right]. \tag{1.41}$$

With the photon initially completely in the incoming state $|in\rangle$, i.e. $\int |\phi_{in}(t)|^2 dt = 1$, and the atom-cavity system in state $|g, 0\rangle$, the continuity balance yields

$$|c_e(t)|^2 = |c_0|^2 - |c_g(t)|^2 - |c_x(t)|^2 + \int_{-\infty}^{t} [|\phi_{in}(t')|^2 - 2\gamma|c_x(t')|^2]dt', \tag{1.42}$$

including an offset term $|c_0|^2$ to account for a small non-zero initial occupation of $|e, 0\rangle$. The relevance of this term becomes obvious in the following. From (1.40, 1.41, 1.42), we obtain the Rabi frequency of the driving pulse,

$$\Omega(t) = \frac{2\left[i\dot{c}_x(t) + i\gamma c_x(t) - g c_g(t)\right]}{\sqrt{|c_0|^2 - |c_g(t)|^2 - |c_x(t)|^2 + \int_{-\infty}^{t}[|\phi_{in}(t')|^2 - 2\gamma|c_x(t')|^2]dt'}}, \tag{1.43}$$

necessary for full impedance matching over all times. In turn this assures complete absorption of the incoming photon by the atom-cavity system. We emphasize here the close similarity of this novel expression with the analytic form of the driving pulse needed for the emission of shaped photons, (1.31). This is not a coincidence. The photon absorption discussed here is nothing else than a time-reversal of the photon emission process. If we disregard any losses and also assume the final occupation of $|e, 0\rangle$ after a photon emission equals the initial occupation of that state prior to a photon absorption, then the required Rabi frequency $\Omega(t)$ for absorption is the exact mirror image in time of the Rabi frequency used for photon generation.

Let us now consider physically realistic photons restricted to a finite support of well-defined start and end times, t_{start} and t_{stop}, starting smoothly with $\phi_{in}(t_{start}) = \frac{d}{dt}\phi_{in}(t_{start}) = 0$, but of non-zero second derivative. Therefore (1.41)

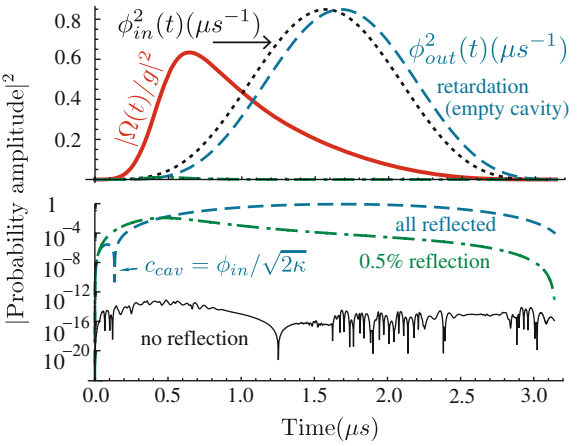

Fig. 1.13 Impedance matching (from [14]): incoming $\sin^2$ photon (*dotted*). Case **a** Empty cavity, all reflected (*dashed*); case **b** system prepared in $|g, 0\rangle$, small reflection (*dash-dotted*); case **c** small initial population in $|e, 0\rangle$, reflection suppressed (*thin solid*). The control pulse (*thick solid*) is derived to match case (**c**)

yields $\Omega(t_{start})c_e(t_{start}) \neq 0$. This necessitates a small initial population in state $|e, 0\rangle$ because otherwise perfect impedance matching with $|c_0|^2 = 0$ is only possible with photons of infinite duration.

To illustrate the power of the procedure and the implications of the constraints to the initial population, we apply the scheme to a typical photon shapes that one may obtain from atom-cavity systems. We consider a cavity with parameters similar to one of our own experimental implementations, with $(g, \kappa, \gamma) = 2\pi \times (15, 3, 3)$ MHz and a resonator length of $L = 100\,\mu$m. As an example, we assume that a symmetric photon with $\phi_{in}(t) \propto \sin^2(\pi t/\tau_{photon})$ arrives at the cavity. For a photon duration of $\tau_{photon} = 3.14\,\mu$s, Fig. 1.13 shows $\phi_{in}(t)$, $\Omega(t)$ and the probability amplitude of the reflected photon, $\phi_{out}(t)$, as a function of time. The latter is obtained from a numerical solution of (1.38) for the three cases of (a) an empty cavity, (b) an atom coupled to the cavity initially prepared in $|g, 0\rangle$, with $|c_0| = 0$, and (c) a small fraction of the atomic population initially in state $|e, 0\rangle$, with $|c_0|^2 = 0.5\,\%$. In all three cases, the Rabi frequency $\Omega(t)$ of the control pulse is identical. It has been calculated analytically assuming a small value of $|c_0|^2 = 0.5\,\%$ (this choice is arbitrary and only limited by practical considerations, as will be discussed later). From these simulations, it is obvious the photon gets fully reflected if no atom is present (case a), albeit with a slight retardation due to the finite cavity build-up time. Because the direct reflection of the coupling mirror is in phase with the incoming photon and the light from the cavity coupled through that mirror is out-of phase by π, the phase of the reflected photon flips around as soon as $c_{cav}(t) = \phi_{in}(t)/\sqrt{2\kappa}$. This shows up in the logarithmic plot as a sharp kink in $\phi_{out}(t)$ around $t = 0.13\,\mu$s.

The situation changes dramatically if there is an atom coupled to the cavity mode. For instance, with the initial population matching the starting conditions used to derive $\Omega(t)$, i.e. case (c) with $\rho_0 = 0.5\,\%$, no photon is reflected. The amplitude of $|\phi_{out}(t)|^2$ remains below 10^{-12}, which corresponds to zero within the numerical precision. However, for the more realistic case (b) of the atom-cavity system well

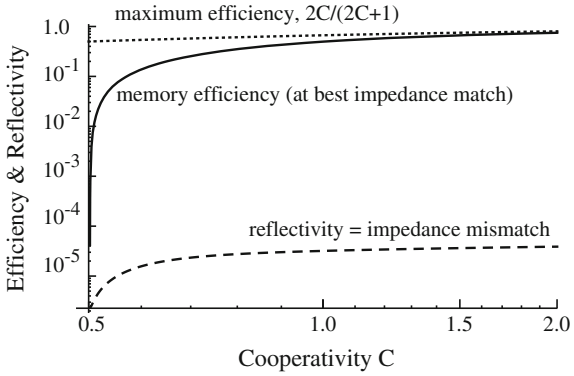

Fig. 1.14 Storage efficiency (mapping the photon to $|e, 0\rangle$, *solid line*) and impedance mismatch (back-reflecting the photon, *dashed line*) as a function of the cooperativity, $C = g^2/(2\kappa\gamma)$ (from [14]). The *dotted line* shows the maximum possible efficiency. Both efficiency and impedance mismatch have been numerically calculated for $\kappa = \gamma = 2\pi\,3\,\text{MHz}$ using symmetric $\sin^2$ pulses of $3.14\,\mu\text{s}$ duration, with control pulses modelled according to (1.41–1.43) to achieve optimum impedance match

prepared in $|g, 0\rangle$, the same control pulse is not as efficient, and the photon is reflected off the cavity with an overall probability of 0.5 %. This matches the "defect" in the initial state preparation, and can be explained by the finite cavity build-up time leading to an impedance mismatch in the onset of the pulse.

We emphasise that this seemingly small deficiency in the photon absorption might become significant with photons of much shorter duration. For instance, in the extreme case of a photon duration $\tau_{photon} < \kappa^{-1}$, building up the field in the cavity to counterbalance the direct reflection by means of destructive interference is achieved most rapidly without any atom. Any atom in the cavity will act as a sink, removing intra-cavity photons. With an atom present, a possible alternative is to start off with a very strong initial Rabi frequency of the control pulse. This will project the atom-cavity system initially into a dark state, so that the atom does not deplete the cavity mode. Nonetheless, the initial reflection losses would still be as high as for an empty cavity.

To illustrate the interplay of impedance matching and memory efficiency, Fig. 1.14 shows the reflection probability and the memory efficiency (excitation transfer to $|e, 0\rangle$) as a function of the cooperativity, $C = g^2/(2\kappa\gamma)$. Obviously, the impedance matching condition is always met, but the efficiency varies. For $C > 1$, it asymptotically reaches the predicted optimum [88] of $2C/(2C + 1)$, but it drops to zero at $C = 1/2$ (i.e. for $g = \kappa = \gamma$). In this particular case, the spontaneous emission loss via the atom equals the transmission of the coupling mirror. Hence the coupled atom-cavity system behaves like a balanced Fabry-Perot cavity, with one real mirror being the input coupler, and the spontaneously emitting atom acting as output coupler. Therefore the photon goes into the cavity, but is spontaneously emitted by

the atom and gets not mapped to $|e, 0\rangle$. This limiting case furthermore implies that impedance matching is not possible for $C < 1/2$, as the spontaneous emission via the atom would then outweigh the transmission of the coupling mirror. The application of our formalism therefore fails in this weak coupling regime (actually, the evaluation of (1.42) would then yield values of $|c_e|^2 < 0$, which is not possible).

The photon reabsorption scheme discussed here, together with the earlier introduced method for generating tailored photons [41, 80, 81], constitute the key to analytically calculating the optimal driving pulses needed to produce and absorb arbitrarily shaped single-photons (of finite support) with three level Λ-type atoms in optical cavities. This is a sine qua non condition for the successful implementation of a quantum network. It is expected that this simple analytical method will have significant relevance for those striving to achieve atom-photon state transfer in cavity-QED experiments, where low losses and high fidelities are of paramount importance.

1.6 Future Directions

We have discussed a large variety of ways for producing single photons from simple quantum systems. The majority of these photon-production methods lead to on-demand emission of narrowband and indistinguishable photons into a well defined mode of the radiation field, with efficiencies that can be very close to unity. Therefore these photons are ideal for all-optical quantum computation schemes, as proposed by Knill et al. [2]. These sources are expected to play a significant role in the implementation of quantum networking [12] and quantum communication schemes [89].

The atom- and ion-based sources have already shown to be capable of entangling and mapping quantum states between atoms and photons [45, 46]. Processes like entanglement swapping and teleportation between distant atoms or ions, that have first been studied without the aid of cavities [69, 70, 86, 90, 91] are beginning to benefit enormously from the introduction of cavity-based techniques [17, 47, 48], as their success probability scales with the square of the efficiency of the photon generation process. The high efficiency of cavity-based photon sources also opens up new avenues towards a highly scalable quantum network, which is essential for providing cluster states in one-way quantum computing [92] and for the quantum simulation of complex solid-state systems [93].

Acknowledgments Hereby I express my gratitude to all my colleagues and co-workers in my present and past research groups at the University of Oxford and the MPQ in Garching. It has been their engagement and enthusiasm, teamed up with the support from the European Union, the DFG and the EPSRC, which lead to the discovery of the phenomena and the development of the techniques discussed in this chapter.

References

1. D.P. DiVincenzo, Real and realistic quantum computers. Nature **393**, 113–114 (1998)
2. E. Knill, R. Laflamme, G.J. Milburn, A scheme for efficient quantum computing with linear optics. Nature **409**, 46–52 (2001)
3. A. Reiserer, G. Rempe, Cavity-based quantum networks with single atoms and optical photons, (2014), arXiv:1412.2889
4. A. Kuhn, D. Ljunggren, Cavity-based single-photon sources. Contemp. Phys. **51**, 289–313 (2010)
5. G.S. Solomon, C. Santori, A. Kuhn, *Single Emitters in Isolated Quantum Systems*. Experimental Methods in the Physical Sciences, vol. 45, Chapter 13. (Elsevier Science, 2013), pp. 467–539
6. E.T. Jaynes, F.W. Cummings, Comparison of quantum and semiclassical radiation theories with application to the beam maser. Proc. IEEE **51**, 89–109 (1963)
7. B.W. Shore, P.L. Knight, The Jaynes-Cummings model. J. Mod. Opt. **40**, 1195 (1993)
8. E.M. Purcell, Spontaneous emission probabilities at radio frequencies. Phys. Rev. **69**, 681 (1946)
9. D. Kleppner, Inhibited spontaneous emission. Phys. Rev. Lett. **47**, 233–236 (1981)
10. H.J. Carmichael, Photon antibunching and squeezing for a single atom in a resonant cavity. Phys. Rev. Lett. **55**, 2790–2793 (1985)
11. F. De Martini, G. Innocenti, G.R. Jacobovitz, P. Mataloni, Anomalous spontaneous emission time in a microscopic optical cavity. Phys. Rev. Lett. **59**, 2955–2958 (1987)
12. J.I. Cirac, P. Zoller, H.J. Kimble, H. Mabuchi, Quantum state transfer and entanglement distribution among distant nodes in a quantum network. Phys. Rev. Lett. **78**, 3221–3224 (1997)
13. D.P. DiVincenzo, The physical implementation of quantum computation. Fortschr. Phys. **48**, 771 (2000)
14. J. Dilley, P. Nisbet-Jones, B.W. Shore, A. Kuhn, Single-photon absorption in coupled atom-cavity systems. Phys. Rev. A **85**, 023834 (2012)
15. A.D. Boozer, A. Boca, R. Miller, T.E. Northup, H.J. Kimble, Reversible state transfer between light and a single trapped atom. Phys. Rev. Lett. **98**, 193601 (2007)
16. M. Mücke et al., Electromagnetically induced transparency with single atoms in a cavity. Nature **465**, 755–758 (2010)
17. H.P. Specht et al., A single-atom quantum memory. Nature **473**, 190 (2011)
18. A. Kuhn, M. Hennrich, T. Bondo, G. Rempe, Controlled generation of single photons from a strongly coupled atom-cavity system. Appl. Phys. B **69**, 373–377 (1999)
19. N.V. Vitanov, M. Fleischhauer, B.W. Shore, K. Bergmann, Coherent manipulation of atoms and molecules by sequential laser pulses. Adv. At. Mol. Opt. Phys. **46**, 55–190 (2001)
20. D.J. Heinzen, J.J. Childs, J.E. Thomas, M.S. Feld, Enhanced and inhibited spontaneous emission by atoms in a confocal resonator. Phys. Rev. Lett. **58**, 1320–1323 (1987)
21. S.E. Morin, C.C. Yu, T.W. Mossberg, Strong atom-cavity coupling over large volumes and the observation of subnatural intracavity atomic linewidths. Phys. Rev. Lett. **73**, 1489–1492 (1994)
22. L.A. Lugiato, Theory of optical bistability, in *Progress in Optics*, vol. XXI, ed. by E. Wolf (Elsevier Science Publishers, B. V., 1984), pp. 71–216
23. C.K. Law, J.H. Eberly, Arbitrary control of a quantum electromagnetic field. Phys. Rev. Lett. **76**, 1055 (1996)
24. C.K. Law, H.J. Kimble, Deterministic generation of a bit-stream of single-photon pulses. J. Mod. Opt. **44**, 2067–2074 (1997)
25. A. Kuhn, G. Rempe, Optical cavity QED: fundamentals and application as a single-photon light source, in *Experimental Quantum Computation and Information*, vol. 148, ed. by F. De Martini, C. Monroe (IOS-Press, Amsterdam, 2002), pp. 37–66
26. A. Kuhn, M. Hennrich, G. Rempe, Strongly-coupled atom-cavity systems, in *Quantum Information Processing*, ed. by T. Beth, G. Leuchs (Wiley-VCH, Berlin, 2003), pp. 182–195
27. S.E. Harris, Electromagnetically induced transparency with matched pulses. Phys. Rev. Lett. **70**, 552–555 (1993)

28. S.E. Harris, Electromagnetically induced transparency. Phys. Today **50**, 36 (1997)
29. L.V. Hau, S.E. Harris, Z. Dutton, C.H. Behroozi, Light speed reduction to 17 metres per second in an ultracold atomic gas. Nature **397**, 594–598 (1999)
30. D.F. Phillips, A. Fleischhauer, A. Mair, R.L. Walsworth, M.D. Lukin, Storage of light in atomic vapor. Phys. Rev. Lett. **86**, 783–786 (2001)
31. A. Messiah, *Quantum Mechanics*, vol. 2, Chapter 17. (Wiley, New York, 1958)
32. J. Kim, O. Benson, H. Kan, Y. Yamamoto, A single photon turnstile device. Nature **397**, 500–503 (1999)
33. C. Brunel, B. Lounis, P. Tamarat, M. Orrit, Triggered source of single photons based on controlled single molecule fluorescence. Phys. Rev. Lett. **83**, 2722–2725 (1999)
34. B. Lounis, W.E. Moerner, Single photons on demand from a single molecule at room temperature. Nature **407**, 491–493 (2000)
35. C. Kurtsiefer, S. Mayer, P. Zarda, H. Weinfurter, Stable solid-state source of single photons. Phys. Rev. Lett. **85**, 290–293 (2000)
36. R. Brouri, A. Beveratos, J.-P. Poizat, P. Grangier, Photon antibunching in the fluorescence of individual color centers in diamond. Opt. Lett. **25**, 1294–1296 (2000)
37. P. Michler et al., Quantum correlation among photons from a single quantum dot at room temperature. Nature **406**, 968–970 (2000)
38. C. Santori, M. Pelton, G. Solomon, Y. Dale, Y. Yamamoto, Triggered single photons from a quantum dot. Phys. Rev. Lett. **86**, 1502–1505 (2001)
39. Z. Yuan et al., Electrically driven single-photon source. Science **295**, 102–105 (2002)
40. A. Kuhn, M. Hennrich, G. Rempe, Deterministic single-photon source for distributed quantum networking. Phys. Rev. Lett. **89**, 067901 (2002)
41. P.B.R. Nisbet-Jones, J. Dilley, D. Ljunggren, A. Kuhn, Highly efficient source for indistinguishable single photons of controlled shape. New J. Phys. **13**, 103036 (2011)
42. M. Hennrich, T. Legero, A. Kuhn, G. Rempe, Photon statistics of a non-stationary periodically driven single-photon source. New J. Phys. **6**, 86 (2004)
43. J. McKeever et al., Deterministic generation of single photons from one atom trapped in a cavity. Science **303**, 1992–1994 (2004)
44. M. Hijlkema et al., A single-photon server with just one atom. Nat. Phys. **3**, 253–255 (2007)
45. T. Wilk, S.C. Webster, A. Kuhn, G. Rempe, Single-atom single-photon quantum interface. Science **317**, 488 (2007)
46. B. Weber et al., Photon-photon entanglement with a single trapped atom. Phys. Rev. Lett. **102**, 030501 (2009)
47. S. Ritter et al., An elementary quantum network of single atoms in optical cavities. Nature **484**, 195–200 (2012)
48. C. Nölleke et al., Efficient teleportation between remote single-atom quantum memories. Phys. Rev. Lett. **110**, 140403 (2013)
49. Y. Colombe et al., Strong atom-field coupling for bose-einstein condensates in an optical cavity on a chip. Nature **450**, 272–276 (2007)
50. M. Trupke et al., Atom detection and photon production in a scalable, open, optical microcavity. Phys. Rev. Lett. **99**, 063601 (2007)
51. B. Dayan et al., A photon turnstile dynamically regulated by one atom. Science **319**, 1062–1065 (2008)
52. T. Aoki et al., Efficient routing of single photons by one atom and a microtoroidal cavity. Phys. Rev. Lett. **102**, 083601 (2009)
53. M. Pöllinger, D. O'Shea, F. Warken, A. Rauschenbeutel, Ultrahigh-Q tunable whispering-gallery-mode microresonator. Phys. Rev. Lett. **103**, 053901 (2009)
54. A. Rauschenbeutel et al., Step by step engineered many particle entanglement. Science **288**, 2024 (2000)
55. A. Wallraff et al., Strong coupling of a single photon to a superconducting qubit using circuit quantum electrodynamics. Nature **431**, 162 (2004)
56. X. Maître et al., Quantum memory with a single photon in a cavity. Phys. Rev. Lett. **79**, 769–772 (1997)

57. S. Brattke, B.T.H. Varcoe, H. Walther, Generation of photon number states on demand via cavity quantum electrodynamics. Phys. Rev. Lett. **86**, 3534–3537 (2001)
58. F. Brennecke et al., Cavity qed with a bose-einstein condensate. Nature **450**, 268–271 (2007)
59. V. Vuletić, S. Chu, Laser cooling of atoms, ions, or molecules by coherent scattering. Phys. Rev. Lett. **84**, 3787–3790 (2000)
60. V. Vuletić, H.W. Chan, A.T. Black, Three-dimensional cavity Doppler cooling and cavity sideband cooling by coherent scattering. Phys. Rev. A **64**, 033405 (2001)
61. J. McKeever et al., State-insensitive cooling and trapping of single atoms in an optical cavity. Phys. Rev. Lett. **90**, 133602 (2003)
62. P. Maunz et al., Cavity cooling of a single atom. Nature **428**, 50–52 (2004)
63. J.K. Thompson, J. Simon, H. Loh, V. Vuletić, A high-brightness source of narrowband. Identical-photon pairs. Science **313**, 74–77 (2006)
64. K.M. Fortier, S.Y. Kim, M.J. Gibbons, P. Ahmadi, M.S. Chapman, Deterministic loading of individual atoms to a high-finesse optical cavity. Phys. Rev. Lett. **98**, 233601 (2007)
65. M. Keller, B. Lange, K. Hayasaka, W. Lange, H. Walther, Continuous generation of single photons with controlled waveform in an ion-trap cavity system. Nature **431**, 1075–1078 (2004)
66. G.R. Guthörlein, M. Keller, K. Hayasaka, W. Lange, H. Walther, A single ion as a nanoscopic probe of an optical field. Nature **414**, 49–51 (2001)
67. C. Russo et al., Raman spectroscopy of a single ion coupled to a high-finesse cavity. Appl. Phys. B **95**, 205–212 (2009)
68. H.G. Barros et al., Deterministic single-photon source from a single ion. New J. Phys. **11**, 103004 (2009)
69. B.B. Blinov, D.L. Moehring, L.-M. Duan, C. Monroe, Observation of entanglement between a single trapped atom and a single photon. Nature **428**, 153–157 (2004)
70. J. Volz et al., Observation of entanglement of a single photon with a trapped atom. Phys. Rev. Lett. **96**, 030404 (2006)
71. S. Olmschenk et al., Quantum teleportation between distant matter qubits. Science **323**, 486–489 (2009)
72. T. Bondo, M. Hennrich, T. Legero, G. Rempe, A. Kuhn, Time-resolved and state-selective detection of single freely falling atoms. Opt. Comm. **264**, 271–277 (2006)
73. D.F.V. James, P.G. Kwiat, W.J. Munro, A.G. White, Measurement of qubits. Phys. Rev. A **64**, 052312 (2001)
74. J. Altepeter, E. Jeffrey, P. Kwiat, Photonic state tomography. Adv. At. Mol. Opt. Phys. **52**, 105–159 (2005)
75. A. Reiserer, N. Kalb, G. Rempe, S. Ritter, A quantum gate between a flying optical photon and a single trapped atom. Nature **508**, 237–240 (2014)
76. J.L. O'Brien, G.J. Pryde, A.G. White, T.C. Ralph, D. Branning, Demonstration of an all-optical quantum controlled-NOT gate. Nature **426**, 264–267 (2003)
77. T. Legero, T. Wilk, M. Hennrich, G. Rempe, A. Kuhn, Quantum beat of two single photons. Phys. Rev. Lett. **93**, 070503 (2004)
78. T. Legero, T. Wilk, A. Kuhn, G. Rempe, Characterization of single photons using two-photon interference. Adv. At. Mol. Opt. Phys. **53**, 253 (2006)
79. T. Legero, T. Wilk, A. Kuhn, G. Rempe, Time-resolved two-photon quantum interference. Appl. Phys. B **77**, 797–802 (2003)
80. G.S. Vasilev, D. Ljunggren, A. Kuhn, Single photons made-to-measure. New J. Phys. **12**, 063024 (2010)
81. P.B.R. Nisbet-Jones, J. Dilley, A. Holleczek, O. Barter, A. Kuhn, Photonic qubits, qutrits and ququads accurately prepared and delivered on demand. New J. Phys. **15**, 053007 (2013)
82. A.J. Bennett et al., Experimental position-time entanglement with degenerate single photons. Phys. Rev. A **77**, 023803 (2008)
83. H.J. Kimble, The quantum internet. Nature **453**, 1023–1030 (2008)
84. K.S. Choi, H. Deng, J. Laurat, H.J. Kimble, Mapping photonic entanglement into and out of a quantum memory. Nature **452**, 67–71 (2008)

85. D.N. Matsukevich et al., Entanglement of remote atomic qubits. Phys. Rev. Lett. **96**, 030405 (2006)
86. B. Sun, M.S. Chapman, L. You, Atom-photon entanglement generation and distribution. Phys. Rev. A **69**, 042316 (2004)
87. D.F. Walls, G.J. Milburn, *Quantum Optics* (Springer, Heidelberg, 1994)
88. A.V. Gorshkov, A. André, M. Fleischhauer, A.S. Sørensen, M.D. Lukin, Universal approach to optimal photon storage in atomic media. Phys. Rev. Lett. **98**, 123601 (2007)
89. H.-J. Briegel, W. Dür, J.I. Cirac, P. Zoller, Quantum repeaters: the role of imperfect local operations in quantum communication. Phys. Rev. Lett. **81**, 5932–5935 (1998)
90. J. Beugnon et al., Quantum interference between two single photons emitted by independently trapped atoms. Nature **440**, 779–782 (2006)
91. P. Maunz et al., Quantum interference of photon pairs from two remote trapped atomic ions. Nat. Phys. **3**, 538–541 (2007)
92. R. Raussendorf, H.-J. Briegel, A one-way quantum computer. Phys. Rev. Lett. **86**, 5188–5191 (2001)
93. H.P. Büchler, M. Hermele, S.D. Huber, M.P.A. Fisher, P. Zoller, Atomic quantum simulator for lattice gauge theories and ring exchange models. Phys. Rev. Lett. **95**, 040402 (2005)

Chapter 2
A Highly Efficient Single Photon-Single Quantum Dot Interface

Loic Lanco and Pascale Senellart

Abstract Semiconductor quantum dots are a promising system to build a solid state quantum network. A critical step in this area is to build an efficient interface between a stationary quantum bit and a flying one. In this chapter, we show how cavity quantum electrodynamics allows us to efficiently interface a single quantum dot with a propagating electromagnetic field. Beyond the well known Purcell factor, we discuss the various parameters that need to be optimized to build such an interface. We then review our recent progresses in terms of fabrication of bright sources of indistinguishable single photons, where a record brightness of 79 % is obtained as well as a high degree of indistinguishability of the emitted photons. Symmetrically, optical nonlinearities at the very few photon level are demonstrated, by sending few photon pulses at a quantum dot-cavity device operating in the strong coupling regime. Perspectives and future challenges are briefly discussed.

2.1 Motivations

To a large extent, semiconductor quantum dots (QDs) can be considered as artificial atoms. Strong confinement of the carriers in the three direction of space results in discrete energy levels and the coulomb interaction between carriers lead to a direct correspondence between the number of carriers in the QD and the energy levels [1]. These properties make semiconductor QDs promising to implement quantum functionalities in a solid state system [2]. Like real atoms, QDs can emit single photons [3] or entangled photon pairs [4, 5]. The large oscillator strength of the transitions leads to a recombination time below one nanosecond allowing

L. Lanco · P. Senellart (✉)
CNRS-LPN Laboratoire de Photonique Et de Nanostructures, Route de Nozay, 91460 Marcoussis, France
e-mail: pascale.senellart@lpn.cnrs.fr

L. Lanco
Université Paris Diderot, Paris 7, 75205 Paris Cedex 13, France
e-mail: loic.lanco@lpn.cnrs.fr

P. Senellart
Physics Department, Ecole Polytechnique-RD128, 91763 Palaiseau Cedex, France

A. Predojević and M.W. Mitchell (eds.), *Engineering the Atom-Photon Interaction*, Nano-Optics and Nanophotonics, DOI 10.1007/978-3-319-19231-4_2

operation of the source in the GHz frequency range [6, 7]. Finally, despite the coupling of the carriers to their vibrational and electrostatic environment, the emitted photons have been shown to present high degrees of indistinguishability, up to 96 % [8–13].

The anharmonicity of the energy levels in a QD also naturally opens the route toward single photon optical non-linearities [14–16, 77]. The optical absorption of a photon resonant to a QD transition leads to the creation of an electron hole pair which spectrally shifts the resonance for the absorption of a second photon. Such non-linearities could be used to implement optical quantum logic gates, with a gate operation speed determined by the QD radiative transition rate [17].

Finally, benefiting from the semiconductor technological possibilities, it is also possible to deterministically inject a carrier in a QD, using doped structures and electrical contacts [18]. The spin of such a carrier can be used as a stationary quantum bit: while an electron spin presents coherence times in the few ns range [19, 20], a hole spin can present a coherence time as long as 200 ns [21–24]. Since the main source of spin dephasing is the hyperfine interaction, spin echo techniques applied on the nuclear spin bath have allowed greatly increasing the electron spin coherence time [25]. Spin-orbit coupling in the excited charge state of the QD results in polarization selection rules for the optical transitions making it possible to optically manipulate and measure the spin. Applying a magnetic field in the Voigt configuration has also allowed full manipulation of the spin using virtual Raman optical transition [26] and, very recently, spin photon entanglement has been reported [27, 28].

All these properties have put the QD system in an interesting position to implement integrated quantum functionalities. To go beyond the demonstrations of principle, a major challenge is to make every functionality efficient. Indeed, QD based single photon sources present the attractive features of a solid state light source with true quantum statistics but suffer from low brightness, simply because total internal reflexion limits to a few percents the photons exiting the semiconductor. Techniques must be developed to collect every photon emitted by a QD. Symmetrically, optical quantum gates relying on the QD anharmonicity will only be demonstrated if one can ensure that every photon sent on a device will interact with the QD. Several approaches are pursued to build an efficient photon-QD interface [6, 13, 29–32]. In the last few years, the most successful ones have consisting in inserting the QD in a photonic structure, either a photonic wire [29, 30] or a microcavity [13]. The first approach relies on the single mode structure of a thin nanowire to guide the light emitted by the QD. This approach presents the advantage of offering a broadband high collection efficiency and could be applied to spectrally broad single photon emitters, like NV centers in diamond and colloidal QDs. In the case of QDs, the proximity the surface has made the QD emission more sensitive to spectral diffusion phenomena [33] and dephasing of the carriers may be a limitation for obtaining indistinguishable photons.

Using cavity quantum electrodynamics has been shown to be very efficient to build such an interface, and also to reduce the effect of dephasing induced by the solid state environment [34–36]. When coupling a single QD to a confined optical mode, the light matter interaction is increased leading to an acceleration of

spontaneous emission (Purcell effect) [37] or to new light-matter mixed states (strong coupling regime) [38–40]. Together with a full control on both the emission rate and the radiation pattern of the QD emitted photons, this approach basically reduces the QD excited state lifetime hence its sensitivity to phonon assisted mechanisms [34], pure dephasing [8] and spin-flip processes [36]. First proposed in 1999 [41], the cavity based interface has faced many technological challenges regarding its implementation, because the QD must be precisely spatially and spectrally matched to the cavity mode, whereas QD mostly grow with random spatial and spectral properties.

This chapter reviews the recent progress made in this research line using a deterministic technique to couple a QD to a micro pillar cavity [42]. In the first part, we discuss the physics of such a cavity based interface. While the Purcell factor and coupling to mode figures of merit are commonly discussed, we show that other parameters are critical for making the interface efficient.We also briefly describe the technology we have developed to have a full control of the devices. In a second part, we review the progresses we have made in terms of fabrication of quantum light sources: brightness, indistinguishability of the emitted photons, purity of the single photon emission, electrically controlled sources. We also briefly present a first application using a QD based bright source to implement an entangling quantum logic gate. In a third part, we present a study of the giant optical non-linearity for a QD-pillar device operating in the strong coupling regime. We further show that such a device allows monitoring single quantum events at the microsecond time scale. In the last part, we discuss future challenges and objectives: spin-photon interface, scalability, limitations or possibilities provided by the solid state environment.

2.2 Efficient Quantum Dot-Photon Interfacing

2.2.1 Basics of Cavity-QED in a Quantum Dot-Micropillar Device

Figure 2.1a displays a sketch of a typical QD-pillar cavity system. Fabricating such a device requires, first, to fabricate a planar sample through molecular beam epitaxy: a layer of self-assembled InGaAs QDs is embedded into a GaAs cavity, sandwiched between two-distributed Bragg mirrors (alternating GaAs/AlGaAs layers). These Bragg mirrors induce the confinement of light in the vertical direction. Lateral confinement is then obtained by etching a cylindrical micropillar, with a typical diameter of a few microns: a confined cavity mode is obtained with a cavity mode frequency ω_C. In parallel, confinement of carriers in an InGaAs quantum dot leads to discrete energy levels, with a transition at frequency ω_{QD} between the QD ground state ($|\text{ground}\rangle$) and its first excited state ($|\text{excited}\rangle$). A maximal light-matter interaction is obtained when $\omega_{QD} \approx \omega_C$ (spectral matching), and when the InGaAs quantum dot is located at a maximum of the cavity mode intensity, i.e. at the center of the micropillar for the fundamental mode (spatial matching).

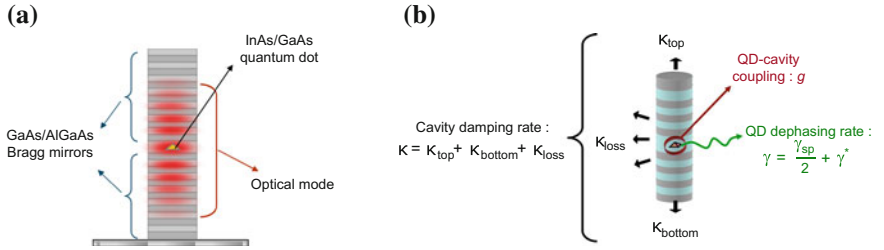

Fig. 2.1 **a** Typical structure of a quantum-dot/micropillar system. **b** Physical quantities describing the device behavior

The important physical quantities governing the physics of such a cavity-QED device are sketched in Fig. 2.1b:

- The **QD-cavity coupling strength** g: it describes the coherent interaction between the QD optical transition and the confined cavity mode. More precisely, it describes the rate at which a photon in the confined mode can be coherently converted into an electron-hole pair in the quantum dot, and vice-versa.
- The **cavity damping rate** κ: it describes the incoherent dissipation associated to photons escaping the cavity. This damping rate is given by the sum of several contributions, through $\kappa = \kappa_{\text{top}} + \kappa_{\text{bottom}} + \kappa_{\text{loss}}$. In the latter expression κ_{top} and κ_{bottom} are the damping rates associated to photons escaping through the top and bottom mirrors, while κ_{loss} is the damping rate associated to unwanted leakage through the unperfect micropillar sidewalls.[1]
- The **QD decay rate** γ_{sp}: it describes the rate of the unwanted spontaneous emission of photons outside the cavity mode (as opposed to emission in the confined cavity mode, which is the desired emission channel).
- The **QD pure dephasing rate** γ^*: it describes the rate at which the QD loses its coherence through pure dephasing processes. The total QD dephasing rate, denoted γ, is then the sum of a lifetime-limited contribution and of this pure dephasing contribution γ^*, through: $\gamma = \frac{\gamma_{sp}}{2} + \gamma^*$.

The objective for a QD-cavity device is to increase the strength of the coherent coupling g, as compared to the incoherent processes described by κ and γ. In this respect, two regimes are usually introduced in cavity-QED:

- The *strong-coupling regime* [43], where g is higher than both $\kappa/4$ and $\gamma/4$. In such a case, if the QD is in its excited state at a given time, it will be able to coherently emit a photon, absorb it, reemit it, reabsorb it, and so on, before dissipation occurs. In quantum words, the system experiences a Rabi oscillation at frequency g between two states: $|\text{excited}\rangle \otimes |0 \text{ photon}\rangle$ and $|\text{ground}\rangle \otimes |1 \text{ photon}\rangle$.

[1] We note that our cavity damping rate κ is an intensity damping rate, whereas other references define κ as a field damping rate: there is a factor 2 difference between these two possible definitions.

- The *weak-coupling regime* [37], where g is smaller than either $\kappa/4$ or $\gamma/4$. In such a regime dissipative processes are faster than the coherent evolution, and therefore no Rabi oscillations can be observed.

Both the weak and the strong-coupling regimes provide a wide range of possibilities for quantum physics applications. For instance, large values can be obtained for the QD emission rate in the confined mode, denoted Γ, which is given by $\Gamma = \frac{2g^2}{\kappa}$ in the weak-coupling regime [44]: this emission rate can be significantly higher than the emission rate γ_{sp} outside the cavity mode, ensuring the emission of easily collectable photons (see Sect. 2.3). A well-known figure of merit in cavity-QED is thus the Purcell factor $F_p = \frac{\Gamma}{\gamma_{sp}}$ [37].[2] Because γ_{sp} is fixed by the properties of the QD material, optimizing the Purcell factor F_p requires increasing the coupling strength g while at the same time decreasing the cavity damping rate κ. The optimization of κ requires a significant number of GaAs/AlGaAs pairs in each Bragg mirror (typically more than 16 pairs in each mirror, to reach quality factors above a few thousands) and minimizing sidewall losses κ_{loss}, while the optimization of g requires etching micropillars with small mode volumes and thus small diameters (typically less than a few microns) [39]. On top of that, the spectral matching condition ($\omega_{QD} \approx \omega_C$) and the spatial matching condition (QD at the micropillar center) also have to be fulfilled. The following section describes how both these requirements can be deterministically achieved with a specific in-situ lithography technique [42].

2.2.2 Deterministic QD-Cavity Coupling Through In Situ Lithography

Since 2005, many groups have worked on the deterministic coupling between a single QD and a cavity mode, using either top-down [42, 45] or bottom-up approaches [46, 47]. The first technological challenge, regarding this implementation, comes from the fact that QDs grow with random spatial locations on a planar surface (as is, for instance, the bottom mirror of a Bragg cavity). It is thus most probable, that, for a given quantum dot inside a randomly-etched micropillar, the QD location will not be at the maximum of the electromagnetic field. The second technological challenge comes from the wide inhomogeneous spreading of the QD transition frequencies ω_{QD}, on a spectral range corresponding to a few tens of nanometers. In comparison, temperature adjustments allow tuning of the spectral mismatch $\omega_{QD} - \omega_C$ in a spectral range corresponding to approximately one nanometer only (for a typical temperature variation range between 4 and 50 K). For a randomly-etched micropillar, the overall probability to find a spectrally matched QD at its center is thus of the order of 10^{-3}.

[2] The Purcell Factor is usually defined as the ratio between the emission rate in the cavity mode, Γ, and the emission rate for a quantum dot in bulk GaAs, γ_{bulk}, but in a micropillar device γ_{sp} is usually equal to γ_{bulk}.

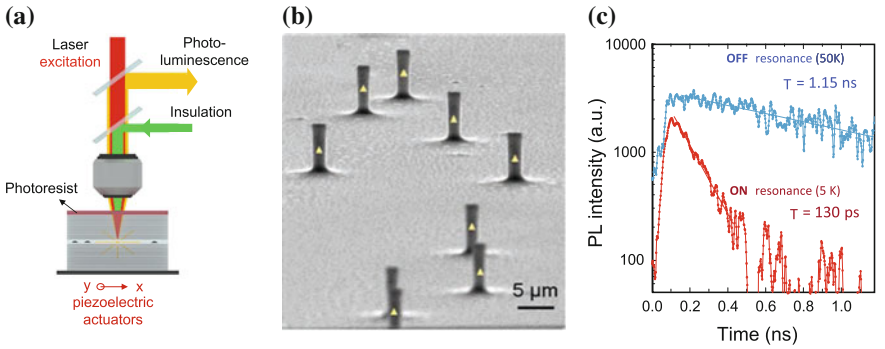

Fig. 2.2 **a** Principle of in situ lithography. **b** SEM image of several deterministically-coupled micropillars. **c** Experimental demonstration of the Purcell effect with a deterministically-coupled pillar

Standard dry etching of micropillars, starting from a planar Bragg cavity sample, requires a lithography step allowing to first define the positions and sizes of the micropillars. In the *in situ lithography* technique developed in 2008 [42], this step is performed inside a low-temperature cryostat. As sketched in Fig. 2.2a, the planar sample is spin-coated with a positive photoresist and brought to low temperature; a 850 nm laser line is then used to excite the QD emission without exposing the resist. The emitted photoluminescence is analyzed with a spectrometer, allowing one to select a QD emission line and measure its intensity. Mapping this QD emission intensity as a function of the QD position, within the focused laser beam, allows measuring the QD position with 50 nm accuracy. A second laser, at 532 nm, spatially superimposed to the 850 nm one, is then used to expose a disk centered on the QD. Furthermore, the diameter of the exposed disk is adjusted in order to tune the micropillar diameter; this, in turn, allows tuning the pillar fundamental mode frequency ω_C and matching it to the QD emission frequency ω_{QD}. The exposed disk is later used as a mask to etch the micropillar around the selected QD. This step is repeated as many times as desired for different QDs, so that one can fabricate many optimally coupled QD-pillar cavities on a single wafer, as illustrated in Fig. 2.2b.

A typical demonstration of the Purcell effect obtained with such devices is displayed in Fig. 2.2c. When the QD emission frequency ω_{QD} is tuned off resonance from the mode frequency ω_C, emission in the confined mode remains negligible, and the QD emission lifetime is mainly governed by γ_{sp}. On the contrary, when ω_{QD} is tuned on resonance with ω_C, emission in the confined mode becomes prominent: the QD emission lifetime is given by $\Gamma + \gamma_{sp} = (F_p + 1)\gamma_{sp}$. From the lifetime measurements displayed in Fig. 2.2c a Purcell factor $F_p = 7.8$ is deduced.

2.2.3 Critical Parameters: Beyond the Purcell Factor

Controlling the QD emission rate is one thing; another is to take advantage of this control in order to develop a really efficient QD-photon interface. Such an interfacing must, ideally, go both ways: transfer of information from an incident photon to a QD, and from a QD to an extracted photon. The perspectives offered by an efficient QD-photon interface are very wide, as will also be discussed in the last section of this chapter (Sect. 2.5). In the following we will mainly focus on two major aspects of QD-photon interfacing: the development of ultrabright sources of indistinguishable single photons [13] (Sect. 2.3) and the demonstration of an optical nonlinearity with few-photon pulses [14] (Sect. 2.4). In the former application, the QD-pillar device is used to *emit* single photons with specific properties. In the latter, it is used to *receive* incident photons, and subsequently transmit or reflect them, depending on the QD state. Here we discuss the critical parameters which characterize the quality of a QD-pillar device for both applications.

As regards photon emission, quantum communication applications ideally require deterministically-triggered emission of indistinguishable single photons. One thus has to control at the same time:

- The *fraction of photons emitted in the mode*, denoted β. Indeed, only photons emitted in the confined mode can be efficiently collected through the cavity top mirror. Γ being the emission rate in the mode, and γ_{sp} the emission rate outside this mode, the fraction β is given by $\beta = \frac{\Gamma}{\Gamma+\gamma_{sp}}$, i.e. $\beta = \frac{F_p}{F_p+1}$ with F_p the Purcell factor defined above. A large Purcell factor is required to obtain $\Gamma \gg \gamma_{sp}$, i.e. emission in the mode with a fraction β close to unity.
- The *single-photon wavepacket indistinguishability*, usually denoted $\frac{T_2}{2T_1}$. This is a figure of merit indicating if the single-photon wavepacket is close to the Fourier-transform limit, where the photon coherence time T_2 equals twice its lifetime T_1. In our case $T_1^{-1} = \Gamma + \gamma_{sp}$ (sum of the emission rates into and outside the confined mode), while $T_2^{-1} = \frac{\Gamma+\gamma_{sp}}{2} + \gamma^*$ also includes the pure dephasing described by γ^*. A large Purcell factor is usually required to obtain $\frac{\Gamma}{2} \gg \gamma^*$, i.e. negligible dephasing and thus a wavepacket close to the Fourier-transform ideal limit.

These two separate conditions $\Gamma \gg \gamma_{sp}$ and $\frac{\Gamma}{2} \gg \gamma^*$ can be fulfilled both at the same time if $\frac{\Gamma}{2} \gg \gamma$, where γ is the total QD dephasing time previously defined: $\gamma = \frac{\gamma_{sp}}{2} + \gamma^*$. Because $\frac{\Gamma}{2} = \frac{g^2}{\kappa}$, this allows introducing a fundamental quantity which is the device **cooperativity**, denoted C:

$$C = \frac{g^2}{\kappa\gamma} \tag{2.1}$$

This cooperativity is a well-known figure of merit in cavity-QED, first introduced with cold atoms [48]. It compares the strength of the coherent interaction (governed by g) to that of the incoherent processes (governed by κ and γ), and indicates how

strongly the presence of the QD transition modifies the optical properties of the device.

We point out that different notations are sometimes adopted in the literature. As an example, in atom cavity-QED the pure dephasing term γ^* can be considered equal to zero, as is in chapter by A. Kuhn of this book. In such a case the spontaneous emission rate γ_{sp} is equal to twice the total dephasing rate, and the Purcell Factor (denoted f in chapter by A. Kuhn and F_p here) is equal to twice the cooperativity. We also note that with our definition, the cavity damping rate κ is an intensity damping rate, whereas it is a field damping rate in chapter by A. Kuhn: the cavity linewidth is thus equal to κ in the present chapter, but to 2κ in chapter by A. Kuhn.

Another crucial quantity to be optimized is the **top-mirror output-coupling efficiency**, denoted η_{top}:

$$\eta_{\text{top}} = \frac{\kappa_{\text{top}}}{\kappa} \tag{2.2}$$

This top-mirror output coupling efficiency gives the fraction of photons from the confined cavity mode that escape through the top mirror. This derives from the fact that the cavity damping rate is the sum of contributions from several channels: $\kappa = \kappa_{\text{top}} + \kappa_{\text{bottom}} + \kappa_{\text{loss}}$, so that $\frac{\kappa_{\text{top}}}{\kappa}$ measures the probability for escaping through the top-mirror channel. For single-photon emission applications, it is crucial to approach $\eta_{\text{top}} \approx 1$ in order to collect efficiently photons from the cavity mode: this requires an asymmetric design with a highly reflective bottom mirror (so that $\kappa_{\text{top}} \gg \kappa_{\text{bottom}}$), as well as low sidewall losses (so that $\kappa_{\text{top}} \gg \kappa_{\text{loss}}$). As will be discussed in Sect. 2.4, η_{top} also plays a crucial role in resonant excitation experiments where photons are received and then reflected or transmitted by the device.

Finally, regarding photon reception experiments, one must not forget the requirement that photons have to be injected efficiently into the fundamental cavity mode: to do so, one has to optimize the spatial overlap between the free space optical beam and the confined mode (exactly as one would do to efficiently inject light into an optical fiber). The overlap integral between these two spatial shapes gives us another figure of merit, the *input-coupling efficiency* of our experiment, denoted η_{in}. Contrary to C and η_{top}, which are related to the quality of the device technology, η_{in} is governed by the experiment and can be optimized with a careful optical alignment. Because the fundamental mode of the pillar cavity present a high overlap with a gaussian mode, η_{in} values close to unity can be obtained [49, 50].

2.3 Ultrabright Single Photon Sources

2.3.1 Why Are Bright Single Photon Sources Desirable?

Although single QDs have been shown to emit single photons as early as 14 years ago [3], most optical quantum communication and quantum computation protocols

are still mostly implemented using parametric down conversion (PDC) sources. The main reason for this is that PDC sources present the main advantage of generating highly indistinguishable photons at room temperature. Their main limitation is their photon statistic, which is at best Poissonian (for non heralded sources) and which strongly limits the operation rate of the source in order to minimize multi-photon events. Over the years, multi-photon events have been dealt with error correction protocols and the number of entangled photons has recently reached a record value of eight [51]. Yet, the low brightness and the multi photon events of PDC sources may soon put a strong barrier to the scalability of photonics quantum networks, simply because the measurement time exponentially increases with the number of photons.

A QD based single photon source, even highly indistinguishable, is not of much interest if one cannot collect more than few percents of the emitted photons, 5–10 % being the typical operation rate of non-heralded PDC sources. On the contrary, a very bright QD source of highly indistinguishable photons could have strong potential in this context. Recent progresses in the community indicate that such a source is within reach. We now present the recent progresses we made in term of QD based single photon sources for quantum information processing by inserting QDs in micro pillar cavities.

2.3.2 *Demonstration of Single Photon Sources with Record Brightness*

We define the brightness of the source as the number of collected photon per excitation pulse in the first collection lens. For a high excitation power, one can assume that at least an electron hole pair is created in the QD. The QD high quantum efficiency means that this electron hole pair will radiatively recombine with a probability close to one [52, 53]. This first step describes the photon creation efficiency. To obtain a bright source, high creation efficiency must be combined with high collection efficiency. As explained in Sect. 2.2, in the weak coupling regime, the collection efficiency is given by the coupling to the mode $\beta = \frac{F_P}{F_P+1}$ multiplied by the out coupling efficiency η_{top}. To collect all the emission from one side of the pillar, we use an highly asymmetric cavity, where the transmission of the top mirror strongly exceeds the one of the bottom one $\kappa_{\text{top}} \gg \kappa_{\text{bottom}}$. In this case, η_{top} is only limited by the side losses and is given by $\eta_{top} = \frac{\kappa_{\text{top}}}{\kappa} = \frac{Q}{Q_0}$ where Q and Q_0 are the quality factor of the pillar and planar cavities. The dashed line in Fig. 2.3a show this ratio for a typical etching process, starting from a planar cavity with $Q_0 = 3000$. During the pillar etching process, some roughness can develop on the pillar sidewalls, resulting in a decreasing Q when decreasing the pillar diameter. The corresponding β (dotted line) increases as the mode volume decreases. As a result, the collection efficiency $\eta_{top}\beta$ presents an optimum around 80 % obtained for a pillar diameter around 2–3 μm here.

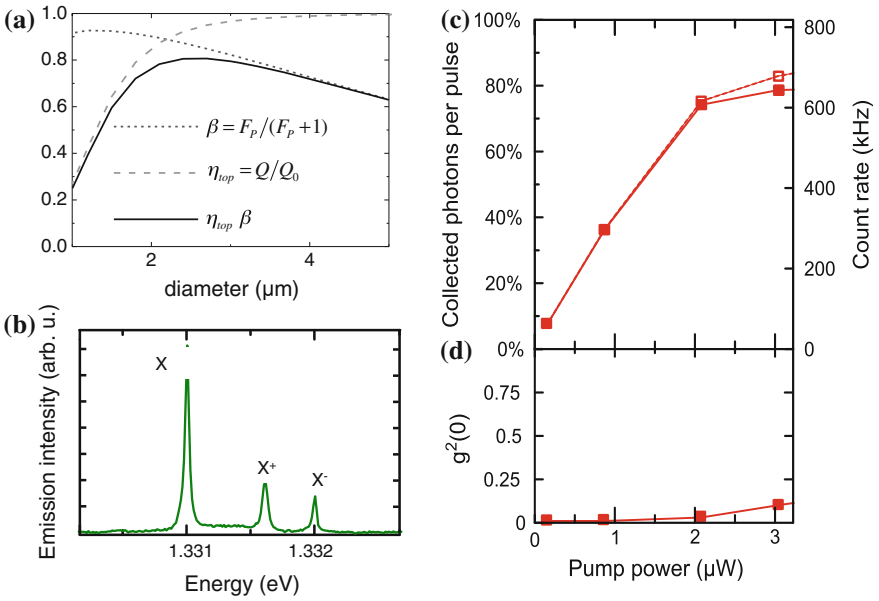

Fig. 2.3 Ultrabright single photon source. **a** *Dashed line* $\eta_{top} = \frac{Q}{Q_0}$ as a function of the pillar diameter. *Dotted line* coupling to the mode $\beta = \frac{F_P}{F_P+1}$. *Solid line* extraction efficiency $\eta_{top}\beta$. **b** Example of a QD spectrum under non-resonant excitation where several charged exciton emission lines are observed. **c** Count rate on the detector (*right axis*) and brightness (*left axis*) as a function of the excitation power. *Solid line* correspond to raw data ($\mathcal{B}$), *dashed line* is corrected from multi photon emission ($\mathcal{B}_{corr} = \mathcal{B}\sqrt{1-g^{(2)}(0)}$). **d** $g^{(2)}(0)$ as a function of the incident power. The multiphoton emission is very small at low powers, and slightly increases when higher powers are used

To reach such a high value, we need to consider the actual typical spectrum of a QD under non-resonant excitation (see Fig. 2.3b). The QD emission spectrum consists in discrete emission lines, each corresponding to a well defined charge state of the QD. Although the samples are not intentionally doped, several emission lines can be observed, the neutral exciton (X), the positively charged exciton (X^+) and the negatively charged exciton (X^-). The observation of these three lines shows that depending on the excitation cycles, the QD will be in either one of these states. To reach a creation efficiency close to one, ideally, the QD should be in only one of these states with a high probability. Gated structures can be used to control this charge state [18]. In this first demonstration, no electrical control of the source is used. We use the possibility to select the QDs presenting only a single emission line during the in-situ lithography process.

Several dozens of sources are therefore fabricated selecting QDs with a bright single emission line and spectrally matched to pillar cavity mode with diameter around 2–3 μm. The source brightness is measured using a simple experimental setup consisting of a collection objective, mirrors and cubes and a spectrometer coupled to

an avalanche photo diode (APD). Each optical component transmission or detection efficiency has been carefully measured using an attenuated pulsed laser at the QD emission wavelength. Figure 2.3c presents the number of counts measured on the APD as a function of a pulsed excitation power at 82 MHz. At high power, when the probability to create at least an electron hole pair is close to one, a 0.65 MHz count rate is measured on the detector. Taking into account the overall setup efficiency of 0.97 %, this corresponds to a brightness around $\mathscr{B} = 83 \pm 8\,\%$. The purity of the single photon source is also measured through photon correlation measurements (Fig. 2.3d). A very low $g^{(2)}(0)$ below 0.05 is observed up saturation. The corrected brightness $\mathcal{B}_{corr} = \mathcal{B}\sqrt{1 - g^{(2)}(0)}$ amounts to $78 \pm 8\,\%$, a record value for a single photon source. Brightness ranging between 60 and 79 % have been obtained in this first generation sample, with $\eta_{top} \approx 1$ and $\mathcal{B} \approx \beta$, with Purcell factors ranging in the 2–3.5 range. In a new generation of sample, similar values have been obtained using an adiabatic design for the cavity as proposed in [54]. Such a design reduces the effect of sidewall losses, allowing to maintain higher quality factors for smaller pillar diameters. Brightness in the $75 \pm 7\,\%$ range are obtained with $\beta \approx 1$ and $B \approx \eta_{top}$, with Purcell factors around 10. In between these two regimes, i.e. with slightly smaller F_P, brightnesses in the 90 % range should be reached.

2.3.3 Purity of the Single Photon Emission

While the QD emission usually presents a quantum statistic with $g^{(2)}(0) < 0.5$, the observed values for the second order autocorrelation function $g^{(2)}(0)$ can significantly vary from one device to another and from one measurement to another on the same device. In the literature, two phenomena are mainly proposed to explain the residual $g^{(2)}(0)$: multiple capture processes [55] and cavity feeding effects [56–58]. We now discuss these various phenomena and show that only recapture processes affect the single photon purity for deterministically coupled devices and how one can systematically obtain a nice single photon purity with the appropriate excitation conditions.

When increasing the excitation power, some emission background is sometimes observed together with the discrete emission lines of the QD [59]. Because of the strong phonon and coulomb interaction with their solid state environment, few percent of QD emission is emitted on a broad spectral range. When the QD is in a cavity, this broad emission is enhanced by the cavity resonance, leading to the so called cavity feeding effect, namely the observation of an emission at the cavity resonance, even when no QD optical transition is resonant to the cavity. When several QDs are inserted in the device, the emission at the cavity mode energy can arise from several spectrally non-resonant QDs. Such emission at the cavity energy can significantly decrease the single photon purity.

However, we show that when a single QD is coupled to the cavity line, cavity feeding effects do not explain a bad single photon purity. The emission spectrum of

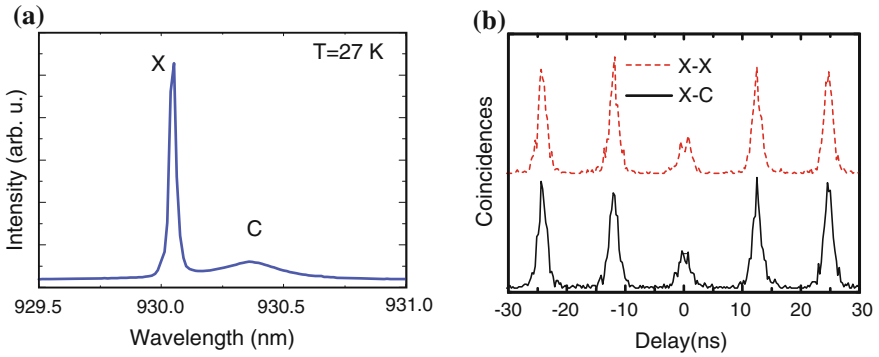

Fig. 2.4 Origin of the cavity emission line. **a** Spectrum of a deterministically coupled QD-pillar device for a non-zero detuning between the QD exciton line and the cavity resonance. Two emission lines are observed: the D exciton line and a emission line close to the cavity resonance. **b** Photon correlation measurements. *Red* auto-correlation of the exciton line. *Black* cross correlation between the exciton and cavity line

a deterministically coupled QD device when the QD resonance is not matched to the cavity line is presented in Fig. 2.4a. Two emission lines are observed, one corresponding to the QD resonance, the other close to the cavity resonance. Figure 2.4b. presents the measured auto correlation function of the exciton line where $g^{(2)}_{X,X}(0) \approx 0.4$. The same value is observed for the cross correlation between the exciton and the cavity line $g^{(2)}_{C,X}(0) = g^{(2)}_{X,X}(0)$. If the cavity mode arised from several QD emission lines then $g^{(2)}_{C,X}(0) > g^{(2)}_{X,X}(0)$. This observation shows that the cavity like emission arises from the very same QD line and can be accounted for by the phonon sidebands. It cannot explain the bad single photon purity illustrated here.

To explain the bad single photon purity presented here, Fig. 2.5 recalls the main mechanisms involved in the single photon generation for a QD system pumped non-resonantly. A pulsed non-resonant excitation creates a population of carriers n_{QW} in the wetting layer or GaAs barriers. These carriers recombine radiatively or non-radiatively with a rate r_{QW} or are captured in the QD with a rate r_{cap}. Assuming that there is only a single confined exciton state in the QD, the QD exciton and biexciton states radiatively recombine with rates r_X and r_{XX}. The guarantee for a good single photon source is that when the QD exciton recombines, there are no carriers left in the barriers that can be captured in the QD, namely that $r_X, r_{XX} \ll r_{QW}, r_{cap}$. As a result, several mechanisms can degrade the single photon purity.

On one hand, a very high quality barrier where carriers can spatially diffuse on long time and spatial scales would decrease r_{QW}, r_{cap}. Increasing temperature can also increase the lifetime of the carriers in the barrier. On the other hand, shortening the exciton radiative lifetime should also reduce the single photon purity under non-resonant pumping. This is what is evidenced in Fig. 2.5. $g^{(2)}_{X,X}(0)$ is plotted as a function of temperature (bottom scale) corresponding to a detuning with the cavity mode (top scale). These measurements are taken for an excitation power close to saturation. High value for $g^{(2)}_{X,X}(0)$ are observed for the whole temperature range.

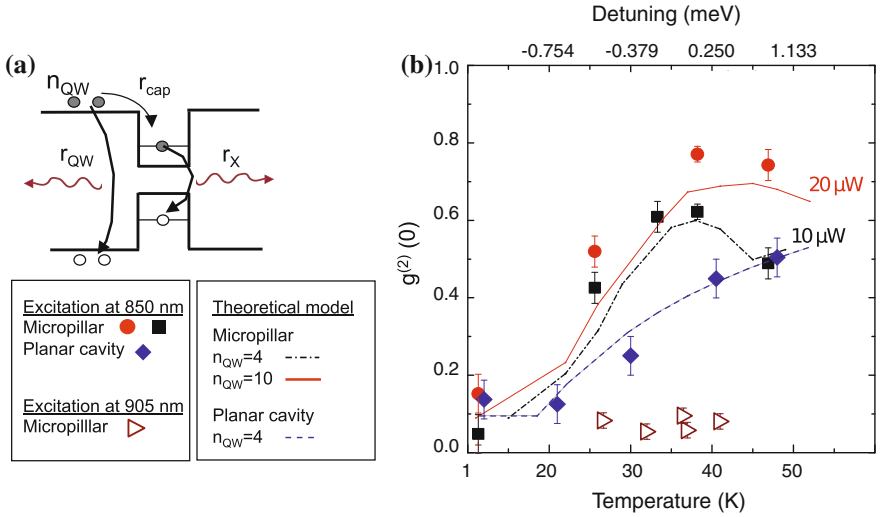

Fig. 2.5 Influence of multiple capture processes on the single photon emission. **a** Schematics of the processes involved in the QD single photon emission under on resonant excitation (see text). **b** Exciton auto-correlation function under non-resonant excitation as a function of the temperature for a QD in a pillar cavity (*circles* and *squares*) and planar cavity (*diamonds*). *Symbols* are experimental data, lines theoretical predictions detailed in [60]. *Triangles* Exciton auto-correlation function under quasi-resonant excitation. For the QD in the pillar device, the detuning from the cavity mode is indicated on the top scale

As a reference, the $g^{(2)}_{X,X}(0)$ for a QD in the planar structure (not experiencing Purcell effect) is shown; a continuous degradation of the single photon purity is observed increasing temperature, because of a decreased of r_{QW}, r_{cap}. For the QD in the cavity, the single photon purity is further degraded when the QD is brought in resonance with the cavity mode, increasing r_X.

Because the single photon purity is degraded by multiple capture mechanisms, a good single photon purity can be obtained by a direct creation of the carriers inside the QD: the relaxation of carriers between confined energy levels is very efficient and hardly temperature dependent. This is what is demonstrated with the open symbols in Fig. 2.5b: a very good single photon purity, with $g^{(2)}_{X,X}(0) < 0.08$ is observed on the whole temperature and detuning range.

2.3.4 *High Indistinguishability Through a Control of the QD Environment*

Chapter by Schneider, Gold, Lu, Höfling, Pan and Kamp recalls the requirements for obtaining indistinguishable photons, namely the photons should be identical in

polarization, energy, spatial and temporal mode. Finally, the most demanding requirement concerns the emission of single photons with a Fourier transform limited spectrum. This last requirement immediately brings the question of environment induced dephasing for an emitter in a solid state system. Several mechanisms can limit the photon indistinguishability. Coupling with acoustic phonons leads to the appearance of phonon sideband emission [61–63], while coupling with optical phonons induces pure dephasing of the zero phonon line. Moreover, charges in the QD surrounding (either fluctuating charges in traps or optically created charges in the barrier) create a fluctuating electric field, leading to a Stark induced fluctuation of the emission energy. Depending on the relative time scale between the charge fluctuations and the exciton radiative recombination, this charge noise will result in a homogeneous broadening (pure dephasing) or an inhomogeneous one (spectral diffusion) [64]. Finally, obtaining indistinguishable photons also depends on the dynamics of carrier relaxation and emission in the system. Very high pumping, which creates many electron hole pairs in the QD, delay the emission of the exciton [65] and lead to a strong jitter in the QD emission dynamics.

Despite these possible limitations, QDs have been shown to emit indistinguishable photons as early as 2002 [8], with mean wave packet overlap as large as 80 %. Since then, many works have reported on the emission of indistinguishable photons [9–12]. In most works, the indistinguishability is below 80 % and the origin of this limitation is not clear. Very recently, pure resonant excitation has allowed the observation of indistinguishability of 96 % [12], bringing the QD source close to the quality of PDC sources. Yet, this was obtained for a low source brightness.

We have studied the indistinguishability of a QD-pillar single photon source as a function of the source brightness. When creating the carriers in the surrounding barriers (Fig. 2.6, green symbols), a high photon indistinguishability, characterized by a mean wavepacket overlap $M = 0.82$, is observed at a source brightness of 30 %. When increasing the source brightness, M continuously decreases: additional carriers optically created in the QD surrounding create a fluctuating electrostatic environment. To circumvent this effect, carriers are directly created in the excited state of the QD (red symbols). Surprisingly, the source indistinguishability is even lower, independently of the source brightness. Considering these two sets of measurements, we deduce that under low power non-resonant excitation, non-resonantly created carriers fill deep traps around the QD and stabilize its electrostatic environment. To combine high brightness with high indistinguishability, we have therefore used a two color excitation scheme (blue symbols): a strong pumping directly creating excitons into an excited QD state together with a weak non-resonant pumping to fill traps. Doing so, we demonstrate a mean wavepacket overlap as high as 92 % (82 %) for a source brightness of 53 % (65 %). These values are close to the best values ever reported on QD system, combined here with a high brightness.

Finally, we analyze the dynamics of the indistinguishability by performing a temporal post selection of the emitted photons. Figure 2.7 presents the indistinguishability of the source as a function of the time bin for the analysis. This temporal post

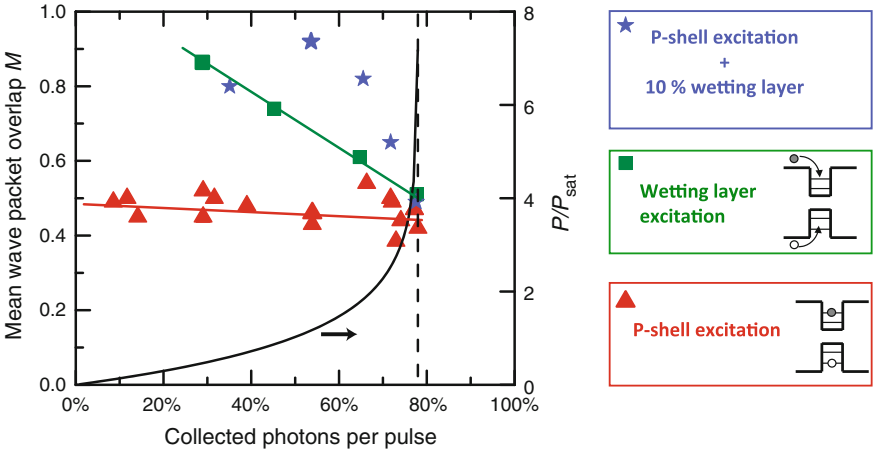

Fig. 2.6 Brightness and indistinguishability. Mean wave packet overlap characterizing the indistinguishability of successively emitted photons as a function of the source brightness. The *right scale* shows the excitation power normalized to the saturation excitation power corresponding to a given brightness. *Triangles* quasi resonant excitation in the QD. *Squares* excitation in the wetting layer. *Stars* two color excitation scheme: quasi resonant excitation (90 % of the time integrated count rate) combined with wetting layer continuous wave excitation (10 % of the time integrated count rate)

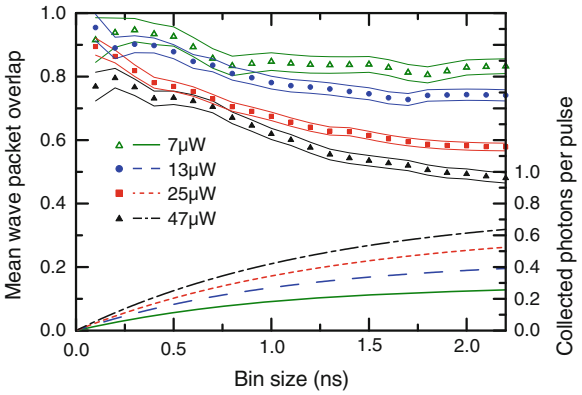

Fig. 2.7 Brightness and post temporal selection. Measured photon mean wave packet overlap as function of the time bin size of detection for three excitation powers in the wetting layer. The *lines* indicate the experimental error bars. The brightness corresponding to the time bin size is shown on the *right scale*

selection reduces the brightness of the source as indicated on the right axis. The measurements presented here correspond to an excitation in the wetting layer. For all excitation powers, a higher indistinguishability is observed at shorter time delay: the earlier the photon is emitted after the excitation pulse, the less the exciton has experienced dephasing.

2.3.5 *Electrically Controlled Sources*

Inserting the QD in a doped structure and applying an electric field is a very efficient tool in the context of building a solid state quantum network. It first allows deterministically injecting an electron or hole in the QD [18] in order to build a spin based quantum memory. It has also been used to control the coupling between the two linearly polarized exciton states and produce entangled photon pairs [66] (see chapter by Trotta and Rastelli). Applying an electric field can allow tuning the QD emission energy through the Stark effect, an interesting property to implement quantum interferences between two sources [67]. Finally, a doped structure and an applied bias around the QD layer helps stabilizing the QD charge environment and reduce charge induced dephasing.

Combining an electrical control with a good extraction efficiency is technologically challenging. Pioneer works have developed a technology consisting in planarizing a micropillar sample and defining an anular contact on top of a micropillar [68]. Another approach has consisted in using oxide aperture cavities [6]. In such structures, the carrier injection is very close to the quantum dot layer, a favorable approach to obtain fast operation of the electrical control. On the other hand, a precise control over the oxidation process is needed to control the cavity energy.

We have proposed another approach to obtain an electrical control of a QD in a cavity [69]. The cavity consists in a micropillar, connected with one dimensional wires to a larger frame, where the electrical contact is defined (Fig. 2.8a). To study the optical properties of the connected pillar cavity, a preliminary study was conducted on a high quality factor sample embedding a large density of QDs. For the same pillar diameter, the connected pillar cavity fundamental mode presents a slightly lower energy, evidencing a lower optical confinement as the field partially penetrates in the connected wires (Fig. 2.8b). Comparing the quality factor for connected versus isolated pillars for the same confinement (same mode energy), we find that while

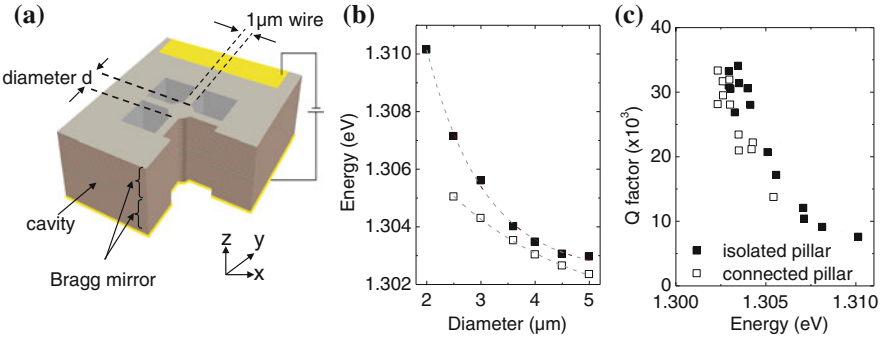

Fig. 2.8 Connected pillar cavity. **a** Schematic of the connected pillar structure used to implement electrical contacts on a cavity. **b** Energy of the connected micropillar (*open*) and isolated (*solid*) pillar fundamental mode as a function of pillar diameter. **c** Quality factor of the fundamental mode as a function of the mode energy for isolated (*solid*) and connected (*open*) pillars

connected pillar cavities present slightly lower quality factors, the latter can still reach $Q = 30{,}000$. Such high quality factors show that connected pillar cavities could be used to reach the strong coupling regime. Concerning light extraction efficiency, the slightly reduced quality factor compared to isolated pillars may indicate some additional side losses, due to light guided in the wires. However, since the out coupling efficiency depends on $\eta_{\text{top}} = \frac{\kappa_{\text{top}}}{\kappa_{\text{top}} + \kappa_{\text{bottom}} + \kappa_{\text{loss}}}$, it can still be brought close to one by adjusting the parameters so that $\kappa_{\text{top}} \gg \kappa_{\text{loss}}, \kappa_{\text{bottom}}$.

To deterministically insert a single QD in such a cavity, we have extended the in-situ lithography technique in order to write any pattern in the resist, centered on a selected QD. This requires having a control on the absolute sample position with respect to the laser beam. Using a customized attocube confocal microscope, such a control was possible with a 10 nm accuracy, using high accuracy capacitive sensors. The pillars, centered on a single QD, were connected to a 25 μm × 25 μm frame, the latter being connected to a 100 μm wide mesa. After resist development, metallic deposition and etching of the pillar structure, a second standard optical lithography step was used to define contacts on the large mesa structure. Figure 2.9a presents an optical microscope image of a final device, where two connected pillars are visible on the right side. Figure 2.9b presents emission spectrum obtained under optical excitation when no bias is applied. The cavity line is slightly detuned from both the

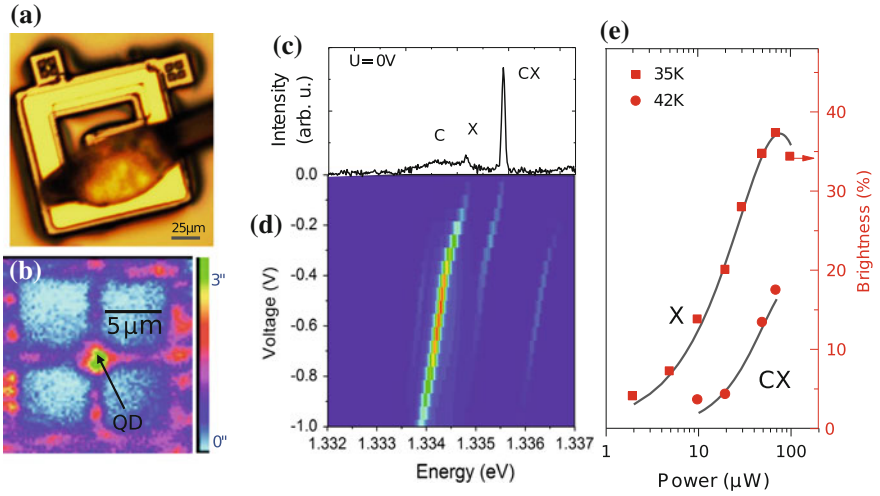

Fig. 2.9 Electrically tunable bright single photon source. **a** Microscope image of a device. The electrical contact and bonding are realized on a 100 μm wide mesa. The pillars are connected to a 25 μm wide frame overlapping the large mesa. **b** Emission scan of the device (the sample is moved with respect to excitation and confocal detection line). The emission is selected in a 5 nm wide spectral range around the cavity resonance. **c** Emission spectrum without applied bias. The cavity (C), exciton (X) and charged exciton (X) lines are seen. **d** Emission intensity as a function of applied bias. **e** Brightness as a function of excitation power for the X line (*squares*) and CX line (*circles*). Lines are guides to the eyes

neutral X and charged CX exciton QD lines. The present structure embeds a p-i-n junction with a QD layer surrounded by barriers so as to allow the Stark tuning of the QD optical transition. By increasing the voltage, the QD transition can be tuned over a 1.4 meV spectral range, throughout the cavity resonance (Fig. 2.9). Finally, an emission map of the device where the emission in a 5 nm spectral range around the cavity mode is selected is presented in Fig. 2.9d. The intense emission of the QD centered in the connected pillar is clearly evidenced, showing the Purcell enhanced extraction efficiency.

As for single pillars, a calibrated experimental setup is used to measure the single photon source brightness (Fig. 2.9e). In this experiment, the charge state of the QD was not well controlled, so that the QD under study is in the neutral and charged exciton state with 0.69 and 0.31 relative probabilities. When bringing either neutral or charged exciton lines in resonance with the cavity mode, the measured brightness reaches respectively 37 ± 7 and 17 ± 6 %. This corresponds to an extraction efficiency of 54 %, limited here by the low Purcell factor of the source ($F_P = 0.8 \pm 0.08$, $\eta_{\text{top}} \approx 1$, $\beta = 0.44$).

In this first technological realization, we demonstrated the electrical tunability for a bright single photon source. With a different doping structure, the same technology can be used to control the charge state of the QD and build a deterministic spin-photon interface. Resonant spectroscopy is currently investigated in such structures. While the charge state of the QD in cavities has been shown to be sometime unstable under resonant spectroscopy [16], preliminary tests indicate a significantly improved situation in gated structures.

2.3.6 Implementation of an Entangling CNOT Gate

To demonstrate the potential of QD based bright single photon sources for quantum information processing we have implemented an entangling controlled-NOT (C-NOT) gate [70]. Indeed, a universal quantum computer can be built with solely C-NOT gates and arbitrary local rotations, the latter being trivial in optics. A C-NOT gate flips the state of a target qubit depending on the state of a control qubit. Here the two qubits are single photons successively generated by a single QD-pillar based source with a brightness of 78 ± 7 %. The information is encoded on the polarization of the photons.

Figure 2.10a illustrates a possible implementation of an optical C-NOT gate. We first consider only the path concerning the target qubit, in a linear superposition of H and V polarization $|target\rangle_{in} = \alpha|H\rangle + \beta|V\rangle$. This polarization encoding is transformed into a path encoding using a polarizing beam splitter and a half-wave-plate. The two paths are then sent to the two inputs of a Mach-Zender interferometer (MZI). At the output of the interferometer, another half wave plate and polarizing beam splitter return from path to polarization encoding. If the phase difference between the two arms of the MZI is π, the target qubit is flipped into the $|target\rangle_{out} = \alpha|V\rangle + \beta|H\rangle$. To implement a C-NOT gate, the MZI is set to a zero phase difference between the

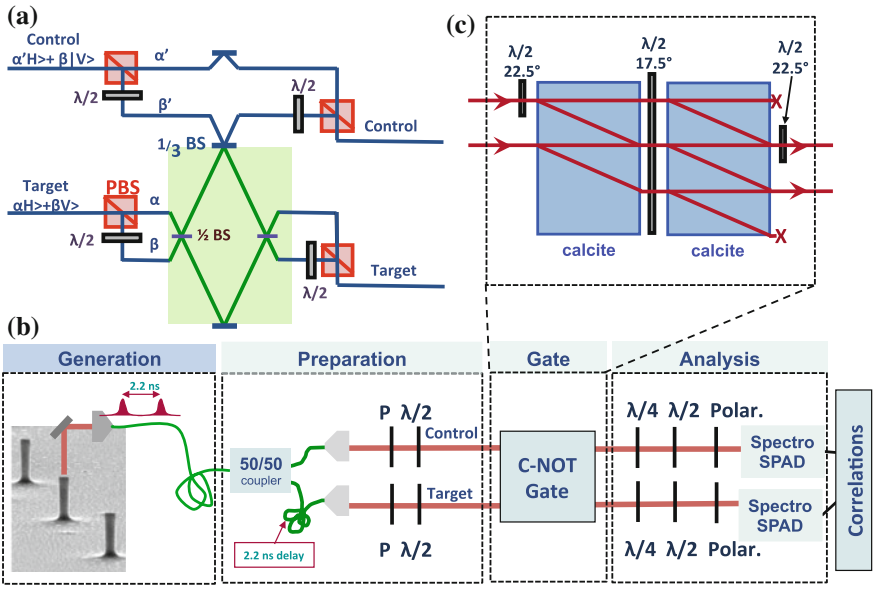

Fig. 2.10 Implementation of a C-NOT gate. **a** Schematic of a possible implementation for a C-NOT gate. **b** Experimental setup used to entangle two photons generated by a QD based single photon source using a C-NOT gate. **c** Zoom on the C-NOT gate implemented using calcite crystals and wave plates. See text for details

two arms, and the π phase shift of one arm is induced by the controlled qubit. To do so, one arm of the MZI embeds a 1/3 beam splitter. The control qubit (upper part of Fig. 2.10a) is path encoded, one path being sent on the 1/3 beam splitter of the MZI. When the control and target qubit are indistinguishable, their quantum interference results in an effective π phase shift between the two MZI arms. It can be shown that such a conceptually simple scheme acts as a quantum C-NOT gate on single photons. However, such an experimental scheme is hard to implement because it requires stabilization of the optical paths. Here we use a simpler way to implement such a gate proposed in 2003 [71] and illustrated in Fig. 2.10b. It relies on two calcite crystals implementing the path encoding and the interferometer and an internal half wave late implementing the 1/3 beam splitters.

Two photons generated by the source with a delay of 2.3 ns are coupled to a single mode fiber. The coupling efficiency into the fiber is 82 % as measured by comparing the count rate with and without the fiber coupling. The two photons are then non-deterministically split on a 50/50 fiber beam splitter and temporally overlapped using a 2.3 ns delay line on one arm of the fiber splitter. The two photons are then sent to the free space C-NOT gate setup, where waveplates before and after the gate allows controlling and analyzing the qubit polarization.

The measured truth table of the gate in the linear H and V polarization basis is presented in Fig. 2.11a together with the calculated truth table for a mean wave

packet overlap M characterizing the indistinguishability of the two photons. In the ideal case, $M = 1$, the target qubit is flipped from H to V (and vice versa) when the control qubit is set to V. The observed truth table deviates from the ideal one because the indistinguishability of the photon is not ideal. The measurements are consistent with an experimental photon overlap of $M = 0.5$. Note that this value is not the photon mean wave packet overlap as presented in Fig. 2.6 where the photon indistinguishability was deduced after correcting from the setup imperfection. Here, the raw photon wavepacket overlap is deduced from these measurements. The deduced value is consistent with ones reported earlier for a source operated at a brightness of 75 %. The probability of obtaining the correct output averaged over four possible inputs is measured to 68.4 % for a maximal source brightness. Because the photon exhibits a better indistinguishability at short time delay (Fig. 2.7), the probability of obtaining the correct output increases to 73 % for a source brightness of 17 %.

To prove the entangling capability of the gate, the control qubit is set to $|D\rangle = (|V\rangle+|H\rangle)/\sqrt{2}$, and the target qubit to $|H\rangle$. The output of an ideal gate is then the maximally entangled state $\Phi^+ = (|V, V\rangle + |H, H\rangle)/\sqrt{2}$. The fidelity of the two photon state generated experimentally is deduced by measuring the polarization of the correlation in three polarization bases [72, 73]:

$$E_{\alpha,\beta} = \frac{A_{\alpha,\alpha} + A_{\beta,\beta} - A_{\alpha,\beta} - A_{\beta,\alpha}}{A_{\alpha,\alpha} + A_{\beta,\beta} + A_{\alpha,\beta} + A_{\beta,\alpha}}$$

where $A_{\beta,\alpha}$ is the zero delay peak area in the correlation measurements for the output control photon detected in β polarization and the output target photon in α polarization. The fidelity to the Bell state is given by $F_{\Phi^+} = \left(1+E_{H,V}+E_{D,A}-E_{R,L}\right)/4$ where D,A refer to the diagonal and the anti-diagonal polarisation, and R and L to right and left circular polarizations.

For entanglement measurements, the source brightness has been set to $I_{max} = 65\,\%$ so as to benefit from a better degree of indistinguishability of the photons. The fidelity to the Bell state F_{Φ^+} is presented in Fig. 2.11b as a function of time bin, with the corresponding source brightness indicated on the right scale. For the maximum brightness, the fidelity to the Bell state is above the 0.5 limit for quantum correlations. When reducing the time bin, the fidelity increases up to 0.710 ± 0.036. The theoretical fidelity to the Bell state $F_{\Phi^+} = \frac{1+M}{2(2-M)}$ is plotted on Fig. 2.11c as a function of the mean wavepacket overlap, M. For maximum brightness, a fidelity of 0.5 correspond to M = 0.5 (circle). For a time bin of 400 ps, the measured fidelity gets as high as 0.71, corresponding to mean wavepacket overlap larger than M = 0.76 (triangle).

While we have reported the first implementation of an entangling C-NOT gate using a QD based single photon source, our study shows that a significant improvement of the indistinguishability is still needed to make QD based sources suitable for optical quantum computing. We discuss in Sect. 2.5 ways to reach such a goal.

(a)

Input	$p^*_{\|HH\rangle}$	$p^*_{\|HV\rangle}$	$p^*_{\|VH\rangle}$	$p^*_{\|VV\rangle}$
$\|HH\rangle$	1	0	0	0
$\|HV\rangle$	0	1	0	0
$\|VH\rangle$	0	0	$2\times(1\text{-}M)$	1
$\|VV\rangle$	0	0	1	$2\times(1\text{-}M)$

Input	$p^*_{\|HH\rangle}$	$p^*_{\|HV\rangle}$	$p^*_{\|VH\rangle}$	$p^*_{\|VV\rangle}$
$\|HH\rangle$	1.12(9)	α	0.01(1)	α
$\|HV\rangle$	α	0.97(8)	α	0.04(2)
$\|VH\rangle$	β	α	$2\times0.50(6)$	0.92(9)
$\|VV\rangle$	α	β	0.75(9)	$2\times0.50(7)$

$\alpha<0.005$ $\beta<0.01$

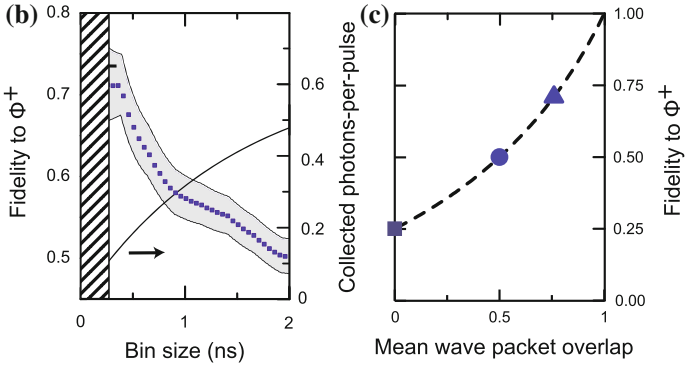

Fig. 2.11 Entangling capability of the gate. **a** theoretical (*top*) and experimental (*bottom*) truth table of the gate. M is the mean wave packet overlap of the photons. **b** Fidelity to the Bell state as a function of the bin size (*left axis*) and corresponding brightness (*right axis*). **c** Fidelity to the Bell state as a function of the mean wave packet overlap. *Line* theoretical curve, *symbols* measured point for a brightness of 50 % (*circle*) and 17 % (*triangle*)

2.4 Nonlinear Optics with Few-Photon Pulses

In this section, we now address a symmetric situation, where a QD in a cavity is studied to implement a single photon router.

2.4.1 Motivations: Photon Blockade and Photon Routing

A two-level system is, by nature, a strongly nonlinear system: it may interact with a first photon but, once the two-level transition is saturated, it will not interact with

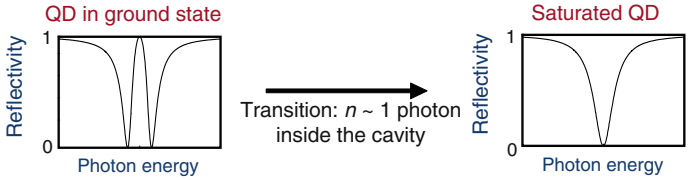

Fig. 2.12 Theoretical reflectivity spectra for a strongly-coupled cavity-QED device, in the two limiting cases of a quantum dot in the ground state and of a saturated quantum dot transition

a second one. In the absence of a cavity structure, taking advantage of this with a quantum dot is very inefficient: most of the photons incident on the quantum dot will not interact with it. It is much more useful to use a QD in a cavity-QED device, as in such a case the optical properties of the system can dramatically depend on the QD state. As an example, Fig. 2.12 describes the theoretical reflectivity spectrum of a strongly-coupled device having both high cooperativity $C \gg 1$ (see definition in 2.1) and a top-mirror output-coupling adjusted to $\eta_{\text{top}} = 50\,\%$ (for example with a symmetrical design where $\kappa_{\text{top}} = \kappa_{\text{bottom}} = \frac{\kappa}{2}$, and $\kappa_{\text{loss}} = 0$). When the quantum dot is in its ground state, the reflectivity spectrum presents two dips associated to the two eigenstates of the system, separated by the Rabi splitting $2g$. When the QD transition is saturated, on the contrary, the reflectivity spectrum presents a single Lorentzian dip associated to the cavity mode resonance. A continuous transition between these two behaviors can be obtained when, increasing the incident power, the average number of photons in the cavity approaches unity. This nonlinear effect has been named "giant optical nonlinearity" due to this extremely low photon number nonlinearity threshold [44].

How can such an effect be exploited for practical applications? The main idea is that the transmission/reflection probability for a second photon will be modified if a first one has already been incident on the device. One can use this nonlinearity to engineer quantum light from a classical laser beam: this is the *photon-blockade effect* ensuring, for instance, that no more than one photon at the same time will be transmitted by the cavity [74]. Another important device for quantum applications would be a *single-photon router*: a device so nonlinear that, if two photons are simultaneously incident on it, the first one will get transmitted and the second one reflected [75]. This would constitute a major breakthrough for quantum information and communication. Indeed, contrary to the coalescence of indistinguishable photons on a beamsplitter cube (see previous section), it would allow the engineering of a *deterministic* interaction between two photons, mediated by the cavity-QED device.

Towards this final objective of single-photon routing, several realizations have already been obtained in various types of microcavity systems. Recently, resonant spectroscopy on coupled QD-cavity devices, in the form of photonic crystals [15, 16, 76–78] or microdisks [79, 80], has demonstrated giant optical nonlinearity and fast optical switching. These works all concluded that optical nonlinearity is obtained when close to unity photon numbers are reached *inside* the cavity. However, hundreds of incident photons were required to obtain a single intracavity photon.

For future quantum applications, distinguishing between the intracavity photon number and the number of *incident photons per pulse* is crucial. An optical nonlinearity behavior at the level of one to two incident photons per pulse is needed: as described below, the current record is an optical nonlinear threshold at 8 photons per pulse recently achieved using a QD-micropillar device [14].

2.4.2 Observation of Nonlinearities at the Few-Photon Scale

The results described here have been obtained with a QD-pillar device which is in the strong-coupling regime thanks to a very high quality factor Q = 29,000, for a 2.1 μm diameter. This could be obtained using the in-situ lithography technique on a sample where the bottom and top Bragg mirrors are constituted by 36 and 32 pairs, respectively, so that they have equal reflectivities and thus equal damping rates $\kappa_{top} = \kappa_{bottom}$. A simplified sketch of a resonant excitation setup, allowing the measurement of a device reflectivity spectrum with high spectral resolution, is displayed in Fig. 2.13. The sample is placed inside a helium vapor cryostat, altogether with a focusing lens, the sample position being controlled with nanopositioners inside the cryostat. A CW or pulsed laser is injected into and reflected from the micropillar with a finely tunable photon energy $\hbar\omega$. Non-polarizing beamsplitters are used to split the incident and reflected beams: the incident power is measured with a first avalanche photodiode, a second one being used to measure the reflected power. The input-coupling efficiency η_{in} is optimized thanks to a careful optical alignment.

Figure 2.14a presents the reflectivity spectrum measured, at low incident power, at the resonance temperature $T = 35.9$ K: The system is in a pronounced strong-coupling regime, the two reflectivity dips being associated with the exciton-photon eigenstates of the system, having equal excitonic and photonic parts. Figure 2.14b presents a reflectivity spectrum measured at a different $T = 34.8$ K where the asymmetrical shape arises from the unequal excitonic and photonic parts for the exciton-photon eigenstates. A final characterization of the device behavior at low power, Fig. 2.14c shows an experimental map of the reflectivity measured as a function of both temperature and photon energy $\hbar\omega$, where the darker areas correspond to lower

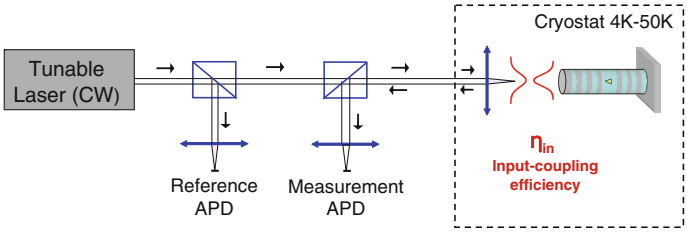

Fig. 2.13 Simplified sketch of a resonant excitation setup for reflection spectroscopy measurements

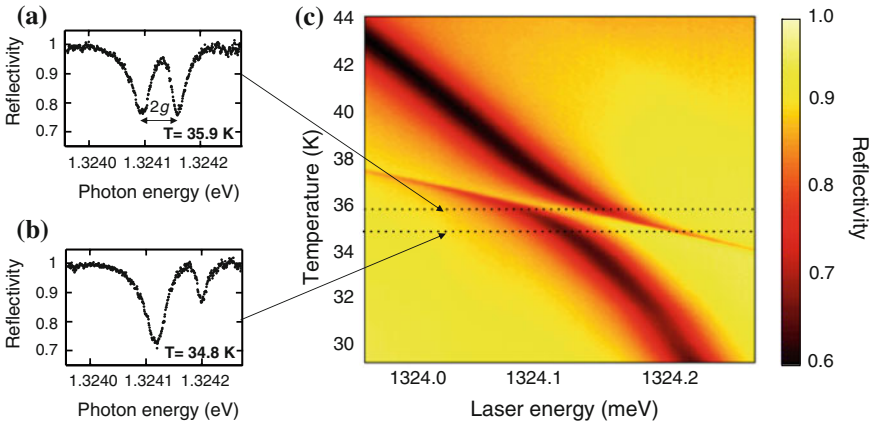

Fig. 2.14 **a** and **b** Reflectivity spectra at low incident power, for different temperatures $T = 35.9\,\mathrm{K}$ and $T = 34.8\,\mathrm{K}$. **c** Reflectivity map as a function of device temperature and laser photon energy

reflectivities. The low-reflectivity regions directly evidence the temperature dependence of the two coupled exciton-photon eigenstates, and their anticrossing when the device temperature is tuned [49].

Figure 2.15a–c illustrate the nonlinear behavior of this device under CW excitation with a varying pump power [14]. A transition is observed from the low-power regime (two reflectivity dips) to the high-power regime (single reflectivity dip). Fitting these experimental data allows determining the figures of merit of our cavity-QED device: a good cooperativity ($C = 2.5$) and a near-unity input-coupling ($\eta_{\mathrm{in}} = 95\,\%$), but a relatively low top-mirror output-coupling ($\eta_{\mathrm{top}} = 8\,\%$ instead of $50\,\%$ for an ideal device). The high cooperativity is related to the very good contrast, at low power, between the two reflectivity dips. The quite low top-mirror output coupling $\eta_{\mathrm{top}} = 8\,\%$ is the reason why the minimal reflectivity is not zero, contrary to the ideal situation described in Fig. 2.12.

Finally, Fig. 2.15d reports a reflectivity measurement under pulsed excitation, with an optimized optical pulse whose spectral width matches that of the cavity mode resonance. The device reflectivity is plotted as a function of N, the number of incident photons in each pulse. As can be seen, a nonlinearity threshold at 8 incident photons per pulse is obtained [14]. This constitutes a record value which became achievable thanks to the near-unity input coupling efficiency in our micropillar: the previous record was a threshold at 80 photons per pulse with a photonic crystal cavity [15]. Figure 2.15d also shows that the experimental data fit with the predictions of cavity-QED, using the same parameters as used with the CW experiment ($C = 2.5$, $\eta_{\mathrm{in}} = 95\,\%$, $\eta_{\mathrm{top}} = 8\,\%$).

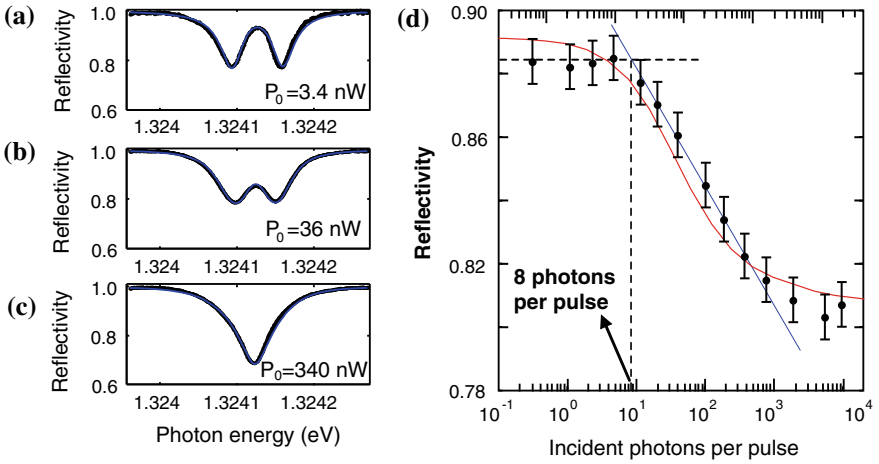

Fig. 2.15 **a**–**c** Reflectivity spectra for various incident powers, illustrating the nonlinear transition under CW excitation. **d** Pulsed excitation: reflectivity measurement displaying a record nonlinearity threshold at 8 incident photons per pulse

2.4.3 Device Optimization: Towards a Single-Photon Router?

Looking at the device figures of merit, it is clear that the improvement margin lies in the top-mirror out-coupling, which should be brought closer to the 50 % ideal value. This requires decreasing the loss damping rate and/or increasing the mirror damping rates, so that $\kappa_{\text{loss}} \ll \kappa_{\text{top}} = \kappa_{\text{bottom}}$. Reducing the sidewall losses by increasing the pillar diameter, or increasing the mirror damping rate by decreasing the number of layers in the Bragg mirrors, is a first way to do so. This, however, would require a careful optimization as it could also degrade the device cooperativity. Another possibility is to use adiabatic cavities, following Lermer et al. [54], which allows decreasing κ_{loss} without increasing the pillar diameter; it provides a way to increase both the top-mirror output coupling η_{top} and the cooperativity C (through the decrease of the total damping rate $\kappa = \kappa_{\text{top}} + \kappa_{\text{bottom}} + \kappa_{\text{loss}}$).

To illustrate the impact that such an improvement would have on the nonlinear device, Fig. 2.16a displays the theoretical device reflectivity as a function of N for increasing output couplings η_{top}. We find that a factor six increase in η_{top} decreases the expected threshold by a factor 30 [14]. As sketched in Fig. 2.16b, this is explained by the fact that the reflected beam results from the interference between two fields: a directly-reflected field and a field that has been injected into the cavity (input coupling η_{in}), has interacted with the quantum dot (cooperativity C), and has been re-extracted out through the top mirror (output coupling η_{top}). Increasing η_{top} is thus crucial to significantly increase the strength of this interference.

Furthermore, one finds that a nonlinearity threshold lower than 1 can be obtained with an optimized top-mirror output coupling, so that for $N = 1$ incident photon per

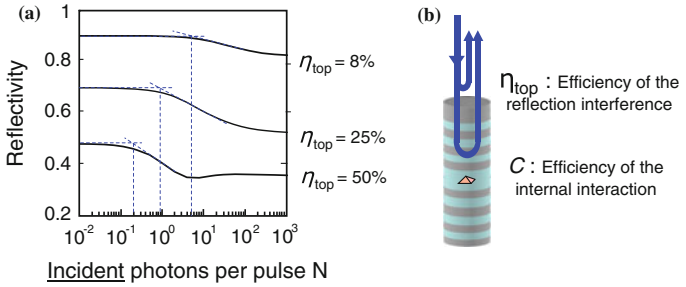

Fig. 2.16 **a** Predicted nonlinear behaviors under pulse excitation, for various top-mirror output couplings η_{top}. **b** Sketch of the interference, in the reflected beam, between the directly-reflected field and the field which has interacted with the quantum dot and been reextracted out through the top-mirror

pulse the system will be precisely in the region of highest nonlinearity. This paves the way toward the realization of single-photon routers and quantum logic gates operating with single-photon incident pulses. However, we must point out that the calculations presented here are performed with attenuated coherent pulses, rather than with true one-photon or two-photon pulses. Actually the road towards *deterministic* single-photon routers (which transmit a first photon with 100 % probability and reflect a second one with 100 % probability) is still long: it will not only require technological improvements but also experimental schemes a bit more complex than the two-level system nonlinearity [81].

2.4.4 Resonant Excitation: Application to Fast Optical Nanosensing

A quantum-dot strongly-coupled to a cavity mode is an extremely sensitive device whose optical properties can be controlled in several other ways. For instance, it can be sensitive even to very small electrostatic fluctuations, like those induced by the motion of carriers in the vicinity of the quantum dot. Indeed, a slight modification of the QD electrostatic environment can induce a small variation of the QD optical transition frequency ω_{QD}. This variation, in turn, can strongly change the device reflectivity and be readily detected with an appropriate resonant excitation setup. Using a strongly-coupled device very similar to the one used for the optical nonlinearity measurements, it has recently been possible to monitor in real-time single quantum events, corresponding to a carrier being captured and then released by a material defect. The experiment could be performed at the microsecond time scale [82]: this measurement rate is five orders of magnitude faster than for previous optics experiments of single-charge sensing, because of the close to shot-noise-limited detection setup and of the enhanced light-matter interaction. Figure 2.17a displays a

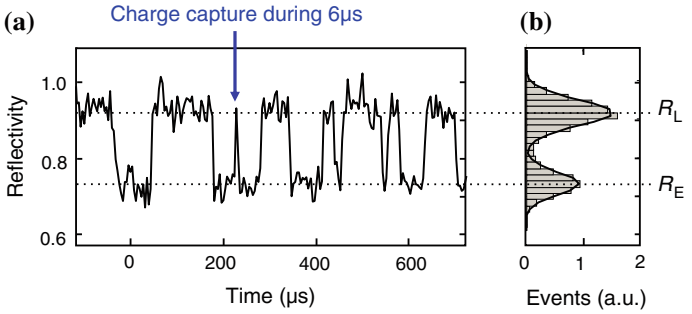

Fig. 2.17 **a** Real-time reflectivity measurement, monitoring the capture and subsequent release of individual carriers by a single material defect. **b** Histogram showing that the reflectivity randomly jumps between two values, R_L and R_E, respectively corresponding to a loaded or to an empty trap

typical real-time reflectivity signal illustrating the monitoring of single-charge jumps between two states (loaded/empty material trap). The vertical arrow, for example, indicates an event where a single charge has been captured by the material trap and then released 6 μs later. The clear distinction between the loaded and empty states is also illustrated in the reflectivity histogram of Fig. 2.17b: the overlap between the two distributions is small enough to allow identifying the system state, at any time, with a less than 0.2 % error probability. This powerful resonant excitation technique can also be applied to the real-time monitoring of other rapid quantum events such as the spin flips of a single electron or hole resident in a charged quantum dot: such an experiment would constitute the building block a spin-photon interface.

2.5 Future Challenges

The recent advances in QD based technologies make them very good candidates for fabricating the next generation of single photon sources used in optical quantum computing. While the source brightness has reached very high values, the indistinguishability of bright single photon sources needs further improvements. In this matter, controlling the electrostatic environment of the QD appears as a critical step. While such a control is more difficult to obtain in photonic structures like micropillars and nanowires where the QD is close to etched surfaces, preliminary results on connected pillar devices indicate that such a control is within reach.

A very bright source of highly indistinguishable photons would have immediate applications in optical quantum computing, where a large number of photons successively emitted by the same source would be temporally overlapped using appropriate delay lines. Some comment should however been made here: in most experiments, the indistinguishabilities of the successively emitted photons is tested with a limited time delay between the two photons (typically several nanoseconds). Indistinguishabilities on long time scales has not been tested yet. We note however that a recent

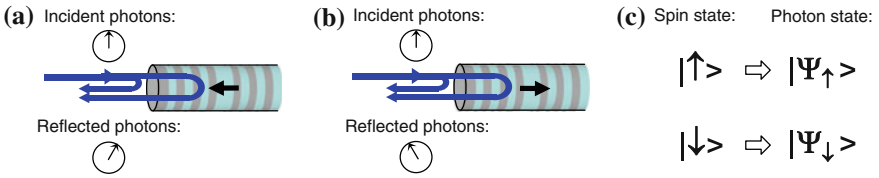

Fig. 2.18 **a** and **b** Illustration of spin-dependent polarization rotation, induced by a single quantum dot spin. **c** Mapping from a spin state to a photon polarization state

study of the charge noise on gated QDs shows Fourier transform limited linewidth on a time scale as long as 20 μs [83].

In the long term, demonstrating the possibility to use several sources is crucial for the scalability of a QD based quantum network. Quantum interferences between remote QD sources have first been demonstrated in 2010 [67, 84]. Impressive progresses have been reported recently using pure resonant excitation [85]. Similar experiments are currently conducted using deterministically coupled QD-pillar bright sources. To that end, QD with similar optical transitions energies are inserted in pillars presenting the same diameter. Preliminary results show that the Purcell effect relaxes the requirement on the spectral matching between the two sources. It can also enable quantum interferences with a single photon source presenting a very low degree of indistinguishability for successively emitted photons.

In Sect. 2.4, we saw that single photon switches based on a single QD coupled to a cavity are within reach, with a reasonable improvement of the current technology. While such optical non linearities are highly desirable, they present a limitation for applications: the photons must overlap temporally within the cavity lifetime. A promising approach to engineer an interaction between *delayed* photons is to insert a spin in a cavity: this requires a charged quantum dot, containing a resident carrier whose spin state can be used as an optically-accessible quantum memory. The basic concept at the heart of a spin-photon interface is illustrated in Fig. 2.18a, b: if an input beam with a given polarization is injected into a QD-micropillar device, the reflected output beam will be rotated clockwise or counter-clockwise, depending on the spin state [86, 87]. In quantum words (see Fig. 2.18c), the reflected photons will be in the polarization state $|\Psi_\uparrow\rangle$ if the QD spin is in state $|\uparrow\rangle$, and in the polarization state $|\Psi_\downarrow\rangle$ if the spin is in state $|\downarrow\rangle$. This is the well known Faraday/Kerr rotation effect, a phenomenon widely used to optically characterize magnetic materials, but applied here to quantum physics with a single spin.

As with the previous experiments based on resonant excitation, the device figures of merit which will govern the efficiency of the polarization rotation are the cooperativity C and the top-mirror output-coupling η_{top}. Analytical calculations show that, for realistic values of C and η_{top}, the two possible output polarization states can be made orthogonal: $<\Psi_\uparrow|\Psi_\downarrow\rangle = 0$. Such a configuration provides the possibility to reach a maximal entanglement between the state of the spin qubit and the polarization state of the output photon. Let us suppose that, before the interaction with a photon, the spin is first prepared in a coherent superposition $\frac{1}{\sqrt{2}}(|\uparrow\rangle + |\downarrow\rangle)$. Then, after

interaction with an incident photon, the bipartite spin-photon system will end up in a maximally-entangled state of the form $\frac{1}{\sqrt{2}}\left(|\Psi_{\uparrow}\rangle \otimes |\uparrow\rangle + |\Psi_{\downarrow}\rangle \otimes |\downarrow\rangle\right)$.

In contrast to the recent spin-photon entanglement demonstrations [27, 28], the interaction of a photon with such devices would allow the entanglement between a spin and a photon generated by an external source. Such a situation has been theoretically predicted to open new paradigms in quantum optics like delayed photon entanglement [88], deterministic logic gates [89] or fault-tolerant quantum computing [90]. Recent measurements show that deterministically inserting a single spin in a pillar cavity indeed allows obtaining a rotation of the polarization by few degrees depending on the spin state.

Beyond the potential for quantum information processing, QD deterministically coupled to pillar cavities also opens the possibility to explore cavity quantum electrodynamics in a regime rarely explored by the atomic community, namely the broad emitter limit. Indeed, in the founding work by Purcell as well as for all experimental realizations with real atoms, the emitter presents a monochromatic spectrum with respect to the cavity linewidth. With solid state emitters, broadening induced by the environment gives rise to new phenomena. We recently demonstrated that phonon assisted emission lead to cavity pulling phenomena for a single QD coupled to a cavity with moderate quality factor [91]. Recent developments show that phonon assisted Purcell effect can be used to obtain bright single photon sources, where strong coupling to the environment provides a built-in spectral tuning of the QD emission to the cavity resonance.

Acknowledgments The authors acknowledge their coworkers who have made all these results possible: Aristide Lemaitre, Isabelle Sagnes, Paul Voisin, Olivier Krebs, Adrien Dousse, Olivier Gazzano, Jan Suffczynski, Steffen Michaelis de Vasconcellos, Anna Nowak, Simone Luca Portalupi, Valérian Giesz, Niccolo Somaschi, Chirstophe Arnold, Vivien Loo, Justin Demory, Marcelo de Almeida, Andrew White and Alexia Auffeves. This work was partially supported by the French ANR DELIGHT, ANR MIND, ANR CAFE, ANR QDOM, the ERC starting grant 277885 QD-CQED, the CHISTERA project SSQN, the French Labex NANOSACLAY, and the RENATECH network.

References

1. J.Y. Marzin, J.M. Gérard, A. Izraël, D. Barrier, G. Bastard, Photoluminescence of single inas quantum dots obtained by self-organized growth on GaAs. Phys. Rev. Lett. **73**, 716–719 (1994). http://dx.doi.org/10.1103/PhysRevLett.73.716
2. M. Bayer, O. Stern, P. Hawrylak, S. Fafard, A. Forchel, Hidden symmetries in the energy levels of excitonic /'artificial atoms/'. Nature **405**, 923–926 (2000). http://dx.doi.org/10.1038/35016020
3. P. Michler et al., A quantum dot single-photon turnstile device. Science **290**, 2282–2285 (2000). http://dx.doi.org/10.1126/science.290.5500.2282
4. N. Akopian et al., Entangled photon pairs from semiconductor quantum dots. Phys. Rev. Lett. **8**, 130501 (2006). http://dx.doi.org/10.1103/PhysRevLett.96.130501
5. R.J. Young et al., Improved fidelity of triggered entangled photons from single quantum dots. New J. Phys. **8**, 29 (2006). http://dx.doi.org/10.1088/1367-2630/8/2/029

6. S. Strauf et al., High-frequency single-photon source with polarization control. Nat. Photonics **1**, 704–708 (2007). http://dx.doi.org/10.1038/nphoton.2007.227
7. D.J.P. Ellis et al., Cavity-enhanced radiative emission rate in a single-photon-emitting diode operating at 0.5 GHz. New J. Phys. **10**, 043035 (2008). http://stacks.iop.org/1367-2630/10/i=4/a=043035
8. C. Santori, D. Fattal, J. Vuckovic, G.S. Solomon, Y. Yamamoto, Indistinguishable photons from a single-photon device. Nature **419**, 594–597 (2002). http://dx.doi.org/10.1038/nature01086
9. S. Ates et al., Post-selected indistinguishable photons from the resonance fluorescence of a single quantum dot in a microcavity. Phys. Rev. Lett. **103**, 167402 (2009). http://dx.doi.org/10.1103/PhysRevLett.103.167402
10. R.M. Stevenson et al., Indistinguishable entangled photons generated by a light-emitting diode. Phys. Rev. Lett. **108**, 040503 (2012). http://dx.doi.org/10.1103/PhysRevLett.108.040503
11. M. Muller, S. Bounouar, K.D. Jons, M. Glassl, P. Michler, On-demand generation of indistinguishable polarization-entangled photon pairs. Nat. Photonics **8**, 224–228 (2014). http://dx.doi.org/10.1038/nphoton.2013.377
12. Y.-M. He et al., On-demand semiconductor single-photon source with near-unity indistinguishability. Nat. Nano. **8**, 213–217 (2013). http://dx.doi.org/10.1038/nnano.2012.262
13. O. Gazzano et al., Bright solid-state sources of indistinguishable single photons. Nat. Commun. **4**, 1425 (2013). http://dx.doi.org/10.1038/ncomms2434
14. V. Loo et al., Optical nonlinearity for few-photon pulses on a quantum dot-pillar cavity device. Phys. Rev. Lett. **109**, 166806 (2012). http://dx.doi.org/10.1103/PhysRevLett.109.166806
15. R. Bose, D. Sridharan, H. Kim, G.S. Solomon, E. Waks, Low-photon-number optical switching with a single quantum dot coupled to a photonic crystal cavity. Phys. Rev. Lett. **108**, 227402 (2012). http://dx.doi.org/10.1103/PhysRevLett.108.227402
16. A. Reinhard et al., Strongly correlated photons on a chip. Nat. Photonics **6**, 93–96 (2011). http://dx.doi.org/10.1038/nphoton.2011.321
17. H. Kim, R. Bose, T.C. Shen, G.S. Solomon, E. Waks, A quantum logic gate between a solid-state quantum bit and a photon. Nat. Photonics **7**, 373–377 (2013). http://dx.doi.org/10.1038/nphoton.2013.48
18. S. Laurent, et al., Electrical control of hole spin relaxation in charge tunable InAs/GaAs quantum dots. Phys. Rev. Lett. **94**, 147401 (2005). http://dx.doi.org/10.1103/PhysRevLett.94.147401
19. A. Greilich et al., Mode locking of electron spin coherences in singly charged quantum dots. Science **313**, 341–345 (2006). http://dx.doi.org/10.1126/science.1128215
20. X. Xu et al., Coherent population trapping of an electron spin in a single negatively charged quantum dot. Nat. Phys. **4**, 692–695 (2008). http://dx.doi.org/10.1038/nphys1054
21. A.J. Ramsay et al., Fast optical preparation, control, and readout of a single quantum dot spin. Phys. Rev. Lett. **100**, 197401 (2008). http://dx.doi.org/10.1103/PhysRevLett.100.197401
22. B.D. Gerardot et al., Optical pumping of a single hole spin in a quantum dot. Nature **451**, 441–444 (2008). http://dx.doi.org/10.1038/nature06472
23. K. De Greve et al., Ultrafast coherent control and suppressed nuclear feedback of a single quantum dot hole qubit. Nat. Phys. **7**, 872–878 (2011). http://dx.doi.org/10.1038/nphys2078
24. D. Brunner et al., A coherent single-hole spin in a semiconductor. Science **325**, 70–72 (2009). http://dx.doi.org/10.1126/science.1173684
25. D. Press et al., Ultrafast optical spin echo in a single quantum dot. Nat. Photonics **4**, 367–370 (2010). http://dx.doi.org/10.1038/nphoton.2010.83
26. D. Press, T.D. Ladd, B. Zhang, Y. Yamamoto, Complete quantum control of a single quantum dot spin using ultrafast optical pulses. Nature **456**, 218–221 (2008). http://dx.doi.org/10.1038/nature07530
27. W.B. Gao, P. Fallahi, E. Togan, J. Miguel-Sanchez, A. Imamoglu, Observation of entanglement between a quantum dot spin and a single photon. Nature **491**, 426–430 (2012). http://dx.doi.org/10.1038/nature11573
28. K. De Greve et al., Quantum-dot spin-photon entanglement via frequency downconversion to telecom wavelength. Nature **491**, 421–425 (2012). http://dx.doi.org/10.1038/nature11577

29. J. Claudon et al., A highly efficient single-photon source based on a quantum dot in a photonic nanowire. Nat. Photonics **4**, 174–177 (2010). http://dx.doi.org/10.1038/nphoton.2009.287
30. M.E. Reimer et al., Bright single-photon sources in bottom-up tailored nanowires. Nat. Commun. **3**, 1266 (2012). http://dx.doi.org/10.1038/ncomms1746
31. M. Munsch et al., Dielectric gaas antenna ensuring an efficient broadband coupling between an inas quantum dot and a gaussian optical beam. Phys. Rev. Lett. **110**, 177402 (2013). http://dx.doi.org/10.1103/PhysRevLett.110.177402
32. A. Laucht et al., A waveguide-coupled on-chip single-photon source. Phys. Rev. X **2**, 011014 (2012). http://dx.doi.org/10.1103/PhysRevX.2.011014
33. I. Yeo et al., Surface effects in a semiconductor photonic nanowire and spectral stability of an embedded single quantum dot. Appl. Phys. Lett. **99**, 233106 (2011). http://dx.doi.org/dx.doi.org/10.1063/1.3665629
34. S. Varoutsis et al., Restoration of photon indistinguishability in the emission of a semiconductor quantum dot. Phys. Rev. B **72**, 041303 (2005). http://dx.doi.org/10.1103/PhysRevB.72.041303
35. A. Dousse et al., Ultrabright source of entangled photon pairs. Nature **466**, 217–220 (2010). http://dx.doi.org/10.1038/nature09148
36. A. Dousse et al., A quantum dot based bright source of entangled photon pairs operating at 53 k. Appl. Phys. Lett. 97, 081104 (2010). http://dx.doi.org/dx.doi.org/10.1063/1.3475487
37. J.M. Gérard et al., Enhanced spontaneous emission by quantum boxes in a monolithic optical microcavity. Phys. Rev. Lett. **81**, 1110–1113 (1998). http://dx.doi.org/10.1103/PhysRevLett.81.1110
38. T. Yoshie et al., Vacuum rabi splitting with a single quantum dot in a photonic crystal nanocavity. Nature **432**, 200–203 (2004)
39. J.P. Reithmaier et al., Strong coupling in a single quantum dot?semiconductor microcavity system. Nature **432**, 197–200 (2004)
40. E. Peter et al., Exciton-photon strong-coupling regime for a single quantum dot embedded in a microcavity. Phys. Rev. Lett. **95**, 067401 (2005). http://dx.doi.org/10.1103/PhysRevLett.95.067401
41. J.-M. Gerard, B. Gayral, Strong purcell effect for inas quantum boxes in three-dimensional solid-state microcavities. J. Lightwave Technol. **17**, 2089 (1999). http://www.jlt.osa.org/abstract.cfm?URI=jlt-17-11-2089
42. A. Dousse et al., Controlled light-matter coupling for a single quantum dot embedded in a pillar microcavity using far-field optical lithography. Phys. Rev. Lett **101**, 267404 (2008). http://dx.doi.org/10.1103/PhysRevLett.101.267404
43. L.C. Andreani, G. Panzarini, J.-M. Gérard, Strong-coupling regime for quantum boxes in pillar microcavities: theory. Phys. Rev. B **60**, 13276–13279 (1999). http://dx.doi.org/10.1103/PhysRevB.60.13276
44. A. Auffèves-Garnier, C. Simon, J.-M. Gérard, J.-P. Poizat, Giant optical nonlinearity induced by a single two-level system interacting with a cavity in the purcell regime. Phys. Rev. A **75**, 053823 (2007). http://dx.doi.org/10.1103/PhysRevA.75.053823
45. A. Badolato et al., Deterministic coupling of single quantum dots to single nanocavity modes. Science **308**, 1158–1161 (2005). http://dx.doi.org/10.1126/science.1109815
46. P. Gallo et al., Integration of site-controlled pyramidal quantum dots and photonic crystal membrane cavities. Appl. Phys. Lett. **92**, 263101 (2008). http://dx.doi.org/dx.doi.org/10.1063/1.2952278
47. D. Dalacu et al., Deterministic emitter-cavity coupling using a single-site controlled quantum dot. Phys. Rev. B **82**, 033301 (2010). http://dx.doi.org/10.1103/PhysRevB.82.033301
48. Q.A. Turchette, R.J. Thompson, H.J. Kimble, One-dimensional atoms. Appl. Phys. B **60**, S1–S10 (1995). http://www.springerlink.com/content/t007u7mx5663042v/
49. V. Loo et al., Quantum dot-cavity strong-coupling regime measured through coherent reflection spectroscopy in a very high-q micropillar. Appl. Phys. Lett. **97**, 241110 (2010). http://dx.doi.org/10.1063/1.3527930
50. C. Arnold et al., Optical bistability in a quantum dots/micropillar device with a quality factor exceeding 200,000. Appl. Phys. Lett. **100**, 111111 (2012). http://dx.doi.org/10.1063/1.3694026

51. X.-C. Yao et al., Observation of eight-photon entanglement. Nat. Photonics **6**, 225–228 (2012). http://dx.doi.org/10.1038/nphoton.2011.354
52. J. Bleuse et al., Inhibition, enhancement, and control of spontaneous emission in photonic nanowires. Phys. Rev. Lett. **106**, 103601 (2011). http://dx.doi.org/10.1103/PhysRevLett.106.103601
53. O. Gazzano et al., Evidence for confined tamm plasmon modes under metallic microdisks and application to the control of spontaneous optical emission. Phys. Rev. Lett. **107**, 247402 (2011). http://dx.doi.org/10.1103/PhysRevLett.107.247402
54. M. Lermer et al., Bloch-wave engineering of quantum dot micropillars for cavity quantum electrodynamics experiments. Phys. Rev. Lett. **108**, 057402 (2012). http://dx.doi.org/10.1103/PhysRevLett.108.057402
55. E. Peter et al., Fast radiative quantum dots: from single to multiple photon emission. Appl. Phys. Lett. **90**, 223118 (2007). http://dx.doi.org/dx.doi.org/10.1063/1.2744475
56. M. Kaniber et al., Investigation of the nonresonant dot-cavity coupling in two-dimensional photonic crystal nanocavities. Phys. Rev. B **77**, 161303 (2008). http://dx.doi.org/10.1103/PhysRevB.77.161303
57. J. Suffczyński et al., Origin of the optical emission within the cavity mode of coupled quantum dot-cavity systems. Phys. Rev. Lett. **103**, 027401 (2009). http://dx.doi.org/10.1103/PhysRevLett.103.027401
58. M. Winger et al., Explanation of photon correlations in the far-off-resonance optical emission from a quantum-dot–cavity system. Phys. Rev. Lett. **103**, 207403 (2009). http://dx.doi.org/10.1103/PhysRevLett.103.207403
59. S. Strauf et al., Self-tuned quantum dot gain in photonic crystal lasers. Phys. Rev. Lett. **96**, 127404 (2006). http://dx.doi.org/10.1103/PhysRevLett.96.127404
60. V. Giesz et al., Influence of the purcell effect on the purity of bright single photon sources. Appl. Phys. Lett. **103**, 33113 (2013). http://dx.doi.org/dx.doi.org/10.1063/1.4813902
61. L. Besombes, K. Kheng, L. Marsal, H. Mariette, Acoustic phonon broadening mechanism in single quantum dot emission. Phys. Rev. B **63**, 155307 (2001). http://dx.doi.org/10.1103/PhysRevB.63.155307
62. I. Favero et al., Acoustic phonon sidebands in the emission line of single inas/gaas quantum dots. Phys. Rev. B **68**, 233301 (2003). http://dx.doi.org/10.1103/PhysRevB.68.233301
63. E. Peter et al., Phonon sidebands in exciton and biexciton emission from single gaas quantum dots. Phys. Rev. B **69**, 041307 (2004). http://dx.doi.org/10.1103/PhysRevB.69.041307
64. A. Berthelot et al., Unconventional motional narrowing in the optical spectrum of a semiconductor quantum dot. Nat. Phys. **2**, 759–764 (2006). http://dx.doi.org/10.1038/nphys433
65. J. Hours, P. Senellart, E. Peter, A. Cavanna, J. Bloch, Exciton radiative lifetime controlled by the lateral confinement energy in a single quantum dot. Phys. Rev. B **71**, 161306 (2005). http://dx.doi.org/10.1103/PhysRevB.71.161306
66. A.J. Bennett et al., Electric-field-induced coherent coupling of the exciton states in a single quantum dot. Nat. Phys. **6**, 947–950 (2010). http://dx.doi.org/10.1038/nphys1780
67. R.B. Patel, A.J. Bennett, J. Anthony, I. Farrer, C.A. Nicoll, D.A. Ritchie, A.J. Shields, Two-photon interference of the emission from electrically tunable remote quantum dots. Nat. Photonics **4**, 632–635 (2010). http://dx.doi.org/10.1038/nphoton.2010.161
68. T. Heindel et al., Electrically driven quantum dot-micropillar single photon source with 34. Appl. Phys. Lett. **96**, 011107 (2010). http://dx.doi.org/10.1063/1.3284514
69. A.K. Nowak et al., Deterministic and electrically tunable bright single-photon source. Nat. Commun. **5**, 3240 (2014). http://dx.doi.org/10.1038/ncomms4240
70. O. Gazzano et al., Entangling quantum-logic gate operated with an ultrabright semiconductor single-photon source. Phys. Rev. Lett. **110**, 250501 (2013). http://dx.doi.org/10.1103/PhysRevLett.110.250501
71. J.L. O'Brien, G.J. Pryde, A.G. White, T.C. Ralph, D. Branning, Demonstration of an all-optical quantum controlled-not gate. Nature **426**, 264–267 (2010). http://dx.doi.org/10.1038/nature02054

72. A.G. White et al., Measuring two-qubit gates. J. Opt. Soc. Am. B **24**, 172–183 (2007). http://dx.doi.org/10.1364/JOSAB.24.000172
73. D.F.V. James, P.G. Kwiat, W.J. Munro, A.G. White, Measurement of qubits. Phys. Rev. A **64**, 052312 (2001). http://dx.doi.org/10.1103/PhysRevA.64.052312
74. K.M. Birnbaum et al., Photon blockade in an optical cavity with one trapped atom. Nature **436**, 87–90 (2005). http://dx.doi.org/doi:10.1038/nature03804
75. D.E. Chang, A.S. Sorensen, E.A. Demler, M.D.A. Lukin, Single-photon transistor using nanoscale surface plasmons. Nat. Phys. **3**, 807–812 (2007). http://dx.doi.org/10.1038/nphys708
76. D. Englund et al., Controlling cavity reflectivity with a single quantum dot. Nature **450**, 857–861 (2007). http://dx.doi.org/10.1038/nature06234
77. D. Englund et al., Ultrafast photon-photon interaction in a strongly coupled quantum dot-cavity system. Phys. Rev. Lett. **108**, 093604 (2012). http://dx.doi.org/10.1103/PhysRevLett.108.093604
78. T. Volz et al., Ultrafast all-optical switching by single photons. Nat. Photonics **6**, 607–611 (2012)
79. K. Srinivasan, O. Painter, Mode coupling and cavity-quantum-dot interactions in a fiber-coupled microdisk cavity. Phys. Rev. A **75**, 023814 (2007). http://dx.doi.org/10.1103/PhysRevA.75.023814
80. K. Srinivasan, C.P. Michael, R. Perahia, O. Painter, Investigations of a coherently driven semiconductor optical cavity qed system. Phys. Rev. A **78**, 033839 (2008). http://dx.doi.org/10.1103/PhysRevA.78.033839
81. S. Rosenblum, S. Parkins, B. Dayan, Photon routing in cavity qed: beyond the fundamental limit of photon blockade. Phys. Rev. A **84**, 033854 (2011). http://dx.doi.org/10.1103/PhysRevA.84.033854
82. C. Arnold et al., Cavity-enhanced real-time monitoring of single-charge jumps at the microsecond time scale. Phys. Rev. X **4**, 021004 (2014). http://dx.doi.org/10.1103/PhysRevX.4.021004
83. A.V. Kuhlmann et al., Charge noise and spin noise in a semiconductor quantum device. Nat. Phys. **9**, 570–575 (2013). http://dx.doi.org/10.1038/nphys2688
84. E.B. Flagg et al., Interference of single photons from two separate semiconductor quantum dots. Phys. Rev. Lett. **104**, 137401 (2010). http://dx.doi.org/10.1103/PhysRevLett.104.137401
85. W. Gao et al., Quantum teleportation from a propagating photon to a solid-state spin qubit. Nat. Commun. **4** (2013). doi:10.1038/ncomms3744; http://dx.doi.org/10.1038/ncomms3744
86. J. Berezovsky et al., Nondestructive optical measurements of a single electron spin in a quantum dot. Science **314**, 1916–1920 (2006). http://dx.doi.org/10.1126/science.1133862
87. M. Atature, J. Dreiser, A. Badolato, A. Imamoglu, Observation of faraday rotation from a single confined spin. Nat. Phys. **3**, 101–106 (2007). http://dx.doi.org/10.1038/nphys521
88. C.Y. Hu, W.J. Munro, J.G. Rarity, Deterministic photon entangler using a charged quantum dot inside a microcavity. Phys. Rev. B **78**, 125318 (2008). http://dx.doi.org/10.1103/PhysRevB.78.125318
89. C. Bonato et al., CNOT and Bell-state analysis in the weak-coupling cavity QED regime. Phys. Rev. Lett **104**, 160503 (2010). http://dx.doi.org/10.1103/PhysRevLett.104.160503
90. M.N. Leuenberger, Fault-tolerant quantum computing with coded spins using the conditional faraday rotation in quantum dots. Phys. Rev. B **73**, 075312 (2006). http://dx.doi.org/10.1103/PhysRevB.73.075312
91. D. Valente et al., Frequency cavity pulling induced by a single semiconductor quantum dot. Phys. Rev. B **89**, 041302 (2014). http://dx.doi.org/10.1103/PhysRevB.89.041302

Part II
Light Meets a Single Atom

Chapter 3
Photon-Atom Coupling with Parabolic Mirrors

Markus Sondermann and Gerd Leuchs

Abstract Efficient coupling of light to single atomic systems has gained considerable attention over the past decades. This development is driven by the continuous growth of quantum technologies. The efficient coupling of light and matter is an enabling technology for quantum information processing and quantum communication. And indeed, in recent years much progress has been made in this direction. But applications aside, the interaction of photons and atoms is a fundamental physics problem. There are various possibilities for making this interaction more efficient, among them the apparently 'natural' attempt of mode-matching the light field to the free-space emission pattern of the atomic system of interest. Here we will describe the necessary steps of implementing this mode-matching with the ultimate aim of reaching unit coupling efficiency. We describe the use of deep parabolic mirrors as the central optical element of a free-space coupling scheme, covering the preparation of suitable modes of the field incident onto these mirrors as well as the location of an atom at the mirror's focus. Furthermore, we establish a robust method for determining the efficiency of the photon-atom coupling.

3.1 Coupling to an Atom: The Role of Dipole Radiation

3.1.1 General Considerations

When discussing the interaction of photons and atoms it is a good idea to make some simplifying approximations. First, we neglect the complexity of nature and

M. Sondermann (✉) · G. Leuchs
Department of Physics, University of Erlangen-Nuremberg, Staudtstr. 7/B2,
91058 Erlangen, Germany
e-mail: markus.sondermann@fau.de

G. Leuchs
Max Planck Institute for the Science of Light, Guenther-Scharowsky-Str. 1/Bldg. 24,
91058 Erlangen, Germany

G. Leuchs
Department of Physics, University of Ottawa, Ottawa, ON K1N 6N5, Canada
e-mail: gerd.leuchs@mpl.mpg.de

A. Predojević and M.W. Mitchell (eds.), *Engineering the Atom-Photon Interaction*,
Nano-Optics and Nanophotonics, DOI 10.1007/978-3-319-19231-4_3

assume that the atom has only two energy levels. Then, we take advantage of the fact that the extent of the atom in real space is much smaller than the wavelength of the light emitted by the atom and make the so-called *dipole approximation* [1, 2]. The dipole approximation allows us to treat the atom as an electric dipole while neglecting magnetic dipoles and higher-order multipoles. Within this approximation the interaction energy of the atom and the light field is given by the scalar product of the electric field vector at the position of the atom and the electric dipole moment of the atomic transition:

$$H_I = -\boldsymbol{\mu} \cdot \mathbf{E}. \tag{3.1}$$

This suggests to put as much as possible of the incident electric field into the vector component parallel to the atomic dipole in order to maximize the interaction energy. Despite of some applications such as laser cooling where one can just put more power into the incident beam to adjust the interaction strength, more sophisticated methods are mandatory when for example coupling a single photon to an atom, where the amount of available energy is naturally limited.[1]

There are various strategies for enhancing the interaction of photons and atoms.[2] One is to enhance the field strength by placing the atom in the near field of a suitable antenna, which can enhance the local field strength far above the value given by the diffraction limited focusing of the incident field in the absence of the antenna [3–5]. The approach followed most frequently in the past decades is to place the atom in an anti-node of the electric field of a high quality resonator (see [6–9] for reviews and also the chapters by Lanco and Senellart and A. Kuhn). It is the small cavity mode volume and the fact that the light field interacts with the atom over many cavity round-trips [10] that enhances the interaction. Recently, impressive progress in the field of so-called *cavity quantum-electrodynamics* was achieved (see e.g. [11–14]).

This chapter (and also the ones by Slodička, Hétet, Hennrich and Blatt and Piro and Eschner) is devoted to the coupling of atoms and the light field in *free space*. Contrary to the approaches mentioned above, efficient free-space photon-atom coupling is not based on modifying the boundary conditions of the electro-magnetic field but rather on suitably shaping the field itself. Remember the dipole approximation mentioned above. It is the very name of this approximation that suggests how to couple light efficiently to the atom: shape the incident field as to resemble the kind of dipole radiation emitted by the atom! This mode-matching argument is basically the same as when thinking of coupling light efficiently into a single-mode optical fibre and follows directly from time-reversal symmetry arguments (see [15–19] and references therein).

---

[1] There is no state of the light field, more intense than a single photon, which will transform into a single photon state when projecting onto a certain mode function. Such a projection is equivalent to attenuation.

[2] If not explicitly mentioned otherwise, the term *atom* is used to designate any kind of single quantum target.

3.1.2 Defining a Coupling Efficiency

Thinking about coupling in a more mathematical way, the same conclusion as above is obtained as follows: As an alternative to describing the electric field as a superposition of an infinite number of plane waves one can select electric and magnetic multipole functions as the basis of choice [20–22]. Following [21], it is only the electric-dipole component that produces a finite electric field at the origin of a spherical wave. Therefore, the maximum electric field strength in free space is produced by an electric-dipole wave. This field strength is found to be [21]

$$E_{\max} = \frac{\sqrt{2P}}{\lambda\sqrt{\varepsilon_0 c_0}} \cdot \sqrt{\frac{8\pi}{3}}. \tag{3.2}$$

This is the maximum field strength parallel to the atomic dipole moment that can be obtained for a given input power P and wavelength λ. Here, ε_0 and c_0 are the vacuum permittivity and speed of light, respectively.

In practice, the dipole mode is not pure but contains components from orthogonal electric dipoles and/or magnetic dipoles or higher order multipoles. This can be due to a finite solid angle from which the incident light is focused, deviations of the incident radiation pattern from the ideal dipole pattern, or a combination of these. One can account for such deviations from a pure dipole-mode by multiplying (3.2) with a single overlap parameter [22, 23], but from an experimentalist's perspective it is favourable to distinguish between different sources of field reduction. This can be done by introducing two parameters that describe the experimental geometry [24]. The first one is the solid angle covered by the focusing optics obtained when weighting with the angular intensity pattern of the atomic dipole:

$$\Omega_\mu = \int D_\mu(\vartheta, \varphi) \sin\vartheta \, d\vartheta d\varphi, \tag{3.3}$$

with the integration performed over the (potentially incomplete) solid angle set by the focusing geometry. The symbol $\mu = \pi, \sigma_\pm$ parametrizes a specific dipole radiation pattern D_μ given by $D_\pi(\vartheta) = \sin^2\vartheta$ for a linear dipole or $D_{\sigma_\pm}(\vartheta) = (1 + \cos^2\vartheta)/2$ for a circular dipole [25], respectively. The second parameter is the overlap of the incident field distribution $\mathbf{E}_{\text{inc}}(\vartheta, \varphi)$ with the field distribution of the dipole's radiation pattern $\mathbf{E}_\mu(\vartheta, \varphi)$, again obtained by integrating over the focusing solid angle:

$$\eta = \frac{\int \mathbf{E}^\star_{\text{inc}} \cdot \mathbf{E}_\mu \sin\vartheta \; d\vartheta d\varphi}{\sqrt{\int |\mathbf{E}_{\text{inc}}|^2 \sin\vartheta \; d\vartheta d\varphi \cdot \int |\mathbf{E}_\mu|^2 \sin\vartheta \; d\vartheta d\varphi}}. \tag{3.4}$$

With these quantities (3.2) can be rewritten as [24]

$$E_{\text{focus}} = \frac{\sqrt{2P}}{\lambda\sqrt{\varepsilon_0 c_0}} \cdot \sqrt{\Omega_\mu} \cdot \eta. \tag{3.5}$$

For sending the ideal dipole pattern ($\eta = 1$) and focusing from full solid angle ($\Omega_\mu = 8\pi/3$) (3.2) is recovered.

The overlap parameter η is very useful in practice. In this respect, we should highlight two points: Since the fields $\mathbf{E}_{\mathrm{inc}}$ and $\mathbf{E}_\mu$ are complex quantities, it is generally possible to let η also account for distortions of the phase front of the incident light or aberrations induced by the focusing optics (see also [26]). Furthermore, the field distribution of the incident field *after* transformation into a spherical wave by the focusing optics is usually not accessible for measurement. However, η can also be calculated in the plane of the entrance pupil of the focusing optics [24]. One just has to calculate how the dipole radiation pattern is transformed into a plane propagating mode by the focusing device.

Generating the time-reversed version of the latter mode is exactly what maximizes the interaction Hamiltonian for a given input power and focusing geometry.[3] Corresponding calculations for a parabolic mirror can be found e.g. in [10, 24, 27] and for other optical elements in [24]. The calculation of overlaps of optimized modes generated in an experiment is treated in [28] and in the next section.

We end this section by finding a suitable definition for the coupling efficiency in free space. As outlined in [28], such a definition can be motivated in analogy to the necessary condition for strong coupling in cavity quantum-electrodynamics. The important quantity in this condition is the square of the single-photon Rabi-frequency of the cavity field. This frequency is proportional to the atomic dipole moment and the field obtained from confining the energy of a single photon in the volume of the cavity mode. In close analogy, apart from proportionality factors our free-space coupling efficiency should be given by $|H_I|^2$, which scales with the intensity of the electric field component polarized parallel to the atomic dipole moment. The importance of the mode-matching argument treated above is highlighted by normalizing $|H_I|^2$ to the ideal case described by (3.2). This suggests to define the coupling efficiency G as [17, 28]

$$G = \frac{|E_{\mathrm{focus}}|^2}{E_{\mathrm{max}}^2} = \frac{\Omega_\mu}{8\pi/3} \cdot \eta^2. \tag{3.6}$$

When reviewing recent experiments in free space, we will highlight the role of the coupling efficiency in more detail.

3.2 Dipole-Mode Generation with a Parabolic Mirror

3.2.1 Finding the Optimum Field Mode

From the discussion in the previous section it has become obvious that one should focus from (almost) the entire solid angle. One suitable setup immediately coming to

[3] We consciously neglect effects related to a nonzero detuning between the incident field and the atomic resonance.

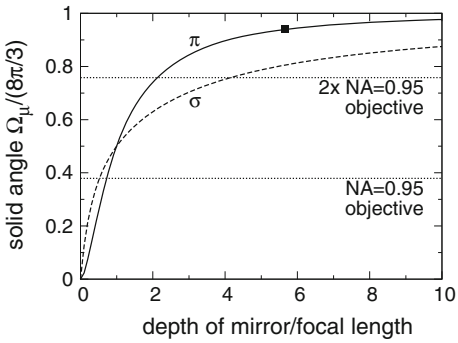

Fig. 3.1 Weighted solid angle Ω_μ covered by a parabolic mirror. The *solid* (*dashed*) *line* denotes the case of a linear (*circular*) dipole transition with the quantization axis parallel to the optical axis of the mirror. The *symbol* marks the geometry used in our experiments. The *dotted lines* display Ω_μ for one and two NA = 0.95 lenses and a linear dipole transition with the quantization axis perpendicular to the optical axis (best case, worse for other orientations)

mind is the setup of the so-called 4π-microscopy [29] which consists of two high NA lenses with coinciding focal points. Although some of the experiments performed in recent years in principle provide the possibility for focusing with two lenses [30–32] and thus doubling the solid angle coverage, such an experiment has not been reported. This might be due to technical issues related to the necessity of achieving constructive interference between the waves focused by the two objectives. But this might also be due to the large band of solid angles located symmetrically around the optical axis which are not covered by the highest numerical aperture (NA) of a commercial objective in vacuum, i.e. NA = 0.95. In the best case, the missing 0.05 to achieve NA = 1 corresponds to losses of 24 % for the weighted solid angle for a 4π-microscopy setup. Moreover, in most experiments, especially the ones on trapped ions, the used NA is considerably smaller.

Another possibility for focusing from essentially full solid angle is using a parabolic mirror that has a depth much larger than the focal length [10, 27, 33, 34]. As is obvious from Fig. 3.1, when the ratio of the depth h of the parabola and the focal length f surpasses the limit $h/f \approx 2.12$ a parabolic mirror setup outperforms 4π-microscopy setups. It is also evident from the figure that the configuration of a π-transition with the quantization axis parallel to the mirror's optical axis yields the largest values of Ω_μ for finite sized parabolic mirrors covering more than half of the solid angle.[4] Therefore, we have chosen to use this configuration in our experiments [26, 28, 35, 36].

Next, we derive the field distribution to be sent onto the parabolic mirror for optimized coupling to an atom in the above configuration. Following [24, 27], one has to trace the emission pattern of the atomic dipole-radiation towards the parabolic surface, relating emission angles ϑ to distances r from the optical axis by $\vartheta = 2\arctan(r/(2f))$. Furthermore, one has to account for the proper transformation of

[4] The half solid angle case corresponds to $h/f = 1$.

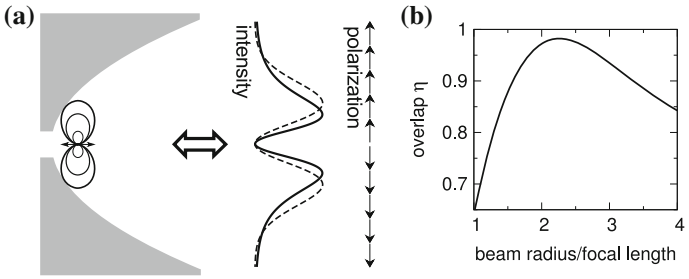

Fig. 3.2 **a** Basic layout of a setup optimizing light-matter coupling in free space. A single atom is located in the focus of a parabolic mirror with depth much larger than its focal length. A beam with the intensity distribution given by the square of (3.7) (*solid line*) and with radial polarization (*arrows*) is focused by the parabolic mirror. For comparison, the intensity distribution of the doughnut mode with largest overlap η is also displayed (*dashed line*). **b** Overlap of a radially polarized doughnut mode with the ideal dipole distribution as a function of the doughnut mode's beam radius for the geometry used in our experiment ($h/f = 5.67$ and $\Omega_\mu = 0.94 \cdot 8\pi/3$)

power emitted per solid angle into power per surface area. This finally yields the amplitude distribution of a linear dipole collimated by the parabolic mirror:

$$E_\pi(r) = E_0 \cdot \frac{r}{(r^2/(4f)^2 + 1)^2}. \tag{3.7}$$

Likewise, one finds the corresponding polarization pattern. For our configuration, the field in the exit pupil of the parabolic mirror is radially polarized. These findings are illustrated in Fig. 3.2.

The generation of the mode defined by (3.7) might be rather intricate [27]. Fortunately, there exists a mode that can have large overlaps with the ideal mode [15, 24, 27] and which is routinely generated in experiments: a radially polarized mode with the amplitude distribution of a Laguerre-Gaussian beam of zeroth radial and first azimuthal order. In the following, we will call this mode shortly 'doughnut mode' for simplicity, although the latter term is used in literature for a plethora of modes with ring shaped amplitude pattern. The amplitude distribution of a doughnut mode can be written as

$$E(r) = E_0 \cdot r \cdot \mathrm{e}^{-\frac{r^2}{w^2}} \tag{3.8}$$

with the beam radius w. For any given parabolic mirror, the overlap parameter η is maximized by tuning w [24].[5] For our geometry ($h/f = 5.67$ and $\Omega_\mu = 0.94 \cdot 8\pi/3$) the overlap is maximized by $w = 2.26f$ to be $\eta = 98.2\,\%$ (see Fig. 3.2b). The intensity profile of this optimum doughnut mode is displayed as a dashed line in Fig. 3.2a. Using the above values of Ω_μ and η, we could in principle achieve overall coupling efficiencies of $G \approx 0.9$ with our setup.

[5] This is of course also true for other focusing optics or dipole configurations and correspondingly other suitable 'standard' field modes as e.g. a fundamental Gaussian mode, see [24] for some examples.

However, one has to keep in mind that expanding the incident beam towards a size which maximizes η might result in clipping considerable parts of the beam and hence in losses, which can be considered as a 'no-go' when focusing single photons onto an atom. This is a considerable effect in setups with small to medium sized numerical apertures, e.g. the NA = 0.4 objectives used in [31, 37]. Hence it is required to maximize the product of the power transmitted through the aperture and η^2 for a given entrance pupil. However, for the parabolic mirrors used in our experiments the relative power loss for the doughnut mode with maximum η is on the order of 10^{-3}. We therefore can safely neglect such effects.

On the other side, when using doughnut modes for focusing with parabolic mirrors it is not too meaningful to use parabolic mirrors with even larger solid angle coverage than in our setup: The gain of solid angle Ω_μ is compensated by a reduction of the maximum value attainable for η, which results in a saturation of the coupling efficiency at $G \approx 0.92$ [24]. Of course, the latter value depends on the choice of the focusing geometry, the dipole configuration, and the optical mode used to approximate the ideal dipole radiation.

3.2.2 Generation and Characterization of Field Modes Tailored for Efficient Free-Space Coupling

We now turn towards the experimental generation and characterization of the optimum doughnut mode for focusing onto an atom. There are various methods for generating radially polarized doughnut modes [38–45]. We have chosen to generate the doughnut mode by means of a segmented half-wave plate [46, 47]. This is mainly motivated by the fact that this technique is rather robust and especially suitable for wavelengths in the ultraviolet spectral range, which we are targeting [10, 28, 35, 36]. For details about the actually used polarization converter and the optical setup we refer to [28].

One example of a generated mode is given in Fig. 3.3. The local intensity as well as the local polarization ellipse of the electric-field vector are obtained performing a spatially resolved measurement of the Stokes parameters (the ellipticity angle is omitted in the figure, cf. [28] for details). Taking the square root of the local intensity and processing the polarization angles one can reconstruct the local electric-field vector. With the obtained field vectors one can compute the overlap η with the ideal field distribution given by (3.7). We routinely achieve values of $\eta = 0.98$ [28] which is practically the maximum value attainable in our setup.

So far we did not discuss the properties of the phase front of the incident field. Under ideal conditions, a spherical wave emerging from the focus of the parabolic mirror leaves the mirror's aperture with a flat phase front. Likewise the phase front of the incident field that impinges onto the mirror and is focused onto the atom should be flat. Unfortunately, current mirror manufacturing capabilities are not precise enough to guarantee the diffraction limited focusing of an incident beam that is free of

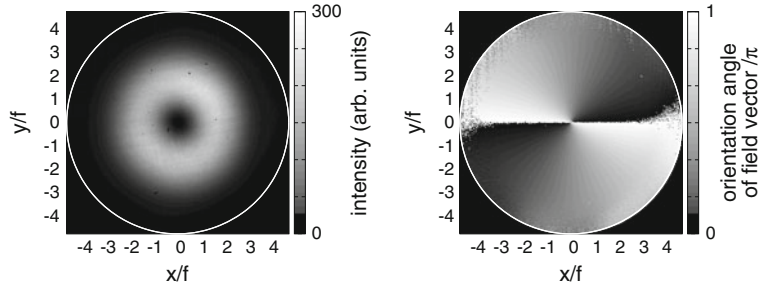

Fig. 3.3 Example of a radially polarized doughnut mode generated at a wavelength of 370 nm and optimized to drive the $S_{1/2}$,$m_j = \pm 1/2 \rightarrow P_{1/2}$,$m_j = \pm 1/2$ transition of a singly ionized ytterbium ion. The intensity distribution (*left*) and the orientation angle of the local polarization ellipse of the field vector (*right*) are reconstructed from a spatially resolved measurement of the Stokes parameters. The *circle* indicates the entrance pupil of the parabolic mirror

aberrations. The mirrors we use in our experiments typically deviate from the parabolic shape by ± 150 nm [35], which is on the order of a wavelength of the involved atomic transitions. We determine such deviations by an interferometric setup that is adapted to our purpose [35]. Other methods involving e.g. profilometers are not applicable due to the tight geometry of the used mirrors—the focal length is 2.1 mm and the aperture radius is 10 mm.

In principle the deviations of the parabolic mirror can be compensated for by using phase plates which imprint the conjugate of the mirror's deviations onto the incident beam. Proof-of-principle experiments at a wavelength of 633 nm yielded aberration compensations enabling a *Strehl ratio*[6] of 99 % for a focused doughnut mode at 633 nm [28].

3.3 Overview of Experiments on Photon-Atom Coupling in Free Space

In this section we discuss various kinds of experiments on photon-atom coupling in free space performed in recent years. They all have in common that the key to a successful observation of the phenomena under investigation lies in mode-matching the incident field to the dipolar radiation pattern of the addressed atomic transition. We will highlight for each type of experiment how it could benefit from full solid angle focusing or the use of parabolic mirrors, respectively.

[6] The Strehl ratio defines the maximum intensity in the focal region for a focusing system exhibiting aberrations as a fraction of the intensity obtained without aberrations [48]. Whereas in the latter reference a plane wave is considered, we apply this figure of merit for the case of a doughnut mode.

3.3.1 Shifting the Phase of a Coherent Beam

For the experiments described here—and also for the ones on attenuating a faint beam—the typical experimental setup is as follows [49–51]: A continuous laser beam is focused onto the atom. Depending on the detuning Δ of the incident light with respect to the atomic resonance a certain amount of light is scattered by the atom with a detuning dependent phase shift.[7] The light passing the atom and the scattered light are both collected by some optical element, e.g. a second lens of the same numerical aperture as the focusing optics. Upon diverging from the atom, the incident light suffers a phase shift of 90° due to the Gouy effect [53–55]. For simplicity, the latter contribution is artificially attributed to the phase of the scattered light in most literature. The phase that is then usually measured is the phase of the superposition of the scattered light and the incident light.

This scenario is illustrated in Fig. 3.4a in a phase-space picture. The phase angle of the scattered field is solely determined by the detuning Δ, whereas the amplitude of the scattered field is determined by Δ and especially G. The latter statement is obvious from the fact that the power of the scattered light in terms of power of the incident light is given by $4G/(1 + 4\Delta^2/\Gamma^2)$ [17, 56] with Γ being the rate of spontaneous emission from the excited atomic state. This so-called *scattering ratio* [53, 54] can be as large as four for a perfect dipole-wave incident from full solid angle and on resonance with the atomic transition.[8] From the fact that the scattering ratio scales with the coupling efficiency G one can draw the following conclusion: No matter how large the detuning is, the influence of the scattered light on the final superposition with the incident light grows with increasing G and is maximized for $G = 1$, cf. Fig. 3.4 and the discussion following (3.9). In other words, the phase obtained for the superposition field 'is drawn' towards the phase of the scattered field with increasing G.

In the discussion so far we have not included effects related to a finite amount of population in the atom's excited state. The excited-state population can be quantified by $S/(2 + 2S)$ using the *saturation parameter* S, which is proportional to G and depends on detuning, see also (3.13). This parameter influences the phase shift in

[7] The phase shift of the light *scattered* by an atom, i.e. the response of a driven harmonic oscillator, has been measured recently [52].

[8] Values for the scattering ratio exceeding unity might seem unphysical at first sight because one might suspect a violation of energy conservation. Here we argue that this is not the case. Energy is always associated with the total field not with individual interfering components. One might write a propagating field as the sum of two fields E_1 and E_2, one 180° out of phase with respect to the other. The total energy has of course a well defined value. But the individual fields $E_{1,2}$ are not well defined. You can choose a field with a larger E_1 as long as the amplitude of field E_2 is also increased such that the sum is as before.

In the specific problem of elastic scattering of a beam resonant with the atomic transition it can even be required that the scattered power has to be larger than the incident one. Due to the 180° phase shift between the scattered and the transmitted incident light there would otherwise be a net loss of energy under efficient-coupling conditions, since in elastic scattering no energy is transferred onto the atom.

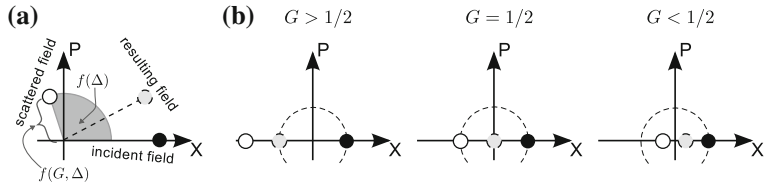

Fig. 3.4 Illustration of phase shift experiments in phase-space diagrams. **a** Depending on the detuning Δ and the coupling efficiency G the field scattered by the atom (*open circle*) has a certain amplitude and phase. The superposition of the incident field (*filled circle*) and the coherently scattered field (*open circle*) yields the resulting field (*dashed circle*). **b** Illustration of the influence of G for the special case $\Delta = 0$. The phase of the resulting field can either be equal to 0 or π. The *dashed line* marks the amplitude of the incident coherent state

two ways: For increasing saturation parameter the scattering ratio decreases. Furthermore, the scattered light contains an increasing fraction of frequency components that are not coherent with the incident light and hence cannot contribute to the superposition with the incident field. A corresponding experiment can be found in [50]. We summarize the above discussion, assuming negligible saturation, in writing the resulting phase shift, i.e. the phase of the superposition of scattered and incident light in comparison to the case of no atom being present, as [17, 56]

$$\phi = \arg\left(1 + 4\frac{\Delta^2}{\Gamma^2} - 2G - i \cdot 4G\frac{\Delta}{\Gamma}\right) \tag{3.9}$$

It is apparent from the above equation that the maximum achievable phase shift is $\phi = \pi$ for $\Delta = 0$ (resonant excitation) and $G > 1/2$. This phase arises from a $\pi/2$ phase for the coherently scattered resonant light and the Gouy phase. However, for $G < 1/2$ (less than half solid angle and/or too low field overlap) the amount of scattered light is too small to counteract the incident field. For $G > 1/2$ (focusing from more than half solid angle with sufficiently mode-matched incident light), the amount of scattered light is large enough to flip the phase of the superposition with the incident field. A corresponding illustration is given in Fig. 3.4b.

Although it seems that it is enough to have 'G just slightly larger than $1/2$', there are good reasons for increasing G towards unity. The closer G is to $1/2$ the smaller is the detuning interval in which ϕ increases from $\pi/2$ towards π, making an experimental observation of a π phase shift increasingly difficult (cf. [56]).

The maximum phase shift observed so far in an experiment in free space was about 3° [50] using a setup with $G < 1/2$.

3.3.2 Extinction of a Weak Coherent Beam

An experiment closely related to imprinting a phase shift onto a coherent beam is attenuating such a beam with a single atom [30, 37, 54, 57–60]. In such experiments

the incident beam is typically focused and recollimated with two lenses of equal numerical aperture. In the absence of the atom all light is transmitted through the two-lens setup. If an atom resides in the focus of the incident beam, the interference between incident and scattered light results in a decrease of the number of transmitted photons. The exact strength of this extinction depends again on the scattering ratio [53, 54]: For focusing from half solid angle with a properly mode matched wave resulting in $G = 1/2$, the scattering ratio reaches two, with the consequence that the incident light and the light scattered into the solid angle cone of the second lens interfere destructively. In other words, a single atom can perfectly reflect a resonant coherent beam [53, 54, 61]. The partial reflection of an incident beam was measured in [59]. In [62] the back scattering from a single ion was exploited for utilizing a single ion as a mirror of an optical resonator (see also the chapter by Slodička, Hétet, Hennrich and Blatt). The smallest transmission observed so far for a single quantum emitter in free space was about 78 % [58].

The transmitted power fraction T of a resonant incident beam inducing negligible saturation of the atom can be derived straightforwardly, again assuming the same numerical aperture for focusing and light collection: The scattering ratio is given by $4G$, i.e. the light scattered into the solid angle outside the collection optics is given by $4G \cdot [1 - \Omega_\mu/(8\pi/3)]$. This yields

$$T = 1 - 4G \cdot \left(1 - \frac{\Omega_\mu}{8\pi/3}\right). \tag{3.10}$$

Obviously, for $\Omega_\mu = 8\pi/3$ one gets full transmission. This solution is however trivial, since for a full-solid-angle optics no photons are lost due to scattering.

More interesting is the case of $T = 0$, which can be realized with a full-solid-angle parabolic mirror. If the incident light is transversely limited to exactly half of the solid angle (the portion of the parabola defined by $r \leq 2f$) one has $\Omega_\mu = 4\pi/3$. If furthermore $\eta = 1$ one obtains $G = 1/2$ and hence $T = 0$ according to (3.10). In such a setup, the part of the mirror with $r > 2f$ acts as a second 'objective' collimating the transmitted light. A possible layout of such an experiment is sketched in Fig. 3.5.

3.3.3 Absorption of Single Photons

In the experiments discussed so far the light focused onto the atom was of sufficiently low intensity to avoid a non-negligible excitation of the atom, i.e., the number of photons per excited-state lifetime was much smaller than one. In contrast to this, in the experiments reported in [31, 32] the explicit aim was to excite the atom with single photons. In [31] the absorption of a heralded and spectrally filtered single photon by a single ion is reported (see chapter by Piro and Eschner). The reported absorption efficiency is on the order of 0.03 %. In [32] weak coherent states have been focused onto a single atom and an absorption efficiency of about 4 % is reported for pulses containing two photons on average.

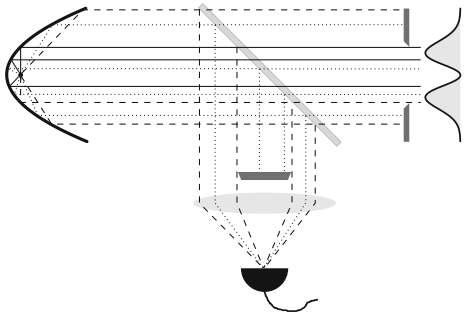

Fig. 3.5 Layout of an extinction experiment using a parabolic mirror. The incident light (*solid lines*) is limited to half solid angle by an aperture with diameter $4f$. Light passing the atom (*dashed lines*) and the scattered light (*dotted lines*) are picked off by a beam splitter. Light scattered 'backwards' is blocked by an aperture stop of diameter $4f$

As outlined in [28] the probability for the absorption of a photon by a two-level atom is given by

$$P_{\mathrm{a}} = G \cdot \eta_t^2. \tag{3.11}$$

The parameter η_t describes the temporal overlap of the field envelope of the incident single photon with the field envelope that maximizes absorption. The latter is given by an increasing exponential pulse, as described in detail in the next section. According to (3.11) the upper bound for the absorption of single photons by atoms in our parabolic mirror setup is given by $G = 0.94$ when sending the ideal radiation pattern and $G = 0.9$ when sending an optimized radially-polarized doughnut mode.

We finish this section highlighting a link between the elastic scattering of a monochromatic wave discussed before and the absorption of photons, see [63]. For this purpose we treat the interaction of the atom with all spectral components of the focused pulse as an elastic scattering problem. We compute the phase and amplitude of the superposition of the incident field and the coherently scattered field for each spectral component of the incident pulse. This yields the spectrum and hence the temporal evolution of the scattered pulse. Performing such a calculation for an exponentially increasing pulse with a time constant matching the excited state's lifetime yields an outgoing pulse envelope containing exponentially increasing and decreasing components.[9] The fraction of the exponentially decreasing components is given by G, quantifying the amount of absorbed and spontaneously re-emitted photons [63]. For $G = 1$ full absorption is obtained, as one would expect from time-reversal symmetry arguments discussed below. But this finding should be taken with care, since time-reversal symmetry arguments demand the use of a single-photon Fock state. Nevertheless, the above treatment should be valid for weak coherent state pulses as used in [32] or the ones created in [28].

[9] The decreasing components should of course be observable for any incident pulse with non-zero temporal overlap η_t.

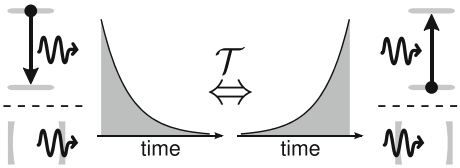

Fig. 3.6 Illustration of the time-reversal arguments for coupling to a single atom or into an empty optical resonator as treated in Sect. 3.4.3

3.4 Absorbing a Single Photon: Temporal Mode Shaping

3.4.1 Choosing the Right Mode

As mentioned above, the temporal envelope of the focused electric field is of importance when exciting a single atom with a single photon. This can be motivated heuristically as follows (see also [10, 15, 16]): The atom and the continuum of all free-space field modes form a closed system. For such a system, the Schrödinger equation is invariant under time reversal. Assuming the atom in its excited state and the electro-magnetic field in the vacuum state as the initial condition, a photon will be emitted spontaneously over the course of time. As is well known, a spontaneously emitted photon has an exponentially decaying field envelope with a decay constant equal to the excited-state lifetime. Applying the time reversal operation—we just assume we could do so in practice—would result in an exponentially increasing photon travelling towards the atom, promoting the atom to the excited state as outlined in Fig. 3.6.

Applying the time-reversal operation in practice, which implies phase-conjugating a single photon, is carefully speaking subject to technical difficulties—and also the evolution in the atom's motional degrees of freedom has to be handled [16]. Moreover, the phase-conjugation process induces excess quantum noise [64, 65]. It is therefore the idea to shape a photon to resemble a perfect copy of a time-reversed spontaneously emitted photon.[10] This implies the spatial mode-matching arguments raised in Sect. 3.1 but also requires 'temporal mode-matching', as expressed by the temporal overlap-parameter η_t in (3.11).

In practice, the assumption of working with two-level atoms is usually not justified and there is more than one possible decay channel from the excited state. Hence, spontaneous emission would result in a superposition of the decays via all these channels, entangling the emitted photon and the remaining atom. The reverse process, absorption of a photon, would ideally start from such an entangled state. This is extremely challenging if not self forbidding. We therefore seek an atomic species providing as small as possible branching ratios in the excited state's decay as well as a π-transition. Any even numbered isotope of doubly ionized ytterbium (YbIII) is such a species. It is also a good choice from a practical point of view, since singly-ionized ytterbium (YbII) is a well-established ion used in many quantum-optics experiments

[10] It can be shown in a fully quantum-mechanical calculation that an exponentially rising pulse with proper time-constant indeed leads to full excitation of the atom [66].

and for atomic clocks. YbII also offers a strong π-transition (see Fig. 3.10), serving as our test-system for all techniques enabling efficient free-space coupling.[11]

3.4.2 Generation of Exponentially Increasing Pulses

The fact that most ions have to be addressed by ultraviolet light makes the generation of single-photon Fock states with proper temporal envelope a cumbersome task (see [28] for citations on shaped photons with more 'accessible' wavelengths). Nevertheless, the use of whispering-gallery-mode resonators [68] made of appropriately chosen materials might facilitate shaped single photons at UV wavelengths.

For the time being and as a preliminary test, we resort to using suitably shaped weak coherent states [28]. We generate these states by modulating a continuous laser beam with an acousto-optic modulator (AOM).[12] The AOM is driven with a voltage signal generating exponentially rising pulses in the first diffraction order. The voltage signal is proportional to $\arcsin[\exp(t/(2\tau))] \cdot \sin(\omega_{\mathrm{RF}} t)$,[13] where $\tau = 1/\Gamma$ is the excited-state lifetime and ω_{RF} the frequency with which the AOM is driven. The obtained pulses are attenuated towards mean photon numbers about 0.1 and characterized by statistics on the times of photon detection events obtained from a photo-multiplier tube, cf. [28] for details.

From the obtained histograms (see Fig. 3.7) we reconstruct the field amplitude's envelope $E_{\mathrm{inc}}(t)$ by taking the square root of the number of events per time bin. We then compute the overlap of $E_{\mathrm{inc}}(t)$ with the ideal envelope $E_{\mathrm{ideal}}(t) = e^{\frac{\Gamma}{2}t} \cdot \theta(-t)$ obtained from time-reversal symmetry arguments:

$$\eta_t = \frac{\int_{-\infty}^{\infty} E_{\mathrm{inc}}(t) \cdot E_{\mathrm{ideal}}(t) dt}{\sqrt{\int_{-\infty}^{\infty} |E_{\mathrm{inc}}(t)|^2 dt / \Gamma}}. \tag{3.12}$$

For the data shown in Fig. 3.7 we obtain $\eta_t = 0.96$ for the YbII transition and $\eta_t = 0.99$ for the YbIII transition. The slightly lower overlap in the case of the YbII transition is due to the fact that the drop-off at the end of the pulse, which amounts to 5 ns enforced by the finite decay time of the acoustic grating inside the AOM, is on the order of the lifetime of 8 ns. Hence, the drop of intensity at the end of the pulse

[11] YbIII has been created by electron-impact ionization from a cloud of trapped YbII ions [67]. We recently accomplished the controlled photo-ionization from YbII to YbIII.

[12] A similar technique employing electro-optic modulation is reported in [69]. In contrast to this, other authors directly modulate the waveform of a single photon upon receiving a trigger signal from a heralding photon, see [70], and the chapter by Chuu and Du. Last but not least, in a recent experiment single-photon Fock states with increasing exponential envelope have been achieved by manipulating a heralding photon with an asymmetric cavity prior to detection [71]. Both photons originated from a cascaded decay in a cold atomic ensemble.

[13] This expression arises from the fact that the power scattered into the first diffraction order of the AOM is proportional to the sine of the acoustic power establishing the diffraction grating.

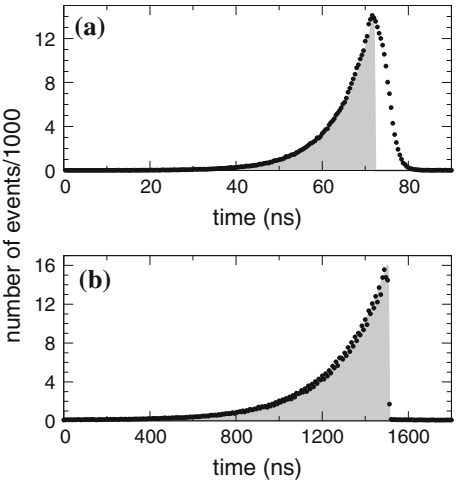

Fig. 3.7 Weak coherent-state pulses generated to drive an atomic transition with 8 ns excited-state lifetime (YbII $^2P_{1/2} \rightarrow {}^2S_{1/2}$ (**a**)) and 230 ns excited-state lifetime (YbIII $^3P_1 \rightarrow {}^1S_0$ (**b**)). The average photon number per pulse is about 0.1. Histogram data of photon detection times are denoted by *circles*. Each histogram contains more than 4×10^5 events. The *shaded area* depicts the optimum pulse shape

is not as step-like as required. Nevertheless, both pulse shapes envision absorption probabilities close to G, neglecting the non-ideal level structure of YbII [28].

3.4.3 An Analogous Experiment: Coupling to a Resonator

An experiment conceptually analogous to absorbing a single photon—but with significantly reduced technical complexity—is the coupling of pulses into an empty optical resonator [72]. Imagine a finite amount of energy being stored inside the resonator at a certain point in time. This electro-magnetic field will leave the resonator via exponential decay, where the time constant of the decay is given by the decay time of the intra-cavity field. If the resonator consists of only two mirrors with one of them having unit reflectivity, the field leaves the cavity through the mirror with sub-unit reflectivity. Now time-reversal arguments tell us that the energy of a properly shaped, exponentially increasing pulse sent towards the cavity is stored completely inside the cavity. In other words, no light is reflected from the cavity as long as the incident pulse continues to grow [72].

Recently, we have implemented a corresponding experiment [73], shaping the pulses in the same way as described above in the generation of the weak coherent-state pulses. The non-confocal resonator, which was used in our experiment, consisted of a mirror with a reflectivity of $R_1 = 97.96\,\%$ and $R_2 = 99.94\,\%$ and had an intensity decay time of 39 ns. In the experiment, incident light was spatially mode matched to

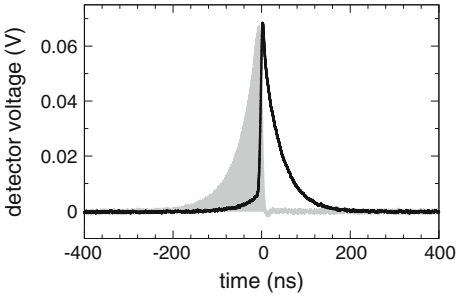

Fig. 3.8 Response of an empty optical resonator to a pulse with increasing exponential envelope and a time constant matching the cavity's decay-time. *Black line* reflected signal for resonant excitation. *Shaded area* reflected signal for large detuning from the cavity resonance, being in good approximation identical with the incident pulse

the resonator mode, sent onto the resonator via the mirror with reflectivity R_1 and tuned into resonance. The temporal envelope of the reflected pulse was monitored with a photo diode. The outcome of such an experiment is presented in Fig. 3.8.

The finite amount of light leakage through the second mirror, preventing measurements of the cavity transmission with sufficient bandwidth, as well as non-perfect spatial mode-matching necessitate a somewhat more involved analysis [73]. Despite the imperfections, we achieved 88 % energy storage efficiency for the generated pulses and even 94 % efficiency for the spatially mode-matched fraction.[14] Deviations from unity are due to a non-unit temporal field overlap $\eta_t = 0.986$ and leakage through the second mirror. In analogy to the single-atom experiment this leakage corresponds to a solid-angle coverage of 97 %. The achieved large efficiencies hint at the power of time-reversal-symmetry based arguments when optimizing the coupling of light and matter. As a further example, true single-photon Fock states with increasing exponential temporal envelope have been efficiently coupled to a cavity recently, c.f. [76].

3.5 Trapping Ions in Parabolic Mirrors

3.5.1 Parabolic Mirror Ion Trap

So far we did not discuss a most important issue of photon-atom coupling with parabolic mirrors: How do we place the atom at the focus of the parabolic mirror? As already mentioned above, we have chosen to work with atomic ions. This demands for an ion trap potential that can be located precisely enough to place the ions within the tight focal spot of the incident beam. Simultaneously, the ion trap geometry should

[14] Similar efficiencies where obtained recently in experiments for microwave pulses [74, 75].

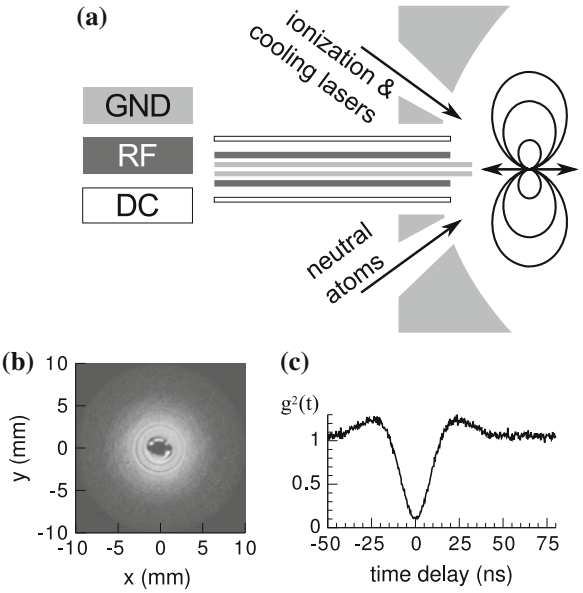

Fig. 3.9 **a** Schematics of the parabolic-mirror ion-trap, consisting of two concentric tubular electrodes for the radio-frequency (*RF*) signal and ground (*GND*) potential. The aluminium parabolic mirror is also grounded. Rod electrodes (*DC*) enable micro-motion compensation. **b** A single YbII ion's fluorescence imaged in the aperture plane of the parabolic mirror. *White colour* indicates large intensity. **c** Second-order intensity correlation function (anti-bunching) obtained from approx. $8 \cdot 10^5$ fluorescence counts in 60 s

maintain the large solid-angle optical access to the ion. These tasks are solved by adapting a 'stylus trap' [77] and combining it with a parabolic mirror. The aluminium parabolic mirror replaces the planar ground electrode of the stylus trap [36, 77]. Two tubular electrodes providing ground potential and the radio-frequency signal, respectively, are mounted concentrically and attached to a piezo-driven translation stage. The latter allows for adjusting the minimum of the trapping potential with nm-accuracy relative to the mirror's focus. The layout is sketched in Fig. 3.9. The level scheme relevant for laser cooling YbII and for the coupling experiments outlined in Sect. 3.6 is depicted in Fig. 3.10.

The radiation from a single YbII ion's fluorescence as collimated by the parabolic mirror is displayed in Fig. 3.9b. The cooling transition has been saturated in this experiment. The figure shows an image of the intensity distribution at the output plane of the paraboloid. The spatial distribution of the measured fluorescence photons corresponds to the one of an isotropic point source, as which a saturated YbII ion can be considered [36]. The thin, concentric, ring-shaped features originate from surface distortions of the parabolic mirror, see discussion below and in Sect. 3.6. The central dark spot is attributed to the opening for the trap electrodes.

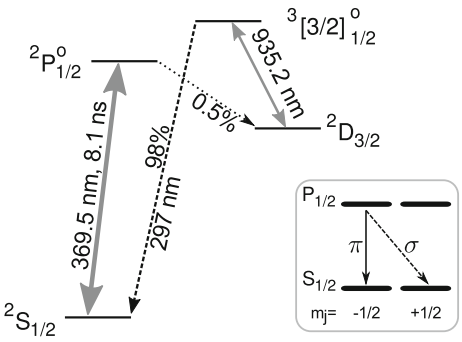

Fig. 3.10 Energy levels of YbII most relevant for our experiments. The *inset* details the levels addressed in our photon-atom coupling experiments

3.5.2 Fluorescence Collection

The large solid angle covered by a deep parabolic mirror is not only beneficial for focusing onto an atom, but also—as suggested by the time-reversal symmetry arguments raised before—for the efficient collection of photons emerging from the atom. The latter is of importance in any application in which the internal state of an atom has to be determined.

For our mirror geometry we demonstrated the collection of 54 % of the emitted fluorescence photons [36]. This number is basically limited by two constraints: As mentioned above, a saturated YbII ion emits on average as an isotropic point source. For the latter the solid angle covered by our mirror amounts to 81 % instead of the 94 % when considering the emission of a linear dipole aligned with the mirror's optical axis. The second constraint stems from the surface quality of the used mirror. The nominal reflectivity of aluminium, when averaging over all angles of incidence corresponding to the surface of our mirror, should amount to roughly 87 %. Instead, the measured reflectivity amounts to 67 %. Such a low value is mainly attributed to a too large surface roughness of the parabolic mirror, which might be caused by a non-optimum manufacturing process. Using a mirror with better surface properties along with collecting from a linear-dipole emitter should boost the collection efficiency to 82 %.

Nevertheless, according to current literature the number of two million photons per second actually counted in our setup outperforms other setups using neutral atoms or ions.

3.6 Experimental Determination of the Coupling Efficiency

With the different aspects treated so far we now have basically all tools at hand for conducting experiments on efficient light-matter coupling. What we did not discuss, however, is a reliable way of determining the coupling efficiency G experimentally. In principle, one could conduct the experiment one would like to do (e.g. phase

shift or extinction measurements) and compare the achieved results with theory in order to find a reasonable value for G that consistently reproduces the experiment. But there are some obstacles. As both the phase shift and the extinction induced by a single atom are caused by the interference of incident and scattered light, any incoherent scattering due to saturation of the atom reduces the corresponding figure of merit [50, 56, 58]. Also the amount of light scattered back into the solid-angle cone of the focusing optics, as measured in [59], is influenced by the saturation of the atom's excited state. This is due to the fact that the scattering ratio is decreasing for increasing saturation parameter [22, 56].

One could solve such problems by determining the atomic saturation in an additional experiment. But there is a simpler solution in measuring *only* a saturation curve and relating the power needed to achieve a certain saturation parameter S to the one necessary under ideal conditions, i.e. at $G = 1$ [26]. The saturation parameter S induced by light with detuning Δ and incident power P is given by [56]

$$S = G \cdot \frac{8P}{\hbar\omega_0\Gamma} \cdot \frac{1}{1 + 4\Delta^2/\Gamma^2}, \tag{3.13}$$

where ω_0 is the resonance frequency of the atomic transition. For example, the minimum power ($G = 1$) to achieve a unit saturation parameter on resonance is $\hbar\omega_0\Gamma/8$, see also [61].

In the experiment one measures the amount of fluorescence counts as a function of the incident power and fits the result to a function proportional to

$$\frac{\Gamma}{2} \cdot \frac{S(P)}{1 + S(P)}, \tag{3.14}$$

which is the rate of photons scattered by a two-level atom in the steady state. The only difficulty arises from distinguishing the scattered photons from the incident ones. This could be done by monitoring e.g. the Stokes-shifted fluorescence when coupling to a molecule [58]. Working with YbII ions one could monitor the photons emitted on the auxiliary transition $^3[3/2]_{1/2} \rightarrow {}^2S_{1/2}$ at 297 nm which is part of the typical scheme applied for laser-cooling YbII [78].

Here we pursue another method and split incident and scattered light spatially. The spatial separation is accomplished by restricting the incident light to half of the solid angle as depicted in the extinction setup in Fig. 3.5. In other words, we cool the YbII ion with a radially polarized doughnut mode focused by the parabolic mirror while restricting the incident light to radii $r \leq 2f$.[15] Furthermore, one has to use the same kind of aperture in the detection path as in the excitation path in order to detect only backward scattered light [26]. The result of such an experiment is given in Fig. 3.11.

[15] The cooling laser beam at 370 nm that enters through an auxiliary opening of the parabolic mirror (cf. Fig. 3.9) is blocked during the saturation measurements.

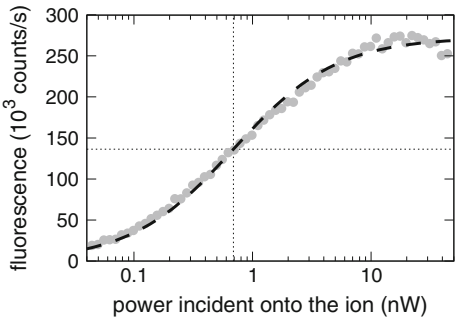

Fig. 3.11 Saturation curve (*symbols*) obtained cooling an YbII ion with a doughnut mode incident from $r \leq 2f$ at a detuning $\Delta = \Gamma/2$. The *dashed line* denotes the result of fitting (3.14) to the experimental data. The *dotted lines* indicate the power and fluorescence rate at $S = 1$

A least-squares fit yields a power of 690 pW for achieving $S = 1$. Using the parameters $\Gamma^{-1} = 8.1$ ns, $\Delta = \Gamma/2$ and $\omega_0 = 2\pi c_0/370$ nm (3.13) thus delivers $G = 0.024$. However, we have to take into account that (3.13) is valid for a two-level atom, which is not the appropriate description of YbII. The focused radially polarized mode only drives the π-transition which has a relative oscillator strength of $1/3$ in comparison to $2/3$ for the $\sigma_\pm$-transitions for the levels $S_{1/2}$ and $P_{1/2}$. Hence we have to apply a correction factor of three in order to obtain $G = 0.072$.[16]

This coupling efficiency is among the largest achieved in a free-space setup so far, but it is seven times below the expected value: Focusing from half solid angle, the maximum achievable coupling efficiency amounts to $G = 0.5$. The non-perfect overlap of $\eta = 0.98$ measured for the incident doughnut modes is so close to the ideal value that it can only explain a tiny portion of the discrepancy. Most probably the discrepancy arises from the fact that the aberrations of the non-perfect parabolic surface have not been compensated during the measurement. From an interferometric characterization [35] of the parabolic mirror performed before mounting it in the vacuum chamber and simulations of the focal intensity based on the corresponding results we predict a Strehl ratio of 87 % for focusing from $r \leq 2f$. The obtainable coupling efficiency including the aberrations and η thus amounts to 41 %.

This value is still much larger than the measured one. We speculate that the surface of the parabolic mirror might be subjected to unknown distortions which are not recognizable in the interferometric measurements performed at visible wavelengths. But also distortions of the incident wavefront by the viewport of the vacuum chamber might play a role. In any case, the measurement of the coupling efficiency as performed here provides a sensitive tool hinting at any open issues.

[16]This reasoning assumes that the quantization axis is parallel to the optical axis of the parabola. But one can show that for any orientation of the quantization axis the same correction factor has to be applied when treating a $S_{1/2} \rightarrow P_{1/2}$ transition.

3.7 Outlook

The experimental demonstrations of coupling light to a single atom in free space have been made with different systems. The best experimental performance in relation to the phase shift of the full transmitted beam, the extinction of the irradiating beam and the absorption of a single photon are are still far from the theoretical best possible values and thus far away from the maximum possible efficiency. The parabolic mirror set-up emphasized here offers the opportunity of improving upon all these numbers. Nevertheless, demonstrating close to 100 % absorption efficiency remains a particular challenge, since the requirements on mode-matching in the spatial and temporal domain have to be fulfilled with highest quality. This is especially difficult at the short wavelength of the linear-dipole transition of the almost ideal two-level system YbIII, which we successfully trapped recently. We hope to report on light-matter-interaction experiments with a single YbIII ion in the near future.

Acknowledgments We gratefully acknowledge the contributions of Marianne Bader, Benoit Chalopin, Martin Fischer, Andrea Golla, Simon Heugel and Robert Maiwald to our experimental endeavours. We thank the *Deutsche Forschungsgemeinschaft* for financial support. G.L. also acknowledges financial support from the *European Research Council* under the Advanced Grant 'PACART'.

References

1. L. Mandel, E. Wolf, *Optical Coherence and Quantum Optics* (Cambridge University Press, Cambridge, New York, 1995)
2. M.O. Scully, M.S. Zubairy, *Quantum Optics* (Cambridge University Press, Cambridge, 1997)
3. M. Moskovits, Surface-enhanced spectroscopy. Rev. Mod. Phys. **57**, 783–826 (1985)
4. S. Kühn, U. Håkanson, L. Rogobete, V. Sandoghdar, Enhancement of single-molecule fluorescence using a gold nanoparticle as an optical nanoantenna. Phys. Rev. Lett. **97**, 017402 (2006)
5. L. Novotny, N. van Hulst, Antennas for light. Nat. Photonics **5**, 83–90 (2011)
6. J.M. Raimond, M. Brune, S. Haroche, Manipulating quantum entanglement with atoms and photons in a cavity. Rev. Mod. Phys. **73**, 565–582 (2001)
7. H. Walther, B.T.H. Varcoe, B.-G. Englert, T. Becker, Cavity quantum electrodynamics. Rep. Prog. Phys. **69**, 1325–1382 (2006)
8. H.J. Kimble, Strong interactions of single atoms and photons in cavity qed. Phys. Scr. **T76**, 127–137 (1998)
9. G. Rempe, Atoms in an optical cavity: quantum electrodynamics in confined space. Contemp. Phys. **34**, 119–129 (1993)
10. M. Sondermann et al., Design of a mode converter for efficient light-atom coupling in free space. Appl. Phys. B **89**, 489–492 (2007)
11. H. Specht et al., A single-atom quantum memory. Nature **473**, 190–193 (2011)
12. S. Ritter et al., An elementary quantum network of single atoms in optical cavities. Nature **484**, 195–200 (2012)
13. C. Sames et al., Antiresonance phase shift in strongly coupled cavity qed. Phys. Rev. Lett. **112**, 043601 (2014)
14. T. Tiecke et al., Nanophotonic quantum phase switch with a single atom. Nature **508**, 241–244 (2014)

15. S. Quabis, R. Dorn, M. Eberler, O. Glöckl, G. Leuchs, Focusing light to a tighter spot. Opt. Comm. **179**, 1–7 (2000)
16. G. Leuchs, M. Sondermann, Time-reversal symmetry in optics. Phys. Scr. **85**, 058101 (2012)
17. G. Leuchs, M. Sondermann, Light matter interaction in free space. J. Mod. Opt. **60**, 36–42 (2013)
18. A. Silberfarb, I.H. Deutsch, Continuous measurement with traveling-wave probes. Phys. Rev. A **68**, 013817 (2003)
19. D. Pinotsi, A. Imamoglu, Single photon absorption by a single quantum emitter. Phys. Rev. Lett. **100**, 093603 (2008)
20. C. Cohen-Tannoudji, J. Dupont-Roc, G. Grynberg, *Photons and Atoms* (John Wiley and Sons, New York, 1989)
21. I.M. Basset, Limit to concentration by focusing. J. Mod. Opt. **33**, 279–286 (1986)
22. S.J. van Enk, Atoms, dipole waves, and strongly focused light beams. Phys. Rev. A **69**, 043813 (2004)
23. Y. Wang, J. Minář, L. Sheridan, V. Scarani, Efficient excitation of a two-level atom by a single photon in a propagating mode. Phys. Rev. A **83**, 063842 (2011)
24. M. Sondermann, N. Lindlein, G. Leuchs, Maximizing the electric field strength in the foci of high numerical aperture optics. Phys. Opt. (2008). arXiv:0811.2098
25. J.D. Jackson, *Classical Electrodynamics*, 3rd edn. (Wiley, New York, 1999)
26. M. Fischer et al., Efficient saturation of an ion in free space. Appl. Phys. B **117**, 797–801 (2014)
27. N. Lindlein et al., A new 4π-geometry optimized for focusing onto an atom with a dipole-like radiation pattern. Laser Phys. **17**, 927–934 (2007)
28. A. Golla et al., Generation of a wave packet tailored to efficient free space excitation of a single atom. Eur. Phys. J. D **66**, 190 (2012)
29. S. Hell, E.H.K. Stelzer, Properties of a 4pi confocal fluorescence microscope. J. Opt. Soc. Am. A **9**, 2159–2166 (1992)
30. M.K. Tey et al., Strong interaction between light and a single trapped atom without the need for a cavity. Nat. Phys. **4**, 924–927 (2008)
31. N. Piro et al., Heralded single-photon absorption by a single atom. Nat. Phys. **7**, 17–20 (2011)
32. S.A. Aljunid et al., Excitation of a single atom with exponentially rising light pulses. Phys. Rev. Lett. **111**, 103001 (2013)
33. C.W. Gardiner, Inhibition of atomic phase decays by squeezed light: a direct effect of squeezing. Phys. Rev. Lett. **56**, 1917–1920 (1986)
34. N. Bokor, N. Davidson, 4π focusing with single paraboloid mirror. Opt. Commun. **281**, 5499–5503 (2008)
35. G. Leuchs et al., Interferometric null test of a deep parabolic reflector generating a Hertzian dipole field. Appl. Opt. **47**, 5570–5584 (2008)
36. R. Maiwald et al., Collecting more than half the fluorescence photons from a single ion. Phys. Rev. A **86**, 043431 (2012)
37. L. Slodička, G. Hétet, S. Gerber, M. Hennrich, R. Blatt, Electromagnetically induced transparency from a single atom in free space. Phys. Rev. Lett. **105**, 153604 (2010)
38. Z. Bomzon, G. Biener, V. Kleiner, E. Hasman, Radially and azimuthally polarized beams generated by space-variant dielectric subwavelength gratings. Opt. Lett. **27**, 285–287 (2002)
39. Z. Ghadyani et al., Concentric ring metal grating for generating radially polarized light. Appl. Opt. **50**, 2451–2457 (2011)
40. M. Stalder, M. Schadt, Linearly polarized light with axial symmetry generated by liquid-crystal polarization converters. Opt. Lett. **21**, 1948–1950 (1996)
41. S. Tidwell, D. Ford, W. Kimura, Generating radially polarized beams interferometrically. Appl. Opt. **29**, 2234–2239 (1990)
42. S. Tidwell, G. Kim, W. Kimura, Efficient radially polarized laser beam generation with a double interferometer. Appl. Opt. **32**, 5222–5229 (1993)
43. R. Oron et al., The formation of laser beams with pure azimuthal or radial polarization. Appl. Phys. Lett. **77**, 3322–3324 (2000)

44. C. Maurer, A. Jesacher, S. Fürhapter, S. Bernet, M. Ritsch-Marte, Tailoring of arbitrary optical vector beams. New J. Phys. **9**, 78 (2007)
45. J. Lin, P. Genevet, M.A. Kats, N. Antoniou, F. Capasso, Nanostructured holograms for broadband manipulation of vector beams. Nano Lett. **13**, 4269–4274 (2013)
46. R. Dorn, S. Quabis, G. Leuchs, Sharper focus for a radially polarized light beam. Phys. Rev. Lett. **91**, 233901 (2003)
47. S. Quabis, R. Dorn, G. Leuchs, Generation of a radially polarized doughnut mode of high quality. Appl. Phys. B **81**, 597–600 (2005)
48. M. Born, E. Wolf, *Principles of Optics*, 6th edn. (Pergamon Press, Oxford, 1991)
49. S.A. Aljunid et al., Phase shift of a weak coherent beam induced by a single atom. Phys. Rev. Lett. **103**, 153601 (2009)
50. M. Pototschnig et al., Controlling the phase of a light beam with a single molecule. Phys. Rev. Lett. **107**, 063001 (2011)
51. G. Hétet, L. Slodička, N. Röck, R. Blatt, Free-space read-out and control of single-ion dispersion using quantum interference. Phys. Rev. A **88**, 041804 (2013)
52. A. Jechow et al., Controllable optical phase shift over one radian from a single isolated atom. Phys. Rev. Lett. **110**, 113605 (2013)
53. G. Zumofen, N.M. Mojarad, V. Sandoghdar, M. Agio, Perfect reflection of light by an oscillating dipole. Phys. Rev. Lett. **101**, 180404 (2008)
54. M.K. Tey et al., Interfacing light and single atoms with a lens. New J. Phys. **11**, 043011 (2009)
55. T. Tyc, Gouy phase for full-aperture spherical and cylindrical waves. Opt. Lett. **37**, 924–926 (2012)
56. M. Sondermann, G. Leuchs, The phase shift induced by a single atom in free space. J. Europ. Opt. Soc. Rap. Public. **8**, 13502 (2013)
57. A.N. Vamivakas et al., Strong extinction of a far-field laser beam by a single quantum dot. Nano Lett. **7**, 2892–2896 (2007)
58. G. Wrigge, I. Gerhardt, J. Hwang, G. Zumofen, V. Sandoghdar, Efficient coupling of photons to a single molecule and the observation of its resonance fluorescence. Nat. Phys. **4**, 60–66 (2008)
59. S.A. Aljunid et al., Interaction of light with a single atom in the strong focusing regime. J. Mod. Opt. **58**, 299–305 (2011)
60. Y.L.A. Rezus et al., Single-photon spectroscopy of a single molecule. Phys. Rev. Lett. **108**, 093601 (2012)
61. P. Kochan, H.J. Carmichael, Photon-statistics dependence of single-atom absorption. Phys. Rev. A **50**, 1700–1709 (1994)
62. G. Hétet, L. Slodička, M. Hennrich, R. Blatt, Single atom as a mirror of an optical cavity. Phys. Rev. Lett. **107**, 133002 (2011)
63. M. Sondermann, G. Leuchs, Scattering of an exponential pulse by a single atom. Rom. Rep. Phys. **65**, 638–645 (2013)
64. Y. Yamamoto, H.A. Haus, Preparation, measurement and information capacity of optical quantum states. Rev. Mod. Phys. **58**, 1001–1020 (1986)
65. A.L. Gaeta, R.W. Boyd, Quantum noise in phase conjugation. Phys. Rev. Lett. **60**, 2618–2621 (1988)
66. M. Stobinska, G. Alber, G. Leuchs, Perfect excitation of a matter qubit by a single photon in free space. EPL **86**, 14007 (2009)
67. M.M. Schauer et al., Isotope-selective trapping of doubly charged yb ions. Phys. Rev. A **82**, 062518 (2010)
68. M. Förtsch et al., A versatile source of single photons for quantum information processing. Nat. Commun. **4**, 1818 (2013)
69. H.L. Dao, S.A. Aljunid, G. Maslennikov, C. Kurtsiefer, Preparation of an exponentially rising optical pulse for efficient excitation of single atoms in free space. Rev. Sci. Instrum. **83**, 083104 (2012)
70. P. Kolchin, C. Belthangady, S. Du, G.Y. Yin, S.E. Harris, Electro-optic modulation of single photons. Phys. Rev. Lett. **101**, 103601 (2008)

71. B. Srivathsan, G.K. Gulati, A. Cerè, B. Chng, C. Kurtsiefer, Reversing the temporal envelope of a heralded single photon using a cavity. Phys. Rev. Lett. **113**, 163601 (2014)
72. S. Heugel, A.S. Villar, M. Sondermann, U. Peschel, G. Leuchs, On the analogy between a single atom and an optical resonator. Laser Phys. **20**, 100–106 (2010)
73. M. Bader, S. Heugel, A.L. Chekhov, M. Sondermann, G. Leuchs, Efficient coupling to an optical resonator by exploiting time-reversal symmetry. New J. Phys. **15**, 123008 (2013)
74. T. Palomaki, J. Harlow, J. Teufel, R. Simmonds, K. Lehnert, Coherent state transfer between itinerant microwave fields and a mechanical oscillator. Nature **495**, 210–214 (2013)
75. J. Wenner et al., Catching time-reversed microwave coherent state photons with 99.4% absorption efficiency. Phys. Rev. Lett. **112**, 210501 (2014)
76. C. Liu et al., Efficiently loading a single photon into a single-sided fabry-perot cavity. Phys. Rev. Lett. **113**, 133601 (2014)
77. R. Maiwald et al., Stylus ion trap for enhanced access and sensing. Nat. Phys. **5**, 551–554 (2009)
78. A.S. Bell et al., Laser cooling of trapped ytterbium ions using a four-level optical excitation scheme. Phys. Rev. A **44**, 20–23 (1991)

Chapter 4
Free Space Interference Experiments with Single Photons and Single Ions

Lukáš Slodička, Gabriel Hétet, Markus Hennrich and Rainer Blatt

Abstract Trapped ion crystals have proved to be one of the most viable physical implementations of quantum registers and a promising candidate for a scalable realization of quantum networks. The latter will require the development of an efficient interface between trapped ions and photons. We describe two research directions that are currently investigated to realize such photonic quantum interfaces in free space using high numerical aperture optics. The first approach investigates how strong focusing of light onto a single ion can increase the interaction strength to achieve efficient interaction between a photon and the ion. The second approach uses a probabilistic measurement on scattered photons to generate entanglement between two ions that could be used to distribute information in a quantum network. For both approaches a higher numerical aperture would increase the efficiency of the interface.

L. Slodička (✉)
Department of Optics, Palacký University, 17. listopadu 1192/12, 771 46, Olomouc, Czech Republic
e-mail: slodicka@optics.upol.cz

G. Hétet
Laboratoire Pierre Aigrain, Ecole Normale Supérieure-PSL Research University, CNRS, Université Pierre et Marie Curie-Sorbonne Universités, Université Paris Diderot-Sorbonne Paris Cité, 24 rue Lhomond, 75231 Paris Cedex 05, France
e-mail: gabriel.hetet@lpa.ens.fr

M. Hennrich · R. Blatt
University of Innsbruck, Technikerstr. 25, 6020 Innsbruck, Austria
e-mail: markus.hennrich@uibk.ac.at

M. Hennrich
Department of Physics, Stockholm University, Roslagstullsbacken 21, 106 91 Stockholm, Sweden

R. Blatt
Institute for Quantum Optics and Quantum Information, Austrian Academy of Sciences, Technikerstr. 21a, 6020 Innsbruck, Austria
e-mail: rainer.blatt@uibk.ac.at

A. Predojević and M.W. Mitchell (eds.), *Engineering the Atom-Photon Interaction*, Nano-Optics and Nanophotonics, DOI 10.1007/978-3-319-19231-4_4

4.1 Coupling to a Single Ion in Free Space

Atom-photon interfaces are a key element for constructing a quantum network [1–3]. Here, the interface maps quantum information from stationary to flying qubits and vice versa. Usually photons are employed as flying qubits due to their robustness in preserving quantum information during propagation, while atoms are used for storing and computing the quantum information in stationary nodes. The efficient mapping of quantum information from atoms to photons and back demands controlled photon emission and absorption with a very high probability. This condition can be achieved in a strong coupling regime where the information is exchanged between atoms and photons several times before it decoheres. The standard way to achieve strong atom-photon coupling is by using either small high finesse cavities, which increase the interaction between a single atom and a photon [4–6] as described in chapter by A. Kuhn, or large atomic ensembles for continuous variable quantum interfaces [7–9] treated in chapter by Chuu and Du.

In free space, i.e. without an enhancing cavity, the coupling of a single atom and light is generally considered to be weak. Nevertheless, it can be significantly increased if the light covers a large solid angle, for instance by using large aperture lenses [10] or mirrors [11]. In such a setup it is possible to observe effects where a single atom can notably modify the light field. For instance, several experiments have recently demonstrated that a single quantum particle, like a single rubidium atom [12], a molecule [13–15], or a quantum dot [16] can cause extinction of more than 10 %, and a phase shift of 1° [17] for the transmitted light. Also, a single molecule has been shown to act as a nonlinear switch [18]. These experiments are first steps towards realizing photonic quantum gates and quantum memories with single atoms in free space.

In this chapter we will discuss several experiments in which single ions are placed at the focus of high numerical aperture optics for efficient atom-light interaction. In Sect. 4.1 of this chapter we will review several experiments on direct free space coupling of a single trapped ion with light. Here, the high numerical aperture optics allow the observation of effects which are usually only observed with large atomic ensembles or single atoms in high finesse cavities, including electromagnetically induced transparency [19], coherent back scattering [20], and Faraday rotation induced on a propagating laser field [21]. Very similar ideas and experiments discussing the efficient absorption of single photons by single ions are described also in the chapters by Leuchs and Sondermann and by Piro and Eschner.

Later in Sect. 4.2 we will treat probabilistic methods to exchange quantum information over a distance. Here, a projective measurement on the fluorescence photons scattered by two atoms projects them into an entangled state, which then for instance could be used to link distant registers in a quantum network using protocols like quantum teleportation or entanglement swapping.

4.1.1 Electromagnetically Induced Transparency from a Single Atom in Free Space

The controlled storage and retrieval of photonic quantum information from an atomic medium is often based on a phenomenon called electromagnetically induced transparency (EIT) [22] or its excitation in the form of stimulated Raman adiabatic passage (STIRAP) [23]. This technique has been widely used to control the storage of weak light pulses or single photons in atomic ensembles [8, 9, 24] and high-finesse cavities [25, 26]. For EIT, atoms in a lambda-type three-level system are driven by a weak probe laser and a strong control laser in Raman configuration. Due to a destructive quantum interference effect the control laser suppresses the absorption of the resonant probe light. Consequently, by changing the control laser intensity it is possible to switch the medium between transmitting and absorbing the probe light. Seen from a different point of view, the control laser intensity changes the group velocity of the probe laser. Thus, adiabatic ramping of the control laser intensity can slow down and even stop a single probe photon. In this way the photon is stored in the long-lived atomic ground states of the medium and can be retrieved by a time-reversal of the storage process [1, 22]. An extension of this scheme can store a photonic quantum state, for instance encoded in the polarization of light, in superpositions of atomic ground states [27], thus realizing a memory for the photonic quantum information.

Effective switching between transmission and absorption can only be achieved in optically thick media. Therefore, until recently the application of EIT was restricted to ensembles of many atoms [22]. In contrast, (discrete variable) quantum information processing is based on single well-defined qubits (for example single atoms or ions) where each qubit can be individually manipulated to perform quantum gates. A quantum network which combines these two technologies requires strong single atom-single photon interaction within the interface nodes to distribute quantum information over the nodes of the quantum network.

Trapped ions are at the moment one of the most advanced systems for quantum information processing [28]. Also, since ions of the same species are identical, they are very well suited as indistinguishable light sources [29, 30] at the distant locations of a quantum network. Furthermore, the precise control over the electronic and motional states of the ions in Paul traps makes them ideal to investigate the coupling of radiation to single absorbers. In the following, we will present first steps towards a free-space single ion quantum interface by demonstrating an extinction of a weak probe laser of 1.3 %, electromagnetically induced transparency from a single trapped ion, and the corresponding phase shift response.

4.1.1.1 Extinction and Phase Shift Measurements

The experiments that we will describe in this chapter show the relation between the input and the transmitted light field in the presence of an atom [21]. The following simple theoretical model can describe the basic properties of the extinction and

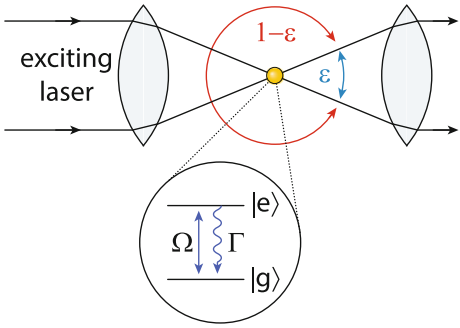

Fig. 4.1 Schematic view of a single atom irradiated by continuous laser light. The atom is illuminated from a fraction of the solid angle ε and radiates into full solid angle. The fluorescent light in general contains both elastic and inelastic components, nevertheless, for weak excitation the elastic component dominates. In the forward direction the elastically scattered part of the fluorescent light interferes with the transmitted laser beam (ε). In the backward direction $(1-\varepsilon)$ the fluorescent light is observed

reflection of a weak probe field from a single atom. This approach uses a perturbative input-output formalism to relate the input field, $\hat{E}_{\text{in}}$, and the output field, $\hat{E}_{\text{out}}$, through their interaction with the atom [31] as schematically depicted in Fig. 4.1. In Markov approximation, the output field in forward direction can be described as a superposition of the transmitted input field and the emitted field of the radiating atomic dipole as

$$\hat{E}_{\text{out}}(t) = \hat{E}_{\text{in}}(t) + i\sqrt{2\gamma_{\text{in}}}\hat{\sigma}(t), \tag{4.1}$$

where $\hat{\sigma}(t)$ is the atomic coherence and γ_{in} is an effective coupling coefficient of the input field to the atom. The coupling coefficient can also be expressed by the total decay rate of the excited state γ and the fraction ε of the full solid angle covered by the incoming field as $\gamma_{\text{in}} = \varepsilon\gamma$. The atom reacts on the excitation by the input field, thus the atomic coherence $\hat{\sigma}(t)$ can be calculated by solving Bloch equations of the two-level atom in the weak excitation limit and in steady state, which gives

$$\hat{\sigma} = \frac{i\sqrt{2\gamma_{\text{in}}}}{\gamma + i\Delta}\hat{E}_{\text{in}}, \tag{4.2}$$

where Δ is the frequency detuning of the probe light from the excited state. Finally, the transmission of the intensity of the probe field $T = |E_{\text{out}}/E_{\text{in}}|^2$ in steady state reads

$$T(\Delta) = |1 - 2\varepsilon\mathscr{L}(\Delta)|^2, \tag{4.3}$$

where the amplitude of the atomic coherence is proportional to $\mathscr{L}(\Delta) = \gamma/(\gamma + i\Delta)$ for a two level atom. Furthermore, the phase shift ϕ of the transmitted light field is

$$\phi(\Delta) = \arg\left[1 - 2\varepsilon\mathscr{L}(\Delta)\right]. \tag{4.4}$$

Please note that this simple theory predicts perfect extinction of the transmitted probe field, and thus full reflection for a weak resonant input field covering half of the full solid angle ($\varepsilon = 0.5$). This results from the interference between the transmitted input beam and the radiated dipole field, which yields a considerable decrease in the forward mode amplitude [13, 32]. In the experiment described below, we use a lens with numerical aperture NA = 0.4 (i.e. $\varepsilon = 4\,\%$), so we expect a probe beam extinction of 16 % from (4.3) from this basic theoretical model. More refined models [12, 13, 33] include effects like the polarization of the input beam and the exact mode overlap between the transmitted beam and the dipole emission pattern which becomes especially important when the input beam is focused to the atom from a large solid angle with a high numerical aperture lens beyond the paraxial approximation. From the model of [12], we expect an extinction of around 13 % for our experimental parameters. A higher extinction is possible for larger solid angles. Nevertheless, if one wants to use a single atom in free space as a quantum interface, for an efficient sender one will need to collect the emitted photon from full solid angle. Also, an efficient quantum receiver will demand reversal of the emission process, thus the single photon input mode will have to match the full dipole radiation pattern and the reversed temporal mode of the atomic emission as detailed in [11] and chapter by Leuchs and Sondermann.

In the following we will describe how we measure the single ion transmission, the phase shift, and the EIT effect in our experiment. The experimental setup consists of a high numerical aperture objective [34] to focus the probe field onto a single trapped ion and a second objective to collect the transmitted light onto a detector, shown in Fig. 4.2a. The barium ion is trapped and cooled in a standard spherical Paul trap. As already mentioned before, good extinction of the probe field can only be achieved if the incoming probe beam and dipole emission pattern are carefully overlapped. This mode-matching is done using an expanding telescope and a custom-designed objective with a numerical aperture of NA = 0.4 ($\varepsilon = 4\,\%$). A magnetic field of 5 Gauss applied along the probe beam propagation direction defines the quantization axis. The probe field is linearly polarized perpendicular to the quantization axis, collected after the ion using a second high numerical aperture lens, and then analyzed using a polarimetric set-up and photo-multiplier tubes (PMT). In practice, we detect the transmitted polarization alternately at $+45$ or $-45°$ with respect to the input polarization.

The level scheme of $^{138}Ba^{+}$ is shown in Fig. 4.2b. The probe field is tuned to the $6S_{1/2} \rightarrow 6P_{1/2}$ transition and with our choice of quantization axis, its polarization can be decomposed onto left and right circularly polarized modes that drive σ_{-} and σ_{+} transitions in the ion, respectively. The two polarization modes do not have the same detuning from their respective transitions and thus may experience different indices of refraction. We set the intensity of the probe field well below saturation so that most of the light is elastically scattered. The probe field supplies only weak cooling to the ion. Therefore the ion is cooled additionally by a red detuned 493 nm laser field perpendicular to the probe direction and a laser at 650 nm, co-propagating

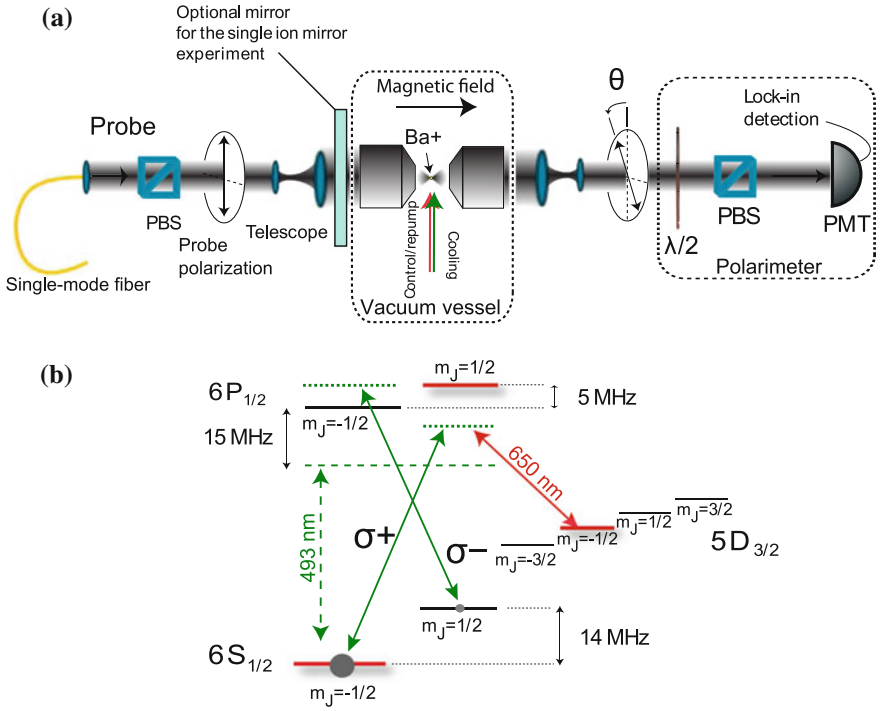

Fig. 4.2 **a** Scheme of the experimental set-up used to measure EIT and the corresponding phase shift on a single atom [21]. The probe field is defined in horizontal polarization by passing through a polarizing beam-splitter (PBS). The laser beam is then expanded by a telescope and focused by a high numerical aperture lens in vacuum (NA = 0.4) onto the ion. Depending on the intensity of the control laser, the single ion changes the transmission of the probe light and rotates its polarization, which after re-collimation is detected by polarimetry. **b** Level scheme of $^{138}Ba^{+}$ and probe and control laser fields used in the experiment. The input probe field at 493 nm is decomposed in the two circular polarizations which excite two branches of the spin-half system with different detunings. The laser field at 650 nm is used as the control field in the EIT measurements and for repumping population from the $5D_{3/2}$ level

with the cooling beam, for pumping out population from the $5D_{3/2}$ level. For the characterization of the Faraday rotation we use a lock-in method where the 650 nm repumping laser is switched on and off at a rate of 5 kHz to precisely measure the polarization rotation signal. When the repumping laser is off the population of the atom is pumped into the $5D_{3/2}$ state. Since the probe beam drives the transition between $6S_{1/2}$ and $6P_{1/2}$, it does not feel the presence of an ion that resides in $5D_{3/2}$. Thus, the modulation of the repumping laser also modulates the effect of the atom on the probe field. The photo-multiplier signal is demodulated and low-pass filtered with a time constant of 1 s.

The intensity of the light at the PMT measured at $+45°$ with respect to the input polarization can be written as

$$I_{45} = \frac{1}{2}|E^{+}_{\text{out}}e^{i\pi/4} + E^{-}_{\text{out}}e^{-i\pi/4}|^2, \tag{4.5}$$

where

$$E^{+}_{\text{out}} = (1 - 2\varepsilon\mathscr{L}^{+})\tfrac{1}{\sqrt{2}}E_{\text{in}} \quad \text{and} \tag{4.6}$$

$$E^{-}_{\text{out}} = (1 - 2\varepsilon\mathscr{L}^{-})\tfrac{1}{\sqrt{2}}E_{\text{in}} \tag{4.7}$$

are the corresponding output fields of σ^+ and σ^- polarization, respectively. The real and imaginary parts of

$$\mathscr{L}^{\pm} = \frac{\rho_{\pm}\gamma}{\gamma + i\Delta^{\pm}} \tag{4.8}$$

correspond to absorption and phase-lag of the two scattered circularly polarized field modes with regards to the input field, respectively. Here, $\Delta^{\pm} = \Delta \pm \Delta_B$ are the detunings of the σ^+ and σ^- polarized fields from their respective transitions. The two ground state populations ρ_+ (ρ_-) of the σ_+ (σ_-) transition correspond to the states $6S_{1/2}$, $m_J = -1/2$ ($m_J = +1/2$), respectively. Δ is the probe laser detuning with respect to the $6S_{1/2} \rightarrow 6P_{1/2}$ transition without Zeeman shift, and Δ_B is the frequency offset of the two resonances due to the Zeeman splitting. The $\pm\pi/4$ phase shifts in (4.5) are due to the rotation of the polarization direction between input and detected polarization induced by the $\lambda/2$ waveplate that allows us to characterize the Faraday rotation.

To measure the Faraday rotation angle $\theta = \frac{1}{2}\arctan(s_2/s_1)$, here defined as half the rotation angle from horizontal polarization towards 45° polarization on the Poincaré sphere, we need to record the Stokes parameter $s_1 = I_0 - I_{90}$, and $s_2 = 2I_{45} - s_0$, with $s_0 = I_0 + I_{90}$. Please note that for our small extinction values the Stokes parameter s_1 can be approximated by $s_1 \approx s_0 \approx I_0$, which can be measured directly by removing the polarizing beam-splitter. After re-inserting the beam-splitter and adjusting the waveplate accordingly, we can access the Stokes parameter $s_2 \approx 2I_{45} - I_0$. The Faraday rotation angle $\theta \approx \frac{1}{2}\arctan((2I_{45} - I_0)/I_0)$ is directly related to the phase shift induced by the atom. It can be shown, using the approximation $\arg(1 - 2\varepsilon z) \approx -2\varepsilon\text{Im}(z)$ in the limit of small ε, that

$$\theta = \frac{1}{2}\arg\left[1 - 2\varepsilon(\mathscr{L}^{+} - \mathscr{L}^{-})\right], \tag{4.9}$$

which is half of the phase lag experienced by the output with respect to the input field. A measurement of I_{45} and I_0 thus provides a measurement of the Faraday rotation of the light across the atom together with the phase difference acquired by the two circularly polarized modes.

We characterize the Faraday rotation of the probe field by measuring the phase shift θ and the transmission I_0, which are plotted in Fig. 4.3a as a function of the probe frequency detuning Δ. As can be seen from the measurement of I_0, an optical pumping mechanism by the cooling and repumping lasers causes a strong

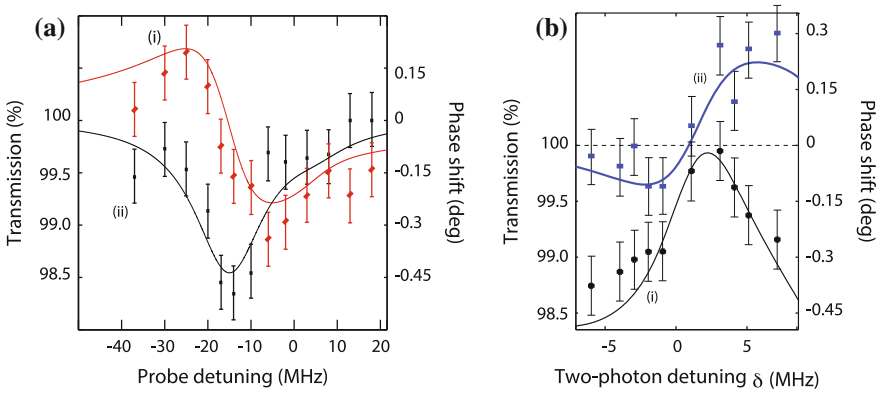

Fig. 4.3 **a** Transmission I_0 (*ii*) and phase shift θ (*i*) of a probe field transmitted through a single trapped barium ion as a function of probe beam detuning [21]. The transmission spectrum is fitted by a Lorentzian profile with a width of 11 MHz. The peak probe beam extinction is 1.35 %. **b** Transmission (*i*) and phase shift (*ii*) of a probe field transmitted through a single trapped barium ion as a function of probe beam detuning close to a dark resonance

unbalancing between the two ground states populations. In principle, one would expect to observe two identical absorption lines at $+5$ and -14 MHz (shifted with respect to the symmetric case due to dipole shifts) for the σ_+ and σ_- transitions of the probe light from $6S_{1/2}$ to $6P_{1/2}$, respectively. Here, the optical pumping induced by the cooling and repumping lasers traps population in the $|6S_{1/2}, m_J = +1/2\rangle$ level so that only the σ_- transition can be detected by the probe field. This manifests itself in the 1.5 % extinction that is seen -14 MHz red-detuned from the central line for the σ^- and in the almost completely suppressed extinction for the other σ^+ mode at 5 MHz. With this state preparation, trace (i) displays a clear dispersive profile across the resonance of the σ_- transition and the σ^+ polarized mode is almost not phase shifted. Even with our small magnetic field, the pumping technique thus allows us to isolate a single two-level atom and to reach a maximum of 0.3° phase-shift. Solid lines show the result of a fit of the data using the above four-levels calculations, with $\varepsilon = 0.8\,\%$, $\Delta_B = 9$ MHz, $\rho_- = 0.9$ and $\rho_+ = 0.1$. With these parameters, good agreement is found with the experimental results.

4.1.1.2 Electromagnetically Induced Transparency and Associated Phase Shift with a Single Atom

In the above measurements, the cooling and repumping beams were tuned to a dark resonance with the intention to pump the population of the ion into one of the $S_{1/2}$ levels and therefore minimize the population in the $D_{3/2}$ state which is not interacting with the probe laser. Nevertheless, the transverse cooling beam can also be turned off and the ion be cooled by the linearly polarized probe field itself. In such

a configuration the probe undergoes electromagnetically induced transparency (EIT) [19] where the population in the excited state of the Λ scheme (see Fig. 4.2b) is canceled due to a quantum interference between the two excitation pathways leading to the $P_{1/2}$ excited state.

Under weak probe excitation, the probe transmission as a function of the two-photon detuning $\delta = \Delta_g - \Delta_r$ can be found by solving the Bloch equations [35] and using the above input-output relations. We neglect here the angular dependence of the extinction (due to polarization). That is, we suppose that the probe has a polarization profile that matches the dipole field. This is a good approximation for the relatively small numerical aperture we use in this experiment. We can thus replace the function $\mathscr{L}$ by

$$\mathscr{L}_\Lambda(\delta) = \frac{\gamma(\gamma_0 - i\delta)}{(\gamma_0 - i\delta)(\gamma + i\Delta_g) + \Omega_r^2}, \tag{4.10}$$

in (4.3), where Ω_r is the Rabi frequency of the red laser field, γ_0 the ground state dephasing rate, γ the natural linewidth of the two transitions (assumed to be the same for simplicity). An important condition for EIT to take place is $\gamma\gamma_0 \ll \Omega_r^2$, i.e. the pumping rate to the dark state must be much faster than any ground state decoherence process. Independent frequency fluctuations of the two laser fields, magnetic field fluctuations, and atomic motion induced Doppler shifts, must be therefore reduced. When this is the case, extinction of the resonant probe can be completely inhibited, within a small range of control laser detuning Ω_r^2/γ, creating an EIT window. This is what we observed in this experiment.

In the experiment we found that the motion induced decoherence yields broadening of tens of kHz, which reduced the EIT when the control and the probe were orthogonal to each other. However, the effect of Doppler shifts due to the ion motion could be eliminated when we used co-propagating control and probe fields. Since for optimum EIT conditions we could not use the cooling fields which would have reduced the transparency achieved through EIT, so the ion needed to be cooled by the probe itself. Consequently, the probe beam was more intense and red detuned, which resulted in reduced extinction efficiencies of about 0.6 %. Additionally, we have to note here that due to the multi-level structure of barium, a single three level system can only be perfectly isolated from the others through optical pre-pumping. Therefore, Stark-shifts induced by the other levels and double-Λ type couplings contribute to a slight reduction of the EIT contrast.

The results of the measurement of the probe transmission versus the two-photon detuning δ are shown in Fig. 4.3b trace (i). In this EIT regime, a rapid change of the transmission is found as a function of the two-photon detuning and an almost complete cancellation of the transmission is measured at $\delta = 0$.

Associated with such a steep change of the probe transmission, we also expect a fast roll-off of the phase. Figure 4.3b—trace (ii) shows the measurement of the phase θ of the probe field, using the same polarimetric technique as in the measurement described in the previous section. Here again, close to the dark resonance, the Faraday rotation angle yields the phase-shift induced by the atom. The clear dispersive shape

of θ across the two-photon resonance is here a sign of the EIT induced phase-shift from the ion where a maximum phase lag of 0.3° is observed. The solid lines show a fit to the experimental results using 8-level Bloch equations, consisting of the two $S_{1/2}$, the two $P_{1/2}$ and the four $D_{3/2}$ states. Here we replace the two-level atom Lorentzian functions $\mathscr{L}^{\pm}$ in (4.4) by the newly found susceptibilities. The theory describes well the data with the repumping and probe field intensities as the only two free parameters. The asymmetry of the dispersion and transmission profiles that we measured is due to a slight overlap with neighboring dark-resonances and our detuned driving of the Λ scheme. The distinctive feature of this interference effect is that the flipping of the phase shift sign occurs only over a couple of MHz. Increasing the slope steepness further can in fact be done by performing the experiment with smaller probe and repumping powers which can be implemented by appropriate switching of the laser cooling beams involved in the experiment. Achieving a very steep phase shift dependence across the atomic spectrum would open the way for reading out the motional and internal energy of the atom.

Tightly focusing a weak, detuned, linear polarized probe field onto a single barium ion thus enables observation of both the direct extinction of a weak probe field and electromagnetically induced transparency from a single barium ion. Besides demonstrating further the potential of these effects for fundamental quantum optics and quantum information science, these experimental results will trigger interest for quantum feedback to the motional state of single atoms, as proposed in [36] using EIT, for dispersive read out of atomic qubits and for ultra-sensitive single atom magnetometery.

In the following we will now discuss another effect observed with a similar experimental apparatus where we show that a single atom can act as a mirror of an optical cavity.

4.1.2 Single Ion as a Mirror of an Optical Cavity

Atom-photon interactions are essential in our understanding of quantum mechanics. Besides the two processes of absorption and emission of photons, coupling of radiation to atoms raises a number of questions that are worth investigating for a deeper theoretical and thus interpretational insight. The modification of the vacuum by boundaries is amongst the most fundamental problems in quantum mechanics and is widely investigated experimentally. We here present the very first steps towards merging the field of cavity QED with free-space coupling, using an ion trap apparatus.

Here we report an experiment where we set up an atom-mirror system [20]. As shown Fig. 4.2a, we place a mirror in the path of the probe beam in front of the ion. The idea of this geometry is to form an atom-mirror cavity system consisting of the normal mirror and the ion acting as the second mirror. We observe the modification of the probe transmission and reflection of this atom-mirror cavity. Here, the atomic coupling to the probe is modified by the single mirror in a regime where the probe intensity is already significantly altered by the atom without the mirror. In principle,

in the limit of an even higher numerical-aperture lens, the mirror-induced change in the vacuum-mode density around the single atom could modulate the atom's coupling to the probe, the total spontaneous decay and the Lamb shift, so that the atom would behave as the mirror of a high-finesse cavity.

As before, for extinction of a laser field by the ion in free space, we use a very weak probe beam resonant with the $S_{1/2}(m_J = +1/2) - P_{1/2}(m_J = -1/2)$ transition. In the case of coherent reflection of a laser field by a single atom, the backscattered field must interfere with the driving laser. To verify this, we construct the system shown in Fig. 4.2a by inserting a dielectric mirror 30 cm away from the atom into the probe path, with a reflectivity $|r|^2 = 1 - |t|^2 = 25\,\%$. We align it so that the ion is re-imaged onto itself and shine the resonant probe through it. Using the Fabry-Pérot cavity transmissivity, and modeling the atom as a mirror with amplitude reflectivity 2ε [31], one can naively assume that the intensity transmissivity of the probe reads

$$T = \left| \frac{t(1-2\varepsilon)}{1 - 2r\varepsilon e^{i\phi_L}} \right|^2, \tag{4.11}$$

where $\phi_L = 2k_L R$, R is the atom-mirror distance and k_L the input probe wavevector. The finesse $\mathscr{F} = \pi 2\varepsilon r/(1-(2\varepsilon r)^2)$ of such a cavity-like set-up can in fact be made very large by using a high numerical aperture lens such that $\varepsilon \to 50\,\%$ together with a highly reflective dielectric mirror. By tuning the distance between the dielectric mirror and the ion, one would therefore expect a dependence of the transmitted signal on the cavity length, provided that the temporal coherence of the incoming field is preserved upon single-atom reflection.

The operation of our ion-mirror system is shown in Fig. 4.4b, where we simultaneously recorded the reflected and transmitted intensity. As the mirror position is scanned, we indeed observed clear sinusoidal oscillations of the intensity on a wavelength scale. These results reveal that the elastic back-scattered field is interfering with the transmitted probe, and that the position of the ion is very well defined, meaning that it is well within the Lamb-Dicke regime. Reflected and transmitted intensity

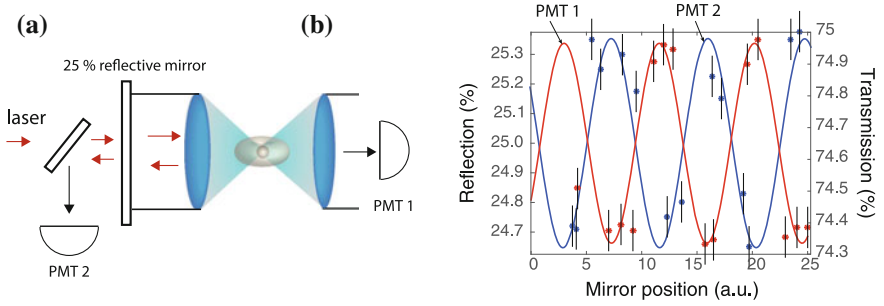

Fig. 4.4 **a** Experimental setup with an optical cavity formed by the mirror and the single ion. PMT 1 and 2 measure the transmitted and the reflected probe laser intensity, respectively. **b** Reflection and transmission signal of the ion-mirror cavity as a function of the mirror position [20]

have opposite phase, as is predicted for a Fabry-Pérot cavity response. The slight shift in the two sinusoidal fitting functions is within the measurement error bars.

We now investigate whether the naive Fabry-Pérot interpretation that we used to describe our results is valid. One could indeed wonder how the modification of the quantum vacuum around the atom affects our results. It is clear that the dielectric mirror imposes new boundary conditions that change the vacuum mode density close to the atom, but it is less obvious how much this change contributes to the probe intensity modulation that we observe in this experiment. One can in fact show [20] that solving the multimode Heisenberg equations in a time-dependent perturbation theory gives

$$T = |t|^2 \left| 1 - \frac{2 g_\varepsilon \overline{g}^*}{\tilde{\gamma} + i\tilde{\Delta}} \right|^2, \tag{4.12}$$

assuming the input probe to be resonant with the atomic transition. Here, g_ε denotes the atomic coupling strength in the probe mode, $\overline{g}$ is the mean coupling to all the modes, $\tilde{\gamma}$ and $\tilde{\Delta}$ are the decay and level shifts modified by the presence of the mirror, respectively. Their value can be calculated using the appropriate spatial mode function for this system [37] and we can then show that

$$\frac{g_\varepsilon \overline{g}^*}{\tilde{\gamma} + i\tilde{\Delta}} = \frac{\varepsilon(1 - re^{i\phi_L})}{1 - 2r\varepsilon e^{i\phi_L}}. \tag{4.13}$$

After combining this relation with (4.12) we obtain the same transmissivity as was obtained by modeling the atom as a mirror with reflectivity 2ε (4.11). Interestingly, the QED calculations yield the same mathematical results as the direct Fabry-Pérot calculation.

In this QED approach, it was not necessary to invoke multiple reflections off the atom for the Fabry-Pérot like transmission to appear. The transmission of the probe through the single atom+mirror system is mathematically equivalent to a cavity, therefore the origin of the peaked transmission profile can be interpreted either as a cavity effect or as a line-narrowing effect due to the QED-induced changes of the spontaneous emission rate and level shift. In the second interpretation, the observed oscillations can be interpreted as a change of the coupling between the atom and the probe mode, due to the modification of the mode density at the position of the ion induced by the mirror. For very high numerical optics the change of the extinction contrast would be analogous to an almost complete cancellation and enhancement by a factor of two of the atomic coupling constant in the probe mode. Deviations from the sinusoidal shape due to line narrowing would already be visible for a lens covering a solid angle of more than 10 %.

4.2 Probabilistic Entanglement Between Distant Ions

Long-lived entanglement between distant physical systems is an essential primitive for quantum communication networks [2, 3], and distributed quantum computation [38–40]. There are several protocols generating entanglement between distant matter qubits [41], like single atoms. The majority of them exploit traveling light fields as mediators of the entanglement generation process. A way to generate distant entanglement is based on the spontaneous generation of entanglement between an atom and a single photon during the emission process followed by the absorption of the photonic state in a second atom [1]. This method can generate entanglement deterministically, if the photon collection and absorption processes are highly efficient. Nevertheless, photon losses in experimental realizations might render it necessary to first detect a successful photon absorption in order to herald the successful entanglement generation. Another approach generates the entanglement probabilistically by detecting single photons that were scattered by two atoms. The projective measurement on the photons heralds an entangled state of the two atoms [2, 3, 42, 43].

The realization of heralded entanglement between distant atomic ensembles [44, 45] was amongst the first major experimental achievements in this field. Probabilistic generation of heralded entanglement between single atoms [43] was demonstrated using single trapped ions [46] with an entanglement generation rate given by the probability of coincident detection of two photons coming from the ions [47, 48]. More recently, single neutral atoms trapped at distant locations were entangled using the deterministic entanglement protocol described above [27]. Nevertheless, the efficiency of this realization was still limited due to losses to approximately 2 %. A heralding mechanism will therefore be essential for efficient entanglement and scalability of quantum networks using realistic channels [41]. The distant entanglement could also be used for one-way quantum computation schemes [49, 50]. Such schemes for distributed quantum information processing would require only projective measurements and single qubit operations to perform quantum calculation [41]. For future quantum information applications it therefore will be important to realize *heralded* distant entanglement with the possibility of *single qubit operations* and with *high entanglement generation rate* at the same time.

4.2.1 Single-Photon and Two-Photon Protocols

The main limitation for generation of heralded distant entanglement between single atoms with high rate is imposed by relatively small overall detection efficiencies η of fluorescence photons emitted by atoms trapped in free space [47]. For state-of-the-art experimental setups employing high numerical aperture optics close to single trapped neutral atoms or ions, η is on the order of 10^{-3} [32, 51–54]. There is a large effort in the experimental quantum optics community towards increasing this number both by employing very high numerical aperture optics in the form

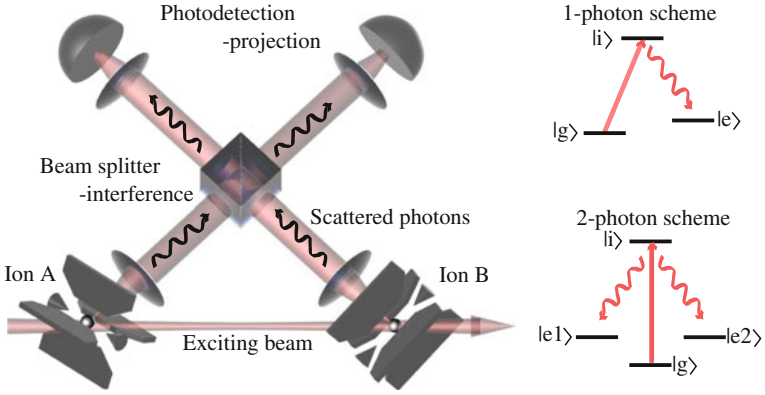

Fig. 4.5 Both one- and two-photon entanglement protocols use the same steps for generating heralded entanglement of distant atoms. After electronic excitation the atoms decay back to a ground state, while spontaneously emitting a photon. The scattered photons interfere to make it indistinguishable which of the two atoms has scattered the photon. Finally, the photons are detected and project the atoms into entangled state. For the two-photon protocol, two photons must be emitted from two distant atoms and the detection corresponds to the projection onto one of the Bell states in the photon basis. For the single photon scheme, only one photon has to be emitted and detected. Depicted energy levels correspond to the typical schemes employed for the two protocols with $|g\rangle$, $|i\rangle$ and $|e\rangle$ corresponding to the initial ground state, auxiliary excited state and final state after Raman process, respectively

of spherical [55] or parabolic [56, 57] mirrors and by developing single-photon detectors with high quantum efficiency. However, even with these improvements it will be hard to increase the overall detection efficiency by more than one order of magnitude in the near future.

We compare the efficiency of the two known heralded entanglement generation protocols based on the single-photon [42] and two-photon [43] detection. Both protocols are based on the atomic excitation, indistinguishability and interference of the emitted photons and on state-projective detection, as illustrated in Fig. 4.5.

We define two dimensionless measures crucial for the performance of any practical quantum information network [47]. Fidelity between the generated state described by the density matrix ρ and the desired maximally entangled two qubit state $|\psi\rangle$,

$$F = \langle\psi|\rho|\psi\rangle \tag{4.14}$$

and success probability P_s, corresponding to probability with which this state can be generated for given overall detection efficiency η.

Following the simplified model in the work of Zippilli et al. [47], the fidelity and success rate of the single-photon protocol are given by

$$F_1 \sim (1 - p_e)/(1 - \eta p_e) \quad \text{and} \quad P_{s,1} \sim 2\eta p_e(1 - \eta p_e). \tag{4.15}$$

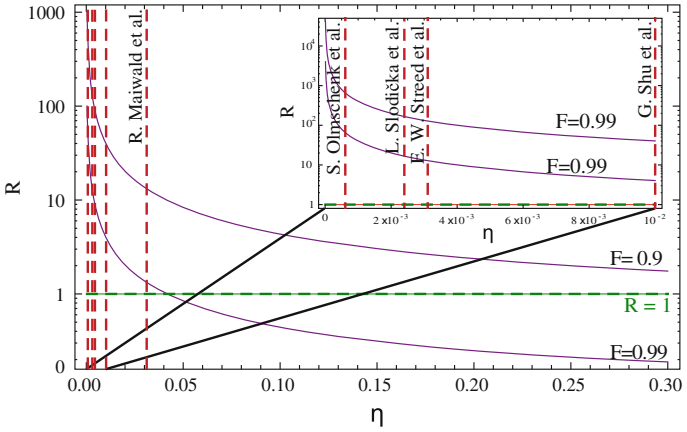

Fig. 4.6 Success probability ratio of entanglement generation for the single-photon and two-photon protocols. For current ion-trapping experimental setups [51, 55, 58–60] the overall collection and detection efficiency is limited to few percents. For such realistic detection efficiencies, the single-photon entanglement generation scheme has potential to be several orders of magnitude faster than the two-photon scheme. The three highest detection efficiencies values are from experiments where fluorescence was detected directly, without coupling to optical fiber

Here p_e is the probability of the successful excitation and emission of a single photon by a single ion. For a given value of p_e, the fidelity increases with overall detection efficiency because the likelihood of detecting events where two photons are scattered increases. For a two-photon protocol, the effect of detection efficiency on generated state fidelity is negligible, because both atoms need to be excited and only coincidence detection events trigger entanglement, and thus the fidelity of the generated state with the maximally entangled state is assumed to be $F_2 = 1$. However, the rate and success probability of entanglement generation depend here quadratically on η,

$$P_{s,2} \sim \eta^2, \tag{4.16}$$

since the two photons need to be detected at the same time.

Figure 4.6 shows the ratio of success probabilities $R = P_{s,1}/P_{s,2}$ of the two protocols for fixed values of the generated states fidelities as a function of detection efficiency. For a given desired fidelity the two-photon scheme is faster only for high overall detection efficiencies. There is a large advantage in using the single-photon scheme for experimental setups with detection efficiencies below 10^{-2}. For most of currently realized single-atom experiments, the theoretical gain in entanglement generation rate using the single-photon scheme thus corresponds to several orders of magnitude. In addition, even for unrealistically high detection efficiencies of more than 90 %, the single-photon scheme can give higher success rates of generated entangled states with high fidelities. This is due to the high detection probability

of double excitations in this limit, which correspond to the fundamental source of infidelity in the single-photon protocol.

4.2.2 Generation of Entanglement by a Single Photon Detection

The entanglement of distant single atoms through the detection of a single photon was proposed in the seminal work of Cabrillo et al. [42]. In this scheme, two atoms (A,B) are both initially prepared in the same long-lived electronic state $|gg\rangle$, see Fig. 4.5. Each atom is then excited with a small probability p_e to another long-lived state $|e\rangle$ through a spontaneous Raman process ($|g\rangle \rightarrow |i\rangle \rightarrow |e\rangle$) by weak excitation of the $|g\rangle \rightarrow |i\rangle$ transition and spontaneous emission of the single photon on the $|i\rangle \rightarrow |e\rangle$ transition. Here $|i\rangle$ denotes an auxiliary atomic state with short lifetime. This Raman process entangles each of the atom's internal states $|s\rangle$ with the emitted photon number $|n\rangle$, so the state of each atom and its corresponding light mode can be written as

$$|s, n\rangle = \sqrt{1 - p_e}|g, 0\rangle e^{i\phi_L} + \sqrt{p_e}|e, 1\rangle e^{i\phi_D}. \tag{4.17}$$

The phases ϕ_L and ϕ_D correspond to the phase of the exciting laser at the position of the atoms and the phase acquired by the spontaneously emitted photons on their way to the detectors, respectively. The total state of the system consisting of both atoms and the light modes can be written as

$$\begin{aligned}|s_\mathrm{A}, s_\mathrm{B}, n_\mathrm{A}, n_\mathrm{B}\rangle = (1 - p_e)e^{i(\phi_{\mathrm{L,A}}+\phi_{\mathrm{L,B}})}|gg, 00\rangle \\ + \sqrt{p_e(1 - p_e)}(e^{i(\phi_{\mathrm{L,A}}+\phi_{\mathrm{D,B}})}|eg, 10\rangle + e^{i(\phi_{\mathrm{L,B}}+\phi_{\mathrm{D,A}})}|ge, 01\rangle) \\ + p_e e^{i(\phi_{\mathrm{D,A}}+\phi_{\mathrm{D,B}})}|ee, 11\rangle.\end{aligned} \tag{4.18}$$

Indistinguishability of the photons from the two atoms is achieved by overlapping their corresponding modes, for example using a beam splitter. Single photon detection then projects the two-atom state onto the entangled state

$$|\Psi^\phi\rangle = \frac{1}{\sqrt{2}}(|eg\rangle + e^{i\phi}|ge\rangle), \tag{4.19}$$

with a probability of $1 - p_e^2$, where p_e^2 is the probability of simultaneous excitation of both atoms. The phase of the generated entangled state ϕ corresponds to the sum of the phase differences acquired by the exciting beam at the position of the two atoms and the phase difference acquired by the photons from the respective atoms upon traveling to the detector,

$$\phi = (\phi_{\mathrm{L,B}} - \phi_{\mathrm{L,A}}) + (\phi_{\mathrm{D,A}} - \phi_{\mathrm{D,B}}). \tag{4.20}$$

The only limiting factor for the fidelity of the generated state with respect to the maximally entangled state emerging from the presented simplified model is the probability of simultaneous excitation of the two atoms p_e^2. However, this can be made arbitrarily small at the expense of entanglement generation success probability P_s, as demonstrated in Fig. 4.6. The phase of the generated state depends on the relative length of the excitation and detection paths, which therefore need to be stabilized with sub-wavelength precision. Random changes of these path-lengths caused by atomic motion or air density fluctuations change the phase of the entangled state in (4.21) in an incoherent way, which can considerably reduce the fidelity of the generated state. In the experiment we stabilize the phase ϕ with interferometric methods to $\phi = 0$. The heralded detection of a single photon should then generate the maximally entangled target state

$$|\Psi^+\rangle = \frac{1}{\sqrt{2}}(|eg\rangle + |ge\rangle). \tag{4.21}$$

4.2.3 Experimental Realization

For the experimental realization of the single-photon entanglement generation scheme two barium ions are trapped in a linear Paul trap setup. As shown in Fig. 4.7, laser light at 493 nm is used to Doppler-cool the ions and to detect their electronic states by means of electron shelving, and a laser field at 650 nm pumps the atoms back to the $6P_{1/2}$ level from the metastable $5D_{3/2}$ state. By carefully adjusting the cooling and trapping parameters, the ions are always well within the Lamb-Dicke limit so that the photon recoil during the Raman scattering process is mostly carried by the trap. This ensures that only minimal information is retained in the motion of the

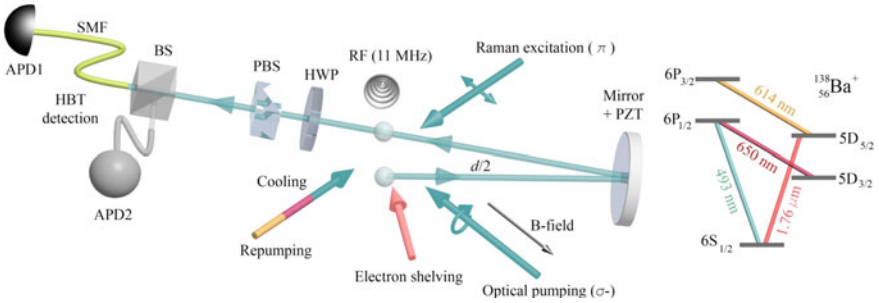

Fig. 4.7 Scheme of the experimental setup for entanglement generation by a single photon detection and relevant electronic level scheme of $^{138}Ba^+$ [59]. Fluorescence of the two ions is overlapped using a distant mirror which sets the effective distance between them to $d = 1$ m. A half wave plate (HWP), a polarizing beam splitter (PBS) and a single-mode optical fiber select the polarization and the spatial mode before an avalanche photodiode (APD1). A non-polarizing beam-splitter and an additional avalanche photodiode (APD2) can be inserted to form a Hanbury-Brown-Twiss setup

ion about which atom has scattered the photon during the entanglement generation process. The fluorescence photons are efficiently collected by two high numerical aperture lenses (NA ≈ 0.4) placed 14 mm away from the atoms. A magnetic field of 0.41 mT is applied at an angle of 40° with respect to the two-ion axis and defines the quantization axis. After passing through a polarizing beam splitter that blocks the π-polarized light and lets σ-polarized light pass, the spatial overlap of the photons is guaranteed by collecting the atomic fluorescence of the first ion in a single mode optical fiber, whilst the fluorescence of the second ion is sent to a distant mirror that retro-reflects it in the same optical fiber. The fluorescence of the two ions (including the Raman scattered light) is then detected by an avalanche photodiode with a quantum efficiency of 60 %.

In order to produce a pure entangled state of two qubits, the phase ϕ of the generated state, defined in (4.20), must be controlled with high precision. This is achieved by a measurement of the phase of the interference produced by the elastic scattering of the 493 nm Doppler-cooling beam from the two ions. Scattered photons will follow the same optical paths as the photons scattered by the Raman beam just in opposite directions. Observation of their interference can be then used for stabilization of the relative phase of the exciting Raman beam at the position of the two ions.

Every experimental sequence of this measurement starts by Doppler-cooling of the two ions. Then the ion-mirror distance $d/2$ is stabilized by locking the position of the measured interference fringe to a chosen position. The electronic states of the ions are then prepared to the Zeeman substate $|6S_{1/2,(m=-1/2)}\rangle = |g\rangle$ by optical pumping with a circularly polarized 493 nm laser pulse propagating along the magnetic field. Next, a weak horizontally polarized laser pulse excites both ions on the $S_{1/2} \leftrightarrow P_{1/2}$ transition with a probability $p_e = 0.07$. From the excited state the ion can decay to the other Zeeman sublevel $|6S_{1/2,(m=+1/2)}\rangle = |e\rangle$, see Fig. 4.8. The electronic state of each ion is at this point entangled with the number of photons $|0\rangle$ or $|1\rangle$ in the σ^- polarized photonic mode. Provided that high indistinguishability of the two photonic channels is assured and that simultaneous excitation of both atoms is negligible, detection of a single σ^- photon on the APD projects the two-ion state onto the maximally entangled state given by (4.21).

Following the detection of a Raman scattered σ^- photon, the two-atom state is coherently manipulated to allow for measurements in a different basis used for the estimation of the generated state. As shown in Fig. 4.8, this is done by first applying radio-frequency (RF) pulses that are resonant with the $|g\rangle \leftrightarrow |e\rangle$ transition of both atoms at transition frequency of 11.5 MHz. Finally, discrimination between the two Zeeman sub-levels of the $6S_{1/2}$ state is done by shelving the population of the $|g\rangle$ state to the metastable $5D_{5/2}$ level using a narrowband 1.76 µm laser. The fluorescence rate on the $6S_{1/2} \leftrightarrow 6P_{1/2}$ transition [59] allows distinguishing between having no excitation at all ρ_{gg}, a single delocalized excitation ρ_{ge} or ρ_{eg}, and two excitations ρ_{ee} in the two-atoms system. These events can be separated with 98 % probability, which enables efficient reconstruction of the relevant parts of the two-atom density matrix. The 614 nm laser field then resets the ions to the $6S_{1/2}$ state and the same experiment is repeated 100 times.

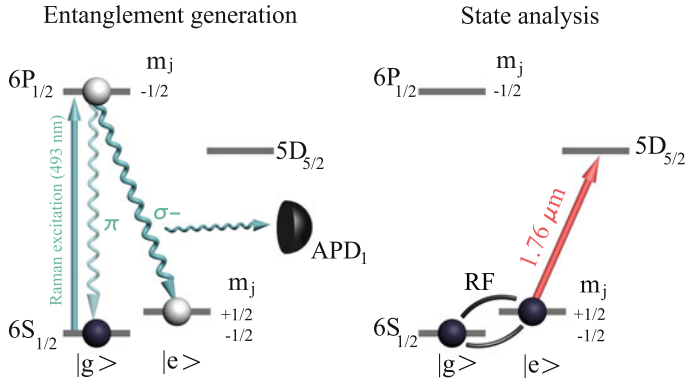

Fig. 4.8 Experimental sequence [59]. Spontaneous Raman scattering from $|g\rangle$ to $|e\rangle$ triggers emission of a single photon from the two atoms. Upon successful detection of a σ^- photon, state analysis comprising coherent radio-frequency (RF) pulses at 11.5 MHz, and electron shelving to the $5D_{5/2}$ level are performed

4.2.3.1 Estimation of the Generated State

The success rate and fidelity of the generated entangled state of distant ions can be estimated by measuring the overlap of the generated state with the desired entangled state every time the heralding photon is detected. It is sufficient to measure only certain parts of the density matrix which contribute to this overlap [59]. The fidelity $F = \langle \Psi^+ | \rho | \Psi^+ \rangle$ of the general two-qubit state ρ with the desired maximally entangled state $|\Psi^+\rangle$ reads

$$F = \frac{1}{2}[\rho_{ge} + \rho_{eg} + 2\mathrm{Re}(\rho_{eg,ge})]. \tag{4.22}$$

The fidelity thus depends only on the sum of diagonal populations ρ_{ge} and ρ_{eg} and on the real part of the off-diagonal term $\rho_{eg,ge}$ that expresses the mutual coherence between them. All these terms can be accessed using the collective rotations

$$\hat{R}(\theta, \phi) = \exp\left[-i\frac{\theta}{2}\left(\cos\phi\hat{S}_x + \sin\phi\hat{S}_y\right)\right], \tag{4.23}$$

followed by the measurement of parity operator

$$\hat{P} = \hat{p}_{gg} + \hat{p}_{ee} - \hat{p}_{eg} - \hat{p}_{ge}, \tag{4.24}$$

where $\hat{p}_{ij}$ are the projection operators on states $|ij\rangle, i, j \in \{g, e\}$ in different bases [61] and $\hat{S}_{x,y} = \hat{\sigma}^{(1)}_{x,y} \otimes I^{(2)} + I^{(1)} \otimes \hat{\sigma}^{(2)}_{x,y}$ is the total angular momentum operator in x- or y-direction for both ions. The rotation angle θ and rotation axis ϕ on the Bloch sphere are determined by the duration and the phase of the RF pulses, respectively.

For the state $|\Psi^+\rangle$, it can be readily shown that

$$\mathrm{Tr}\left[\hat{P}\hat{R}(\pi/2,\phi)|\Psi^+\rangle\langle\Psi^+|\hat{R}^\dagger(\pi/2,\phi)\right]=1 \tag{4.25}$$

for all ϕ. A parity measurement on the $|\Psi^+\rangle$ entangled state is therefore invariant with respect to the change of the rotation pulse $\hat{R}(\pi/2,\phi)$ phase ϕ. In order to measure the parity oscillations for this state, it first has to be rotated by a global $\hat{R}(\pi/2,\pi/2)$ pulse, corresponding to a $\hat{\sigma}_y$ rotation on both qubits with the pulse area of $\pi/2$.

4.2.3.2 Entanglement Generation Results

The electronic state of two ions is analyzed after each heralding photon detection. Figure 4.9a shows that in $(89\pm3)\,\%$ of the heralded events only one of the atoms was excited to the $|e\rangle$ state. This is in good agreement with the excitation probability $p_e = 0.07 \pm 0.03$ of each ion and the measured dark-count rate of the employed avalanche photodiode of 10 counts/s.

Figure 4.9b, trace (ii), shows the results of the parity operator $\hat{P}$ measurements that are, as explained above, preceded by two global RF rotations $\hat{R}(\pi/2,\pi/2)\hat{R}(\pi/2,\phi)$

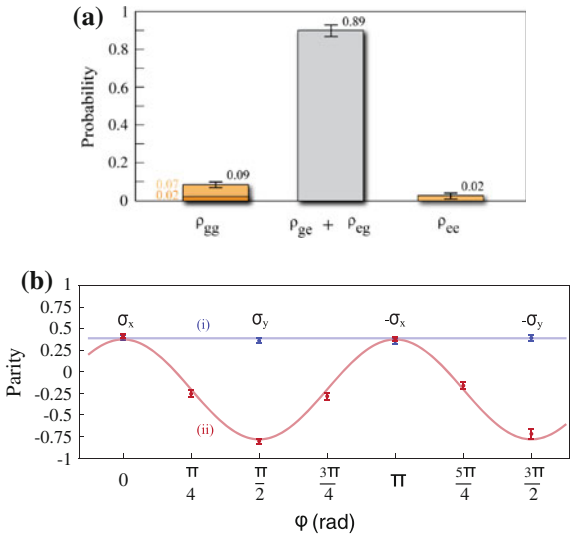

Fig. 4.9 Characterization of the entangled state [59]. **a** Two-atom state populations after the detection of a σ^- photon showing that the total probability of measuring the state with a single excitation is $(89\pm3)\,\%$. Spurious populations of the $|gg\rangle$ state are caused by double excitations of each ion (0.07) and dark count rate of the employed avalanche diode (0.02). State $|ee\rangle$ is populated due to the simultaneous excitation of the two ions. **b** Parity measurements as a function of the RF-phase. Trace (*ii*) corresponds to the measurement of the atomic populations after two global rotations $\hat{R}(\pi/2,\pi/2)\hat{R}(\pi/2,\phi)$. In the measurement of trace (*i*) only a single global RF-pulse $\hat{R}(\pi/2,\phi)$ is applied

for estimation of the quantum coherence of the generated state. The first applied pulse $\hat{R}(\pi/2, \pi/2)$ performs the unitary rotation $\hat{R}(\pi/2, \pi/2)|\Psi^+\rangle \rightarrow |\Phi^-\rangle$, where $|\Phi^-\rangle = \frac{1}{\sqrt{2}}(|gg\rangle - |ee\rangle)$. The second RF-pulse with same duration but with a phase ϕ then performs the rotation $\hat{R}(\pi/2, \phi)|\Phi^-\rangle$. The measured parity signal clearly oscillates as a function of phase ϕ with contrast of $(58.0 \pm 2.5)\,\%$ and period of π, a proof that we indeed succeed in preparing an entangled two-ion state close to $|\Psi^+\rangle$ [61]. The mean value of the parity operator at zero phase $\langle \hat{P} \rangle_{\phi \rightarrow 0}$ corresponds to the difference between the inner parts and outer-most coherence terms of the density matrix. The measured value corresponds to $2\mathrm{Re}(\rho_{\mathrm{ge,eg}} - \rho_{\mathrm{gg,ee}}) = 0.38 \pm 0.03$. To precisely quantify the fidelity of the generated state with $|\Psi^+\rangle$, the real part of the coherence term $\rho_{ge,eg}$ needs to be estimated. This is done by measuring the parity without the first RF rotation. Trace (i) of Fig. 4.9b shows the expectation value of the parity as a function of the phase ϕ of the single RF-pulse. The invariance of the measurement result with respect to the phase ϕ proves that $\rho_{gg,ee} = 0 \pm 0.03$, so that indeed only the coherence corresponding to the state $|\Psi^+\rangle$ is measured. The estimated fidelity of the generated state with the maximally entangled state $|\Psi^+\rangle$ is $F = (63.5 \pm 2)\,\%$. The threshold for an entanglement is thus surpassed by more than six standard deviations. The coherence between the $|ge\rangle$ and $|eg\rangle$ states of $(38 \pm 3)\,\%$ is limited by three main processes [59]. First, imperfect populations of $|ge\rangle$ and $|eg\rangle$ states set a limit of 89 % [62]. Around 4 % of the coherence loss can be attributed to the finite coherence time of the individual atomic qubits (120 μs) due to collective magnetic field fluctuations. Although the generated $|\Psi^+\rangle$ state is intrinsically insensitive against collective dephasing [63, 64], a loss of coherence is indeed expected after a rotation of $|\Psi^+\rangle$ out of the decoherence-free subspace. The highest contribution to the coherence loss can be attributed to atomic motion, which can provide information about which atom emitted the photon. Around 55 % of the coherence is lost due to the atomic recoil kicks during the Raman scattering.

The overall fidelity of the maximally entangled state $|\Psi^+\rangle$ with the experimentally generated one is limited mainly by the imperfect populations of the desired $|ge\rangle$ and $|eg\rangle$ states and coherence loss due to the atomic recoil kicks during the Raman scattering. The effect of motion-induced decoherence can be reduced by cooling the radial modes to the motional ground state [65] or by choosing a forward Raman scattering scenario [42]. Error bars in the presented measurements results correspond to one standard deviation and are estimated statistically from several experimental runs each giving approximately 120 measurement outcomes. Up to 60 % of the measurement error is caused by the quantum projection noise. Additional uncertainty comes from slow magnetic field drift with a magnitude of several tens of nT making the RF-driving off-resonant by tens of kHz.

An important advantage of the single-photon heralding mechanism is the possibility of achieving a high entanglement generation rate. In the presented experiment, the entanglement generation rate has reached (14.0 ± 1.5) events/minute with an experimental duty cycle of 2.3 kHz [59]. The probability of successful entanglement generation per each experimental trial estimated from the single photon detection efficiency and the measured probability of Raman scattering is $P_{\mathrm{succ}} = 2p_e\eta = 1.1 \times 10^{-4}$ that

corresponds to 15.4 successful entanglement generation events/minute. The factor two here corresponds to the probability of detecting a single photon from one of two ions. The efficiency of detecting a single Raman-scattered photon was estimated to be $\eta = 8 \times 10^{-4}$. It was derived from the detection probability of a single Raman scattered photon given by the collection efficiency of high-NA lenses ($\sim$0.04), the single-mode fiber coupling efficiency ($\sim$0.1) and by the avalanche-photodiode detection efficiency ($\sim$0.6). Additional factors of 0.5 and 0.66 come from the polarization filtering of unwanted π-polarized photons and from the probability for the ion to decay back to the $|g\rangle$ state after the Raman pulse excitation, respectively. The single ion excitation probability was $p_e = (0.07 \pm 0.03)\,\%$. For comparison, the two-photon heralding entanglement scheme proposed by Simon et al. [43] would for the employed experimental setup give approximately $P_{\mathrm{succ}} \approx 2\eta^2 = 1.3 \times 10^{-6}$, so about two orders of magnitude smaller success probability of entanglement generation. For simplicity, $p_e = 1$ was assumed here for the two-photon scheme and an additional factor of 2 accounted from the two possible contributions to coincidence detection events.

4.2.4 Summary

In this chapter we have reviewed two methods for free-space coupling between single ions and photons: the coupling of a weak probe laser to a single ion in free space (Sect. 4.1), and the probabilistic generation of entanglement between two ions by detecting a single scattered photon (Sect. 4.2). Both method rely on high-numerical aperture optics in order to achieve a sufficiently high efficiency.

In the experiments presented in Sect. 4.1 we have investigated the free-space interaction of a single ion to a weak near-resonant probe field. The coupling mediated by a single objective covering 4 % of the full solid angle resulted in an extinction of the probe field of 1.5 %, a phase shift of up to 0.3°, and the observation of electromagnetically-induced transparency from single atom. Current experimental efforts to increase the numerical aperture should significantly improve the interaction strength (see chapter by Leuchs and Sondermann), which will likely lead to a number of direct applications of these effects in the field of quantum information, quantum feedback or single atom magnetometry. Utilization of a single ion as an optical mirror in a Fabry-Pérot-like cavity set-up enabled the observation of almost full suppression and enhancement by a factor of two of the atomic coupling constant in the laser probe mode. Besides the appealing quantum memory applications of such a set-up [66], the single ion mirror has the potential to become useful for the realization of an optical switch similar to the single atom transistors using EIT. Furthermore, the presented experiment enables to study the quantum electrodynamics in an exciting regime where both the free-space coupling of the probe beam and the modification of the vacuum mode density at the position of an ion play an important role [37].

In Sect. 4.2 of this chapter we have summarized an experimental realization of a proposal by Cabrillo et al. [42] where the detection of a single scattered photon generates entanglement between two ions. This presents an important step towards the realization of the quantum information networks with ions and photons. The maximally entangled state $|\Psi^+\rangle$ was produced with a fidelity of 63.5 % and with entanglement generation rates of 14 events/minute, which is more than two orders of magnitude higher than the rate obtainable with protocols relying on a two-photon coincidence events with the presented experimental parameters. These results can be further improved by cooling all of the involved motional modes close to their ground state [65] or by choosing a different excitation direction to minimize residual which-way information.

There are some obvious questions regarding the technical difficulties related to phase stability requirements and photon recoil problems of the single-photon entanglement generation scheme. For generation of the entanglement between distant atoms, the paths of the excitation and detection channels need to be interferometrically stable. This issue has been addressed by the community developing fiber links for comparing remote optical clocks. Recently, coherent laser light transfer over more than 900 km has been shown with a precision exceeding the requirements of the single-photon protocol [67]. The problem of a which-way information available due to the atomic recoil upon scattering of single photon can be eliminated by changing the geometry of the system. These improvements, together with the experimental results presented, have potential to enable efficient creation and distribution of entanglement between distant sites with well-defined and controllable atomic qubits.

Acknowledgments We would like to thank all our colleagues who were involved in this work over the course of the years, in particular Nadia Röck, Philipp Schindler, Daniel Higginbottom, François Dubin, Alexander Glätzle, Muir Kumph, Gabriel Araneda, Sebastian Gerber, Daniel Rotter, Pavel Bushev, Yves Colombe, and Jürgen Eschner. The work reported in this chapter has been supported by the Austrian Science Fund FWF (SINFONIA, SFB FoQuS), by the European Union (CRYTERION), by the Institut für Quanteninformation GmbH, and a Marie Curie International Incoming Fellowship within the 8th European Framework Program. The writing of this chapter was supported by the European Research Council project QuaSIRIO.

References

1. J.I. Cirac, P. Zoller, H.J. Kimble, H. Mabuchi, Quantum state transfer and entanglement distribution among distant nodes in a quantum network. Phys. Rev. Lett. **78**, 3221–3224 (1997)
2. H.-J. Briegel, W. Dür, J.I. Cirac, P. Zoller, Quantum repeaters: the role of imperfect local operations in quantum communication. Phys. Rev. Lett. **81**, 5932–5935 (1998)
3. L. Duan, M. Lukin, I. Cirac, P. Zoller, Long-distance quantum communication with atomic ensembles and linear optics. Nature **414**, 413–418 (2001)
4. M. Brune et al., From Lamb shift to light shifts: vacuum and subphoton cavity fields measured by atomic phase sensitive detection. Phys. Rev. Lett. **72**, 3339–3342 (1994)
5. P.W.H. Pinkse, T. Fischer, P. Maunz, G. Rempe, Trapping an atom with single photons. Nature **404**, 365–368 (2000)

6. C.J. Hood, T.W. Lynn, A.C. Doherty, A.S. Parkins, H.J. Kimble, The atom-cavity microscope: Single atoms bound in orbit by single photons. Science **287**, 1447–1453 (2000)
7. B. Julsgaard, J. Sherson, J. Cirac, J. Fiurášek, E. Polzik, Experimental demonstration of quantum memory for light. Nature **432**, 482–486 (2004)
8. L.V. Hau, S.E. Harris, Z. Dutton, C.H. Behroozi, Light speed reduction to 17 metres per second in an ultracold atomic gas. Nature **397**, 594–598 (1999)
9. D. Phillips, A. Fleischhauer, A. Mair, R. Walsworth, M. Lukin, Storage of light in atomic vapor. Phys. Rev. Lett. **86**, 783–786 (2001)
10. Y.R.P. Sortais et al., Diffraction-limited optics for single-atom manipulation. Phys. Rev. A **75**, 013406 (2007)
11. M. Sondermann et al., Design of a mode converter for efficient light-atom coupling in free space. Appl. Phys. B: Lasers Opt. **89**, 489–492 (2007)
12. M. Tey et al., Strong interaction between light and a single trapped atom without the need for a cavity. Nat. Phys. **4**, 924–927 (2008)
13. G. Zumofen, N. Mojarad, V. Sandoghdar, M. Agio, Perfect reflection of light by an oscillating dipole. Phys. Rev. Lett. **101**, 180404 (2008)
14. I. Gerhardt et al., Strong extinction of a laser beam by a single molecule. Phys. Rev. Lett. **98**, 33601 (2007)
15. G. Wrigge, I. Gerhardt, J. Hwang, G. Zumofen, V. Sandoghdar, Efficient coupling of photons to a single molecule and the observation of its resonance fluorescence. Nat. Phys. **4**, 60–66 (2007)
16. A.N. Vamivakas et al., Strong extinction of a far-field laser beam by a single quantum dot. Nano Lett. **7**, 2892–2896 (2007)
17. S.A. Aljunid et al., Phase shift of a weak coherent beam induced by a single atom. Phys. Rev. Lett. **103**, 153601 (2009)
18. J. Hwang et al., A single-molecule optical transistor. Nature **460**, 76–80 (2009)
19. L. Slodička, G. Hétet, S. Gerber, M. Hennrich, R. Blatt, Electromagnetically induced transparency from a single atom in free space. Phys. Rev. Lett. **105**, 153604 (2010)
20. G. Hétet, L. Slodička, M. Hennrich, R. Blatt, Single atom as a mirror of an optical cavity. Phys. Rev. Lett. **107**, 133002 (2011)
21. G. Hétet, L. Slodička, N. Röck, R. Blatt, Free-space read-out and control of single-ion dispersion using quantum interference. Phys. Rev. A **88**, 041804 (2013)
22. M. Fleischhauer, A. Imamoğlu, J.P. Marangos, Electromagnetically induced transparency: optics in coherent media. Rev. Mod. Phys. **77**, 633–673 (2005)
23. K. Bergmann, H. Theuer, B. Shore, Coherent population transfer among quantum states of atoms and molecules. Rev. Mod. Phys. **70**, 1003–1025 (1998)
24. M.D. Eisaman et al., Electromagnetically induced transparency with tunable single-photon pulses. Nature **438**, 837–841 (2005)
25. A.D. Boozer, A. Boca, R. Miller, T.E. Northup, H.J. Kimble, Reversible state transfer between light and a single trapped atom. Phys. Rev. Lett. **98**, 193601 (2007)
26. M. Mücke et al., Electromagnetically induced transparency with single atoms in a cavity. Nature **465**, 755–758 (2010)
27. S. Ritter et al., An elementary quantum network of single atoms in optical cavities. Nature **484**, 195–200 (2012)
28. H. Häffner, C. Roos, R. Blatt, Quantum computing with trapped ions. Phys. Rep. **469**, 155 (2008)
29. P. Maunz et al., Quantum interference of photon pairs from two remote trapped atomic ions. Nat. Phys. **3**, 538541 (2007)
30. S. Gerber et al., Quantum interference from remotely trapped ions. New J. Phys. **11**, 013032 (2009)
31. P. Kochan, H.J. Carmichael, Photon-statistics dependence of single-atom absorption. Phys. Rev. A **50**, 1700–1709 (1994)
32. M.K. Tey et al., Interfacing light and single atoms with a lens. New J. Phys. **11**, 043011 (2009)

33. S.J. van Enk, Atoms, dipole waves, and strongly focused light beams. Phys. Rev. A **69**, 043813 (2004)
34. J. Eschner, C. Raab, F. Schmidt-Kaler, R. Blatt, Light interference from single atoms and their mirror images. Nature **413**, 495–498 (2001)
35. A. Imamoğlu, S.E. Harris, Lasers without inversion: interference of dressed lifetime-broadened states. Opt. Lett. **14**, 1344–1346 (1989)
36. P. Rabl, V. Steixner, P. Zoller, Quantum-limited velocity readout and quantum feedback cooling of a trapped ion via electromagnetically induced transparency. Phys. Rev. A **72**, 043823 (2005)
37. G. Hétet, L. Slodička, A. Glätzle, M. Hennrich, R. Blatt, QED with a spherical mirror. Phys. Rev. A **82**, 063812 (2010)
38. L. Jiang, J.M. Taylor, A.S. Sørensen, M.D. Lukin, Distributed quantum computation based on small quantum registers. Phys. Rev. A **76**, 062323 (2007)
39. J.I. Cirac, A.K. Ekert, S.F. Huelga, C. Macchiavello, Distributed quantum computation over noisy channels. Phys. Rev. A **59**, 4249 (1999)
40. D. Gottesman, I.L. Chuang, Demonstrating the viability of universal quantum computation using teleportation and single-qubit operations. Nature **402**, 390–393 (1999)
41. L.M. Duan, C. Monroe, Colloquium: quantum networks with trapped ions. Rev. Mod. Phys. **82**, 1209 (2010)
42. C. Cabrillo, J.I. Cirac, P. Garcia-Fernández, P. Zoller, Creation of entangled states of distant atoms by interference. Phys. Rev. A **59**, 1025–1033 (1999)
43. C. Simon, W.T.M. Irvine, Robust long-distance entanglement and a loophole-free Bell test with ions and photons. Phys. Rev. Lett. **91**, 110405 (2003)
44. C. Chou et al., Measurement-induced entanglement for excitation stored in remote atomic ensembles. Nature **438**, 828–832 (2005)
45. C. Chou et al., Functional quantum nodes for entanglement distribution over scalable quantum networks. Science **316**, 1316–1320 (2007)
46. D.L. Moehring et al., Entanglement of single-atom quantum bits at a distance. Nature **449**, 68–71 (2007)
47. S. Zippilli et al., Entanglement of distant atoms by projective measurement: the role of detection efficiency. New J. Phys. **10**, 103003 (2008)
48. L. Luo et al., Protocols and techniques for a scalable atom-photon quantum network. Fortschritte der Physik **57**, 1133–1152 (2009)
49. R. Raussendorf, H.J. Briegel, A one-way quantum computer. Phys. Rev. Lett. **86**, 51885191 (2001)
50. Duan, L.-M. and Raussendorf, R. Efficient quantum computation with probabilistic quantum gates. Physical Review Letters 95 (2005)
51. E.W. Streed, B.G. Norton, A. Jechow, T.J. Weinhold, D. Kielpinski, Imaging of trapped ions with a microfabricated optic for quantum information processing. Phys. Rev. Lett. **106**, 010502 (2011)
52. E. Streed, A. Jechow, B. Norton, D. Kielpinski, Absorption imaging of a single atom. Nat. Commun. **3**, 933 (2012)
53. B. Darquié et al., Controlled single-photon emission from a single trapped two-level atom. Science **309**, 454–456 (2005)
54. S. Olmschenk et al., Quantum logic between distant trapped ions. Int. J. Quantum Inf. **8**, 337–394 (2010)
55. G. Shu, C.K. Chou, N. Kurz, M. Dietrich, B. Blinov, Efficient fluorescence collection and ion imaging with the "tack" ion trap. JOSA B **28**, 2865–2870 (2011)
56. R. Maiwald et al., Stylus ion trap for enhanced access and sensing. Nat. Phys. **5**, 551–554 (2009)
57. M. Stobińska, G. Alber, G. Leuchs, Perfect excitation of a matter qubit by a single photon in free space. Europhys. Lett. **86**, 14007 (2009)
58. S. Olmschenk et al., Quantum teleportation between distant matter qubits. Science **323**, 486–489 (2009)

59. L. Slodička et al., Atom-atom entanglement by single-photon detection. Phys. Rev. Lett. **110**, 083603 (2013)
60. R. Maiwald et al., Collecting more than half the fluorescence photons from a single ion. Phys. Rev. A **86**, 043431 (2012)
61. C.A. Sackett et al., Experimental entanglement of four particles. Nature **404**, 256–259 (2000)
62. M.I. Shirokov, Cauchy inequality and uncertainty relations for mixed states. Int. J. Theoret. Phys. **45**, 141–151 (2006)
63. D. Kielpinski et al., A decoherence-free quantum memory using trapped ions. Science **291**, 1013–1015 (2001)
64. C.F. Roos et al., Bell states of atoms with ultralong lifetimes and their tomographic state analysis. Phys. Rev. Lett. **92**, 220402 (2004)
65. L. Slodička et al., Interferometric thermometry of a single sub-Doppler-cooled atom. Phys. Rev. A **85**, 043401 (2012)
66. Y. Wang, J. Minář, G. Hétet, V. Scarani, Quantum memory with a single two-level atom in a half cavity. Phys. Rev. A **85**, 013823 (2012)
67. K. Predehl et al., A 920-kilometer optical fiber link for frequency metrology at the 19th decimal place. Science **336**, 441–444 (2012)

Chapter 5
Single Photon Absorption by a Single Atom: From Heralded Absorption to Polarization State Mapping

Nicolas Piro and Jürgen Eschner

Abstract Together with photon emission, the absorption of a single photon by a single atom is a fundamental process in matter-light interaction that manifests its quantum mechanical nature. As an experimentally controlled process, it is a key tool for the realization of quantum technologies. In particular, in an atom/photon based quantum network scenario, in which localized atomic particles are used as quantum information processing nodes while photons are used as carriers of quantum information between distant nodes, controlling both emission and absorption of single photons by single atoms is required for quantum coherent state mapping between the two entities. Most experimental efforts to date have focused on establishing the control of single photon emission by single trapped atoms, and the implementation of quantum networking protocols using this interaction. In this chapter, we describe experimental efforts to control the process of single photon absorption by single trapped ions. We describe a series of experiments in which polarization entangled photon pairs, generated by a spontaneous parametric down-conversion source, are coupled to a single ion. First the source is operated to generate heralded single photons, and coincidences between the absorption event of one photon of the pair and the detection of the heralding partner photon are observed. We then show how polarization control in the process is established, leading to the manifestation of the photonic polarization entanglement in the absorption process. Finally, we introduce protocols in which this interaction scheme is harnessed to perform tasks in a quantum network, such as entanglement distribution among distant nodes of the network, and we demonstrate a specific protocol for heralded, high-fidelity photon-to-atom quantum state transfer.

N. Piro (✉)
École Polytechnique Fédérale de Lausanne, Lausanne, Switzerland
e-mail: nicolas.piro@gmail.com

J. Eschner
Universität des Saarlandes, Saarland, Germany
e-mail: juergen.eschner@physik.uni-saarland.de

A. Predojević and M.W. Mitchell (eds.), *Engineering the Atom-Photon Interaction*,
Nano-Optics and Nanophotonics, DOI 10.1007/978-3-319-19231-4_5

5.1 Introduction

At its most fundamental level, matter-light interaction involves the absorption and emission of single photons by single atomic particles. While being well understood theoretically, these processes have only recently started to be explored experimentally under controlled conditions. The motivation for realizing photon-atom interaction experiments at the single particle level is two-fold: first, from the fundamental perspective, such studies allow performing tests of the quantum theory describing the interaction; second, controlling the interaction opens new routes to developing technologies that use quantum mechanical phenomena as a resource, in particular for purposes of quantum information processing.

Experiments with single trapped atomic ions have proven to provide optimal conditions for quantum information processing, fulfilling the requirements of providing long-coherence qubits [1], high-fidelity state manipulation and detection schemes [2], as well as controlled coherent interaction of several quantum bits allowing deterministic generation of entanglement [3], quantum logic gates [4] and quantum error correction [5]. Meanwhile, single photons are optimal carriers of quantum information, allowing the transfer of quantum states and the distribution of entanglement over long distances [6]. The quantum-coherent link between single atomic particles and single photons then emerges as a key requirement to develop quantum networks, in which quantum information is processed and stored in atom-based quantum nodes, while photons are used to communicate quantum states between the nodes [7, 8].

Several experiments have concentrated on establishing quantum-coherent links between single trapped atoms and emitted photons, taking advantage of the intrinsic quantum correlations in the emission process [9, 10]. Recent experiments even showed how to entangle distant trapped atomic particles by allowing the emitted photons to interfere and subsequently performing a correlation measurement on the photons [11, 12]. However, a fully bidirectional link requires also control over the absorption process in a quantum coherent fashion. Here we concentrate on recent progress with single ions and single photons. A cavity-based approach with neutral atoms is also being pursued [13]. A bidirectional link has also been established between atomic ensembles [14], but these do not possess the quantum computation capabilities provided by ion chains.

The control of single photon absorption not only allows one to transfer quantum states encoded in a photonic degree of freedom onto an internal degree of freedom of the atom. It also enables taking advantage of the widely developed quantum photonic technologies, such as quantum light sources, in the realm of atom-based quantum networks. In particular, one can think of implementing protocols to entangle distant atoms by generating the entanglement via optical means, e.g. using the process of spontaneous parameteric down-conversion (SPDC), and subsequently mapping the states of the two photons onto two distant atoms by an entanglement swapping process. Such absorption-based schemes could benefit from the high generation rates for entangled photon pairs available in state-of-the-art sources and thereby provide an attractive alternative to emission-based schemes.

In this context, we review in this chapter a series of experiments in which entangled photon pairs, generated with an SPDC source, interact with a single trapped $^{40}Ca^{+}$ ion. The spectral properties of the photons are tailored to optimally interact with the single atom, thereby enabling several photon-atom entanglement schemes.

We first present in Sect. 5.2 schemes that allow one to observe single atom-photon interaction processes, to map quantum states from photons to $^{40}Ca^{+}$ ions and to perform entanglement swapping between photon pairs and distant trapped ions. In Sect. 5.3 we describe the experimental apparatus we developed to implement and study these interaction schemes, consisting of a pair of $^{40}Ca^{+}$ ion trap setups and an SPDC photon pair source designed to produce narrowband polarization-entangled photon pairs tunable to two optical transitions in $^{40}Ca^{+}$. We present the results of various interaction experiments in Sect. 5.4. Finally, in Sect. 5.5 we discuss future possibilities of these experiments and the conclusions of this research. In an appendix we provide some details regarding the data analysis techniques used to detect the photon-atom interaction.

5.2 Single Photon-Single Atom Interaction and Entanglement Schemes

The detailed level scheme, including the Zeeman structure, of $^{40}Ca^{+}$ is depicted in Fig. 5.1. For quantum information processing applications, two types of qubits can be chosen: an optical qubit formed by one magnetic sublevel of $S_{1/2}$ and one sublevel of $D_{5/2}$, or a Zeeman (or RF-)qubit formed by the two sublevels of $S_{1/2}$. The entanglement transfer schemes considered in this work use the latter.

5.2.1 Single Photon Absorption Schemes

We consider here four possible schemes addressing either the $D_{3/2} \leftrightarrow P_{3/2}$ transition at 850 nm wavelength or the $D_{5/2} \leftrightarrow P_{3/2}$ transition at 854 nm, see Fig. 5.2.

Schemes (a) and (b) are based on the detection of quantum jumps: the ion undergoes continuous excitation by a 397 nm laser driving the $S_{1/2} \leftrightarrow P_{1/2}$ transition (and at the same time Doppler-cooling the ion) and an 866 nm laser driving the $D_{3/2} \leftrightarrow P_{1/2}$ transition and repumping the ion out of the metastable $D_{3/2}$ level. In this closed cycle, the ion emits a continuous stream of 397 nm fluorescence photons, typically at a few 10^5 s^{-1} rate, that are recorded with a single-photon counter or a CCD camera. In scheme (a), the single photon source is tuned to the 850 nm line, and the absorption of a photon, followed by spontaneous decay into the metastable $D_{5/2}$ state, puts the ion out of the 397/866 nm transition cycle, hence halting the emission of 397 nm fluorescence. This sudden drop in fluorescence is termed a bright-to-dark quantum jump. In this case it signals the absorption of a single 850 nm photon by the atom.

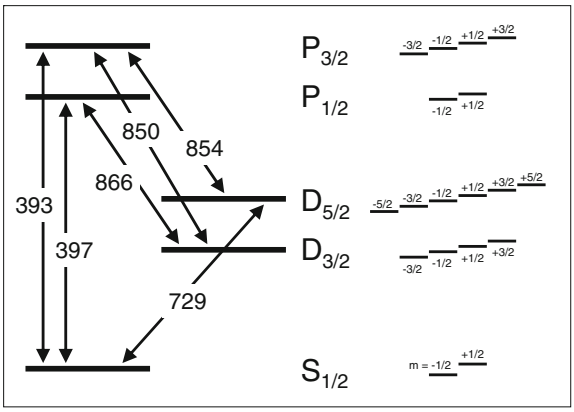

Fig. 5.1 Level scheme and transition wavelengths (given in nm) of the $^{40}Ca^{+}$ ion, without (*left*) and with (*right*) magnetic sublevels. Splittings are not to scale; the g_J-factors of the states, from *bottom* to *top*, are $(2, \frac{4}{5}, \frac{6}{5}, \frac{2}{3}, \frac{4}{3})$. The D levels are metastable with ~1 s natural lifetime. The excited levels $P_{1/2}$ and $P_{3/2}$ decay preferentially to the ground state manifold $S_{1/2}$, emitting a 397 and 393 nm photon, respectively. The lower excited state $P_{1/2}$ also decays to $D_{3/2}$, with about 6.4 % branching ratio. The upper excited state $P_{3/2}$ also decays to $D_{5/2}$ or $D_{3/2}$, with branching ratios of about 5.9 and 0.66 %, respectively. Magnetic sublevels of $S_{1/2}$ and $D_{5/2}$ are used to form optical qubits, which are coherently manipulated by laser excitation of the 729 nm electric quadrupole transition. The sublevels of $S_{1/2}$ form a Zeeman qubit manipulated by radio frequency (RF) radiation

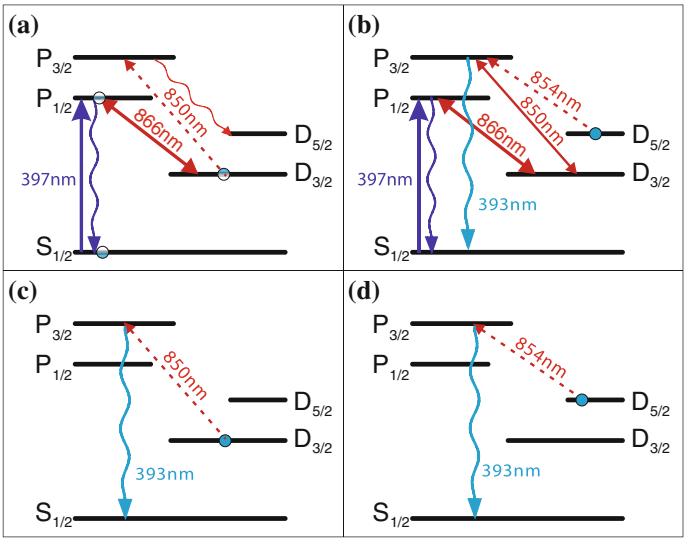

Fig. 5.2 Schemes to detect the absorption of a single photon by a single $^{40}Ca^{+}$ ion. Absorption happens either on the 854 nm (**b**, **d**) or the 850 nm transition (**a**, **c**); it is signaled by either a quantum jump (**a**, **b**) or a single emitted photon (**c**, **d**). See main text for more details

In scheme (b), the photon source is tuned to the transition at 854 nm. An additional weak laser at 850 nm is introduced to induce transitions of the ion into the $D_{5/2}$ state, in which fluorescence emission is suppressed. Now, the absorption of a single 854 nm photon followed by a spontaneous decay to $S_{1/2}$ or $D_{3/2}$ reinitiates the stream of fluorescence emission. Hence the absorption of a single photon is signaled by the onset of fluorescence, or a dark-to-bright quantum jump.

In schemes (c) and (d), the ion is previously prepared in one of the metastable states $D_{3/2}$ or $D_{5/2}$ by optical pumping techniques or by coherent excitation, as described in Sect. 5.4. During the exposure to the single photon source, no other lasers drive the ion. The absorption of an 850 or 854 nm photon, in each case, is now signaled by the emission of a single 393 nm photon, when this is detected by a single photon counter. As we will see, schemes (c) and (d) have the advantage that they do not destroy the final state of the ion and thus enable quantum states to be transferred from the photon to the ion.

While schemes for detecting 850 and 854 nm photon absorption events are both feasible, the 854 nm schemes are significantly more efficient due to a combination of two factors: firstly, the oscillator strength of the $D_{5/2} \leftrightarrow P_{3/2}$ transition is about 6 times larger than that of the $D_{3/2} \leftrightarrow P_{3/2}$ transition; secondly, upon excitation to $P_{3/2}$, the probability of decaying to $D_{5/2}$ (required by scheme (a)) is only 5.9 % [15], while decay to $S_{1/2}$ (required in (b)) happens with nearly 94 % probability. Overall, scheme (b) is about 100 times more efficient the scheme (a). The first factor also makes scheme (d) about one order of magnitude more efficient than scheme (c).

5.2.2 *Photon-Atom State Transfer and Entanglement Swapping Schemes*

Entanglement swapping schemes between photons and atoms rely on the possibility of mapping the polarization state of the photon onto the internal state of the ion. In particular, an arbitrary photon state $|\Psi_p\rangle = \alpha\,|\uparrow\rangle + \beta\,|\downarrow\rangle$ must be transferred to the state $|\Psi_i\rangle = \alpha\,|+\rangle + \beta\,|-\rangle$, where $|\uparrow\rangle$, $|\downarrow\rangle$ are two arbitrary polarization basis vectors, and $|+\rangle$, $|-\rangle$ represent an atomic qubit pair of states.

One possible proposed state transfer scheme is illustrated in Fig. 5.3 [16, 17]. Here the atomic qubit is chosen to be $|\pm\rangle = |S_{1/2}, m = \pm 1/2\rangle$. The ion is manipulated with a laser pulse sequence consisting of three main phases. It is first laser cooled by means of the 397 and 866 nm lasers as usual. Then it is prepared in a symmetric superposition of the states $|D_{5/2}, m = \pm 3/2\rangle$ by means of four pulses: first, a σ^- polarized 397 nm beam pumps the ion to the $|S_{1/2}, m = -1/2\rangle$ state; then, a resonant RF $\pi/2$-pulse creates a symmetric superposition of the two sublevels of $S_{1/2}$; finally, two 729 nm π-pulses coupling the respective $S_{1/2} \leftrightarrow D_{5/2}$ transitions convert this state into the desired $|D_{5/2}, m = \pm 3/2\rangle$ superposition.

At this point, the ion is exposed to a single photon at 854 nm, for example from an SPDC source, and a single photon detector monitoring the 393 nm photons is

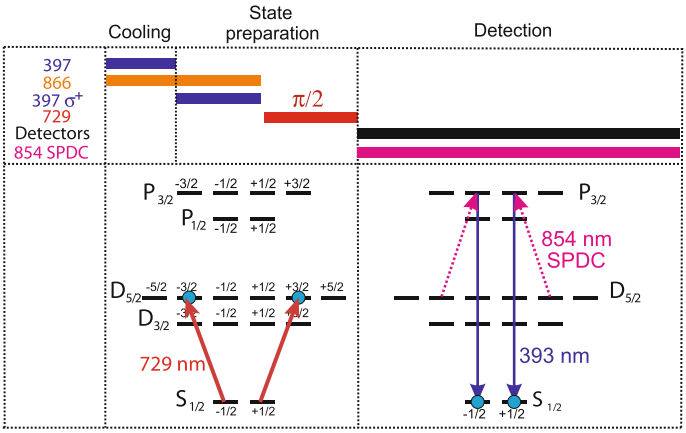

Fig. 5.3 Scheme to transfer the polarization state of an 854 nm photon onto the atom [16, 17]

gated on. The SPDC photon is prepared in an arbitrary polarization state $|\Psi_p\rangle = \alpha\,|H\rangle + \beta\,|V\rangle$; upon its absorption, the ion undergoes a Raman transition to the ground state emitting a 393 nm photon which, if detected, heralds the absorption event. The process is coherent, i.e., the absorbed polarization is converted into a corresponding superposition of the RF-qubit in $S_{1/2}$, as long as it remains impossible to determine which $P_{3/2}$ Zeeman substate the ion decays from. This condition holds if the 393 nm photon is detected with a time resolution whose inverse is much larger than the frequency splitting between the two involved, equally polarized $P_{3/2} \rightarrow S_{1/2}$ transitions [18]. Such high time resolution is also needed to keep track of the phase of the final superposition state in $S_{1/2}$, see [17, 19].

5.3 Experimental Setup

The core of the experimental setup is a twin ion trap apparatus capable of trapping single or strings of $^{40}Ca^{+}$ ions. For details on their construction and operation, see [20–22]. These setups are complemented with a source of polarization entangled photon pairs tunable to two transitions in $^{40}Ca^{+}$, described in [23, 24]. Here we focus on the operation of one ion trap setup in conjunction with the single photon source, see Fig. 5.4.

The SPDC photon pair source is based on a laser at 854 nm whose frequency-doubled light pumps a 20-mm long PPKTP crystal designed for degenerate type-II spontaneous parametric down-conversion. As the key purpose of the source is to produce photon pairs with spectral properties matching those of atomic transitions in the $^{40}Ca^{+}$ species, the wavelength of the 854 nm laser is actively locked to the transition, and the photon bandwidth is matched to the atomic absorption linewidth of 22 MHz by means of a cavity filtering system. Photon pairs are generated within a

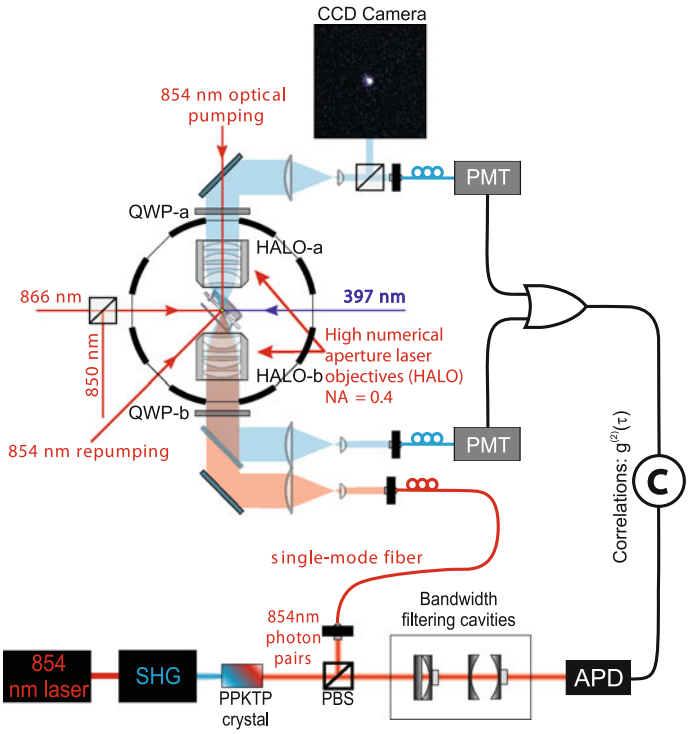

Fig. 5.4 Experimental setup combining an ion trap with an SPDC photon source, the latter being operated as a heralded single-photon source. Two high-numerical aperture laser objectives (HALOs) facilitate the ion-photon coupling. See text for more details

relatively large bandwidth of about 200 GHz. However, due to the narrow linewidth of the pump laser and energy conservation in the SPDC process, the pairs are emitted at symmetric frequencies with respect to the pump, $\omega_s = \omega_p - \omega_i$. Hence, filtering one photon of the pair with filtering cavities locked on resonance to the 854 pump laser, and a design transmission bandwidth of 22 MHz, followed by the detection of the transmitted photon heralds the presence of a partner photon resonant with the atomic transition [23, 24]. The partner photon is coupled into a single mode fiber and directed to the ion trap setup. The photon pair exhibits high-purity polarization entanglement which may be utilised when the polarizing beam splitter separating the pair (PBS in Fig. 5.4) is replaced by a non-polarizing beam splitter [23, 24].

The ion trap setup consists of a linear Paul trap placed between two high-numerical aperature lenses (HALO-a/b in Fig. 5.4) designed to be diffraction-limited and near-achromatic at wavelengths around 397 and 860 nm, with 0.4 numerical aperture. The HALO lenses serve two purposes: to efficiently collect light scattered by the ion, and to tightly focus the single photon beam onto the ion to enhance its absorption probability. Light from the source is first expanded by a magnifying telescope to fill the back-aperture of the objective, and aligned to focus at the ion position.

Fluorescence light from the ion is collected by both objectives and detected by two independent photo-multiplier tubes (PMT), or by a CCD camera (on one side) to image the ion. Photon detection pulses from both PMTs are combined into a single channel. Their detection times, together with the detection times of the source herald photon, are recorded in a computer by means a time-tagged single-photon counting system (PicoHarp).

5.4 Experimental Progress

In this section we present the experimental progress towards establishing a quantum coherent link between single photons and a single atom. Specifically, we first describe a preliminary experiment in which scheme (b) of Fig. 5.2 is implemented in order to detect the absorption of weak 854 nm light by a single $^{40}Ca^{+}$ ion. We then present an experiment where we detect time correlations between the absorption event and the heralding partner photon, establishing the true single-photon nature of the absorption process. In a further experiment, we show how control of the Zeeman substate of the atoms renders the absorption dependent on the polarization of the photon, hence manifesting the polarization entanglement of the photon pair in the absorption process. Finally, we discuss the experimental implementation of a heralded-absorption protocol through which the polarization state of a single absorbed photon is transferred, with high fidelity, onto the qubit state of the ion.

5.4.1 Single Photon Absorption by a Single Ion

As described in Sect. 5.2, the absorption of a single photon by a single atom may be signaled by a change in its fluorescence state, a quantum jump [25–27]. This uses the concept of quantum amplification proposed by Dehmelt as early as 1975 [28]. In the case of the scheme in Fig. 5.2b, the atom starts emitting fluorescence photons upon the absorption of a single 854 nm photon, providing a very efficient signal that witnesses the absorption event.

A simple experiment proves this method. An ion is trapped and illuminated with a 397 and 866 nm lasers, while its fluorescence emission is monitored with a photomultiplier (Fig. 5.4). In addition, a weak 850 nm laser resonant with the $D_{3/2}$ to $P_{3/2}$ transition optically pumps the ion (on a 1-s time scale) to the metastable $D_{5/2}$ state, halting the emission of fluorescence. Eventually, the ion will spontaneously decay back to the ground state and restart the fluorescence emission cycle. This is detected in the form of quantum jumps in the fluorescence count trace, see Fig. 5.5a. The corresponding count histogram (Fig. 5.5b) enables defining the optimal count threshold for discrimination of the on and off states, as described in the Appendix. The distribution of dark period durations in the fluorescence count trace, displayed

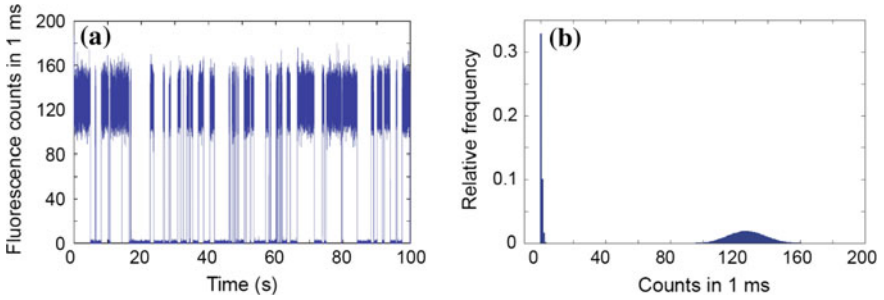

Fig. 5.5 **a** Detected fluorescence rate (in time bins of 1 ms) displaying quantum jumps upon excitation with the cooling (397 nm) and repumping (866 nm) lasers, and a weak optical pumping laser (850 nm). **b** Histogram of fluorescence counts displaying the distributions for the on and off states

in Fig. 5.6a, exhibits an exponential dependence with a decay constant given by the spontaneous decay rate of the $D_{5/2}$ state, measured to be $\tau_0 = 1.11(3)$ s.

When the ion is illuminated by a weak 854 nm light source, in our case the SPDC entangled photon source, the ion has two channels to reenter the fluorescing state (see Fig. 5.2b): either spontaneous decay, or excitation to the $P_{3/2}$ state and decay to the ground state $S_{1/2}$. One should therefore expect a decrease in the lifetime of the metastable $D_{5/2}$ state and, hence, a drop in the average duration of the dark periods in the fluorescence trace. We indeed observe a reduction of the average decay time to $\tau_{\text{on}} = 0.675(3)$ s (Fig. 5.6b), and the corresponding absorption rate is derived as $R_{\text{spdc}} = \tau_{\text{on}}^{-1} - \tau_{\text{off}}^{-1} = 0.53(3)\ \text{s}^{-1}$.

In a subsequent experiment, we prove that the absorption may be attributed to individual SPDC photons. In order to determine the time instant of the absorption event, we extract the first detected fluorescence photon in each dark-bright quantum jump using the technique described in the Appendix. We then calculate the second order correlation function $g^{(2)}(\tau)$ (i.e., the delay time distribution) between this detection and the detection of the heralding SPDC photon (Fig. 5.6c). A sharp coincidence peak at time delay $\tau = 0$ emerging above the random background proves the strong correlation between the two events and, hence, the heralded absorption of single SPDC photons by the ion. We observe 83(9) coincidences in 50 min of acquisition, against a Poisson-distributed background of 13.6(3.7) counts, i.e. at $>22\sigma$ outside the random fluctuations.

These experiments prove the possibility of observing and identifying single photon absorption events by a single ion. But to render such interaction useful for quantum networking technologies, a further level of control is necessary: to match the quantum states from the absorbed photon to the atom, the initial Zeeman substate of the atom must be controlled; in addition, the absorption event must be detected without destroying the final state of the ion, which requires detecting the single photon emitted upon the single-photon excitation, as in Fig. 5.2c, d. In the following we show experiments that achieve these two requirements.

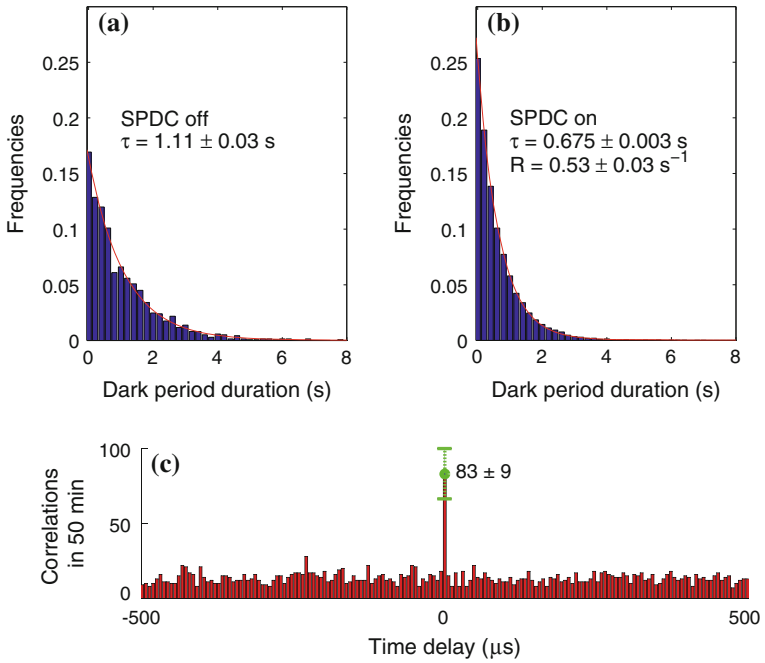

Fig. 5.6 Single photon-single atom interaction data. **a**, **b** Histograms of *dark period durations* with the SPDC source off (**a**) and on (**b**), showing reduction of the $D_{5/2}$ state population upon exposure to the quantum light source. **c** Second-order correlation function (time delay distribution) between the absorption event (the first photon after a *dark-bright* quantum jump) and the detection of a herald photon transmitted through the narrowband filter of the SPDC source

5.4.2 Polarization Control in the Absorption Event

To render the absorption process dependent on the polarization of the incoming photon, the atom must be prepared in a given Zeeman substate, or a coherent superposition of two of them, as discussed in Sect. 5.2.2. Experimentally, this is achieved either by optical pumping techniques or by coherent Rabi pulses driving transitions between the relevent levels.

To show this, we perform an experiment [29] similar to the one reported in the last section, using the pulse sequence described in Fig. 5.7. The ion is first laser cooled by driving it with resonant 866, 850, 854 nm lasers and a red-detuned 397 nm laser. It is then prepared in a mixture of the two outermost Zeeman substates of $D_{5/2}$, by optical pumping with a circularly polarized 854 nm laser, propagating along the quantization axis defined by the applied magnetic field (see Fig. 5.4). The ion becomes sensitive to either σ^- polarized photons, if pumped to the upper two states, or σ^+ if pumped to the lower ones. Finally, in the last step, only the 397 and 866 nm lasers are left on and detectors are activated to monitor the ion fluorescence. Strong time correlations

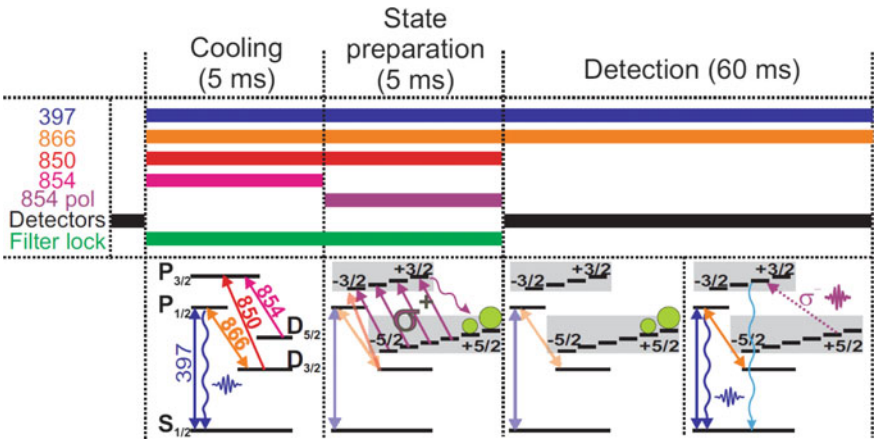

Fig. 5.7 Pulsed sequence used to control the polarization of the absorption process. The ion is laser cooled during 5 ms and then optically pumped to the outer Zeeman substates by means of a circularly polarized 854 nm laser. In the last phase, the pumping laser is turned off and the PMT detectors are activated to monitor fluorescence. Upon a photon absorption event, the ion emits a constant stream of 397 nm fluorescence photons

are again observed between the first detected fluorescence photon and the SPDC heralding photon (Fig. 5.8b).

Most importantly, the absorption process now displays a strong dependence on the photon polarization. This is observed by recording the height of the coincidence peak for different SPDC photon polarizations, varied from R-circular (σ^-) to L-circular (σ^+) (Fig. 5.8c). Full suppression of the correlation rate is found when the photon polarization is orthogonal to the one programmed by the optical pumping.

Additionally, a change of the frequency dependence of the absorption with the photon polarization is observed in a single-photon coincidence spectroscopy experiment: the ion is pumped to either the higher or the lower Zeeman substates, and the photon polarization is adjusted to σ^- and σ^+, respectively. The coincidence rate is then recorded for different detunings of the SPDC photons from the atomic transition center frequency (Fig. 5.8d). The two single-photon absorption spectra are found to be symmetrically displaced from the center frequency of the transition (determined by fluorescence spectroscopy with a horizontally polarized 854 nm laser), due to the differential Zeeman shift between the involved $D_{5/2}$ and $P_{3/2}$ levels. The spectral line widths of ∼45 MHz fit well with the expectation, resulting from convoluting the atomic transition width with the engineered photon spectral width, each ∼22 MHz.

Note that the single-photon spectroscopy is based on absorption-herald coincidences. The photons sent to the ion have the full SPDC bandwidth of ∼200 GHz, and detuning is only applied to the center frequency of the cavities that filter out the heralds. Due to the strict frequency correlation of the photon pair, however, this selects the events when a photon falls within the resonance bandwidth of the ion.

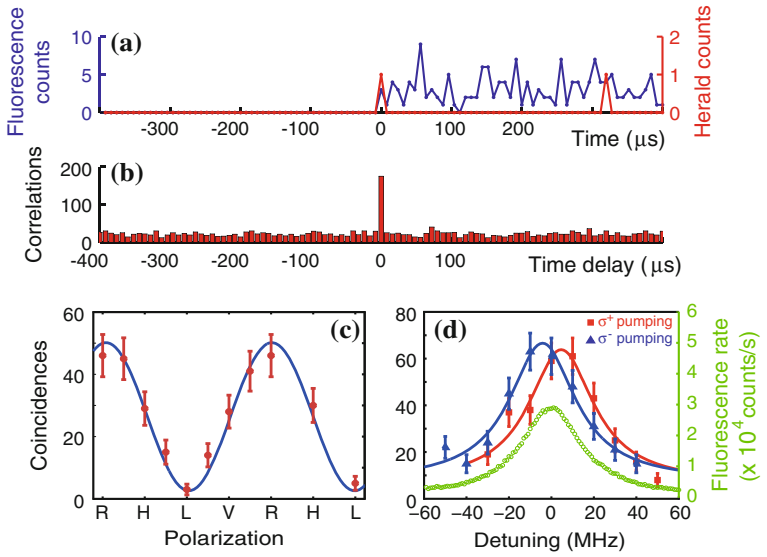

Fig. 5.8 Heralded single-photon absorption with polarization control. **a** Example of a fluorescence onset event (*blue trace*) coinciding with the detection of a heralding photon from the down-conversion source (*red trace*). **b** Extracting such events and calculating the correlation function yields a strong coincidence peak at zero time delay, revealing the single-particle character of the interaction. **c** The polarization dependence of the absorption rate is manifested by measuring the coincidence peak for different settings of the input photon polarization (L/R = left-/right-circular, H/V = horizontal/vertical). **d** Frequency dependence of the absorption-herald coincidence rate recorded for pumping to the lower (*red points*) and upper (*blue points*) Zeeman substates. A reference absorption spectrum of the $D_{5/2} \leftrightarrow P_{3/2}$ transition (*green trace*) is measured using fluorescence spectroscopy with a linearly polarized 854 nm laser that propagates along the quantization axis. *Solid lines* are Lorentzian fits to the data

These experiments demonstrate heralded single-photon absorption with control on the polarization in the interaction. Nevertheless, the polarization entanglement shared by the SPDC photon pairs is destroyed by splitting them with a polarizing beam splitter. To further develop the potential of our methods for quantum information processing, an experiment was performed where the atom interacts with a photon that is polarization-entangled with its heralding partner, in order to verify that the polarization entanglement is indeed manifested in the absorption process [30]. To this end, the photon pairs are now split by means of a non-polarizing beam splitter, such that a coincidence detection between the two arms corresponds to a pair in a maximally entangled polarization state [23, 24].

Entanglement is manifested by measuring the polarization correlation, in this case of absorption and herald, in various bases. As for detection of the herald, there is a polarizer in front of the filter cavities, such that a basis rotation is simply performed by an additional quarter- or half-wave plate. Setting the polarization basis of the absorption is more involved; it is attained by adjusting the orientation of the applied magnetic field and the polarization of the 854 nm laser, with respect to the

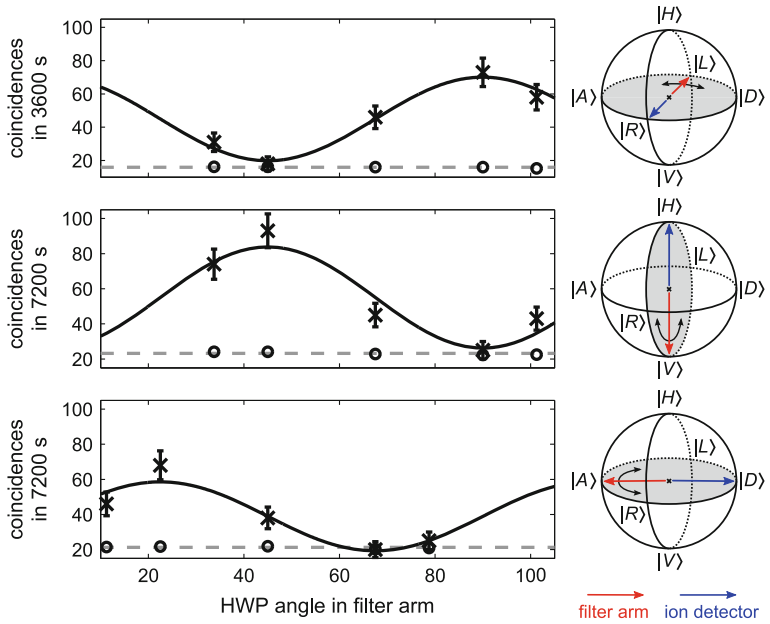

Fig. 5.9 Dependence of absorption-herald coincidences on polarization of the heralding photon for three different polarization bases, R-L (*top*), H-V (*middle*), and D-A (*bottom*). Data points (crosses) are extracted at $\tau = 0$ from the absorption-herald correlation function $g^{(2)}(\tau)$ on a 10 µs time grid; the corresponding background (*circles*), produced by accidental coincidences, is the average over the whole $g^{(2)}(\tau)$ function. Error bars correspond to one standard deviation assuming Poissonian counting statistics. The curves are sinusoidal fits with a fixed period and offset angle. In the right-hand column, we show the Poincaré sphere with the setting of the ion (*blue*) and of the heralding photon detector (*red*, with *black arrows* indicating variation by rotating the HWP). From [30]

incoming SPDC photon wavevector, during the optical pumping which prepares the ion's state before the absorption. Thereby, the ion is made sensitive to only one photon polarization of the respective linear or circular basis. Correlations are then recorded as a function of the half-wave plate (HWP) angle in the heralding photon arm. As displayed in Fig. 5.9, they are observed with high visibilities in the three relevant detection basis, left-/right-circular $\{|R\rangle, |L\rangle\}$, horizontal/vertical linear $\{|H\rangle, |V\rangle\}$, and diagonal/anti-diagonal linear $\{|A\rangle, |D\rangle\}$ [30].

This experiment clearly manifests the polarization entanglement in the single-photon absorption, but the absorbed polarization state is still not preserved in the internal state of the ion, because the latter is destroyed by the continuous 397 nm laser excitation of the fluorescent transition, i.e. by the quantum jump detection technique. The experiment that achieved a full state transfer is described in the following.

5.4.3 Photon-to-Ion State Transfer by Heralded Absorption

The protocol which heralds the absorption event while preserving the state of the ion has been described in Sect. 5.2.2. It was proposed in [16, 31] and is related to an earlier scheme for neutral atoms in cavities [32]. The protocol enhances the previous method in two important aspects (see Fig. 5.3). Firstly, absorption happens out of a pure initial state, either a single Zeeman sublevel or a coherent superposition, but not a mixture as before. Secondly, absorption is heralded by the single photon emitted in the Raman transition from the initial $D_{5/2}$ state to the $S_{1/2}$ ground state manifold.

This has been realized in a recent experiment [17], employing a narrowband laser at 729 nm to coherently excite the $S_{1/2}$ to $D_{5/2}$ transition, plus a radio-frequency field that drives the transition between the two $S_{1/2}$ Zeeman sub-levels. The single absorption event is heralded by detection of the single photon emitted on the $P_{3/2}$ to $S_{1/2}$ transition at 393 nm, without fluorescence excitation. As a result, transfer of the polarization state of photons from a weak laser onto the Zeeman qubit in the $S_{1/2}$ level is demonstrated with over 95 % fidelity, an unprecedented result. Most importantly, the heralding scheme renders the fidelity independent of the success probability.

5.5 Conclusions and Outlook

In conclusion, we have reviewed experiments in which a single trapped ion interacts in a controlled manner with single photons. Resonant, heralded single photons are generated for that purpose with an SPDC-based photon pair source. Single interaction events are detected efficiently thanks to the strong amplification provided by the onset of fluorescence upon the absorption of a photon. Absorption events are observed to be strongly time correlated with the time-resolved detection of the partner photon generated simultaneously by the source. The interaction is further controlled by using a laser pulse sequence that optically pumps the ion such that it only absorbs photons of a given polarization. The observed correlation shows almost full suppression at the wrong polarization. Extending this technique to polarization-entangled photon pairs and observation in three polarization bases, the photonic entanglement is manifested in the heralded absorption processes.

The method is then extended into a protocol for mapping the quantum state of a single photon onto the ground-state Zeeman qubit of the ion. For this, the single photon emitted by the ion after the absorption of the incoming photon, i.e. in a Raman scattering process, is used as a heralding signal of the absorption event. The protocol has been demonstrated using laser photons; implementing it with SPDC photons is work in progress. If the incoming photon is provided by an entangled photon pair source, detection of the herald renders the ion entangled with the partner photon. Subsequently, this second photon can be set up to interact with a second distant trapped atom, or even a quantum particle of different nature, resulting in a

generic scheme to entangle different massive quantum systems via controlled absorption. Such perspectives become even more attractive in view of recent progress in quantum frequency conversion [33], by means of which single photons may be converted between different wavelength regimes, including telecom bands. Hence, the experiments discussed here are key steps towards making heralded absorption suitable for quantum information processing applications.

Other recent approaches to implement controlled single-photon interaction with a trapped ion involve the direct photonic coupling between two distant ions [34] and the cavity-enhanced interaction of an ion with photons from a quantum dot [35]. Protocols that rely on the interference of photons *emitted* by distant atoms to entangle them have already been succesfully implemented with ions [11], neutral atoms [36] and color centers in diamond [37]. The entanglement rates of these schemes are limited by the photon collection efficiency into a single optical mode. We believe that the schemes we propose offer a competitive alternative, in that the high generation rates of state-of-the-art narrow-band photon pair sources [38–40] may alleviate the collection efficiency problem.

Acknowledgments The experiments described in this chapter were carried out by the members of J. Eschner's group at The Institute of Photonic Sciences (until 2009) and at the Universität des Saarlandes; their contributions are most gratefully acknowledged. We also acknowledge financial support by the MICINN (Consolider 2010 project "QOIT"), the BMBF (projects "QuOReP" and "Q.com-Q", CHIST-ERA project "QScale"), the German Scholars Organization/Alfried Krupp von Bohlen und Halbach-Stiftung, the ESF (COST Action "IOTA"), and CONICYT.

Appendix: Data Analysis

The raw data sets produced by the two types of schemes in Fig. 5.2 consist of lists of photon detection times from two channels, the source herald and either the ion laser-induced fluorescence (schemes (a) and (b)), or the single emitted photons (schemes (c) and (d)). With the latter, the single-photon interaction is manifested directly by calculating the second-order correlation function between the two detection events. In schemes (a) and (b) where the absorption is signalled by a change in the fluorescent state of the ion (a jump), a previous data processing step has to be undertaken to extract the time of the first (or last) detected fluorescence photon, which is then assigned to be the moment of the quantum jump. Below we provide some detail on how this preprocessing is performed.

The analysis is performed in three steps: (1) determination of the optimal on-off fluorescence threshold; (2) preselection of detection times around each fluorescence jump; (3) detection of the first (last) photon associated to the fluorescence jump.

Step 1 establishes a criterion to decide whether in a given time interval the ion is in the *on* or *off* fluorescent state. First, the time axis is divided into bins of size t_b, and the fluorescence trace, i.e. the number $n_\mathrm{f}(i)$ of detections in bin i, is computed. From the trace, a histogram of fluorescent counts is extracted. This histogram statistically corresponds to the sum of two independent Poisson distributions $P_{\mathrm{on/off}}(\bar{n}_{\mathrm{on/off}}, n)$,

with mean values $\bar{n}_{\mathrm{on/off}}$ given by the average detection rate for the on and off states in the specified time bin size. The optimal threshold used to discriminate the two states is then given by $n_{\mathrm{th}} = \min_n \{P_{\mathrm{on}}(\bar{n}_{\mathrm{off}}, n) + P_{\mathrm{off}}(\bar{n}_{\mathrm{on}}, n)\}$, with $\bar{n}_{\mathrm{off}} > n > \bar{n}_{\mathrm{on}}$.

Step 2 is performed by running a moving average over the fluorescence trace, $\bar{n}_{\mathrm{f}}(i)$ of window size N, given by the desired number of detection events to be extracted, storing the last N detection times in a buffer. Every time the condition $\bar{n}_{\mathrm{f}}(i) < n_{\mathrm{th}} < \bar{n}_{\mathrm{f}}(i \pm 1)$ is met (using $+$ $(-)$ sign for detecting the change to the *on* (*off*) fluorescing state) the last N stored detection times are extracted.

Step 3 is performed directly on the detection times t_i extracted in Step 2. They are scanned for the condition $t_i > \tau_{\mathrm{th}} > t_{i\pm1}$, where the sign is chosen to detect the first (+) or last (-) fluorescence photon. The optimal delay threshold τ_{th} to discriminate the *on* and *off* state is chosen by maximizing the probability of successfully detecting an atom transition, namely, the probability of *not* detecting a photon in the *off* state after a time τ_{th} and detecting one in the *on* state before a time τ_{th}. Assuming a rate of fluorescence photon detection r_{on} and a dark count rate of r_{off} in the *off* state, this probability is given by $p_{\mathrm{det}} = \exp(-r_{\mathrm{off}}\tau_{\mathrm{th}})\left[1 - \exp(-r_{\mathrm{on}}\tau_{\mathrm{th}})\right]$, which takes a maximum value at $\tau_{\mathrm{th}} = r_{\mathrm{on}}^{-1} \log(1 + r_{\mathrm{on}}/r_{\mathrm{off}})$.

References

1. C. Langer et al., Long-lived qubit memory using atomic ions. Phys. Rev. Lett. **95**, 060502 (2005)
2. D. Leibfried, R. Blatt, C. Monroe, D. Wineland, Quantum dynamics of single trapped ions. Rev. Mod. Phys. **75**, 281–324 (2003)
3. Q.A. Turchette et al., Deterministic entanglement of two trapped ions. Phys. Rev. Lett. **81**, 3631–3634 (1998)
4. C. Monroe, D.M. Meekhof, B.E. King, W.M. Itano, D.J. Wineland, Demonstration of a fundamental quantum logic gate. Phys. Rev. Lett. **75**, 4714–4717 (1995)
5. J. Chiaverini et al., Realization of quantum error correction. Nature **432**, 602–605 (2004)
6. R. Ursin et al., Entanglement-based quantum communication over 144 km. Nat. Phys. **3**, 481–486 (2007)
7. J.I. Cirac, P. Zoller, H.J. Kimble, H. Mabuchi, Quantum state transfer and entanglement distribution among distant nodes in a quantum network. Phys. Rev. Lett. **78**, 3221 (1997)
8. H.J. Kimble, The quantum internet. Nature **453**, 1023–1030 (2008)
9. B.B. Blinov, D.L. Moehring, L.M. Duan, C. Monroe, Observation of entanglement between a single trapped atom and a single photon. Nature **428**, 153 (2004)
10. J. Volz et al., Observation of entanglement of a single photon with a trapped atom. Phys. Rev. Lett. **96**, 030404 (2006)
11. D.L. Moehring et al., Entanglement of single-atom quantum bits at a distance. Nature **449**, 68–71 (2007)
12. J. Hofmann et al., Heralded entanglement between widely separated atoms. Science **337**, 72 (2012)
13. S. Ritter et al., An elementary quantum network of single atoms in optical cavities. Nature **484**, 195–200 (2012)
14. T. Chaneliere et al., Storage and retrieval of single photons transmitted between remote quantum memories. Nature **438**, 833–836 (2005)
15. R. Gerritsma et al., Precision measurement of the branching fractions of the $4p^2P_{3/2}$ decay of Ca II. Eur. Phys. J. D **50**, 13–19 (2008)

16. P. Müller, J. Eschner, Single calcium-40 ion as quantum memory for photon polarization: a case study. Appl. Phys. B **114**, 303–306 (2014)
17. C. Kurz et al., Experimental protocol for high-fidelity heralded photon-to-atom quantum state transfer. Nat. Commun. **5**, 5527 (2014)
18. E. Togan et al., Quantum entanglement between an optical photon and a solid-state spin qubit. Nature **466**, 730 (2010)
19. M. Schug et al., Quantum interference in the absorption and emission of single photons by a single ion. Phys. Rev. A **90**, 023829 (2014)
20. F. Rohde, Remote ion traps for quantum networking: two-photon interference and correlations, in *PhD thesis, ICFO—The Institute of Photonic Sciences* (2009)
21. C. Schuck, Interfacing single ions and single photons for quantum networks, in *PhD thesis, ICFO, The Institute Of Photonics Sciences* (2010)
22. M. Almendros et al., Bandwidth-tunable single-photon source in an ion-trap quantum network. Phys. Rev. Lett. **103**, 213601 (2009)
23. A. Haase, N. Piro, J. Eschner, M.W. Mitchell, Tunable narrowband entangled photon pair source for resonant single-photon single-atom interaction. Opt. Lett. **34**, 55–57 (2009)
24. N. Piro, A. Haase, M.W. Mitchell, J. Eschner, An entangled photon source for resonant single-photon-single-atom interaction. J. Phys. B: Atom. Mol. Opt. Phys. **42**, 114002 (2009)
25. W. Nagourney, J. Sandberg, H. Dehmelt, Shelved optical electron amplifier: observation of quantum jumps. Phys. Rev. Lett. **56**, 2797–2799 (1986)
26. T. Sauter, W. Neuhauser, R. Blatt, P.E. Toschek, Observation of quantum jumps. Phys. Rev. Lett. **57**, 1696–1698 (1986)
27. J.C. Bergquist, R.G. Hulet, W.M. Itano, D.J. Wineland, Observation of quantum jumps in a single atom. Phys. Rev. Lett. **57**, 1699–1702 (1986)
28. H. Dehmelt, Proposed $10^{14}\Delta\nu < \nu$ laser fluorescence spectroscopy on Tl^{+} mono-ion oscillator II (spontaneous quantum jumps). Bull. Am. Phys. Soc. **20**, 60 (1975)
29. N. Piro et al., Heralded single-photon absorption by a single atom. Nat. Phys. **7**, 17–20 (2011)
30. J. Huwer et al., Photon entanglement detection by a single atom. New J. Phys. **15**, 025033 (2013)
31. N. Sangouard, J.-D. Bancal, P. Müller, J. Ghosh, J. Eschner, Heralded mapping of photonic entanglement into single atoms in free space: proposal for a loophole-free bell test. New J. Phys. **15**, 085004 (2013)
32. S. Lloyd, M.S. Shahriar, J.H. Shapiro, P.R. Hemmer, Long distance, unconditional teleportation of atomic states via complete bell state measurements. Phys. Rev. Lett. **87**, 167903 (2001)
33. S. Zaske et al., Visible-to-telecom quantum frequency conversion of light from a single quantum emitter. Phys. Rev. Lett. **109** (2012)
34. M. Schug, J. Huwer, C. Kurz, P. Müller, J. Eschner, Heralded photonic interaction between distant single ions. Phys. Rev. Lett. **110**, 213603 (2013)
35. M. Steiner, H.M. Meyer, J. Reichel, M. Köhl, Photon emission and absorption of a single ion coupled to an optical-fiber cavity. Phys. Rev. Lett. **113**, 263003 (2014)
36. M. Lettner et al., Remote entanglement between a single atom and a bose-einstein condensate. Phys. Rev. Lett. **106**, 210503 (2011)
37. H. Bernien et al., Heralded entanglement between solid-state qubits separated by three metres. Nature **497**, 86–90 (2013)
38. F. Wolfgramm et al., Bright filter-free source of indistinguishable photon pairs. Opt. Express **16**, 18145–18151 (2008)
39. E. Pomarico et al., Waveguide-based opo source of entangled photon pairs. New J. Phys. **11**, 113042 (2009)
40. Z.-Y. Zhou, D.-S. Ding, Y. Li, F.-Y. Wang, B.-S. Shi, Cavity-enhanced bright photon pairs at telecom wavelengths with a triple-resonance configuration. J. Opt. Soc. Am. B **31**, 128–134 (2014)

Part III
Light Meets Many Atoms

Chapter 6
Narrowband Biphotons: Generation, Manipulation, and Applications

Chih-Sung Chuu and Shengwang Du

Abstract In this chapter, we review recent advances in generating narrowband biphotons with long coherence time using spontaneous parametric interaction in monolithic cavity with cluster effect as well as in cold atoms with electromagnetically induced transparency. Engineering and manipulating the temporal waveforms of these long biphotons provide efficient means for controlling light-matter quantum interaction at the single-photon level. We also review recent experiments using temporally long biphotons and single photons.

6.1 Introduction

Entangled photon pairs, termed *biphotons*, have been benchmark tools in the field of quantum optics for testing fundamental quantum mechanics as well as for developing applications in quantum information technology, including realization of the Einstein-Podolsky-Rosen paradox [1, 2], test of violation of Bell's inequality [3–5], quantum cryptography and key distribution [6], quantum teleportation [7, 8], quantum computation [9], etc. Traditional methods of producing biphotons include spontaneous parametric down conversion (SPDC) [10–12] and spontaneous four-wave mixing (SFWM) [13–15] in nonlinear solid-state materials. Photons from these nonlinear processes in free space forward-wave configuration usually have broad bandwidth (>THz) and short coherence time (<ps) such that their temporal quantum waveform can not be directly resolved by existing commercial single-photon counters (which have a typical resolution of about ns).

C.-S. Chuu (✉)
Department of Physics and Frontier Research Center on Fundamental and Applied Sciences of Matters, National Tsing Hua University, Hsinchu 30013, Taiwan
e-mail: cschuu@phys.nthu.edu.tw

S. Du
Department of Physics, The Hong Kong University of Science and Technology, Clear Water Bay, Kowloon, Hong Kong, People's Republic of China
e-mail: dusw@ust.hk

A. Predojević and M.W. Mitchell (eds.), *Engineering the Atom-Photon Interaction*, Nano-Optics and Nanophotonics, DOI 10.1007/978-3-319-19231-4_6

These broadband biphotons are not suitable for recently proposed protocols of long-distance quantum communication and quantum network based on photon-atom interaction [16, 17], because an efficient photon-atom quantum interface requires single flying photons having a bandwidth sufficiently narrower than the atomic resonance (typically in MHz). To reduce their bandwidth, optical cavity may be used for active filtering [18–21]. However, multiple cavity modes are resonated simultaneously due to the broad gain linewidth of the forward-wave parametric interaction and the biphotons are generated in multiple longitudinal modes. Additional passive filters locked to the desired mode of the resonant cavity is thus necessary to obtain single mode output with reduced generation rate and increased complexity.

Phase-matching condition plays an important role in determining the photon bandwidth in these nonlinear process. The loose constraint of phase matching in the forward-wave configuration make it difficult to generate ultranarrow-bandwidth biphotons. To overcome this problem, one may use the cluster effect in a monolithic cavity with double-pass pumping. An alternative solution is to take the backward-wave configuration where the produced paired photons propagate in opposing directions. In this chapter, we review recent advances in generating narrowband biphotons with long coherence time using forward-wave and backward-wave parametric interaction. In particular, we describe the monolithic resonant down-conversion with cluster effect [22, 23] and the resonant SFWM in cold atoms with electromagnetically induced transparency (EIT) [24–26].

6.2 Monolithic Resonant Parametric Down-Conversion with Cluster Effect

A resonant parametric down-converter can generate single-mode biphotons without external filtering when its gain linewidth is narrower than the spacing of adjacent resonant modes. For a doubly resonator where the signal and idler fields are simultaneously resonant, the mode spacing is determined by the cluster spacing $\Delta\Omega_c$ between the simultaneous resonant signal the idler modes. The cluster spacing can be calculated by solving the following equations [27],

$$\begin{aligned} \pm 1 &= M(\omega)\Delta\Omega_c^2 + N(\omega)\Delta\Omega_c, \\ M(\omega) &= [L/(2\pi c)]\{2[n_s^{'}(\omega) + n_i^{'}(\omega_i)] + \omega_s n_s^{''}(\omega) + \omega_i n_i^{''}(\omega_i)\}, \\ N(\omega) &= [L/(\pi c)][n_s - n_i + \omega_s n_s^{'}(\omega_s) - \omega_i n_i^{'}(\omega_i)], \end{aligned} \tag{6.1}$$

where n_s and n_i are the refractive indices at the signal and idler frequencies, and $n_{s,i}^{'}$ and $n_{s,i}^{''}$ are the first and second frequency derivatives, respectively.

If we assume that the idler mode spacing Δ_i is slightly less than the signal mode spacing Δ_s and the group velocity dispersion is negligible, the cluster spacing can also be obtained by multiplying the idler mode spacing by the number of idler modes

between two doubly resonant modes,

$$\Delta\Omega_c \cong \frac{\Delta_s\,\Delta_i}{\Delta_s - \Delta_i}. \tag{6.2}$$

For small $\Delta_s - \Delta_i$, the cluster spacing will be much larger than the signal or idler mode spacing. Moreover, since $\Delta\Omega_c$ decreases with the length of cavity, a monolithic doubly resonator has the largest possible cluster spacing and can be used to reduce the number of resonant modes within the gain curve.

For parametric down-conversion of the forward wave type, a monolithic doubly resonator by itself is not enough for generating biphotons in a single longitudinal mode. This is because the gain linewidth of the parametric interaction is larger than the cluster spacing, which allows biphotons to be generated in multiple longitudinal modes. As an example, we consider a 3 cm long monolithic PPKTP crystal pumped by a continuous-wave 532 nm laser. At type-II phase matching, the gain linewidth $\Delta f_{sp} = 0.885c/(|n_s^{(g)} - n_i^{(g)}|L) = 93.2$ GHz and the cluster spacing $\Delta\Omega_c = c/(2|n_s^{(g)} - n_i^{(g)}|L) = 52.6$ GHz where $n_{s,i}^{(g)}$ are the group indices at the signal and idler frequencies and L is the crystal or cavity length. Because $\Delta f_{sp} > \Delta\Omega_c$, multimode biphotons are generated and external filters are required to eliminate biphotons in unwanted modes to obtain single-mode biphotons. This results in reduced biphoton generation rate in additional to increased complexity of the biphoton source.

6.2.1 Single-Mode Output

To obtain single-mode biphotons without additional filtering, it is necessary to increase the mode spacing and reduce the gain linewidth. This can be achieved by using double-pass pumping, for example, by depositing a high reflection coating at the pump frequency on the output face of the crystal. The double-pass pumping effectively doubles the length of the parametric interaction or reduces the gain linewidth by half. The broaden gain linewidth $\Delta f_{dp} = 0.443c/(|n_s^{(g)} - n_i^{(g)}|L)$ is thus smaller than the cluster spacing $\Delta\Omega_c = c/(2|n_s^{(g)} - n_i^{(g)}|L)$. Consider the previous example with a double-pass pump. The gain linewidth $\Delta f_{dp} = 46.6$ GHz is now narrower than the cluster spacing $\Delta\Omega_c = 52.6$ GHz, so biphotons can be generated in a single longitudinal mode without the need of additional filtering.

The principle of single-mode operation is illustrated in Fig. 6.1a, where the solid curve is the gain profile and the vertical lines represent the frequencies of the simultaneously resonant signal and idler modes. With one resonant mode aligned to the center of the gain curve, the adjacent modes are outside the gain region. For comparison, the gain curve of a monolithic resonator with single-pass pumping is also shown as a dotted curve where more than one resonant signal and idler pairs are present within the gain curve.

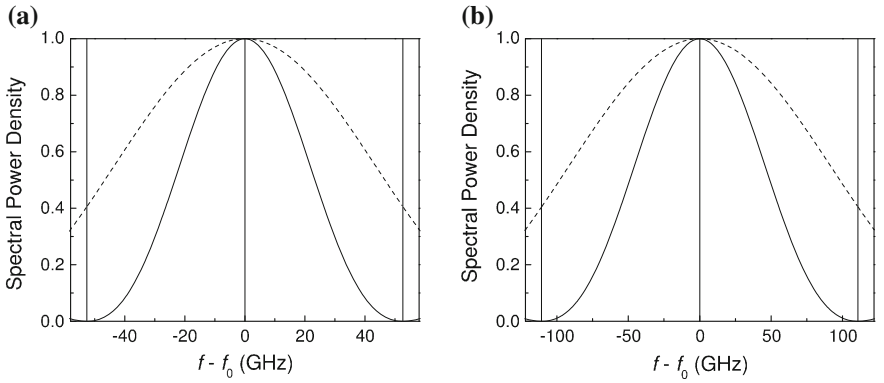

Fig. 6.1 Single-mode operation is shown as compared to multi-mode operation. The *solid* and *dotted curves* are the gain profiles (spectral power density) of a doubly resonant forward-wave parametric down-converters with double-pass and single-pass pumping, respectively. The *vertical lines* represent the frequencies of the simultaneously resonant signal and idler pairs with one mode taken at the center frequency f_0 of the gain curve. Quasi-phasematching is chosen for **a** degenerate and **b** non-degenerate frequencies

As another example, we consider the generation of single-mode non-degenerate biphotons. We assume a 3-cm long monolithic PPKTP crystal pumped by a double-pass 525.5 nm laser. Such source may be useful for applications such as quantum repeater [28]. For example, the signal photons at 795 nm can be stored in nearby atomic memories while idler photons at 1550 nm can be sent through a fiber to interfere on a distant beam splitter for creating entanglement between two remote locations. As shown in Fig. 6.1b, the gain linewidth $\Delta f_{dp} = 98.1\,\text{GHz}$ is narrower than the cluster spacing $\Delta\Omega_c = 110.7\,\text{GHz}$ and the biphotons are generated in a single longitudinal mode.

6.2.2 Experimental Realization

Chuu et al. [23] have demonstrated a miniature ultrabright source of narrowband biphotons using a monolithic resonant parametric down-converter without external filtering. A schematic of the experimental setup is shown in Fig. 6.2. The biphoton source uses a nonlinear crystal of which the end faces are spherically polished and deposited with a high reflection coating at the signal and idler wavelengths to form a monolithic cavity. The high reflection coating on one end face is also highly reflective at the pump wavelength for double-pass pumping. The combination of monolithic cavity, double-pass pumping, and type-II phase matching allows the generation of single-mode biphotons near degeneracy. When the pump is increased above threshold to produce parametric oscillation, the output is single-mode, as observed by a scanning Fabry Perot interferometer. This suggests that only a single cluster mode is present.

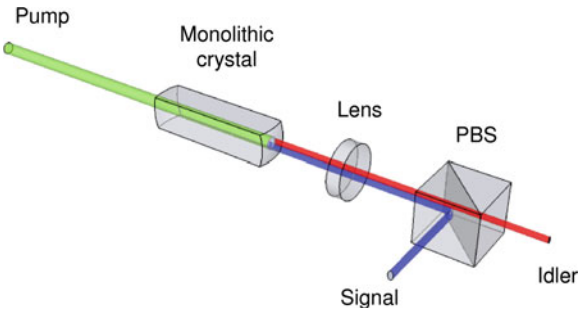

Fig. 6.2 A monolithic doubly resonant parametric down-converter for generating single-mode biphotons [23]. The pump is double-passed by the end face of the monolithic crystal, which has a high reflection coating at the signal, idler, and pump wavelengths. The lens is used to collimate the signal and idler fields. The PBS (polarizing beam splitter) separates the signal and idler fields before they are detected by the single-photon detection modules (not shown)

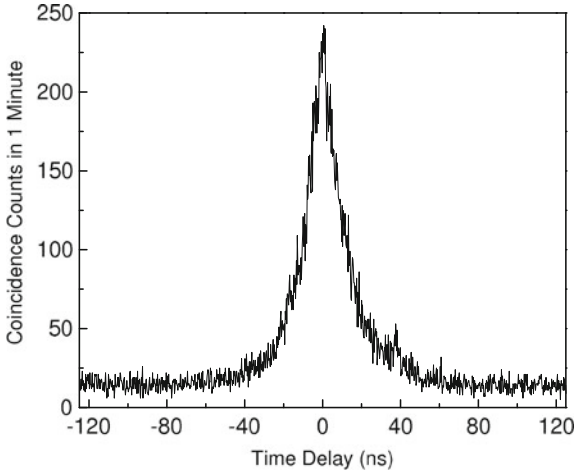

Fig. 6.3 Glauber correlation function of the biphotons [23]. The coincidence counts are measured as a function of the time delay between the signal and idler photons at a pump power of 700 μW. The function has two exponential decays with decay constants of 13.29 ± 0.14 and 11.33 ± 0.12 ns for time delay greater than or less than zero. The biphoton correlation time is 17.07 ± 0.13 ns

A typical coincidence measurement of the biphoton wavepacket is shown in Fig. 6.3. The measured curve shows two asymmetric exponential decays possibly due to the different reflectivity for orthogonal polarizations. The biphoton correlation time is found to be $T_c \cong 17$ ns and the biphoton bandwidth is $\Delta\omega \cong 2\pi \cdot 8$ MHz. Correcting for the collection efficiency, the generation rate is $R = 1.10 \times 10^5$ biphotons/(s mW) which gives a spectral brightness of $R/\Delta\omega = 1.34 \times 10^4$ biphotons/(s MHz mW).

6.3 Backward-Wave Biphoton Generation

Parametric down-conversion of the backward-wave type provides an alternative way to realize an ultrabright biphoton source without external filtering. As compared to conventional forward-wave schemes, such as spontaneous parametric down

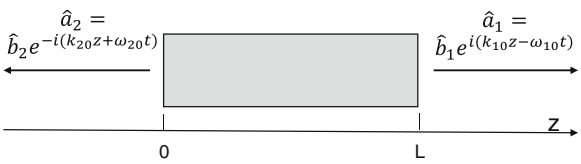

Fig. 6.4 Schematics of backward-wave biphoton generation from a nonlinearly driven medium in free space

conversion (SPDC) in nonlinear crystals, the backward geometry allows a much tighter constraint of phase matching that leads to substantially narrow linewidth.

6.3.1 General Formulism: Free Space

The backward-wave biphoton generation in free space is schematically illustrated in Fig. 6.4, where the generated field $\hat{a}_1$ propagates along the +z direction and $\hat{a}_2$ along the −z direction. For SPDC with $\chi^{(2)}$ nonlinearity, this geometry can be achieved by quasiphase matching [29] to submicron periodicity and driven by a single pump laser beam [30–32]. For SFWM driven by $\chi^{(3)}$ nonlinearity, the phase matching condition can be satisfied by aligning two coherent driving laser beams [26, 33]. As compared to conventional forward-wave schemes, the backward-wave geometry allows a much tighter constraint of phase matching that leads to substantially narrow linewidth.

We describe the spontaneously generated paired photons as quantized field operators

$$\begin{aligned}\hat{a}_1(z,t) &= \hat{b}_1(z,t)e^{i(k_{10}z-\omega_{10}t)} \times e^{-i\Delta k_0 Z/2},\\ \hat{a}_2(z,t) &= \hat{b}_2(z,t)e^{-i(k_{20}z+\omega_{20}t)} \times e^{-i\Delta k_0 Z/2},\end{aligned} \tag{6.3}$$

where ω_{i0} are the central angular frequencies and $k_{i0} = \omega_{i0}/c$ are the wave numbers in vacuum, and Δk_0 is the phase matching in vacuum. $\hat{b}_i(z,t)$ are their slowly varying envelopes and follow the Fourier transform

$$\hat{b}_i(z,t) = \frac{1}{\sqrt{2\pi}} \int \hat{b}_i(z,\omega)e^{-i\omega t}d\omega. \tag{6.4}$$

The frequency domain field operators are governed by the following Heisenberg-Langevin coupled equations [34]:

$$\begin{aligned}\left[\frac{\partial}{\partial z} + \alpha_1(\omega) - i\frac{\Delta k_0}{2}\right]\hat{b}_1(z,\omega) &= \kappa_1(\omega)\hat{b}_2^{\dagger}(z,-\omega) + \hat{F}_1(z,\omega),\\ \left[\frac{\partial}{\partial z} + g_2(\omega) + i\frac{\Delta k_0}{2}\right]\hat{b}_2^{\dagger}(z,-\omega) &= \kappa_2(\omega)\hat{b}_1(z,\omega) + \hat{F}_2^{\dagger}(z,-\omega),\end{aligned} \tag{6.5}$$

where $\alpha_1(\omega) = -i\frac{\omega_{10}}{2c}\chi_1(\omega_{10}+\omega)$ and $g_2(\omega) = -i\frac{\omega_{20}}{2c}\chi_2^*(\omega_{20}-\omega)$ describe the linear propagation effects with the linear susceptibilities χ_i, $\kappa_i(\omega)$ are the nonlinear parametric coupling coefficients, and $\hat{F}_i(z,\omega)$ are the Langevin noise operators. Neglecting the Langenvin noise operators that contribute to uncorrelated noise photons, the above equations reduce to

$$\begin{aligned}\left[\frac{\partial}{\partial z}+\alpha_1(\omega)-i\frac{\Delta k_0}{2}\right]\hat{b}_1(z,\omega) &= \kappa_1(\omega)\hat{b}_2^\dagger(z,-\omega),\\ \left[\frac{\partial}{\partial z}+g_2(\omega)+i\frac{\Delta k_0}{2}\right]\hat{b}_2^\dagger(z,-\omega) &= \kappa_2(\omega)\hat{b}_1(z,\omega),\end{aligned} \tag{6.6}$$

which are subject to the boundary conditions $[\hat{b}_1(0,\omega),\hat{b}_1^\dagger(0,\omega')] = [\hat{b}_2(L,\omega),\hat{b}_2^\dagger(L,\omega')] = \delta(\omega-\omega')$ and $\langle\hat{b}_1^\dagger(0,\omega')\hat{b}_1(0,\omega)\rangle = \langle\hat{b}_2^\dagger(L,\omega')\hat{b}_2(L,\omega)\rangle = 0$. The general solution to (6.6) is given as

$$\begin{aligned}\hat{b}_1(L,\omega) &= A(\omega)\hat{b}_1(0,\omega)+B(\omega)\hat{b}_2^\dagger(L,-\omega),\\ \hat{b}_2^\dagger(0,-\omega) &= C(\omega)\hat{b}_1(0,\omega)+D(\omega)\hat{b}_2^\dagger(L,-\omega),\end{aligned} \tag{6.7}$$

where

$$\begin{aligned}A(\omega) &= \frac{Qe^{-(\alpha_1+g_2)L/2}}{q\sinh(QL/2)+Q\cosh(QL/2)},\\ B(\omega) &= \frac{2\kappa_1}{q+Q\coth(QL/2)},\\ C(\omega) &= \frac{-2\kappa_2}{q+Q\coth(QL/2)},\\ D(\omega) &= \frac{Qe^{(\alpha_1+g_2)L/2}}{q\sinh(QL/2)+Q\cosh(QL/2)}.\end{aligned} \tag{6.8}$$

Here $q(\omega) = \alpha_1(\omega) - g_2(\omega) - i\Delta k_0$ and $Q(\omega) = \sqrt{q^2(\omega)+4\kappa_1(\omega)\kappa_2(\omega)}$. The single photon rates can be calculated from

$$\begin{aligned}R_1 &= \langle\hat{b}_1^\dagger(L,t)\hat{b}_1(L,t)\rangle = \frac{1}{2\pi}\int|B(\omega)|^2d\omega,\\ R_2 &= \langle\hat{b}_2^\dagger(0,t)\hat{b}_2(0,t)\rangle = \frac{1}{2\pi}\int|C(\omega)|^2d\omega.\end{aligned} \tag{6.9}$$

The two-photon Glauber correlation function can be determined by

$$G_{12}^{(2)}(\tau) = \langle\hat{b}_1^\dagger(L,t+\tau)\hat{b}_2^\dagger(0,t)\hat{b}_2(0,t)\hat{b}_1(L,t+\tau)\rangle = |\psi(\tau)|^2 + R_1R_2, \tag{6.10}$$

where the two-photon wave function is

$$\psi(\tau) = \langle \hat{b}_2(0,t)\hat{b}_1(L,t+\tau)\rangle = \frac{1}{2\pi}\int B(\omega)D^*(\omega)e^{-i\omega\tau}d\omega. \tag{6.11}$$

Alternatively, the two-photon wave function can also be obtained from

$$\psi(\tau) = \langle \hat{b}_1(L,t+\tau)\hat{b}_2(0,t)\rangle = \frac{1}{2\pi}\int A(\omega)C^*(\omega)e^{-i\omega\tau}d\omega. \tag{6.12}$$

When the system is conservative and the commutation relation of the field operators is preserved, (6.11) and (6.12) are equivalent. When the Langevin noise fluctuations exist, (6.11) and (6.12) become approximated solutions [35]. The photon pair generation rate can be calculated from

$$R = \int |\psi(\tau)|^2 d\tau. \tag{6.13}$$

The normalized two-photon cross-correlation function is

$$g_{12}^{(2)}(\tau) = \frac{G_{12}^{(2)}(\tau)}{R_1R_2} = 1 + \frac{|\psi(\tau)|^2}{R_1R_2}. \tag{6.14}$$

It is instructive to see what parameters play important role in determining the two-photon wave function under some reasonable approximations. To ensure the spontaneous photon generation remains below the threshold and multi-photon-pair events are suppressed, we work in the low parametric gain regime, i.e., $|\kappa_1(\omega)\kappa_2(\omega)| \ll |q^2|$. We further take $\kappa_1 \simeq \kappa_2 \simeq \kappa$ and assume the linear loss and gain of the medium to the generated fields can be neglected for the generated fields (i.e., $\chi_i = \chi_i^*$). Under these conditions, the ABCD parameters in (6.8) can be written approximately

$$\begin{aligned} A &\simeq e^{i\Delta k_1 L}e^{i\Delta k_0 L/2},\\ B &\simeq \kappa L\,\mathrm{sinc}(\Delta kL/2)e^{i\Delta kL/2},\\ C &\simeq -\kappa L\,\mathrm{sinc}(\Delta kL/2)e^{i\Delta kL/2},\\ D &\simeq e^{-i\Delta k_2 L}e^{i\Delta k_0 L/2}, \end{aligned} \tag{6.15}$$

where $\Delta k_i = \chi_i\omega_{i0}/(2c)$ and $\Delta k = \Delta k_1 - \Delta k_2 + \Delta k_0$. The biphoton wave function in (6.11) then becomes

$$\psi(\tau) = \frac{L}{2\pi}\int \kappa(\omega)\Phi(\omega)e^{-i\omega\tau}d\omega, \tag{6.16}$$

where $\Phi(\omega)$ is the longitudinal detuning function

$$\Phi(\omega) = \text{sinc}\left[\frac{\Delta k(\omega)L}{2}\right] e^{i[\Delta k_1(\omega)+\Delta k_2(\omega)]L/2}. \tag{6.17}$$

Equations (6.16) and (6.17) are the same as those obtained following a perturbation treatment in the interaction picture [26]. The biphoton joint spectrum is determined by two factors: the nonlinear parametric coupling coefficient $\kappa(\omega)$ and the longitudinal detuning function $\Phi(\omega)$ from the linear phase-matching and propagation effects.

6.3.2 General Formalism: Resonant SPDC

Doubly resonant optical cavity plays an important role in obtaining single-mode output for ultrabright biphoton generation. Here we develop the theory of resonant biphoton generation in the Heisenberg picture.

We denote the signal and idler fields internal to the cavity by the standing-wave cavity operators

$$\begin{aligned} a_s(t,z) &= b_s(t)\exp(-i\Omega_q t)\sin(k_q z) \\ a_i(t,z) &= b_i(t)\exp(-i\Omega_r t)\sin(k_r z) \end{aligned} \tag{6.18}$$

where $b_s(t)$ and $b_i(t)$ are the slowly varying envelopes, Ω_q and Ω_r are the cold cavity frequencies, $k_q = q\pi/L$ and $k_r = r\pi/L$. We assume that only one pair of signal and idler fields is resonant with the qth and rth cavity modes simultaneously (we will justify this in the following section). Since only the components nonorthogonal to the qth and rth cavity mode interact with the signal and idler fields respectively, the generated dipole moment operators for the signal and idler fields, which are proportional to $b_i(t)\exp(-i\Omega_q t)\exp(ik_q z)\exp(i\Delta k z)$ and $b_s(t)\exp(-i\Omega_r t)\exp(ik_r z)\exp(i\Delta k z)$ where the phase mismatch $\Delta k = k_p - k_r - k_q$, are projected against $\sin(k_q z)$ and $\sin(k_r z)$.

Using the input-output coupling formalism [36, 37], the equations for the evolution of $b_s(t)$ and $b_i(t)$ and their relation to the incident fields are

$$\begin{aligned} \frac{\partial b_s(t)}{\partial t} + \frac{\Gamma_s}{2} b_s(t) &= -i\kappa\, b_i^\dagger(t) + \sqrt{\gamma_s}\, b_s^{\text{in}}(t) \\ \frac{\partial b_i^\dagger(t)}{\partial t} + \frac{\Gamma_i}{2} b_i^\dagger(t) &= i\kappa\, b_s(t) + \sqrt{\gamma_i}\, b_i^{\text{in}\dagger}(t), \end{aligned} \tag{6.19}$$

where $b_s^{\text{in}}(t)$ and $b_i^{\text{in}}(t)$ are the fields incident on the resonant cavity and κ is the coupling constant. With $\{\Delta_s, \Delta_i\}$ and $\{r_s, r_i\}$ denoting the spacing of the cavity modes and the mirror reflectivity, respectively, the output coupling rates of the signal and idler fields are $\gamma_s = \Delta_s(1 - r_s)$ and $\gamma_i = \Delta_i(1 - r_i)$. With ξ_s and ξ_i defined as

the single-pass power loss for the signal and idler fields in the crystal, the total cavity decay rates are $\Gamma_s = 2\xi_s\Delta_s + \gamma_s$ and $\Gamma_i = 2\xi_i\Delta_i + \gamma_i$.

The slowly varying output fields $b_s^{\text{out}}(t)$ and $b_i^{\text{out}\dagger}(t)$ are related to the internal and incident fields by

$$\begin{aligned} b_s^{\text{out}}(t) &= \sqrt{\gamma_s}\, b_s(t) - b_s^{\text{in}}(t) \\ b_i^{\text{out}\dagger}(t) &= \sqrt{\gamma_i}\, b_i^{\dagger}(t) - b_i^{\text{in}\dagger}(t). \end{aligned} \tag{6.20}$$

They can be solved by transforming the coupled equations to the frequency domain with the Fourier pair

$$\begin{aligned} b(t) &= \int_{-\infty}^{\infty} b(\omega') \exp(-i\omega' t) d\omega' \\ b(\omega) &= \frac{1}{2\pi} \int_{-\infty}^{\infty} b(t') \exp(i\omega t') dt' \end{aligned} \tag{6.21}$$

and converting to rapidly varying quantities

$$\begin{aligned} a(\omega_{s,i}) &= b(\omega_{s,i} - \Omega_{q,r}) \\ a^{\dagger}(\omega_{s,i}) &= b^{\dagger}(\omega_{s,i} + \Omega_{q,r}) \end{aligned} \tag{6.22}$$

The output fields $a_s^{\text{out}}(\omega)$ and $a_i^{\text{out}\dagger}(-\omega_i)$ can then be expressed in terms of incident fields $a_s^{\text{in}}(\omega)$ and $a_i^{\text{in}\dagger}(-\omega_i)$,

$$\begin{aligned} a_s^{\text{out}}(\omega) &= A(\omega)\, a_s^{\text{in}}(\omega) + B(\omega)\, a_i^{\text{in}\dagger}(-\omega_i) \\ a_i^{\text{out}\dagger}(-\omega_i) &= C(\omega)\, a_s^{\text{in}}(\omega) + D(\omega)\, a_i^{\text{in}\dagger}(-\omega_i), \end{aligned} \tag{6.23}$$

with commutators $[a_j^{\text{in}}(\omega_1), a_k^{\text{in}\dagger}(\omega_2)] = [a_j^{\text{out}}(\omega_1), a_k^{\text{out}\dagger}(\omega_2)] = \frac{1}{2\pi}\delta_{jk}\delta(\omega_1 - \omega_2)$. For small gain the coefficients are given by

$$\begin{aligned} A(\omega) &= \frac{\gamma_s - \Gamma_s/2 + i(\omega - \Omega_q)}{\Gamma_s/2 - i(\omega - \Omega_q)} \\ B(\omega) &= \frac{-i\kappa\sqrt{\gamma_s\gamma_i}}{[\Gamma_s/2 - i(\omega - \Omega_q)][\Gamma_i/2 + i(\omega_i - \Omega_r)]} \\ C(\omega) &= \frac{i\kappa\sqrt{\gamma_s\gamma_i}}{[\Gamma_s/2 - i(\omega - \Omega_q)][\Gamma_i/2 + i(\omega_i - \Omega_r)]} \\ D(\omega) &= \frac{\gamma_i - \Gamma_i/2 - i(\omega_i - \Omega_r)}{\Gamma_i/2 + i(\omega_i - \Omega_r)} \end{aligned} \tag{6.24}$$

With (6.23) and (6.24), we obtain the spectral power density at the signal frequency

$$S(\omega) = \frac{1}{2\pi}|B(\omega)|^2 = \frac{8\gamma_s\gamma_i\kappa^2}{\pi[4(\omega-\Omega_q)^2+\Gamma_s^2][4(\omega_i-\Omega_r)^2+\Gamma_i^2]}, \tag{6.25}$$

with the biphoton linewidth $\Delta\omega = [(\sqrt{\Gamma_s^4+6\Gamma_s^2\Gamma_i^2+\Gamma_i^4}-\Gamma_s^2-\Gamma_i^2)/2]^{1/2}$, and the total paired count rate at exact phase matching,

$$R = \frac{1}{2\pi}\int_{-\infty}^{\infty}|B(\omega')|^2 d\omega' = \frac{4\gamma_s\gamma_i\kappa^2}{\Gamma_s\Gamma_i(\Gamma_s+\Gamma_i)}. \tag{6.26}$$

Compared to a non-resonant forward-wave SPDC of the same crystal length and pumping power (6.13), the generation rate of a lossless resonant backward-wave SPDC is thus increased by a factor of

$$\eta_r \approx \frac{8\mathscr{F}}{\pi r^{1/2}}\frac{|v_s-v_i|}{(v_s+v_i)}, \tag{6.27}$$

where $\mathscr{F}$ is the cavity finesse, r is the mirror reflectivity, and $v_{s,i}$ are the group velocities of the signal and idler photons. The spectral brightness is increased by a factor of $\eta_b = \eta_r\Delta\omega_G/\Delta\omega$ with $\Delta\omega_G$ being the gain linewidth of the parametric interaction.

If the generation rate of biphotons is small as compared to the inverse of the temporal length of the biphoton, the accidental two-photon events may be neglected and the time domain Glauber correlation function (namely the biphoton wavepacket) is given by [38]

$$\begin{aligned} G^{(2)}(\tau) &= \left|\frac{1}{2\pi}\int_{-\infty}^{\infty}A(\omega')C^*(\omega')e^{i\omega'\tau}\mathrm{d}\omega'\right|^2 + \left|\frac{1}{2\pi}\int_{-\infty}^{\infty}|B(\omega')|^2 d\omega'\right|^2 \\ &\approx \frac{4\Gamma_s\Gamma_i\kappa^2}{(\Gamma_s+\Gamma_i)^2}\times\begin{cases} e^{\Gamma_s\tau}, & \tau<0 \\ e^{-\Gamma_i\tau}, & \tau>0. \end{cases} \end{aligned} \tag{6.28}$$

where $\tau = t_i - t_s$ is the time delay between the arrival of the signal and idler photons. The biphoton correlation time is then $T_c = (\ln 2)(1/\Gamma_s + 1/\Gamma_i)$. The asymmetry of biphoton wavepacket in τ is due to the order of detection of the signal and idler photons.

6.3.3 Single-Mode Output

The narrow gain linewidth of the backward-wave parametric interaction is advantageous for generating single-mode biphotons in a monolithic doubly resonant

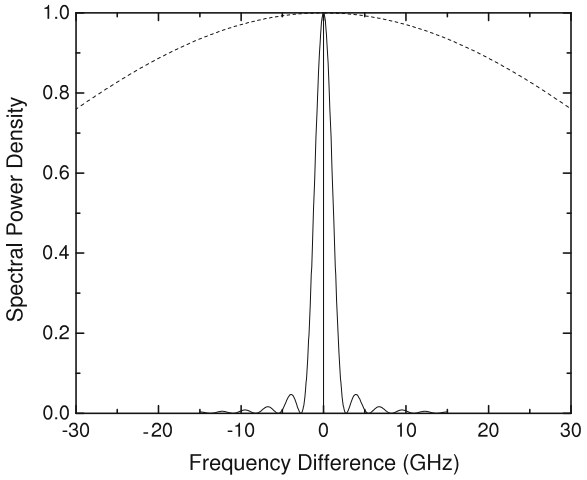

Fig. 6.5 Gain profile of backward-wave parametric interaction (*solid*) as compared to that of a forward-wave interaction (*dash*). The *vertical line* at 0 denotes a mode pair of the resonant cavity that is taken at the degenerate frequency. The next mode pair, separated by the cluster spacing is outside the gain linewidth of the backward-wave parametric interaction [22]

down-converter. Consider a 3 cm long PPKTP crystal placed inside a cavity of the same length. The cluster spacing $\Delta\Omega_{\rm Cl} \cong 2\pi \cdot 1.75\,{\rm cm}^{-1}$ and the gain linewidth of the parametric interaction $\Delta\omega_G \cong 2\pi \cdot 0.08\,{\rm cm}^{-1}$. Since $\Delta\Omega_{\rm Cl}$ is much broader than $\Delta\omega_G$, there will only be one doubly resonant mode within the gain linewidth when the cavity is properly tuned. This is shown in Fig. 6.5 where the gain curves of the forward-wave type (red) is also shown for comparison.

The properties of the single-mode biphotons can be calculated as for the case of forward-wave interaction. We assume a cavity finesse of 1000. The time-domain biphoton wavepacket is plotted in Fig. 6.6a, which is slightly asymmetric due to the different ring-down times at the signal and idler frequencies. The biphoton correlation time is 68 ns. The spectral power density of the biphotons is plotted in Fig. 6.6b and has a Lorentzian shape. The biphoton linewidth is $2\pi \cdot 2.1$ MHz. For exact phase matching, the spectral brightness of the generated biphotons is $8.16 \cdot 10^4\ {\rm s}^{-1}{\rm MHz}^{-1}$ per mW of pump power and, as compared to a non-resonant forward-wave source of the same material, pumping power, and length, is about 80,000 times higher.

6.3.4 Experimental Challenge

The backward-wave parametric interaction was proposed in the 1960s for implementing a mirrorless oscillator in the infrared regime [39]. The experimental demonstration, however, was not realized until 40 years later [32] because of the required quasi-phase matching with sub-micron periodicity [30, 31].

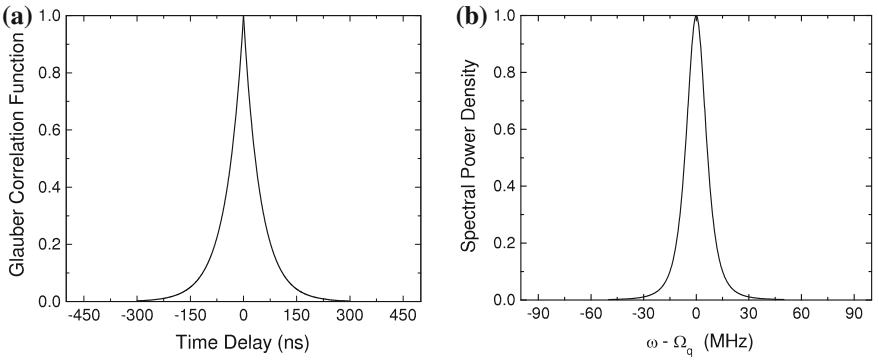

Fig. 6.6 **a** Time domain biphoton wavepacket of the backward-wave spontaneous down-conversion within a resonant cavity. **b** Spectral power density at the signal frequency [22]

To construct a backward-wave source as described above, a 532 nm laser may be used as the pump source to generate biphotons at the degenerate frequency of 1.064 μm. For type-II phase matching, a KTP crystal periodically poled with a periodicity of $\Lambda = 872$ nm is required to accomplish the third-order ($m = 3$) quasi phase matching so that $k_p = K_G + k_s - k_i$, where the lattice k-vector $K_G = 2\pi m/\Lambda$. Realization of such source thus needs a KTP crystal that is periodically poled with a sub-micron periodicity. Although challenging, it can be done with current structuring technique [32].

6.4 Spontaneous Four-Wave Mixing with Electromagnetically Induced Transparency

Here we describe narrowband biphoton generation via SFWM with EIT [40, 41] in cold atoms. The modeled four-level double-Λ atomic system and backward-wave configuration are shown in Fig. 6.7. $|1\rangle$ and $|2\rangle$ are two long-lived ground states (such as the two hyperfine ground states of alkali atoms) and between them there is no electric dipole transition. $|3\rangle$ and $|4\rangle$ are two excited states (in some scheme they can be the same state). A pump laser (ω_p) excites atoms at the transition $|1\rangle \rightarrow |4\rangle$ with a detuning Δ_p. A coupling laser (ω_c) dresses the states $|2\rangle$ and $|3\rangle$ resonantly. In the presence of continuous-wave counter-propagating pump and coupling lasers, phase-matched backward paired Stokes (ω_s) and anti-Stokes (ω_{as}) photons are spontaneously produced following the transitions $|4\rangle \rightarrow |2\rangle$ and $|3\rangle \rightarrow |1\rangle$, respectively. We assume the pump laser is far detuned from the transition $|1\rangle \rightarrow |4\rangle$ and its excitation is weak such that the majority of atomic population remains in the ground state $|1\rangle$. Under this ground-state approximation, we further assume that both the pump and coupling laser beams are undepleted in the atomic medium. As shown in Fig. 6.7a, the coupling laser and the weak generated anti-Stokes field form a

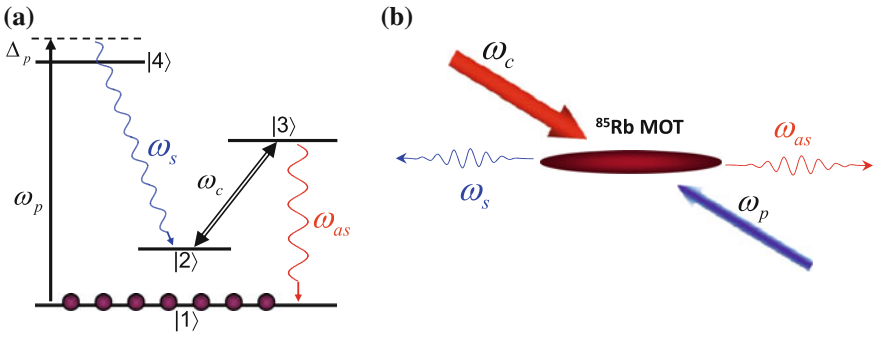

Fig. 6.7 Biphoton generation via SFWM in a four-level double-Λ atomic system. **a** The atomic energy level diagram. **b** The backward-wave biphoton generation geometry

standard three-level Λ EIT scheme. As a result, the coupling laser not only participates in the SFWM nonlinear process but also renders the medium transparent for the resonantly generated anti-Stokes photons. This EIT resonance dramatically enhances the SFWM nonlinear photon conversion efficiency. Moreover, in this system, the anti-Stokes photons propagate with a slow group velocity due to the EIT effect [42] while the Stokes photons travel nearly with the speed of light in vacuum. Below we show that this group velocity mismatching is the key to manipulating the phase-matching spectrum and thus the biphoton bandwidth. In the backward-wave configuration paired Stokes and anti-Stokes photons can propagate collinearly with the pump and coupling beams, and can also propagate in a right-angle geometry, depending on how well the relationship $\mathbf{k}_p + \mathbf{k}_c = 0$ is satisfied, where $\mathbf{k}_{p,c}$ are wave vectors of the pump and coupling fields.

The cold atoms (without Doppler broadening effect) are confined within a long, thin cylindrical volume of a length L and atomic density is N. The experiments reviewed in this chapter are mostly done with cold atoms in a two-dimensional (2D) magneto-optical trap (MOT) [43]. To adapt the theory in Sect. 6.3.1, we replace the field index 1 with *as* and 2 with *s*. The nonlinear parametric coupling coefficients (κ_{as} and κ_s) for the SFWM process are connected to the third-order nonlinear susceptibilities ($\chi_{as}^{(3)}$ and $\chi_s^{(3)}$):

$$\kappa_{as}(\omega) = i\frac{\omega_{as0}}{2c}\chi_{as}^{(3)}(\omega_{as0}+\omega)E_pE_c,$$
$$\kappa_s(\omega) = i\frac{\omega_{s0}}{2c}\chi_s^{(3)*}(\omega_{as0}-\omega)E_p^*E_c^*. \tag{6.29}$$

Here E_p and E_c are the electric field amplitude of the pump and coupling laser beams, respectively. Under the ground-state approximation, the third-order nonlinear susceptibility for the generated anti-Stokes and Stokes fields are

$$\chi_{as}^{(3)}(\omega_{as0}+\omega)=\frac{N\mu_{13}\mu_{32}\mu_{24}\mu_{41}/(\varepsilon_0\hbar^3)}{(\Delta_p+i\gamma_{14})[|\Omega_c|^2-4(\omega+i\gamma_{13})(\omega+i\gamma_{12})]}$$
$$=\frac{-N\mu_{13}\mu_{32}\mu_{24}\mu_{41}/(\varepsilon_0\hbar^3)}{4(\Delta_p+i\gamma_{14})(\omega-\Omega_e/2+i\gamma_e)(\omega+\Omega_e/2+i\gamma_e)}, \tag{6.30}$$

and

$$\chi_{s}^{(3)}(\omega_{as0}-\omega)=\frac{N\mu_{13}\mu_{32}\mu_{24}\mu_{41}/(\varepsilon_0\hbar^3)}{(\Delta_p+i\gamma_{14})[|\Omega_c|^2-4(\omega-i\gamma_{13})(\omega-i\gamma_{12})]}$$
$$=\frac{-N\mu_{13}\mu_{32}\mu_{24}\mu_{41}/(\varepsilon_0\hbar^3)}{4(\Delta_p+i\gamma_{14})(\omega-\Omega_e/2-i\gamma_e)(\omega+\Omega_e/2-i\gamma_e)}. \tag{6.31}$$

μ_{ij} are the electric dipole matrix elements, $\Omega_c=\mu_{23}E_c/\hbar$ is the coupling Rabin frequency, and γ_{ij} are dephasing rates, respectively. $\Delta_p=\omega_p-\omega_{41}$ is the pump detuning from the atomic transition $|1\rangle\rightarrow|4\rangle$. $\omega=\omega_{as}-\omega_{as0}$ is the detuning of the anti-Stokes photons from the transition $|1\rangle\rightarrow|3\rangle$, and we take $\omega_{as0}=\omega_{31}$ as the anti-Stokes central frequency. From (6.30) and (6.31), we have $\chi_{as}^{(3)}(\omega_{as0}+\omega)=\chi_{s}^{(3)}(\omega_{as0}+\omega)$. As the pump laser is far detuned ($\Delta_p\gg\gamma_{14}$), we further obtain $\chi_{as}^{(3)}(\omega_{as0}+\omega)\simeq\chi_{s}^{(3)*}(\omega_{as0}-\omega)$. $\Omega_e=\sqrt{|\Omega_c|^2-(\gamma_{13}-\gamma_{12})^2}$ is the effective coupling Rabi frequency. $\gamma_e=(\gamma_{12}+\gamma_{13})/2$ is the effective dephasing rate. The third-order nonlinear susceptibility has two resonances separated by Ω_e and each is associated with a linewidth of $2\gamma_e$. These two resonances here indicate two SFWM paths. In one path the frequency of the anti-Stokes photons is $\omega_{as0}+\Omega_e/2$ and the frequency of the correlated Stokes photons is $\omega_{42}+\Delta_p-\Omega_e/2$. In the other path the anti-Stokes photons have frequency at $\omega_{as0}-\Omega_e/2$ while the paired Stokes photons at $\omega_{42}+\Delta_p+\Omega_e/2$. Consequently, the interference between these two types of biphotons will appear in the two-photon temporal correlation, as shall be discussed in Sect. 6.4.1. The results obtained here agree with the dressed-state picture [44–46].

The linear susceptibilities at the anti-Stokes and Stokes frequencies are, respectively,

$$\chi_{as}(\omega_{as0}+\omega)=\frac{4N|\mu_{13}|^2(\omega+i\gamma_{12})/(\varepsilon_0\hbar)}{|\Omega_c|^2-4(\omega+i\gamma_{13})(\omega+i\gamma_{12})}, \tag{6.32}$$

$$\chi_{s}(\omega_{s0}-\omega)=\frac{N|\mu_{24}|^2(\omega-i\gamma_{13})/(\varepsilon_0\hbar)}{|\Omega_c|^2-4(\omega-i\gamma_{13})(\omega-i\gamma_{12})}\frac{|\Omega_p|^2}{\Delta_p^2+\gamma_{14}^2}, \tag{6.33}$$

where $\Omega_p=\mu_{14}E_p/\hbar$ is the pump Rabi frequency. The complex wave numbers of Stokes and anti-Stokes photons are obtained from the relations $k_s=(\omega_s/c)\sqrt{1+\chi_s}$ and $k_{as}=(\omega_{as}/c)\sqrt{1+\chi_{as}}$, where the imaginary parts indicate the Raman gain

and EIT loss, respectively. In an ideal EIT system with zero ground-state dephasing, i.e., with $\gamma_{12} = 0$, the linear susceptibility is $\chi_{as}(\omega_{as0}) = 0$, implying zero linear absorption of the anti-Stokes photons. This allows the nonlinear optics occurring on atomic resonance without absorption and hence enhances the efficiency of the nonlinear interaction.

Taking $|\Omega_p| \ll \Delta_p$, (6.32) and (6.33) give $k_{as} \simeq k_{as0} + \omega/V_g + i\alpha$ and $\chi_s \simeq 0$ so that the wave-number mismatching is approximately $\Delta k \simeq \omega/V_g + i\alpha$. Here k_{as0} is the central wave number of the anti-Stokes field, V_g is its group velocity, and α, the imaginary part of the anti-Stokes wave number, characterizes the EIT finite loss caused by the non-zero ground-state dephasing rate γ_{12}. Now (6.17) can be approximated as

$$\Phi(\omega) \simeq \mathrm{sinc}\Big(\frac{\omega L}{2V_g} + i\frac{\alpha L}{2}\Big)\exp\Big(i\frac{\omega L}{2V_g} - \frac{\alpha L}{2}\Big). \tag{6.34}$$

In (6.34), $\alpha = 2N\sigma_{13}\gamma_{12}\gamma_{13}/(|\Omega_c|^2 + 4\gamma_{12}\gamma_{13})$ where $\sigma_{13} = 2\pi|\mu_{13}|^2/(\varepsilon_0\hbar\lambda_{13}\gamma_{13})$ is the on-resonance absorption cross section of the transition $|1\rangle \rightarrow |3\rangle$. The longitudinal detuning function of (6.34) has a full-width-at-half-maximum (FWHM) phase-matched bandwidth determined by the sin function, $\Delta\omega_g = 2\pi \times 0.88/\tau_g$, where $\tau_g = L/V_g$ is the anti-Stokes group delay time. The group delay time can be estimated from $\tau_g = L/V_g \simeq (2\gamma_{13}/|\Omega_c|^2)OD$ with the optical depth defined as $OD = N\sigma_{13}L$.

Therefore, there are two important characteristic frequencies that determine the shape of the biphoton waveform. The first is the coupling effective Rabi frequency Ω_e , which determines the two-resonance spectrum of the nonlinear susceptibility. The second is phase-matching bandwidth $\Delta\omega_g$. In the time domain, they correspond to the Rabi time $\tau_r = 2\pi/\Omega_e$ and the group delay time τ_g. The competition between τ_r and τ_g will determine which effect plays a dominant role in governing the feature of the two-photon correlation. Therefore, in the following we will discuss the two-photon joint-detection measurement in two regimes, damped Rabi oscillation and group delay.

6.4.1 Damped Rabi Oscillation Regime

We first look at the regime where the nonlinear spectrum plays a dominant role and the optical properties of the two-photon amplitude (6.16) are mainly determined by the nonlinear coupling coefficient. This regime requires that the effective coupling Rabi frequency Ω_e be smaller than the phase-matching bandwidth $\Delta\omega_g$, i.e., $\Omega_e < \Delta\omega_g$, or equivalently, $\tau_r > \tau_g$, so that we can treat the longitudinal detuning function as $\Phi(\omega) \simeq 1$. The biphoton spectral generation rate is proportional to $|\kappa L|^2 \propto |\chi^{(3)}L|^2$. Hence both biphoton spectrum intensity and emission rate are proportional to OD^2. The two-photon temporal correlation function exhibits a damped Rabi oscillation

resulting from the interference between the two resonances of the nonlinear coupling coefficient.

We consider the case of $\Omega_c > |\gamma_{13} - \gamma_{12}|$ first, which implies a real effective coupling Rabi frequency Ω_e. Following (6.16), the two-photon wave amplitude now is determined by the Fourier transform of the nonlinear coupling coefficient (6.29) to give

$$\begin{aligned}\psi(\tau) &= BLe^{-\gamma_e\tau}e^{-i\varpi_{as}\tau}\sin\left(\frac{\Omega_e\tau}{2}\right)\Theta(\tau),\\ &= \frac{i}{2}BLe^{-\gamma_e\tau}e^{-i\varpi_{as}\tau}[e^{-i\Omega_e\tau} - e^{i\Omega_e\tau}]\theta(\tau).\end{aligned} \tag{6.35}$$

Here $B = -i\frac{N\mu_{13}\mu_{32}\mu_{24}\mu_{41}\sqrt{\varpi_{as}\varpi_s}}{4c\varepsilon_0\hbar^3\Omega_e(\Delta_p+i\gamma_{14})}$ and $\Theta(\tau)$ is the Heaviside step function, i.e., $\Theta(\tau) = 1$ for $\tau \geq 0$, and $\Theta(\tau) = 0$ for $\tau < 0$. The physics of (6.35) is understood as follows. Because the two-photon state is entangled, it cannot be factorized into a function of t_{as} times a function of t_s. $|\psi|^2$, depends only on the relative time delay τ, which implies that the pair is randomly generated at any time. The first term in the bracket on the RHS of (6.35) represents the two-photon amplitude of paired anti-Stokes at $\omega_{as0} + \Omega_e/2$ and Stokes at $\omega_{s0} - \Omega_e/2$; while the second term is the two-photon amplitude of paired anti-Stokes at $\omega_{as0} - \Omega_e/2$ and Stokes at $\omega_{s0} + \Omega_e/2$. Equivalently, this frequency entangled state can be written as $|\omega_{as0} + \Omega_e/2\rangle_{as}|\omega_{s0} - \Omega_e/2\rangle_s - |\omega_{as0} - \Omega_e/2\rangle_{as}|\omega_{s0} + \Omega_e/2\rangle_s$. To further see the interference, let us look at the two-photon Glauber correlation function,

$$G^{(2)}(\tau) = \frac{1}{2}|BL|^2e^{-2\gamma_e\tau}\big[1 - \cos(\Omega_e\tau)\big]\Theta(\tau), \tag{6.36}$$

which displays a damped Rabi oscillation with an oscillation period of $2\pi/\Omega_e$ and a damping rate of $2\gamma_e$. The heaviside function $\Theta(\tau)$ shows that the anti-Stokes photon is always generated after its paired Stokes photon by following the FWM path shown in Fig. 6.7a. The two-photon correlation function also shows the well-known anti-bunching effect [$G^{(2)}(0) \leq G^{(2)}(\tau)$]. Similarly to the polarization entangled Bell states, the visibility of the Rabi oscillation, resulting from the two-photon interference in time domain, can be taken as an evidence for the time-frequency entanglement.

Figure 6.8a shows the first experimental demonstration of this type of biphoton source by Balić et al. [33]. Figure 6.8a corresponds to the case of $\tau_e > \tau_r$ and the oscillations are clearly resolved. Figure 6.8b is the case of $\tau_e < \tau_r$ where only the first oscillation is observable and other disappear because of the fast dephasing rate γ_e.

Rabi oscillations have also been observed in three-level and two-level atomic systems [47–49].

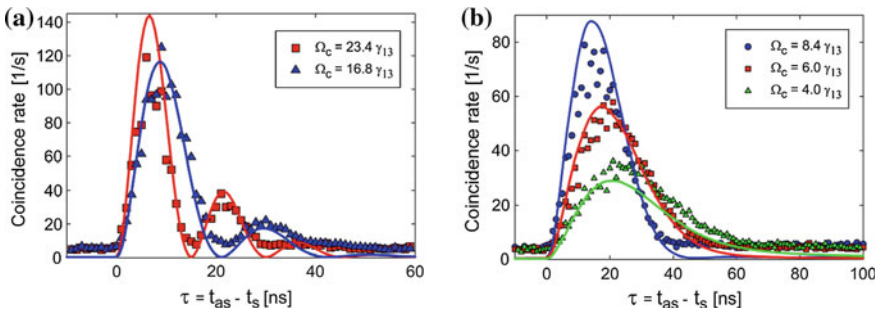

Fig. 6.8 **a** Two-photon correlation function in the damped Rabi oscillation regime. The missing of other oscillation periods in (**b**) is due to the short dephasing time of about 33 ns. The experimental parameters used here are $\gamma_{13} = \gamma_{14} = 2\pi \times 3\,\text{MHz}$, $\gamma_{12} = 0.6\gamma_{13}$, $OD = 11$, $\Delta_p = -7.5\gamma_{13}$, and $\Omega_p = 0.8\gamma_{13}$. Data are taken from [33]

6.4.2 Group Delay Regime

Suggested by Balic et al. [33] and demonstrated by Du et al. [24], the group delay regime is defined as $\tau_g > \tau_r$ and the EIT slow-light effect can be used to control the biphoton temporal coherence time. The group delay condition is equivalent to $\Omega_e > \Delta\omega_g \approx 2\pi/\tau_g$, i.e., the biphoton bandwidth is determined by phase matching. For this reason, in this subsection we treat the third-order nonlinear susceptibility as a constant over the phase-matching spectrum. As a consequence, the double resonances of biphoton generation are suppressed. The two-photon correlation tends to be rectangular shaped, more like that of the conventional SPDC photons. We obtain the biphoton wave function approximately as $\psi(\tau) \simeq \kappa_0 L\tilde{\Phi}(\tau)$, where κ_0 is the on-resonance nonlinear coupling constant and $\tilde{\Phi}(\tau) = 1/(2\pi)\int \Phi(\omega)e^{-i\omega\tau}d\omega$ is Fourier transform of the longitudinal detuning function. When the EIT bandwidth $[\Delta\omega_{tr} \simeq |\Omega_c|^2/(2\gamma_{13}\sqrt{OD})]$ is wider than the phase-matching bandwidth, the anti-Stokes loss is negligible and the two-photon wave function approaches a rectangular shape. However, when the EIT loss is significant, the biphoton waveform follows an exponential decay.

When $\Delta\omega_{tr} > \Delta\omega_g$, we ignore the EIT linear loss and rewrite (6.34) as

$$\Phi(\omega) \simeq \text{sinc}\left(\frac{\omega L}{2V_g}\right)\exp\left(i\frac{\omega L}{2V_g}\right). \tag{6.37}$$

We then obtain the biphoton wave function

$$\psi(\tau) \simeq \kappa_0 L\tilde{\Phi}(\tau) = \kappa_0 V_g \Pi(\tau; 0, L/V_g)e^{-i\varpi_{as}\tau}. \tag{6.38}$$

The rectangular function is defined as $\Pi(\tau; \tau_1, \tau_2) = \theta(\tau-\tau_1)-\theta(\tau-\tau_2)$. Equation (6.38) shows that the anti-Stokes photon is always delayed with respect to its paired Stokes photon because of the slow light effect. The two-photon correlation time is

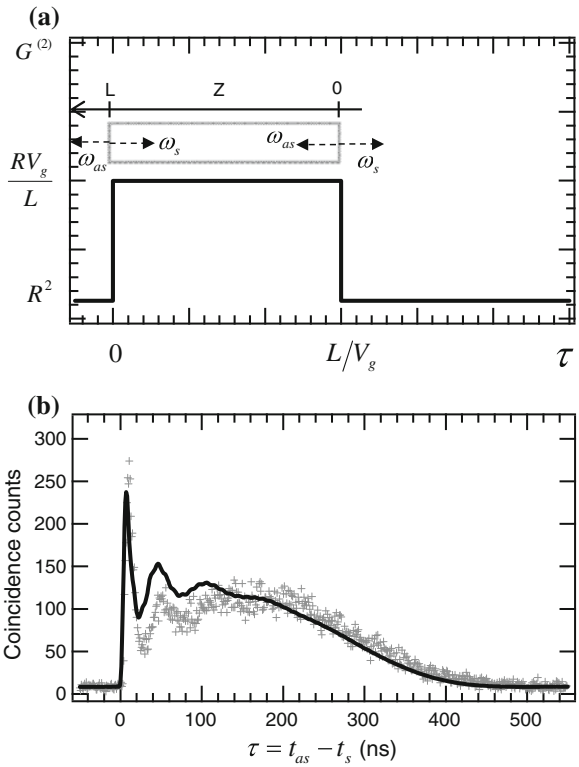

Fig. 6.9 Two-photon correlation function in the group delay regime. **a** Ideal *rectangular-shape* correlation with a relative group delay L/V_g and pair emission rate R. **b** Experimental data (*red*) and theoretical curve (*solid blue line*) obtained from the Heisenberg-Langevin theory. Data are taken from [24]

determined by the group delay $\tau_g = L/V_g$. Using (6.13) we get the photon pair generation rate

$$R = |\kappa_0|^2 V_g L. \tag{6.39}$$

Thus in the group delay regime the total rate of paired counts scales linearly as OD even though the spectral generation rate, $\kappa_0 L \Phi(\omega)$, scales as OD^2. This is because the bandwidth reduces linearly with optical depth [33]. As illustrated in Fig. 6.9a, the rectangular-shape waveform can be understood in the following picture. When the photon pair is produced from the front surface ($z = L$), the anti-Stokes photon has no delay and both photons arrive at detectors simultaneously. When emitted from the back surface ($z = 0$), the anti-Stokes photon is delayed relative to the Stokes photon by τ_g. Since the photon pair generation probability density is evenly distributed in the medium, a rectangular shape shows up in the biphoton temporal waveform. Figure 6.9a shows an ideal rectangular-shape correlation with a group delay of $\tau_g = L/V_g$. For conventional SPDC photons, the sub-ps rectangular-shaped biphoton waveform has only been indirectly confirmed in [50]. For the SFWM in cold atoms discussed here, we find that to observe the rectangular

shape, the condition $\Delta\omega_{tr} > \Delta\omega_g$ sets a lower bound for the optical depth. Using $\Delta\omega_{tr} \simeq |\Omega_c|^2/(2\gamma_{13}\sqrt{OD})$ and $\Delta\omega_g \simeq 2\pi/\tau_g \simeq \pi|\Omega_c|^2/(\gamma_{13}OD)$, we obtain $OD > 4\pi^2$. Or equivalently, it requires the EIT delay-bandwidth product greater than two [51].

In Fig. 6.9b the experimental demonstration of a near-rectangular-shape correlation is obtained at the optical depth around 53 [24]. The experimental parameters used here are $\gamma_{13} = \gamma_{14} = 2\pi \times 3$ MHz, $\gamma_{12} = 0.02\gamma_{13}$, $OD = 53$, $\Delta_p = 48.67\gamma_{13}$, $\Omega_p = 1.16\gamma_{13}$, and $\Omega_c = 4.20\gamma_{13}$, respectively. The EIT transparency width is estimated around 3.63 MHz and the phase-matching spectral width about 2.93 MHz. It is found that the exponential-decay behavior at the tail is due to the finite EIT loss, which alters the correlation function away from the ideal rectangular shape.

The sharp peak shown in the leading edge of the two-photon coincidence counts in Fig. 6.9b is the first observed Sommerfeld-Brillouin precursor at the biphoton level [52]. In the stationary-phase approximation, starting from (6.16) one can show that the sharp peak results from the beating of biphotons which are generated outside of the EIT opacity window. The detailed analysis of the precursor generation at the two-photon level has been presented in [52].

Following (6.38), one expects the length L/V_g of the rectangular function increases if one reduces the anti-Stokes group velocity V_g by reducing the coupling laser power. However, (6.38) is valid only when the EIT is preserved. When the EIT loss becomes significant, the biphoton has an exponential decay waveform [26]. Therefore at a certain OD, there is a limitation to prolonging the coherence time while maintaining the rectangular-like shape. Most recently, by pushing the OD to 130, the two-photon coherence time was extended to nearly 2 μs, as shown in Fig. 6.10, which corresponds to a FWHM bandwidth of 0.43 MHz [25].

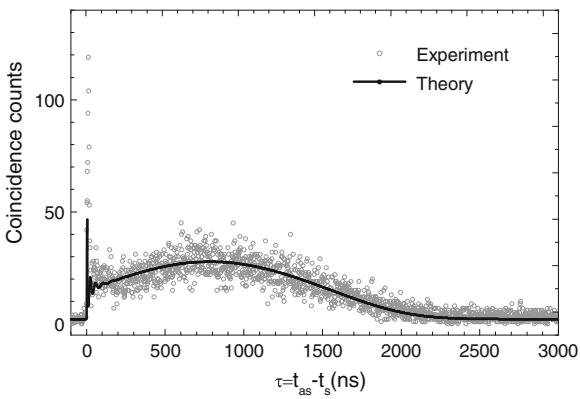

Fig. 6.10 Biphotons with coherence time up to about 2 μs. Operating parameters are: OD = 130, $\Omega_c = 2\pi \times 7.77$ MHz and $\Omega_p = 2\pi \times 1.14$ MHz. Data are taken from [25]

6.5 Manipulation of Narrowband Single Photons

The long coherence time of these narrow-band biphotons allows us to not only directly resolve their temporal waveform with existing commercial single photon detectors (with a typical resolution of 1 ns) but also manipulate their quantum waveform with external phase-amplitude modulators [53, 54]. In addition, compared with SPDC using a single pump laser, there are more freedoms to manipulate the biphoton generation in SFWM with two driving lasers. We will show in this section how to engineer the biphoton quantum states by controlling the temporal [55, 56] and spatial patterns [25, 35] as well as the polarizations [48, 57] of the classical driving fields.

(1) **Electro-Optical Modulation of Heralded Single Photons**

It is well know that time-frequency entangled photon pairs can be used to efficiently produce heralded single photons with well defined relative time origin. Here we describe how single photons may be modulated so as to produce single-photon waveforms whose amplitude and phase are functions of time. As shown in Fig. 6.11, The detection of a Stokes photon at D_1 triggers the function generator that drives the electro-optic modulator (EOM) to shape the waveform of the anti-Stokes photon. In this way the heralded anti-Stokes photon temporal wave function (phase and amplitude) may be shaped in the same manner as one modulates a classical light pulse.

When a Stokes photon is detected at D_s ($z_s = 0$), the heralded single anti-Stokes photon wave packet shaped by the EOAM can be described as

$$\begin{aligned}\Psi(z,\tau) &= \langle 0|m(\tau)\hat{a}_{as}(z,\tau)\hat{a}_s(0,0)|\Psi_{s,as}\rangle \\ &= m(\tau - z/c)\psi(\tau - z/c)e^{i(k_{as0}z-\omega_{as0}\tau)}.\end{aligned} \tag{6.40}$$

where $|\Psi_{s,as}\rangle$ is the two-photon time-frequency entangled state [26], and $m(\tau)$ is the modulation. It is clear that the heralded single-photon waveform is directly modulated by the EOM. Therefore, within the coherence time, the single-photon waveform can

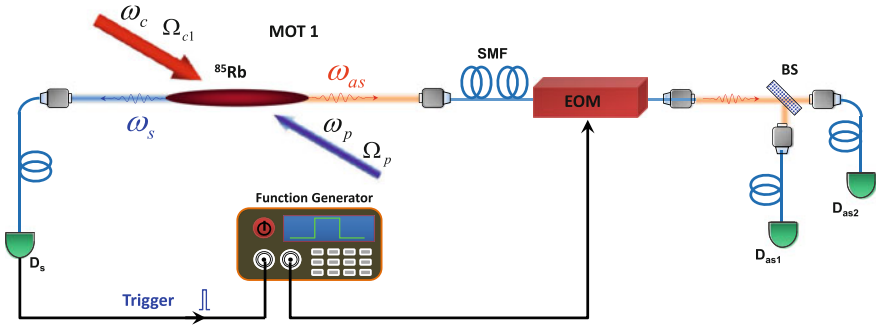

Fig. 6.11 Schematic of heralded single photon generation and conditional modulation with an EOM

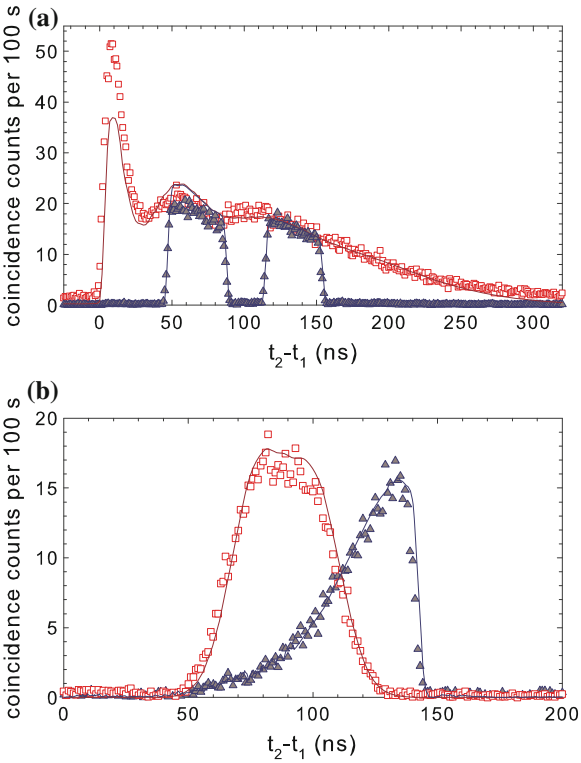

Fig. 6.12 Waveforms of heralded anti-Stokes photons. **a** Modulated and unmodulated waveforms. **b** Waveforms with Gaussian and rising exponential shapes. Data are taken from [53]

be arbitrarily shaped. As shown in Fig. 6.12, The heralded single photons can be modulated into two rectangular pulses, Gaussian or time reversed exponential [53].

The importance of the electro-optic method is its speed and ability to modulate phase as well as amplitude. The technique provides the technology for studying the response of atoms to shaped single photon waveforms on a time-scale comparable to the natural linewidth.

(2) **Quantum Fourier Cosine Transform: Modulation and Measurement of Biphoton Waveform**

As described previously, the Stokes-anti-Stokes two-photon temporal waveform is directly measured as coincidence counts between two single photon detectors. However, if the speed of the detectors is slow as compared to the two-photon correlation time, the biphoton temporal waveform can not resolved by the resolution of the detectors. That is the reason why the wide-band SPDC biphoton waveform can not be directly measured by the existing commercial single photon detectors. Here we describe an approach to the problem of measurement of biphoton waveforms using slow detectors. Figure 6.13 shows the essential idea. The Stokes and anti-Stokes photons are incident on synchronously driven sinusoidal amplitude modulators (MOD1 and MOD2). The coincidence count rate between single-photon counting modules

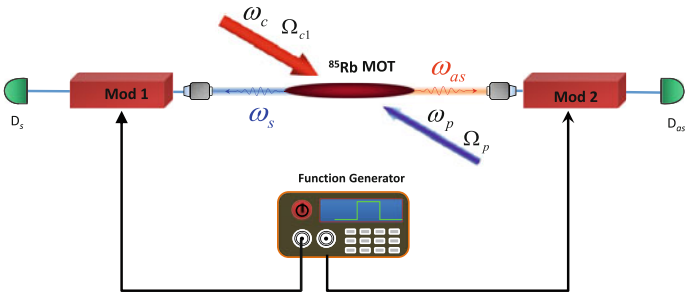

Fig. 6.13 Modulation and measurement of time-energy entangled photons synchronously driven sinusoidal modulators and slow detectors

(SPCMs) is measured as a function of the sinusoidal modulation frequency. The SPCMs are slow as compared to the pulse width of the biphoton waveform. With τ equal to the relative arrival time of the Stokes and anti-Stokes photons, the inverse Fourier transform of the (frequency domain) measurement of coincidence counts versus frequency yields the Glauber correlation function $G^{(2)}(\tau)$ and therefore the square of the absolute value of the biphoton wave function [54].

The modulated correlation function can be written as

$$G_M^{(2)}(t, t+\tau) = |m_1(t)|^2 |m_2(t+\tau)|^2 G_0^{(2)}(\tau), \tag{6.41}$$

where m_1 and m_2 are the two amplitude modulation functions. $G_0^{(2)}(\tau)$ is the unmodulated Glauber correlation function. We average $G_M^{(2)}(t, t+\tau)$ over a period T of the modulating frequency to form the time averaged correlation function

$$\overline{G_M^{(2)}(\tau)} = \frac{1}{T}\int_0^T G_M^{(2)}(t, t_\tau)dt. \tag{6.42}$$

Combining (6.41) and (6.42), we obtain

$$\begin{aligned} \overline{G_M^{(2)}(\tau)} &= M(\tau) G_0^{(2)}(\tau), \\ M(\tau) &= \frac{1}{T}\int_0^T |m_1(t)|^2 |m_2(t+\tau)|^2 dt \end{aligned} \tag{6.43}$$

where $M(\tau)$ is the intensity correlation function of the modulators. Here we assume both channels are modulated by the same sinusoidal amplitude modulation $m_1(t) = m_2(t) = \cos(\omega t + \varphi)$. Then we have $M(\tau) = 1/4 + 1/8\cos(2\omega\tau)$, and the integrated coincidence count becomes

$$\int_0^\infty \overline{G_M^{(2)}(\tau)} d\tau = \frac{1}{8}\int_0^\infty [2 + \cos(2\omega\tau)] G^{(0)}(\tau) d\tau. \tag{6.44}$$

We neglect the dc term and normalize to obtain the Fourier cosine transform pair

$$F(2\omega) = \sqrt{\frac{2}{\pi}} \int_0^\infty G^{(0)}(\tau) \cos(2\omega\tau) d\tau,$$
$$G^{(0)}(\tau) = \sqrt{\frac{2}{\pi}} \int_0^\infty F(2\omega) \cos(2\omega\tau) d\omega. \tag{6.45}$$

Therefore the two-photon correlation function can be obtained by an inverse Fourier cosine transform from integrated coincidence counts (by slow detectors).

The proof of principle of the above Fourier technique in measuring biphoton waveform was demonstrated with narrow-band biphotons and the slow detectors are simulated with integration [54]. The result agrees well with the directly measured waveforms. For practical applications, this technique can be extended to short biphotons.

(3) **Shaping Biphoton Temporal Waveforms with Temporally Modulated Classical Fields**

By passing long single photons through electro-optical modulators (EOM), it is possible to modulate one of the paired photons or their correlation function. However, these external modulators always introduce losses and attenuations. As shown in Fig. 6.7, due to the two-photon resonance condition in the SFWM process in the double-Λ atomic system, the central frequency of the Stokes photon follows the pump laser, while the central frequency of the anti-Stokes photon follows the coupling laser (in the group delay regime). As a result, if we add a modulation to the pump (coupling) laser, the modulation will affect the generated Stokes (anti-Stokes) photon. As compared to the SPDC source with a single pump laser, the SFWM scheme with two driving lasers allows more freedoms to manipulate the biphoton state by controlling the two classical driving lasers.

When the pump and coupling lasers are periodically modulated, As shown in Fig. 6.14b, the driving laser fields are decomposed in frequency domain into

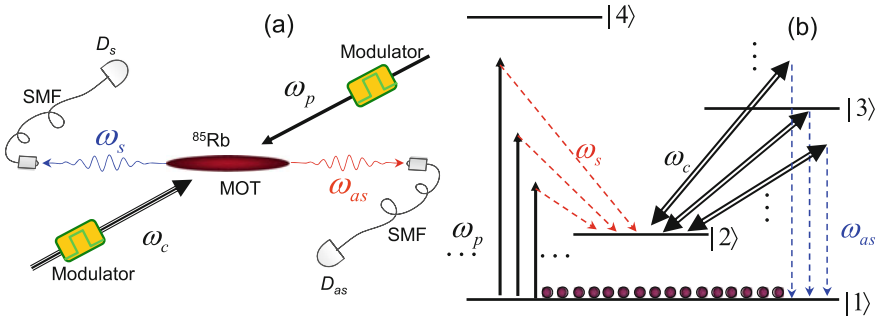

Fig. 6.14 Schematic of biphoton generation with modulated driving-laser fields. **a** Experimental configuration. **b** Atomic energy level diagram for multichannel biphoton generation

discrete frequency components. As a result, biphoton generation follows many possible SFWM paths. The interference between these multichannel FWMs provides a controllable way to manipulate and engineer the biphoton wave packets. Under the condition that the atomic optical depth in the transition $|1\rangle \rightarrow |3\rangle$ is high, the EIT slow light effect is significant, and there is no spectral overlap between these SFWM channels, following the theory by Du et al. [55], the biphoton wave amplitude can be obtained analytically

$$\Psi(t_s, t_{as}) = \frac{c\varepsilon_0}{2\sqrt{\bar{I}_p \bar{I}_c}} E_p(t_s) E_c(t_{as}) \psi_0(t_{as} - t_s) \times e^{-i\omega_{s0} t_s} e^{-i\omega_{as0} t_{as}}, \tag{6.46}$$

where $E_p(t_s)$ and $E_c(t_{as})$ are the complex envelopes of the pump and coupling laser fields. $\bar{I}_p$ and $\bar{I}_c$ are the pump and coupling laser average intensities. $\psi_0(t_{as} - t_s)e^{-i\omega_{s0}t_s}e^{-i\omega_{as0}t_{aS}}$ is the original two-photon wave packet without modulation on the driving fields. As shown in (6.46), the two-photon time-frequency entanglement information is preserved while the pump and coupling field profiles are mapped into the biphoton waveform. The Stokes and anti-Stokes temporal correlation function is

$$G^{(2)}(t_s, t_{as}) \equiv |\Psi(t_s, t_{as})|^2 = \frac{I_p(t_s) I_c(t_{as})}{\bar{I}_p \bar{I}_c} G_0^{(2)}(t_{as} - t_s), \tag{6.47}$$

where $I_p(t_s)$ and $I_c(t_{as})$ are the pump and coupling laser intensity temporal profiles. $G_0^{(2)}(\tau) = |\psi_0(\tau)|^2$ is the correlation function without modulation. Therefore the time-averaged correlation becomes

$$\overline{R}(\tau) = \mathrm{C}(\tau) R_0(\tau), \tag{6.48}$$

where $\mathrm{C}(\tau) \equiv \lim_{\Delta T \rightarrow \infty} \frac{1}{\Delta T \bar{I}_p \bar{I}_c} \int_0^{\Delta T} I_p(t) I_c(t + \tau) dt$ is the time-averaged pump-coupling correlation function. Equations (6.46)–(6.48) show that it is possible to manipulate the biphoton temporal wave packet and its correlation functions in a controllable way. The proof of principle has been experimentally demonstrated in [56].

(4) **Shaping Biphoton Temporal Waveforms with Spatially Modulated Classical Fields**

Following Rubin's group delay picture [12], in the ideal group delay regime, the rectangular waveform reflects the uniform spatial distribution of the photon pair generation probability. This is indeed ensured in our previous theoretical model where the atomic density, pump and coupling laser fields are assumed to be uniform. It is noticed that the biphoton generation probability is proportional to the pump field intensity. Therefore, if the pump field is spatially modulated along the longitudinal direction of the biphoton generation, this spatial modulation will affect the biphoton temporal waveform. This effect was first reported in a recent experiment for

achieving the two-photon coherence time up to about 2 μs [25]. In this experiment, the transverse Gaussian amplitude profile of the pump laser beam is projected to the biphoton longitudinal direction and revealed in the two-photon correlation function. This effect becomes only apparent at a high OD of more than 100—at OD < 60, the theory in Sect. 6.3.1 still holds and the pump field can be treated as a plane wave even though in reality it is in a gaussian mode.

In [25], the pump-coupling laser beams are aligned with am angle of 2.8^o to the biphoton longitudinal z-axis and the pump beam transverse Gaussian profile is projected to the z-axis. Taking into account the pump field profile effect, we modify (6.11) to have

$$\psi(\tau) = \frac{1}{2\pi}\int d\omega\kappa(\omega)\mathrm{F}(\Delta k)e^{i(k_{as}+k_s)L/2}e^{-i\omega\tau}, \tag{6.49}$$

where the longitudinal detuning function is replaced by $\mathrm{F}(\Delta k)e^{i(k_{as}+k_s)L/2}$. $\mathrm{F}(\Delta k)$ is the Fourier transform of the pump field profile $f(z) = 1/(2\pi)\int dkF(k)e^{ikz}$ along the z-axis. In the group delay regime, the spatial phase propagation in (6.49) can approximated as

$$(k_{as} + k_s)L/2 \simeq \phi_0 + \omega\tau_g/2, \tag{6.50}$$

where ϕ_0 is a constant phase factor. The two-photon spectrum is mainly determined by the phase-matching longitudinal function $\mathrm{F}[\Delta k(\omega)]$, and $\kappa(\omega) \simeq \kappa_0$ varies slowly in frequency. The we can reduce (6.49) to

$$\psi(\tau) \simeq \kappa_0 V_g f(L/2 - V_g\tau)e^{i\phi_0}. \tag{6.51}$$

It is clear that the pump field spatial variation is mapped into the two-photon quantum temporal waveform with its origin delayed by $L/(2V_g) = \tau_g/2$. The two-photon temporal correlation time is determined by the group delay τ_g of the slow anti-Stokes photon.

Figure 6.15 shows the experimental results at OD $= 130$ [25]. There are two main features of the two-photon correlation function. The fast oscillating spike at the leading edge is the biphoton optical precursor which travels at the speed of light in vacuum [52]. The later, slowly varying long waveform is generated from the narrow EIT window. The Gaussian shape reveals the pump laser intensity profile as we expected from (6.51).

The detailed discussion of the effects of the nonuniformity of the driving fields on the biphoton waveform and biphoton engineering with spatially modulated driving lasers can be found in [35].

(5) **Polarization Entanglement**

The SFWM scheme provides a natural entanglement mechanism in the time-frequency domain, but it is extremely difficult to produce polarization entanglement because of the polarization selectivity of EIT in a non-polarized atomic medium [58].

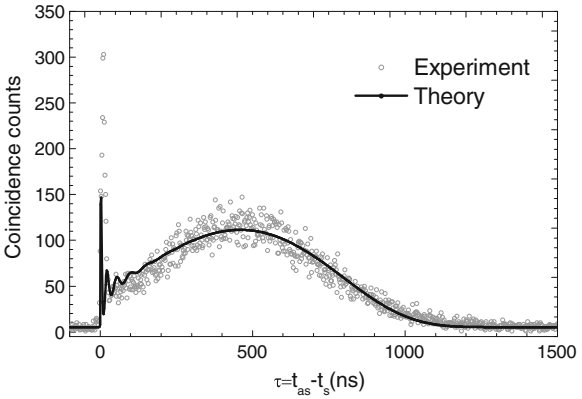

Fig. 6.15 Biphoton temporal waveform reveals the Spatial Gaussian profile of the pump laser beam. Operating parameters are: OD = 130, $\Omega_c = 2\pi \times 11.34\,\text{MHz}$ and $\Omega_p = 2\pi \times 1.14\,\text{MHz}$. Data are taken from [25]

The "writing-reading" technique with optical pumping provides a solution to polarization entanglement but results in reducing time-frequency entanglement [59].

Figure 6.16 shows a schematics for polarization entanglement generation in a right angle geometry [48]. A single pump laser is retro-reflected and serve both pump and coupling laser beams in the SFWM process. The perfect phase matching condition allows spontaneously generated paired photons to be emitted at right angle. To produce entanglement in polarization, we make use of the degenerate Zeeman sub states of each hyperfine energy level. By choosing the 2D MOT longitudinal symmetry axis as the quantization axis (z-axis), Zeeman states with $\Delta M_F = 0$ are coupled by the linearly-polarized pump beams. Conservation of angular moment along the z-axis allows two possible circular polarization configurations as shown in Fig. 6.16a: $|\sigma_s^+\sigma_{as}^-\rangle$ and $|\sigma_s^-\sigma_{as}^+\rangle$. From the symmetry of our system, the quantum state of the paired Stokes and anti-Stokes photons at the two detectors are described by

$$|\Psi_{s,as}(t_s, t_{as})\rangle = \psi(\tau)e^{-i\omega_{s0}t_s}e^{-i\omega_{as0}t_{as}} \times \frac{1}{\sqrt{2}}(|\sigma_s^+\sigma_{as}^-\rangle + |\sigma_s^-\sigma_{as}^+\rangle). \quad (6.52)$$

However, in this right angle configuration, because of some forbidden transition between the Zeeman sub states which can not be coupled by the coupling laser, the anti-Stokes photons do not see a complete EIT. As a result, the system can only work at a low OD in the Rabi oscillation regime [48].

Figure 6.17 shows a more robust scheme for generating polarization entanglement for narrowband biphotons in the group delay regime [57]. The pump laser beam is equally split into two beams after the first polarization beam splitter (PBS1). These two beams, with opposite circular polarizations (σ^+ and σ^-) after two quarter-wave plates, then intersect at the MOT with an angle of $\pm 2.5°$ to the longitudinal axis.

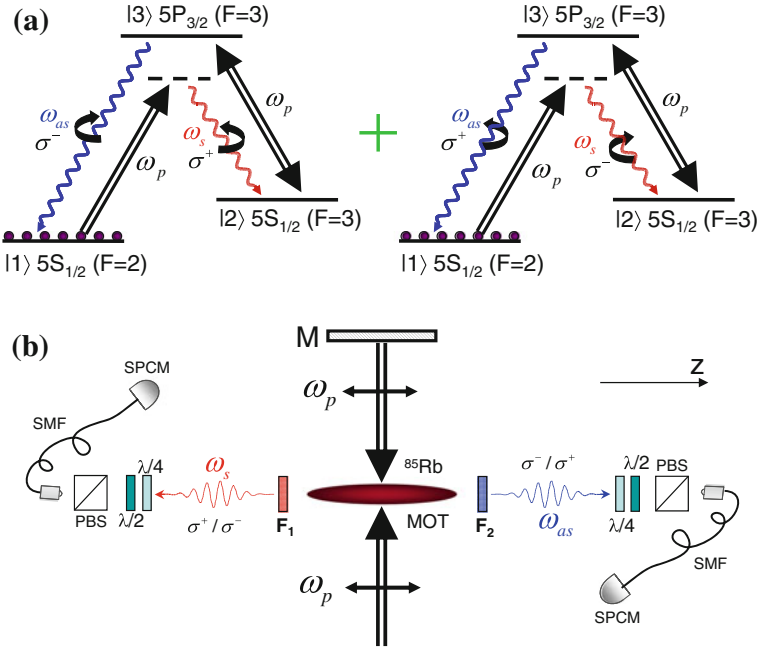

Fig. 6.16 Polarization entanglement generation in a right-angle SFWM configuration. **a** ^{85}Rb energy level diagram with two possible polarization configurations for the spontaneously emitted photon pairs. **b** Experimental setup with a right-angle geometry. Two sets of quarter-wave plates, half-wave plates, and PBSs are inserted for measuring polarization correlation and quantum state tomography. The figure is taken from [48]

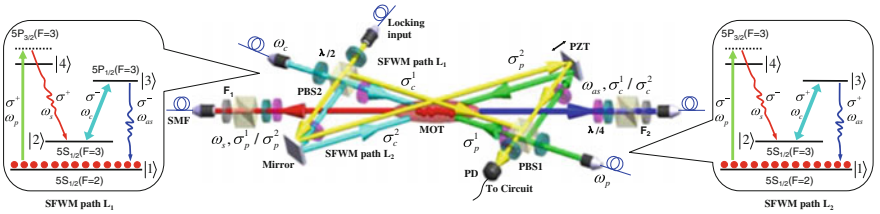

Fig. 6.17 Experimental setup for producing subnatural-linewidth polarization-entangled photon pairs. The polarization entanglement is created by the quantum interference of the two spatially symmetric SFWM processes driven by two counter-propagating pump-coupling beams (L_1 and L_2). The inserted energy level diagrams are two possible SFWM channels for L_1 and L_2, respectively. The figure is taken from [57]

Similarly, the two coupling laser beams after PBS2 with opposite circular polarizations overlap with the two pump beams from opposite directions. In presence of these two pairs of counter-propagating pump-coupling beams, phase-matched Stokes and anti-Stokes paired photons are produced along the longitudinal axis. In each SFWM

path, the polarizations of the Stokes and anti-Stokes photons match those of the corresponding pump and coupling fields.

To obtain the polarization entanglement, we must stabilize the phase difference between the two SFWM spatial paths. This is achieved by injecting a reference laser beam from the second input of PBS2. The two reference beams split after PBS2 are then recombined after PBS1 and detected by a photo detector (PD, a half wave plate and a PBS are used to obtain the interference), as shown in Fig. 6.17. This is a standard Mach-Zehnder interferometer to the reference laser. Locking the phase difference of the two arms of the Mach-Zehnder interferometer with a feedback electronics stabilizes the phase of the two SFWM paths. To avoid its interaction with the cold atoms, the reference beams are slightly displaced relative to the pump-coupling beams but pass through the same optical components.

By properly choosing the driving laser polarizations and the phase between the two SFWM paths, all four polarization-entangled Bell states can be realized for subnatural-linewidth biphotons [57].

6.6 Applications

In the past, experimental manipulation of a single photon interacting with atoms have been mostly focused in the frequency domain. Now with the narrowband biphoton generation technique described in this chapter, it is possible to control the quantum interaction between a single photon and atoms in time domain. In this section, we review the applications of heralded single photons whose waveforms are shaped by an EOM. A general schematics is illustrated in Fig. 6.18. We work with two-MOT setup. Narrowband Stokes and anti-Stokes biphotons are spontaneously produced from cold atoms in the first MOT (MOT1). After detection of a Stokes photon, its heralded anti-Stokes photon, after shaping by an EOM, is directed to the cold atoms

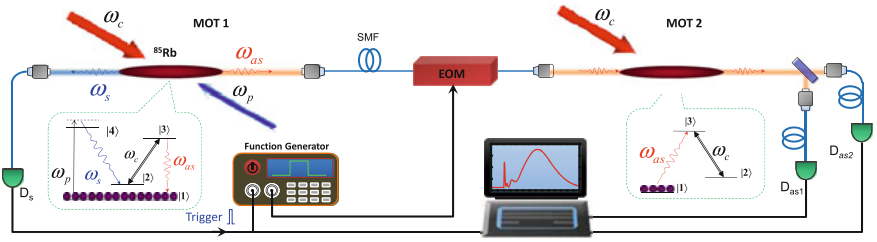

Fig. 6.18 Schematics of experimental setup for studying photon-atom quantum interaction. Narrow-band paired Stokes and anti-Stokes photons are produced from a cold atomic ensemble in MOT1. The anti-Stokes photons pass through an EOM driven by a function generator triggered by the detection of Stokes photons at D_s. We then send the heralded anti-Stokes photons with amplitude modulation to the second cold ^{85}Rb atomic ensemble at MOT2. The figure is taken from [77]

in the second MOT (MOT2). The atoms in MOT2 can be either a three-level EIT system with a coupling laser or a two-level system without the coupling laser. In the following we show three examples on how the photon-atom interaction in MOT2 can be precisely controlled by manipulating the temporal waveform of the heralded single photons.

(1) **Optical Precursor of a Single Photon**

Now it has been well accepted that both phase velocity and group velocity of light in a dispersive medium can exceed c, the speed of light in vacuum [60, 61]. Then, what is the information velocity of light? Could it be faster than c and violate Einstein's causality in the special relativity? Answering this question motivated early study of optical precursors by Sommerfeld and Brillouin in 1914 [62–64]. They showed theoretically that the front of a step-modulated optical pulse (as a carrier of 1 bit information) propagating in a dispersive medium always travels at c. This front, in the form of a transient wave now known as the Sommerfeld-Brillouin precursor, is then followed by the main pulse traveling at its group velocity. Study of optical precursors is of great interests not only for fundamental reasons since it is related to Einstein's causality, but also for applications because of its connection to the maximum speed of optical information transmission [65–72]. Now it is clear that the precursor is the fastest part in the propagation of an optical pulse even in a superluminal medium [68, 69, 71]. Classical precursors are entirely based on macroscopic electromagnetic wave propagation.

A single photon is described by quantum mechanics. What is the speed of a single photon in a dispersive medium? In quantum mechanics, an observable physical quantity, such as the speed, usually takes many possible (discrete or continuous) eigenvalues. Some may argue that a single photon event may possibly violate Einstein's causality while the expectation value of its speed never exceeds c. Although The propagation effect of single photons through slow and fast light media has been studied previously [73–76], all of these experiments focused on the group velocity picture. It remains a question whether there is a speed limit for a single photon in the quantum nonclassical world. The detection of single-photon precursor may shine light to this question as well as the understanding of quantum information transmission.

Optical precursor of a single photon was first observed making use of narrowband heralded single photon with a step-shaped waveform [77], with the experimental setup shown in Fig. 6.18. The modulated heralded anti-Stokes photon waveform is shown in Fig. 6.19a. After the anti-Stokes photon has passed through the EIT medium in MOT2 (OD=20), the precursor is clearly seen at the rising edge and separated from the delayed main waveform, shown in Fig. 6.19b. To test single-photon causal propagation in a superluminal medium, we turn off the coupling laser in MOT2 to work in a two-level system, which has a negative group delay, as shown in Fig. 6.19d. we observe a peak advance of at least 40 ns and with about 10 % transmission compared to the propagation through vacuum. However, as shown in Fig. 6.19c, there is no observable advancement relative to the rising edge in the single photon waveform. That is, using the quantum mechanics interpretation, there is no

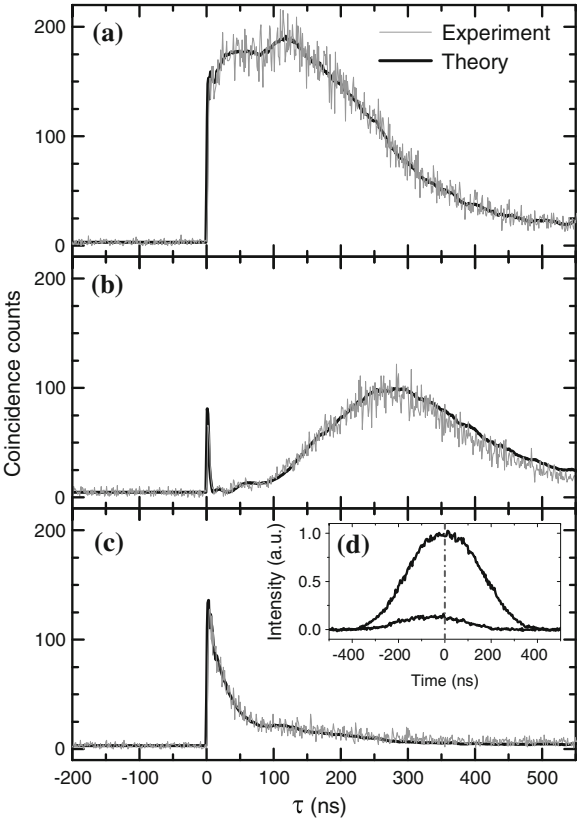

Fig. 6.19 Single-photon optical precursors from a step amplitude modulation. **a** The heralded anti-Stokes photon waveform with a step modulation. **b** and **c** are two-photon coincidences after the anti-Stokes photons passing through the EIT system ($\Omega_{c2} = 3.5\gamma_{13}$, OD = 20) and two-level system ($\Omega_{c2} = 0$, OD = 2.5) in MOT2 respectively. Inset (**d**) shows a gaussian pulse propagation in the two-level system with a peak advancement of about 40 ns (the *lower curve*) compared to the reference pulse (the *upper curve*). Data are taken from [77]

observable probability for single photon traveling faster than c. This result indicates that the optical precursor is always the fastest part even in superluminal propagation and Einstein's causality holds.

The observation of optical precursor of heralded single photons [77] confirms the speed limit of a single photon in a dispersive medium, which is indeed the speed of light in vacuum. The information velocity of a single photon does not follow its group velocity. It also suggests that the causality holds for a single photon.

(2) **Optimal Storage and Retrieval of Single-Photon Waveform**

The second application example of narrowband heralded single photons with arbitrary waveform shaping is for optical quantum memory. The efficiency of a photon-atom quantum interface strongly depends on the temporal shape of single photons [78]. Although storage of of weak coherent pulses have been demonstrated with high efficiencies up to 87 % [79, 80], obtaining such high efficiency with single photons remains a technical challenge due to the difficulty in having narrowband single photons with optimal temporal waveform at the operation frequency [81–83].

Making use of heralded narrowband single photons with an optimal waveform shaped by EOM, Du *et al* reported an experimental demonstration of efficient storage

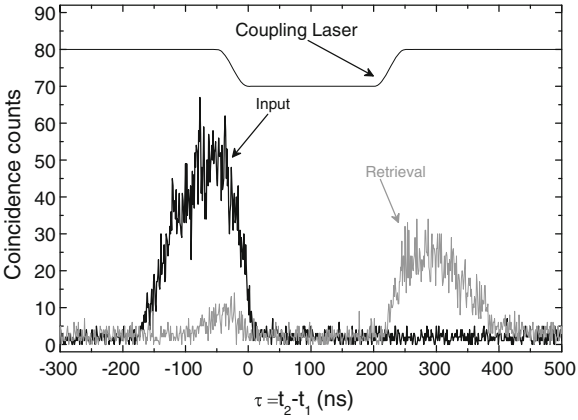

Fig. 6.20 Optimal storage and retrieval of single photons with a storage efficiency of $(49 \pm 3)\%$. **a** The optimal input (*red curve*) and output (retrieval, *green curve*) heralded single-photon waveforms. **b** The time-reversed retrieved photon waveform matches the input photon waveform after normalization. Data are taken from [84]

and retrieval of narrow-band single-photon waveforms using EIT in a cold atomic ensemble [84]. With the ability to control both single-photon wave packets and the memory bandwidth, the storage efficiency is obtained up to $(49 \pm 3)\%$. The experimental result is shown in Fig. 6.20. To our knowledge, it represents the highest storage efficiency for a single-photon waveform to date. Because an efficiency above 50 % is necessary to operate a memory for error correction protocols in one-way quantum computation [85], this result brings the atomic quantum light-matter interface closer to practical quantum information applications.

(3) **Coherent Control of Single-Photon Absorption and Reemission in a Two-Level Atomic Ensemble**

When an optical pulse propagates through a dispersive medium, the absorption and emission can coherently modify its spectral-temporal components and lead to many fundamental and important optical phenomena, such as attenuation, amplification, distortion, slow and fast light effects [40, 42, 86–88]. For a single photon in the absorptive medium, the remission can only occur after the absorption, as required by the causality. Although this quantum time order has been observed as the antibunching effect in resonance fluorescence [49, 89], the processes in these experiments are chaotic. After a single photon enters a two-level atomic medium and gets absorbed, the spontaneously remitted photon usually goes to 4π solid angle randomly.

It turns out a directed "spontaneous" emission excited by a single photon is possible if the timing of absorption is traceable [90]. Moreover, this direct "spontaneous" emission can be manipulated in time domain by controlling the single-photon temporal waveform [91]. For example, making use of the destructive interference between the emission (or scattering) and the incident photon wave packet, the probability of remitting the photon during the absorption can be completely suppressed when the incident photon has an exponential growth waveform with a time constant equal to the excite-state lifetime. The remission process only starts after the incident photon waveform is switched off and thus can be controlled on demand.

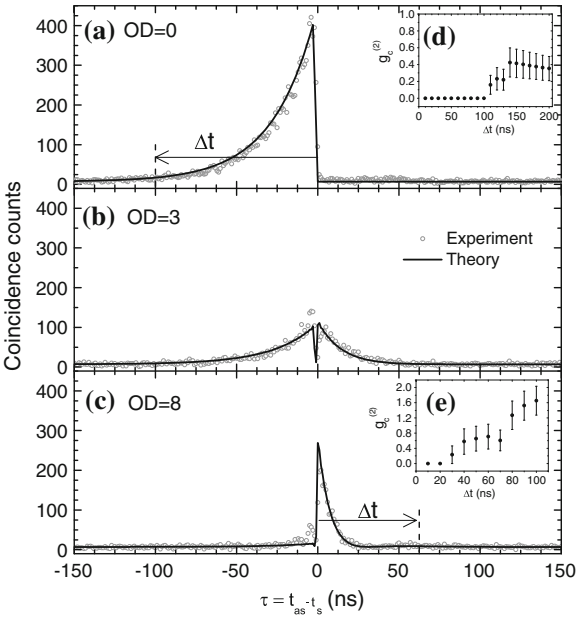

Fig. 6.21 Coherent control of single-photon absorption and reemission in a two-level laser-cooled atomic ensemble. Heralded anti-Stokes photon waveforms after passing through the two-level atomic ensemble at **a** OD = 0 (vacuum), **b** OD = 3, and **c** OD = 8. **d** and **e** show the measured conditional autocorrelation $g_c^{(2)}$ for confirmation of the single-photon quantum nature. Data are taken from [91]

We illustrate the process in Fig. 6.18, where we turn off the coupling laser in MOT2 and have the atoms there in a two-level system. With the EOM modulation, we produce single anti-Stokes photons with an exponential growth waveform with a time constant equal to $1/(2\gamma_{13}) = 26.5$ ns for the incident anti-Stokes photons, as shown in Fig. 6.21a. Here $2\gamma = 2\pi \times 6$ MHz is the population decay rate in the excite state. At $\tau = t_2 - t_1 = 0$, the waveform is switched off with a fall time of 3 ns. After passing through the atoms, the photons are coupled into a SMF to be detected by a SPCM. Figure 6.21b shows the result at OD = 3. At this modest OD, during the exponential growth period ($\tau < 0$), the photon waveform is only partially absorbed. After the incident photon is switched off at $\tau = 0$, this partially absorbed waveform is released (re-emitted) following a exponential decay curve which is determined by the lifetime $[1/(2\gamma)]$ of the excited state. As we increase the OD, the incident photon gets absorbed more heavily. At OD = 8, as shown in Fig. 6.21c, the photon is completely absorbed and the probability in finding the remitted photon at $\tau < 0$ is nearly zero due to the destructive interference. As expected, at $\tau > 0$, the interference between the incident waveform and the emission disappears and we observe the remitted photon. Consequently, the absorption and reemission of the single photon is completely separated in time domain.

This technique can be used to efficiently excite a single quantum absorber in a cavity by a single photon [92, 93]. The result may find potential applications in the quantum networks which require efficient conversion between flying single-photon states and local atomic states [17].

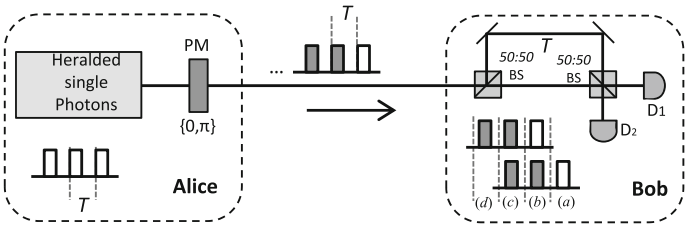

Fig. 6.22 Schematics of single-photon differential phase shift quantum key generation and distribution

(4) **Single-Photon Differential-Phase-Shift Quantum Key Distribution**

Due to the long coherence time of the heralded single photon, its wave packet can be encoded into many time bins with phase-amplitude modulation. It thus become an ideal information carrier for the differential phase shift quantum key distribution (DPS-QKD) [94, 95]. Traditionally, discrete polarization quantum states have been widely used due to their simplicity [96]. However, the fiber length of such a polarization-based QKD system is limited by the birefringence effect that causes the polarization fluctuation on the receiver. This limit can be overcome by the DPS-QKD scheme that is polarization independent. The DPS-QKD also shows tolerance to photon-number-splitting (PNS) attacks [95, 97].

A simplified schematics of the first single-photon DPS-QKD system is illustrated in Fig. 6.22 [98]. Alice divides the single photon into N ($\geq$3) time slots (with a period of T). The keys are encoded by the random relative phase shift between consecutive pulses in 0 or π. Bob detects the incoming photon using an unbalanced M-Z interferometer setup with a path time delay difference equal to T. Taking $N = 3$ as an example, the detection at Bob's site yields four possible time-slot outputs, (a)–(d), as shown in Fig. 6.22. As Bob detect a photon, he records the time and which detector clicks. If the detector clicks at the (b) or (c) time slot, Bob tells Alice only the time slot information through a classical channel; otherwise, Bob discards the photon. Using the time-slot information and her phase encoding records, Alice knows which detector clicked at Bob's site. Defining the clicks at D_1 and D_2 as "0" and "1" respectively, Alice and Bob can obtain a confidential bit string as a sharing key. The photon sent from Alice to Bob can be written as one of the following four states: $(|1_1 0_2 0_3\rangle \pm |0_1 1_2 0_3\rangle \pm |0_1 0_2 1_3\rangle)/\sqrt{3}$, where $1_{i=1,2,3}$ represents one photon at time slot i. As nonorthogonal with each other, the four states cannot be perfectly identified by a single measurement, as shown by the noncloning theorem [99], which guarantees the security of the scheme.

In the original DPS-QKD proposal [94], a single photon is split into N paths with different lengths and then recombined with passive beam splitters. This brings unavoidable loss, which results in a low key creation efficiency [$\propto (N-1)/N^2$] when N is large. Meanwhile, the phase stabilization between different paths becomes a serious problem N increases. In the experimental demonstration of single-photon DPS-QKD, each heralded narrowband single photon is modulated into many time

slots (N up to 15) using a pair of phase and amplitude EOMs [98]. Without using beam splitters, the entire key creation efficiency scales as $(N-1)/N$ and approaches 100 % at the limit of large N [98, 100]. The details of the experiment are described in [98].

6.7 Summary

In summary, we have reviewed recent development in narrowband biphoton generation. For the SFWM in cold atomic medium, EIT effect is used not only for resonantly enhancing the $\chi^{(3)}$ nonlinearity by eliminating the resonance absorption but also for tuning the phase-matching bandwidth with its slow-light effect. For the monolithic resonant backward-wave and forward-wave SPDC with cluster effect and double-pass pumping, it is possible to realize a miniature ultrabright biphoton source. These narrowband biphotons with long coherence time from tens nanoseconds to several microseconds can be used to produce heralded single photons with arbitrarily shaped temporal waveforms by phase-amplitude modulations. We also reviewed their applications in manipulating temporal quantum interactions between single photons and atoms, as well as in the quantum key distribution. Most recently, it was demonstrated that a single photon with time-reversed exponential growth waveform can be loaded into a single-sided Fabry Pérot cavity with near-unity efficiency [101, 102]. With the time-resolved quantum-state tomography [103, 104], their further applications in quantum network and quantum information processing are to be explored.

Acknowledgments C.-S.C. acknowledges support from the Taiwan Ministry of Science and Technology (NSC101-2112-M-007-001-MY3, MOST103-2112-M-007-015-MY3) and National Tsing Hua University (101N7014E1, 103N2014E1). S. Du acknowledges the support from the Hong Kong Research Grants Council (Project Nos. 601411, 601113, and HKU8/CRF/11G).

References

1. A. Einstein, B. Podolsky, N. Rosen, Phys. Rev. **47**, 777 (1935)
2. J.C. Howell, R.S. Bennink, S.J. Bentley, R.W. Boyd, Phys. Rev. Lett. **92**, 210403 (2004)
3. J.S. Bell, Phys. (N.Y.) **1**, 195 (1965)
4. J.F. Clauser, M.A. Horne, A. Shimony, R.A. Holt, Phys. Rev. Lett. **23**, 880 (1969)
5. A. Aspect, P. Grangier, G. Roger, Phys. Rev. Lett. **47**, 460 (1981)
6. A.K. Ekert, Phys. Rev. Lett. **67**, 661 (1991)
7. C.H. Bennett, G. Brassard, C. Crépeau, R. Jozsa, A. Peres, W.K. Wootters, Phys. Rev. Lett. **70**, 1895 (1993)
8. J. Yin, J.-G. Ren, H. Lu, Y. Cao, H.-L. Yong, Y.-P. Wu, C. Liu, S.-K. Liao, F. Zhou, Y. Jiang, X.-D. Cai, P. Xu, G.-S. Pan, J.-J. Jia, Y.-M. Huang, H. Yin, J.-Y. Wang, Y.-A. Chen, C.-Z. Peng, J.-W. Pan, Nature **488**, 185 (2012)
9. M. Neilson, I. Chuang, *Quantum Computation and Quantum Information* (Press, Cambridge, 2000)
10. S.E. Harris, M.K. Oshman, R.L. Byer, Phys. Rev. Lett. **18**, 732–734 (1967)

11. D. Burnham, D. Weinberg, Phys. Rev. Lett. **25**, 84 (1970)
12. M.H. Rubin, D.N. Klyshko, Y.H. Shih, A.V. Sergienko, Theory of two-photon entanglement in type-II optical parametric down-conversion. Phys. Rev. A **50**, 5122 (1994)
13. X. Li, P.L. Voss, J.E. Sharping, P. Kumar, Phys. Rev. Lett. **94**, 053601 (2005)
14. J. Fan, A. Migdall, L.J. Wang, Opt. Lett. **30**, 3368 (2005)
15. O. Cohen, J.S. Lundeen, B.J. Smith, G. Puentes, P.J. Mosley, I.A. Walmsley, Phys. Rev. Lett. **102**, 123603 (2009)
16. L.-M. Duan, M.D. Lukin, J.I. Cirac, P. Zoller, Nature **414**, 413 (2001)
17. H.J. Kimble, Nature **453**, 1023 (2008)
18. Z.Y. Ou, Y.J. Lu, Phys. Rev. Lett. **83**, 2556 (1999)
19. C.E. Kuklewicz, F.N.C. Wong, J.H. Shapiro, Phys. Rev. Lett. **97**, 223601 (2006)
20. X.H. Bao, Y. Qian, J. Yang, H. Zhang, Z.-B. Chen, T. Yang, J.-W. Pan, Phys. Rev. Lett. **101**, 190501 (2008)
21. M. Scholz, L. Koch, O. Benson, Phys. Rev. Lett. **102**, 063603 (2009)
22. C.-S. Chuu, S.E. Harris, Phys. Rev. A **83**, 061803(R) (2011)
23. C.-S. Chuu, G.Y. Yin, S.E. Harris, Appl. Phys. Lett. **101**, 051108 (2012)
24. S. Du, P. Kolchin, C. Belthangady, G.Y. Yin, S.E. Harris, Phys. Rev. Lett. **100**, 183603 (2008)
25. L. Zhao, X. Guo, C. Liu, Y. Sun, M.M.T. Loy, S. Du, Optica **1**, 84 (2014)
26. S. Du, J. Wen, M.H. Rubin, J. Opt. Soc. Am. B **25**, C98 (2008)
27. R.C. Eckardt, C.D. Nabors, W.J. Kozlovsky, R.L. Byer, J. Opt. Soc. Am. B **8**, 646 (1991)
28. H.-J. Briegel, W. Dur, J.I. Cirac, P. Zoller, Phys. Rev. Lett. **81**, 5932 (1998)
29. M.M. Fejer, G.A. Magel, D.H. Jundt, R.L. Byer, IEEE J. Quantum Electron. **28**, 2631 (1992)
30. C. Canalias, V. Pasiskevicius, V. Clemens, F. Laurell, Appl. Phys. Lett. **82**, 4233 (2003)
31. C. Canalias, V. Pasiskevicius, M. Fokine, F. Laurell, Appl. Phys. Lett. **86**, 181105 (2005)
32. C. Canalias, V. Pasiskevicius, Nat. Photonics **1**, 459 (2007)
33. V. Balic, D.A. Braje, P. Kolchin, G.Y. Yin, S.E. Harris, Phys. Rev. Lett. **94**, 183601 (2005)
34. P. Kolchin, Phys. Rev. A **75**, 033814 (2007)
35. L. Zhao, Y. Su, S. Du, arXiv:1409.3341 [quant-ph] (2014)
36. M.J. Collett, C.W. Gardiner, Phys. Rev. A **30**, 1386 (1984)
37. S. Sensarn, I. Ali-Khan, G.Y. Yin, S.E. Harris, Phys. Rev. Lett. **102**, 053602 (2009)
38. S.E. Harris, Phys. Rev. Lett. **98**, 063602 (2007)
39. S.E. Harris, Appl. Phys. Lett. **9**, 114 (1966)
40. S.E. Harris, Phys. Today **50**, 36 (1997)
41. M. Fleischhauer, A. Imamoglu, J.P. Marangos, Rev. Mod. Phys. **77**, 633 (2005)
42. L.V. Hau, S.E. Harris, Z. Dutton, C.H. Behroozi, Nature (London) **397**, 594 (1999)
43. S. Zhang, J.F. Chen, C. Liu, S. Zhou, M.M.T. Loy, G.K.L. Wong, S. Du, Rev. Sci. Instrum. **83**, 073102 (2012)
44. J.-M. Wen, S. Du, M.H. Rubin, Phys. Rev. A **75**, 033814 (2007)
45. J.-M. Wen, S. Du, M.H. Rubin, Phys. Rev. A **76**, 013825 (2007)
46. J.-M. Wen, S. Du, Y. Zhang, M. Xiao, M.H. Rubin, Phys. Rev. A **77**, 033816 (2008)
47. P. Kolchin, S. Du, C. Belthangady, G.Y. Yin, S.E. Harris, Phys. Rev. Lett. **97**, 113602 (2006)
48. H. Yan, S. Zhang, J.F. Chen, M.M.T. Loy, G.K.L. Wong, S. Du, Phys. Rev. Lett. **106**, 033601 (2011)
49. S. Du, J. Wen, M.H. Rubin, G.Y. Yin, Phys. Rev. Lett. **98**, 053601 (2007)
50. A.V. Sergienko, Y.H. Shih, M.H. Rubin, J. Opt. Soc. Am. B **12**, 859 (1994)
51. S.E. Harris, L.V. Hau, Phys. Rev. Lett. **82**, 4611 (1999)
52. S. Du, C. Belthangady, P. Kolchin, G.Y. Yin, S.E. Harris, Opt. Lett. **33**, 2149–2151 (2008)
53. P. Kolchin, C. Belthangady, S. Du, G.Y. Yin, S.E. Harris, Phys. Rev. Lett. **101**, 103601 (2008)
54. C. Belthangady, S. Du, C.-S. Chuu, G.Y. Yin, S.E. Harris, Phys. Rev. A **80**, 031803(R) (2009)
55. S. Du, J. Wen, C. Belthangady, Phys. Rev. A **79**, 043811 (2009)
56. J.F. Chen, S. Zhang, H. Yan, M.M.T. Loy, G.K.L. Wong, S. Du, Phys. Rev. Lett. **104**, 183604 (2010)
57. K. Liao, H. Yan, J. He, S. Du, Z.-M. Zhang, S.-L. Zhu, Phys. Rev. Lett. **112**, 243602 (2014)
58. Y.C. Chen, C.W. Lin, I.A. Yu, Phys. Rev. A **61**, 053805 (2000)

59. D. Matsukevich, A. Kuzmich, Science **306**, 663 (2004)
60. S. Chu, S. Wong, Phys. Rev. Lett. **48**, 738 (1982)
61. L.J. Wang, A. Kuzmich, A. Dogariu, Nature **406**, 277 (2000)
62. A. Sommerfeld, Ann. Phys. **44**, 177 (1914)
63. L. Brillouin, Ann. Phys. **44**, 203 (1914)
64. L. Brillouin, *Wave Propagation and Group Velocity* (Academic Press, New York, 1960)
65. K.E. Oughstun, G.C. Sherman, *Electromagnetic Pulse Propagation in Causal Dielectrics* (Springer, Berlin, 1994)
66. J. Aaviksoo, J. Kuhl, K. Ploog, Phys. Rev. A **44**, R5353 (1991)
67. S.-H. Choi, U.L. Österberg, Phys. Rev. Lett. **92**, 193903 (2004)
68. H. Jeong, A.M.C. Dawes, D.J. Gauthier, Phys. Rev. Lett. **96**, 143901 (2006)
69. D. Wei, J.F. Chen, M.M.T. Loy, G.K.L. Wong, S. Du, Phys. Rev. Lett. **103**, 093602 (2009)
70. J.F. Chen, H. Jeong, L. Feng, M.M.T. Loy, G.K.L. Wong, S. Du, Phys. Rev. Lett. **104**, 223602 (2010)
71. J.F. Chen, M.M.T. Loy, G.K.L. Wong, S. Du, J. Opt. **12**, 104010 (2010)
72. S. Du, Physics **42**, 315 (2013)
73. M.D. Eisaman, A. André, F. Massou, M. Fleischhauer, A.S. Zibrov, M.D. Lukin, Nature **438**, 837 (2005)
74. A.M. Steinberg, P.G. Kwiat, R.Y. Chiao, Phys. Rev. Lett. **71**, 708 (1993)
75. A.M. Steinberg, R.Y. Chiao, Phys. Rev. A **51**, 3525 (1995)
76. N. Akopian, L. Wang, A. Rastelli, O.G. Schmidt, V. Zwiller, Nat. Photonics **5**, 230 (2011)
77. S. Zhang, J.F. Chen, C. Liu, M.M.T. Loy, G.K.L. Wong, S. Du, Phys. Rev. Lett. **106**, 243602 (2011)
78. A.V. Gorshkov, A. André, M. Fleischhauer, A.S. Sørensen, M.D. Lukin, Phys. Rev. Lett. **98**, 123601 (2007)
79. A.L. Alexander, J.J. Longdell, M.J. Sellars, N.B. Manson, Phys. Rev. Lett. **96**, 043602 (2006)
80. M. Hosseini, B.M. Sparkes, G. Campbell, P.K. Lam, B.C. Buchler, Nature Commun. **2**, 174 (2011)
81. C. Clausen, I. Usmani, F. Bussières, N. Sangouard, M. Afzelius, H. de Riedmatten, N. Gisin, Nature **469**, 508 (2011)
82. E. Saglamyurek, N. Sinclair, J. Jin, J.A. Slater, D. Oblak, F. Bussières, M. George, R. Ricken, W. Sohler, W. Tittel, Nature **469**, 512 (2011)
83. E. Saglamyurek, N. Sinclair, J. Jin, J.A. Slater, D. Oblak, F. Bussières, M. George, R. Ricken, W. Sohler, W. Tittel, Phys. Rev. Lett. **108**, 083602 (2012)
84. S. Zhou, S. Zhang, C. Liu, J.F. Chen, J. Wen, M.M.T. Loy, G.K.L. Wong, S. Du, Opt. Express **20**, 24124 (2012)
85. M. Varnava, D.E. Browne, T. Rudolph, Phys. Rev. Lett. **97**, 120501 (2006)
86. M. Tanaka, M. Fujiwara, H. Ikegami, Phys. Rev. A **34**, 4851 (1986)
87. F.Y. Wu, S. Ezekiel, M. Ducloy, B.R. Mollow, Phys. Rev. Lett. **38**, 1077 (1977)
88. Md. AminulIslam Talukder, Y. Amagishi, M. Tomita, Phys. Rev. Lett. **86**, 3546 (2001)
89. H.J. Kimble, M. Dagenais, L. Mandel, Phys. Rev. Lett. **39**, 691 (1977)
90. M.O. Scully, E.S. Fry, C.H. Raymond Ooi, K. Wodkiewicz, Phys. Rev. Lett. **96**, 010501 (2006)
91. S. Zhang, C. Liu, S. Zhou, C.-S. Chuu, M.M.T. Loy, S. Du, Phys. Rev. Lett. **109**, 263601 (2012)
92. R. Johne, A. Fiore, Phys. Rev. A **84**, 053850 (2011)
93. D. Pinotsi, A. Imamoglu, Phys. Rev. Lett. **100**, 093603 (2008)
94. K. Inoue, E. Waks, Y. Yamamoto, Phys. Rev. Lett. **89**, 037902 (2002)
95. K. Wen, K. Tamaki, Y. Yamamoto, Phys. Rev. Lett. **103**, 170503 (2009)
96. C.H. Bennett, G. Brassard, Quantum cryptography: public key distribution and coin tossing. In *Proceedings of IEEE International Conference on Computers, Systems, and Signal Processing, Bangalore*, p. 175. India (IEEE, New York, 1984)
97. E. Waks, H. Takesue, Y. Yamamoto, Phys. Rev. A **73**, 012344 (2006)
98. C. Liu, S. Zhang, L. Zhao, P. Chen, C.-H.F. Fung, H.F. Chau, M.M.T. Loy, S. Du, Opt. Express **21**, 9505 (2013)

99. N. Gisin, G. Ribordy, W. Tittel, H. Zbinden, Rev. Mod. Phys. **74**, 145–195 (2002)
100. H. Yan, S. Zhu, S. Du, Chin. Phys. Lett. **28**, 070307 (2011)
101. C. Liu, Y. Sun, L. Zhao, S. Zhang, M.M.T. Loy, S. Du, Phys. Rev. Lett. **113**, 133601 (2014)
102. B. Srivathsan, G.K. Gulati, A. Cere, B. Chng, C. Kurtsiefer, Phys. Rev. Lett. **113**, 163601 (2014)
103. P. Chen, C. Shu, X. Guo, M.M.T. Loy, S. Du, arXiv:1409.5747 [quant-ph] (2014)
104. F.A. Beduini, J.A. Zielinska, V.G. Lucivero, Y.A. de Icaza Astiz, M.W. Mitchell, Phys. Rev. Lett. **113**, 183602 (2014)

Chapter 7
Generation, Characterization and Use of Atom-Resonant Indistinguishable Photon Pairs

Morgan W. Mitchell

Abstract We describe the generation of atom-resonant indistinguishable photon pairs using nonlinear optical techniques, their spectral purification using atomic filters, characterization using multi-photon interference, and application to quantum-enhanced sensing with atoms. Using either type-I or type-II cavity-enhanced spontaneous parametric down-conversion, we generate pairs of photons in the resonant modes of optical cavities with linewidths comparable to the natural linewidths of strong atomic transitions. The cavities and pump lasers are tuned so that emission occurs in a mode or a pair of orthogonally-polarized modes that are resonant to the D_1 line, at 794.7 nm. The emission from these frequency-degenerate modes is separated from other cavity emission using ultra-narrow atomic frequency filters, either a Faraday anomalous dispersion optical filter (FADOF) with a 445 MHz linewidth and 57 dB of out-of-band rejection or an induced dichroism filter with an 80 MHz linewidth and $\geq$ 35 dB out-of-band rejection. Using the type-I source, we demonstrate interference of photon pair amplitudes against a coherent state and a new method for full characterization of the temporal wave-function of narrow-band photon pairs. With the type-II source we demonstrate high-visibility super-resolving interference, a high-fidelity atom-tuned NooN state, and quantum enhanced sensing of atoms using indistinguishable photon pairs.

7.1 Introduction

Interference of indistinguishable photons is one of the most striking non-classical phenomena. When two indistinguishable photons meet at a beamsplitter, each entering from a different port, an interference of two-photon amplitudes leads them to "coalesce" and to exit in the same direction, even though there is no force causing

M.W. Mitchell (✉)
ICFO – Institut de Ciencies Fotoniques, Av. Carl Friedrich Gauss,
3, 08860 Castelldefels, Barcelona, Spain
e-mail: morgan.mitchell@icfo.es

M.W. Mitchell
ICREA – Institució Catalana de Recerca i Estudis Avançats, 08015 Barcelona, Spain

A. Predojević and M.W. Mitchell (eds.), *Engineering the Atom-Photon Interaction*,
Nano-Optics and Nanophotonics, DOI 10.1007/978-3-319-19231-4_7

them to interact [1, 2]. This and similar multi-photon interference effects have been harnessed for quantum teleportation [3], entanglement swapping [4], linear optics quantum information processing [5], quantum-enhanced sensing [6], and quantum simulation [7], among other applications. A similar effect concerns the interference of indistinguishable photon pairs sharing a single mode against other sources of photon pairs. This is the mechanism by which squeezed vacuum, which consists of pairs of indistinguishable photons, alters the noise distribution in an interferometer [8], a phenomenon central to quantum-enhanced sensing [9, 10] and continuous-variable quantum information processing [11].

Most of the above-mentioned applications were developed with broadband photons that, due to a strong spectral mismatch, could at best interact inefficiently with atoms or other material systems. Generation of indistinguishable, atom-resonant photons is an attractive goal if we wish to interact states exhibiting non-classical interference with atomic quantum information processors (see chapters by Leuchs and Sondermann, Piro and Eschner, and Slodička, Hétet, Hennrich and Blatt), atomic quantum memories (see chapter by Chuu and Du), or atomic sensors [12–16]. Using cavity-QED methods, atom-resonant indistinguishable photons can be produced with exquisite control over their wave-functions (see the chapter by A. Kuhn), but at a high cost in system complexity.

In this chapter we describe generation of pairs of indistinguishable photons using cavity-enhanced spontaneous parametric down-conversion (CESPDC) [17–19] and extremely narrow-band optical filters [20, 21] to select the atom-resonant component of the emission. We describe also applications: using pairs of indistinguishable high-coherence photons, we demonstrate a full measurement of the two-photon temporal wave function, including both amplitude and phase [22], generate an atom-tuned Noon state [19], and use this state to probe an atomic magnetometer, demonstrating the use of indistinguishable photon pairs for sensing of an atomic system beyond the standard quantum limit [23].

7.1.1 CESPDC Sources

Spontaneous parametric down-conversion (SPDC) is a proven method to generate non-classical states of light, including single-mode and two-mode squeezed states, entangled photon pairs, and states with multiple pairs of photons. Although photon production by SPDC is probabilistic, heralded single photons, heralded entangled states, and heralded versions of more exotic states including so-called “Schrödinger kitten” states, can be generated from SPDC output using single-photon detectors to indicate when the source has produced the desired state. Quantum states can also be generated “on demand” if active elements are also incorporated (see the chapter by Yoshikawa, Makino and Furusawa).

A strength of SPDC is the simplicity of the parametric interaction, which can produce very pure correlations in frequency, polarization, and photon number. In contrast, parametric interactions do not naturally produce narrowband output, and

some engineering is required to generate SPDC output that is bandwidth-compatible with atomic resonance lines or other material spectroscopic features. Due to the strong frequency correlations, narrow-band filtering of one SPDC output can be used to select desired frequency content in the other output, as in the chapter by Piro and Eschner. Placing the SPDC process inside a resonant cavity, "cavity-enhanced SPDC," (CESPDC) [24] gives a resonant enhancement to photon pairs coinciding with the cavity modes while suppressing those frequencies that do not fit. Cavity-enhancement techniques often benefit from techniques such as group-velocity mismatching and even backward-wave phase-matching that further restrict the SPDC output (see the chapters by Chuu and Du, de Riedmatten and Afzelius and Zhao, Bao, Zhao and Pan).

In this chapter we will describe two very similar CESPDC sources, the first using type-I phase matching, and thus capable of producing fully-degenerate photon pairs, i.e. produced in the same cavity mode and thus with the same frequency, polarization, and spatial mode. The second CESPDC source uses type-II phase matching, and is tuned so that one H-polarized mode, and one V-polarized mode are both resonant at half the frequency of the pump. In this way, we generate photon pairs that are indistinguishable in all respects except for polarization. We will sometimes refer to these devices as sub-threshold optical parametric oscillators (OPOs), the term usually used in frequency conversion and continuous-variable quantum optics for these same devices.

7.1.2 Atomic Frequency Filters

Atomic filters use atomic media, usually atomic vapors, to generate intrinsically narrow-band spectral features, and typically achieve transmission bandwidths from a few MHz to a few GHz. The "traditional" uses of atomic filters are in astronomy [25], laser ranging and surveying, and daylight optical communications, where they are used to detect signals at specific frequencies while giving excellent blocking, better than $1{:}10^5$, over a very wide rejection band. As we will describe, these features combine well with the output of our CESPDC source, which has a linewidth of only a few MHz, free-spectral range (FSR) of a few hundred MHz and emission extending over hundreds of GHz. Proper matching of an atomic filter to a CESPDC source can then select a single output line while efficiently rejecting the rest of the SPDC output.

While atomic media naturally present strong and narrow absorption features, what we require is a filter with narrowband *transmission*. This requires some kind of optical trickery, to convert the absorption resonances into transmission features. Equally importantly, the filter must have a strong rejection of the unwanted frequencies. While traditional optics, in the form of cascaded optical cavities, can in principle perform this task perfectly, i.e. with arbitrarily high rejection and unit transmission, this approach requires careful mode-matching and active tuning of the filters, and is ultimately limited by the quality of the cavity optics [26–28]. Atomic filters are an

interesting option for their stability, multi-mode capability, high transmission, and very high out-of-band rejection, limited by the quality of the polarizers. To date, atomic filters continue to outperform cavity filters in these figures of merit.

7.2 Atom-Resonant Indistinguishable Photon Pairs in a Single Mode

In this section we describe a series of experiments to generate indistinguishable photon pairs in a single polarization mode, using type-I parametric downconversion. Section 7.2.1 describes the source, Sect. 7.2.2 describes the atomic filter, Sect. 7.2.3 describes measurements of the spectral purity achieved, Sect. 7.2.4 demonstrates interference of two-photon amplitudes between a narrow-band SPDC source and a CW laser, and Sect. 7.2.5 applies this interference to biphoton wave-function measurement. Additional details can be found in [20–22, 29].

7.2.1 Type-I CESPDC Source

We use a doubly-resonant degenerate OPO [17] containing a type-I PPKTP crystal, phase-matched for second-harmonic generation from 794.7 to 397.4 nm. A schematic is shown in Fig. 7.1. A continuous wave external cavity diode laser at 794.7 nm is

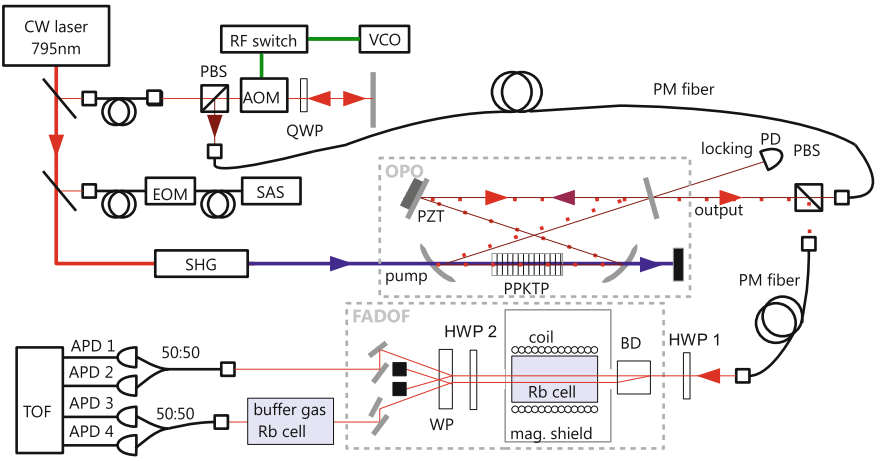

Fig. 7.1 Experimental setup of the type-I OPO, the FADOF filter and detection system. *Symbols PBS* polarizing beam splitter, *AOM* acousto-optic modulator, *EOM* electro-optic modulator, *APD* avalanche photodiode, *BD* calcite beam displacer, *WP* Wollaston prism, *TOF* time-of-flight analyzer, *SAS* saturated absorption spectroscopy, *VCO* voltage controlled oscillator, *PM* polarization maintaining fiber, *HWP* half-wave plate, *QWP* quarter-wave plate, *PD* photodiode

stabilized at a frequency ω_0, 2.7 GHz to the red of the Rb D_1 line centre. As described in [21], an electro-optic modulator (EOM) adds sidebands to a saturated spectroscopy absorption signal in order to get an error signal at the desired frequency. We double the laser frequency by cavity-enhanced second harmonic generation using a LBO crystal to generate a 397.4 nm pump beam for the OPO. The cavity length is stabilized to maintain a TEM00, V-polarized cavity mode at frequency ω_0, thus resonating the SPDC production of indistinguishable photon pairs at this frequency.

With this configuration, photon pairs are generated at all the resonance frequencies of the OPO cavity that fall inside the 150 GHz-wide phase matching envelope of the PPKTP crystal. The OPO output is thus composed of hundreds of frequency modes, each of 8.4 MHz bandwidth, separated by the 501 MHz FSR. We note that in this type-I scenario, group velocity mismatching techniques are not applicable, because the pairs of generated photons differ only in longitudinal mode. Filtering can in principle separate the desired, degenerate-mode photon pairs from the background pairs, but the requirements are quite stringent: The filter must be able to distinguish between one cavity mode and the next, separated by the FSR. Moreover, to achieve a high spectral purity in the output, the filter needs a very high out-of-band rejection. Finally, high transmission efficiency is always desirable so as to not lose the photon pairs. As we shall see, these requirements are well-matched to a specific kind of atomic frequency filter.

7.2.2 A FADOF at the Rb D_1 Line

We now describe a Faraday Anomalous-Dispersion Optical Filter (FADOF) at the D_1 line of Rb at 795 nm. This line, efficiently detected with Si detectors, accessible with a variety of laser technologies, and showing large hyperfine splittings, is a favorite for coherent and quantum optics with warm atomic vapors. Applications include electromagnetically-induced transparency [30], stopped light [31], optical magnetometry [12, 32], laser oscillators [33], polarization squeezing [34, 35], quantum memory [36], and high-coherence heralded single photons [37, 38].

A FADOF consists of an atomic vapor cell between two crossed polarizers, while a homogeneous magnetic field along the propagation direction induces circular birefringence in the vapor. The crossed polarizers block transmission away from the absorption line, while the absorption itself blocks resonant light. Between these, Faraday rotation just outside the Doppler profile can give high transmission for a narrow range of frequencies. FADOF is simple and robust, but performance depends critically on optical properties of the atomic vapor. Fortunately, first-principles modeling of the atomic vapor agrees very well with experiment, as shown in Fig. 7.2. Public-domain codes are available for calculating FADOF spectra for Rb [21], Na [39, 40] and several other alkali species [41].

Similar FADOFs have been developed for several other alkali atom resonances—Cs D_2 [42] and $6S_{1/2} \rightarrow 7P_{3/2}$ [43, 44] lines, Rb D_2 line [45, 46], Rb $5S_{1/2} \rightarrow 6P_{3/2}$ [47], K (three lines) [48], Na D lines [49], and for Ca [50]. Several of these show

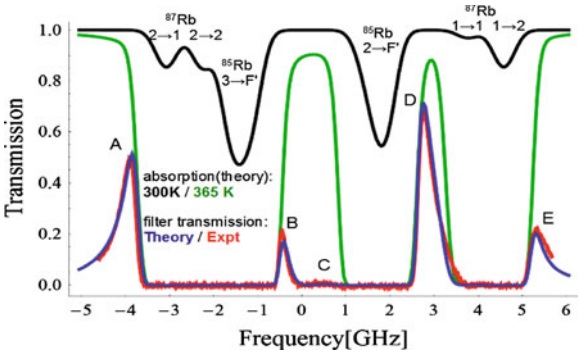

Fig. 7.2 Features of the Rb D_1 FADOF spectrum for a cell of 10 cm internal length containing natural abundance rubidium with no buffer gas. The calculated absorption spectrum at 300 K is shown in *black*, with distinct peaks due to the ^{85}Rb and ^{87}Rb transitions. The calculated spectrum at 365 K is shown in *green*, and shows very strong absorption in three regions. When this medium is placed between crossed polarizers in the presence of a magnetic field of $B = 4.5$ mT, strong Faraday rotation at the line-edges leads to sharp transmission peaks an points *A*–*E*. Calculated transmission spectra are shown in *blue*, experimental spectra are shown in *red*. The feature *D*, which occurs between two lines, is particularly advantageous, as it is both stronger (higher transmission), and narrower than other lines, because its tail is absorbed by the ^{87}Rb $F = 1 \rightarrow F'$ transitions

transmission above 90 %, and/or linewidths below 1 GHz. Filter figures of merit are shown in Table 7.1. An important figure of merit used in the FADOF literature is the Equivalent Noise Bandwidth ENBW $= [\max_\nu T(\nu)]^{-1} \int T(\nu) d\nu$, where $T(\nu)$ is the filter transmission versus frequency ν [46]. For narrowband signals in broadband noise, a filter achieves the signal-to-noise ratio of an ideal filter with bandwidth ENBW.

When quantified by the ENBW, the Rb D_1 line gives superior performance to other species and lines, due to what appears to be a fortunate accident of the hyperfine splittings. For either pure ^{85}Rb or pure ^{87}Rb, the FADOF transmission at these field strengths shows four peaks, with the strongest ones at the extremes of the spectrum and with long tails. The strong ^{87}Rb peaks are visible as peak A and E of Fig. 7.2. The strong ^{85}Rb peaks include the peak D and one at -2.5 GHz, but in the natural-abundance vapor this latter peak is completely obscured by the ^{87}Rb absorption. The long tail of peak D is blocked by absorption from the ^{87}Rb $F = 1 \rightarrow F' = 1$ transition, improving the ENBW.

7.2.2.1 A Dual-Channel FADOF

The filter used here is a small modification of that described in Sect. 7.2.2 and in [21]. We take advantage of the multi-mode, imaging property of the FADOF to filter simultaneously two orthogonal polarizations: instead of the crossed polarizers, we use a beam displacer before the cell, so that the two orthogonal polarizations travel

Table 7.1 Comparison of reported FADOF transmission for different atoms and wavelengths λ

Atom	λ(nm)	References			T_{max}	B_T(GHz)	B_N(GHz)
K	405	[48]			0.93	1.2	6
^{87}Rb	420	[47]			0.98	2.5	5.9
Ca	423	[50]			0.55	1.5	–
Cs	455	[43]			0.96	0.9	3.3
Cs	455	[44]			0.86	1.5	–
Na	589	[49]			0.85	1.9	5.1
Na	590	[49]			0.37	10.5	8.3
K	766	[48]			0.96	0.9	5
K	770	[48]			–	–	–
Rb	780	[46]			0.93	1.3	4.7
Cs	852	[42]			0.90	0.6	–
B(mT)				T(K)			
Rb	795	[21]	18.0	353	0.92	0.48	2.1
Rb	795	[21]	5.9	378	0.91	1.10	2.7
Rb	795	[21]	4.5	365	0.71	0.45	1.2
Rb	795	[21]	2.0	345	0.04	0.32	0.8

T_{max} Peak transmission. B_T Full-width at half-maximum bandwidth of main transmission peak. B_N Equivalent-noise bandwidth (*ENBW*). – Value not reported. Reference [48] shows a K 770 nm FADOF curve very similar to K 766 nm

along independent parallel paths in the cell. After the cell we use a Wollaston prism to separate the near-resonant filtered light from the unrotated one. The optical axes of the two polarizing elements are oriented with precision mounts, and an extinction ratio of 1.8×10^{-6} is reached.

Additionally, the setup has been supplemented with a half-waveplate placed before the Wollaston prism (HWP 2 in Fig. 7.1), which enables us to, in effect, turn on and off the filter. In the "FADOF on" condition, the waveplate axis is set parallel to the Wollaston axis (and thus the waveplate has no effect on the filter behaviour), the magnetic field is 4.5 mT and the temperature is 365 K. In the "FADOF off" condition, no magnetic field is applied, the temperature of the cell is also 365 K and HWP 2 is set to rotate the polarization by 90 degrees, in effect swapping the outputs, so that almost all the light is transmitted through the setup without being filtered.

We optimized the filter using a common criterion for experiments with photon pairs: we maximize the ratio of coincidences due to photon pairs belonging to the degenerate mode to coincidences due to other photon pairs. Because of energy conservation, the two photons in any SPDC pair will have frequencies symmetrically placed with respect to the degenerate mode; to prevent the pair from reaching the detectors, it suffices to block at least one of the photons. In terms of filter performance, this means that it is possible to have near-perfect filtering even with transmission in some spectral windows away from the degenerate mode, provided the transmission is asymmetrical (Fig. 7.3). Using this criterion we find the optimal conditions for the

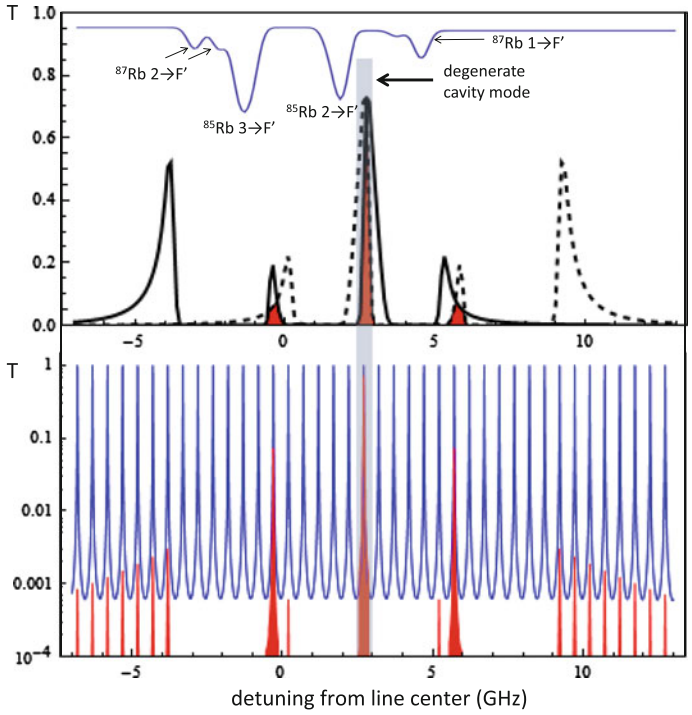

Fig. 7.3 Spectral matching of FADOF to CESPDC source. *Upper plot* reference transmission spectrum of room temperature natural abundance Rb (*blue*), filter spectrum (*black*) and a mirror filter spectrum with respect to the degenerate cavity mode (*black dashed*). *Red shaded* regions indicate transmission of correlated photon pairs. *Lower plot* cavity output spectrum (*blue*) and FADOF-filtered cavity spectrum (*red*). The degenerate cavity mode coincides with the FADOF peak. Both figures have the same frequency scale

filter performance at the field and temperature values given above. The optimum filter performance requires the degenerate mode to coincide with the FADOF transmission peak at a fixed frequency (2.7 GHz to the red from the center of the Rb D_1 line).

7.2.3 Spectral Purification of Degenerate Photon Pairs from Type-I CESPDC

We now show how such an atomic filter can separate indistinguishable, atom-resonant photon pairs from a much stronger broadband background of non-degenerate photon pairs, the natural output of a sub-threshold OPO or CESPDC source.

Using the FADOF described in Sect. 7.1.2 we observe 70 % transmission of the degenerate mode through the filter, simultaneous with out-of-band rejection by 57 dB,

sufficient to reduce the combined non-degenerate emission to a small fraction of the desired, degenerate mode emission. For comparison, a recently-described monolithic filter cavity achieved 60 % transmission and 45 dB out-of-band rejection [28]. We test the filter by coincidence detection of photon pairs from the OPO output, which provides a stringent test of the suitability for use at the single-photon level. We observe for the first time fully-degenerate, near atom-resonant photon pairs, as evidenced by correlation functions and atomic absorption measurements. The 96 % spectral purity we observe surpasses the previous record of 94 % [38], and is in agreement with theoretical predictions.

7.2.3.1 Detection

The distribution of arrival times of photons in a Hanbury-Brown-Twiss configuration is useful to check that the filter effectively suppresses the non-degenerate modes of the type-I OPO described in the previous section. We collect the OPO output in a polarization maintaining fiber and send it through the filter setup. The filtered light is then coupled into balanced fiber beam splitters that send the photons to avalanche photo-detectors (APDs), connected to a time-of-flight analyzer (TOF) that allows us to measure the second order correlation function $G^{(2)}(T)$ (see Fig. 7.1).

Since we are using single photon detectors, we need to reduce as much as possible the background due to stray light sources in the setup. The main source of background light is the counter-propagating beam that we inject in the OPO in order to lock the cavity length to be resonant at ω_0. We solve this problem using a chopped lock: the experiment switches at 85 Hz between periods of data acquisition and periods of stabilization. During periods of data acquisition, the AOM is off, and thus no locking beam is present. During periods of stabilization, the AOM is on, and an electronic gate circuit is used to block electronic signals from the APDs, preventing recording of detections due to the locking beam photons. In addition, the polarization of the locking beam is orthogonal to that of the OPO output.

7.2.3.2 Effect of Filtering on Arrival Time Distribution

The relative arrival-time distribution for photon pairs produced by the CESPDC source is a Dirac comb, with a separation given by the cavity round-trip time, times a double exponential with a time constant given by the cavity ring-down time [29, 51]. Here the cavity round-trip time is slightly less than 2 ns, whereas the resolution of our time-to-digital converter is 1 ns. Evidence for the comb structure is visible in the measured distribution, shown in Fig. 7.4. This agrees well with the theoretical expectation, described in the Appendix, as does the 26 ns full-width at half-maximum (FWHM) of the double-exponential envelope. When the filter is "on," we expect to see an unmodulated double exponential of the same width. While the filter blocks the unwanted modes, it has little reshaping effect on the degenerate mode, which is

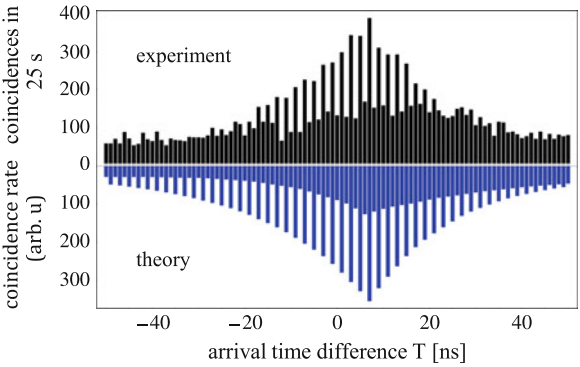

Fig. 7.4 Histograms of arrival time differences for FADOF off compared to theoretical model (both include the background due to accidental coincidences and the artefacts resulting from 1 ns resolution of the counting electronics)

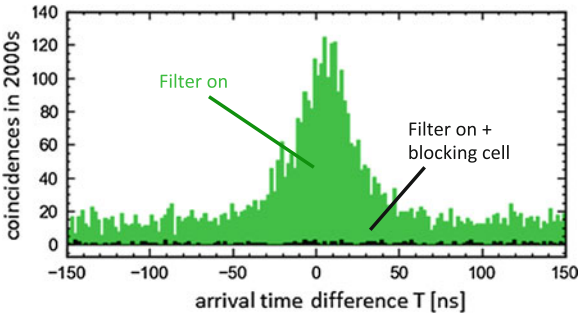

Fig. 7.5 Histograms of the differences of arrival times of the photon pairs for FADOF on (*green*) and FADOF on with hot cell on the path (*black bars* at *bottom* of graph). No background has been subtracted

much narrower than, and centred on, the peak of the filter pass-band. In agreement with these expectations we observe a double-exponential distribution with no visible modulation with the same FWHM width. This is shown in Fig. 7.5.

7.2.3.3 Spectral Purity

According to the theoretical filter spectrum from [21], we estimate that 98 % of the atom-resonant photon pairs come from degenerate mode (see Fig. 7.3). In order to test how much light outside the Rubidium D_1 line can pass through our FADOF, we split the light equally between the two different polarization paths of the filter setup by means of a half-wave plate put before the beam displacer (HWP 1 in Fig. 7.1). A natural-abundance Rb vapor cell, with 10 Torr of N_2 buffer gas and heated until it is opaque for resonant light, is inserted in one of the paths after the filter. The collisionally-broadened absorption from this cell blocks the entire FADOF transmission window, allowing us to compare the arrival time histograms with and without the resonant component.

The number of photons detected after passing through the hot Rb cell is comparable to the detector dark counts, meaning that most of the filtered light is at the chosen frequency ω_0. We define the spectral purity P_S of the FADOF as $P_S \equiv 1 - c_{HC}/c_F$,

where c_{HC} (c_F) is the number of photon pairs which were recorded within a coincidence windows of 50 ns in the path with (without) the hot cell. Considering raw coincidences (no background subtraction), we obtain $P_S = 0.98$, meaning that the filtered signal is remarkably pure, as only the 2 % of the recorded pairs are out of the filter spectrum. This 2 % agrees with measurements of the polarization extinction ratio with the FADOF off, i.e., it is due to technical limitations of the polarization optics and could in principle be improved. From the filter spectrum, we know that, of the photon pairs within the Rb resonance line, 98 % come from the degenerate cavity mode, we conclude that 96 % of the pairs exiting the filter come from the degenerate mode.

7.2.4 Interference of Biphoton Amplitudes from Distinct Sources

An SPDC process naturally generates a state of the form

$$|\psi\rangle \propto |0\rangle + \sum_{k_s,k_i} f(k_s,k_i) a^\dagger_{k_s} a^\dagger_{k_i} |0\rangle + \ldots, \tag{7.1}$$

where k_s and k_i index the modes of the signal and idler fields, respectively, and f is a complex-valued function analogous to the wave function encountered in non-relativistic quantum mechanics. Following this analogy, one might expect that observations can only indicate f up to an unobservable global phase. A bit of reflection shows, however, that even the global phase of f is observable, so long as the two-photon part of the wave-function exists in superposition with other parts, most importantly the zero-photon contribution $|0\rangle$.

Consider the simplest scenario, in which signal and idler are the same mode, and differ at most by their times of arrival t, t'. This is in fact the case when we consider the filtered output of the CESPDC source described above. The SPDC state becomes

$$|\psi\rangle \propto |0\rangle + \int dt\, dt'\, \psi(t,t') a^\dagger(t) a^\dagger(t') |0\rangle + \ldots, \tag{7.2}$$

where ψ now plays the role of f. The phase of ψ can be made visible by interfering the state against another state containing both a zero-photon and a two-photon component. A natural candidate is the continuous-wave coherent state with amplitude α:

$$|\alpha\rangle \propto |0\rangle + \alpha \int dt\, a^\dagger(t)|0\rangle + \frac{\alpha^2}{2} \int dt\, dt'\, a^\dagger(t) a^\dagger(t')|0\rangle + \ldots \tag{7.3}$$

We can imagine combining at a polarizing beamsplitter the states $|\psi\rangle$, with vertical polarization, and $|\alpha\rangle$, with horizontal polarization, to obtain a state

$$|\Psi\rangle \equiv |\psi\rangle_V \otimes |\alpha\rangle_H \tag{7.4}$$

$$= \left[1 + \alpha \int dt\, a_H^\dagger(t) + \int dt\, dt'\, \psi(t,t') a_V^\dagger(t) a_V^\dagger(t') + \frac{\alpha^2}{2} \int dt\, dt'\, a_H^\dagger(t) a_H^\dagger(t') + \ldots\right] |0\rangle_V \otimes |0\rangle_H \tag{7.5}$$

with a two-photon component

$$\int dt\, dt' \left[\psi(t,t') a_V^\dagger(t) a_V^\dagger(t') + \frac{\alpha^2}{2} a_H^\dagger(t) a_H^\dagger(t')\right] |0\rangle_V \otimes |0\rangle_H . \tag{7.6}$$

Interference of these two terms can be obtained by coincidence detection in a basis that is neither V nor H. For example, the rate of detection of a photon pair, at times t and t', both in the state $|\phi\rangle \equiv (\exp[-i\phi]|H\rangle + |V\rangle)/\sqrt{2}$, is found by projection onto $|\phi\rangle^{\otimes 2}$ to give

$$R_\phi(t,t') \propto \left|\psi(t,t') + \frac{\alpha^2}{2} \exp[2i\phi]\right|^2 , \tag{7.7}$$

which clearly depends on the phase of ψ. It should be noted that observing this interference requires both narrow-band photon pairs, so that the detection times can be resolved, and a stable phase relation between α and ψ. To maintain this phase relationship, we use the OPO also as a phase-sensitive amplifier, a well-established technique from continuous-variable quantum optics.

The experimental setup is shown in Fig. 7.6. A continuous-wave diode laser at 794.7 nm generates both the coherent reference beam and, after being amplified and doubled in frequency, a 397.4 nm pump beam for the OPO, described in [17], which generates a vertically-polarized (V) squeezed vacuum state via SPDC in a periodically poled KTP crystal. The cavity length is actively stabilized with a Pound-Drever-Hall lock, to keep one longitudinal V mode resonant at the laser frequency. The locking beam is H polarized, counter-propagating, and shifted in frequency by an acousto-optic modulator (AOM), to match the frequency of an H-polarized mode. The AOM RF power is chopped and the detectors are electronically gated: coincidence data are acquired only when the locking light is off. With these measures, the contribution of locking light to the accidental coincidences background is minimised.

The V-polarized squeezed vacuum is combined with the H-polarized coherent reference at a polarizing beamsplitter to generate a beam with co-propagating squeezed and reference components. A polarization transformation, chosen so that $|\phi\rangle \equiv (\exp[-i\phi]|H\rangle + |V\rangle)/\sqrt{2}$ arrives to one detector, is implemented with a quarter- and a half-waveplate, before coupling into a polarization-maintaining fiber.

At the fiber output, the two polarization components are filtered with the two-polarization FADOF described in Sect. 7.2.3, in order to isolate the squeezed vacuum and block with high efficiency the hundreds of non-degenerate frequency modes generated by the OPO. The maximum transmission frequency of this filter is located

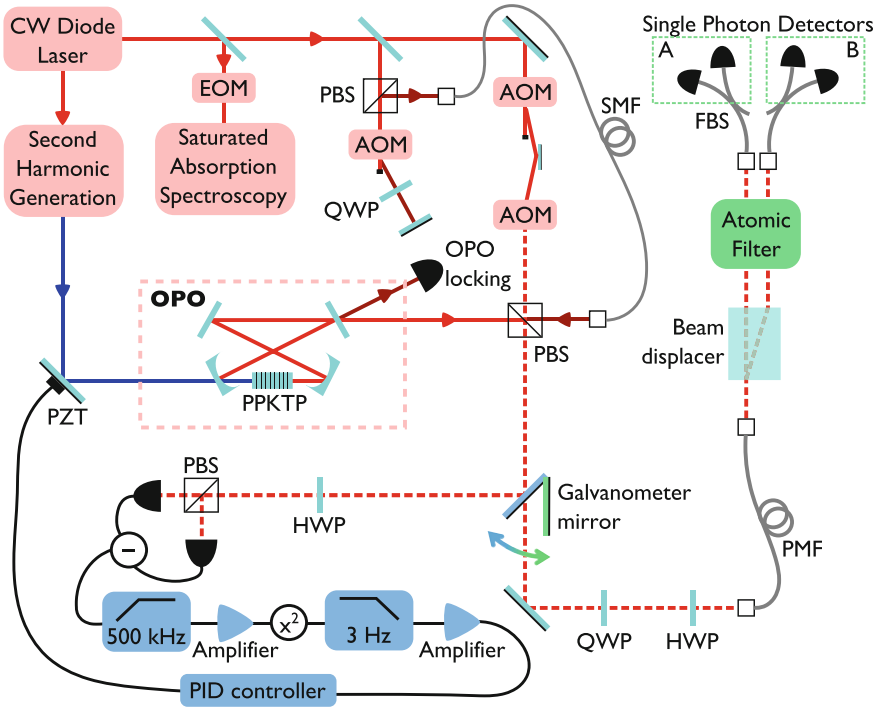

Fig. 7.6 Experimental setup. *AOM* (*EOM*) acousto- (electro-) optic Modulator. *PBS* polarizing beam splitter. *QWP* (*HWP*) quarter- (half-)wave plate. *PZT* piezoelectric actuator. *SMF* single mode fiber. *PMF* polarization maintaining fiber. *FBS* fiber beam splitter

at 2.7 GHz to the red of the center of the rubidium D_1 line, and the laser frequency is stabilized at this particular frequency by using an integrated electro-optic modulator to add sidebands to the laser prior to the saturated absorption spectroscopy.

The relative phase ϕ_{rel} between the coherent and the squeezed beam is stabilized by a quantum noise lock: One Stokes component is detected with a balanced polarimeter, and the noise power in a 3 Hz bandwidth above 500 kHz is computed analogically using a multiplier circuit. This signal is fed back by a servo loop to a piezo-electric actuator on a mirror in the pump path, to stabilize the pump phase by a side-of-fringe lock. A galvanometer mirror is used to switch between the single-photon counting and stabilization setups at a frequency of ∼100 Hz. The reference beam power is increased during the stabilization part of the cycle, to reach the shot-noise-limited regime optimal for detection of the squeezing and operation of the noise lock. Two cascaded AOMs, whose RF power is chopped synchronously with the galvanometer mirror, modulate the coherent reference beam power, so that it has high power when the light is entering the stabilization setup and low power when the photon counting part is active. The system can maintain a fixed ϕ_{rel} over several hours.

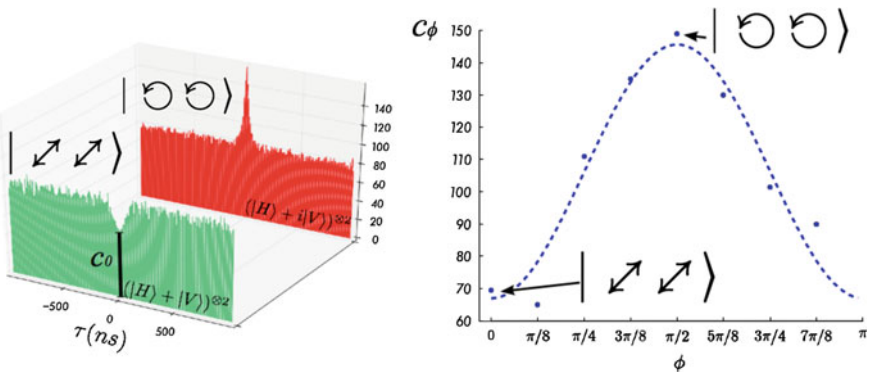

Fig. 7.7 Time-resolved interference of the two-photon amplitude from CESPDC against the two-photon amplitude from a coherent state. *Left* Arrival-time distribution, photon pair rate as a function of time difference τ, for photons pairs either both diagonally-polarized or both circularly-polarized. A τ-independent coherent state contribution interferes with a CESPDC contribution that has a double-exponential form centred on $\tau = 0$, with a FWHM width of 26 ns. As seen in the two histograms, the interference can be either constructive or destructive. *Right* Height of the interference peak versus the phase ϕ appearing in the two-photon state $(\exp[-i\phi]|H\rangle + |V\rangle)/\sqrt{2}$. As expected for a two-photon interference, and strikingly different from single-photon interference, the period of oscillation is π

Results are shown in Fig. 7.7, and clearly show both constructive and destructive interference of the two-photon wave-function against the coherent state.

7.2.5 Full Reconstruction of the Biphoton Wave-function

The form of (7.7) suggests a method to measure the two-photon wave-function, including not only its amplitude, but also its phase. If the term $\frac{\alpha^2}{2}\exp[2i\phi]$ is under our control, it should be possible by setting this term and measuring the resulting coincidence rates, to infer the complex value of $\psi(t, t')$. This idea was made precise in [22], and the above setup was used to reconstruct the biphoton wave-function shown in Fig. 7.8.

The results are consistent with a double-exponential amplitude with 26 ns full-width at half-maximum (FWHM), as expected for a squeezed vacuum state from an OPO with the 8.1 MHz FWHM bandwidth independently-measured on our system. The phase of $\psi_{VV}^{(\lambda)}$, consistent with a non-zero constant value, is reconstructed with a statistical uncertainty that decreases with increasing $|\psi_{VV}^{(\lambda)}|$, reaching $\sigma_\phi \approx \pm 6$ degree near $\tau = 0$. A constant phase is expected for an ideal OPO, while a phase defect could signal cavity or crystal imperfections [52, 53]. The phase offset is tunable via the side-of-fringe lock that sets the relative phase of the squeezed vacuum and reference, and is another indication of interference at the two-photon level.

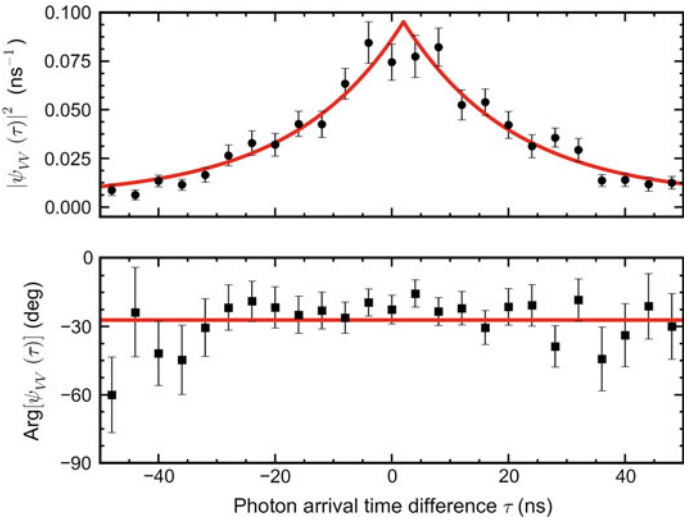

Fig. 7.8 Squared amplitude (*above*) and phase (*below*) of the reconstructed two-photon wave function for the squeezed vacuum state. The *solid line* shows the predicted, double exponential amplitude describing an ideal squeezed vacuum state from our OPO with an independently-measured 8.1 MHz bandwidth, with the amplitude and the offset fitted to the data. *Error bars* show $\pm 1\sigma$ statistical uncertainty assuming Poisson statistics

7.3 Generation of Spectrally-Pure, Atom-Resonant NooN States

In this section we describe a series of experiments to generate atom-tuned photon pairs from Type-II SPDC. Section 7.3.1 presents a motivation in terms of NooN states and their interest for quantum-enhanced sensing, Sect. 7.3.2 describes the SPDC source and characterization of the generated states, Sect. 7.3.3 describes the atomic filter, Sect. 7.3.4 describes measurements of the spectral purity achieved, and Sect. 7.3.5 describes the application of atom-tuned NooN states to quantum-enhanced sensing of magnetic fields using an atomic ensemble as a sensor.

7.3.1 NooN States

We now describe the generation of atom-tuned photon pairs of orthogonal polarization, with one photon H-polarized and one V-polarized, but indistinguishable in all other degrees of freedom. Such a state can be written

$$|\psi\rangle = a_H^\dagger a_V^\dagger |0\rangle = \frac{1}{2}\left(a_L^\dagger a_L^\dagger - a_R^\dagger a_R^\dagger\right)|0\rangle \tag{7.8}$$

where the circular polarization modes are defined by $a_L = (a_H + ia_V)/\sqrt{2}$, $a_R = (a_H - ia_V)/\sqrt{2}$. When written in terms of the photon numbers n_L, and n_R in the L, R modes respectively, and using the notation $|n_L, n_R\rangle_{L,R}$, this state is

$$|\psi\rangle = \frac{1}{\sqrt{2}}\left(|N,0\rangle_{L,R} + |0,N\rangle_{L,R}\right) \tag{7.9}$$

with $N = 2$, an example of a "NooN" state, named for the letters that appear in the kets $|\cdot\rangle$.

Consider a linear polarization interferometer that operates by Faraday rotation. This imposes a differential phase ϕ between the L and R parts of the state, transforming the NooN state as

$$\frac{1}{\sqrt{2}}\left(|N,0\rangle_{L,R} + |0,N\rangle_{L,R}\right) \rightarrow \frac{1}{\sqrt{2}}\left(|N,0\rangle_{L,R} + e^{iN\phi}|0,N\rangle_{L,R}\right). \tag{7.10}$$

Note that the phase acts N times on the second part of the state, because it contains N photons. This implies that any signal derived from this state must vary with $N\phi$, producing an N-fold acceleration of any interferometric signal. If we consider that ϕ is an unknown phase, this accelerated interference implies an N-fold increase in the Fisher information [54], allowing estimation of ϕ with uncertainty $\delta\phi = 1/N$, improving upon the standard quantum limit of $\delta\phi = 1/\sqrt{N}$, the best obtainable with non-entangled states.

A major motivation of this work is to test the suitability of entangled states for quantum enhanced sensing with atoms. In atomic media, interferometric phase shifts are necessarily accompanied by absorption, implying deposition of energy in the probed medium. Absorption also degrades any quantum advantage, as described by recent theory [55, 56]. To further complicate matters, in real media the phase shift and absorption may depend on the same unknown quantity. In a trade-off of rotation strength versus transparency, we employ a NooN state in a 7MHz spectral window detuned four Doppler widths from the nearest ^{85}Rb resonance. We generate this, as above, with a CESPDC source and an ultra-narrow atom-based filter.

7.3.2 Type-II CESPDC Source

As laser source we use a continuous-wave (CW) diode laser, stabilized to the D_1 transition of atomic rubidium at 795 nm and then frequency doubled to generate a 397.5 nm pump that is passed through a mode-cleaning single-mode fiber and then focused into the center of a 20 mm-long periodically-poled $KTiOPO_4$ (PPKTP) crystal in a cavity, forming the OPO (Fig. 7.9). A pump beam waist of 30 μm is achieved with a telescope. This beam waist was chosen to be larger than the optimum for degenerate down-conversion according to Boyd and Kleinman [57] in order to reduce possible effects of thermal lensing [58] and gray-tracking [59]. The crystal is

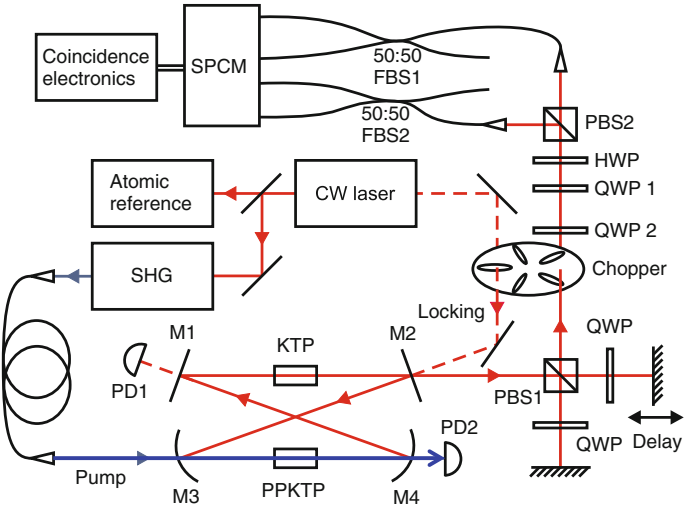

Fig. 7.9 Type-II CESPDC. *Source* PPKTP, phase-matched nonlinear crystal; *KTP* compensating crystal; *M1–M4* cavity mirrors; *PBS* polarizing beam splitter; *HWP* half wave plate; *QWP* quarter wave plate; *SMF* single-mode fiber; *PD* photodiode

poled for type-II degenerate down-conversion, and produces orthogonally-polarized signal and idler photons. Due to crystal birefringence, these photons experience temporal walk-off that would, if un-compensated, render the photons temporally distinguishable. A second, unpoled, KTP crystal of the same length and crystal cut, and rotated about the beam direction by 90°, is added to the long arm of the cavity in order to introduce a second walk-off equal in magnitude but opposite in sign [51].

The ring cavity is formed by two flat mirrors (M1, M2) and two concave mirrors (M3, M4) with a radius of curvature of 100 mm. The effective cavity length of 610 mm corresponds to a FSR of 490 MHz. This geometry provides a beam waist of 42 μm for the resonant down-converted beam at the center of the crystal, which matches the 30 μm pump beam waist. Cavity length is controlled by a piezoelectric transducer on mirror M1. The output coupler M2 has a reflectivity of 93 % at 795 nm. All other cavity mirrors are highly reflecting ($R > 99.9\,\%$) at 795 nm and highly transmitting at 397.5 nm ($R < 3\,\%$) resulting in a single-pass through the nonlinear crystal for the blue pump beam. The crystal end faces are AR coated for 397.5 and 795 nm. The measured cavity finesse of 70 results in a cavity linewidth of 7 MHz.

While the walk-off per round trip is compensated by the KTP crystal, there is an uncompensated walk-off of in average half a crystal-length, because of the different positions inside the PPKTP, at which a photon pair could be generated. This leads to a remaining temporal distinguishability at the output of the cavity that is completely removed by delaying the horizontally polarized photon of each pair with a Michelson-geometry compensator: a polarizing beam splitter, retro-reflecting mirrors, and quarter wave-plates set to 45° introduce an adjustable delay while

preserving spatial mode overlap. After recombination the pairs are sent through a half wave plate (HWP2) that together with PBS2 determines the measurement basis. Both output ports of PBS2 are coupled into single-mode fibers(SMF) connected to single photon counting modules (Perkin Elmer SPCM-AQ4C). The pulse events are registered and processed by coincidence electronics (FAST ComTec P7888) with a resolution of 1 ns.

The OPO cavity is actively stabilized by injecting an auxiliary beam, derived from the same diode laser, into the cavity via the output coupler (M2). This light is detected in transmission by a photodiode (PD1). Frequency modulation at 20 MHz, applied via the laser diode current, is used to lock to the peak of the cavity transmission. To eliminate the background noise caused by this auxiliary beam and to protect the SPCMs, the locking and measuring intervals are alternated using a mechanical chopper at a frequency of about 80 Hz with a duty cycle of 24 %.

A general polarization analyzer, consisting of a quarter wave plate (QWP1) followed by a half wave plate (HWP) and a polarizing beam splitter (PBS2) is used to determine the measurement basis as shown in Fig. 7.9. To generate a NOON state in the H/V basis another quarter wave plate (QWP2) can be added. The two output ports of PBS2 are coupled to single-mode fibers and split with 50:50 fiber beam splitters. The four outputs are connected to a set of single photon counting modules (Perkin Elmer SPCM-AQ4C). Time-stamping was performed by coincidence electronics with a resolution of 2 ns. By considering a time window of 150 ns, which is longer than the coherence time of each individual photon, we can evaluate the coincidences between any two of the four channels.

7.3.2.1 Characterization of the NooN State

Rotating the HWP before the detection setup allows us to demonstrate the greater resolution available with the NooN state, as shown in Fig. 7.10 (left). First, sending just a single polarization and detecting the rate of single-photon arrivals, we observe the expected oscillations with a period, in HWP angle, of 90°. Then, sending NooN states and detecting in coincidence, we observe a two-fold reduction in the oscillation period simultaneous with high visibility, due to the two-photon coherence of the NooN state. The sinusoidal fit function of the coincidences shows a visibility of 90 %.

The achieved high visibility of the state is the requirement for a high-fidelity NOON state. We introduce another quarter wave plate (QWP2) before the analyzing part of the setup to create a two-photon NOON state in the H/V basis, which can be written $1/\sqrt{2}(|H_1, H_2\rangle + e^{2i\phi}|V_1, V_2\rangle)$. Since the output state of the cavity $|HV\rangle$ is already a NOON state in the circular basis $|HV\rangle = i/\sqrt{2}(|L_1, L_2\rangle - |R_1, R_2\rangle)$, this state can be transferred into a NOON state in the H/V basis by sending it through an additional quarter wave plate at 45 degrees.

We also use quantum state tomography, as in [60], to measure the polarization density matrix of the NooN state [19]. In Fig. 7.10 (right) real and imaginary parts of the reconstructed density matrix of a NooN state are displayed. The coherence

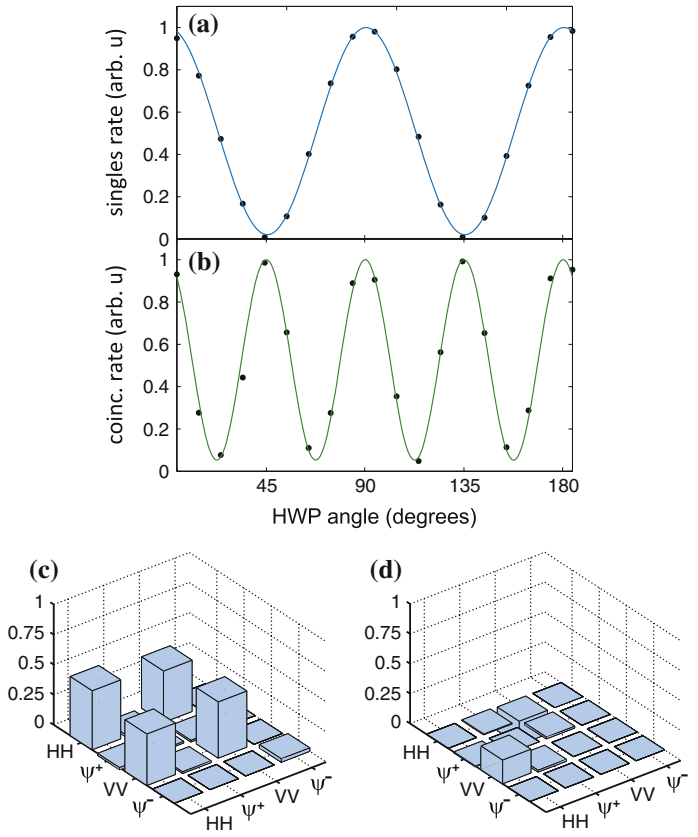

Fig. 7.10 Multi-photon interference and state characterization. *Left panels* Resolution of one- and two-photons states under rotations. **a** Single-photon rotation measurement showing ordinary oscillations with a period of 90° in the HWP angle. In this measurement only the H polarized part of the pair-photon state was sent to the analyzer. *Vertical axis* shows normalized singles rate at the transmitted port of PBS2. **b** High-visibility super-resolving phase measurement. Normalized coincidence detection between reflected and transmitted port of PBS2 for a NooN state input. The shorter period of the coincidence counts oscillations indicates super-resolution. *Right panels* Results of quantum state tomography to characterize the NooN state. **c** Real and **d** imaginary part of the polarization density matrix of the pair-photon state transformed to a two-photon NOON state in the H, V basis, showing a nearly equal superposition of $|HH\rangle$ and $|VV\rangle$

of the state is partly imaginary leading to a phase of $2\phi = 0.20$ between HH and VV components (Fig. 7.10(b)), which is however of no importance in the following. The fidelity of this state with the corresponding ideal two-photon NooN state $1/\sqrt{2}(|H_1, H_2\rangle + e^{2i\phi}|V_1, V_2\rangle)$ is 99 %, making the state suitable for applications such as phase estimation [6].

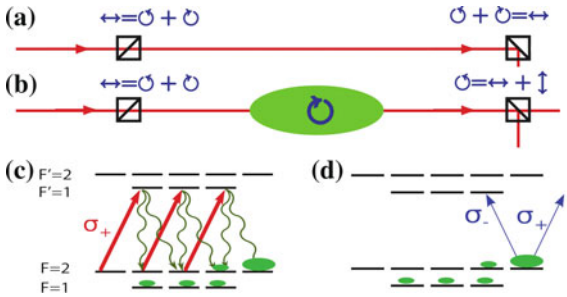

Fig. 7.11 Principle of the circular dichroism filter. **a** Non-resonant photons are blocked, either by the first or by the second PBS. **b** Resonant photons are linearly polarized after the first PBS, may become circularly polarized by interaction with the circularly dichroic atomic medium, and then have a chance of passing the second PBS. In this way, atom-resonant light can pass the filter. In the ideal case of a perfect circular absorber, the transmission would still only be 25 %. **c** optical pumping, shown here on the D_1 line, moves atomic population toward the states $F = 2, m_F = 2$ and $F = 2, m_F = 1$. **d** from these states, the atoms cannot absorb more σ_+ light on the $F = 2 \rightarrow F' = 1$ transition, creating a strong circular dichroism at this frequency

7.3.3 Induced Dichroism Atomic Filter

As with the Type-I OPO described earlier, only a small portion of the SPDC output of the Type-II OPO is atom-resonant, and a narrow-band filter is necessary to select this atom-resonant portion. We use an induced dichroism atomic filter (see Fig. 7.11), similar in several ways to the FADOF of Sect. 7.1.2, to separate the frequency-degenerate output of the CESPDC from the rest of the output. The filter, described in references [37, 38], has an 80 MHz FWHM passband centered on ω_{NooN} and $>$ 35 dB out-of-band rejection, so that only atom-tuned photons are detected. A representative spectrum is shown in Fig. 7.13.

As shown in Fig. 7.12 (right), a YVO_4 crystal separates horizontally and vertically polarized photons by 1 mm. The polarization modes travel parallel to each other through a hot rubidium cell of isotopically pure ^{87}Rb, optically pumped by a single-frequency laser resonant to the F=2→F'=3 transition of the D_2 line of ^{87}Rb (not shown). Due to Doppler shifts, the optical pumping only effects a portion of the thermal velocity distribution, and creates a circular dichroism with a sub-Doppler linewidth of about 80 MHz. A second YVO_4 crystal introduces a second relative displacement, which can re-combine or further separate the photons, depending on polarization. Separated photons are collected, while re-combined photons are blocked. A half wave plate is used to switch between the "active" configuration, in which only photons that change polarization in the cell are collected, and the "inactive" configuration, in which photons that do not change are collected. In the "active" configuration, the system acts as an "interaction-free measurement" detector for polarized atoms: a photon is collected only if it experiences a polarization change, i.e., if it is resonant with the optically pumped atoms, which absorb one circular component of the photon polarization state. The filter transmission is shown

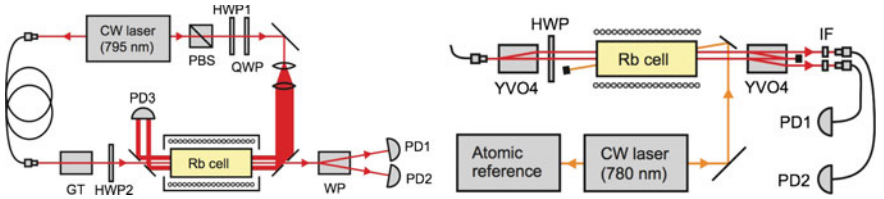

Fig. 7.12 Two arrangements for induced dichroism filtering. *Left* Pumping on the D_1 transition with geometric separation of the pump and probe beams, as in [37]. By combining the pump and probe beams using pierced mirrors, the pump beam propagates in a ring-shaped beam, coaxial with the probe beam, to achieve optical pumping of the atoms before they reach the probe beam, but without geometrical overlapping that beam. *Right* Pumping on the D_2 transition at 780 nm with overlapped beams, as in [38]. The wavelength difference between the pump and probe allows pump light to be filtered using commercial interference filters (*IF*), and the use of YVO_4 walkoff crystals as polarizers allows both polarizations to be filtered and collected. In both arrangements, the pump and probe are counter-propagating, giving rise to sub-Doppler resonances

in Fig. 7.13. Neighboring modes of the degenerate mode at the rubidium transition are already 490 MHz detuned and therefore outside of the filter linewidth of 80 MHz. The out-of-band extinction ratio is $\geq$35 dB. The filter transmission is optimized by adjusting the overlap between pump and single-photon mode, the rubidium vapor temperature and the magnitude of a small orienting applied magnetic field. The temperature is set to 65 °C, which corresponds to an atomic density of 5×10^{11} cm^{-3}. The measured filter transmission of 10.0 % for horizontal polarization and 9.5 % for vertical polarization is limited by pump power and in principle can reach 25 % [37].

To avoid contamination of the single-photon mode by scattered pump light, the pump enters the vapor cell at a small angle and counter-propagating to the single-photon mode. Interference filters centered on 795 nm further reject the 780 nm pump light with an extinction ratio of $>10^5$. The measured contribution from pump photons is below the detectors' dark count rate. Each output is coupled into single-mode fiber.

7.3.4 Spectral Purity Measurement

The CESPDC source, shown in Fig. 7.9, was filtered using the geometry of Fig. 7.12 (right), to produce in-principle spectrally pure photon pairs. The geometry of the filter and detection setup are shown in Fig. 7.14 (left). To test the spectral purity, one photon was detected as a herald, and the other subjected to further spectral filtering using a cell of Rb vapor. The cell could be maintained at room temperature, causing little absorption, or at a high temperature, in which case it efficiently blocked resonant photons. Figure 7.14 (right) shows the results: with the cold blocking cell, a double-exponental arrival-time distribution is observed, as expected. When the blocking cell is heated, the coincidences drop to the dark-count level. We estimate the fraction of atom-resonant photons among the heralded single photons is at least 94 % [38].

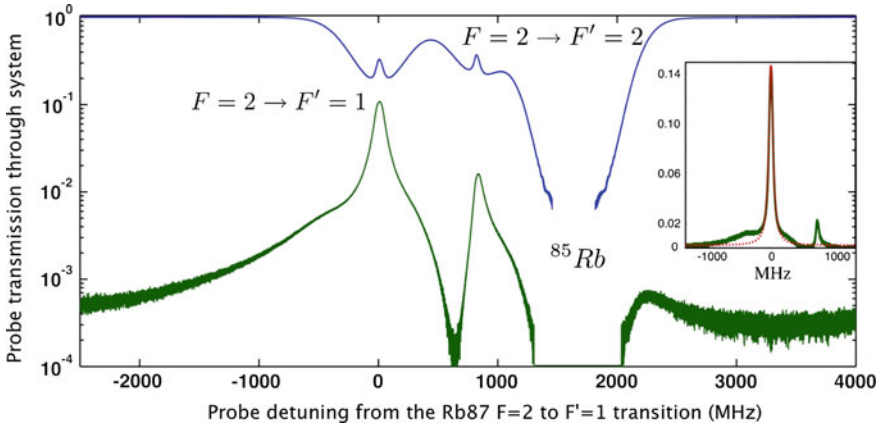

Fig. 7.13 Transmission of the circular dichroism filter, obtained with the configuration of Fig. 7.12 (*left*). Blank areas around 1500 MHz indicate regions where the transmission was unmeasurably low, due to the strong extinction of the ^{85}Rb transition

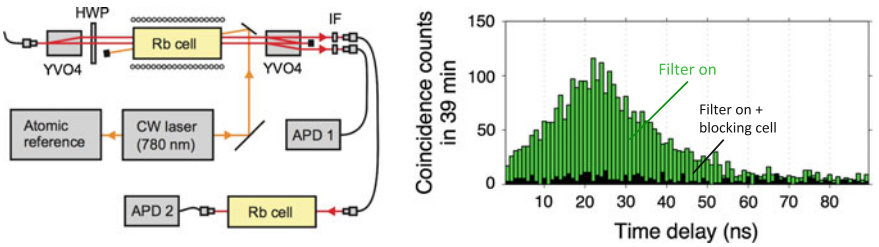

Fig. 7.14 Induced dichroism filter spectral purity measurement. *Left* Schematic of the setup. *Right* Arrival-time correlations with the second vapor cell cold (*green*) and hot (*black*). When the second vapor cell is hot, it blocks the output to the dark count level of the detectors, implying at least 94 % atom-resonant photons

7.3.5 Quantum-Enhanced Sensing of Atoms Using Atom-Tuned NooN States

We now apply the atom-tuned NooN states for sensing of Faraday rotation in a hot atomic ensemble. Because the Faraday rotation is a resonant phenomenon, it is essential to have near-resonant photons for this purpose. We use a ^{85}Rb atomic spin ensemble, similar to ensembles used for optical quantum memories [61] and quantum-enhanced atom interferometry [15, 16, 62]. Non-destructive dispersive measurements on these systems, used for storage and readout of quantum information or to produce spin squeezing, are fundamentally limited by scattering-induced depolarization [14, 61, 63, 64]. This provides an experimentally-grounded motivation for the idea that the number of probe photons is a limiting resource when

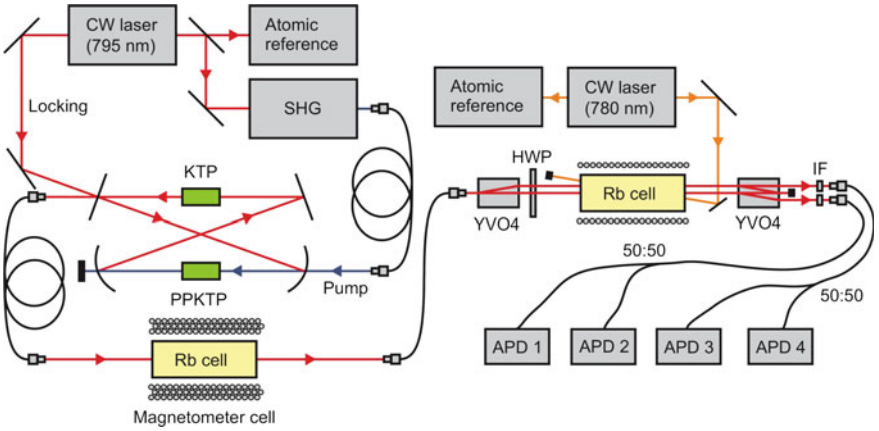

Fig. 7.15 Schematic of the setup for probing of an atomic magnetometer with atom-resonant NooN states. Photon pairs are generated by CESPDC as in Fig. 7.9, passed through a heated cell containing isotopically-enriched ^{85}Rb and immersed in a longitudinal magnetic field, filtered as in Fig. 7.12 (right), and detected with a pair of Hanbury-Brown and Twiss setups. The three possible coincidence outcomes: *HH*, *HV*, and *VV* can then be monitored as a function of the applied B field

measuring this system; the number of probe photons cannot be increased without increasing the damage to the spin ensemble.

The setup is shown schematically in Fig. 7.15. Narrowband NooN states at ω_{NooN}, the optical frequency of the $5^2\mathrm{S}_{1/2}\mathrm{F}{=}2 \rightarrow 5^2\mathrm{P}_{1/2}\mathrm{F}'{=}1$ transition of the D_1 line of ^{87}Rb, are generated by CESPDC, as described above, and sent through the ensemble. The ensemble of ^{85}Rb atoms is contained in an anti-reflection coated vapor cell with internal length $L = 75$ mm, in a temperature-controlled oven at 70° C, together with a 0.5 % residual ^{87}Rb component. An applied axial magnetic field B of up to 60 mT produces resonantly-enhanced Faraday rotation of the optical polarization. After leaving the vapor cell, the photons are separated in polarization, frequency filtered, and detected with single-photon counters. Two counters on each polarization output record all possible outcomes, i.e., coincidences of HH, HV, and VV polarizations.

7.3.5.1 Physics of Near-Resonant Faraday Rotation

The cell, with an internal path of 75 mm and containing purified ^{85}Rb with a small (0.5%) admixture of ^{87}Rb, no buffer gas, and no wall coatings that might preserve polarization, is modeled as a thermal equilibrium, Doppler-broadened vapor subject to Zeeman shifts in the intermediate regime. The atomic structure is calculated by diagonalization of the atomic Hamiltonians $H_{\mathrm{At}}^{(\mathrm{iso})} = H_0^{(\mathrm{iso})} + H_{\mathrm{HFS}}^{(\mathrm{iso})} + H_{\mathrm{Z}}^{(\mathrm{iso})}$, where $H_0^{(\mathrm{iso})}$ is the energy structure of the isotope $^{\mathrm{iso}}$Rb including fine-structure contribution, $H_{\mathrm{HFS}}^{(\mathrm{iso})} = g_{\mathrm{HFS}}\mathbf{J}\cdot\mathbf{I}$ is the hyperfine contribution, and $H_{\mathrm{Z}}^{(\mathrm{iso})} = \mathbf{b}\cdot(g_J\mathbf{J} + g_I\mathbf{I})$ is the Zeeman contribution. All atomic parameters are taken from references [65, 66].

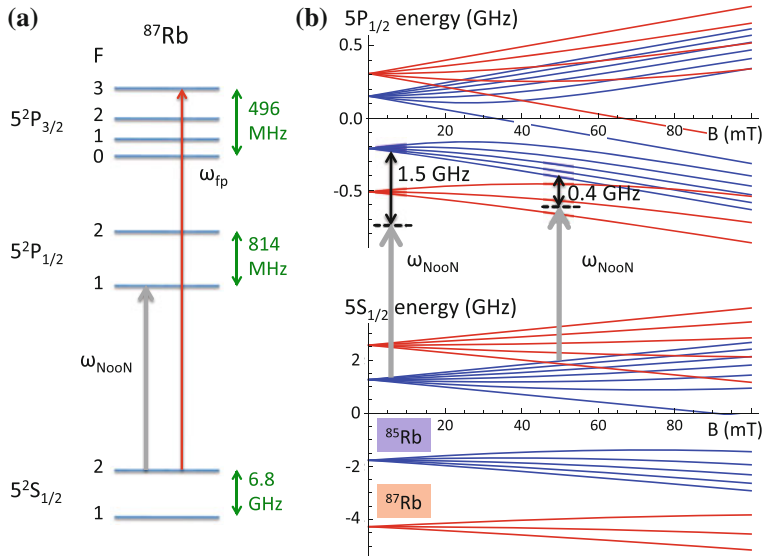

Fig. 7.16 Energy level diagrams relevant to Faraday rotation on the D_1 line of Rb. **a** Energy levels of ^{87}Rb relevant to generation and filtering (not to scale). The frequency of the NooN state ω_{NooN} is tuned to the $5^2S_{1/2}F = 2 \rightarrow 5^2P_{1/2}F' = 1$ transition of the D_1 line of ^{87}Rb. The optical pumping laser of the filter, with frequency ω_{fp}, addresses the $5^2S_{1/2}F = 2 \rightarrow 5^2P_{3/2}F' = 3$ transition of the D_2 line of ^{87}Rb. The 15 nm separation from the detection wavelength allows a high extinction using interference filters centered on ω_{NooN}. **b** D_1 energy levels of the probed ensemble versus field strength B, showing ^{85}Rb levels in blue and ^{87}Rb levels in red. At zero field ω_{NooN} is 1.5 GHz detuned from the nearest ^{85}Rb transition. With increasing B, the nearest ^{85}Rb transition moves closer to resonance, increasing the Faraday rotation. The Doppler-broadened absorption begins to overlap ω_{NooN} near $B = 50$ mT

The matrices $H_{\mathrm{At}}^{(\mathrm{iso})}$ are numerically diagonalized to find field-dependent energy eigenstates, illustrated in Fig. 7.16, from which the complex linear optical polarizability is calculated, including radiative damping. The complex refractive index $n_{\pm}$ for $\sigma_{\pm}$ polarizations is computed including Doppler broadening and a temperature-dependent atom density given by the vapor pressure times the isotope fraction, and the transfer function for the cell is calculated from the integral of the index along the beam path, including the measured drop in field strength of 15 % from the center to the faces of the cell. Transmission spectroscopy, shown in Fig. 7.17, agrees well with theory.

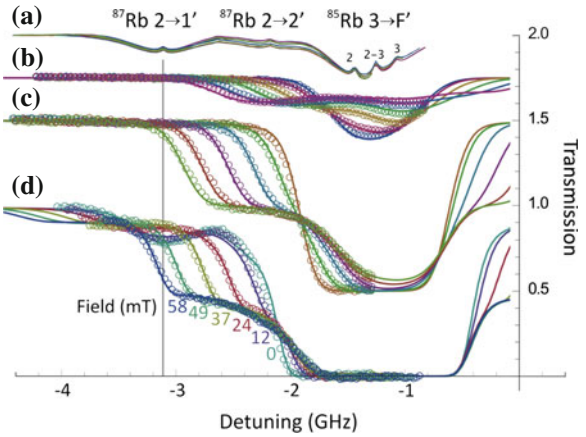

Fig. 7.17 Spectroscopic characterization of the rubidium atomic ensemble. *Circles* show measured values, *curves* show predictions of first-principles model (see text). **a** Saturated-absorption spectra acquired with a natural-abundance cell at room temperature, as a frequency reference. *Horizontal axis* shows detuning from the center of the D_1 spectral line. **b–d** Transmission spectra for the cell containing ^{85}Rb plus 0.5 % ^{87}Rb at temperatures of 22°C, 53°C and 83°C, respectively. For each temperature, spectra with measured field strengths (in mT) of 0, 12, 24, 37, 49, and 58 are shown, in order of increasing line broadening. *Grey vertical line* shows ω_{NooN}, the probe detuning. This operating point gives strong Faraday rotation with low absorption over the range 0–49 mT. Absorption from the small residual ^{87}Rb component can be seen in **d**. For clarity, parts **a–c** have been offset vertically by 1, 0.75, and 0.5, respectively

Figures 7.16 and 7.17 illustrate the optical physics of this magneto-optic rotation: The probe photons are red detuned from the ^{85}Rb transitions, and experience the same positive contribution to the refractive index at zero field. When the B-field is applied, however, the nearby ^{85}Rb $F = 3 \rightarrow F'$ transitions split, with the now circularly-polarized transitions moving closer or farther from the probe frequency in function of their polarization. This provides a growing refractive index contribution for one circular polarization, and a decreasing contribution for the other, i.e. a circular birefringence giving rise to polarization rotation. Due to the proximity to resonance, the rotation angle increases non-linearly with B until at around B = 50 mT the ^{85}Rb $F = 3 \rightarrow F'$ lines begin to overlap with the probe frequency and significant absorption begins.

7.3.5.2 Faraday Rotation Signals with Atom-Tuned NooN States

As seen in Fig. 7.18, all coincidence outcomes oscillate as a function of B, with two-fold super-resolution relative to the single-photon oscillation, visible in the singles counts due to a small imbalance between H and V in the input state. The interference visibilities are all $\geq$ 90%, well above the 33 % classical limit for HH and VV visibility [67]. Also shown are predicted coincidence rates [23], which show good agreement.

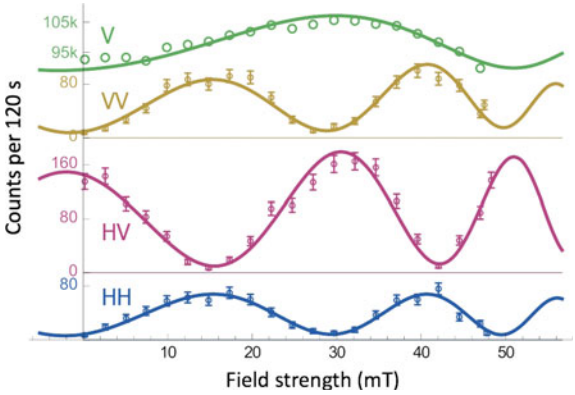

Fig. 7.18 High-visibility super-resolving Faraday rotation probing using optical NooN states. *Top curve* for phase reference, singles detection rate (V polarization) versus field strength B shows one oscillation in the range $B = 0$ to 50 mT. *Other curves* coincidence detections HH, HV, and VV show two oscillations in the same range (super-resolution) and high visibility. *Symbols* show measured data (no background subtracted), with $\pm 1\sigma$ statistical uncertainties. *Curves* show predicted coincidence rates using a first-principles atomic susceptibility calculation illustrated in Fig. 7.16 with a NooN state ρ found by quantum state tomography

An analysis of the Fisher information from these coincidence rates confirm the utility of entangled states for probing atomic ensembles. The NooN state achieves a factor 1.30 ± 0.05 more Fisher information per photon than the standard quantum limit (SQL). i.e. it gives more information per photon than can be extracted using any state consisting of non-entangled photons. It achieves this advantage at a field of $B = 37$ mT, near the point at which absorption begins to become important. Perhaps more important to eventual application, the NooN state gives also an advantage in Fisher information per scattered photon, the figure of merit for low-damage probing. As described in [23] the NooN state gives an advantage of 1.40 ± 0.06 over the SQL.

Among other things, this exercise uncovered a previously unknown feature of quantum-enhanced sensing in imperfect interferometers, in this case those with losses. Here, as one can expect for most interferometric measurements on material systems, the loss depends on the measured quantity (here B). This dependence makes a positive contribution to the Fisher information, offsetting the well-known [68] reduction of Fisher information due to loss of photons.

7.4 Conclusions

We have described two experimental projects to generate high- spectral purity indistinguishable photon pairs using cavity-enhanced SPDC and extremely narrowband optical filters based on resonant optical effects in atomic ensembles. Combining these techniques, we have demonstrated bright sources of entangled photons pairs,

with both high two-photon coherence, for example 99 % fidelity with a two-photon NooN state, and high spectral purity, $\geq 94\,\%$ atom-resonant heralded single photons for a type-II source and $\geq 98\,\%$ atom resonant photon pairs for a type-I source. The potential for interaction with atoms is clearly shown by the generation and use of atom-tuned NooN states to beat the standard quantum limit in non-destructive probing of an atomic magnetometer. As this work goes forward, it will be interesting to see how indistinguishable photon pairs can interact with other atomic systems, for example atomic quantum memories and atomic quantum information processors.

Acknowledgments The work reported here involved many people over many years. I would especially like to thank Marta Abad, Federica Beduini, Alessandro Cerè, Nicolas Godbout, Valentina Parigi, Ana Predojević, Chiara Vitelli, Florian Wolfgramm, Xinxing Xing, and Joanna Zielińska, each of whom contributed something unique and essential to the work reported here, e.g. inventing a first-of-its-kind source or filter, providing insights into the physics of atomic optical instruments, or persuading difficult lasers (and their suppliers) to cooperate with our plans. Aephraim Steinberg was essential to getting the photon pair research started. The contributions of Zehui Zhai, Yannick de Icaza Astiz and Gianvito Lucivero are also much appreciated. The research was supported by various Catalan, Spanish, European, Canadian and philanthropic grants over the years. The writing of this chapter was supported by the Spanish MINECO project MAGO (Refer FIS2011-23520), by the European Research Council project AQUMET, and by Fundació Privada CELLEX.

Appendix: Second-Order Correlation Functions of Filtered Output

In this section we consider the second order correlation function of the field operators a_{out} in a form:

$$G^{(2)}(T) \propto \langle a^{\dagger}_{\text{out}}(t) a^{\dagger}_{\text{out}}(t+T) a_{\text{out}}(t+T) a_{\text{out}}(t) \rangle \tag{7.11}$$

for multimode (unfiltered) and single-mode (filtered) output of the OPO.

As shown by Lu et al. [69], $G^{(2)}(T)$ describing the output of a single-mode, far-below-threshold OPO has the form of double exponential decay

$$G^{(2)}_{\text{single}}(T) \propto e^{-|T|(\gamma_1+\gamma_2)}, \tag{7.12}$$

where the reflectivity of the output coupler is $r_1 = \exp[-\gamma_1 \tau]$, the effective reflectivity resulting from intracavity losses is $r_2 = \exp[-\gamma_2 \tau]$ and τ is the cavity round-trip time. An ideal narrowband filter would remove all the nondegenerate cavity-enhanced spontaneous down-conversion CESPDC modes, reducing the $G^{(2)}(T)$ to $G^{(2)}_{\text{single}}(T)$. This filtering effect was demonstrated in [38] for a type-II OPO and an induced dichroism atomic filter.

In [69] it is also predicted that when the filter is off, so that the output consists of N cavity modes, $G^{(2)}(T)$ takes the form

$$G^{(2)}_{\text{multi}}(T) \propto G^{(2)}_{\text{single}}(T)\frac{\sin^2[(2N+1)\pi T/\tau]}{(2N+1)\sin^2[\pi T/\tau]} \tag{7.13}$$

$$\approx G^{(2)}_{\text{single}}(T)\sum_{n=-\infty}^{\infty}\delta(T-n\tau), \tag{7.14}$$

i.e., with the same double exponential decay but modulated by a comb with a period equal to the cavity round-trip time τ. In our case the bandwidth of the output contains more than 200 cavity modes, and the fraction in (7.13) is well approximated by a comb of Dirac delta functions.

The comb period of $\tau = 1.99$ ns is comparable to the $t_{\text{bin}} = 1$ ns resolution of our counting electronics, a digital time-of-flight counter (Fast ComTec P7888). This counter assigns arrival times to the signal and idler arrivals relative to an internal clock. We take the "window function" for the ith bin, i.e., the probability of an arrival at time T being assigned to that bin, to be

$$f^{(i)}(T) = \begin{cases} 1, & \text{if } T \in [it_{bin}, (i+1)t_{bin}]\,, \\ 0, & \text{otherwise}\,. \end{cases} \tag{7.15}$$

Without loss of generality we assign the signal photon's bin as $i = 0$, and we include an unknown relative delay T_0 between signal and idler due to path length, electronics, cabling, and so forth. For a given signal arrival time t_s, the rate of idler arrivals in the ith bin is $\int dt_i\, f^{(i)}(t_i)G^{(2)}_{\text{multi}}(t_i - t_s - T_0)$ (t_i is the idler arrival time). This expression must be averaged over the possible t_s within bin $i = 0$. We also include the "accidental" coincidence rate $G^{(2)}_{\text{acc}} = t_{\text{bin}}R_1R_2$, where R_1, R_2 are the singles detection rates at detectors 1, 2, respectively. The rate at which coincidence events are registered with i bins of separation is then

$$G^{(2)}_{\text{multi,det}}(i) = \frac{1}{t_{\text{bin}}}\int dt_s\, f^{(0)}(t_s)\int dt_i\, f^{(i)}(t_i)G^{(2)}_{\text{multi}}(t_i - t_s - T_0) + G^{(2)}_{\text{acc}} \tag{7.16}$$

$$= \sum_{n=-\infty}^{\infty} G^{(2)}_{\text{single}}(n\tau)\frac{1}{t_{\text{bin}}}\int_0^{t_{\text{bin}}} dt_s\, f^{(i)}(t_s + T_0 + n\tau) + G^{(2)}_{\text{acc}}. \tag{7.17}$$

We take T_0 is a free parameter in fitting to the data. Note that if we write $T_0 = kt_{\text{bin}} + \delta$ then the simultaneous events fall into kth bin and $\delta \in [-t_{\text{bin}}/2, t_{\text{bin}}/2]$ determines where the histogram has the maximum visibility due to the beating between the 1 ns sampling frequency of the detection system and the 1.99 ns comb period. APD time resolution is estimated to be 350 ps FWHM (manufacturer's specification), i.e. significantly less than the TOF uncertainty, and is not included here.

References

1. Y.H. Shih, C.O. Alley, New type of Einstein-Podolsky-Rosen-Bohm experiment using pairs of light quanta produced by optical parametric down conversion. Phys. Rev. Lett. **61**, 2921–2924 (1988). doi:10.1103/PhysRevLett.61.2921
2. C.K. Hong, Z.Y. Ou, L. Mandel, Measurement of subpicosecond time intervals between two photons by interference. Phys. Rev. Lett. **59**, 2044–2046 (1987). doi:10.1103/PhysRevLett.59.2044
3. D. Bouwmeester et al., Experimental quantum teleportation. Nature **390**, 575–579 (1997). doi:10.1038/37539
4. J.-W. Pan, D. Bouwmeester, H. Weinfurter, A. Zeilinger, Experimental entanglement swapping: entangling photons that never interacted. Phys. Rev. Lett. **80**, 3891–3894 (1998)
5. J.L. O'Brien, G.J. Pryde, A.G. White, T.C. Ralph, D. Branning, Demonstration of an all-optical quantum controlled-not gate. Nature **426**, 264–267 (2003). doi:10.1038/nature02054
6. M.W. Mitchell, J.S. Lundeen, A.M. Steinberg, Super-resolving phase measurements with a multiphoton entangled state. Nature **429**, 161–164 (2004). doi:10.1038/nature02493
7. S. Aaronson, A. Arkhipov. *The Computational Complexity of Linear Optics* (2010)
8. L.-A. Wu, H.J. Kimble, J.L. Hall, H. Wu, Generation of squeezed states by parametric down conversion. Phys. Rev. Lett. **57**, 2520–2523 (1986). doi:10.1103/PhysRevLett.57.2520
9. The LIGO Scientific Collaboration. A gravitational wave observatory operating beyond the quantum shot-noise limit. Nat. Phys. **7**, 962–965 (2011). doi:10.1038/nphys2083
10. J. Aasi et al., Enhanced sensitivity of the ligo gravitational wave detector by using squeezed states of light. Nat. Photon. **7**, 613–619 (2013). doi:10.1038/nphoton.2013.177
11. S. Braunstein, A. Pati, *Quantum Information with Continuous Variables* (Springer, New York, 2010)
12. F. Wolfgramm et al., Squeezed-light optical magnetometry. Phys. Rev. Lett. **105**, 053601 (2010). doi:10.1103/PhysRevLett.105.053601
13. M. Koschorreck, M. Napolitano, B. Dubost, M.W. Mitchell, Sub-projection-noise sensitivity in broadband atomic magnetometry. Phys. Rev. Lett. **104**, 093602 (2010). doi:10.1103/PhysRevLett.104.093602
14. M. Koschorreck, M. Napolitano, B. Dubost, M.W. Mitchell, Quantum nondemolition measurement of large-spin ensembles by dynamical decoupling. Phys. Rev. Lett. **105**, 093602 (2010). doi:10.1103/PhysRevLett.105.093602
15. R.J. Sewell et al., Magnetic sensitivity beyond the projection noise limit by spin squeezing. Phys. Rev. Lett. **109**, 253605 (2012). doi:10.1103/PhysRevLett.109.253605
16. R.J. Sewell et al., Ultrasensitive atomic spin measurements with a nonlinear interferometer. Phys. Rev. X **4**, 021045 (2014). doi:10.1103/PhysRevX.4.021045
17. A. Predojević, Z. Zhai, J.M. Caballero, M.W. Mitchell, Rubidium resonant squeezed light from a diode-pumped optical-parametric oscillator. Phys. Rev. A **78**, 063820 (2008). doi:10.1103/PhysRevA.78.063820
18. F. Wolfgramm et al., Bright filter-free source of indistinguishable photon pairs. Opt. Express **16**, 18145–18151 (2008). doi:10.1364/OE.16.018145
19. F. Wolfgramm, A. Cerè, M.W. Mitchell, Noon states from cavity-enhanced down-conversion: high quality and super-resolution. J. Opt. Soc. Am. B **27**, A25–A29 (2010). doi:10.1364/JOSAB.27.000A25
20. J.A. Zielińska, F.A. Beduini, V.G. Lucivero, M.W. Mitchell, Atomic filtering for hybrid continuous-variable/discrete-variable quantum optics. Opt. Express **22**, 25307–25317 (2014). doi:10.1364/OE.22.025307
21. J.A. Zielińska, F.A. Beduini, N. Godbout, M.W. Mitchell, Ultranarrow Faraday rotation filter at the Rb D_1 line. Opt. Lett. **37**, 524–526 (2012). doi:10.1364/OL.37.000524
22. F.A. Beduini, J.A. Zielińska, V.G. Lucivero, Y.A. de Icaza Astiz, M.W. Mitchell, Interferometric measurement of the biphoton wave function. Phys. Rev. Lett. **113**, 183602 (2014). doi:10.1103/PhysRevLett.113.183602

23. F. Wolfgramm, C. Vitelli, F.A. Beduini, N. Godbout, M.W. Mitchell, Entanglement-enhanced probing of a delicate material system. Nat. Photon. **7**, 28–32 (2013). doi:10.1038/nphoton.2012.300
24. Z.Y. Ou, Y.J. Lu, Cavity enhanced spontaneous parametric down-conversion for the prolongation of correlation time between conjugate photons. Phys. Rev. Lett. **8**, 2556–2559 (1999). doi:10.1103/PhysRevLett.83.2556
25. Y. Öhman, On some new auxiliary instruments in astrophysical research VI. A tentative monochromator for solar work based on the principle of selective magnetic rotation. Stockholms Obs. Ann. **19**, 9–11 (1956)
26. J.S. Neergaard-Nielsen, B.M. Nielsen, H. Takahashi, A.I. Vistnes, E.S. Polzik, High purity bright single photon source. Opt. Express **15**, 7940–7949 (2007). doi:10.1364/OE.15.007940
27. A. Haase, N. Piro, J. Eschner, M.W. Mitchell, Tunable narrowband entangled photon pair source for resonant single-photon single-atom interaction. Opt. Lett. **34**, 55–57 (2009). doi:10.1364/OL.34.000055
28. P. Palittapongarnpim, A. MacRae, A.I. Lvovsky, Note: a monolithic filter cavity for experiments in quantum optics. Rev.Sci. Instrum. **83**, 066101 (2012). doi:10.1063/1.4726458
29. J.A. Zielińska, M.W. Mitchell, *Theory of high gain cavity-enhanced spontaneous parametric down-conversion* (2014)
30. X. Yang, S. Li, C. Zhang, H. Wang, Enhanced cross-kerr nonlinearity via electromagnetically induced transparency in a four-level tripod atomic system. J. Opt. Soc. Am. B **26**, 1423–1424 (2009). doi:10.1364/JOSAB.26.001423
31. R.M. Camacho, P.K. Vudyasetu, J.C. Howell, Four-wave-mixing stopped light in hot atomic rubidium vapour. Nat. Photon. **3**, 103–106 (2009). doi:10.1038/nphoton.2008.290
32. V.I. Yudin et al., Vector magnetometry based on electromagnetically induced transparency in linearly polarized light. Phys. Rev. A **82**, 033807 (2010). doi:10.1103/PhysRevA.82.033807
33. W.F. Krupke, R.J. Beach, V.K. Kanz, S.A. Payne, Resonance transition 795-nm rubidium laser. Opt. Lett. **28**, 2336–2338 (2003). doi:10.1364/OL.28.002336
34. J. Ries, B. Brezger, A.I. Lvovsky, Experimental vacuum squeezing in rubidium vapor via self-rotation. Phys. Rev. A **68**, 025801 (2003). doi:10.1103/PhysRevA.68.025801
35. I.H. Agha, G. Messin, P. Grangier, Generation of pulsed and continuous-wave squeezed light with ^{87}Rb vapor. Opt. Express **18**, 4198–4205 (2010). doi:10.1364/OE.18.004198
36. M. Hosseini, G. Campbell, B.M. Sparkes, P.K. Lam, B.C. Buchler, Unconditional room-temperature quantum memory. Nat. Phys. **7**, 794–798 (2011). doi:10.1038/nphys2021
37. A. Cere et al., Narrowband tunable filter based on velocity-selective optical pumping in an atomic vapor. Opt. Lett. **34**, 1012–1014 (2009). doi:10.1364/OL.34.001012
38. F. Wolfgramm, Y.A. de Icaza Astiz, F.A. Beduini, A. Cerè, M.W. Mitchell, Atom-resonant heralded single photons by interaction-free measurement. Phys. Rev. Lett. **106**, 053602 (2011). doi:10.1103/PhysRevLett.106.053602
39. I. Gerhardt, Software—sodium data. Available at http://gerhardt.ch/sodium.php
40. W. Kiefer, R. Low, J. Wrachtrup, I. Gerhardt, Na-Faraday rotation filtering: the optimal point. Sci. Rep. **4**, 6552 (2014). doi:10.1038/srep06552
41. M.A. Zentile et al., Elecsus: A program to calculate the electric susceptibility of an atomic ensemble. Comput. Phys. Commun. **189**, 162–174 (2015). doi:10.1016/j.cpc.2014.11.023
42. J. Menders, K. Benson, S.H. Bloom, C.S. Liu, E. Korevaar, Ultranarrow line filtering using a cs faraday filter at 852 nm. Opt. Lett. **16**, 846–848 (1991). doi:10.1364/OL.16.000846
43. B. Yin, T. Shay, Faraday anomalous dispersion optical filter for the Cs 455 nm transition. Photon. Technol. Lett. IEEE **4**, 488–490 (1992). doi:10.1109/68.136496
44. Y. Wang, Cs faraday optical filter with a single transmission peak resonant with the atomic transition at 455 nm. Opt. Express **20**, 25817–25825 (2012). doi:10.1364/OE.20.025817
45. B. Yin, L.S. Alvarez, T.M. Shay, *The rb 780-nanometer faraday anomalous dispersion optical filter: Theory and experiment* (Technical report, Jet Propulsion Laboratory, 1994)
46. D.J. Dick, T.M. Shay, Ultrahigh-noise rejection optical filter. Opt. Lett. **16**, 867–869 (1991). doi:10.1364/OL.16.000867

47. L. Ling, G. Bi, Isotope ^{87}Rb Faraday anomalous dispersion optical filter at 420 nm. Opt. Lett. **39**, 3324–3327 (2014). doi:10.1364/OL.39.003324
48. B. Yin, T. Shay, A potassium Faraday anomalous dispersion optical filter. Opt. Commun. **94**, 30–32 (1992). doi:10.1016/0030-4018(92)90400-L
49. H. Chen, C.Y. She, P. Searcy, E. Korevaar, Sodium-vapor dispersive faraday filter. Opt. Lett. **18**, 1019–1021 (1993). doi:10.1364/OL.18.001019
50. Y.C. Chan, J.A. Gelbwachs, Fraunhofer-wavelength magnetooptic atomic filter at 422.7 nm. IEEE J. Quantum Electron. **29**, 2379–2384 (1993). doi:10.1109/3.245569
51. C.E. Kuklewicz, F.N.C. Wong, J.H. Shapiro, Time-bin-modulated biphotons from cavity-enhanced down-conversion. Phys. Rev. Lett. **97**, 223601 (2006). doi:10.1103/PhysRevLett.97.223601
52. O. Kuzucu, F.N.C. Wong, Pulsed sagnac source of narrow-band polarization-entangled photons. Phys. Rev. A **77**, 032314 (2008). doi:10.1103/PhysRevA.77.032314
53. K.A. O'Donnell, A.B. U'Ren, Time-resolved up-conversion of entangled photon pairs. Phys. Rev. Lett. **103**, 123602 (2009). doi:10.1103/PhysRevLett.103.123602
54. L. Pezzè, A. Smerzi, Quantum theory of phase estimation, in *Proceedings of the International School of Physics "Enrico Fermi"*, ed. by G.M. Tino, M.A. Kasevich (IOS Press, Amsterdam, 2014), pp. 691–741
55. U. Dorner et al., Optimal quantum phase estimation. Phys. Rev. Lett. **102**, 040403 (2009). doi:10.1103/PhysRevLett.102.040403
56. B.M. Escher, R.L. de Matos Filho, L. Davidovich, General framework for estimating the ultimate precision limit in noisy quantum-enhanced metrology. Nat. Phys. **7**, 406–411 (2011). doi:10.1038/nphys1958
57. G.D. Boyd, D.A. Kleinman, Parametric interaction of focused gaussian light beams. J. Appl. Phys. **39**, 3597–3639 (1968). doi:10.1063/1.1656831
58. R.L. Targat, J.-J. Zondy, P. Lemonde, 75%-efficiency blue generation from an intracavity PPKTP frequency doubler. Opt. Commun. **247**, 471–481 (2005). doi:10.1016/j.optcom.2004.11.081
59. B. Boulanger, M.M. Fejer, R. Blachman, P.F. Bordui, Study of $KTiOPO_4$ graytracking at 1064, 532, and 355 nm. Appl. Phys. Lett. **65**, 2401–2403 (1994). doi:10.1063/1.112688
60. R.B.A. Adamson, L.K. Shalm, M.W. Mitchell, A.M. Steinberg, Multiparticle state tomography: Hidden differences. Phys. Rev. Lett. **98**, 043601 (2007). doi:10.1103/PhysRevLett.98.04360
61. B. Julsgaard, J. Sherson, J.I. Cirac, J. Fiurasek, E.S. Polzik, Experimental demonstration of quantum memory for light. Nature **432**, 482–486 (2004). doi:10.1038/nature03064
62. R.J. Sewell, M. Napolitano, N. Behbood, G. Colangelo, M.W. Mitchell, Certified quantum non-demolition measurement of a macroscopic material system. Nat. Photon. **7**, 517–520 (2013). doi:10.1038/nphoton.2013.100
63. L.B. Madsen, K. Mølmer, Spin squeezing and precision probing with light and samples of atoms in the gaussian description. Phys. Rev. A **70**, 052324 (2004). doi:10.1103/PhysRevA.70.052324
64. M. Napolitano et al., Interaction-based quantum metrology showing scaling beyond the Heisenberg limit. Nature **471**, 486–489 (2011). doi:10.1038/nature09778
65. D.A. Steck, Rubidium 85 D line data, revision 2.1.4 (2010), http://steck.us/alkalidata. Accessed 23 Dec 2010
66. D.A. Steck, Rubidium 87 D line data, revision 2.1.4 (2010), http://steck.us/alkalidata. Accessed 23 Dec 2010
67. I. Afek, O. Ambar, Y. Silberberg, Classical bound for mach-zehnder superresolution. Phys. Rev. Lett. **104**, 123602 (2010). doi:10.1103/PhysRevLett.104.123602
68. N. Thomas-Peter et al., Real-world quantum sensors: evaluating resources for precision measurement. Phys. Rev. Lett. **107**, 113603 (2011). doi:10.1103/PhysRevLett.107.113603
69. Y.J. Lu, Z.Y. Ou, Optical parametric oscillator far below threshold: experiment versus theory. Phys. Rev. A **62**, 033804 (2000). doi:10.1103/PhysRevA.62.033804

Part IV
Storage and Retrieval of Non-classical States

Chapter 8
On-Demand Release of a Heralded Quantum State from Concatenated Optical Cavities

Jun-ichi Yoshikawa, Kenzo Makino and Akira Furusawa

Abstract We describe a concatenated-cavities system that is capable of creation, storage, and on-demand release of a heralded optical quantum state. Here, two optical cavities are concatenated, where one is a memory cavity to store a quantum state inside, and the other, placed at the output of the memory cavity, is a shutter cavity to control the release from the memory cavity. When quantum entanglement is created by means of parametric down conversion and shared between two frequency modes inside the memory cavity, it is possible to eject one mode promptly while keeping the other mode inside the cavity. A projective measurement on the ejected mode results in probabilistic and heralded reduction of the stored mode into a quantum state through the quantum correlation. Once a quantum state is successfully created and stored in this way inside the memory cavity, it can be released on demand by quickly shifting the resonance of the shutter cavity. This scheme was first experimentally demonstrated for a heralded single-photon state, which we also describe here.

8.1 Introduction

Photons are almost the only resource for quantum communication when the communication distance is not very short. In particular, photons in the telecom wavelength range are especially suited for transfer through optical fibers. On the other hand, there is a great demand for storing photonic information locally. An important example that joins these two communication tasks is the quantum repeater for long-distance quantum communication [1, 2], in which local stations keep their photonic information until all of them are linked by entanglement. Therefore, it is a common view that

J. Yoshikawa (✉) · K. Makino · A. Furusawa
Department of Applied Physics, School of Engineering, The University of Tokyo,
7-3-1 Hongo,Bunkyo-ku, Tokyo 113-8656, Japan
e-mail: yoshikawa@ap.t.u-tokyo.ac.jp

K. Makino
e-mail: makino@alice.t.u-tokyo.ac.jp

A. Furusawa
e-mail: akiraf@ap.t.u-tokyo.ac.jp

A. Predojević and M.W. Mitchell (eds.), *Engineering the Atom-Photon Interaction*,
Nano-Optics and Nanophotonics, DOI 10.1007/978-3-319-19231-4_8

the transfer of photonic quantum information to static matter systems is an indispensable technique for future quantum information protocols. However, a problem is that most kinds of quantum memories restrict the optical wavelength. It is determined by the absorption lines of the matter systems, and is typically far from the telecom wavelength. Of course, this problem can be solved by wavelength conversion based on nonlinear optics, and indeed a certain effort has been made in this direction [3, 4]. Here we describe an alternative possibility, namely, quantum memories with optical cavities. Photons are moving back and forth between mirrors constructing a cavity, and this situation can be considered as the photons being virtually stopped. In this case, the wavelength of light can be arbitrarily chosen from the continuous domain of near-infrared and optical wavelength regions, where high-reflectivity mirrors are available.

There has been a series of works on all-optical quantum memories, especially using nanocavities intending future incorporation into integrated optical quantum circuits [5, 6]. However, what we describe here is somewhat in a different stream. We address switchable concatenated cavities in free space where photon-pair generation and quantum memory storage are elegantly unified. Our approach is based on an experimental success in storage and on-demand release of *pure* single photons [7], which became in fact a first demonstration to control the release timing of a quantum state with a negative Wigner function. The negativity of a Wigner function is a witness of strong nonclassicality, only obtainable when a non-Gaussian quantum state is sufficiently pure. In the case of a single-photon state, the single-photon fraction $\langle 1|\hat{\rho}|1\rangle$ higher than $1/2$ is a sufficient condition for a negative Wigner function, where $\hat{\rho}$ is a single-mode density operator and $|1\rangle$ is a single-photon state vector.

Control of highly *pure* photons by quantum memories is important, not only in quantum communication, but especially in quantum computation with optical quantum states. In particular, it is known that pure photons processed by a network of beamsplitters followed by photon-number-resolving detectors are, when supported by quantum memories, sufficient for efficient quantum computation [8]. But for such linear-optical quantum computation to be fault-tolerant, the product of the photon-source efficiency (i.e., single-photon fraction in emitted single modes) and the detection efficiency must be higher than $2/3$ in a known scheme [9]. Besides, in a simulation of continuous-variable systems, it is pointed out that a system without negativity in its Wigner function representation is simulable [10]. Although there seems to be no such clear boundary for purities in quantum communication at the moment but rather storage lifetime seems to be more important, the high-purity may also open a new realm in quantum communication [11].

High-purity single photons as traveling wavepackets have been experimentally created using a probabilistic, heralding scheme [12] that exploits nonlinear optical effects of parametric down conversion and reduction of wavepackets by photon detection. In parametric down conversion, the pairs of signal and idler photons are randomly created, and the detection of an idler photon heralds a signal photon. The resulting heralded single photons are often highly pure, because their generation does not rely on strong coupling with matter systems, in which case collection of a strongly-confined photon into a single traveling wavepacket is typically poor in

efficiency. In addition, another advantage of the heralding scheme is that the wavelength of the photon can be chosen from a wide range, by utilizing for instance a periodically-poled crystal for the quasi-phase-matching of the parametric down conversion. Moreover, the capabilities of a heralding scheme extend beyond heralded single photons. The heralding scheme can also create arbitrary superposition of plural photonic states, and indeed, heralded creation of superposition of up to three photons has been reported [13]. The disadvantage of the probabilistic nature can be circumvented if we could manage highly-efficient quantum memories. And furthermore, if the quantum memories are all-optical, composed of optical cavities, they do not spoil the free choice of the optical wavelength, a big advantage of the heralding scheme. The experiment described in this chapter [7] is a significant step toward this midterm goal.

As explained later, high purity of heralded single photons in the experimental demonstration [7] is partly owing to a one-step mechanism, in which the memory cavity is directly excited, accompanied by a photon emission serving as a herald. In contrast, in the case of a two-step mechanism, in which a photon pair is first generated and then a photon is stored in a quantum memory, the coupling efficiency of the flying photon into the quantum memory becomes a concern, but this cumbersomeness is avoided in the one-step mechanism. This one-step mechanism is in analogy with the atomic-ensemble quantum memory scheme with Raman transitions, where a collective spin state of the quantum memory is excited, accompanied by an emission of a Stokes photon serving as a herald. This atomic-ensemble counterpart has been a target of intensive studies since it was proposed by Dual et al. as a promising building block of a quantum repeater [1], and finally, just after the report of the concatenated-cavities scheme, high-purity single photons from an atomic-ensemble quantum memory was also reported [14]. Curiously, the characteristics of these two demonstrations were comparable. The single-photon fractions of the released single-photon states were significantly better than 50 %, which is sufficient for a negative Wigner function [12], while the memory lifetimes were of the order of 1 μs. These heralding schemes with quantum memories are potentially extended to a variety of optical quantum states [13], and additionally Gaussian processing after the memory release further broadens the available quantum states. Indeed, squeezing operation on a single-photon state was experimentally demonstrated [15], giving an output state well approximated by a superposition of two coherent states [16], a state often referred to as a Schrödinger's kitten state. When this squeezer is combined with the controlled single photons described here, it means that a Schrödinger's kitten state is in principle also available on demand.

In Sect. 8.2, the working principle of the concatenated-cavities quantum memory, in which a photon-pair generator is integrated, is described. In Sect. 8.3, the first experimental demonstration applied to the control of heralded single photons is described. In Sect. 8.4, this chapter is summarized. In Appendix 1, the mathematical model of the concatenated cavities is described. In Appendix 2, the longitudinal mode in homodyne detection is briefly explained.

8.2 Working Principle

In this section, we describe the working principle of the one-step mechanism of the memory excitation accompanied by a herald, as well as the mechanism of the on-demand memory release. First we explain the case of heralded single-photon states, and then we extend the scheme to general optical quantum states.

Figure 8.1 helps to understand the working principle of the concatenated-cavities memory system, in which a photon-pair generator is integrated. Two cavities are concatenated, where the one, referred to as a memory cavity, is a cavity to store photons inside, while the other, referred to as a shutter cavity, is a cavity to select which photon to eject from the memory cavity to the external world. The memory cavity contains a nonlinear-optical crystal, and the photon pairs are directly generated inside the memory cavity by spontaneous parametric down conversion. Since the photons in the memory cavity have to pass through the shutter cavity to be ejected, their lifetimes inside the memory cavity are dependent on their optical frequencies, and controllable through the resonance points of the shutter cavity. This mechanism enables earlier release of the idler photon as a herald, as well as on-demand release of the heralded signal photon, as explained below.

The system takes two phases. One is the phase of heralding and storing, whose schematic diagram is depicted in Fig. 8.1a and the corresponding frequency-domain diagram is depicted in Fig. 8.1b, while the other is the phase of releasing, whose schematic diagram is depicted in Fig. 8.1c and the corresponding frequency-domain diagram is depicted in Fig. 8.1d. Note that the frequency-domain diagrams are only conceptual ones for basic understanding, and, to be precise, the bandwidths of the stand-alone memory cavity should be very narrow. Cavities have many frequency modes as their longitudinal modes, which are equally spaced by their own free spectrum ranges. The signal and idler photons are probabilistically but simultaneously created in different frequency modes of the memory cavity. Here, along with the ordinary heralding scheme, the pumping level for the parametric down conversion must be sufficiently low in order to suppress unwanted multiphoton components. Initially, the resonance point of the shutter cavity is matched to the frequency of the idler field, but not to that of the signal field. In this phase, a created idler photon is immediately ejected through the shutter cavity, while the partner signal photon is confined inside the memory cavity. The idler field is monitored by a photon detector, and the detection of an idler photon heralds a signal photon, which is existing as an excitation of the cavity mode. In this way the heralded single photon is stored in the cavity mode until the experimental conditions are changed. The pumping might be stopped at this point to prevent further photon creation. At the timing when the signal photon is desired by an external user, it can be released by fast switching to the releasing phase. In the releasing phase, the resonance point of the shutter cavity is shifted to be matched to the frequency of the signal field. Then, the intracavity signal field in a single-photon state is rapidly released. This releasing process and the resulting shape of the traveling wavepacket is described in Appendix 1.

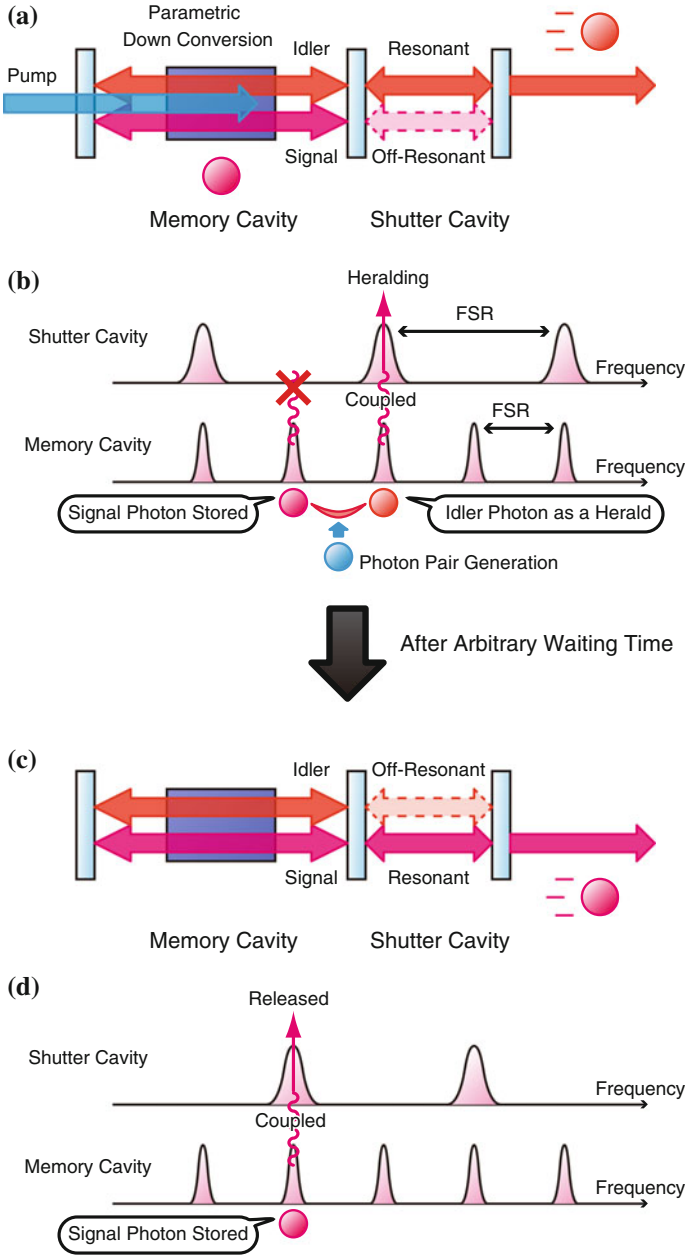

Fig. 8.1 Diagram of the scheme to unify a concatenated-cavities quantum memory system and a heralding system. **a** Schematic diagram of the system at the herald and storage stage. **b** Frequency-domain diagram of the system at the herald and storage stage. **c** Schematic diagram of the system at the release stage. **d** Frequency-domain diagram of the system at the release stage. *FSR* free spectral range

A key point for understanding this method is the fact that, when one of the frequency modes is selected as the signal, a photon is actually stretched uniformly inside the memory cavity. Therefore, this memory does not have a periodic behavior with respect to the round-trip time of photons inside the memory cavity, and in principle the release timing can be arbitrarily chosen from continuous time, unlike a simple storage-loop switching scheme [17].

So far we discussed the scheme for a heralded single-photon state, which is the simplest case. It can be extended to more general heralded quantum states by appropriately modifying the heralding detection setup [13]. Intuitively, the ideal two-mode quantum state of the signal and the idler in the ordinary parametric down conversion may be written as $|0,0\rangle + q|1,1\rangle + q^2|2,2\rangle + \ldots$ with $0 \leq q < 1$, and the quantum correlation in this entangled state can be used for heralded creation of a variety of quantum states. Concretely speaking, when n idler photons are detected, the signal state becomes the n-photon state $|n\rangle$. Furthermore, when the idler field interferes with a coherent field before the photon detection, the information of the origins of detected photons is erased, which leads to heralded creation of a photon-number superposition state in the signal mode. This scheme is so far demonstrated with traveling wavepackets for up to three photons $c_0|0\rangle + c_1|1\rangle + c_2|2\rangle + c_3|3\rangle$ [13]. In the case of traveling wavepackets, the n idler photons must be detected simultaneously. In contrast, in the case of the one-step mechanism of memory excitation described here, due to the asymmetry between the signal and the idler, the detection events of the idler photons do not have to be simultaneous.The signal field inside the memory cavity can be excited step by step by each of the idler detection events. This explains a significant boost expected when the heralding source is combined with a memory system. All such probabilistic quantum states created inside the concatenated-cavities memory system can be released on demand.

Several variants of the above scheme are possible. Actually, the idler is not necessarily looped in the shutter cavity, but instead extracted with a single path. This is possible when the signal and idler photons are very far in wavelength, or distinguishable by polarization. Of course, we can separate the concatenated cavities and the photon-pair source. The concatenated cavities without the nonlinear optical crystal can also be used as a quantum memory to catch the flying photons, keep them for a while, and release them when required. However, interestingly, the unification of these two elements increases quantum memory capabilities. This method is not limited to the heralding scheme for preparing nonclassical quantum states, but it may also enable processing of, e.g., by squeezing or photon addition [18], the stored intracavity state.

8.3 Experimental Demonstration for a Heralded Single-Photon State

The scheme of the concatenated-cavities quantum memory with integration of a photon-pair generator is first demonstrated for timing control of heralded single photons [7]. Below we explain this experiment.

8.3.1 Experimental Methods

Figure 8.2 shows the simplified experimental setup [7].

The two concatenated cavities are, unlike the diagram in Fig. 8.1, not Fabry-Pérot cavities but ring cavities. The round-trip length of the memory cavity, 1.4 m, is about twice as long as that of the shutter cavity, 0.7 m. The bow-tie-shaped memory cavity contains a periodically-poled crystal for parametric down conversion. Its quasi-

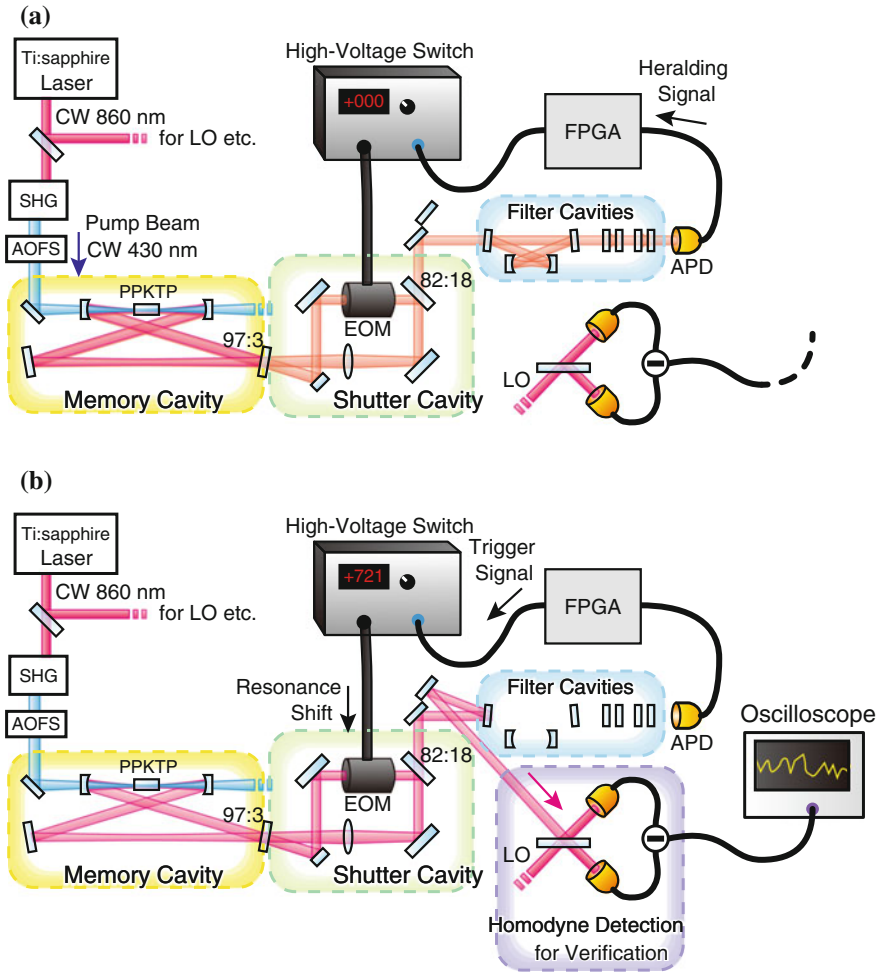

Fig. 8.2 Simplified experimental setup of concatenated-cavities quantum memory for heralded single photons [7]. **a** Setup at the herald and storage stage. **b** Setup at the release stage. *CW* Continuous wave; *SHG* second harmonic generator; *AOFS* acousto-optic frequency shifter; *PPKTP* periodically-poled $KTiOPO_4$ crystal; *EOM* electro-optic modulator; *APD* silicon avalanche photodiode; *FPGA* field-programmable gate array; *LO* optical local oscillator

phase-matching of type-0 produces photon pairs in the same polarization. The signal and idler modes for the heralding scheme are taken as adjacent frequency modes of the memory cavity, which are separated by 2.2×10^2 MHz. The shutter cavity contains an electro-optic modulator (EOM) for fast switching of the resonance. There are two outcoupling mirrors in the concatenated cavities. One is between the cavities (97 % reflectivity and 3 % transmissivity), and the other is at the exit of the shutter cavity (82 % reflectivity and 18 % transmissivity). The former one corresponds to the strength of oscillation between the two cavities, while the latter corresponds to the strength of damping from the coupled system. The magnitude relationship between these two factors determines whether the system is over-damped or under-damped. The concrete mathematical expressions describing the concatenated-cavities system are shown in Appendix 1. Comparing the transmissivities of 3 and 18 %, it might seem as if the damping is strong, but, in fact, the system is still in the under-damped region, as we will see in the experimental results.

There are three filter cavities placed after the concatenated-cavities system. At the output of the concatenated cavities, both the signal and idler fields are in the same beam path, but they must be directed to different apparatus. Therefore, the first filter cavity has the role to spatially separate the signal and idler. The additional two filter cavities further removes photons of irrelevant frequencies in the idler path. Then, the idler beam is directed to a photon detector, which is a module containing an avalanche photodiode. The filtration of the idler is necessary because the photon detector is sensitive to photons in a broad frequency range, and because fake heralding signals by irrelevant photons degrades the purity of the heralded single-photon state. In addition to the signal and idler frequency modes for the heralding scheme, the parametric down conversion inside the memory cavity also creates photons in different frequency mode pairs in which the energy conservation condition and the quasi-phase-matching condition are satisfied. The bandwidth of the quasi-phase-matching is estimated to be in the order of several hundreds gigahertz, and the filter cavities extract the target idler frequency mode from this broadband.

When the photon detector absorbs a photon, an electric pulse signal is generated, which is sent to a field-programmable gate array (FPGA) as a heralding signal. At the FPGA, a variable delay from 0 to 300 ns is added. Then, a logic signal is sent to a high-voltage switching driver, which applies around a thousand volts to the EOM in the shutter cavity with a rise time of several nanoseconds. The intrinsic delay in the response of the high-voltage switch is about 150 ns, which can be improved. The applied voltage is tuned so that the resonance point of the shutter cavity is correctly matched to the signal frequency, which corresponds to suppressing the imaginary component of the time-domain longitudinal mode function $\psi(t)$ of the released signal photons as much as possible, in the analysis explained in Appendix 2. The pumping beam is not cut after heralding signals in this demonstration, because the probability of creating an additional photon during the storage is very small.

The released signal wavepackets, reflected by the first filter cavity, are directed to a homodyne detector for characterization. It is based on interference with an optical local oscillator, which is a strong coherent beam. The quadrature distribution obtained by homodyne detection is explained below. As will be noted, a key point here is that

a single mode of the light field can be characterized with homodyne detection, in contrast to characterization based on photon detection. Finally, the electric signal from the homodyne detector is digitized by an oscilloscope and stored for analysis.

8.3.1.1 Homodyne Detection and Quadrature Distribution

Here we intend to describe the quadrature distribution obtained by homodyne detection, but before that, we review the mathematical expression of a quantized light field.

As widely known, a single mode of a light field with a well-defined optical frequency Ω is described by a harmonic oscillator with the same frequency. Taking the normalized frequency $\Omega = 1$ and the Dirac constant $\hbar = 1$, the Hamiltonian of a harmonic oscillator is $\hat{\mathscr{H}} = \hat{x}^2 + \hat{p}^2$. Here, $\hat{x}$ and $\hat{p}$ are the position and momentum operators of the harmonic oscillator, but in the case of a light field, the cosine and sine components of the field amplitude, called quadrature amplitudes, correspond to $\hat{x}$ and $\hat{p}$. The quadrature amplitudes have continuous real-value spectrum, and do not mutually commute, $[\hat{x}, \hat{p}] = i$, where i is the imaginary unit.

The quantization is well described by two non-Hermitian operators $\hat{a} = (\hat{x} + i\hat{p})/\sqrt{2}$ and $\hat{a}^\dagger = (\hat{x} - i\hat{p})/\sqrt{2}$, which are annihilation and creation operators of photons in the particle picture, respectively, but also complex and complex-conjugate amplitude operators in the wave picture, respectively. They satisfy the bosonic commutation relation $[\hat{a}, \hat{a}^\dagger] = 1$, and the Hamiltonian is diagonalized by the number operator $\hat{n} = \hat{a}^\dagger\hat{a}$ as $\hat{H} = \hat{n} + 1/2$. Starting from the vacuum state $|0\rangle$ defined by $\hat{n}|0\rangle = 0$, an arbitrary n-photon state $|n\rangle$, defined by $\hat{n}|n\rangle = n|n\rangle$, $n \in \mathbb{N}$, is uniquely constructed with creation operators as $|n\rangle = (1/\sqrt{n!})(\hat{a}^\dagger)^n|0\rangle$.

Both the discrete eigenstates $\{|n\rangle\}_{n\in\mathbb{N}}$ of the photon number operator $\hat{n}$ and the continuous eigenstates $\{|x\rangle\}_{x\in\mathbb{R}}$ or $\{|p\rangle\}_{p\in\mathbb{R}}$ of the quadrature operator $\hat{x}$ or $\hat{p}$ can be a basis of this Hilbert space, where $\langle n|n'\rangle = \delta_{n,n'}$ is the Kronecker delta, and $\langle x|x'\rangle = \delta(x - x')$ or $\langle p|p'\rangle = \delta(p - p')$ is the Dirac delta function. An arbitrary pure state $|\phi\rangle$ can be expressed in these bases as

$$|\phi\rangle = \sum_{n=0}^{\infty} c_n|n\rangle = \int_{-\infty}^{\infty} dx\, \phi(x)|x\rangle = \int_{-\infty}^{\infty} dp\, \phi'(p)|p\rangle. \tag{8.1}$$

The continuous wavefunctions $\phi_n(x)$ of the number states are well known as $\phi_n(x) = \langle x|n\rangle = H_n(x)\exp(-x^2/2)/\sqrt{2^n n!\sqrt{\pi}}$, where $H_n(x)$ is the nth Hermite polynomial.

Photon detection reveals the particle-like aspect of a light field click by click, basically observing the photon number $\hat{n}$, while homodyne detection can be said to reveal the wave-like aspect, observing a quadrature $\hat{x}\cos\theta + \hat{p}\sin\theta$ with an arbitrary optical phase $\theta \in [0, 2\pi)$ in general. Homodyne detection is based on interference with a strong local-oscillator light beam, and the phase θ in the measurement is determined by the optical phase of the local oscillator. In the case of $\theta = 0$, corresponding to measuring $\hat{x}$, homodyne detection on $|\phi\rangle$ randomly outputs a real value $x \in \mathbb{R}$ with

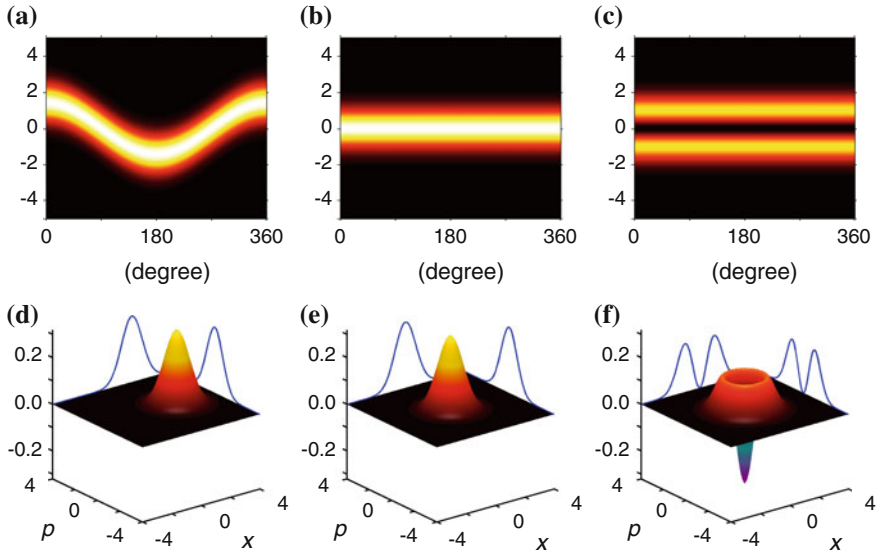

Fig. 8.3 Quadrature distributions for various measurement phases (*top*), and the corresponding Wigner functions (*bottom*), for ideal states. For the *top panels*, the horizontal axis is the phase θ of a homodyne measurement, the vertical axis is the value of the quadrature amplitude $\hat{x}\cos\theta + \hat{p}\sin\theta$, which is obtained probabilistically by an ideal homodyne measurement, and the brightness shows the probability density. For the *bottom panels*, beside the Wigner function $W(x, p)$, marginal distributions $P(x)$ and $P'(p)$ are attached, which are rescaled by a factor of $1/2$. **a** and **d** A coherent state. **b** and **e** A vacuum state. **c** and **f** A single-photon state

probability density $|\phi(x)|^2$. Since a quantum state collapses after a measurement, the distribution $|\phi(x)|^2$ is never obtained from a single object of the quantum state. The distribution $|\phi(x)|^2$ is obtained from the repeated preparation of an identical state $|\phi\rangle$ followed by an identical measurement. The information of $|\phi(x)|^2$ is still insufficient to characterize the quantum state $|\phi\rangle$, because the information of the argument $u(x)$ of the complex wavefunction $\phi(x) = |\phi(x)|e^{iu(x)}$ is equally important. However, if we obtain such distributions for all phases $\theta \in [0, 2\pi)$, they are sufficiently informative to fully identify the quantum state. The above characterization scheme of quantum states is called quantum homodyne tomography [19].

Figure 8.3a–c show a few examples of the quadrature distributions when the measurement phase θ is scanned from 0 to 2π. The horizontal axis is the measurement phase θ, while vertical axis is the value of $\hat{x}\cos\theta + \hat{p}\sin\theta$, and the probability density is visualized by the brightness.

Figure 8.3a is a coherent state $|\alpha\rangle = \exp(-|\alpha|^2/2)\sum_{n=0}^{\infty}(\alpha^n/\sqrt{n!})|n\rangle$ with the mean amplitude $\alpha = 1$. A coherent state is a quantum state of an ordinary laser light beam. It shows a wave-like oscillation with respect to the phase θ. This kind of a phase-dependent oscillation in general originates from coherent superposition of different photon-number states.

Figure 8.3b, c are a vacuum state and a single-photon state. Such energy eigenstates, and also their incoherent mixtures, are phase-insensitive in general. The vacuum state in Fig. 8.3b is the minimum-energy state, and what we see here are random fluctuations with a Gaussian distribution $|\phi_0(x)|^2$, owing to the uncertainty principle between a position and a momentum. On the other hand, the single-photon state in Fig. 8.3c has a non-Gaussian distribution $|\phi_1(x)|^2$, which has two peaks and a dip at the center.

When a single-photon state is impure and contaminated by a vacuum as $\hat{\rho} = \eta|1\rangle\langle 1| + (1-\eta)|0\rangle\langle 0|$, the quadrature distribution becomes simply their average $\eta|\phi_1(x)|^2 + (1-\eta)|\phi_0(x)|^2$, and therefore the dip at the center in the quadrature distribution becomes shallower than the pure single-photon case. In other words, we can estimate the purity of the single-photon state from the depth of the dip at the center. More generally, when a phase-insensitive quadrature distribution $P(x)$ is decomposed as $P(x) = \sum_{n=0}^{\infty} \eta_n |\phi_n(x)|^2$, the state is $\hat{\rho} = \sum_{n=0}^{\infty} \eta_n |n\rangle\langle n|$.

A feature of the homodyne detection, in contrast to photon detection which is sensitive to all the entering optical photons, is that only the light field interfering with the local-oscillator light beam is detected. That is, the local oscillator not only amplifies the quadrature signal at a quantum level but also plays a role of a filter. Therefore, the information can be extracted from a single mode of the light field, and the coherence of the confirmed photons is guaranteed by the detection scheme itself, which are important so as to claim pure single photons.

A Wigner function $W(x, p)$ is a phase-space representation of a quantum state, and is intimately connected to the quadrature distributions. When quadrature distributions of $\hat{x}$ and $\hat{p}$ are $P(x)$ and $P'(p)$ respectively, they are related to the Wigner function as

$$P(x) = \int_{-\infty}^{\infty} dp\, W(x, p), \qquad P'(p) = \int_{-\infty}^{\infty} dx\, W(x, p), \tag{8.2}$$

and the similar relation applies to a general quadrature $\hat{x}\cos\theta + \hat{p}\sin\theta$. A distinction of a Wigner function $W(x, p)$ from an ordinary simultaneous probability distribution is that a Wigner function may take negative values.

By way of illustration, Wigner functions corresponding to the quadrature distributions in Fig. 8.3a–c are shown in Fig. 8.3d–f. A coherent state $|\alpha\rangle$, including a vacuum state as its special case with $\alpha = 0$, has a Gaussian function as the Wigner function, which is always positive, as shown in Fig. 8.3d, e. On the other hand, a pure single-photon state $|1\rangle$ has a non-Gaussian Wigner function rotationally symmetric around the origin, with a large negative dip at the origin, as shown in Fig. 8.3f. In fact, it is theoretically known that any quantum state with a non-Gaussian Wigner function has negative values somewhere in the Wigner function when the state is sufficiently pure [20]. In the case of a single-photon state, when the single-photon fraction $\langle 1|\hat{\rho}|1\rangle$ is above $1/2$, the corresponding Wigner function has a negative value at the origin $W(0, 0)$, which can be considered as a sign of strong nonclassicality.

In the experiment, the homodyne detection is also utilized for the estimation of the longitudinal mode of the released single-photon wavepackets. This is described in Appendix 2.

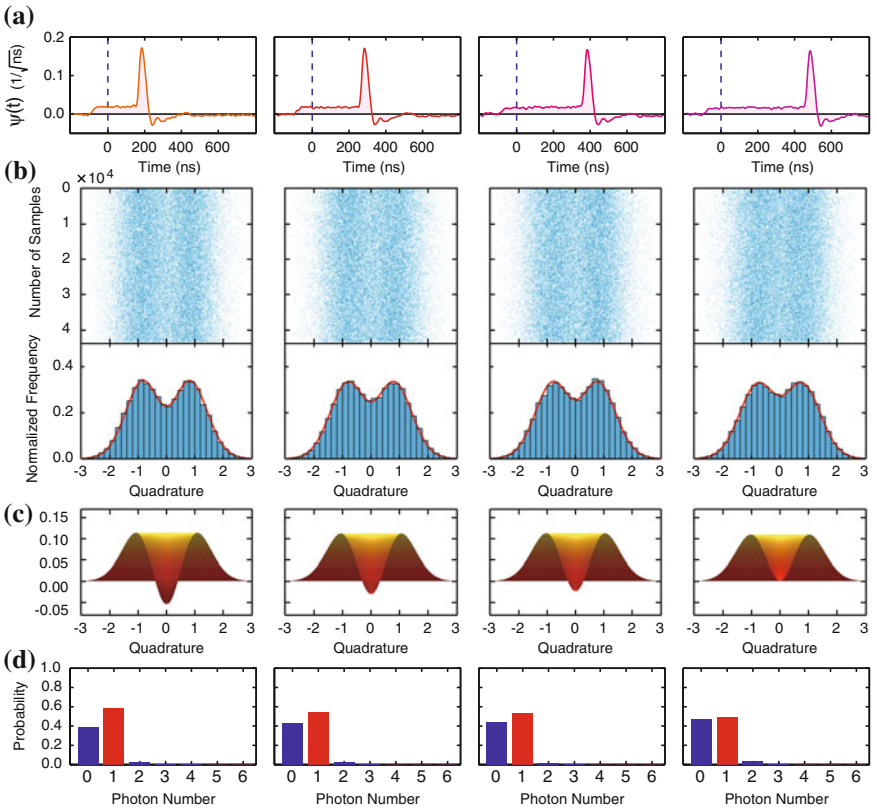

Fig. 8.4 Experimental results for various storage times [7]. The intrinsic storage time is about 150 ns, and the variable storage time is added to it. The variable storage time is 0, 100, 200, and 300 ns from *left* to *right*, respectively. **a** Longitudinal mode function in the time domain. The horizontal axis is the relative time, where 0 ns corresponds to the timing of the heralding signal. **b** Quadrature distribution. The measurement is repeated for 4.3×10^4 times. **c** Sectional side view of the Wigner function. The negative value at the origin is -0.054, -0.030, -0.024, and 0.001 from *left* to *right*, respectively. **d** Photon number distribution. The single-photon fraction $\langle 1|\hat{\rho}|1\rangle$ is 58.2, 54.6, 53.1, and 49.7 % from *left* to *right*, respectively, where the error bar is about ± 0.5 %

8.3.2 Experimental Results

Figure 8.4 shows the experimental results for various release timings. The variable storage time is 0, 100, 200, and 300 ns from left to right.

Figure 8.4a shows the longitudinal mode function $\psi(t)$ of the released wavepackets in the time domain, whose explanation is supplemented in Appendix 2. The horizontal axis is the relative time where 0 ns corresponds to the timing of the heralding signal. For the leftmost panel of the immediate release, we can see the amplitude suddenly grows from about 150 ns and then rapidly shrinks within about 50 ns,

which means the signal state is released at this timing. As mentioned in Sect. 8.3.1, the intrinsic storage time of 150 ns is due to the delayed response of the resonance-shifting EOM driver, which can be shortened. There is already a nonzero amplitude before the release from about −50 ns, which shows leakage of the photon due to imperfect decoupling at the shutter. Then in the right three panels, we can see the position of the peak is correctly shifted in accordance with the variable storage time added. The important thing is that the shape of the wavepackets does not depend on the release timing, except for the leakage before the release. As mentioned in Sect. 8.3.1, the cavity parameters are somewhat in the domain of under-damping, and this appears as the overshoot of the mode function down to negative values.

Figure 8.4b shows the quadrature distributions, obtained by integrating the homodyne signal by using the mode function $\psi(t)$ in Fig. 8.4a as a weight function, as explained in Appendix 2. In all of the four panels, we see a clear dip at the center, which is the characteristics of a single-photon quadrature distribution. The phase independence of the quadrature distribution is confirmed from the fact that the quadrature distribution does not differ between the two cases of the local oscillator phase scanned and unscanned.

Figure 8.4c, d show the sectional side view of the Wigner function and the photon-number distribution, respectively, calculated from the quadrature distribution in Fig. 8.4b. Due to optical losses in the cavity memory system during storage, the single-photon fraction gradually decreases, and the dip at the origin of the Wigner function gets gradually smaller. However, high purity to show negative values of the Wigner function is kept for the variable storage time in the order of 100 ns. The above results successfully demonstrate the timing-control of high-purity single photons with a negative Wigner function.

The results are collected in Fig. 8.5 for easy comparison. Figure 8.5a is the collection of the four mode functions $\psi(t)$ in Fig. 8.4a, where the equal intervals are clearly seen. Figure 8.5b shows the square of the mode functions $|\psi(t)|^2$. In fact, a mode function $\psi(t)$ is an envelope of the field amplitude, so the energy distribution, or the photon density, is proportional to its square. With these squared functions, we can see that contribution of the leakage before release is small. Figure 8.5c summarizes the decay of the single-photon fraction $\langle 1|\hat{\rho}|1\rangle$ with exponential fitting, from which the photon lifetime in the memory is estimated to be in the order of 1 μs when the system is in the storage phase.

8.4 Summary

We described a scheme to utilize concatenated cavities as a quantum memory system, where each memory excitation is probabilistically succeeded, heralded by detection of a photon. We also described a first experiment of this quantum memory, where the release timing of a heralded single photon was controlled, which is actually the first demonstration of releasing quantum states with a negative Wigner function on demand. The single-photon fraction of above 50 %, a sufficient condition for a

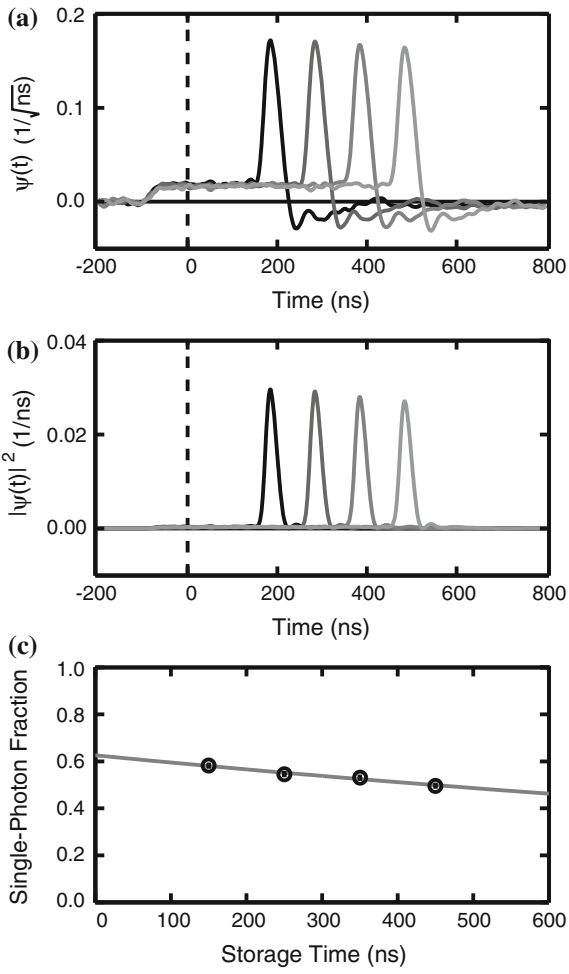

Fig. 8.5 Experimental dependency on the storage time [7]. **a** Longitudinal mode function $\psi(t)$, corresponding to probability amplitude, for various storage times. **b** Squared mode function $|\psi(t)|^2$, corresponding to probability density, for various storage times. The variable storage time is 0, 100, 200, and 300 ns, and the intrinsic storage time is about 150 ns. **c** Decay of the single-photon fraction $\langle 1|\hat{\rho}|1\rangle$ with respect to the storage time, including the intrinsic 150 ns. *Circles* are experimental values. The result of fitting with an exponential curve $\eta(t) = \eta(0)\exp(-t/\tau)$ is $\eta(0) = 62.6\,\%$ and $\tau = 1.98$ μs

negative Wigner function, was kept for the variable storage time of the order of 100 ns, which is sufficiently significant compared to the temporal width of the released single-photon wavepackets of about 50 ns. This scheme may be considered as an all-optical analogy of the Raman-transition type of the atomic-ensemble quantum memory scheme [1]. An advantage of the concatenated-cavities quantum memory is less restriction in the optical wavelength, compared to the quantum memories based on matter systems. The scheme can be potentially extended to multi-photon, phase-sensitive quantum states.

Appendix 1: Mathematical Model of Concatenated Cavities

Here we describe the mathematical model of the concatenated-cavities system, from which the longitudinal mode of the released wavepackets is predicted.

The optical frequency of the signal mode is denoted by Ω, and we consider the case where the resonance point of the shutter cavity is matched to the signal frequency Ω at time $t = 0$. The system Hamiltonians for individual cavities are

$$\hat{\mathscr{H}}_1(t) = \hbar\Omega\hat{a}_1^\dagger(t)\hat{a}_1(t), \qquad \hat{\mathscr{H}}_2(t) = \hbar\Omega\hat{a}_2^\dagger(t)\hat{a}_2(t), \tag{8.3}$$

where $\hat{a}_1(t)$ and $\hat{a}_2(t)$ are annihilation operators for the fields inside the memory and shutter cavities, respectively, obeying the equal-time commutation relation

$$[\hat{a}_k(t), \hat{a}_\ell^\dagger(t)] = \delta_{k\ell}. \tag{8.4}$$

The two cavities are linearly coupled, which is expressed by an interaction Hamiltonian,

$$\hat{\mathscr{H}}_{\rm int}(t) = \hbar[\varepsilon\hat{a}_1^\dagger(t)\hat{a}_2(t) + \varepsilon^*\hat{a}_2^\dagger(t)\hat{a}_1(t)], \tag{8.5}$$

where $\varepsilon \in \mathbb{C}$ is a parameter of the coupling, which can be taken as a real number without loss of generality by redefinition of the optical phase of $\hat{a}_1$ or $\hat{a}_2$, and $|\varepsilon|$ corresponds to the coupling strength. The total system Hamiltonian of the concatenated cavities is the sum of them,

$$\hat{\mathscr{H}}_{\rm sys}(t) = \hat{\mathscr{H}}_1(t) + \hat{\mathscr{H}}_2(t) + \hat{\mathscr{H}}_{\rm int}(t). \tag{8.6}$$

In addition to the above intrasystem evolution, the shutter cavity is coupled to an external field. Because the external field has a broad bandwidth, the commutation relation is well approximated by a Dirac delta function,

$$[\hat{b}_{\rm in}(t), \hat{b}_{\rm in}^\dagger(t')] = \delta(t - t'), \tag{8.7a}$$

$$[\hat{b}_{\rm out}(t), \hat{b}_{\rm out}^\dagger(t')] = \delta(t - t'). \tag{8.7b}$$

where $\hat{b}_{\rm in}(t)$ is an annihilation operator of the external incoming field, which enters into the shutter cavity at time t, and $\hat{b}_{\rm out}(t)$ is that of the external outgoing field, which leaves from the shutter cavity at time t. In the following, we will sometimes omit the argument (t) for simplicity. Overall time evolution obeys the quantum Langevin equation [21] as

$$\frac{d}{dt}\hat{a}_1 = -\frac{i}{\hbar}[\hat{a}_1, \hat{\mathscr{H}}_{\rm sys}], \tag{8.8a}$$

$$\frac{d}{dt}\hat{a}_2 = -\frac{i}{\hbar}[\hat{a}_2, \hat{\mathscr{H}}_{\rm sys}] - \frac{\gamma}{2}\hat{a}_2 - \sqrt{\gamma}\hat{b}_{\rm in}, \tag{8.8b}$$

where $\gamma \geq 0$ is the damping rate. The time-reversed Langevin equation can be expressed in the same way as

$$\frac{d}{dt}\hat{a}_1 = -\frac{i}{\hbar}[\hat{a}_1, \hat{\mathscr{H}}_{\rm sys}], \tag{8.9a}$$

$$\frac{d}{dt}\hat{a}_2 = -\frac{i}{\hbar}[\hat{a}_2, \hat{\mathscr{H}}_{\rm sys}] + \frac{\gamma}{2}\hat{a}_2 - \sqrt{\gamma}\hat{b}_{\rm out}. \tag{8.9b}$$

The above two sets of equations are connected by the boundary condition at the exit of the shutter cavity,

$$\hat{b}_{\rm out}(t) - \hat{b}_{\rm in}(t) = \sqrt{\gamma}\hat{a}_2(t). \tag{8.10}$$

Note that the coefficients of the Langevin equations, i.e. $\gamma/2$ for $\hat{a}_2$ and $\sqrt{\gamma}$ for $\hat{b}_{\rm in}$, are derived from the requirement to preserve the commutation relation during an infinitesimal time evolution $\delta t \ll 1/\gamma$, which is checked as below.

$$\begin{aligned}
&[\hat{a}_2(t+\delta t), \hat{a}_2^\dagger(t+\delta t)] - [\hat{a}_2(t), \hat{a}_2^\dagger(t)] \\
&= -\left[\hat{a}_2(t), \frac{i\delta t}{\hbar}[\hat{a}_2^\dagger(t), \hat{\mathscr{H}}_{\rm sys}(t)] + \frac{\gamma\delta t}{2}\hat{a}_2^\dagger(t)\right] \\
&\quad -\left[\frac{i\delta t}{\hbar}[\hat{a}_2(t), \hat{\mathscr{H}}_{\rm sys}(t)] + \frac{\gamma\delta t}{2}\hat{a}_2(t), \hat{a}_2^\dagger(t)\right] \\
&\quad +\left[\sqrt{\gamma}\int_0^{\delta t} d\tau \hat{b}_{\rm in}(t+\tau), \sqrt{\gamma}\int_0^{\delta t} d\tau \hat{b}_{\rm in}^\dagger(t+\tau)\right] + O(\delta t^2) \\
&= O(\delta t^2).
\end{aligned} \tag{8.11}$$

Here, for the terms containing $\hat{\mathscr{H}}_{\rm sys}(t)$, the Jacobi identity $[[\hat{X}, \hat{Y}], \hat{Z}] + [[\hat{Z}, \hat{X}], \hat{Y}] + [[\hat{Y}, \hat{Z}], \hat{X}] = 0$ simplifies the calculation.

By substituting (8.6) into the Langevin equation (8.8), we obtain

$$\frac{d}{dt}\hat{a}_1 = -i\Omega\hat{a}_1 - i\varepsilon\hat{a}_2, \tag{8.12a}$$

$$\frac{d}{dt}\hat{a}_2 = -i\Omega\hat{a}_2 - i\varepsilon^*\hat{a}_1 - \frac{\gamma}{2}\hat{a}_2 - \sqrt{\gamma}\hat{b}_{\rm in}. \tag{8.12b}$$

We take a rotating frame by the following replacement,

$$\hat{a}_1 \to \hat{a}_1 e^{-i\Omega t}, \qquad \hat{a}_2 \to \hat{a}_2 e^{-i\Omega t}, \tag{8.13a}$$

$$\hat{b}_{\rm in} \to \hat{b}_{\rm in} e^{-i\Omega t}, \qquad \hat{b}_{\rm out} \to \hat{b}_{\rm out} e^{-i\Omega t}, \tag{8.13b}$$

which simplifies the equations, canceling the terms proportional to Ω,

$$\frac{d}{dt}\hat{a}_1 = -i\varepsilon\hat{a}_2, \tag{8.14a}$$

$$\frac{d}{dt}\hat{a}_2 = -i\varepsilon^*\hat{a}_1 - \frac{\gamma}{2}\hat{a}_2 - \sqrt{\gamma}\hat{b}_{\mathrm{in}}. \tag{8.14b}$$

Note that this rotation frame at the optical frequency Ω is experimentally naturally taken when the light field is subject to homodyne detection with a local oscillator at the optical frequency Ω.

Using (8.14a) to eliminate $\hat{a}_2$ from (8.14b), we find that the system obeys the second-order differential equation,

$$\frac{d^2}{dt^2}\hat{a}_1 + \frac{\gamma}{2}\frac{d}{dt}\hat{a}_1 + |\varepsilon|^2\hat{a}_1 - i\varepsilon\sqrt{\gamma}\hat{b}_{\mathrm{in}} = 0. \tag{8.15}$$

Solution of the Released Wavepackets

We consider the situation in which the memory cavity is initially isolated and holds a single photon for $t < 0$, and then the interaction suddenly starts at $t = 0$ and eventually the photon is ejected to an external field. In this case, we are interested in how the term of $\hat{a}_1(0)$ is transferred to $\hat{b}_{\mathrm{out}}(t)$ for $t \geq 0$.

Since we are considering only linear coupling, we can suppose the following form of solution, for $t \geq 0$.

$$\begin{aligned}\hat{a}_1(t) &= h_{1\to1}(t)\hat{a}_1(0) + h_{2\to1}(t)\hat{a}_2(0) \\ &\quad + \int_0^t d\tau\, h_{\mathrm{in}\to1}(t-\tau)\hat{b}_{\mathrm{in}}(\tau),\end{aligned} \tag{8.16a}$$

$$\begin{aligned}\hat{a}_2(t) &= h_{1\to2}(t)\hat{a}_1(0) + h_{2\to2}(t)\hat{a}_2(0) \\ &\quad + \int_0^t d\tau\, h_{\mathrm{in}\to2}(t-\tau)\hat{b}_{\mathrm{in}}(\tau),\end{aligned} \tag{8.16b}$$

$$\begin{aligned}\hat{b}_{\mathrm{out}}(t) &= h_{1\to\mathrm{out}}(t)\hat{a}_1(0) + h_{2\to\mathrm{out}}(t)\hat{a}_2(0) \\ &\quad + \int_0^t d\tau\, h_{\mathrm{in}\to\mathrm{out}}(t-\tau)\hat{b}_{\mathrm{in}}(\tau),\end{aligned} \tag{8.16c}$$

where $h_{\mu\to\nu}(t)$ is the transfer coefficient from μ to ν, which is considered as a complex-valued analytic function with respect to time. By this supposition, the differential equations of the operators are converted to the differential equations of complex-valued functions. The objective is to solve $h_{1\to\mathrm{out}}(t)$, which predicts the longitudinal mode of the released wavepackets, except for the leakage before the release.

Substituting (8.16) into (8.14) and taking the coefficients of $\hat{a}_1(0)$, we find the relation that determines $h_{1\to 2}(t)$ uniquely from $h_{1\to 1}(t)$ as

$$\frac{d}{dt}h_{1\to 1}(t) = -i\varepsilon h_{1\to 2}(t). \tag{8.17}$$

On the other hand, substituting (8.16) into (8.10), we find that $h_{1\to \mathrm{out}}(t)$ is proportional to $h_{1\to 2}(t)$,

$$\sqrt{\gamma}h_{1\to 2}(t) = h_{1\to \mathrm{out}}(t). \tag{8.18}$$

Combining (8.17) and (8.18), we obtain,

$$h_{1\to \mathrm{out}}(t) = \frac{i\sqrt{\gamma}}{\varepsilon}\frac{d}{dt}h_{1\to 1}(t). \tag{8.19}$$

Therefore, if the system parameter $h_{1\to 1}(t)$ can be found, then the objective $h_{1\to \mathrm{out}}(t)$ is uniquely determined. The differential equation for $h_{1\to 1}(t)$ is obtained from (8.15) as

$$\left(\frac{d^2}{dt^2} + \frac{\gamma}{2}\frac{d}{dt} + |\varepsilon|^2\right)h_{1\to 1}(t) = 0. \tag{8.20}$$

The initial conditions for $h_{1\to 1}(t)$ are as follows.

$$h_{1\to 1}(0) = 1, \tag{8.21a}$$

$$\frac{d}{dt}h_{1\to 1}(t)\Big|_{t=0} = -i\varepsilon h_{1\to 2}(0) = 0. \tag{8.21b}$$

The system decay in (8.20) is characterized by the damping ratio ξ,

$$\xi = \frac{\gamma}{4|\varepsilon|}. \tag{8.22}$$

The decay is classified into three types.

- When $0 < \xi < 1$, the system is under-damped, where damped oscillation occurs.
- When $\xi = 1$, the system is critically damped, where the system parameter rapidly decays to zero.
- When $\xi > 1$, the system is over-damped, where the system parameter gradually decays without oscillation.

Under-Damping

When $4|\varepsilon| > \gamma$, the system parameter $h_{1\to 1}(t)$ is damped with oscillation. The solution of the differential equation is

$$h_{1\to 1}(t) = C_1 \exp\left(-\frac{\gamma t}{4}\right) \cos\left(\frac{t}{4}\sqrt{16|\varepsilon|^2 - \gamma^2}\right) + C_2 \exp\left(-\frac{\gamma t}{4}\right) \sin\left(\frac{t}{4}\sqrt{16|\varepsilon|^2 - \gamma^2}\right), \tag{8.23}$$

where C_1 and C_2 are free parameters which are fixed by the initial condition in (8.21) as follows.

$$C_1 = 1, \qquad C_2 = \frac{\gamma}{\sqrt{16|\varepsilon|^2 - \gamma^2}}. \tag{8.24}$$

Finally, using (8.19), the coefficient at the output becomes,

$$\begin{aligned} h_{1\to \text{out}}(t) &= \frac{i\sqrt{\gamma}}{\varepsilon}\frac{d}{dt} h_{1\to 1}(t) \\ &= -\frac{4i\varepsilon^*\sqrt{\gamma}}{\sqrt{16|\varepsilon|^2 - \gamma^2}} \exp\left(-\frac{\gamma t}{4}\right) \sin\left(\frac{t}{4}\sqrt{16|\varepsilon|^2 - \gamma^2}\right). \end{aligned} \tag{8.25}$$

The correctness of the normalization is checked as

$$\int_0^\infty dt |h_{1\to \text{out}}(t)|^2 = 1. \tag{8.26}$$

Critical Damping

When $4|\varepsilon| = \gamma$, the system parameter $h_{1\to 1}(t)$ is critically damped. The solution of the differential equation is

$$h_{1\to 1}(t) = (C_1 + C_2 t) \exp\left(-\frac{\gamma}{4} t\right). \tag{8.27}$$

From the initial condition in (8.21),

$$C_1 = 1, \qquad C_2 = \frac{\gamma}{4}. \tag{8.28}$$

Finally, using (8.19), the coefficient at the output becomes,

$$\begin{aligned} h_{1\to \text{out}}(t) &= \frac{i\sqrt{\gamma}}{\varepsilon}\frac{d}{dt} h_{1\to 1}(t) \\ &= -i\varepsilon^*\sqrt{\gamma} t \exp\left(-\frac{\gamma}{4} t\right). \end{aligned} \tag{8.29}$$

The correctness of the normalization is checked by integration as in (8.26).

Over Damping

When $4|\varepsilon| < \gamma$, the system parameter $h_{1\to 1}(t)$ is over-damped. The solution of the differential equation is

$$h_{1\to 1}(t) = C_1 \exp\left[-\frac{\gamma t}{4}\left(1 - \frac{\sqrt{\gamma^2 - 16|\varepsilon|^2}}{\gamma}\right)\right] + C_2 \exp\left[-\frac{\gamma t}{4}\left(1 + \frac{\sqrt{\gamma^2 - 16|\varepsilon|^2}}{\gamma}\right)\right]. \tag{8.30}$$

From the initial condition in (8.21),

$$C_1 = \frac{1}{2}\left(1 + \frac{\gamma}{\sqrt{\gamma^2 - 16|\varepsilon|^2}}\right), \qquad C_1 = \frac{1}{2}\left(1 - \frac{\gamma}{\sqrt{\gamma^2 - 16|\varepsilon|^2}}\right). \tag{8.31}$$

Finally, using (8.19), the coefficient at the output becomes,

$$\begin{aligned} h_{1\to \mathrm{out}}(t) &= \frac{i\sqrt{\gamma}}{\varepsilon}\frac{d}{dt}h_{1\to 1}(t) \\ &= -\frac{2i\varepsilon^*\sqrt{\gamma}}{\sqrt{\gamma^2 - 16|\varepsilon|^2}}\left\{\exp\left[-\frac{\gamma t}{4}\left(1 - \frac{\sqrt{\gamma^2 - 16|\varepsilon|^2}}{\gamma}\right)\right]\right. \\ &\quad \left. - \exp\left[-\frac{\gamma t}{4}\left(1 + \frac{\sqrt{\gamma^2 - 16|\varepsilon|^2}}{\gamma}\right)\right]\right\}. \end{aligned} \tag{8.32}$$

The correctness of the normalization is checked by integration as in (8.26).

Correspondence of the Parameters

An important question is how the parameters ε and γ in the Langevin equations correspond to the parameters of the optical setup such as the cavity lengths and the transmissivities of the coupling mirrors. They can be determined from the consistency with the time evolution of classical light fields.

Here the round-trip length of the memory cavity is denoted by ℓ_1, that of the shutter cavity by ℓ_2, the energy transmissivity and reflectivity of the coupling mirror between the two cavities by T_c and R_c, respectively, those between the shutter cavity and the external field by T_o and R_o, respectively, and the light speed by c. Then, the round-trip times of light in the memory cavity and the shutter cavity are $\tau_1 = \ell_1/c$ and $\tau_2 = \ell_2/c$, respectively.

We first consider the damping rate γ. We consider how the field inside the shutter cavity reduces by the leakage by γ, when it is disconnected from the memory cavity

by setting $\varepsilon = 0$. During a passage of time δt much smaller than the system time scale $\delta t \ll (1/\gamma)$, the intracavity classical field amplitude decreases by a factor of $1 - (\gamma/2)\delta t$, from the Langevin equation. On the other hand, during this time, the field circulates $(c/\ell_2)\delta t$ times inside the cavity, which reduces the field amplitude by a factor of $(\sqrt{R_o})^{(c/\ell_2)\delta t}$. By equating these two factors,

$$\left(1 - \frac{\gamma}{2}\delta t\right) \approx (\sqrt{R_o})^{(c/\ell_2)\delta t} = (1 - T_o)^{(c/2\ell_2)\delta t} \approx \left(1 - \frac{cT_o}{2\ell_2}\delta t\right), \tag{8.33}$$

the following relation is derived,

$$\gamma \approx \frac{cT_o}{\ell_2} = \frac{T_o}{\tau_2}. \tag{8.34}$$

On the other hand, for the coupling strength ε, the derivation is a bit tricky due to the interference of the intracavity fields. We also consider the consistency with the time evolution of classical fields during a small amount of time $\delta t \ll (1/|\varepsilon|)$. For simplicity, we consider the situation where initially the classical field amplitude is nonzero only in the memory cavity but zero in the shutter cavity. Then, we evaluate the classical field leaked to the shutter cavity by a time passage, where the field amplitude linearly increases with respect to time $\propto \delta t$, rather than attenuation in the memory cavity, where the change of the field amplitude is not linear but quadratic $\propto \delta t^2$. However, in this case, we must keep in mind the different amplitudes of a photon (or equivalently, different magnitudes of the vacuum fluctuation) between the two cavities. A photon is uniformly stretched in the cavity, so the amplitude become larger when the cavity is smaller. This difference is compensated by multiplying the factor $\sqrt{\ell_2/\ell_1}$. Classically, $\sqrt{T_c}$ times the field amplitude in the memory cavity enters the shutter cavity per time ℓ_2/c, and this compensated by the photon amplitude ratio $\sqrt{\ell_2/\ell_1}$ leads to the following relation

$$|\varepsilon| \approx \sqrt{T_c} \times \frac{c}{\ell_2} \times \sqrt{\frac{\ell_2}{\ell_1}} = \frac{c\sqrt{T_c}}{\sqrt{\ell_1\ell_2}} = \frac{\sqrt{T_c}}{\sqrt{\tau_1\tau_2}}. \tag{8.35}$$

As a natural result, the parameters of the two cavities ℓ_1 and ℓ_2 appear in a symmetric form in $|\varepsilon|$. As noted before, the argument of the complex parameter ε is arbitrarily chosen by appropriately redefining the phase of the intracavity fields $\hat{a}_1$ and $\hat{a}_2$.

Worth noting is that γ is proportional to T_o but ε is proportional to $\sqrt{T_c}$. Therefore, the transmissivities of the two coupling mirrors must be designed very asymmetrically.

The theoretical predictions from the above calculations are in good agreement with the experimental results in Sect. 8.3.2, except for the leakage before the release.

Appendix 2: Wavepacket Estimation by Continuous Homodyne Detection

Although we have taken a single mode from the first in Sect. 8.3.1.1, real situation in homodyne detection is somewhat different, as follows. Homodyne detection with a continuous-wave local oscillator continuously outputs the measurement values of instant quadratures $\hat{x}(t)\cos\theta + \hat{p}(t)\sin\theta = [\hat{b}(t)e^{-i\theta} + \hat{b}^\dagger(t)e^{i\theta}]/\sqrt{2}$. We note that here we are equating the position in the longitudinal direction with the time t, through the constant speed of light. And also we note that here a rotating frame is taken in accordance with the optical frequency Ω of the local oscillator. That is to say, the situation corresponds to continuous measurements on the field $\hat{b}_{\mathrm{out}}(t)$ in Appendix 1, after the shift to the rotating frame in (8.13). A single-photon state is associated with a specific longitudinal mode function $\psi(t)$. Annihilation and creation operators on the longitudinal mode $\psi(t)$ are defined as $\hat{a}_\psi = \int dt\, \psi(t)\hat{b}(t)$ and $\hat{a}_\psi^\dagger = \int dt\, \psi^*(t)\hat{b}^\dagger(t)$, where the normalization condition is $\int dt\, |\psi(t)|^2 = 1$ for the bosonic commutation relations of $[\hat{b}(t), \hat{b}^\dagger(t')] = \delta(t-t')$ and $[\hat{a}_\psi, \hat{a}_\psi^\dagger] = 1$. Note that this normalization condition coincides with (8.26). By using this creation operator $\hat{a}_\psi^\dagger$, a pure single-photon state is defined as $\hat{a}_\psi^\dagger|\emptyset\rangle = \int dt\, \psi^*(t)\hat{b}^\dagger(t)|\emptyset\rangle$, where $|\emptyset\rangle$ denotes a multimode vacuum state $\hat{b}(t)|\emptyset\rangle = 0, t \in \mathbb{R}$.

Then, the quadrature distribution of a single-photon state shown in Fig. 8.3 is obtained from measurements of $\hat{x}_\psi = (\hat{a}_\psi + \hat{a}_\psi^\dagger)/\sqrt{2}$. A measurement outcome x_ψ of the single-mode quadrature $\hat{x}_\psi$ can be actually calculated from a set of measurement outcomes $\{x(t)\}$ of the instant quadratures $\{\hat{x}(t)\}$, only when the mode function $\psi(t)$ is a real function, based on the relation

$$\begin{aligned}\hat{x}_\psi &= \int dt\, \frac{1}{\sqrt{2}}[\psi(t)\hat{b}(t) + \psi^*(t)\hat{b}^\dagger(t)] \\ &= \int dt\, \{\mathrm{Re}[\psi(t)]\hat{x}(t) - \mathrm{Im}[\psi(t)]\hat{p}(t)\},\end{aligned} \tag{8.36}$$

where $\mathrm{Re}[\alpha]$ and $\mathrm{Im}[\alpha]$ denote the real part and the imaginary part of a complex number α, respectively. The mode function $\psi(t)$ of a single-photon state is indeed a real function in the ideal case. In the calculation of $h_{1\to\mathrm{out}}(t)$ in (8.25), (8.29), (8.32) in Appendix 1, the arguments are constantly $\arg(-i\varepsilon^*)$ for all of the three cases, and this constant argument can be canceled by the redefinition of the optical phase. However, the mode function $\psi(t)$ can be experimentally a complex function with a varying argument, when the resonance point of the shutter cavity is improper or drifting. In this case, if the optical phase of the local oscillator of the homodyne detection is dynamically varied in accordance with the mode function, then the value of the desired quadrature $\hat{x}_\psi$ can be calculated, but such adaptation is experimentally very demanding.

With the procedure explained below, the real mode function $\psi(t)$ of a single-photon state is estimated. The estimation is supported by the situation where the

irrelevant modes are not excited but in a vacuum state. An ideal single-photon state has a quadrature variance three times larger than that of a vacuum state.

$$\langle 1|\hat{x}^2|1\rangle = \langle 0|\hat{a}\frac{(\hat{a}+\hat{a}^\dagger)^2}{2}\hat{a}^\dagger|0\rangle = \frac{3}{2}, \tag{8.37}$$

$$\langle 0|\hat{x}^2|0\rangle = \langle 0|\frac{(\hat{a}+\hat{a}^\dagger)^2}{2}|0\rangle = \frac{1}{2}. \tag{8.38}$$

Therefore, a function $f(t)$ that maximizes the quadrature variance $\langle \hat{x}_f^2 \rangle$ is the best estimation of the photon mode function $\psi(t)$. Experimentally, the estimation is obtained by spectral decomposition of the autocorrelation function $V(t,t') = \langle x(t)x(t')\rangle$ as the eigenfunction with the largest eigenvalue. In the case where the mode function $\psi(t)$ of a single-photon state is a complex function, the estimation gives two real functions. We obtain, up to the normalization, $\mathrm{Re}[\psi(t)e^{i\lambda}]$ with some $\lambda \in [0, 2\pi)$ as a primary mode function that maximize the single-photon component, and $\mathrm{Im}[\psi(t)e^{i\lambda}]$ as a secondary mode function, from the spectral decomposition. Note that the primary mode function $\mathrm{Re}[\psi(t)e^{i\lambda}]$ and the secondary mode function $\mathrm{Im}[\psi(t)e^{i\lambda}]$ are orthogonal with respect to the L^2-norm, owing to the principle of spectral decomposition.

References

1. L.-M. Duan, M.D. Lukin, J.I. Cirac, P. Zoller, Long-distance quantum communication with atomic ensembles and linear optics. Nature **414**, 413–418 (2001)
2. N. Sangouard, C. Simon, H. de Riedmatten, N. Gisin, Quantum repeaters based on atomic ensembles and linear optics. Rev. Mod. Phys. **83**, 33–80 (2011)
3. M.A. Albota, F.N.C. Wong, Efficient single-photon counting at 1.55 μm by means of frequency upconversion. Opt. Lett. **29**, 1449–1451 (2004)
4. B. Albrecht, P. Farrera, X. Fernandez-Gonzalvo, M. Cristiani, H. de Riedmatten, A waveguide frequency converter connecting rubidium-based quantum memories to the telecom c-band. Nat. Commun. **5**, 3376 (2014)
5. A.W. Elshaari, A. Aboketaf, S.F. Preble, Controlled storage of light in silicon cavities. Opt. Express **18**, 3014–3022 (2010)
6. Y. Sato et al., Strong coupling between distant photonic nanocavities and its dynamic control. Nat. Photon. **6**, 56–61 (2012)
7. J. Yoshikawa, K. Makino, S. Kurata, P. van Loock, A. Furusawa, Creation, storage, and on-demand release of optical quantum states with a negative wigner function. Phys. Rev. X **3**, 041028 (2013)
8. E. Knill, R. Laflamme, G.J. Milburn, A scheme for efficient quantum computation with linear optics. Nature **409**, 46–52 (2001)
9. M. Varnava, D.E. Browne, T. Rudolph, How good must single photon sources and detectors be for efficient linear optical computation? Phys. Rev. Lett. **100**, 060502 (2008)
10. A. Mari, J. Eisert, Positive wigner functions render classical simulation of quantum computation efficient. Phys. Rev. Lett. **109**, 230503 (2012)
11. M. Schleier-Smith, H. Tanji-Suzuki, Pure photons for quantum communications. Physics **7**, 6 (2014)

12. A.I. Lvovsky et al., Quantum state reconstruction of the single-photon fock state. Phys. Rev. Lett. **87**, 050402 (2001)
13. M. Yukawa et al., Generating superposition of up-to three photons for continuous variable quantum information processing. Opt. Express **21**, 5529–5535 (2013)
14. E. Bimbard et al., Homodyne tomography of a single photon retrieved on demand from a cavity-enhanced cold atom memory. Phys. Rev. Lett. **112**, 033601 (2014)
15. Y. Miwa et al., Exploring a new regime for processing optical qubits: squeezing and unsqueezing single photons. Phys. Rev. Lett. **113**, 013601 (2014)
16. A.P. Lund, H. Jeong, T.C. Ralph, M.S. Kim, Conditional production of superpositions of coherent states with inefficient photon detection. Phys. Rev. A **70**, 020101(R) (2004)
17. T.B. Pittman, B.C. Jacobs, J.D. Franson, Single photons on pseudodemand from stored parametric down-conversion. Phys. Rev. A **66**, 042303 (2002)
18. A. Zavatta, S. Viciani, M. Bellini, Quantum-to-classical transition with single-photon-added coherent states of light. Science **306**, 660–662 (2004)
19. A.I. Lvovsky, M.G. Raymer, Continuous-variable optical quantum-state tomography. Rev. Mod. Phys. **81**, 299–332 (2009)
20. R.L. Hudson, When is the wigner quasi-probability density non-negative? Rep. Math. Phys. **6**, 249–252 (1974)
21. M.J. Collett, C.W. Gardiner, Squeezing of intracavity and traveling-wave light fields produced in parametric amplification. Phys. Rev. A **30**, 1386–1391 (1984)

Chapter 9
Quantum Light Storage in Solid State Atomic Ensembles

Hugues de Riedmatten and Mikael Afzelius

Abstract In this chapter, we will describe the storage and retrieval of quantum light (heralded single photons and entangled photons) in atomic ensembles in a solid state environment. We will consider ensembles of rare-earth ions embedded in dielectric crystals. We will describe the methods used to create quantum light spectrally compatible with the narrow atomic transitions, as well as possible protocols based on dipole rephasing that can be used to reversibly map the quantum light onto collective atomic excitations. We will review the experimental state of the art and describe in more detail quantum light storage experiments in neodymium and praseodymium doped crystals.

9.1 Introduction

Harnessing strong and coherent interactions between quantum light and matter is an important ability in quantum science. These interactions can be used to build light-matter interfaces enabling reversible quantum state transfer between photons and atoms. One important application of these interfaces is the realization of photonic quantum memories [1–4] which allow storage of quantum information carried by photons. Quantum memories are important devices in quantum information science because they can be used as synchronization devices when many different probabilistic quantum processes are linked together. They are therefore required for scalable protocols using photons, with potential applications in optical quantum computing, generation of multiphoton states from probabilistic pair sources [5], quantum

H. de Riedmatten (✉)
ICFO-The Institute of Photonic Sciences, Barcelona, Spain
e-mail: hugues.deriedmatten@icfo.es

H. de Riedmatten
ICREA-Institució Catalana de Recerca i Estudis Avançats, 08015 Barcelona, Spain

M. Afzelius
Group of Applied Physics, University of Geneva, Geneva, Switzerland
e-mail: mikael.afzelius@unige.ch

A. Predojević and M.W. Mitchell (eds.), *Engineering the Atom-Photon Interaction*,
Nano-Optics and Nanophotonics, DOI 10.1007/978-3-319-19231-4_9

information networks [6] and long-distance quantum communication using quantum repeaters [7–9].

The realization of quantum memories for light requires efficient and reversible mapping of photons onto long lived atomic coherences. This in turn requires strong interactions between light and matter. However, in free space the interaction between a single photon and a single atom is usually weak. One way to overcome the problem is to place the atom in a high finesse cavity which strongly enhances the interaction [10] (see chapter by A. Kuhn). Another way is to use a collection of atoms, where the atom light coupling is enhanced by a factor of $\sqrt{N}$ with N being the number of atoms involved. Single photons are stored in atomic ensembles as collective atomic excitation, sometimes called superatoms. These superatoms have the important property that they can be efficiently converted to single photons in a well defined spatio-temporal mode thanks to a collective interference between all the involved emitters [8]. This so-called collective enhancement is at the heart of most quantum memory protocols in atomic ensembles. The quantum control of collective atomic coherences is therefore a key task in the field of quantum memories.

For applications involving transfer of quantum information over large distances, remote quantum memories must be entangled [8, 11]. This requires that the remote quantum memories must exchange quantum information using e.g. single photons, or that photons emitted by the quantum memories interfere at a central location between the two quantum memories. If optical fibers are used, this means that quantum memories must be connected to the optical fiber network, in particular to photons at telecom wavelengths in order to minimize optical losses in the fiber transmission.

Quantum memories for light were first demonstrated in atomic gases, both room-temperature gases and ensembles of laser-cooled atoms. Several review papers can also be found on that subject [1, 9]. Some solid-state systems offer interesting perspectives as quantum memories for light, such as rare-earth doped crystals [12–16], nitrogen-vacancy centers in diamond [17, 18], phonons in diamond [19, 20] and quantum dots [3, 21, 22] (see also chapter by McMahon and De Greve). Realizing quantum memories in solid-state systems would, in general, have several advantages, such as the absence of atomic motion and the prospects for integrated devices, which may facilitate large-scale deployment of these techniques in future quantum networks. But, controlling light-matter interactions in solid-state materials also poses important challenges, such as preserving the quantum coherence in a solid-state environment.

Here we will discuss rare-earth-ion doped crystals for quantum memories. These crystals provide a large number of atoms naturally trapped in a solid-state matrix, with spectrally narrow optical and spin transitions. Due to their particular electron level structure, they also provide exceptional coherence properties, both for the optical and spin transitions, when cooled to cryogenic temperatures.

This chapter will describe experiments and techniques developed to store non-classical light in rare-earth-ion doped crystals. In Sect. 9.2, we describe in more details the relevant properties of rare-earth-ion doped crystals and the reasons why these are interesting materials for quantum light storage. In Sect. 9.3, we describe quantum memory protocols that have been proposed to store quantum information

in doped crystals. In Sect. 9.4, we review the experimental state-of-the-art of storing non-classical states of light in crystals. In the following two sections we describe the development of two specific sources of non-classical light (Sect. 9.5) and their application to non-classical light storage (Sect. 9.6) in Pr^{3+} and Nd^{3+} ions doped crystals. Finally, in Sect. 9.7, we comment on the prospects for extending quantum light storage to longer storage times in these systems.

9.2 Rare-Earth-Ion Doped Crystals

The energy structure of ions in solid-state materials is usually strongly affected by the lattice of the host crystal, resulting in broad optical transitions with very short optical coherence time. Striking exceptions to this are rare-earth ion impurities in crystals, whose 4f-4f transitions were found to be extremely narrow when the first high-resolution resonance spectra were obtained in the 1970s [23]. The sharp lines are due to the shielding of the 4f electron shell from outermost 5s and 5p electrons, which reduces the coupling of the 4f electrons to the lattice. This explains the atomic-like properties of the lanthanides in a crystal. There exist several excellent books [24, 25] and reviews of optical properties of rare-earth-ion doped crystals [23, 26, 27] and their application in quantum information science [28, 29]. Here we will summarize some properties that are particularly relevant for quantum memory applications.

The effective shielding of the 4f electron shell results in extremely narrow homogeneous and inhomogeneous line widths of the radiative 4f-4f transitions in rare-earth doped crystals. At cryogenic temperatures, the inhomogeneous broadening is the dominating broadening process, analogous to the Doppler broadening of room temperature alkali gases. But in contrast to the dynamical Doppler broadening, where atoms jump between velocity classes due to velocity changing collisions, the inhomogeneous broadening of rare-earth ion doped crystals is to a large degree static. This is a result of the physical origin of the inhomogeneous broadening [30], which can be due to local crystal strain or interactions between dopants [31]. In some cases one can observe a time-dependent broadening of a spectral channel over time, which is known as spectral diffusion [32]. However, this effect is usually weak and is modelled by a time-dependent homogeneous line width [32]. The static inhomogeneous broadening and the large number of spectral channels that can be manipulated with narrowband lasers have important consequences for quantum storage experiments. These features are used in the quantum memory schemes specifically developed for these materials, resulting in capabilities difficult to obtain in gas phase experiments.

The optical inhomogeneous linewidth varies strongly between crystal hosts. In some cases the degree of broadening can be related to the ionic radius mismatch between the rare-earth dopant ion and the lattice ion that it replaces. Usual inhomogeneous broadenings range from a few hundreds of MHz to tens of GHz, although extreme values of around 10 MHz [33] and 250 GHz have been observed [34].

The optical homogeneous linewidth can be extremely narrow (ranging from <1 kHz to 1 MHz) if the sample is cooled to temperatures below 5–10 K [24, 25]. Above this approximative temperature range, the homogeneous linewidth usually increases rapidly, displaying a T^7 or T^9 dependence, due to coupling to phonons (spin-lattice relaxation). Below this temperature range, due to the shielding by the 5s and 5p electrons, the homogeneous linewidth is often limited by magnetic interactions with other rare-earth ion dopants or magnetic constituents of the lattice. This has led to the general understanding that crystal materials with low nuclear spin concentration [35, 36] and low rare-earth ion dopant concentration [32] provides a way of obtaining long coherence times, both for optical and hyperfine transitions. To increase the coherence times of hyperfine levels, it was also realized that one can exploit the non-linear magnetic Zeeman effect of the hyperfine levels in order to find sweet spots where there is a zero first-order Zeeman effect (ZEFOZ) of the hyperfine transition [37]. This effectively decouples the hyperfine transition from the fluctuating magnetic environment, which can increase the hyperfine coherence time with orders of magnitude, akin to clock transitions used in alkali atoms. In addition, one can apply dynamical decoupling schemes to further increase the spin coherence time [38–41]. A recent experiment demonstrated a coherence time of 6 h in Eu^{3+}:Y_2SiO_5 [42] by combining a ZEFOZ transition with dynamical decoupling.

The parity-forbidden 4f-4f transitions are only weakly allowed in crystals, and arise due to admixtures of excited configurations of different parity to the 4f configuration. As a consequence radiative lifetimes are long, usually in the range of 100 μs to 10 ms. The oscillator strengths of transitions relevant to quantum information applications are in the range of 10^{-8}–10^{-6} [43]. The weak absorption probability of individual ions, as compared to the alkali D_1 and D_2 lines, is compensated by the high density of ions typical for a crystal. The doping concentrations are in the range of 10–1000 pm, resulting in typical number densities in the range of 10^{17}–10^{19} ions/cm^3. The absorption coefficients for typical doping levels range from $\alpha = 1$ to 50 cm^{-1}, which often make the transitions close to opaque for a 1 cm long crystal.

We finally comment on the electronic ground-state substructure, which is relevant for quantum information processing in general. The RE^{3+} ions (RE=Pr, Eu, Nd, Tm, etc.) can be divided into Kramers and non-Kramers ions, which have odd or even number of electrons, respectively. This is relevant since the two groups react differently to the interaction with the surrounding lattice ions (crystal-field interaction). In a low-symmetry RE^{3+} doping site, the crystal field interaction completely lifts the electronic ground-state degeneracy for non-Kramers ions. For Kramers ions the crystal-field interaction results gives rise to a series of degenerate doublets, which is due to Kramers time-reversal symmetry. As a consequence the Kramers ions have a strong magnetic dipole moment (order of the Bohr magneton), while non-Kramers ions usually have weak nuclear magnetic moments due to the quenching of the electronic magnetic moment. In some cases, however, the nuclear moment can be strongly enhanced in non-Kramers ions through interactions induced by the crystal-field Hamiltonian. In addition we also need to consider different types of hyperfine interactions. As an example, in Eu^{3+} and Pr^{3+} doped crystals, which are non-Kramers

ions, these ions have three hyperfine states, due to quadrupole-type interactions [24, 25]. The hyperfine level separations in these ions are of the order of 10–100 MHz. In Kramers ions, such as Er^{3+} and Nd^{3+}, a spectrally resolved Zeeman ground-state doublet can be formed by applying a rather weak field (<1 T) [44]. For isotopes with non-zero nuclear spin, the interaction with unquenched electron spin results in a strong hyperfine interaction, of the order of 1 GHz for Kramers ions [45]. These different considerations are important for different aspects of quantum memory applications, since they affect the frequencies used for state preparation of the ions and possible limitations of the memory bandwidth due to interfering optical-hyperfine transitions.

9.3 Quantum Memory Protocols

In this section we will shortly discuss quantum memory protocols that can be used in rare-earth-ion doped crystals. We will particularly discuss the atomic frequency comb protocol, which so far is the only protocol that has been used in these systems for storage of quantum states of light. For the reader who wants an overview of different quantum memory schemes we refer to the many excellent reviews that have been published [1–4, 28].

An important class of quantum memory schemes have been inspired by the photon echo process [28], which is the optical analogue of the spin echo. In the conventional photon echo process the optical pulse to be stored is absorbed by an inhomogeneous ensemble of atoms, typically rare-earth impurity ions in a crystal. The induced atomic coherence then undergo inhomogeneous dephasing, but the dephasing can be reversed by applying an optical π-pulse a time τ after the input pulse. After a time 2τ the atomic coherences are back in phase, which results in a strong collective emission known as a photon echo. Photon echo processes have been investigated for storing and processing coherent states of light since the 1980s [28]. It was therefore natural to consider if the same processes and materials could be used to store the quantum state of a single photon. It was realized, however, that the optical π-pulse used in conventional photon echoes would cause too much spontaneous emission noise, due to the high degree of atomic excitation induced by it [46]. In 2001 Moiseev and Kröll [47] made an initial proposal for a noise free photon-echo quantum memory scheme. The scheme was proposed for Doppler-broadened lines, but sparked the interest for finding a similar scheme adapted to inhomogeneously broadened solid-state ensembles. Around 2005–2006 Nilsson and Kröll [48], Kraus et al. [49] and Alexander et al. [50] proposed a quantum memory scheme where the inhomogeneous dephasing was controlled not by a strong π-pulse, but by an external electric field gradient. The basic idea is to create a narrow spectral feature using optical pumping techniques, which is then broadened using an external field. The scheme was coined controlled reversible inhomogeneous broadening (CRIB), while a later modified version of the scheme was named gradient echo memory (GEM) [51]. Several experimental realizations of the CRIB/GEM storage scheme in rare-earth-ion doped crystals

followed [50, 52], including storage of weak coherent states at the single photon level [13, 53]. It is worth noting that the GEM experiment reported by Hedges et al. [13] demonstrated one of the highest efficiencies reached in any quantum memory, 69 %, and the highest reached in a solid-state memory. In rare-earth-ion doped crystals the CRIB/GEM experiments were implemented using external electric fields, based on the linear Stark shift. In some systems, however, the linear Stark shift is zero due to symmetry considerations [54].

In 2008 the atomic frequency comb (AFC) quantum memory scheme was proposed [12, 55]. The motivation for the scheme was the storage of trains of pulses, so-called temporal multimode storage, which turned out to be difficult using the CRIB scheme due to the scaling of the number of modes as a function of the optical depth of the storage material. In CRIB memories the number of modes scales linearly with the optical depth d of the transition [11], while for AFC it is independent of optical depth, although depending on other critical parameters, as will be discussed later. For electro-magnetically induced transparency (EIT) and Raman techniques, two common light-storage techniques, the number of modes scales as $\sqrt{d}$ [56].

The AFC scheme is based on a spectral tailoring of the inhomogeneous absorption spectrum of an optical transition $|g\rangle - |e\rangle$, where one ideally wants to make a periodic series of narrow, highly absorbing peaks (see Fig. 9.1). This forms the atomic frequency comb, which can be characterized by its spacing Δ and finesse F, in analogy with an optical cavity. A single-photon state, with a bandwidth γ_p larger than Δ, can be completely absorbed by the comb. Indeed, if the input pulse is short enough (meaning $\gamma_p > \Delta$), the effect of the short interaction in time is a spectral averaging of the sharp AFC structure into a smooth distribution, due to Fourier arguments, allowing for uniform absorption over the photons bandwidth. The effective optical depth of the comb is roughly $\tilde{d} = d/F$ [55], depending on the shape of the peaks, where d is the peak absorption depth. The absorption probability is $1 - \exp(-\tilde{d})$, showing that complete absorption can be achieved for high enough d for any finesse F. For a more complete description, we refer the reader to [55].

Conditioned on the absorption of a single photon, the atomic state can be described by a collective Dicke state $\sum_k c_k |g \cdots e_k \cdots g\rangle$ [57], where the amplitudes c_k depend on the detuning and spatial position of the particular atom k. These modes are initially in phase, but the collective state will rapidly dephase into a non-collective state $\sum_k \exp(-i2\pi\delta_k t) c_k |g \cdots e_k \cdots g\rangle$, since each term acquires an individual phase depending on the detuning δ_k of each excited atom. If we consider an AFC having very sharp peaks, then the detunings δ_k are approximately a discrete set such that $\delta_k = m_k \Delta$, where m_k are integers. It follows that the collective state is re-established after a time $1/\Delta$, which leads to a coherent photon-echo [58–60] type re-emission in the forward spatial mode defined by the absorbed photon. We note that the AFC echo can also be interpreted as a slow-light effect induced by the comb structure [61].

The scheme described here can only be used as a delay-line, with a fixed storage time $1/\Delta$. In the following we will refer to this scheme as an *AFC echo scheme*. A recent quantum repeater protocol is entirely based, however, on this scheme, but which requires heavy frequency and time multiplexing to be efficient [62]. It should also be emphasized that the AFC echo scheme provides a dynamical delay-line,

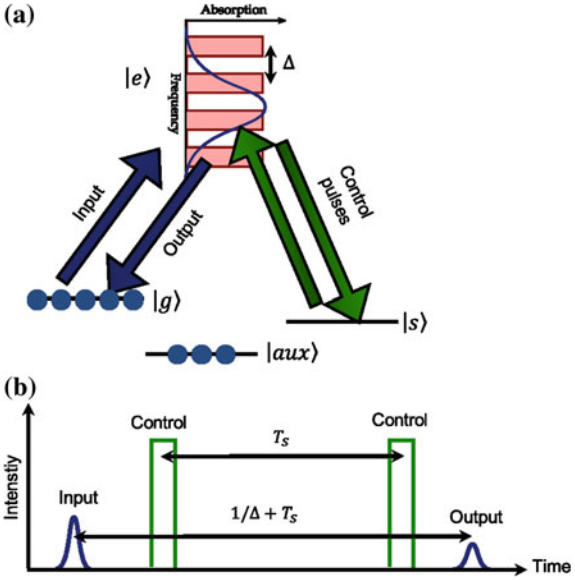

Fig. 9.1 The AFC quantum memory scheme. **a** The input pulse is absorbed on a strongly absorbing transition whose inhomogeneous spectrum is shaped into a comb with periodicity Δ. After the absorption of the input, a control pulse converts the initial optical coherence into a spin coherence, see panel (**b**) for the timing. Another control pulse applied a time T_S after the first one re-establishes the optical coherence, which evolves towards an echo emission after a total storage time $1/\Delta + T_S$. This scheme is the complete AFC spin-wave memory. If the control pulses are not applied, then the input will give rise to an output echo after a total storage time $1/\Delta$, called the AFC echo scheme. We refer to the text for more details on the processes and the required energy structure

which can be re-programmed with a rate related to the comb creation time. The temporal multimode capacity of the AFC scheme does not depend on optical depth, as mentioned above. The number of modes that one can store depends simply on the number of peaks in the comb, which in turn depends on the ratio of the comb periodicity Δ to the total comb bandwidth Γ.

To be able to read out a AFC memory on demand, the original proposal was based on a conversion of the optical excitation into a spin excitation [55]. This can be done by applying an optical control pulse that transfers the single optical excitation to a spin state, for instance a π-pulse, after the absorption of the single photon, but before the appearance of the AFC echo. This requires an additional ground state level $|s\rangle$, such that the states $|g\rangle$, $|e\rangle$ and $|s\rangle$ form a so-called Λ-system. To read out the memory a second control pulse is applied after a spin-wave storage time T_S, after which the collective Dicke state continues to evolve towards the AFC echo emission, after a total storage time $T_S + 1/\Delta$. In addition to providing on-demand read out of the memory, it can also provide a longer total storage time, since the spin coherence time can be orders of magnitude longer than the optical coherence time. In the following we will refer to this scheme as a *AFC spin-wave memory*. The spin-wave storage

requires a coherent spin-transition $|g\rangle$-$|s\rangle$ for storing the spin coherence, but also an additional state $|aux\rangle$ with long population lifetime. The auxiliary ground state $|aux\rangle$ is used for storing population that has been pumped away optically during the AFC creation process. The state $|aux\rangle$ is also needed in the AFC echo scheme described above. The need for three ground-state levels and a coherent spin transition $|g\rangle$-$|s\rangle$ limits the number of known materials that can be used for spin-wave storage.

The efficiency of the complete AFC spin-wave memory depends on several factors. The most important one is the efficiency of the AFC echo, which in turn depends on the optical depth of the material, the comb parameters and the direction of recall. But one also needs to consider the efficiency of the optical control pulses and spin dephasing during the spin-wave storage time T_S. In most cases these factors act independently on the total efficiency, leading to the simple efficiency formula

$$\eta = \eta_{AFC}\eta_C^2\eta_S \tag{9.1}$$

where η_{AFC} is the AFC echo efficiency, η_C the efficiency of one optical control pulse and η_S accounts for loss of efficiency due to spin decoherence. We here assume that the control pulses introduce no decoherence, we only take into account a limited transfer efficiency of population.

The AFC echo efficiency depends on the direction of recall. In forward direction the re-absorption effect in a optically dense medium limits the efficiency to 54 % [63, 64]. In backward recall an interference effect makes it possible to reach 100 % in principle [55, 64]. Backward recall can be achieved by using counter-propagating control pulses, but then only in spin-wave storage. The AFC echo efficiency formulas for both cases are given below

$$\eta_{AFC}^{fw} = \tilde{d}^2 \exp(-\tilde{d})\eta_{deph}, \tag{9.2}$$

$$\eta_{AFC}^{bw} = (1 - \exp(-\tilde{d}))^2\eta_{deph}, \tag{9.3}$$

where η_{deph} is a dephasing factor that accounts for the finite width and shape of the AFC teeth. It should be emphasized that these formulas also apply to the CRIB/GEM scheme. As shown in [55, 64], η_{deph} is simply the Fourier transform of a *single tooth* function in the comb, evaluated at the time of the AFC echo $1/\Delta$. The effective absorption depth $\tilde{d}$ also depends on the exact shape of the AFC teeth. In [55] Gaussian peaks where considered, while in [65] formulas were given for Lorentzian shaped teeth. Later Bonarota et al. [66] showed that square peaks give the highest efficiency for a given peak optical depth d. For square-shaped peaks $\tilde{d} = d/F$ exactly and $\eta_{deph} = \mathrm{sinc}^2(\pi/\mathrm{F})$.

The optical depth is in practice the most crucial parameter, which led to the proposal to put the memory in an optical cavity to enhance the effective interaction length [67, 68]. It was shown that the cavity could be operated in an optimal regime, where the input mirror reflectivity R of an asymmetric cavity is tuned to the effective optical depth of the memory $\tilde{d}$ such that $R = \exp(-2\tilde{d})$, assuming $\tilde{d} < 1$, which

is called an *impedance-matched* cavity. At the impedance-match point complete absorption can in principle be achieved, if all other losses are much smaller than $\tilde{d}$, and the efficiency is then bounded only by the intrinsic dephasing η_{deph}. As a consequence the cavity approach can lead to close to 100 % efficiency, without resorting to the phase-matching operation required for backward recall. Note also that the impedance-matched cavity scheme can be applied to any memory scheme based on control of the inhomogeneous dephasing, e.g. AFC, CRIB or GEM. Recent experimental demonstrations of the cavity scheme reached AFC echo efficiencies with bright pulses of 56 % [69] in Pr^{3+}:Y_2SiO_5 and 53 % [70] in Eu^{3+}:Y_2SiO_5, the highest reported AFC efficiencies to date.

9.4 State of the Art

Although the focus of this chapter is the interaction of quantum light with rare-earth doped solids, we first review a series of experiments that have been performed with weak coherent states at the single photon level. This type of experiment allows the testing of several aspects relevant for quantum light storage, in particular the coherence preservation, the noise added in the storage and retrieval processes as well as the waveform preservation. In addition, although the light at the input is classical, it has been shown that it is possible to infer the quantum character of the storage under certain conditions [10, 13, 62, 71].

The first demonstration of storage and retrieval of light at the single photon level in a solid state device, which was also the first demonstration of the AFC echo scheme, was done in 2008 at the University of Geneva [12]. Weak coherent light pulses were stored for up to 1 µs using the atomic frequency comb scheme in a Nd^{3+}:YVO_4 crystal. Single photon level time-bin qubits were also stored and the coherence was shown to be preserved to a high degree during the storage and retrieval process. Finally, a proof of principle experiment of temporal multimodality of the protocol was done, with the storage and retrieval of 4 temporal modes. The storage and retrieval efficiency was <1 % in that initial demonstration. However, several other single photon level experiments in other materials have since then demonstrated the AFC echo scheme at the single photon level with much higher efficiencies, reaching 9 % efficiency in Tm^{3+}:YAG [65] and 25 % in Pr^{3+}:Y_2SiO_5 [72, 73].

Another aspect that has been improved in recent experiments is the multimode capacity. The reversible mapping of up to 64 weak pulse temporal modes has been demonstrated in a Nd^{3+}:Y_2SiO_5 crystal [74]. The coherence was verified by simultaneously storing and analyzing multiple time-bin qubits. It has also been shown that, combined with phase modulators, AFC can be used as a programmable processor for spectral and temporal manipulation of single qubits [75]. Hong-Ou-Mandel interference between two AFC echoes recalled from Tm doped waveguides has been demonstrated [76]. Finally, the AFC storage was also extended to polarization qubits [71, 77, 78], and more recently to spectrally multiplexed time-bin qubits with selective readout in frequency [62]. Note that for all AFC echo experiments

mentioned above, the storage was done in the excited state only, leading to short and pre-determined storage time. The CRIB/GEM protocol allows on demand read-out even with storage in the excited state, as has been demonstrated at the single photon level in an Er^{3+} doped crystal [53] and in a Pr^{3+} doped crystal [13]. The latter experiment reported the highest efficiency for any solid state memory so far (69 %). It also showed that the memory operated in the quantum regime, meaning that the storage and retrieval fidelity was measured to be higher than the one achievable with a classical memory.

The first demonstration of quantum light storage in solid state device was reported simultaneously in 2011 by two groups, one from the University of Geneva [14] and one from the University of Calgary [15]. Both experiments demonstrated the storage of entangled photons in a rare-earth doped crystal, using the AFC echo scheme. Both experiments used compatible photon pair sources with one photon matching the storage device and the other photon at telecommunication wavelength. The two teams used different storage media with different properties and bandwidth. The Calgary experiment used a broadband AFC in a Tm^{3+} doped Lithium Niobate ($LiNbO_3$) waveguide absorbing light at 793 nm. One photon of the pair was stored for 7 ns in the waveguide, with a storage and retrieval efficiency of 2 % (excluding coupling losses in the waveguide). It was also shown that time-bin entanglement was preserved during the storage and retrieval, and a violation of a Bell inequality was demonstrated between the telecom photon and the stored and retrieved photon. The Geneva experiment used a Nd^{3+} doped crystal absorbing at 883 nm, with a storage bandwidth of 120 MHz and featured a maximal storage time of 200 ns and a maximal efficiency of 20 %. The preservation of energy-time entanglement was demonstrated. These experiments will be described in more detail in Sect. 9.6.1.

These experiments demonstrated for the first time entanglement between a telecom photon and a collective optical atomic excitation in a solid state device. It should be noted however that in both cases the photons were stored as optical atomic excitations, leading to short and only pre-determined storage times.

Following these initial experiments, further developments by the same groups included the storage and retrieval of polarization [77] and time-bin qubits [79] carried by heralded single photons. The Geneva group also reported an experiment demonstrating entanglement between two crystals [80] (it will be described in more detail in Sect. 9.6.1), followed by an experiment demonstrating quantum teleportation of the state of a telecom wavelength photon onto a collective atomic optical excitation [81]. Furthermore, the quantum storage of a 3-dimensional orbital-angular-momentum entangled photon has been reported in a $Nd^{3+}:YVO_4$ crystal by a group in Hefei [82].

In 2014 an experiment demonstrating quantum storage of heralded single photons using the AFC echo scheme in a Pr^{3+} doped crystal absorbing at 606 nm was carried out at ICFO. This material has demonstrated promising properties in the storage of classical light, including long storage times up to 1 min [41, 83] and high storage and retrieval efficiencies as mentioned above [13]. Contrary to materials used in previous demonstrations, it also possesses 3 ground state levels, such that spin-wave storage is in principle possible. However this comes with the drawback that the spacing

between the hyperfine states is small, therefore limiting the storage bandwidth to a few MHz. This poses strong challenges for the realization of a suitable quantum light source. The realization of such a source [84] and the storage experiment [16] will be described in more detail in Sects. 9.5.3 and 9.6.2, respectively.

While the previous experiments have been performed in rare-earth doped crystals, a recent experiment demonstrated that it is also possible to store non classical light states in an amorphous environment. An Er^{3+}-doped standard telecom glass fiber was used as storage device, and photons at telecom wavelengths were stored using the atomic frequency comb scheme, with an efficiency around 1 % and a storage time of 5 ns [85]. The experiment also showed that entanglement was preserved during the storage in the fiber.

Finally, we shortly mention experiments aiming at using crystals as a source of photon pairs with embedded memory. In these protocols, the crystal is illuminated with classical pulses, creating non classical correlations between an emitted photon and a stored collective atomic excitation. The protocols include the rephasing of amplified spontaneous emission (RASE) [86] and a combination of the DLCZ and AFC scheme [87]. First demonstrations of the RASE scheme have been realized, with strong but still classical correlations obtained in $Pr^{3+}:Y_2SiO_5$ [88] in the photon counting regime, and evidence of non-classical correlations obtained with homodyne detection in Tm^{3+}:YAG [89].

9.5 Quantum Light Sources Compatible with Solid State Quantum Memories

In order to achieve strong interactions between a single photon and a crystal, and to achieve high efficiency storage, it is crucial that the quantum light has spectral properties that match those of the quantum memory. The bandwidth of AFC memories is given by the width of the AFC that can be created in the crystal. For obtaining the high-finesse combs necessary to achieve high efficiency storage, the width of the comb is limited by the spacing between the adjacent states in the ground or excited state manifolds. Note that AFC broader than the spacing between ground and excited states can be created, however with a low finesse leading to limited storage efficiencies, see e.g. [15, 90, 91]. In the case where the spacing becomes bigger than the inhomogeneous broadening of the optical transition, the limit is then given by the latter. This situation could be encountered with Kramers ions (e.g. Nd^{3+}, Er^{3+}), where moderate magnetic fields could split the states by several GHz. In principle, high efficiency storage using the AFC echo scheme could therefore reach GHz bandwidth. In practice however, creating high quality combs for long storage times over such a large bandwidth is experimentally challenging. For achieving spin-wave storage, non-Kramers ions such as Pr and Eu are good candidates. In these materials, the spacing between hyperfine states are much smaller, leading to much smaller bandwidths, which can be as low as a few tens of MHz for $Eu^{3+}:Y_2SiO_5$ and 4.6 MHz for the excited state of $Pr^{3+}:Y_2SiO_5$. The creation of single photons with such a narrow

linewidth is experimentally challenging. Designing and implementing narrowband quantum light sources [92–96] that can be interfaced with atoms [97–102] has been the subject of several investigations in recent years. (see also chapters by Chuu and Du, M. Mitchell, and Zhao, Bao, Zhao and Pan).

The quantum light sources compatible with solid-state quantum memories that have been realized up to now make use of spontaneous parametric down conversion (SPDC), where a pump photon is probabilistically split into a photon pair, with energy and momentum conservation. A great advantage of this solution is that it is very flexible in terms of wavelengths of the created photons, which allows the coupling to quantum memories operating at any wavelengths. Moreover, it can create two photons with different frequencies, which can be used for example to create non classical correlations between a quantum memory operating in the visible range and a photon at telecommunication wavelengths. However, the spectrum of the photons emitted by spontaneous down conversion typically goes from 100 GHz to THz, several orders of magnitude larger than the bandwidth of quantum memories. Therefore extensive filtering must be applied in order to generate quantum memory compatible quantum light using spontaneous down conversion.

Filtering can be applied after the source, using passive filters. However this requires extremely bright sources [14], e.g. waveguide sources. The waveguide increases the production rate of photon pairs significantly [103], allowing for an efficient source while pumping it with a low peak-power cw laser. This is particularly important for a strongly filtered source, in order to have a sufficiently high probability of creating a photon pair within the filtered spectral regions. It is important to note that when passive filtering is used, the number of photon pairs per coherence time (or the spectral brightness expressed in pairs per second per mW of pump power and per MHz of bandwidth) does not change with the filter bandwidth [104]. While the rate of created pairs per second decreases with the filter width, the coherence time of the photon increases, leading to a constant spectral brightness.

Another way of implementing a narrow-band quantum light source from spontaneous down conversion is to insert the non linear crystal in an optical cavity [92] (see also chapters by Zhao, Bao, Zhao and Pan, and M. Mitchell). This not only has the advantage of providing filtering, but also enhances the probability of generating a photon within a cavity mode, with respect to the no cavity case. In the ideal case, the enhancement is given by $Q = F^3/(\pi F_0)$ [92], where F is the finesse of the cavity and F_0 is the finesse calculated only from the mirrors reflectivity. In order to reach this enhancement, both signal and idler fields need to be resonant with the cavity.

Beyond the use of SPDC, several other systems could be used as quantum light sources. It could be possible to use the doped crystals themselves as sources of photon pairs with the required spectral properties, as shown with quantum memories based on atomic gases (see. e.g. [9] for a review). However, this turns out to be much more difficult to implement in rare-earth doped solids, due to the very small oscillator strength of the optical transition [105]. Several schemes have been proposed, including the rephasing of amplified spontaneous emission (RASE) [86] and a combination of the DLCZ and AFC scheme [87]. Solid state single photon emitters may also be used as compatible single photon sources, e.g. quantum dots or single

molecules. Quantum dots have typically GHz spectral bandwidths (see chapters by Lanco and Senellart, Schneider, Gold, Lu, Höfling, Pan and Kamp, and McMahon and De Greve), which may be compatible with the AFC echo scheme with broadband combs. The challenge is to tune the quantum dot in resonance with the rare-earth ensemble, without broadening the line. Single molecules in solid state matrices have shown much narrower spectral bandwidth, down to tens of MHz [106], which could be used with spin-wave quantum memories. Again, the challenge is to tune them near resonance. A potential solution for the frequency mismatch is to implement quantum frequency conversion [107] which has been used recently to interface telecom photons to quantum memories [73, 108].

9.5.1 Characterizing Photon Pair Sources

In this section, we discuss various ways to characterize photons pairs emitted by SPDC and to quantify the correlations between signal and idler fields. The state created by single mode SPDC is given by (for $p \ll 1$):

$$|\Psi\rangle_{s,i} = \sqrt{1-p}\sum_{n=0}^{\infty} p^{\frac{n}{2}}|n\rangle_s|n\rangle_i \tag{9.4}$$

where p is the probability to create a photon pair and is proportional to the pump power, and $|n\rangle_s(|n\rangle_i)$ is a n photon Fock state in the signal (idler) mode. This state is known as two-mode squeezed state. It displays very strong quantum correlations between the two modes, i.e. the signal and idler fields.

For a photon pair source, the quality of the correlations between signal and idler fields is usually quantified measuring the second order cross-correlation function $G^{(2)}_{s,i}(\tau)$ between the two fields, by performing a coincidence measurement. The normalized form of $G^{(2)}_{s,i}(\tau)$, denoted as $g^{(2)}_{s,i}(\tau)$ can be expressed as:

$$g^{(2)}_{s,i}(\tau) \equiv \frac{\langle E_s^{\dagger}(t)E_i^{\dagger}(t+\tau)E_i(t+\tau)E_s(t)\rangle}{\langle E_i^{\dagger}(t+\tau)E_i(t+\tau)\rangle\langle E_s^{\dagger}(t)E_s(t)\rangle}, \tag{9.5}$$

where $E^{\dagger}_{s,i}$ $(E_{s,i})$ is the electric field creation (annihilation) operator for the signal and idler fields. For the ideal two mode squeezed state of 9.4, the cross-correlation function is given by:

$$g^{(2)}_{s,i} = 1 + \frac{1}{p} \tag{9.6}$$

We see that the correlation decreases when increasing p. This is the consequence of the creation of multiple pairs. We also see that $g^{(2)}_{s,i}$ can become arbitrarily high

for low excitation probability. However, this comes at the expense of the count rate, since the mean number of photons in the signal mode is given by

$$\bar{n}_s = \frac{p}{1-p} \tag{9.7}$$

This illustrates a fundamental limitation of SPDC: there is a trade off between the degree of quantum correlation and the count rate that can be obtained. In practice, $g^{(2)}_{s,i}$ is determined over a detection window $\Delta\tau$ as:

$$g^{(2)}_{s,i}(\Delta\tau) = \frac{p_{s,i}}{p_s\, p_i} \tag{9.8}$$

where $p_{s,i}$ is the probability to detect a coincidence between signal and idler photons and p_s (p_i) is the probability to detect a signal (idler) photon in a time interval $\Delta\tau$.

The second order cross-correlation function can also be used to gain information on the spectral content of the photon pairs. For example, in the case of doubly-resonant cavity-enhanced downconversion, following the theory used in [100, 102], $G^{(2)}_{s,i}(\tau)$ takes the form:

$$G^{(2)}_{s,i}(\tau) \propto \left| \sum_{m_s,m_i=0}^{\infty} \frac{\sqrt{\gamma_s\,\gamma_i\,\omega_s\,\omega_i}}{\Gamma_s+\Gamma_i} \times \begin{cases} e^{-2\pi\Gamma_s(\tau-(\tau_0/2))}\mathrm{sinc}(i\pi\tau_0\Gamma_s) & \tau \geq \frac{\tau_0}{2} \\ e^{+2\pi\Gamma_i(\tau-(\tau_0/2))}\mathrm{sinc}(i\pi\tau_0\Gamma_i) & \tau < \frac{\tau_0}{2} \end{cases} \right|^2, \tag{9.9}$$

where $\gamma_{s,i}$ are the cavity damping rates for signal and idler, $\omega_{s,i}$ are the central frequencies, $\Gamma_{s,i} = \gamma_{s,i}/2 + i m_{s,i}\,\mathrm{FSR}_{s,i}$ with mode indices $m_{s,i}$ and free spectral ranges $\mathrm{FSR_{s,i}}$, and τ_0 is the transit time difference between the signal and idler photons through the SPDC crystal. Equation 9.9 shows that the second order cross-correlation function for a multimode cavity output displays an oscillatory behavior with peaks separated by the inverse of the cavity free spectral range. The width of the peaks is directly related to the number of spectral modes in the signal and idler fields. For two modes, the oscillation will be sinusoidal, and the width will then decrease with the number of modes. In practice, the minimum width that can be detected is given by the detectors' time resolution.

For the case without cavity, but with single mode Lorentzian filters with width γ_s and γ_i inserted in the signal and idler modes, respectively [109], the cross-correlation function takes the following form we have:

$$g^{(2)}_{s,i}(\tau) = 1 + \frac{4}{p}\frac{\gamma_s\gamma_i}{(\gamma_s+\gamma_i)^2} f(\tau) \tag{9.10}$$

where

$$f(\tau) = \begin{cases} e^{-\gamma_s \tau} & \tau \geq 0 \\ e^{\gamma_i \tau} & \tau < 0 \end{cases} \tag{9.11}$$

This expression is very similar to that of a cavity-enhanced source (equation 9.9) for the special case of a single cavity mode.

Information about the spectral content of the created photons can also be obtained by measuring the unconditional second order autocorrelation function $g^{(2)}_{s,s}$ and $g^{(2)}_{i,i}$, for the signal and idler fields, respectively. For an ideal two mode squeezed state, the unconditional field exhibit thermal statistics with $g^{(2)}_{s,s}(0) = g^{(2)}_{i,i}(0) = 2$. However, if several spectral modes are present, it has been shown [110] that the autocorrelations decrease as $g^{(2)}_{s,s}(0) = g^{(2)}_{i,i}(0) = 1 + 1/K$ where K is the number of modes. By measuring the unconditional second order autocorrelation function, one can therefore bound the number of spectral and temporal modes present in the fields. This is valid as long as the measurement is not limited by noise.

The non-classical nature of the correlation between signal and idler fields can be experimentally assessed with a Cauchy-Schwarz inequality. For a pair of independent classical fields the following inequality must be fulfilled:

$$R = \frac{(g^{(2)}_{s,i})^2}{g^{(2)}_{s,s}\, g^{(2)}_{i,i}} \leq 1 \tag{9.12}$$

If the signal and idler fields exhibit thermal or sub-thermal statistics ($g^{(2)}_{s,s}(0) = g^{(2)}_{i,i}(0) \leq 2$), the measurement of $g^{(2)}_{s,i} > 2$ is therefore a signature of non-classical correlations. However, in order to prove non-classicality without assumptions on the created state, the unconditional autocorrelation functions should be measured as well.

9.5.2 A Quantum Light Source Compatible with Nd Doped Crystals

Here we discuss a filtered SPDC source producing photons at 883 nm (signal) and 1338 nm (idler), which was developed to interface with a Nd^{3+}:Y_2SiO_5 quantum memory operating at 883 nm, having a memory bandwidth of 120 MHz. This particular source has been described in [14, 80], while a similar source, slightly more broadband, of polarization-entangled photons for quantum storage was described in a more recent work [109].

The SPDC source was based on a periodically-poled potassium titanyl phosphate (PPKTP) crystal with an optical waveguide. The PPKTP crystal was pumped by a continuous-wave (cw) 532 nm laser, which is convenient since powerful and frequency stable single-mode Nd:YAG lasers exist at this wavelength. Since one photon should be resonant with the 883 nm transition in Nd^{3+}:Y_2SiO_5, the choice

of the pump laser imposed the wavelength of the idler photon to 1338 nm, in the telecommunication O-band. In principle one could use another pump wavelength to produce an idler photon in the more conventional telecommunication C-band around 1550 nm.

Without external frequency filtering the source produced photons with a bandwidth of about 800 GHz, such that strong filtering of the photon pairs was necessary to match the memory bandwidth of 120 MHz. To this end a combination of diffraction gratings, optical cavities and a fibre-based filter was used. The gratings provided full-width at half-maximum (FWHM) bandwidths of 90 and 60 GHz for the signal and idler photons, respectively. For the signal photon two etalons placed in series resulted in a single longitudinal mode with a bandwidth of 350 MHz. It should also be emphasized that the 6 GHz wide inhomogeneous absorption profile of the Nd^{3+}:Y_2SiO_5 crystal provided additional filtering, since the 120 MHz comb was created within this absorption profile. For the idler photon a home-made narrow-band cavity filtered down the photons to a FWHM linewidth of 43 MHz. A single longitudinal mode of this cavity was selected by a fiber Bragg grating (FBG). The total transmission coefficients from the PPKTP waveguide to the single-mode fibers were 22 and 14 % for signal and idler photons [80], respectively, including fiber coupling. The more recent version of this source [109] reach higher efficiencies, partly because high-efficiency volume Bragg gratings (VBGs) replaced the diffraction gratings.

Strong non-classical correlations between the signal and idler photons can only be obtained if the central frequencies of the filters on each mode satisfy the energy conservation of the SPDC processes. This is a non-trivial task when dealing with highly non-degenerate SPDC sources, particularly when one mode must be resonant with an external quantum memory. A solution to this problem was introduced in the work discussed here. A reference laser that is resonant with the signal filtering system and the quantum memory is injected into the SPDC source. This will create light at the idler wavelength through difference frequency generation (DFG), which obey the necessary energy conservation. This can be used to adjust central frequency of the idler filtering system, alternatively one can also change the wavelength of the pump laser.

The filtered SPDC source can be characterized by the pair creation rate within the filtered modes (spectral brightness) and the second-order auto and cross correlation functions of the signal and idler modes. The intrinsic spectral brightness of the PPKTP waveguide was $6.3 \cdot 10^3$ pairs/(mW $\cdot$ MHz $\cdot$ s) [80], which does not include the transmission through the filtering elements. This means that the probability p to create a pair (in the limit $p \ll 1$) is then $p \approx 2.7 \cdot 10^{-3}$/mW per 10 ns within a 43 MHz wide spectral window. The duration of the detection window should be set with respect to the photon pair coherence time, which in our case is dominated by the 43 MHz filter on the idler side (7 ns coherence time). The spectral brightness of the source including the filtering elements and fiber coupling was $\approx$ 200 pairs/(mW $\cdot$ MHz $\cdot$ s). If we again assume a 43 MHz filtered bandwidth we arrive at a final pair creation rate of 8600 pairs/s per mW pump power.

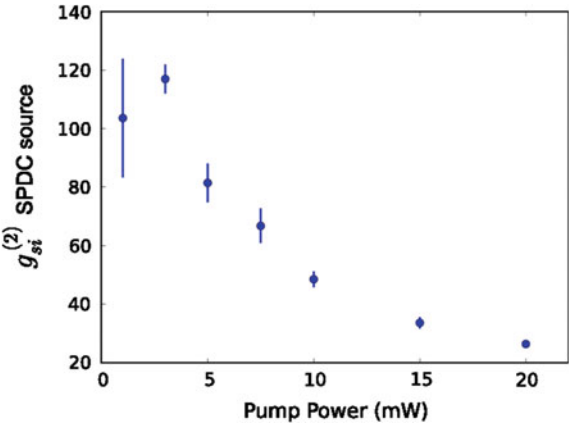

Fig. 9.2 Second-order cross-correlation $g^{(2)}_{s,i}(\Delta\tau)$ function of the filtered SPDC source developed for Nd doped crystals, as a function of the power of the laser pumping the SPDC source. The detection integration window was $\Delta\tau = 10\,\text{ns}$

The second-order auto-correlation functions of both the idler and signal modes were characterized [80], resulting in $g^{(2)}_{i,i}(0) = 1.9$ and $g^{(2)}_{s,s}(0) = 1.8$. These values give effective mode numbers $K = 1.1$ and $K = 1.25$ for the idler and signal modes, which indicate single frequency modes on both the signal and idler side.

In Fig. 9.2 we show the second-order cross-correlation function $g^{(2)}_{s,i}$ of the source as a function of pump power which exhibits the expected $1 + 1/p$ behaviour [14]. Based on the intrinsic spectral brightness we expect a cross-correlation $g^{(2)}_{s,i} \approx 75$ for $P = 5\,\text{mW}$, which is very close to the measured value of about 80. The cross-correlation function is larger than the classical upper bound of 2, where one assumes $g^{(2)}_{i,i}(0) = g^{(2)}_{s,s}(0) = 2$, for all pump powers, clearly demonstrating the strong non-classical correlations of the source.

9.5.3 A Quantum Light Source Compatible with Pr Doped Crystals

In the context of generating quantum light compatible with Pr^{3+}:Y_2SO_5, one of the photons must be at 606 nm, with a bandwidth smaller than 4 MHz. In addition, in order to use this source to generate entanglement between remote crystals, it is desirable to have the second photon of the pair at a telecom wavelength. An experiment showing these properties was reported in [84].

In order to meet these requirements, the following source was used. A pump laser at 426 nm was used to generate widely non degenerate photon pairs at 606 and 1436 nm in a periodically poled lithium niobate crystal. The crystal was placed in a bow tie optical cavity with a free spectral range of 400 MHz and a finesse of around 200 for the signal and idler modes. A special coating was used to achieve high reflectivity (99.99 %) for three mirrors, and a specified reflectivity of 98.5 %

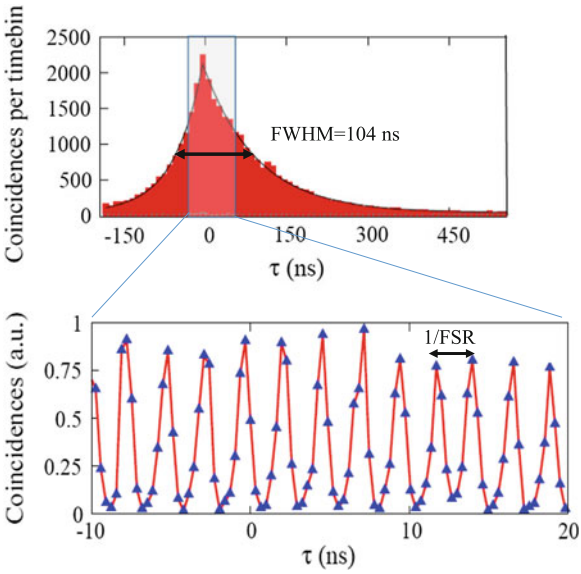

Fig. 9.3 Measured second-order cross-correlation $G^{(2)}_{s,i}(\tau)$ function (non normalized) of the cavity enhanced SPDC source developed for Pr doped crystals [84]. The FWHM correlation time is 104 ns. The zoom displays a higher temporal resolution, allowing to observe the oscillations in the $G^{(2)}_{s,i}(\tau)$, characteristic of multi spectral mode output. From this data, a number of four mode per cluster is inferred

for the output coupler. The SPDC output is modified by the cavity modes. In the case of degenerate photons with the same polarization, the spectrum would be a convolution between the phase matching bandwidth and the cavity modes. However, in the non degenerate case, the signal and idler modes experience different dispersion characteristics in the crystal, which leads to slightly different free spectral ranges. Since both modes have to be resonant with the cavity to enable enhancement, only a subset of modes will be enhanced. These modes are grouped in so called clusters [93, 111]. The width and spacing of the clusters is determined by the dispersion properties of the crystals and the cavity geometry.

In the experiment of [84], the number of modes per cluster was inferred to be around 4, by looking at the oscillations in the $g^{(2)}_{s,i}(\tau)$ function and comparing to equation 9.9 (see Fig. 9.3). This number was also verified by direct measurement of the signal and idler fields with a narrow band filter cavity, scanned over the spectrum. The number of clusters was then inferred by measuring the first order correlation function of the idler field. Within the phase-matching bandwidth of the free space down conversion photons of around Γ_{pm}= 80 GHz, the spectrum of the photons leaving the cavity was finally inferred to be composed of one main cluster containing around four longitudinal modes, and two smaller side clusters separated by 45 GHz from the main one and suppressed by around 80 %. For degenerate photons, the number of longitudinal modes would be given by Γ_{pm}/FSR = 200 modes. The clustering effect therefore leads to a suppression of the number of modes of around 50. Within a longitudinal mode, the photons pair created featured a correlation time of 104 ns (see Fig. 9.3), the longest demonstrated so far with SPDC sources. From the decay of the $G^{(2)}_{s,i}(\tau)$ (fitted with $\exp(-2\pi\Delta\nu\tau)$), spectral-linewidth of $\Delta\nu$ of

1.7 and 2.9 MHz were inferred for the idler field at 1436 nm and the signal field at 606 nm, respectively. The asymmetry can be attributed to the different intra-cavity losses for the two wavelengths. A intrinsic spectral brightness of $8 \cdot 10^3$ pairs/(mW $\cdot$ MHz $\cdot$ s) was inferred, leading to $p \approx 6.4 \cdot 10^{-3}$/mW per 400 ns within a 2 MHz wide spectral window. However due to large optical losses, the spectral brightness before the detectors (inside single mode fibers) was 11 pairs/(mW $\cdot$ MHz $\cdot$ s). In a more recent version of the source, this number was increased to 190 pairs/(mW $\cdot$ MHz $\cdot$ s).

This source still requires additional filtering for selecting a single frequency mode. However, the filtering requirement are considerably relaxed due to the low number of modes present in the spectrum. Side clusters can easily be removed by placing etalons with high transmission efficiency in the signal or idler modes. In order to select a single mode, a narrow band filter cavity with $FSR = 16.8$ GHz and linewidth of 80 MHz has been placed in the signal arm. In this configuration, the measured $G^{(2)}_{s,i}(\tau)$ was measured and no oscillation was observed, confirming that only one mode per cluster was present. The suppression of the side cluster could also be inferred first order autocorrelation.

9.6 Quantum Light Storage Experiments

9.6.1 Quantum Entanglement Storage in Nd:YSO Crystals

In 2008 the first AFC echo storage experiment in a Nd^{3+}:YVO_4 crystal at the single photon level was demonstrated [12], which was the starting point for considering storing true quantum states of light. To this end the filtered SPDC source described in Sect. 9.5.2 was developed. The first Nd:YVO_4 memory had a bandwidth of a few MHz, making the filtering of the SPDC source difficult. A more wideband Quantum memory was therefore developed in a Nd^{3+}-doped crystal Y_2SiO_5, using the $^4I_{9/2}-{}^4F_{3/2}$ transition at 883 nm [14, 74]. This optical transition has an inhomogeneous broadening of about 6 GHz. The ground state was split into a Kramers spin doublet by applying a magnetic field of around 300 mT, producing a Zeeman split of about 11 GHz. The comb structure was created on one of the Zeeman transitions by performing spectral hole burning, i.e. ions were optically pumped into the other Zeeman spin state. In practice this was done by scanning the laser frequency of a narrow-band external-cavity diode laser (EDCL) with a acousto-optic modulator (AOM), while periodically switching off and on the light. The total bandwidth was 120 MHz, limited by the scan range of the AOM. The maximum efficiency at low storage times $1/\Delta$=25 ns was 20 %, close to the optimal value for the optical depth of the crystal. In Fig. 9.4 we show an example of storage of 883 nm signal photons produced by the filtered SPDC source in the crystal [14]. The cross correlation function between the signal and idler modes after storing the signal mode clearly shows

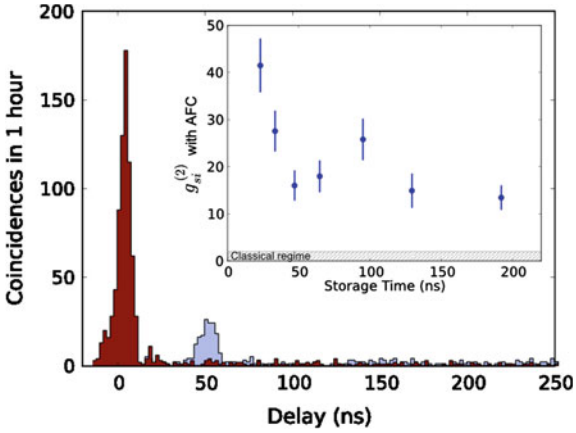

Fig. 9.4 Detection event histogram as a function of time. The peak at around zero time was recorded by making a large transparency hole in the Nd^{3+}:Y_2SiO_5 absorption, therefore it represents the input mode. When creating an AFC with periodicity $\Delta = 20$ MHz, the expected AFC echo appears as a peak at around 50 ns. The excellent signal-to-noise ratio indicates a strong quantum correlation between the idler photon (1338 nm) and the signal photon (883 nm), after the latter has been stored in the memory. The *inset* quantifies this by showing the second-order cross-correlation $g^{(2)}_{s,i}(\Delta\tau)$ function as a function of storage time 1Δ. The $g^{(2)}_{s,i}(\Delta\tau)$ function is significantly larger than the classical limit of 2, for all storage times. The detection integration window was $\Delta\tau = 10$ ns

quantum correlations, for all storage times. This can be interpreted as storing a single photon at 883 nm, heralded by the detection of an idler photon.

The second-order cross-correlation function $g^{(2)}_{s,i}(\Delta\tau)$ after storage of the signal photon is lower than that of the source, cf. Fig. 9.2. In [80] it was shown that it was due to the delay introduced by the memory. Indeed, the signal photons released from the memory are superimposed with uncorrelated signal photons created later during the AFC echo emission, which are transmitted through the memory with a certain probability. This noise source depends on the ratio of the memory transmission to the memory efficiency [80]. A solution to this problem is to turn off the SPDC pump laser before the AFC echo, which was done in the quantum storage experiment in Pr^{3+}:Y_2SiO_5 described below [16].

The photons produced by a SPDC source pumped by a CW pump laser are entangled in energy-time [112], provided that the coherence time of the pump is significantly longer than the coherence time of the signal-idler pair. This condition is naturally met when using a single-mode frequency CW pump laser, as in this case. This energy-time entanglement can be revealed by making projective measurements on different time basis states, on both the signal and idler modes. Practically, one can place Mach-Zehnder (MZ) interferometers in each mode, each MZ having the same path difference ΔT, which is known as a Franson-type set-up [112]. The two-photon interference fringes obtained when varying the phases in each interferometer reveal the energy-time entanglement. The coincidence rate varies like $V\cos(\Delta\phi_s + \Delta\phi_s)$,

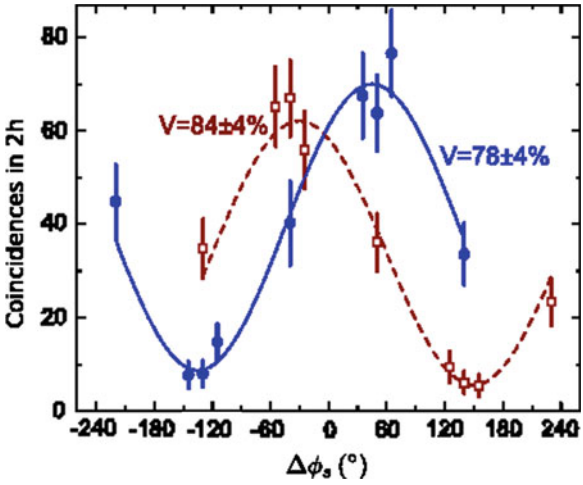

Fig. 9.5 Number of detected signal-idler coincidences as a function of the signal analyser setting $\Delta\phi_s$, for two settings $\Delta\phi_i$ of the idler analyser shown as *square* and *circle symbols*. The *solid* ($V = 78 \pm 4\,\%$) and *dashed* ($V = 84 \pm 4\,\%$) *lines* are fits to the *circles* and *squares*, respectively

where ϕ_s and ϕ_i are the phase settings on the signal and idler interferometers and V is the visibility. More formally the quantum entanglement can be detected by a violation of the Clauser-Horne-Shimony-Holt (CHSH) inequality [113], where the CHSH parameter S is larger than 2 for any entangled state. The violation of the CHSH inequality can also be inferred from a fringe visibility larger than $1/\sqrt{2} \approx 70.7\,\%$.

In the experiment we describe here [14], a particular twist was introduced. While the idler photon was analyzed using a standard interferometer, the signal photon was analyzed inside the Nd^{3+}:Y_2SiO_5 memory. We exploited the fact that more complicated absorption features than periodic combs can be created. Indeed, by creating an absorption structure that was the sum of two combs with different periodicities Δ_1 and Δ_2, we could create an effective unbalanced interferometer within the crystal. By setting $1/\Delta_1 - 1/\Delta_2 = \Delta T$ we could analyze the entanglement *in memory*.

In Fig. 9.5 we show examples of interference fringes as a function of $\Delta\phi_s$ for two values of $\Delta\phi_i$. Both visibilities are well above the limit $\approx 70.7\,\%$, strongly indicating the presence of entanglement. By explicitly measuring a CHSH parameter of $S = 2.64 \pm 0.23$ the entanglement between the idler photon and the photon stored in the crystal was clearly demonstrated.

In parallel to the work described above, Saglamyurek *et al.* also demonstrated storage of a photon entangled with a another photon stored in and released from a rare-earth doped crystal [15]. In their experiment the entangled photons were produced by a bulk periodically poled lithium niobate (PPLN) crystal, which was pumped using a pico-second laser with high peak power. Time-bin entangled photons were produced by splitting the 16 ps pump pulse into two coherent pulses separated by 1.4 ns. The idler photon was at the telecom wavelength 1532 nm, while the signal photon was at 795 nm. The quantum memory was based on a atomic frequency comb created on the $^3H_6$–$^3H_4$ transition at 795 nm in a Thulium-doped lithium niobate crystal (Tm^{3+}:$LiNbO_3$). A particular feature of this experiment was the optical waveguide

on the surface of the Tm^{3+}:$LiNbO_3$ chip. The waveguide technology is widespread in integrated optics and opens up interesting perspectives of combining the storage device with other optical elements. The AFC memory in this experiment was also very broadband, the AFC spanned a range of 5 GHz. This allowed storage of the short 16 ps long photons produced by the filtered SPDC source. This also implies that the degree of filtering was less stringent than in the experiment described previously. A drawback of this material is, however, the short storage time and the low efficiency. The entanglement experiment discussed here demonstrated a storage time of 7 ns, with an AFC echo efficiency of 2 %. The preservation of entanglement was proved by testing the CHSH inequality, resulting in a CHSH parameter of $S = 2.25 \pm 0.06$.

In the next experiment that we will describe the goal was to entangle two Nd^{3+}:Y_2SiO_5 crystals [80]. This could be done by storing each photon out of an entangled pair, but this requires that both photons are resonant with a memory. With only one photon in resonance with the Nd doped crystal at 883 nm, the choice was made instead to store a path-entangled state of a single photon [114]. More specifically, this state can be created by sending a single photon state $|1\rangle$ through a balanced beam-splitter, which creates the state $1/\sqrt{2}(|1\rangle_A|0\rangle_B + |0\rangle_A|1\rangle_B)$ of the spatial output modes A and B of the beam-splitter. This state is sometimes referred to as single-photon entanglement [114]. Now, entanglement between two memories can be realized by placing one memory in each path. This approach was first used by Choi et al. [115] to entangle two spatial modes in the same cloud of laser-cooled caesium atoms, where each mode was stored in the cloud using EIT. In the experiment described here, this approach was used to entangle the modes of two physically distinct crystals and the modes were stored using the AFC scheme [80]. The single photon state was produced by detecting the idler photon from the filtered SPDC source, which creates a state very close to a single photon in the signal mode (a heralded single-photon source).

To characterize the single-photon entanglement one can read out the memories and then perform measurements on the photonic state, which provides a lower bound of the entanglement present while storing the two modes. To detect the entanglement we used the tomographic approach developed by Chou et al. [116], in which the entanglement is quantified through a single parameter, the concurrence C. The concurrence is positive $C > 0$ for an entangled state, more specifically a separable state gives $C = 0$ and a maximally entangled state $C = 1$. To compute the concurrence one needs to measure the probability of finding exactly one signal photon in any of the two modes, p_{01} and p_{10}, and the probability of finding one signal photon in each path, p_{11}. This requires two- and three-fold coincidence measurements, respectively, since one also needs to detect the heralding idler photon. In addition one needs to measure the one-photon visibility V associated with the two paths A and B. The concurrence can then be calculated with the formula: $C = V(p_{10} + p_{01}) - \sqrt{2p_{00}p_{11}}$ [116]. By performing all the necessary measurements for a relatively high pump power of 16 mW, a concurrence of $C = 6.3 \pm 3.8 \cdot 10^{-5}$ was reached, indicating the presence of entanglement [80]. The low concurrence was essentially due to losses, since the detection probabilities include all propagation losses, memory efficiency and detection probabilities. Alternatively one can use an approach where the p_{11} probability is

inferred from the cross-correlation function $g^{(2)}_{s,i}$, which is a much more time efficient experiment as it uses only two-fold detections. Using this approach the presence of entanglement at the pump power of 16 mW could be confirmed, and the concurrence was measured for a range of lower pump powers where the direct method turned out to be too time consuming due to the rarity of three-fold coincidences. The concurrence reached about $C = 1.1 \pm 0.1 \cdot 10^{-4}$ for the lowest pump power of 1 mW, showing the presence of entanglement of the stored modes in the two Nd^{3+}:Y_2SiO_5 crystals.

9.6.2 Quantum Storage of Heralded Single Photon in a Pr^{3+}:Y_2SiO_5 Crystal

As mentioned previously, Pr doped solids have demonstrated exceptional properties for light storage experiments, including long storage times [40, 41, 83] and high efficiencies [13, 69]. Despite these very promising properties, there is currently only one demonstration of storage of quantum light in this system. In this section, we describe in more detail this demonstration, initially reported in [16].

The ultra-narrowband photon pair source described in Sect. 9.5.3 can be used to generate heralded single photons compatible with the Praseodymium doped crystal. For sufficiently high correlations between the two fields, the detection of an idler telecom photon will indeed project the signal mode in a single photon Fock state.

These heralded single photons have been stored in the Pr^{3+}:Y_2SiO_5 as collective optical atomic excitations using the AFC echo scheme. The storage device is a 3 mm thick Y_2SiO_5 sample doped with a Pr^{3+} concentration of 0.05 %. The relevant optical transition connects the $^3H_4$ ground state to the $^1D_2$ excited state at a wavelength of 605.977 nm and features a measured absorption coefficient of 23 cm^{-1}, and an inhomogeneous linewidth of 5 GHz. At zero magnetic field, the ground state and excited states manifolds are split in 3 metastable states, denoted $\pm 1/2_k$, $\pm 3/2_k$ and $\pm 5/2_k$ (see inset of Fig. 9.6), where $k = g, e$ denotes the ground or the excited state. The spacing between the hyperfine states is of the order of a few MHz. This gives an upper limit for the bandwidth as already mentioned. But, since the separation between ground states is much smaller than the inhomogeneous broadening, it also creates a complication for isolating a single class of atoms. A laser sent in the crystal can indeed be resonant with up to 9 distinct classes of atoms, within the inhomogeneous broadening. To select a single class of atoms, the optical pumping scheme first demonstrated by Nilsson et al. was used [117]. After selecting one class of atoms, an atomic frequency comb is created on the $\pm 1/2_g \rightarrow \pm 3/2_e$ transition (see Fig. 9.6 for an example of AFC).

One important issue to couple photons to the solid state atomic ensemble is that the frequency of the photons must be stable within a few hundred kHz. This can be insured by implementing a feedback lock system using the laser used to prepare the atomic frequency comb. One the one hand, the length of the cavity is locked on the

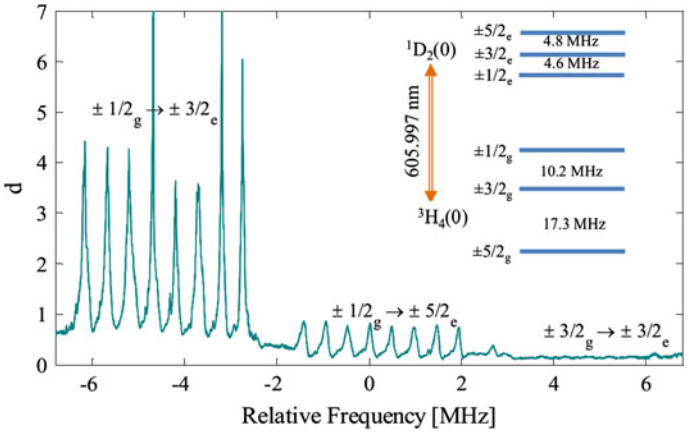

Fig. 9.6 Example of an atomic frequency comb in Pr^{3+}:Y_2SiO_5 . The optical depth (d) is plotted as a function of the relative frequency. The input and output photons are resonant with the $\pm 1/2_g \rightarrow \pm 3/2_e$ transition. *Inset* Relevant energy level scheme of the Pr^{3+}:Y_2SiO_5 crystal, with 3 hyperfine ground states and 3 excited states

laser with a Pound-Drever-Hall scheme. This insures that at least one spectral mode emitted by the cavity enhanced source is resonant with the crystal absorption. On the other hand, the required double resonance for signal and idler modes is insured by adjusting the frequency of the pump laser using a classical signal at the idler wavelength created by difference frequency generation between the pump laser at 426 nm and the laser at 606 nm.

In the experiment, a single longitudinal mode was selected for the idler mode thanks to a Fabry Perot filter cavity. For the heralded single photon, the crystal itself was used as a filter to prevent the modes non resonant with the AFC to reach the detector. The probability to have a single photon in the signal mode before the cryostat conditioned on a detection in the idler mode (called the heralding efficiency η_H) was around a few percents in this experiment, limited by dark counts in the idler detector, noise in the idler mode, cavity escape efficiency and optical losses in the signal mode from the cavity to the crystal.

The heralded single photon at 606 nm was first characterized by measuring the second order correlation $g^{(2)}_{s,i}(\Delta\tau)$ function by sending it through the crystal where a 12 MHz wide transparency window was created (see Fig. 9.7a). In Fig. 9.7b, the values of $g^{(2)}_{s,i}(\Delta\tau)$ for the incoming photons are plotted as a function of the pump power. The value of $g^{(2)}_{s,i}(\Delta\tau)$ increases when the pump power decreases, as expected for a two-mode squeezed state. The non classicality of the input photon was also demonstrated by violating a Cauchy-Schwarz inequality. The detected coincidence count rate was around 0.8 Hz per mW of pump power. By correcting for known optical losses and detection efficiencies, a creation rate outside the cavity of 2.8 kHz /mW was inferred.

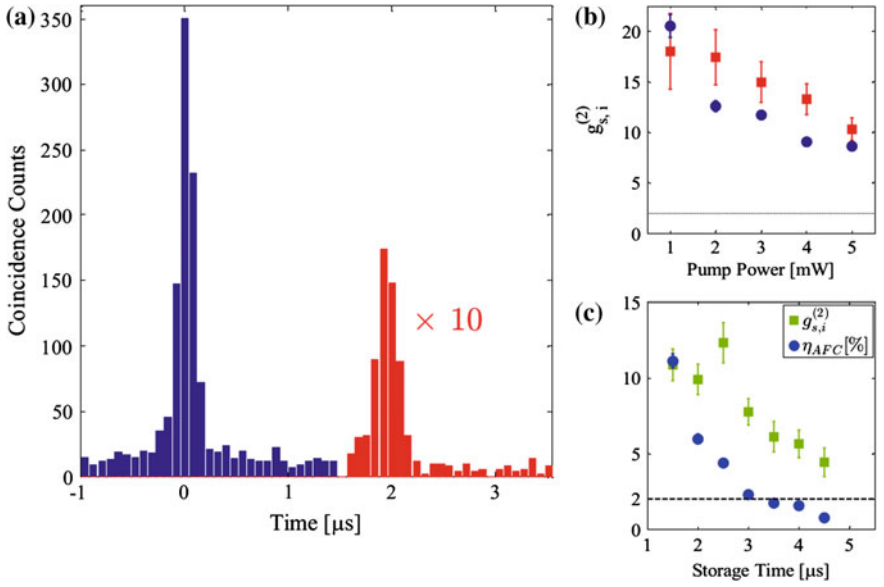

Fig. 9.7 Results of heralded single photon storage in a Pr^{3+}:Y_2SiO_5 crystal [16]. **a** $G^{(2)}_{s,i}(t)$ histogram without (*blue*) and with (*red*) AFC. The preprogrammed storage time is 2 μs and the power of the 426.2 nm pump is 2 mW. **b** The $g^{(2)}_{s,i}$ values as a function of the pump power for the AFC echo (*plain squares*) are compared to those for the input photons (*plain circles*). The *dotted line* corresponds to the classical limit $g^{(2)}_{s,i} = 2$ for two-mode squeezed states. **c** Storage and retrieval efficiency (*blue circle*) and $g^{(2)}_{s,i}$ (*green squares*) as a function of the storage time. For **b** and **c** the data are evaluated for a detection window $\Delta\tau = 400$ ns and the error bars are evaluated from the raw number of counts assuming Poissonian statistics

After having confirmed the non classicality of the input light, the heralded single photon was stored in and retrieved from the crystal the AFC echo scheme. In order to avoid the spurious noise effect described in Sect. 9.6.1, the photon pair source pump light was switched off after detection of an idler photon. The efficiency of the storage and retrieval process was measured to be up to 10 % for short storage times. The second order cross correlation is measured for the stored and retrieved photon as can be seen in Fig. 9.7a. The values of $g^{(2)}_{s,i}$ are also plotted as a function of the pump power in Fig. 9.7b. Surprisingly, the values of $g^{(2)}_{s,i}$ after retrieval are higher than the one for the input photons, for a big range of pump powers. This effect has been attributed to the fact that the memory act as a filter for broadband noise emitted by the photon pair source. Since the pump light is switched off after the detection of an idler photon, the atomic frequency comb delays the signal photon in a noise free region, which therefore increases the signal to noise ratio and the $g^{(2)}_{s,i}(\Delta\tau)$ [16]. This effect highlights that under certain conditions, quantum memories can act as purifiers by storing only the signal and not the noise. It has been observed also in other experiments [73, 118].

The storage time in the crystal can be chosen by tuning the comb periodicity Δ. In theory, the minimal Δ achievable is given by $2\gamma_h F$, where γ_h is the homogeneous linewidth of the optical transition and F the finesse of the comb. However, in practice, several effects will limit the achievable Δ, including power broadening, finite laser linewidth, spin inhomogeneous broadening, crystal vibrations in closed loop cryostats, etc. In the present experiment, non classical correlations between heralding photon and stored and retrieved heralded photons have been observed until a storage time of 4.5 μs (see Fig. 9.7c). This is more than 20 times longer than previous realizations [14, 15] and would allow entanglement between crystals separated by km long distance. The storage and retrieval efficiency dropped by a factor around 10 between 1.5 and 4.5 μs (see Fig. 9.7c). This is mainly due to the fact that the finesse could not be kept constant when decreasing Δ, because of the minimum achievable width of an absorption peak, due to the limitations mentioned above. Longer storage times in the excited state of up to 10 μs have recently been obtained with weak coherent states in Pr^{3+}:Y_2SiO_5 [73]. Note also that excited state storage times of up to 30 μs have been obtained using bright pulses storage in a Eu^{3+}:Y_2SiO_5 crystal [70].

9.7 Prospects for Spin-Wave Storage with Quantum Light

In order to increase the storage time and to achieve an AFC spin wave memory with on demand read-out, it has been proposed to transfer collective optical atomic excitations to collective spin excitations (or spin waves), using control fields (see Sect. 9.3). Proof of principle experiments have been realized in the classical regime for storage of strong pulses [70, 119, 120] and we discuss in this section the prospects to extend this experiments to quantum light. As mentioned in Sect. 9.3, spin wave storage requires materials with at least 3 long lived ground state levels. The best known materials with the required properties are Pr^{3+} and Eu^{3+} doped crystals.

The main experimental challenge for reaching the quantum regime with spin-wave storage is to suppress the noise generated by the control pulses, which are very close in frequency from the single photon output (e.g. from 10 to 17 MHz in Pr^{3+}:Y_2SiO_5 and from 35 to 120 MHz in Eu^{3+}:Y_2SiO_5). In that respect, one advantage of the AFC scheme is that the control pulses are temporally separated from the single photon output, which allows the use of temporal filtering. However, the control pulses also create transient phenomena inside the crystal due to e.g. the interaction with unwanted residual population in the storage state because of imperfect optical pumping. This can give rise to free induction decay and fluorescence, which lead to noise emission simultaneous with the single photon emission. The suppression of this noise requires narrow spectral filtering, which can be realized using e.g. a narrow-band optical cavity [123] or a crystal filter [121, 122]. An interesting figure of merit in the context of single-photon-level spin-wave storage, taking into account the noise generated and the storage and retrieval efficiency, is the mean number of input photons to achieve a signal-to-noise ratio (SNR) of 1 in the output mode, denoted as μ_1. In 2013, an experiment in Eu^{3+}:Y_2SiO_5 achieved $\mu_1 = 2.5$, using a Fabry-Perot narrowband

filter cavity [123]. Very recently, a lower value of μ_1=0.1 has been demonstrated in Eu^{3+}:Y_2SiO_5 [124]. A low value of $\mu_1 = 0.07$ has also been shown in Pr^{3+}:Y_2SiO_5 [125], using a reconfigurable transparency window in an another Pr^{3+}:Y_2SiO_5 crystal as spectral filter. High fidelity storage of time-bin qubits encoded in weak-coherent states at the single photon level was also demonstrated [125], allowing the spin-wave memory to operate in the quantum regime. In order to achieve high fidelity storage of quantum light, it is important to obtain $\mu_1 \ll 1$. This is because in practice, because of various optical losses, it is very difficult to obtain a single photon in front of the memory, with efficiency approaching unity. To achieve quantum storage with high SNR using the photon pair sources presented in Sect. 9.5, the condition $\mu_1 \ll \eta_H$ must be fulfilled, where η_H is the heralding efficiency of the source, including all optical losses from the source to the memory. Such an experiment has so far not been demonstrated.

Beyond the challenge of storing a single photon as a single spin-wave excitation, another important challenge is to increase the spin-wave storage time in this single-excitation regime. The spin-wave memory in a rare-earth-ion doped crystal is limited by the inhomogeneous spin linewidth [119]. This limitation can be lifted by utilizing spin-echo techniques to rephase the inhomogeneous spin dephasing, in which case the storage time is limited by the spin coherence time. But one can push the storage time still further by implementing dynamical decoupling sequences to reach storage times beyond 1s, a technique that has been successfully implemented in EIT storage experiments of strong optical pulses in rare-earth-ion doped crystals [41, 83]. However, the use of spin echo techniques for extending the storage time of ensemble-based quantum memories introduces a new potential source of noise. The challenge lies in avoiding to populate the $|s\rangle$ state with too many atoms, which would lead to spontaneous emission noise in the output when reading out the single spin excitation. At first this might appear to be almost impossible for a single excitation in $|s\rangle$ [126], but it was shown later that the strong collective emission into a particular spatial mode of the stored single excitation provides a very effective spatial filtering of the spontaneous emission noise [127]. The spin-echo technique must be very efficient, however, to avoid this noise, and it remains to be seen if the storage fidelity of a single photon can be high enough when applying spin echo techniques. In a very recent experiment [124] it was shown that spin echo techniques could indeed be used when manipulating an average spin excitation of around 1, in an ensemble composed of 10^{10} Eu^{3+} ions, without adding significant noise to the optical read out of the memory. This was made possible by using a robust and error compensating spin echo sequence which limited the population introduced to the $|s\rangle$ state to well below 1 %. In this way a μ_1 parameter of around 0.3 could be maintained for up to 1 ms of spin-wave storage time, showing that the noise level should in principle allow quantum state storage on a milliseconds time scale. One future goal of this research is to implement dynamical decoupling sequences in order to further extend the spin-wave storage time.

9.8 Outlook

Progress to harness the interaction between quantum light and atomic ensembles in a solid state environment has been fast in recent years. However, the full capabilities of these materials have not yet been exploited in the quantum regime and several challenges remain. For example, an experiment demonstrating simultaneously high efficiency and long storage time of quantum light has not been demonstrated yet. The quantum networking capabilities also need to be improved. Current research directions include work towards the realization of long lived heralded entanglement between remote solid state multimode quantum memories [11]. Such an experiment would pave the way to functional elementary segments of quantum repeaters with multiplexed entanglement generation. These applications would strongly benefit from the realization of a solid state photon pair source with embedded memory [87]. Another research direction actively pursued is to increase the spectral multiplexing capabilities, together with selective frequency read-out [62, 128]. Another promising research direction is the integration of these quantum memories with micro and nanostructures, which would open many interesting opportunities in terms of miniaturization, scalability and integration other optical elements such as quantum light sources and single photon detectors. The coupling of rare-earth ions with nanophotonic structures like photonic crystal waveguides or cavities would also provide increased light-matter interaction and potentially lead to cavity QED experiments with a low number of rare-earth ions [129]. This may also facilitate the detection and manipulation of single rare-earth ions that could be used as quantum bits [130, 131]. Finally, rare-earth ion doped crystals can be used as spin ensemble that can be coupled to superconductive cavities [132, 133], with the long term goal of connecting superconducting qubits and optical photons.

Acknowledgments The results described here has been obtained during several years of work by the teams at the University of Geneva and ICFO. The authors would like to particularly acknowledge the contributions by their co-authors of the work reviewed here, Christoph Clausen, Imam Usmani, Félix Bussières, Nicolas Sangouard, Nicolas Gisin, Daniel Rieländer, Kutlu Kutluer, Mustafa Gundogan, Patrick Ledingham, Margherita Mazzera, Julia Fekete and Matteo Cristiani.

References

1. K. Hammerer, A.S. Sørensen, E.S. Polzik, Quantum interface between light and atomic ensembles. Rev. Mod. Phys. **82**, 1041–1093 (2010)
2. A.I. Lvovsky, B.C. Sanders, W. Tittel, Optical quantum memory. Nat. Photonics **3**, 706–714 (2009)
3. C. Simon et al., Quantum memories. Eur. Phys. J. D—At. Mol. Opt. Plasma Phys. **58**, 1–22 (2010–05-01)
4. F. Bussières et al., Prospective applications of optical quantum memories. J. Mod. Opt. **60**, 1519–1537 (2013)
5. J. Nunn et al., Enhancing multiphoton rates with quantum memories. Phys. Rev. Lett. **110**, 133601- (2013)

6. H.J. Kimble, The quantum internet. Nature **453**, 1023–1030 (2008)
7. H.-J. Briegel, W. Dür, J.I. Cirac, P. Zoller, Quantum repeaters: the role of imperfect local operations in quantum communication. Phys. Rev. Lett. **81**, 5932–5935 (1998)
8. L.-M. Duan, M.D. Lukin, J.I. Cirac, P. Zoller, Long-distance quantum communication with atomic ensembles and linear optics. Nature **414**, 413–418 (2001)
9. N. Sangouard, C. Simon, H. de Riedmatten, N. Gisin, Quantum repeaters based on atomic ensembles and linear optics. Rev. Mod. Phys. **83**, 33–80 (2011)
10. H.P. Specht et al., A single-atom quantum memory. Nature **473**, 190–193 (2011)
11. C. Simon et al., Quantum repeaters with photon pair sources and multimode memories. Phys. Rev. Lett. **98**, 190503–4 (2007)
12. H. de Riedmatten, M. Afzelius, M.U. Staudt, C. Simon, N. Gisin, A solid-state light-matter interface at the single-photon level. Nature **456**, 773–777 (2008)
13. M.P. Hedges, J.J. Longdell, Y. Li, M.J. Sellars, Efficient quantum memory for light. Nature **465**, 1052–1056 (2010)
14. C. Clausen et al., Quantum storage of photonic entanglement in a crystal. Nature **469**, 508–511 (2011)
15. E. Saglamyurek et al., Broadband waveguide quantum memory for entangled photons. Nature **469**, 512–515 (2011)
16. D. Rieländer et al., Quantum storage of heralded single photons in a praseodymium-doped crystal. Phys. Rev. Lett. **112**, 040504 (2014)
17. E. Togan et al., Quantum entanglement between an optical photon and a solid-state spin qubit. Nature **466**, 730–734 (2010)
18. H. Bernien et al., Heralded entanglement between solid-state qubits separated by three metres. Nature **497**, 86–90 (2013)
19. K.C. Lee et al., Macroscopic non-classical states and terahertz quantum processing in room-temperature diamond. Nat. Photonics **6**, 41–44 (2012)
20. D.G. England, P.J. Bustard, J. Nunn, R. Lausten, B.J. Sussman, From photons to phonons and back: a THz optical memory in diamond. Phys. Rev. Lett. **111**, 243601 (2013)
21. K. De Greve et al., Quantum-dot spin-photon entanglement via frequency downconversion to telecom wavelength. Nature **491**, 421–425 (2012)
22. X.-H. Bao et al., Efficient and long-lived quantum memory with cold atoms inside a ring cavity. Nat. Phys. **8**, 517–521 (2012)
23. R.M. Macfarlane, High-resolution laser spectroscopy of rare-earth doped insulators: a personal perspective. J. Lumin. **100**, 1–20 (2002)
24. R. Macfarlane, R. Shelby, *Coherent Transients And Holeburning Spectroscopy In Rare Earth Ions In Solids*. Spectroscopy Of Crystals Containing Rare Earth Ions (Elsevier Science Publishers, Amsterdam, Netherlands, 1987)
25. G. Liu, B. Jacquier (eds.), *Spectroscopic Properties of Rare Earths in Optical Materials* (Springer, Berlin, 2005)
26. R.M. Macfarlane, Inhomogeneous broadening of spectral lines in doped insulators. J. Lumin. **45**, 1–5 (1990)
27. R.M. Macfarlane, Optical stark spectroscopy of solids. J. Lumin. **125**, 156–174 (2007)
28. W. Tittel et al., Photon-echo quantum memory in solid state systems. Laser Photon. Rev. **4**, 244–267 (2010)
29. C. Thiel, T. Böttger, R. Cone, Rare-earth-doped materials for applications in quantum information storage and signal processing. J. Lumin. **131**, 353–361 (2011)
30. A.M. Stoneham, Shapes of inhomogeneously broadened resonance lines in solids. Rev. Mod. Phys. **41**, 82–108 (1969)
31. M. Sellars, E. Fraval, J. Longdell, Investigation of static electric dipole-dipole coupling induced optical inhomogeneous broadening in Eu^{3+}:Y_2SiO_5. J. Lumin. **107**, 150–154 (2004)
32. T. Böttger, C.W. Thiel, Y. Sun, R.L. Cone, Optical decoherence and spectral diffusion at 1.5 μm in Er^{3+}:Y_2SiO_5 versus magnetic field, temperature, and Er^{3+} concentration. Phys. Rev. B **73**, 075101 (2006)

33. R.M. Macfarlane, R.S. Meltzer, B. Malkin, Optical measurement of the isotope shifts and hyperfine and superhyperfine interactions of nd in the solid state. Phys. Rev. B **58**, 5692 (1998)
34. Y. Sun, C.W. Thiel, R.L. Cone, R.W. Equall, R.L. Hutcheson, Recent progress in developing new rare earth materials for hole burning and coherent transient applications. J. Lumin. **98**, 281–287 (2002)
35. R. Macfarlane, R. Shelby, Sub-kilohertz optical linewidths of the $^7f_0$-$^5d_0$ transition in Y_2O_3:Eu^{3+}. Opt. Commun. **39**, 169–171 (1981)
36. R. Yano, M. Mitsunaga, N. Uesugi, Ultralong optical dephasing in Eu^{3+}:Y_2SiO_5. Opt. Lett. **16**, 1884 (1991)
37. E. Fraval, M.J. Sellars, J.J. Longdell, Method of extending hyperfine coherence times in Pr^{3+}:Y_2SiO_5. Phys. Rev. Lett. **92**, 077601–4 (2004)
38. E. Fraval, M.J. Sellars, J.J. Longdell, Dynamic decoherence control of a solid-state nuclear-quadrupole qubit. Phys. Rev. Lett. **95**, 030506 (2005)
39. M.F. Pascual-Winter, R.-C. Tongning, T. Chanelière, J.-L. Le Gouët, Spin coherence lifetime extension in Tm^{3+}:YAG through dynamical decoupling. Phys. Rev. B **86**, 184301 (2012)
40. M. Lovric, D. Suter, A. Ferrier, P. Goldner, Faithful solid state optical memory with dynamically decoupled spin wave storage. Phys. Rev. Lett. **111**, 020503 (2013)
41. G. Heinze, C. Hubrich, T. Halfmann, Stopped light and image storage by electromagnetically induced transparency up to the regime of one minute. Phys. Rev. Lett. **111**, 033601 (2013)
42. M. Zhong, M.P. Hedges, R.L. Ahlefeldt, J.G. Bartholomew, S.E. Beavan, S.M. Wittig, J.J. Longdell, M.J. Sellars, Optically addressable nuclear spins in a solid with a six-hour coherence time. Nature **517**, 177 (2015)
43. D.L. McAuslan, J.J. Longdell, M.J. Sellars, Strong-coupling cavity qed using rare-earth-metal-ion dopants in monolithic resonators: what you can do with a weak oscillator. Phys. Rev. A **80**, 062307 (2009)
44. Y. Sun, T. Böttger, C.W. Thiel, R.L. Cone, Magnetic g tensors for the $^4I_{15/2}$ and $^4I_{13/2}$ states of Er^{3+}:Y_2SiO_5. Phys. Rev. B **77**, 085124–10 (2008)
45. O. Guillot-Noël et al., Hyperfine interaction of Er^{3+} ions in Y_2SiO_5: An electron paramagnetic resonance spectroscopy study. Phys. Rev. B **74**, 214408–214409 (2006)
46. J. Ruggiero, J.-L.L. Gouët, C. Simon, T. Chanelière, Why the two-pulse photon echo is not a good quantum memory protocol. Phys. Rev. A **79**, 053851–8 (2009)
47. S.A. Moiseev, S. Kröll, Complete reconstruction of the quantum state of a single-photon wave packet absorbed by a Doppler-broadened transition. Phys. Rev. Lett. **87**, 173601–4 (2001)
48. M. Nilsson, S. Kröll, Solid state quantum memory using complete absorption and re-emission of photons by tailored and externally controlled inhomogeneous absorption profiles. Opt. Commun. **247**, 393–403 (2005)
49. B. Kraus et al., Quantum memory for nonstationary light fields based on controlled reversible inhomogeneous broadening. Phys. Rev. A **73**, 020302–4 (2006)
50. A.L. Alexander, J.J. Longdell, M.J. Sellars, N.B. Manson, Photon echoes produced by switching electric fields. Phys. Rev. Lett. **96**, 043602–4 (2006)
51. G. Hétet et al., Photon echoes generated by reversing magnetic field gradients in a rubidium vapor. Opt. Lett. **33**, 2323–2325 (2008)
52. G. Hétet, J.J. Longdell, A.L. Alexander, P.K. Lam, M.J. Sellars, Electro-optic quantum memory for light using two-level atoms. Phys. Rev. Lett. **100**, 023601–4 (2008)
53. B. Lauritzen et al., Telecommunication-wavelength solid-state memory at the single photon level. Phys. Rev. Lett. **104**, 080502 (2010)
54. T. Chanelière et al., Tm^{3+}:Y_2O_3 investigated for a quantum light storage application. Phys. Rev. B **77**, 245127 (2008)
55. M. Afzelius, C. Simon, H. de Riedmatten, N. Gisin, Multimode quantum memory based on atomic frequency combs. Phys. Rev. A **79**, 052329–9 (2009)
56. J. Nunn et al., Multimode memories in atomic ensembles. Phys. Rev. Lett. **101**, 260502–4 (2008)
57. R.H. Dicke, Coherence in spontaneous radiation processes. Phys. Rev. **93**, 99–110 (1954)

58. T. Mossberg, A. Flusberg, R. Kachru, S.R. Hartmann, Total scattering cross section for Na on He measured by stimulated photon echoes. Phys. Rev. Lett. **42**, 1665–1669 (1979)
59. N.W. Carlson, Y.S. Bai, W.R. Babbitt, T.W. Mossberg, Temporally programmed free-induction decay. Phys. Rev. A **30**, 1572–1574 (1984)
60. M. Mitsunaga, R. Yano, N. Uesugi, Spectrally programmed stimulated photon echo. Opt. Lett. **16**, 264–266 (1991)
61. M. Bonarota, J.-L.L. Gouët, S.A. Moiseev, T. Chanelière, Atomic frequency comb storage as a slow-light effect. J. Phys. B: At. Mol. Opt. Phys. **45**, 124002 (2012)
62. N. Sinclair et al., Spectral multiplexing for scalable quantum photonics using an atomic frequency comb quantum memory and feed-forward control. Phys. Rev. Lett. **113**, 053603 (2014)
63. S. Moiseev, M. Noskov, The possibilities of the quantum memory realization for short pulses of light in the photon echo technique. Laser Phys. Lett. **1**, 303–310 (2004)
64. N. Sangouard, C. Simon, M. Afzelius, N. Gisin, Analysis of a quantum memory for photons based on controlled reversible inhomogeneous broadening. Phys. Rev. A **75**, 032327–8 (2007)
65. T. Chanelière, J. Ruggiero, M. Bonarota, M. Afzelius, J.-L.L. Gout, Efficient light storage in a crystal using an atomic frequency comb. New J. Phys. **12**, 023025 (2010)
66. M. Bonarota, J. Ruggiero, J.-L. Le Gouët, T. Chanelière, Efficiency optimization for atomic frequency comb storage. Phys. Rev. A **81**, 033803 (2010)
67. S.A. Moiseev, S.N. Andrianov, F.F. Gubaidullin, Efficient multimode quantum memory based on photon echo in an optimal qed cavity. Phys. Rev. A **82**, 022311 (2010)
68. M. Afzelius, C. Simon, Impedance-matched cavity quantum memory. Phys. Rev. A **82**, 022310 (2010)
69. M. Sabooni, Q. Li, S. Kröll, L. Rippe, Efficient quantum memory using a weakly absorbing sample. Phys. Rev. Lett. **110**, 133604 (2013)
70. P. Jobez et al., Cavity-enhanced storage in an optical spin-wave memory. New J. Phys. **16**, 083005 (2014)
71. M. Gündoğan, P.M. Ledingham, A. Almasi, M. Cristiani, H. de Riedmatten, Quantum storage of a photonic polarization qubit in a solid. Phys. Rev. Lett. **108**, 190504 (2012)
72. M. Sabooni et al., Storage and recall of weak coherent optical pulses with an efficiency of 25. Phys. Rev. Lett. **105**, 060501 (2010)
73. N. Maring et al., Storage of up-converted telecom photons in a doped crystal. New J. Phys. **16**, 113021 (2014)
74. I. Usmani, M. Afzelius, H. de Riedmatten, N. Gisin, Mapping multiple photonic qubits into and out of one solid-state atomic ensemble. Nat. Commun. **1**, 12 (2010)
75. E. Saglamyurek et al., An integrated processor for photonic quantum states using a broadband light matter interface. New J. Phys. **16**, 065019 (2014)
76. J. Jin et al., Two-photon interference of weak coherent laser pulses recalled from separate solid-state quantum memories. Nat. Commun. **4**, 103–107 (2013)
77. C. Clausen, F. Bussières, M. Afzelius, N. Gisin, Quantum storage of heralded polarization qubits in birefringent and anisotropically absorbing materials. Phys. Rev. Lett. **108**, 190503 (2012)
78. Z.-Q. Zhou, W.-B. Lin, M. Yang, C.-F. Li, G.-C. Guo, Realization of reliable solid-state quantum memory for photonic polarization qubit. Phys. Rev. Lett. **108**, 190505 (2012)
79. E. Saglamyurek et al., Conditional detection of pure quantum states of light after storage in a Tm-doped waveguide. Phys. Rev. Lett. **108**, 083602 (2012)
80. I. Usmani et al., Heralded quantum entanglement between two crystals. Nat. Photonics **6**, 234–237 (2012)
81. F. Bussières et al., Quantum teleportation from a telecom-wavelength photon to a solid-state quantum memory. Nat. Photonics **8**, 775–778 (2014)
82. Z.-Q. Zhou et al., Quantum storage of high-dimensional orbital-angular-momentum entanglement in a crystal (2014). arXiv:1412.5243
83. J.J. Longdell, E. Fraval, M.J. Sellars, N.B. Manson, Stopped light with storage times greater than one second using electromagnetically induced transparency in a solid. Phys. Rev. Lett. **95**, 063601–4 (2005)

84. J. Fekete, D. Rieländer, M. Cristiani, H. de Riedmatten, Ultranarrow-band photon-pair source compatible with solid state quantum memories and telecommunication networks. Phys. Rev. Lett. **110**, 220502 (2013)
85. E. Saglamyurek et al., Quantum storage of entangled telecom-wavelength photons in an erbium-doped optical fibre. Nat. Photonics (2015). doi:10.1038/nphoton.2014.311
86. P.M. Ledingham, W.R. Naylor, J.J. Longdell, S.E. Beavan, M.J. Sellars, Nonclassical photon streams using rephased amplified spontaneous emission. Phys. Rev. A **81**, 012301 (2010)
87. P. Sekatski, N. Sangouard, N. Gisin, H. de Riedmatten, M. Afzelius, Photon-pair source with controllable delay based on shaped inhomogeneous broadening of rare-earth-metal-doped solids. Phys. Rev. A **83**, 053840 (2011)
88. S.E. Beavan, M.P. Hedges, M.J. Sellars, Demonstration of photon-echo rephasing of spontaneous emission. Phys. Rev. Lett. **109**, 093603 (2012)
89. P.M. Ledingham, W.R. Naylor, J.J. Longdell, Experimental realization of light with time-separated correlations by rephasing amplified spontaneous emission. Phys. Rev. Lett. **109**, 093602 (2012)
90. M. Bonarota, J.-L.L. Gouët, T. Chanelière, Highly multimode storage in a crystal. New J. Phys. **13**, 013013 (2011)
91. H. Linget, T. Chaneliére, J.-L. Le Gouët, P. Berger, L. Morvan, A. Louchet-Chauvet. Phys. Rev. A. **91**, 023804 (2015)
92. Z.Y. Ou, Y.J. Lu, Cavity enhanced spontaneous parametric down-conversion for the prolongation of correlation time between conjugate photons. Phys. Rev. Lett. **83**, 2556 (1999)
93. E. Pomarico et al., Waveguide-based OPO source of entangled photon pairs. New J. Phys. **11**, 113042 (2009)
94. C.-S. Chuu, G.Y. Yin, S.E. Harris, A miniature ultrabright source of temporally long, narrow-band biphotons. Appl. Phys. Lett. **101**, 051108–4 (2012)
95. M. Förtsch et al., A versatile source of single photons for quantum information processing. Nat. Commun. **4**, 1818 (2013)
96. F. Kaiser et al., A versatile source of polarization entangled photons for quantum network applications. Laser Phys. Lett. **10**, 045202 (2013)
97. T. Chanelière et al., Storage and retrieval of single photons transmitted between remote quantum memories. Nature **438**, 833–836 (2005)
98. J.S. Neergaard-Nielsen, B.M. Nielsen, H. Takahashi, A.I. Vistnes, E.S. Polzik, High purity bright single photon source. Opt. Express **15**, 7940–7949 (2007)
99. X.-H. Bao et al., Generation of narrow-band polarization-entangled photon pairs for atomic quantum memories. Phys. Rev. Lett. **101**, 190501–4 (2008)
100. M. Scholz, L. Koch, O. Benson, Statistics of narrow-band single photons for quantum memories generated by ultrabright cavity-enhanced parametric down-conversion. Phys. Rev. Lett. **102**, 063603–4 (2009)
101. A. Haase, N. Piro, J. Eschner, M.W. Mitchell, Tunable narrowband entangled photon pair source for resonant single-photon single-atom interaction. Opt. Lett. **34**, 55–57 (2009)
102. F. Wolfgramm, Y.A. de Icaza Astiz, F.A. Beduini, A. Cer, M.W. Mitchell, Atom-resonant heralded single photons by interaction-free measurement. Phys. Rev. Lett. **106**, 053602 (2011)
103. S. Tanzilli et al., Highly efficient photon-pair source using periodically poled lithium niobate waveguide. Electron. Lett. **37**, 26 (2001)
104. M. Halder et al., High coherence photon pair source for quantum communication. New J. Phys. **10**, 023027 (2008)
105. E.A. Goldschmidt, S.E. Beavan, S.V. Polyakov, A.L. Migdall, M.J. Sellars Storage and retrieval of collective excitations on a long-lived spin transition in a rare-earth ion-doped crystal Optics Express **21**, 10087 (2013)
106. R. Lettow et al., Quantum interference of tunably indistinguishable photons from remote organic molecules. Phys. Rev. Lett. **104**, 123605 (2010)
107. S. Tanzilli et al., A photonic quantum information interface. Nature **437**, 116–120 (2005)
108. B. Albrecht, P. Farrera, X. Fernandez-Gonzalvo, M. Cristiani, H.A. de Riedmatten, Waveguide frequency converter connecting rubidium-based quantum memories to the telecom c-band. Nat. Commun. **5**, 3376 (2014)

109. C. Clausen et al., A source of polarization-entangled photon pairs interfacing quantum memories with telecom photons. New J. Phys. **16**, 093058 (2014)
110. A. Christ, K. Laiho, A. Eckstein, K.N. Cassemiro, C. Silberhorn, Probing multimode squeezing with correlation functions. New J. Phys. **13**, 033027 (2011)
111. E. Pomarico, B. Sanguinetti, C.I. Osorio, H. Herrmann, R.T. Thew, Engineering integrated pure narrow-band photon sources. New J. Phys. **14**, 033008 (2012)
112. J.D. Franson, Bell inequality for position and time. Phys. Rev. Lett. **62**, 2205–2208 (1989)
113. J.F. Clauser, M.A. Horne, A. Shimony, R.A. Holt, Proposed experiment to test local hidden-variable theories. Phys. Rev. Lett. **23**, 880–884 (1969)
114. S.J. van Enk, Single-particle entanglement. Phys. Rev. A **72**, 064306 (2005)
115. K.S. Choi, H. Deng, J. Laurat, H.J. Kimble, Mapping photonic entanglement into and out of a quantum memory. Nature **452**, 67–71 (2008)
116. C.W. Chou et al., Measurement-induced entanglement for excitation stored in remote atomic ensembles. Nature **438**, 828–832 (2005)
117. M. Nilsson, L. Rippe, S. Kröll, R. Klieber, D. Suter, Hole-burning techniques for isolation and study of individual hyperfine transitions in inhomogeneously broadened solids demonstrated in Pr^{3+}:Y_2SiO_5. Phys. Rev. B **70**, 214116–11 (2004)
118. D.L. McAuslan, L.R. Taylor, J.J. Longdell, Using quantum memory techniques for optical detection of ultrasound. Appl. Phys. Lett. **101**, 191112 (2012)
119. M. Afzelius et al., Demonstration of atomic frequency comb memory for light with spin-wave storage. Phys. Rev. Lett. **104**, 040503 (2010)
120. M. Gündoğan, M. Mazzera, P.M. Ledingham, M. Cristiani, H. de Riedmatten, Coherent storage of temporally multimode light using a spin-wave atomic frequency comb memory. New J. Phys. **15**, 045012 (2013)
121. H. Zhang et al., Slow light for deep tissue imaging with ultrasound modulation. Appl. Phys. Lett. **100**, 131102 (2012)
122. S.E. Beavan, E.A. Goldschmidt, M.J. Sellars, Demonstration of a dynamic bandpass frequency filter in a rare-earth ion-doped crystal. J. Opt. Soc. Am. B **30**, 1173–1177 (2013)
123. N. Timoney, I. Usmani, P. Jobez, M. Afzelius, N. Gisin, Single-photon-level optical storage in a solid-state spin-wave memory. Phys. Rev. A **88**, 022324 (2013)
124. P. Jobez, C. Laplane, N. Timoney, N. Gisin, A. Ferrier, P. Goldner, M. Afzelius, Coherent spin control at the quantum level in an ensemble-based optical memory. Phys. Rev. Lett. **114**, 230502 (2015)
125. M. Gündoğan, P.M. Ledingham, K. Kutluer, M. Mazzera, H. de Riedmatten, solid-state quantum memory for time-bin qubits. Phys. Rev. Lett. **114**, 230501 (2015)
126. M. Johnsson, K. Mølmer, Storing quantum information in a solid using dark-state polaritons. Phys. Rev. A **70**, 032320 (2004)
127. K. Heshami, N. Sangouard, J. Minář, H. de Riedmatten, C. Simon, Precision requirements for spin-echo-based quantum memories. Phys. Rev. A **83**, 032315 (2011)
128. C. Thiel, N. Sinclair, W. Tittel, R. Cone, Tm^{3+}:$Y_3Ga_5O_{12}$ materials for spectrally multiplexed quantum memories. Phys. Rev. Lett. **113**, 160501 (2014)
129. T. Zhong, A. Hartz, E. Miyazono, A. Faraon, Towards coupling rare earth ions to a Y_2SiO_5 nanophotonic resonator. In: OSA Technical Digest (online), FTh1B.5–(Optical Society of America, San Jose, California, 2014)
130. R. Kolesov et al., Optical detection of a single rare-earth ion in a crystal. Nat. Commun. **3**, 1029 (2012)
131. T. Utikal et al., Spectroscopic detection and state preparation of a single praseodymium ion in a crystal. Nat. Commun. **5**, 3627 (2014)
132. M.U. Staudt et al., Coupling of an erbium spin ensemble to a superconducting resonator. J. Phys. B: At. Mol. Opt. Phys. **45**, 124019 (2012)
133. S. Probst et al., Anisotropic rare-earth spin ensemble strongly coupled to a superconducting resonator. Phys. Rev. Lett. **110**, 157001 (2013)

Part V
New Sources of Entangled Photon Pairs

Chapter 10
Engineering of Quantum Dot Photon Sources via Electro-elastic Fields

Rinaldo Trotta and Armando Rastelli

Abstract The possibility to generate and manipulate non-classical light using the tools of mature semiconductor technology carries great promise for the implementation of quantum communication science. This is indeed one of the main driving forces behind ongoing research on the study of semiconductor quantum dots. Often referred to as artificial atoms, quantum dots can generate single and entangled photons on demand and, unlike their natural counterpart, can be easily integrated into well-established optoelectronic devices. However, the inherent random nature of the quantum dot growth processes results in a lack of control of their emission properties. This represents a major roadblock towards the exploitation of these quantum emitters in the foreseen applications. This chapter describes a novel class of quantum dot devices that uses the combined action of strain and electric fields to reshape the emission properties of single quantum dots. The resulting electro-elastic fields allow for control of emission and binding energies, charge states, and energy level splittings and are suitable to correct for the quantum dot structural asymmetries that usually prevent these semiconductor nanostructures from emitting polarization-entangled photons. Key experiments in this field are presented and future directions are discussed.

10.1 Engineering of Quantum Dot Photon Sources via Electro-elastic Fields

Initially referred to as quantum boxes [1], semiconductor quantum dots (QDs) are nanostructures made of several thousands of atoms that can self-assemble during hetero-epitaxial growth [2]. QDs are capable to confine the motion of charge carriers in three dimensions and feature discrete energy levels. The latter property, which is a direct consequence of the laws of quantum mechanics, has earned QDs the

R. Trotta (✉) · A. Rastelli
Institute of Semiconductor and Solid State Physics, Johannes Kepler University Linz, Altenbergerstrasse 69, 4040 Linz, Austria
e-mail: rinaldo.trotta@jku.at

A. Predojević and M.W. Mitchell (eds.), *Engineering the Atom-Photon Interaction*, Nano-Optics and Nanophotonics, DOI 10.1007/978-3-319-19231-4_10

well-known nickname of artificial atoms. Looking at these nanostructures with the eyes of a passionate material scientist, there is no doubt that QDs represent one of the most spectacular examples of our ability to manipulate matter at the atomic scale, result of more than 50 years of extensive research in semiconductor and solid state physics. In the last 15 years, however, the interest for QDs has pushed its boundaries into the realm of quantum optics. Seminal works demonstrated that QDs can act as triggered sources of single photons [3] and entangled photon pairs [4–6] and can be easily integrated into conventional optoelectronic devices [7] and optical microcavities [8–10]. The appealing idea of exploiting semiconductor-based sources of non-classical light for quantum technologies has thereby triggered efforts of researchers working at the interface between quantum optics and condensed-matter physics. Nowadays, the quality of the single and entangled photons produced by these nanostructures is reaching levels comparable to trapped atoms [11, 12] or parametric down-converters [13], and advanced quantum optics experiments, such as quantum teleportation [14, 15], have been recently performed.

In spite of these accomplishments, the establishment of QD photon sources as viable building blocks for quantum communication requires a number of extraordinary challenges to be overcome. The need of Fourier-limited [11, 12], bright [10, 16, 17], and site-controlled [18, 19] photon sources remains certainly a problem, and some of the groundbreaking results that have been recently achieved are discussed within this book. There is another issue, however, which becomes crucial as soon as the number of quantum emitters required for the envisioned application increases: different from real atoms, each QD possesses its size, shape, composition [20] and, as consequence, a unique emission spectrum. This hurdle is a direct consequence of the stochastic growth processes and has a dramatic effect, e.g. on the capability of transferring quantum information between distant QD-based qubits [21]. To better explain this point, let us consider Hong-Ou-Mandel two-photon interference [22] between photons emitted by two remote QDs [23, 24], a key operation of existing protocols of large-distance quantum communication [25]. This quantum-mechanical phenomenon consisting in the coalescence of two single photons into a two-photon collective state can be observed when single photons impinge onto a beamsplitter. There, the photon wavepackets should be indistinguishable in all the possible degrees of freedom. While polarization and space overlap can be easily achieved, if we restrict our discussion to Fourier-limited QD photons (see chapter by A. Kuhn) the overlap in energy is what eventually reduces the visibility of two-photon interference. Considering that the inhomogeneous broadening of QD emission is typically tens of meV, the probability of finding two QDs for which photons have the same energy within typical radiative-limited emission linewidth ($\sim\mu$eV) is $< 10^{-4}$. The situation worsens when one requires entangled photons to impinge onto a beamsplitter, i.e., when one aims at quantum teleportation or entanglement swapping between distant nodes [26]. In fact, the capability of QDs to generate photon pairs that have high enough level of entanglement to violate Bell's inequality [27] is hindered by the presence of structural asymmetries, which manifest themselves, via the anisotropic electron-hole exchange interaction [28], in the appearance of an energetic difference between the two bright excitonic states, the well-known fine structure splitting (FSS). When the

FSS is larger than the radiative-limited emission linewidth of the excitonic transition ($\sim$1 μeV), the entanglement is strongly reduced [29]. Recent theoretical calculations [30] show that only a very low portion of as-grown QDs are free of asymmetries (1 over 1000 for standard Stranski-Krastanow QDs) and the numbers increase slightly if very sophisticated growth protocols are employed [18]. Therefore, the probability of finding two as-grown QDs suitable to swap entanglement is considerably small (10^{-9} or less), and it is practically zero in the case of experiments involving several sources. Therefore, the future of QDs for applications critically depends on our capability to precisely control their optical properties within tolerances which are too small to be met even by the most refined fabrication methods. These hurdles have naturally led to the idea of post-growth tuning of the QD emission via the application of external perturbations, such as electric fields [31–34], elastic stress [35–37], magnetic [28, 29], and optical [38] fields. Among the others, piezoelectric-induced strains [37] and vertical electric fields [31] are among the most promising, since they do not require bulky set-ups and they are compatible with compact on-chip technology. The fascinating idea behind the use of these "tuning knobs" is to exploit the same semiconductor matrix that allows for the existence of QDs as the resource for solving problems related to their semiconducting nature itself. Progress in semiconductor technology has opened up the possibility to embed QDs in the intrinsic region of field-effect devices (such of n(p)-i-Schottky or n-i-p diodes) and to precisely control the electric field along the crystal growth direction (vertical electric field) by the simple application of a voltage [31]. Similarly, the integration of semiconductor thin-films containing QDs onto piezoelectric substrates, such as lead-zirconate-titanate (PZT) [35] or lead magnesium niobate-lead titanate (PMN-PT) [37], allows strain fields to be transferred to QDs via electrical means. Using the quantum-confined Stark-effect and variable deformation of the host semiconducting matrix, vertical electric fields and in-plane stress fields offer a precise and reversible way to engineer the QD electronic structure and have been instrumental in bringing into resonance the levels of QD molecules [34, 39], to tune QD levels into resonance with cavity modes [37, 40, 41], and to control binding energies of excitonic complexes [42–44]. Thanks to the broad-band tunability of the QD emission energy [31, 45] they have also enabled the first two experiments showing two-photon interference between remote QDs [23, 24]. Despite these impressive results and the tremendous efforts required to achieve them, having at hand single "tuning knobs" is very often not sufficient to meet some of the very stringent requirements set by advanced quantum optics experiments. A prominent example is represented by the difficulties encountered in erasing the FSS [46]. Theoretical and experimental results have demonstrated that the application of either stress or electric fields to single QDs generally results in a lower bound of the FSS (usually larger than 1 μeV) caused by the coherent coupling of the two bright exciton states [31, 47]. Only a few "hero" QDs can be tuned for entangled photon generation [31], thereby hindering the implementation of QD photon sources in advanced quantum communication protocols [21].

In this chapter, we describe a novel class of hybrid piezoelectric-semiconductor devices that allow large stress and electric fields to be *simultaneously* applied to single semiconductor QDs. Despite the idea to combine independent fields emerges naturally from the need of a tighter control over the properties of the quantum emitters, it has been largely overlooked due to the common opinion that the use of several "knobs" simply extends the tunability of the QD emission properties. In strong contrast, we show that the effect of strain and electric field are complementary and that the resulting *electro-elastic* field allows addressing tasks not solvable with existing approaches.

The chapter is divided as follows: In the first section we discuss the technological steps required to build up the hybrid semiconductor-piezoelectric devices capable of delivering electro-elastic fields to single QDs. We demonstrate immediately the technological relevance of this approach introducing a wavelength-tunable, high-speed and all-electrically-controlled source of single photons. In the following section we focus on the idea of using strain and electric field to achieve independent control of different QD parameters. In particular, we show independent control of (i) charge state and emission energy, (ii) exciton and biexciton energies, and (iii) amplitude and phase of mixing of bright exciton states. The latter achievement means that the electro-elastic fields can be used to tune any QD for the generation of highly polarization-entangled photon-pairs.

10.2 Hybrid Semiconductor-Piezoelectric Quantum Dot Devices: The First High-Speed, Wavelength-Tunable, and All-Electrically-Controlled Source of Single Photons

The hybrid devices discussed here are obtained by merging the semiconductor and piezoelectric technologies. Diode-like (p-i-n or n-i-Schottky) nonanomembranes containing In(Ga)As QDs are integrated onto $[Pb(Mg_{1/3}Nb_{2/3})O_3]_{0.72}[PbTiO_3]_{0.28}$ (PMN-PT) piezoelectric actuators featuring giant piezoelectric response. For details about device fabrication we refer the reader to the specific paper [45].

Figure 10.1 shows a sketch of the final device, which features two electrical tuning knobs: a voltage applied to the nanomembranes (V_d) allows the electric field (F_d) across the QDs (up to $\sim$200 kV/cm) to be controlled, as in standard field-effect devices. Simultaneously, the application of a voltage (V_p) to the PMN-PT results in an out-of-plane electric field F_p that leads to tensile or compressive in-plane strains (up to $\pm 0.2\,\%$ at cryogenic temperatures) in the QD layer. Unlike PZT, PMN-PT is capable of larger in-plane strains, which is crucial for broadband tunability. It is also worth noting that the Au layer between the PMN-PT and the nanomembrane plays a threefold role here: It acts as a stiff strain-transfer layer, as an electrical contact for both the nanomembrane and the PMN-PT, and it represents the bottom mirror of a metal-semiconductor-dielectric-planar cavity [48] featuring extraction efficiencies

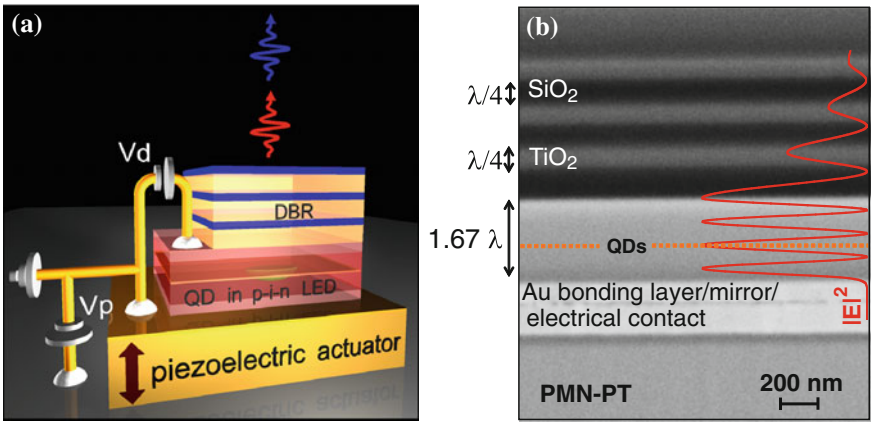

Fig. 10.1 Strain-tunable quantum dot devices. **a** Sketch of the dual-knob device: a p-i-n nanomembrane containing self-assembled QDs is integrated on *top* of a piezoelectric actuator, allowing the in situ application of biaxial strain by tuning the voltage V_p. Electrons and holes are electrically injected by setting V_d. The top distributed bragg reflector (DBR) completes a metal-semiconductor-dielectric planar cavity. **b** SEM image of a cross section of the device prepared by focused ion beam (FIB) cutting. The *solid curve* depicts the square modulus of the electric field inside the cavity. The QD layer is located one λ below the DBR (see *dashed line*), in turn composed by three pairs of SiO_2/TiO_2

as high as 15 %. Finally, depending on the particular design of the diode (n-i-Schottky or n-i-p diode), magnitude and sign of V_d, the electric field can be used to control the QD energy levels via the quantum-confined Stark-effect, to control the charge state of the QD or to inject carriers electrically. The latter operation mode is described in the following, where we report on the realization of the first high-speed, energy-tunable, and all electrically-controlled sources of single photons.

In standard quantum-light-emitting diodes (Q-LEDs), InGaAs QDs are embedded in the intrinsic region of GaAs p-i-n devices [7]. When the applied bias exceeds the turn-on voltage, charge carriers are electrically injected into the QDs and photons of different frequencies are emitted in the recombination processes. In this operation mode, the electric field across the QDs is taken up to inject carriers and cannot be used in a trivial manner to modify sizably the QD electronic properties. Contrarily, the dual-knob device sketched in Fig. 10.1 [45] addresses successfully this hurdle. Figure 10.2a shows several *electro-luminescence* spectra of a single QD as a function of the electric field across the piezoelectric actuator, i.e., as a function of in-plane biaxial strain. Spectra obtained for both tensile (F_p down to −20 kV/cm) and compressive (F_p up to 40 kV/cm) strains are displayed to show that the QD emission lines (X, XX and negative charge exciton, X^-) can be shifted in a ∼20 meV-broad spectral range without loss of intensity or line broadening and, most importantly, during electrical injection. The reported tuning range is comparable with the inhomogeneous broadening of QD emission, meaning that any two QDs in the ensemble can be tuned

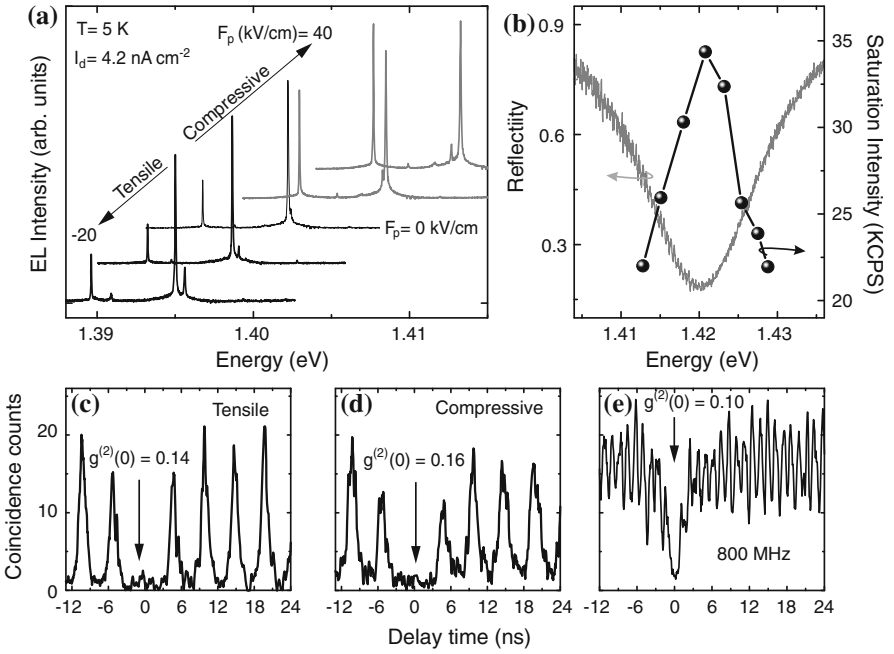

Fig. 10.2 A wavelength-tunable, high-speed, bright, and all electrically controlled source of single photons. **a** Low temperature ($T = 5$ K) electroluminescence spectra of a single QD embedded in the dual-knob device of Fig. 10.1 as a function of the electric field across the piezoelectric actuator and for a fixed current density I_d. *Black thick* (*gray thin*) *lines* correspond to tensile (compressive) strain. The spectrum obtained at $F_p = 0$ is also reported (*black line*). **b** Reflectivity spectrum (*gray line*) for one of the devices. The points connected by a line represent the saturation intensity of the X transition for different values of strain. **c** Autocorrelation measurements for an X embedded in the device under tensile strain. The QD is driven with 300 ps long pulses at 200 MHz. **d** Same as (**c**) for compressive strain. **e** Same as (**c**) for the unstrained case and at 800 MHz

into energetic resonance, an important prerequisite for transferring quantum information between independent quantum emitters via HOM-type interference [22]. It is also interesting to note that during active deformation of the nanomembrane-LEDs, the frequency of the Fabry-Perot mode of the metal-semiconductor-dielectric planar cavity remains almost unaffected (shift up to 1 meV). This "pinning" of the Fabry-Perot mode is interesting because one can design the cavity for a certain frequency and use strain to bring remote QDs into resonance in the spectral position where light extraction efficiency is maximized. In spite of the low quality factor of the cavity ($Q \approx 10^2$), Fig. 10.2c shows a clear enhancement of light extraction efficiency when the X line is tuned trough the center of the cavity mode. Such a low quality factor can also be seen as an advantage for broad-band operation that allows for enhancing the different lines of the same QD (like X and XX), which is fundamental for the efficient generation of entangled photon pairs.

In order to prove that these novel devices deliver non-classical light, we performed autocorrelation measurements. The coincidence counts recorded on the X transition of a single QD at $F_p = -10$ kV/cm, i.e., under applied tensile stress, are shown in Fig. 10.2c [49]. The periodic autocorrelation peaks[1] together with the absence of the peak at zero time-delay provide evidence of photon antibunching and of single-photon emission. The time separation between the neighboring peaks is 5 ns, which corresponds to the repetition rate of 200 MHz used for this experiment. While the normalized value of the second order correlation function at zero time delay $g^{(2)}(0)$ proves unambiguously that the source is a single quantum emitter ($g^{(2)}(0) < 0.5$), it also shows a multi-photon emission probability of 0.14(2). Along with the background and the dark counts of the single photon detectors, this finite probability could originate from carrier recapture phenomena on a time scale comparable with the exciton lifetime, as observed in similar systems [50]. Irrespective of the origin of the non-zero value of the $g^{(2)}(0)$, measurements performed at different F_p (see Fig. 10.2d) show no significant change of the value of $g^{(2)}(0)$. This finding finally proves that the emission of single photons is not degraded by the application of such large stress fields to the LED and that our device can be used as an energy-tunable and bright source of single photons. In addition to the tunability in energy and the high extraction efficiency, our QD-LED allows for high-rate photon generation, another important requirement for high-data rate single photon applications [21]. Figure 10.2e shows autocorrelation measurements of an exciton driven with a train of electrical pulses separated in time by 1.3 ns (corresponding to a repetition rate of 0.8 GHz). We observe a strong suppression of the peak at zero time-delay with $g^{(2)}(0) = 0.10(2)$, similarly to what was found at lower repetition rates (see Fig. 10.2c, d). It is noticeable that the neighbouring peaks start to merge with each other, and that the use of higher repetition rates would result in higher values of the $g^{(2)}(0)$. In fact, the width of the peaks in the autocorrelation measurement is mainly determined by the total jitter on the time interval between the start and stop events registered by the correlation electronics. Considering the rise and the decay time of the exciton transition, a total time jitter of 1.37 ns was estimated, which in turn leads to 2.74 ns-broad peaks in the autocorrelation plot. Being 1.3 ns (2.6 ns) the temporal distance between two (three) consecutive electrical pulses, the neighbouring peaks start to merge while the value of $g^{(2)}(0)$ remains almost unaffected. In order to further increase the speed of our single-photon source, different excitation schemes with appropriate DC bias should be used, so as to reduce the total time jitter via quantum tunnelling of charges out of the QD, an effect induced by band bending. On the other

[1]The electro-luminescence is excited by injecting short electrical pulses (pulse width less than 300 ps, amplitude of −0.7 V and repetition rates up to 0.8 GHz) superimposed to a direct current (DC) bias of $V_d = -1.7$ V, just below the turn-on voltage of the diode.

hand, the device concept can be adapted for the integration of high-Q cavities, where the Purcell effect can be instrumental for increasing not only the speed of the single photon source via reduced radiative recombination times but also its brightness [51].

10.3 Independent Control of Different Quantum Dot Parameters via Electro-elastic Fields

In the previous section we have shown that the electric field can be used to inject carriers electrically into QDs while strain is used to modify the energy of the emitted photons. Exciting possibilities, however, arise when electric field and strain are used in synergy to achieve independent control of different QD parameters, as described in the following experiments.

10.3.1 Independent Control of Charge State and Emission Energy

We now demonstrate [52] how it is possible to obtain independent control of charge state and emission energy in a single QD. In light of recent experiments demonstrating spin-photon entanglement [15, 53] (see chapter by McMahon and De Greve) using X^- transitions in single QDs (excitonic complexes consisting of two electrons and one hole), this possibility is particularly relevant, since it could pave the way towards QD-based quantum networks where remote spins are entangled via HOM interference of the photons emitted by remote QDs during the radiative recombination of the X^-.

For this experiment, we integrate n-i-Schottky diodes (instead of p-i-n LEDs) onto PMN-PT (see sketch of Fig. 10.3a). As shown by Warburton et al. [54], this type of diodes allows single electrons to be injected into the QD with single-electron accuracy.[2] In our device this is demonstrated in Fig. 10.3b, where micro-photoluminescence (μ-PL) spectra of a single QD are reported as a function of V_d. At positive V_d (large electric fields) the μ-PL spectrum is composed by two sharp transitions related to the X and the positively charged excition (X^+). When the electric field across the structure is reduced, such that the lowest state of the QD is aligned with the Fermi level of the n-doped contact, a new peak at lower energy appears and it gains intensity with V_d at the expenses of the X and X^+ transitions. This finding can be easily explained taking into account the *tunneling of a single electron* from the top n-layer into the QD, and the new low-energy transition can be ascribed to the negatively charged exciton (X^-). Subsequent charging events (trapping of additional electrons into the QD) can be clearly seen as V_d is further decreased, and

[2]This takes place when the voltage across the diode shifts the confined levels of QDs below the Fermi energy of the n-doped layer.

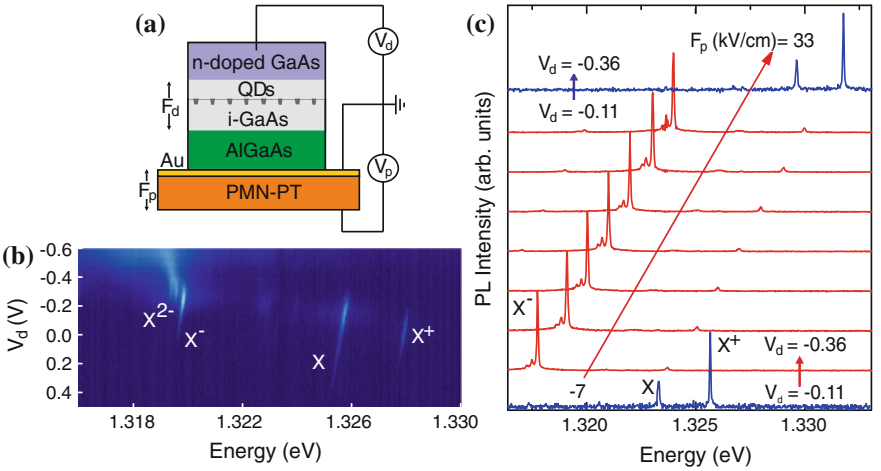

Fig. 10.3 Independent control of charge state and emission energy in single QDs. **a** Sketch of an n-i-Schottky diode containing QDs and integrated onto a PMN-PT actuator, similar as in Fig. 10.1. **b** Micro-photoluminescence map (in false colour scale) of a single QD embedded in the device and as a function of V_d. Several recombination lines ascribable to exciton and charged exciton transitions can be clearly observed. **c** Micro-photoluminescence spectra of a single QD versus V_d and V_p. The latter values were chosen so as to demonstrate independent control of charge state and emission energy in a single QD

two additional lines, most likely related to the X^{2-} [54], appear in the μ-PL spectrum (two electrons are injected into the QD). At even lower electric fields the QD is flooded with electrons and the PL spectrum evolves in a broad band. The μ-PL map reported in Fig. 10.3b contains a plethora of additional information because the energetic-splittings between the different excitonic complexes are a direct result of the combined effect of Coulomb interaction and quantum confinement. In addition, the field-induced shift of the QD emission lines provides information about the QD permanent dipole moment and polarizability [55]. However, here we are mainly interested in discussing the possibility of obtaining simultaneous control of charge state and emission energy. Figure 10.3c shows how this is done: V_d is first tuned so as to charge the QD with one electron (X^-), see the two bottom spectra of Fig. 10.3c. F_p is then used to tune the X^- emission energy while V_d is kept fixed, as shown by the red arrows of Fig. 10.3c. Having the QD in a different strain configuration (different emission energy), we can now discharge it again by independent tuning of V_d at fixed F_p (see the two topmost spectra). Obviously, the experiment can be repeated charging QDs with an additional electron by simply adjusting V_d at the value required to observe X^{2-}.

10.3.2 Independent Control of Exciton and Biexciton Energy

So far, we have used the electric field across the diode for tasks that cannot be addressed with static strains, i.e., to inject carriers electrically and to control the charge state of a QD. We now explore a third and more interesting possibility: we use both fields to reshape the interaction energies among carriers confined in single a QD without affecting the energy of the QD fundamental excitation, i.e., the neutral exciton, X. In particular, we demonstrate for the first time independent and broad-range control of X and XX energy in a single QD. On the one hand, the demonstrated possibility to achieve color coincidence between X and XX photons could allow for testing the degree of entanglement of photon pairs produced using the recently proposed and not yet experimentally demonstrated time reordering-scheme [56]. On the other hand, the broad range control over X and XX energies paves the way towards the development of energy-tunable sources of entangled photons via the time-bin scheme [57], and it would allow entanglement swapping experiments between distant QD-based qubits to be performed.

In the following experiments, we employ p-i-n diodes containing $Al_{0.4}Ga_{0.6}As$ barriers surrounding a 10 nm-thick GaAs quantum well that, in turn, hosts the QDs. The presence of the AlGaAs barriers reduces carrier ionization at very high electric fields [55] and allows the QD emission lines to be shifted in a very broad spectral range when the diode is driven in reverse bias. When combined with the broad-band tunability provided by strain, this device offers unprecedented control over the QD emission properties, as described in the following [42]. Figure 10.4a shows the "additive mode" operation of the device, where strain and electric fields are used in sequence (first F_d and then F_p) to shift the QD emission lines in the same direction. From the μ-PL map of Fig. 10.4a two important features of the device can be readily noticed: (i) The application of stress and electric fields results in a

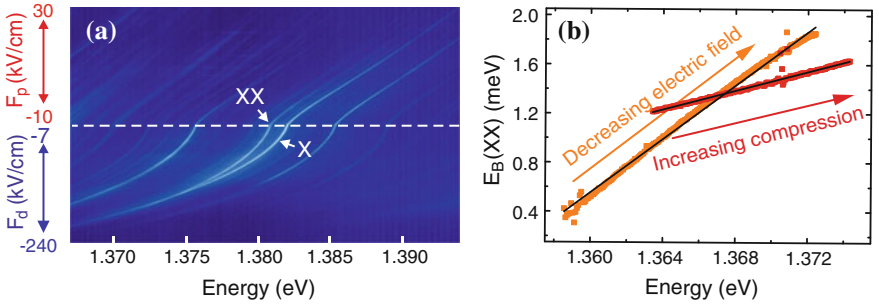

Fig. 10.4 Electro-elastic control of excitons in QDs: "additive mode" operation. **a** Micro-photoluminesnece map (in a false colour scale) of a single QD under the influence of large electric (*bottom part*) and strain (*top part*) fields. Recombination lines ascribed to the exciton (X) and biexciton (XX) transitions are indicated. **b** Biexciton binding energy $E_B(XX)$ of a single QD as a function of the energy of the exciton transition for strain (*red points*) and electric fields (*orange points*). The *black lines* are linear fits to the experimental data

broad-range control of the QD emission lines, which can be as high as 40 meV, one of the largest shift ever reported so far; (ii) The energy separation between the exciton (X) and biexciton (XX) emission lines—which we refer to as the relative biexciton binding energy, defined as $E_B(XX) = E_X - E_{XX}$, where $E_{X,XX}$ indicate the emission energies—is changing at different rates under strain and electric field. The different rates (almost a factor 2) can be better appreciated when $E_B(XX)$ is plotted against E_X, as shown in Fig. 10.4b. While (i) is an expected result, (ii) is an interesting finding since it suggests that the two fields have a different effect on the interaction energies among carriers confined in the same QD. On the one hand, it has been shown [44] that in-plane compressive biaxial strain (increasing exciton energy) increases the confinement potential of electrons and, consequently, their Coulomb repulsion while it leaves holes almost unaffected. On the other hand, an increasing vertical electric field (decreasing exciton energy) pulls electrons and holes apart and, since holes are more localized, the Coulomb repulsion increases much faster for them than for electrons. For a detailed analysis of the field-induced changes of the Couloumb integrals, we refer the reader to the specific paper [42]. Here, we would like to show that the different physical effects produced by the two fields can be used to reshape the electronic properties of single QDs so as to achieve independent control of the X and XX emission energy. To do so, we operate our dual knob device in "subtractive mode", i.e., strain and electric fields are used to shift the energy of the QD emission lines in opposite directions.

Figure 10.5a first shows the tuning and locking of the X energy to the user-defined target energy (E_{targ}). This is achieved using a closed-loop feedback on the piezo-actuator that is capable to stabilize the X frequency with 1 μeV accuracy [45], see Fig. 10.5d. After locking the X to a recombination energy E_{targ}, we increase linearly the magnitude of F_d, while the exciton transition is kept fixed via F_p [the time-evolution of both F_p and F_d is shown in Fig. 10.5c]. In absence of the feedback, all the QD emission lines would redshift due to the quantum-confined Stark effect. However, as the X shift is actively compensated by increasingly compressive strain and the two fields have a different effect on the XX binding energy (see Fig. 10.4), we are able to change the spectral position of the XX transition only. Remarkably, in the QD of Fig. 10.5b the XX changes gradually from a binding to an antibinding configuration at fixed and predefined X energy (E_{targ}). Thus, we are able for the first time [42] to achieve independent control of the XX and X absolute energies. This confirms that the electro-elastic fields allow for reshaping of the interaction energies between carriers confined in a single QD without affecting the energy of the fundamental excitation in a QD, the neutral exciton. We believe that this result shows the real potential of our device, which is capable to address tasks inaccessible with single external fields used alone.

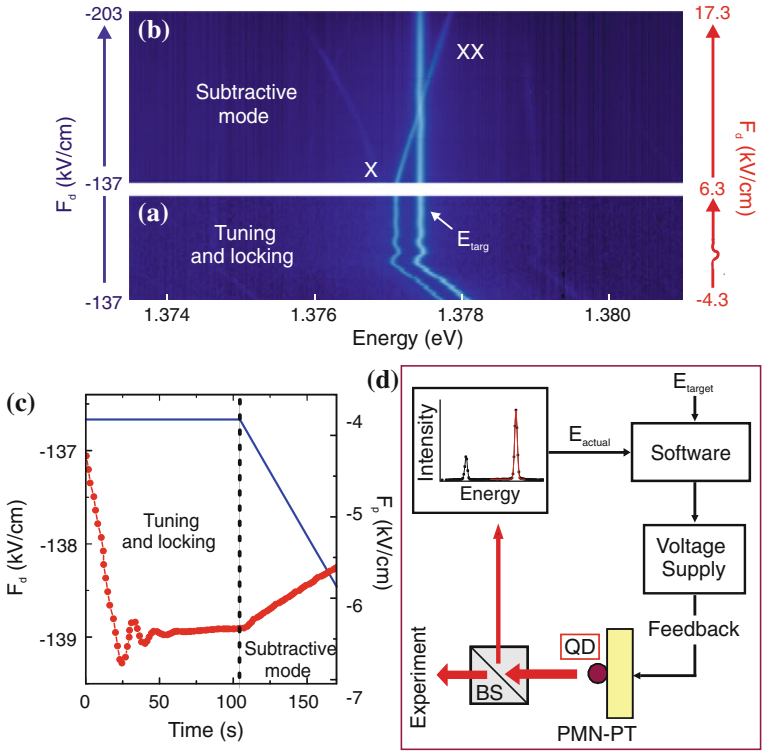

Fig. 10.5 Electro-elastic control of excitons in QDs: "subtractive mode" operation (**a**). Color-coded μ-PL map of a single QD whose X is first tuned to the target energy of $E_{targ} = 1.3774$ eV and then locked at this value via F_p. During the experiment, $F_d \approx -137$ kV/cm. **b** Color-coded μ-PL map of the same QD when the magnitude of F_d is ramped up, while the exciton transition is locked at E_{targ} via F_p, as explained in the main text. **c** Values of F_d (*blue*) and F_p (*red*) as a function of time as recorded during the experiment described in (**a**) and (**b**). **d** Sketch of the closed-loop system used to drive the emission energy of a QD to E_{targ} and for energy stabilization via active feedback. The actual emission energy of the line to be stabilized is first obtained by fitting the μ-PL spectrum and then compared to the E_{targ} to provide feedback to the piezoelectric actuator. For details see [45]

10.4 Controlling and Erasing the Fine Structure Splitting for the Generation of Highly Entangled Photon Pairs

As mentioned in the introduction of this chapter, one of the unique features of our dual-knob device—most probably the most important—is its capability to erase the coherent coupling between the two bright excitonic states, that is, the exciton fine structure splitting (FSS). This is a fundamental requirement for the generation of polarization entangled photon pairs during the radiative decay of the biexciton (XX) to the exciton (X) to the crystal ground state, which has stimulated the efforts of researchers worldwide, who have struggled for more than 10 years after the first

proposal [4] to find a reproducible way to suppress the FSS. In this section we address this issue in detail. In the first part [58] we discuss the theory underlying the FSS and we illustrate the reasons why our device is capable to correct for the structural asymmetries at the origin of the FSS. In the second part [13] we demonstrate that at zero FSS QDs can generate photon pairs featuring a very high degree of polarization entanglement, high enough to violate Bell's inequality without the need of temporal and spectral filtering techniques.

10.4.1 Controlling and Erasing the Exciton Fine Structure Splitting via Electro-elastic Fields

The appearance of an energetic splitting between the two bright excitonic states is a manifestation of the spin-spin coupling of the electron and hole forming the exciton, i.e., the electron-hole exchange interaction [28]. Already at this point a simple question may arise: how can there be an exchange coupling between electrons and holes if this fundamental interaction involves indistinguishable particles? The answer is that in semiconductors physics what we call electron and hole are both perturbations of a many-electron system. In this sense an electron-hole exchange interaction exists, and the first clear report in semiconductors dates back to 1979, when W. Ekardt and co-workers reported on an accurate theoretical and experimental study of bulk GaAs and InP [59]. The determined splittings were found to be considerably small ($\approx$10 μeV) and quite difficult to observe due to the broadening of the involved optical transitions. A few years later, R. Bauer et al. reported on the appearance of doublets in the PL spectra of heavy-hole excitons confined in GaAs/AlGaAs quantum wells [60], which they ascribed to the exchange coupling. Despite this study triggered a lively debate about the origin of these splittings [61, 62], two characteristic features of the exchange interaction became immediately clear: (i) The exchange interaction depends closely on the spatial extent of the exciton wavefunction, and is therefore expected to be enhanced in low dimensional systems; (ii) The symmetry of the excitons is what eventually determines the appearance of energetic splittings in the PL spectra and can be actually exploited to extract information about the microscopic structure of the system under study [61, 63]. Considering (i), it is not surprising that the exchange interaction has a central role in QD physics, and its interplay with quantum confinement is vital for the understanding of the QD optical properties. The first experimental work showing exchange-induced splittings of ground state excitons in QDs appeared in 1996 [64], which also signs the date when the term fine structure splitting (FSS) appeared for the first time for QDs. Since then, many steps toward a complete understanding of the theory underlying the FSS were taken [28, 46, 65]. Its existence suddenly became a "problem" in the early 2000, when Santori et al. [66] showed that suppression of the FSS is fundamental for the efficient generation of polarization entangled photon pairs using the *XX*-*X*-0 radiative decay. As mentioned in the point (ii) above, the latter possibility is strongly connected to

the symmetry of excitons confined in QD: Theoretical calculations show that the coherent coupling of the two bright excitonic states, and hence the FSS, appears every time the QD structural symmetry is lower than D_{2d}. Since this is the case even in ideal lens-shaped Stranski-Kranstanow QDs based on conventional zincblende semiconductors (C_{2v} structural symmetry) alternative growth protocols capable to produce highly symmetric QDs have been developed [18, 67]. Despite impressive progress in this field, however, this approach fails to deliver a substantial number of QDs with FSS <1 μeV. This fact can be qualitatively understood considering that there are inevitable fluctuations in the exact number of atoms composing QDs, their arrangement in the host matrix and intermixing with the substrate and the cap material [20], thus rendering the possibility to grow semiconductor QDs showing specific properties of symmetry a mere theoretical construct. These difficulties have further stimulated the search for alternative routes relying on post-growth tuning of QD properties via the application of stress [35, 36], electric [31], and magnetic [6] fields. It turns out, however, that even with the aid of such "tuning knobs" it is extremely difficult to drive QD excitons towards a universal level crossing, mainly due to the coherent coupling of the two bright states [31, 47]. Suppression of the FSS can be instead achieved using two independent or at least not-equivalent external fields, as strain and electric field provided by our dual-knob device. Before showing how to achieve that experimentally, we discuss the relevant theory. Inspired by the work of Gong et al. [68], we consider the combined effect of a vertical electric field (F) applied along the [001] crystal direction of GaAs and anisotropic biaxial stresses [69, 70] of magnitude $p = p_1 - p_2$, where p_1 and p_2 are the magnitudes of two perpendicular stresses applied along arbitrary directions in the (001) plane. (Note that any in-plane stress configuration can be decomposed in such a way, with $p_{1,2}$ the principal stresses). The effective two-level Hamiltonian for the bright excitons takes the form [58]:

$$H_{ex} = \begin{pmatrix} \eta + \alpha p + \beta F & k + \gamma p \\ k + \gamma p & -(\eta + \alpha p + \beta F) \end{pmatrix} \tag{10.1}$$

Two sets of parameters enter in H_{ex}: (i) the parameters k and η, which are specific of every QD and account for the lowering of the structural symmetry down to C_1, i.e., the most generic case of QDs without structural symmetry; (ii) the parameters of the two perturbations α, γ and β. In particular, α and γ account (via the elastic compliance constants renormalized by the valence band deformation potentials) for the direction of the applied stress while the parameter β (proportional to half of the difference of the exciton dipole moments) is related to the electric field across the diode. Before proceeding further in the analysis it is important to point out that all these parameters combine together in two observables: the magnitude of the FSS and the polarization direction of the exciton emission θ [68]. The latter parameter represents the orientation of the exciton eigenstates with respect to the directions of

the underlying crystal. Finally, diagonalization of the Hamiltonian in (10.1) gives the following values of s and θ:

$$s = \left[(\eta + \alpha p + \beta F)^2 + (k + \gamma p)^2\right]^{1/2}; \; tan(\theta_{\pm}) = \frac{k + \gamma p}{\eta + \alpha p + \beta F \pm s}; \quad (10.2)$$

It can be easily shown that the expression for the FSS has always a minimum at zero when the magnitude of F and p take the values

$$p_{crit} = -\frac{k}{\gamma} \text{ and } F_{crit} = \frac{\alpha k}{\gamma \beta} - \frac{\eta}{\beta} \quad (10.3)$$

In other words, there are *always* values of strain and electric field such that $s = 0$, regardless of the QD structural symmetry, i.e., regardless of the exact values of η and k. At this point, it is important to discuss why exactly two external fields are needed to cancel the FSS and a lower bound for the FSS is instead systematically observed in experiments performed with single tuning knobs [31, 55]. Assuming that only one field acts on QDs, e.g. strain, one can minimize the expression of the FSS reported in (10.2) to find the value of p leading to $s = 0$, that is, $\frac{k}{\eta} = -\frac{2\gamma}{\alpha}$. This equation obviously connects the parameters of the QDs (η and k) to the parameter characterizing the external perturbation (γ and α). Since η and k are unknown and fluctuate from dot to dot, this equation also implies that the $s = 0$ condition can be achieved only if one has *active* control over the direction and magnitude of the applied stress field (γ and α). If this direction is instead fixed—as in all the experiments performed so far—a lower bound of the FSS is generally observed and only the QDs that happen to be "just right" for the chosen perturbation can be tuned to low FSS values. *In strong contrast,* (10.3) *shows that the capability of two independent fields to erase the FSS does not depend on the details of the QD under study*. It is obvious that in real experiments large enough tuning ranges are needed to access the values of p_{crit} and F_{crit} given above. This requirement appears to be satisfied by our device, which allows us to tune systematically all the QDs we measure to $s = 0$.

Figure 10.6a shows the behaviour of the FSS for a QD as a function of F_d and for different values of F_p. In the tensile regime ($F_p < 0$), a lower bound (Δ) for the FSS is observed. Under compressive strain ($F_p > 0$) Δ first decreases to ~0.5 μeV (see Fig. 10.6c), a value comparable with the experimental spectral resolution, and then increases again. Remarkably, the behaviour of the FSS against F_d and F_p is the same in all the measured QDs (see Fig. 10.6b) but for the specific values of F_d and F_p at which the FSS reaches $s = 0$. We have used (10.2) to fit the experimental data (see solid lines in Fig. 10.6a) and we have found an excellent agreement. This confirms not only the existence of a universal method to tune the bright exciton states towards level crossing, but it also points out that the simple theory discussed above—which neglects higher order terms in p and F—is able to grasp the main features of the experiments. Additional information can be inferred looking at the behaviour of the polarization direction of the exciton emission (θ) in relation with the FSS. Figure 10.7

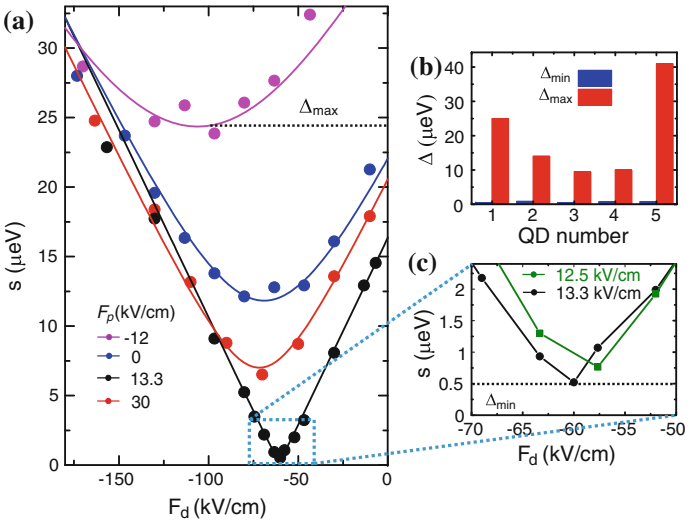

Fig. 10.6 Universal recovery of the bright exciton level degeneracy (**a**). Behavior of the FSS of a single QD as a function of F_d and for different values of F_p. The *solid lines* are fits to the experimental data obtained using (10.2), (10.3) with fixed QD parameters. Δ_{max} indicates the maximum value of Δ (lower bound for the FSS vs. F_d) observed for this QD. **b** Zoom of **a** in the region of small FSS. The data taken at $F_p = 12.5$ kV/cm, not displayed in Fig. 10.3a, are also reported (*green points* connected by *lines*). Δ_{min} indicates the minimum value of Δ observed for this QD. **c** Histogram of Δ_{max} and Δ_{min} for 5 random QDs measured in the same device

shows the dependence (in polar coordinates) of ΔE as a function of the angle the linear polarization analyser forms with the [110] crystal axis, where ΔE is half of the difference between XX and X energies minus its minimum value (see [58] for details). In other words, the length and orientation of the petals give the value of s and θ, respectively. It is clear that when the eigenstates are oriented along the [110] (close to the [100]) or the perpendicular direction, the application of F_d (F_p) leads to $s = 0$. Since the electric field acts as an effective deformations along the [110] direction and the principal stress axis in this device is close to the [100] direction [58], this implies that the excitonic degeneracy can be restored if one external perturbation (e.g. F_d) is used to align the polarization axis of the exciton emission along the axes of the second perturbation (e.g. F_p), which is then able to compensate *completely* for the difference of the confining potentials of the two bright exciton eigenstates, i.e., is able to tune the FSS to zero. This finally shows that the possibility to suppress the FSS is intrinsically connected to the capability of our dual-knob device to achieve independent control of the magnitude of the FSS and the polarization direction of the exciton emission, θ.

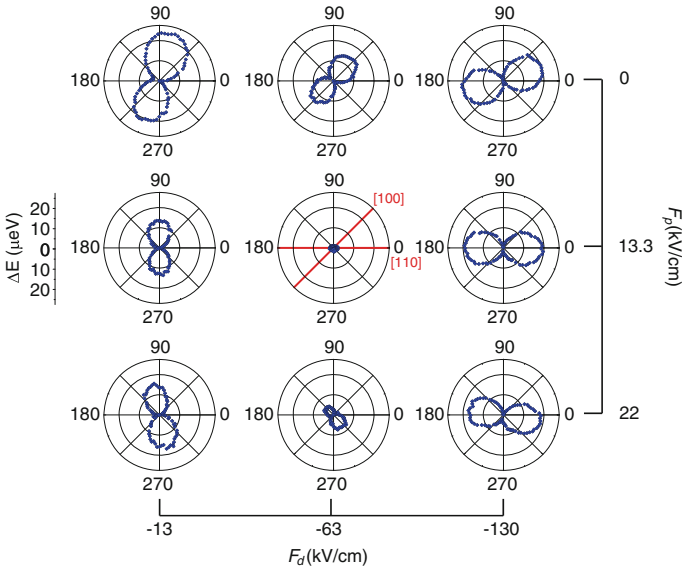

Fig. 10.7 Independent control of exciton fine structure splitting and polarization angle (**a**). Dependence (in polar coordinates) of ΔE versus θ, see text. The length and the orientation of the "petals" give the value of the FSS and θ, respectively. Specific values of F_p and F_d around $FSS \approx 0$ have been used to construct this plot. In the central panel, the [110] and [100] crystal directions of the GaAs matrix hosting the QDs are also indicated

10.4.2 Generation of Highly Entangled Photon Pairs via Electro-elastic Tuning of Single Semiconductor QDs

In the previous section we have demonstrated a universal method to systematically correct for the structural asymmetries that cause the FSS. This opens up the possibility to use arbitrary QDs for the generation of highly entangled photon pairs. When the intermediate X states are degenerate ($s = 0$), photon pairs produced during the XX-X-0 radiative decay are predicted to be in the maximally entangled Bell state $\psi = \frac{1}{\sqrt{2}}(H_{XX}H_X + V_{XX}V_X)$. Figure 10.8 shows XX-X cross-correlation measurements for circular (Fig. 10.8a, d), linear (Fig. 10.8b, e) and diagonal (Fig. 10.8c, f) polarization basis for a QD whose FSS has been tuned to $s = (0.2 \pm 0.3)$ μeV. We observe strong correlation when recording coincidence events for the following projections: $H_{XX}H_X$ (or $V_{XX}V_X$), $D_{XX}D_X$ (or $A_{XX}A_X$) and $R_{XX}L_X$ (or $L_{XX}R_X$). On the other hand, the correlation peaks disappear for $H_{XX}V_X$ (or $V_{XX}H_X$), $D_{XX}A_X$ (or $A_{XX}D_X$) and $R_{XX}R_X$ (or $L_{XX}L_X$). This is exactly the predicted behaviour of photon pairs emitted in the maximally entangled Bell state ψ. By integrating over all the events in the correlation peak at zero time delay it is possible to calculate the correlation visibilities C_{AB}, defined as the difference between co-polarized and cross-polarized correlations divided by their sum. We find

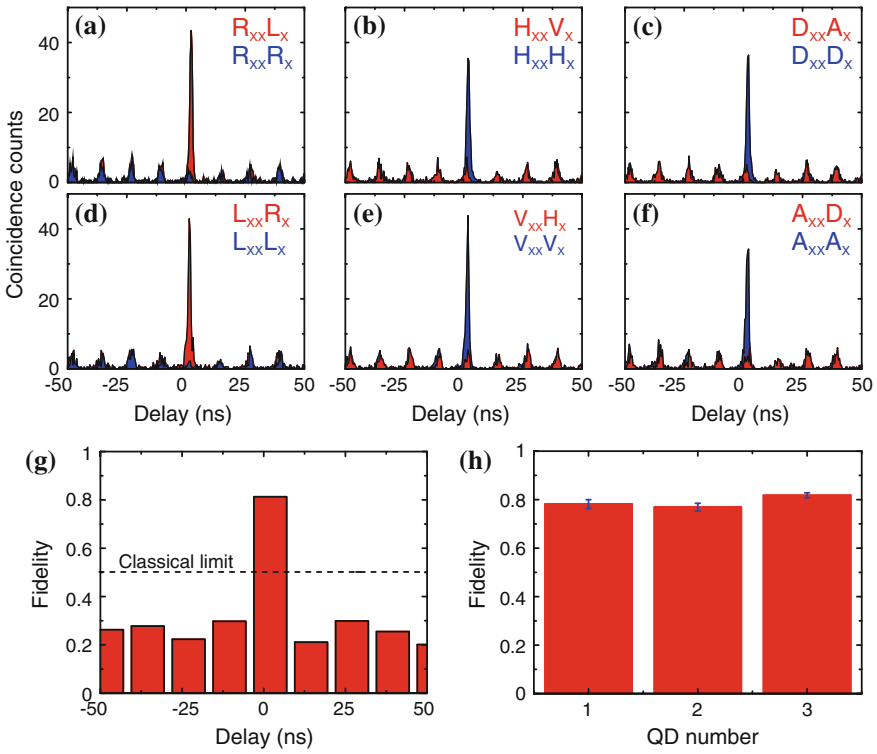

Fig. 10.8 Characterization of the entanglement. **a**–**f** Projective measurements in the polarization basis. The peak at zero delay shows coincidence counts between exciton and biexciton photons for a QD whose FSS has been tuned via the electro-elastic field to zero. The *left*, *central*, and *right* panels correspond respectively to the circular, linear, and diagonal basis. **g** Fidelity versus time delay as obtained from the analysis of the data shown in panels (**a**)–(**f**). The *dashed line* indicates the classical limit. **h** Fidelity values (at zero time delay) for three different QDs from the same device

$C_{HV} = 0.72(5), |C_{RL}| = 0.82(2), C_{DA} = 0.72(5)$. From the correlation visibilities, we can in turn calculate the fidelity to ψ via the following formula [29] $f = (1 + C_{HV} + C_{DA} + |C_{RL}|)/4$ and obtain $f = 0.82(4)$ (see Fig. 10.8g). We have repeated the same measurements in three different QDs tuned to $s = 0$ and we have found very similar values for the fidelity (see Fig. 10.8h). Since these values are always much larger than the classical limit of $f = 0.5$, the experimental data clearly indicate that our strain-tunable device is capable of delivering polarization-entangled photon pairs. However, the fidelity to the Bell state is only an indicator of entanglement and cannot be used to obtain a quantitative estimate. For this reason, we have performed state tomography [71] and reconstructed the density matrix, $\hat{\rho}$, of the two-photon entangled state. The real and imaginary parts of $\hat{\rho}$ for a selected QD are displayed in Fig. 10.9a, b. The matrix clearly satisfies the Peres inseparability criterion [72] for entanglement, being $-0.35(<0)$ the minimum

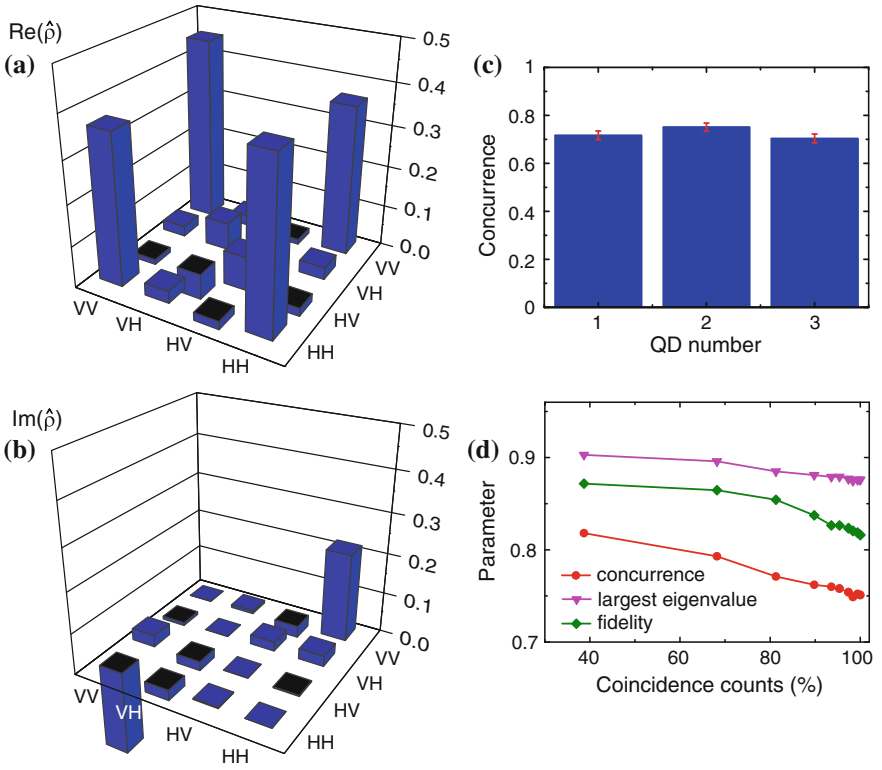

Fig. 10.9 Quantification of the entanglement degree and analysis with temporal post-selection. **a** Real and **b** imaginary part of the two-photon state density matrix as obtained in measurements on a single QD via quantum state tomography. **c** Concurrence values for three different QDs. **d** Temporal post-selection of the parameters characterizing entanglement (concurrence, fidelity, and largest eigenvalue) as a function of the fraction of the recorded coincidence counts (normalized to the total counts calculated for $w = 10$ ns).

eigenvalue of its partial transpose. The $\hat{\rho}$ contains also imaginary components (see Fig. 10.9b), which point out to the presence of a phase delay between $|H_{XX}H_X\rangle$ and $|V_{XX}V_X\rangle$. Therefore, the state is not exactly the maximally entangled Bell state ψ but rather $\psi^* \approx \frac{1}{\sqrt{2}}\left(|H_{XX}H_X\rangle + e^{-i(0.23\pi)}\,|V_{XX}V_X\rangle\right)$, which corresponds to the largest eigenvalue $\lambda = 0.86$ of $\hat{\rho}$. In order to quantify the level of entanglement we have extracted from $\hat{\rho}$ the following metrics [71]: tangle (T), concurrence (C) and entanglement of formation (E_F). For the best QD studied here we obtain $T = 0.56(3)$, $C = 0.75(2)$, $E_F = 0.66(5)$, but very similar values were found for other QDs (see Fig. 10.9c).

It is important to point out that raw data were used in the analysis, without any background subtraction. The measured values are very high compared to previous results using QD-based photon sources [5, 6, 10, 18, 67, 73] and, most importantly, for an electrically-controlled optoelectronic device [7, 31, 74]. In spite of

this achievement, the level of entanglement is not yet ideal and mainly limited by depolarization of the exciton state. This, in turn, can be ascribed to two main mechanisms: (i) fluctuating QD environment [75] and (ii) recapture processes [10]. Point (i) is related to local variations of magnetic and electric fields experienced by the QDs and produced, respectively, by the nuclei of the QD material and by random charges. These fluctuating fields induce a variation of the FSS over time scales much faster than the time required to perform a state tomography, which can therefore reveal $s \approx 0$ only on average. Point (ii) is instead associated with processes in which the intermediate X level is re-excited to the XX level before it decays to the ground state. This mechanism can be optically driven or due to charged carriers trapped in the QD surrounding and produce background photons lowering the correlation visibilities. Temporal post-selection of the emitted photons [7, 10, 76] can be used to alleviate the deleterious effects just discussed, thought at expenses of the brightness of the entangled photon source. We have investigated this strategy in our QDs gradually reducing the temporal window w we choose to integrate the correlation counts later used in the analysis. More specifically, we symmetrically discard photon-pairs arriving at longer positive and negative time delays. This is reasonable because recapture processes produce uncorrelated photons at negative time delays, while in the presence of a fluctuating FSS photons arriving at longer time delays are expected to exhibit lower fidelity to the Bell state. Figure 10.9d shows the evolution of the concurrence (C), fidelity (f) and largest eigenvalue (λ) as a function of the fraction of coincidence counts (normalized to the total counts) recorded during the analysis. The different points correspond to different w, ranging from 10 to 1 ns, being the latter value close to the temporal resolution of the experimental set-up (∼500 ps). A monotonic increase of all the parameters quantifying entanglement can be clearly observed: we first note a slight increase of the parameters for 4 ns $< w <$ 10 ns when less than 10 % coincidence counts are discarded. This behaviour can be easily explained considering the temporal width of the coincidence peak (∼4 ns), and points out the small, albeit deleterious, effect of background photons. A more pronounced effect is instead observed for $w <$ 4 ns: When ∼60 % of the counts are discarded ($w = 1$ ns) a concurrence as high as 0.82 is measured. We believe that the concurrence of our source can be further improved using resonant excitation techniques [12, 77] and faster photon detectors.

The level of entanglement already achieved is particularly significant because it allows us to overcome the Bell limit *without* post-selection of the emitted photons. A first indication of such a possibility is indicated by the level of concurrence. As a rule of thumb, a concurrence of $C \approx 0.7$ (or equivalently a tangle of $T \approx 0.5$) is necessary to violate Bell's inequality [76]. The values we measured in all our QDs are above this threshold (see Fig. 10.9c). Considering the unique capability of our device to drive the FSS through zero, it is extremely interesting to investigate for which values of the FSS we are actually able to violate Bell's inequality. Following [7, 76] we use the following equations for three different planes of the Poincaré sphere: $S_{RC} = \sqrt{2}\,(C_{HV} - C_{RL})$, $S_{RD} = \sqrt{2}\,(C_{HV} - C_{DA})$, $S_{CD} = \sqrt{2}\,(C_{DA} - C_{RL})$. A value larger than 2 of one of these parameters ensures violation the Bell's inequality.

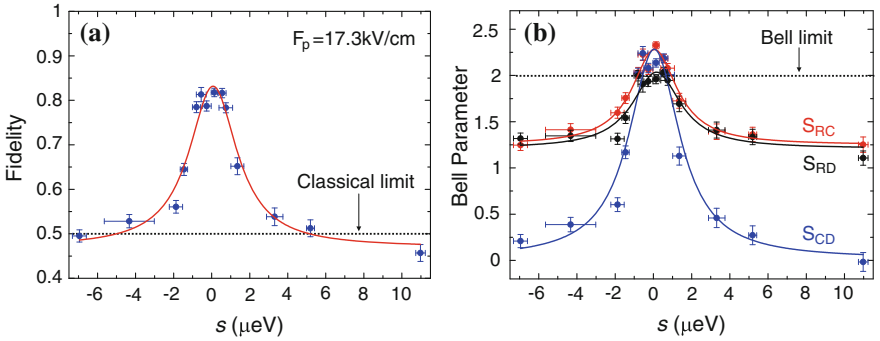

Fig. 10.10 Classical versus Bell limit. **a** Fidelity values for a single QD while the FSS is driven through zero via the electro-elastic fields. The classical limit is indicated by the *dashed line*. The *red line* is a fit to the experimental data using a Lorentzian function. **b** Same as in (**a**) for the three different Bell's parameters introduced in the main text. The Bell limit is indicated by the *dashed line*

Figure 10.10 shows the evolution of these parameters as well as of the fidelity as a function of s. The fidelity (see Fig. 10.10a) first increases, it reaches the non-classical value of 0.82(4) and then it decreases again. As shown by Hudson and co-workers [29], this behaviour can be approximated by a Lorentzian function, whose full-width at half maximum ($\sim$3 μeV) nicely matches the lifetime of the exciton transition ($\tau \approx 1$ ns, being roughly constant for the range of electric fields explored during the experiment). This proves that significant entanglement can be measured once the FSS is reduced below the radiative linewidth of the X transition. Violation of the Bell's inequality in all three planes (see Fig. 10.10b), however, can be achieved only for a very small range of FSS, $s < 1$ μeV, where we measure $S_{RD} = 2.04(0.05)$, $S_{CD} = 2.24(0.07)$, $S_{RC} = 2.33(0.04)$. The latter parameter shows violation of Bell's inequality by more than 8 standard deviations and proves unambiguously that our electrically-driven source can produce non-local states of light. The values of the three Bell parameters further increase well above the limit of 2 using temporal post-selection of the emitted photons, with maximum values of $S_{RD} = 2.22(0.05)$, $S_{CD} = 2.50(0.07)$, $S_{RC} = 2.43(0.04)$ see [13].

To conclude, we further stress the relevance of our results in the perspective of using QDs entanglement resources for applications: It is commonly believed that entanglement is quite tolerant to the presence of a small FSS. Figure 10.3b readily confirms this general idea by showing that the classical limit can be beaten already for FSS $\approx$3 μeV. However, overcoming the classical limit is not sufficient for applications relying on non-local correlations between the emitted photons, such as quantum cryptography and entanglement swapping [21, 26]. One possible criterion to define the "useful" entanglement degree is the violation of Bell's inequality, initially proposed to demonstrate the entanglement non-locality and then used as a base for

quantum cryptography [27]. Figure 10.10b clearly shows that this can be achieved only for FSS <1 μeV, thus ultimately proving the importance of having at hand broad-band "tuning knobs" capable to suppress the FSS [58].

10.5 Conclusions and Outlook

In this chapter, we have introduced a novel class of semiconductor-piezoelectric devices that allows—via the simultaneous application of strain and electric field—for unprecedented control over the electronic and optical properties of self-assembled semiconductor quantum dots. The motivation behind the development of these devices is to use the same semiconductor matrix which allows for the existence of QDs as resource for solving some of the problems arising from their semiconducting nature itself, and in particular those that are hampering their exploitation as sources of non-classical light. In doing so, we have demonstrated the first all-electrically controlled (LED), wavelength-tunable (up to 20 meV), frequency stabilized (down to 1 μeV), high-speed (up to 0.8 GHz) source of single photons. Most importantly, we have shown that the electro-elastic fields generated by our device are able to correct for the structural asymmetries that usually prevent QDs from emitting high-quality polarization entangled photon pairs. We believe that this dual-knob device opens up new frontiers for using QDs in quantum communication science and technology. In particular, it could be exploited in applications based on entanglement non-locality, such as quantum cryptography, as it allows using *any arbitrary* QD to generate triggered entangled photon-pairs featuring high entanglement degree—high enough to violate Bell's inequality without the need of inefficient temporal and spectral filtering techniques. Furthermore, our key idea of combining different external perturbations to achieve independent control of different QD parameters can be further extended in protocols focusing on the distribution of entanglement over the distant nodes of a quantum network, as in quantum relays and repeaters. In these applications, *energy-tunable sources of entangled photons* are needed to match the color of the entangled photons emitted by remote QDs. This is a crucial prerequisite for teleporting entanglement via Hong-Ou-Mandel type two-photon interference. At present, this is out of reach even by the dual-knob device we have discussed in this chapter. In fact, the constraint of exciton level degeneracy requires specific values of strain and electric fields and, as a consequence, specific energies of the X or XX transitions. A different device concept is therefore needed to realize an energy-tunable source of entangled photons. However, having recognized that each QD parameter to control "requires" an independent external field, it is not difficult to envisage that external fields featuring three (or more) independent degrees of freedom will be the key to successfully address this task. We leave this point to future studies [78].

Acknowledgments We thank O.G. Schmidt who continuously supported the different stages of the research presented here, partially performed under his direction at the Institute of Integrative Nanoscience, IFW Dresden. We gratefully acknowledge P.Atkinson and E. Zallo for sample design and growth, and C. Ortix for theoretical support. We also thank J. Wildmann, J.X. Zhang., J.D. Plumhof, S. Kumar, F. Ding, J. Schröter, R.O. Rezaev, and E. Magerl for their important contribution to the work and B. Eichler, R. Engelhardt, F. Binder, S. Bräuer, A. Halilovic, E. Vorhauer, U. Kainz for invaluable support and technical assistance and K. Dörr and A. Herklotz for help with the piezoelectric actuators. The work was supported financially by the European Union Seventh Framework Programme 209 (FP7/2007-2013) under Grant Agreement No. 601126 210 (HANAS), and by Bundesministerium für Bildung und Forschung (BMBF) project QuaHL-Rep (Contract No. 01BQ1032).

References

1. J. Cibert et al., Optically detected carrier confinement to one and zero dimension in gaas quantum well wires and boxes. Appl. Phys. Lett. **49**, 1275–1277 (1986)
2. P. Michler, Single quantum dots: fundamentals, applications and new concepts, vol. 90. (Springer Science & Business Media, 2003)
3. P. Michler et al., A quantum dot single-photon turnstile device. Science **290**, 2282–2285 (2000)
4. O. Benson, C. Santori, M. Pelton, Y. Yamamoto, Regulated and entangled photons from a single quantum dot. Phys. Rev. Lett. **84**, 2513–2516 (2000)
5. N. Akopian et al., Entangled photon pairs from semiconductor quantum dots. Phys. Rev. Lett. **96**, 130501 (2006)
6. R.M. Stevenson et al., A semiconductor source of triggered entangled photon pairs. Nature **439**, 179–182 (2006)
7. C. Salter et al., An entangled-light-emitting diode. Nature **465**, 594–597 (2010)
8. J.P. Reithmaier et al., Strong coupling in a single quantum dot-semiconductor microcavity system. Nature **432**, 197–200 (2004)
9. K. Hennessy et al., Quantum nature of a strongly coupled single quantum dot-cavity system. Nature **445**, 896–899 (2007)
10. A. Dousse et al., Ultrabright source of entangled photon pairs. Nature **466**, 217–220 (2010)
11. Y.-M. He et al., On-demand semiconductor single-photon source with near-unity indistinguishability. Nat. Nanotechnol. **8**, 213–217 (2013)
12. M. Müller, S. Bounouar, K.D. Jöns, M. Glässl, P. Michler, On-demand generation of indistinguishable polarization-entangled photon pairs. Nat. Photon. **8**, 224–228 (2014)
13. R. Trotta, J.S. Wildmann, E. Zallo, O.G. Schmidt, A. Rastelli, Highly entangled photons from hybrid piezoelectric-semiconductor quantum dot devices. Nano Lett. **14**, 3439–3444 (2014)
14. J. Nilsson et al., Quantum teleportation using a light-emitting diode. Nat. Photon. **7**, 311–315 (2013)
15. W. Gao et al., Quantum teleportation from a propagating photon to a solid-state spin qubit. Nat. Commun. **4** (2013)
16. J. Claudon et al., A highly efficient single-photon source based on a quantum dot in a photonic nanowire. Nat. Photon. **4**, 174–177 (2010)
17. M.A. Versteegh et al., Observation of strongly entangled photon pairs from a nanowire quantum dot. Nat. Commun. **5** (2014)
18. G. Juska, V. Dimastrodonato, L.O. Mereni, A. Gocalinska, E. Pelucchi, Towards quantum-dot arrays of entangled photon emitters. Nat. Photon. **7**, 527–531 (2013)
19. R. Trotta et al., Fabrication of site-controlled quantum dots by spatially selective incorporation of hydrogen in ga (asn)/gaas heterostructures. Adv. Mater. **23**, 2706–2710 (2011)
20. A. Rastelli et al., Three-dimensional composition profiles of single quantum dots determined by scanning-probe-microscopy-based nanotomography. Nano Lett. **8**, 1404–1409 (2008)

21. N. Gisin, G. Ribordy, W. Tittel, H. Zbinden, Quantum cryptography. Rev. Mod. Phys. **74**, 145–195 (2002)
22. C. Hong, Z. Ou, L. Mandel, Measurement of subpicosecond time intervals between two photons by interference. Phys. Rev. Lett. **59**, 2044 (1987)
23. R.B. Patel et al., Two-photon interference of the emission from electrically tunable remote quantum dots. Nat. Photon. **4**, 632–635 (2010)
24. E.B. Flagg et al., Interference of single photons from two separate semiconductor quantum dots. Phys. Rev. Lett. **104**, 137401 (2010)
25. L.-M. Duan, M. Lukin, J.I. Cirac, P. Zoller, Long-distance quantum communication with atomic ensembles and linear optics. Nature **414**, 413–418 (2001)
26. J.-W. Pan, D. Bouwmeester, H. Weinfurter, A. Zeilinger, Experimental entanglement swapping: Entangling photons that never interacted. Phys. Rev. Lett. **80**, 3891 (1998)
27. A.K. Ekert, Quantum cryptography based on bell's theorem. Phys. Rev. Lett. **67**, 661 (1991)
28. M. Bayer et al., Fine structure of neutral and charged excitons in self-assembled in (ga) as/(al) gaas quantum dots. Phys. Rev. B **65**, 195315 (2002)
29. A. Hudson et al., Coherence of an entangled exciton-photon state. Phys. Rev. Lett. **99**, 266802 (2007)
30. M. Gong et al., Statistical properties of exciton fine structure splitting and polarization angles in quantum dot ensembles. Phys. Rev. B **89**, 205312 (2014)
31. A. Bennett et al., Electric-field-induced coherent coupling of the exciton states in a single quantum dot. Nat. Phys. **6**, 947–950 (2010)
32. B. Gerardot et al., Manipulating exciton fine structure in quantum dots with a lateral electric field. Appl. Phys. Lett. **90**, 041101–041101 (2007)
33. M. Vogel et al., Influence of lateral electric fields on multiexcitonic transitions and fine structure of single quantum dots. Appl. Phys. Lett. **91**, 051904 (2007)
34. H. Krenner et al., Direct observation of controlled coupling in an individual quantum dot molecule. Phys. Rev. Lett. **94**, 057402 (2005)
35. S. Seidl et al., Effect of uniaxial stress on excitons in a self-assembled quantum dot. Appl. Phys. Lett. **88**, 203113 (2006)
36. C.E. Kuklewicz, R.N. Malein, P.M. Petroff, B.D. Gerardot, Electro-elastic tuning of single particles in individual self-assembled quantum dots. Nano Lett. **12**, 3761–3765 (2012)
37. T. Zander et al., Epitaxial quantum dots in stretchable optical microcavities. Opt. Express **17**, 22452–22461 (2009)
38. A. Muller, W. Fang, J. Lawall, G.S. Solomon, Creating polarization-entangled photon pairs from a semiconductor quantum dot using the optical stark effect. Phys. Rev. Lett. **103**, 217402 (2009)
39. E. Zallo et al., Strain-induced active tuning of the coherent tunneling in quantum dot molecules. Phys. Rev. B **89**, 241303 (2014)
40. A. Laucht et al., Dephasing of exciton polaritons in photoexcited ingaas quantum dots in gaas nanocavities. Phys. Rev. Lett. **103**, 087405 (2009)
41. H. Lin et al., Stress tuning of strong and weak couplings between quantum dots and cavity modes in microdisk microcavities. Phys. Rev. B **84**, 201301 (2011)
42. R. Trotta, E. Zallo, E. Magerl, O.G. Schmidt, A. Rastelli, Independent control of exciton and biexciton energies in single quantum dots via electroelastic fields. Phys. Rev. B **88**, 155312 (2013)
43. M. Kaniber et al., Electrical control of the exciton-biexciton splitting in self-assembled ingaas quantum dots. Nanotechnology **22**, 325202 (2011)
44. F. Ding et al., Tuning the exciton binding energies in single self-assembled ingaas/gaas quantum dots by piezoelectric-induced biaxial stress. Phys. Rev. Lett. **104**, 067405 (2010)
45. R. Trotta et al., Nanomembrane quantum-light-emitting diodes integrated onto piezoelectric actuators. Adv. Mater. **24**, 2668–2672 (2012)
46. R. Singh, G. Bester, Lower bound for the excitonic fine structure splitting in self-assembled quantum dots. Phys. Rev. Lett. **104**, 196803 (2010)

47. J.D. Plumhof et al., Strain-induced anticrossing of bright exciton levels in single self-assembled gaas/al x ga 1-x as and in x ga 1-x as/gaas quantum dots. Phys. Rev. B **83**, 121302 (2011)
48. D. Huffaker, C. Lin, J. Shin, D. Deppe, Resonant cavity light emitting diode with an alxoy/gaas reflector. Appl. Phys. Lett. **66**, 3096–3098 (1995)
49. J. Zhang et al., A nanomembrane-based wavelength-tunable high-speed single-photon-emitting diode. Nano Lett. **13**, 5808–5813 (2013)
50. A. Bennett et al., Single-photon-emitting diodes: a review. Phys. Status Solidi (b) **243**, 3730–3740 (2006)
51. A. Nowak et al., Deterministic and electrically tunable bright single-photon source. Nat. Commun. **5** (2014)
52. R. Trotta, A. Rastelli, Independent control of charge state and emission energy. (2012)
53. W. Gao, P. Fallahi, E. Togan, J. Miguel-Sánchez, A. Imamoglu, Observation of entanglement between a quantum dot spin and a single photon. Nature **491**, 426–430 (2012)
54. R.J. Warburton et al., Optical emission from a charge-tunable quantum ring. Nature **405**, 926–929 (2000)
55. A.J. Bennett et al., Giant stark effect in the emission of single semiconductor quantum dots. Appl. Phys. Lett. **97**, 031104 (2010)
56. J.E. Avron et al., Entanglement on demand through time reordering. Phys. Rev. Lett. **100**, 120501 (2008)
57. H. Jayakumar et al., Time-bin entangled photons from a quantum dot. Nat. Commun. **5** (2014)
58. R. Trotta et al., Universal recovery of the energy-level degeneracy of bright excitons in ingaas quantum dots without a structure symmetry. Phys. Rev. Lett. **109**, 147401 (2012)
59. W. Ekardt, K. Lösch, D. Bimberg, Determination of the analytical and the nonanalytical part of the exchange interaction of inp and gaas from polariton spectra in intermediate magnetic fields. Phys. Rev. B **20**, 3303 (1979)
60. R. Bauer et al., *Proceedings of the 18th International Conference on the Physics of Semiconductors, Stockholm, 1986*. (World Scientific, Singapore, 1987)
61. E. Blackwood, M. Snelling, R. Harley, S. Andrews, C. Foxon, Exchange interaction of excitons in gaas heterostructures. Phys. Rev. B **50**, 14246 (1994)
62. L.C. Andreani, F. Bassani, Exchange interaction and polariton effects in quantum-well excitons. Phys. Rev. B **41**, 7536–7544 (1990)
63. H. Van Kesteren et al., Optically detected magnetic resonance study of a type-ii gaas-alas multiple quantum well. Phys. Rev. Lett. **61**, 129 (1988)
64. D. Gammon, E. Snow, B. Shanabrook, D. Katzer, D. Park, Fine structure splitting in the optical spectra of single gaas quantum dots. Phys. Rev. Lett. **76**, 3005 (1996)
65. R. Seguin et al., Size-dependent fine-structure splitting in self-organized inas/gaas quantum dots. Phys. Rev. Lett. **95**, 257402 (2005)
66. C. Santori, D. Fattal, M. Pelton, G.S. Solomon, Y. Yamamoto, Polarization-correlated photon pairs from a single quantum dot. Phys. Rev. B **66**, 045308 (2002)
67. T. Kuroda et al., Symmetric quantum dots as efficient sources of highly entangled photons: violation of bell's inequality without spectral and temporal filtering. Phys. Rev. B **88**, 041306 (2013)
68. M. Gong, W. Zhang, G.-C. Guo, L. He, Exciton polarization, fine-structure splitting, and the asymmetry of quantum dots under uniaxial stress. Phys. Rev. Lett. **106**, 227401 (2011)
69. S. Kumar et al., Strain-induced tuning of the emission wavelength of high quality gaas/algaas quantum dots in the spectral range of the 87rb d2 lines. Appl. Phys. Lett. **99**, 161118 (2011)
70. S. Kumar et al., Anomalous anticrossing of neutral exciton states in gaas/algaas quantum dots. Phys. Rev. B **89**, 115309 (2014)
71. D.F. James, P.G. Kwiat, W.J. Munro, A.G. White, Measurement of qubits. Phys. Rev. A **64**, 052312 (2001)
72. A. Peres, Separability criterion for density matrices. Phys. Rev. Lett. **77**, 1413 (1996)
73. R. Hafenbrak et al., Triggered polarization-entangled photon pairs from a single quantum dot up to 30?k. New J. Phys. **9**, 315 (2007)

74. M. Ghali, K. Ohtani, Y. Ohno, H. Ohno, Generation and control of polarization-entangled photons from gaas island quantum dots by an electric field. Nat. Commun. **3**, 661 (2012)
75. R.M. Stevenson et al., Evolution of entanglement between distinguishable light states. Phys. Rev. Lett. **101**, 170501 (2008)
76. R. Young et al., Bell-inequality violation with a triggered photon-pair source. Phys. Rev. Lett. **102**, 030406 (2009)
77. H. Jayakumar et al., Deterministic photon pairs and coherent optical control of a single quantum dot. Phys. Rev. Lett. **110**, 135505 (2013)
78. R. Trotta, J. Martín-Sánchez, I. Daruka, C. Ortix, A. Rastelli, Energy-tunable sources of entangled photons: a viable concept for solid-state-based quantum relays. Phys. Rev. Lett. **114**, 150502 (2015)

Chapter 11
Resonant Excitation and Photon Entanglement from Semiconductor Quantum Dots

Ana Predojević

Abstract In this chapter we review the use of semiconductor quantum dots as sources of quantum light. Principally, we focus on resonant two-photon excitation, which is a method that allows for on-demand generation of photon pairs. We explore the advantages of resonant excitation and present a number of results that were made in this excitation regime. In particular, we cover the following topics: photon statistics, coherent manipulation of the ground-excited state superposition, and generation of time-bin entangled photon pairs.

11.1 Introduction

The field of photonic quantum information needs novel, highly efficient, and deterministic sources of single photons and entangled photon pairs. The principal applications of these sources include quantum networks [1–4] and linear optical quantum computing [5]. In particular, quantum light is needed to transfer information in procedures like teleportation [6] and entanglement swapping [7]; the photons are employed as flying qubits that interconnect the nodes of a quantum network, or to run a quantum processor using the methods of linear optical quantum computing.

The vast majority of today's quantum information experiments use single photons and entangled photon pairs that are generated in a process of parametric down-conversion. While this method still stands as the most versatile and successful, semiconductor quantum dot devices are developed because of their potential to deliver a source that is brighter and more reliable but also can be easily integrated within a semiconductor optical circuit. While the initial interest in quantum dots in general was more oriented towards semiconductor and material physics and even chemistry, today's semiconductor quantum dot devices are also very often designed for the

A. Predojević (✉)
Experimental Physics, University of Innsbruck, Technikerstr. 25, 6020 Innsbruck, Austria
e-mail: ana.predojevic@uibk.ac.at

A. Predojević and M.W. Mitchell (eds.), *Engineering the Atom-Photon Interaction*,
Nano-Optics and Nanophotonics, DOI 10.1007/978-3-319-19231-4_11

purposes of quantum information processing. Namely, similar to atoms quantum dots possess discrete energy structure and therefore a valuable asset of an intrinsic sub-Poissonian distribution of the emitted photons. Due to their atom-like energy structure quantum dots can emit single photons [8] but their range of application does not end there. They can also deliver pairs of photons, emitted in a temporary ordered cascade. In addition to their potential to be used as sources of photons, quantum dots can also take the role of a quantum memory. In particular, the quantum dot potential can also trap single carriers (electrons and holes) and the spin on such a carrier can encode a quantum bit (see the chapter by McMahon and De Greve).

In Sect. 11.2 of this chapter we will give the basic specifications that a photon source should fulfil in order to be used in a specific application. Also we will introduce an excitation method that can resonantly create pairs of photons from a quantum dot. We will address this problem from both an experimental and a theoretical point of view. In addition, we will review the use of quantum dots to generate polarization entangled photon pairs. In Sect. 11.3 we will present measurements that exploit the use of resonant excitation. In particular, we will address the coherent control, the effects resonant excitation has on the photon statistics of the emitted light, and finally the generation of time-bin entangled photon pairs emitted by a single semiconductor quantum dot.

11.2 On-Demand Generation of Photon Pairs Using Single Semiconductor Quantum Dots

There are a number of applications that need or benefit from single photons and entangled photon pairs. These include linear optical quantum computing, long distance quantum communication, and up to some level quantum cryptography. Though certain tasks can be performed in a probabilistic manner or even override the use of single photons, the optimum performance and minimal overhead are very often achieved using a deterministic photon source.

Probably the most straightforward example is linear optical quantum computing [9]. Photonic quantum computing using linear elements, as proposed in the seminal paper by Knill et al. [5], is a method to realise a quantum processor. The proposal in its original form assumes an ideal single photon source. Posteriorly, a scheme was shown [10] that allows linear optical quantum computation if the overall efficiency (source $\times$ detector) is higher then 2/3. Nevertheless, to achieve gates outside the post-selection basis[1] one needs much higher photon generation probability combined with a very low probability for emission of more than one photon [11]. Concerning the use of photon sources within quantum networks it is harder to define an efficiency threshold because it would depend on the specific application.[2] Furthermore,

[1] The inefficiency of sources and detectors are commonly bridged using post-selection.

[2] For example for a complex task like distributed quantum computing the threshold will be different than for the simplest form of communication between two network nodes.

quantum networks depends on many additional parameters like the efficiencies of state mapping or generation of atom-photon entanglement. Regardless the specific application, a deterministic photon source would surely increase the information transfer rate. On the other hand, multi-photon contribution, which we will show in continuation is greatly reduced in quantum dots under resonant excitation, has a negative effect on long-distance entanglement distribution [12] as well as quantum key distribution [13].

11.2.1 Quantum Dots and Polarization Entanglement

Before entering the topic of resonant excitation, we will briefly review the use of quantum dots to generate polarization entangled photon pairs. This system has been proposed to be capable of delivering entangled photon pairs [14] through the use of a biexciton-exciton (XX-X) photon cascade. In particular, once the quantum dot potential has trapped two electron-hole pairs (biexciton) the system decays to the ground state via an emission of the temporally ordered photon cascade. This decay can happen via two different paths that give photons with orthogonal polarizations. If these decay paths are indistinguishable the emitted pair of photons are entangled in polarization. Unfortunately this scheme is not straightforward to accomplish due to a geometrical anisotropy of quantum dots that is growth typical and almost unavoidable and that makes the intermediate exciton state split. This splitting (also known as the fine structure splitting—FSS, Fig. 11.1a) causes the two decay paths to be distinguishable. In other words, once the first photon of the cascade is emitted the system is projected in a superposition of the two exciton levels. This superposition evolves in time and therefore averages the phase of the emitted state [15], which causes the measured level of entanglement to be reduced with increasing exciton splitting.

There have been many attempts to overcome the problem of the fine structure splitting. The initial results were focused on selecting the dots with the lowest splitting [16] or employing optical cavities to filter out a narrow indistinguishable spectral region [17]. In [18] it was demonstrated that the optical Stark effect can be used to generate energy degenerate photons. Here, the Stark shift was used to tune the energy of the horizontally polarized exciton and make it degenerate with the vertically polarized one. Another specific approach was shown in [19] where a quantum dot was placed in a system of two strongly coupled micro-pillar cavities. Though the quantum dot itself was weakly coupled to the individual micro-pillars the overall effect was an enhanced emission of both exciton and biexiton photon. This resulted in the immediate emission of the exciton photon after the emission of the biexciton one. Under such experimental conditions the cascade pair is emitted faster than the phase of the generated state, due to the fine structure splitting, could have evolved.

Both fine structure splitting as well as the energies of the exciton and the biexciton can be tuned using an electric field [20], a magnetic field [21], or the material strain. In that respect one should point out the method shown in [22] where both electric field and the material strain were employed simultaneously. This approach allows

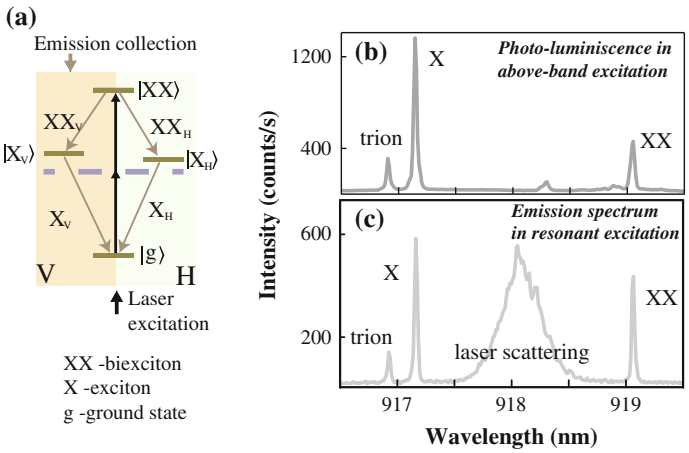

Fig. 11.1 **a** Quantum dot energy scheme. Fine structure splitting is the energy difference between two exciton levels $|X_H - X_V|$. In the process of two-photon resonant excitation a pulsed laser with the energy $E_{laser} = (|XX\rangle - |g\rangle)/2$ (shown as *black arrow* pointing upwards) coherently couples the ground ($|g\rangle$) and the biexciton ($|XX\rangle$) states through a virtual level (*dashed line*). Biexciton recombination takes place through the intermediate exciton states ($|X_{H,V}\rangle$) emitting biexciton ($XX_{H,V}$) and exciton ($X_{H,V}$) photons. **b** Photo-luminescence emitted by a single quantum dot. The excitation laser of wavelength close to 630 nm generates a reservoir of carriers that via multiple phonon scattering occupy the quantum dot levels. Here, we observe three emission lines corresponding to exciton (X), biexciton (XX), and trion. **c** Emission spectrum obtained in two-photon resonant excitation. The laser energy is half way between exciton and biexciton and not resonant to any of these transitions

for modification and removal of the fine structure for any randomly chosen quantum dot.

The origin of the exciton level splitting is growth induced, therefore, a number of experiments were demonstrated where the splitting was reduced via a modification of the growth method. In [23] was explored an alternative method of dot self assembly, namely, the droplet epitaxy on (111)A substrates. Another approach is the growth of so-called pyramidal quantum dots [24] that apart from high geometrical symmetry can provide control of the position where the dot is grown. The use of quantum dots embedded in nanowires [25] is another growth related method that shares some similarities with the pyramidal quantum dots, in particular, intrinsic symmetry and the control of the position of the emitter. Here, it was proposed [26] that the geometrical symmetry of the nanowires will condition the symmetry of the quantum dots embedded within.

At this point it is also important to mention that all above-given results were achieved in above-band excitation. The use of two-photon resonant excitation, in detail explained in continuation, has been shown to improve the degree of entanglement [27].

There are different parameters that characterize two-qubit entanglement [28]; some rather being indicators (like fidelity > 0.5 to the maximally entangled state)

Table 11.1 Characterization of the achieved polarization entanglement given for the experiments where both concurrence and fidelity were reported

	Young (2006) [16]	Juska (2013) [24]	Trotta (2014) [22]	Huber (2014) [25]
Concurrence	0.44(3)	0.16(2)	0.75(2)	0.57(6)
Fidelity	0.70(2)	0.58(3)	0.82(4)	0.76(2)

and others being measures of entanglement (concurrence > 0 [29]). While there are alternative methods to estimate the fidelity, to obtain a value for concurrence one needs to perform state tomography [29]. The results of the experiments that performed state tomography are summarized in Table 11.1. The indicator of the nonlocality of the entanglement measurement—the violation of the Bell inequality—were reported in [22, 23].

11.2.2 Resonant Excitation

A photon generation device employed in quantum information processing tasks must achieve a high success probability to produce a single photon. In atom-like systems such a behaviour is achievable by means of coherent population inversion. Likewise, the discrete energy structure of quantum dots makes this system suitable for driving such a process.

On the other hand, despite the favourable energetic structure it is hard to achieve resonant excitation in semiconductor embedded quantum dots. The first, and most important reason is the excess laser scattering that is hard to distinguish from the single photon signal emitted by the quantum dot. Therefore, the traditional way to excite quantum dots is above-band excitation. Here, one uses a laser with an energy higher than any transition in the quantum dot. This laser creates a multitude of carriers in the vicinity of the quantum dot that can be probabilistically trapped in the quantum dot potential. This process is very nicely illustrated in the Fig. 11.4 of the chapter by Schneider, Gold, Lu, Höfling, Pan and Kamp. While it is possible to both saturate the quantum dot transitions and to achieve very high single photon count rates, the probabilistic nature of this process reduces the suitability of such a source for quantum information protocols. Another negative feature of the above-band excitation is related to how exactly the quantum dot levels are populated. Namely, biexciton photons will be created once the exciton level has been saturated and, therefore, the saturation of the biexciton level itself demands a very large number of carriers in the quantum dot vicinity. Such an experimental configuration is very unfavourable because it promotes the dephasing of the quantum dot levels due to the electric field fluctuations and causes poor photon statistics properties due to processes like carrier re-capture [30].

Two-photon resonant excitation of the biexciton [31] is an experimental implementation that simultaneously solves both problems: laser scattering and

probabilistic generation of photon pairs. Here, one exploits the biexciton binding energy in order to drive the quantum dot system using a virtual resonance that is placed halfway in energy between the exciton and biexciton (see Fig. 11.1a) and therefore is not resonant to any of them. The photo-luminescence obtained in above-band excitation of the quantum dot is shown in Fig. 11.1b. For comparison, the emission spectrum under resonant excitation is shown in Fig. 11.1c. This spectrum shows an additional line coming from the scattered excitation laser light. The physical basis of the phenomenon exploited here, the biexciton binding energy, is the Coulomb interaction present when two electron-hole pairs are trapped inside the quantum dot potential. As the first pair of carriers recombine and the biexciton photon is emitted the energy levels in the quantum dots will change and the second photon to be emitted (exciton photon) will not have the same energy as the biexciton photon. Therefore, one always observes the exciton and biexciton emission as two energetically well separated lines.

It is important to say that the two-photon approach to excite quantum dots is not new, nevertheless, it is quite challenging to apply this method on III-V quantum dots. The previous works [32] addressed II-VI quantum dots that have much larger biexciton binding energy (the difference between the exciton and the biexciton line can be of even more than 10 nm) but have very unfavourable optical properties; they emit photons in the blue and green spectral range that are, due to losses in the optical fibres, not very suitable for quantum communication. The values for the energy difference between biexciton and exciton lines in III-V quantum dots are in the region of 1–2 nm. Therefore, these systems demand a more thoughtful approach to reduce the laser scattering. The early works on III-V quantum dots [33] showed the signatures of resonant excitation, like for example Rabi oscillations, but only in photocurrent measurements and not in the optical signal. The first optical measurements [31] showed Rabi oscillations as well as Ramsey interference measurements, while in [27] it was also shown that resonant excitation can improve the degree of photon entanglement.

Depending on the sample structure and the amount of power needed to excite the quantum dot, the resonant excitation of the biexciton might not be sufficient to fully suppress the laser scattering. Here, we will name two methods to additionally reduce the amount of laser scattering[3]: sample/excitation geometry and design of pulse-bandwidth. The choice of the sample structure and the corresponding geometry of excitation can greatly reduce excess laser scattering. The method of orthogonal propagation paths was first shown in resonant excitation of a single exciton [35]. The schematic of the excitation used in [35] is shown in chapter by Schneider, Gold, Lu, Höfling, Pan and Kamp, Fig. 11.4d. Here, the excitation laser is directed onto the cleaved edge of the sample via an optical fibre that is brought to a distance of a few microns from the sample. This method was also used in [27, 31] with a difference that the laser light was focused onto the cleaved edge of the sample using an objective.

[3] In addition, one of the simplest approaches to minimize the laser scattering is the method of crossed polarisers [34]. It employes an excitation laser that is horizontally polarized (Fig. 11.1a), while the emission is collected only from the vertically polarized ($XX_V - X_V$) cascade.

Micro-cavity quantum dot samples, where the cavity extends all the way to the edges of the sample, are highly suitable structures for the implementation of this type of excitation geometry. Namely, the excitation laser is here focused onto the sample from the side, see Fig. 11.2a, so that the sample distributed Bragg reflector (DBR) structure acts as a waveguide for the laser light. The quantum dot emission is collected from the top using a high numerical aperture objective. For example, the specific sample used in [31] contained self-assembled InAs quantum dots of low density (approximately 10 per μm^2) that were embedded in a 4λ thick, distributed Bragg reflector microcavity consisting of 15.5 lower and 10 upper $\lambda/4$ thick DBR layer pairs of AlAs and GaAs. The cavity mode was resonant at $\lambda = 920$ nm. The results presented in [27] were obtained using a sample with a λ thick cavity that had far fewer upper-reflector DBR pairs.

As mentioned above, the wavelength separation between the exciton and the biexciton line in III-V quantum dots is about 1–2 nm. This value can vary significantly even within the same quantum dot sample. Therefore the flexibility in choice of the excitation laser bandwidth is crucial for this application. There exist quite costly solutions for this problem, like for example lasers with variable pulse length. Nevertheless, in both [27, 31] it was shown that a combination of a short pulse laser (around 2 ps) and a pulse stretcher can fulfil both the variable bandwidth requirement as well as the need to fine tune the wavelength of the pulses. With respect to the design of the pulse stretcher special care should be given to the pulse chirp [27].

11.2.3 Theoretical Description of the Two-Photon Excitation Process

In order to gain better understanding of the problem we introduce here a theoretical model of a three-level system subjected to the resonant two-photon excitation. The approach we present is well known from atomic physics and describes resonant two-photon driving of a discrete-energy system in the presence of level dephasing.

The levels involved are the ground ($|g\rangle$), exciton state ($|x\rangle$), and biexciton state ($|xx\rangle$). The level scheme is shown in Fig. 11.2b. The energy differences between ground state and exciton state, and between exciton state and biexciton state are not equal due to the biexciton binding energy. This electronic configuration allows for a two-photon excitation process where the pump laser is not resonant to any of the single photon transitions, while the two-photon process is resonant. To describe this system we can use the Hamiltonian of the following form:

$$H = \frac{\hbar\Omega_1(t)}{2}(\sigma_{g,x} + \sigma_{g,x}^{\dagger}) + \frac{\hbar\Omega_2(t)}{2}(\sigma_{x,xx} + \sigma_{x,xx}^{\dagger}) + \hbar\sigma_{x,x}(\Delta_x - \Delta_{xx}) - 2\hbar\sigma_{xx,xx}\Delta_{xx}. \tag{11.1}$$

Here, $\Omega_l(t)$, $l = 1,2$ is the Rabi frequency of the pump laser driving both single photon transitions. The transition operators and projectors are given as $\sigma_{i,j} = |i\rangle\langle j|$. The energy difference between the virtual level of the two-photon transition and the

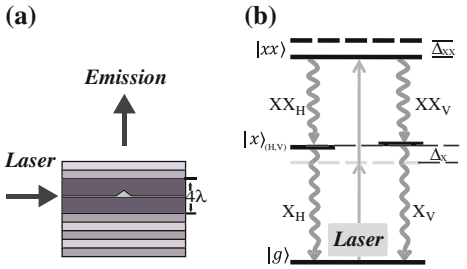

Fig. 11.2 **a** Schematics of the excitation geometry. The laser light is directed from the side onto the cleaved edge of the sample. Here, the 4λ thick structure of the planar micro-cavity acts as a wave-guide for the excitation light. The quantum dot emission is collected from the *top*. **b** Energy level scheme for two-photon excitation of a biexciton. The excitation laser light coherently couples the ground ($|g\rangle$) and the biexciton ($|xx\rangle$) states via the virtual level in two-photon resonance (*dashed gray line*). Biexciton recombination takes place through the intermediate exciton states ($|x_{H,V}\rangle$) emitting biexciton ($XX_{H,V}$) and exciton ($X_{H,V}$) photons. The energy difference between the exciton level and the two-photon virtual resonance is denoted as Δ_x. For driving the two-photon transition off-resonantly we define the detuning Δ_{xx}

exciton energy is Δ_x. This energy difference can also be seen as the laser detuning in a process of a single photon resonant excitation that drives the exciton state. To drive the two-photon transition off-resonantly we define the detuning Δ_{xx}, the difference between the two-photon virtual resonance and the energy of the laser driving the system.

The Hamiltonian in matrix form is given as:

$$H = \hbar \begin{pmatrix} 0 & \frac{\Omega_1(t)}{2} & 0 \\ \frac{\Omega_1(t)}{2} & -\Delta_{xx} + \Delta_x & \frac{\Omega_2(t)}{2} \\ 0 & \frac{\Omega_2(t)}{2} & -2\Delta_{xx} \end{pmatrix}. \tag{11.2}$$

To calculate the state populations and corresponding emission probabilities we need to solve the master equation, here written in Lindblad form [36, 37]

$$\dot{\rho} = -\frac{i}{\hbar}[H, \rho] + \sum_{i=1}^{4} \mathscr{L}_i(\rho). \tag{11.3}$$

Following [36, 37], we use the following Lindblad operator

$$\mathscr{L}_1(\rho) = \frac{\gamma_{xx}}{2}(2\sigma_{x,xx}\rho\sigma^{\dagger}_{x,xx} - \sigma^{\dagger}_{x,xx}\sigma_{x,xx}\rho - \rho\sigma^{\dagger}_{x,xx}\sigma_{x,xx}) \tag{11.4}$$

to describe the spontaneous decay from the biexciton to the intermediate exciton state and the operator

$$\mathscr{L}_2(\rho) = \frac{\gamma_x}{2}(2\sigma_{g,x}\rho\sigma^{\dagger}_{g,x} - \sigma^{\dagger}_{g,x}\sigma_{g,x}\rho - \rho\sigma^{\dagger}_{g,x}\sigma_{g,x}) \tag{11.5}$$

to describe the spontaneous decay from the exciton to the ground state. Unfortunately in quantum dots there are decoherence mechanisms that can put an end to Rabi oscillations before the spontaneous decay does so. The drift of the quantum dot energy levels is a well-known problem that impedes quantum dots from emitting Fourier transform limited photon wave-packets [38]. Therefore it is essential to introduce Lindblad terms that describe the dephasing of the quantum dot levels due to its interaction with the environment. Again following [36, 37], we can introduce the following Lindblad operators to model the dephasing of the biexciton level

$$\mathscr{L}_3(\rho) = \frac{\gamma_{dxx}}{2}(2(\sigma_{xx,xx} - \sigma_{x,x})\rho(\sigma_{xx,xx} - \sigma_{x,x})^\dagger - \rho(\sigma_{xx,xx} - \sigma_{x,x})^\dagger(\sigma_{xx,xx} - \sigma_{x,x}) - (\sigma_{xx,xx} - \sigma_{x,x})^\dagger(\sigma_{xx,xx} - \sigma_{x,x})\rho), \tag{11.6}$$

and respectively to describe the dephasing of the exciton level

$$\mathscr{L}_4(\rho) = \frac{\gamma_{dx}}{2}(2(\sigma_{x,x} - \sigma_{g,g})\rho(\sigma_{x,x} - \sigma_{g,g})^\dagger - \rho(\sigma_{x,x} - \sigma_{g,g})^\dagger(\sigma_{x,x} - \sigma_{g,g}) - (\sigma_{x,x} - \sigma_{g,g})^\dagger(\sigma_{x,x} - \sigma_{g,g})\rho). \tag{11.7}$$

Here, γ_{xx} and γ_x are the spontaneous decay rates and γ_{dxx} and γ_{dx} are the dephasing rates of the biexciton and exciton, respectively. The excitation pulse is considered to have a Gaussian envelope function. Parameters like spontaneous decay and dephasing rates can be determined from experimental lifetime and coherence time measurements, respectively. Using these experimentally measured parameters we can numerically solve the master equation and thereby obtain the theoretical prediction for the populations of the different levels involved ($P_i = \langle \sigma_{ii} \rangle$). The population multiplied with decay rate integrated over time gives the emission probability. The emission probability as a function of the square of the Rabi frequency in resonant excitation shows an oscillating behaviour commonly known as the Rabi oscillations.

The system studied in [31] showed measured lifetimes of $\tau_{xx} = 1/\gamma_{xx} = 405$ ps for the biexciton and $\tau_x = 1/\gamma_x = 771$ ps for the exciton. The coherence lengths of the emitted photons were measured to be $\tau_{dxx} = 1/\gamma_{dxx} = 211$ ps for the biexciton photon and $\tau_{dx} = 1/\gamma_{dx} = 119$ ps for the exciton photon while the excitation pulse was measured to be 4 ps long. The theoretical prediction calculated for these parameters is given in Fig. 11.3a as the dot-dashed curve, which indicates a very high emission probability at the adequate excitation strength. Such a result is not surprising because the excitation pulse length is much shorter than the dephasing mechanisms that were elaborated above. The source of lower than unity emission probability in this model can be attributed to the proximity of the two-photon virtual level to the exciton level ($\Delta_x = 2\pi$ 335 GHz). Therefore, one can expect that in the absence of additional sources of dephasing such a photon source would create photon pairs on demand.

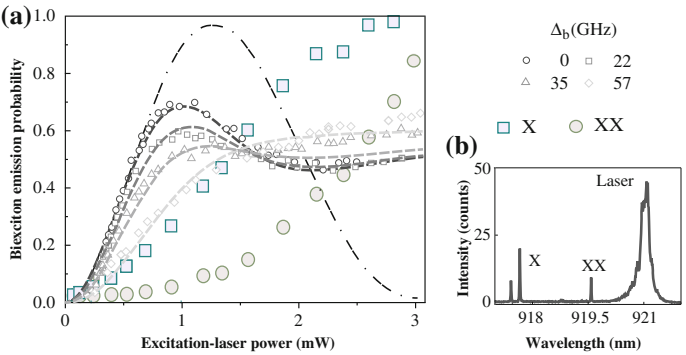

Fig. 11.3 **a** Rabi oscillations of the biexciton. The emission probability was measured for various excitation laser detunings Δ_{xx} from the two-photon resonance. The empty symbols represent the results of these measurements, *circles*, *squares*, *triangles*, and *diamonds* for $\{0, 22, 35, 57\}$ GHz detuning, respectively. *Dashed lines* are simulations employing the theoretical model described in [31]. This model includes additional dephasing processes that are not contained in the four Lindblad operator model described in this text. The model presented here results in the curve that is given as the *dot-dashed line*. The filled symbols stand for data obtained in power dependence measurement of biexciton and exciton photons under incoherent two-photon excitation that was performed using a laser detuned towards lower energy (*red-detuned*) for few nanometers from the two-photon virtual resonance. **b** Photo-luminescence signal obtained in this incoherent excitation regime

Nonetheless, the experimental results shown in both [27, 31] show stronger dephasing of the Rabi oscillations. In [27] this result was attributed to a chirp of the excitation pulse although authors did not exclude the existence of additional sources of dephasing. The findings given in [31] suggest the existence of an underlying incoherent process that dephases the excitation process. In particular, in [31] it was shown that the photo-luminescence signal can be observed even when the quantum dot was addressed using a laser of an energy lower than the biexciton transition, Fig. 11.3b. The power dependence measured under these conditions showed that the exciton photo-luminescence signal increases quadratically with power, while the biexciton signal grows with fourth power. The data obtained in these measurements are shown as full coloured symbols in Fig. 11.3a. While a two-photon process in the surrounding material (GaAs is highly nonlinear) that creates carriers in the vicinity of the quantum dot is possible, such a process would not cause the damping of the Rabi oscillation but rather a background in the photo-luminescence signal. On the other hand a process such as two-photon excitation from the ground state to the continuum would dephase the excitation process.

11.3 Measurements Under Resonant Excitation

Here, we will briefly review several results that were obtained using resonantly excited quantum dots. In particular we will address the topics of the coherent manipulation of the ground-excited state superposition, photon statistics of a resonantly excited quantum dot, and the generation of time-bin entangled photon pairs.

11.3.1 Coherent Control

The coherence of the excitation process allows for the phase of the ground-biexciton state superposition to be coherently manipulated. The traditional way to characterize such a process is to perform a Ramsey interference measurement. To do so, one needs to excite the investigated system using a sequence of two consecutive $\pi/2$ pulses, Fig. 11.4a. The first of these pulses brings the state in an equal superposition of the ground and the biexciton state. Upon this pulse, one lets the system to evolve freely for a time defined by the variable delay between the pulses, Fig. 11.4a. During this free evolution the excitation pseudo-spin is expected to precess along the equator of the Bloch sphere. The second pulse will map the population either back to the ground state or flip it further to the biexciton state, depending on the evolution of the pseudo-spin and the relative phase between the two pulses. A very thorough review of the coherent manipulation of excitons and spins in quantum dot systems is given in [39].

When such an experiment is performed in two-photon excitation it results in Ramsey interference fringes in both the exciton and the biexciton emission [32]. It is important to note here that in the case of the biexiton emission these fringes are a direct result of the laser driving the transition. The interference observed in exciton channel closely follows the behaviour of the biexciton but comes as a consequence of the cascade decay of the system.[4] An example of a decay of the Ramsey visibility fringes is shown in Fig. 11.4c. Due to their lifetime quantum dots are usually excited using laser pulses that are not longer than few picoseconds. Therefore the simplest way to obtain the sequence of Ramsey pulses is by feeding pulsed laser light into a variable-length Michelson interferometer.

Decoherence caused by low frequency noise can be eliminated by applying a refocusing pulse. Such a measurement is commonly called spin echo and requires a sequence of three consecutive pulses of different intensities ($\pi/2, \pi, \pi/2$), illustrated in Fig. 11.4b. Concerning the spin echo measurements, they are straightforward to implement in systems that have long lifetimes and coherence lengths. For example, for a trapped ions system where the coherences are of the order of a milisecond one can use light derived from a cw laser and create the pulse

[4]Note that the Ramsey interference measurement characterizes the coherence of the ground-biexciton state superposition and that by varying the delay between the two Ramsey pulses one can measure the coherence decay of this pseudo spin.

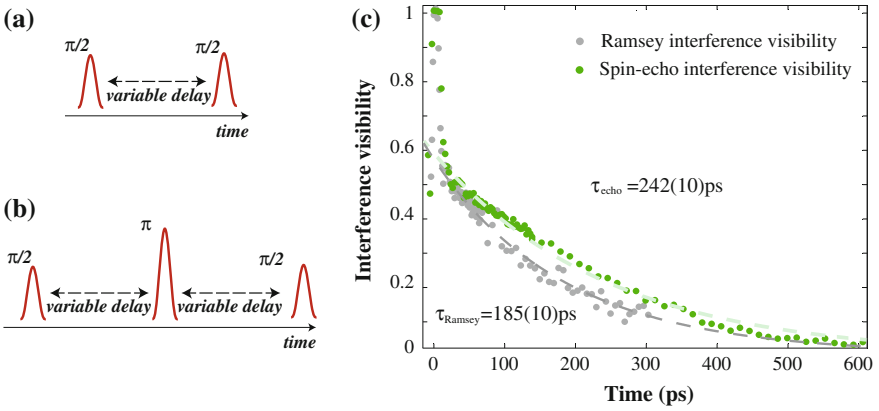

Fig. 11.4 **a** Pulse sequence consisting of two $\pi/2$ pulses applied with variable delay. **b** The spin-echo pulse sequence. **c** Ramsey interference visibility decay experiment monitored with the biexciton photons is shown in *gray*. The data shown in *green* were taken in a spin-echo measurement performed on the same emitter

sequence using an acousto-optical modulator. Unfortunately, and as mentioned before, the pulse lengths needed to drive a spin-echo sequence on a pseudo-spin of a ground-biexciton state superposition of a quantum dot are on the order of few picoseconds. In [31] it was shown that the echo sequence with such pulses can be made by using a Michelson interferometer in double-pass configuration. Such an implementation is capable of delivering the three consecutive pulses necessary for the spin-echo sequence with the middle pulse being a result of the interference between the light passing once through the interferometer with the light passing twice. In Fig. 11.4c are shown two sets of data, one taken in a Ramsey and the other in spin-echo experiment. We observe an increase in the visibility decay from $\tau_{Ramsey} = 185(10)$ ps to $\tau_{echo} = 242(10)$ ps. The measured values indicate the presence of high frequency noise, which could not be refocused by the spin echo technique. On the other hand, the technique itself is limited by the strong incoherent process that happens during the excitation and that is, as mentioned before, also responsible for the dephasing of the Rabi oscillations.

11.3.2 Photon Statistics Under Resonant Excitation

The statistics of the photons emitted by semiconductor quantum dots shows an intrinsically sub-Poissonian distribution [8]. Individual emitters are commonly characterized by a measurement of the autocorrelation [40] parameter (very often also called the $g^{(2)}(0)$ measurement). The choice of this particular method is historically rooted. The use of autocorrelation measurements on quantum dots can be traced back to the first experiments that were capable to address a single quantum dot and where the

main experimental task was to isolate a single emitter from an ensemble of quantum dots. In such an experiment the observation of an autocorrelation parameter lower than 0.5 was a clear confirmation that the observed system was a single emitter. While the autocorrelation is quite easy to implement experimentally from a certain perspective it is a limited resource. Namely, it is an efficiency insensitive measurement that alone cannot deliver the absolute values for the photon generation probabilities p_1 or p_{2+} (probability for a single photon and multiple photons, respectively). On the other hand, and in the limit of the low source efficiency, the autocorrelation parameter can be approximated as $2p_{2+}/(p_1 + 2p_{2+})^2$, [41].

Today the problem of addressing a single isolated quantum dot can be considered no longer challenging and the attention is redirected to the increase of the collection efficiency and reduction of the multi-photon component. The latter, in the case of quantum dots, can be reduced to the problem of multiple excitations. As mentioned before, the traditional way to excite quantum dots is above-band excitation. Apart from a lack of coherence in driving the quantum dot system this excitation method also gives probabilistic statistics for the photon generation and can induce effects that increase the multi-photon component in the statistics of the emitted light like carrier re-capture [30]. The latter is well illustrated in Fig. 11.5. The autocorrelation measurement given in Fig. 11.5a was made on resonantly excited quantum dot, and the autocorrelation parameter extracted from the data reads 0.0315(2). On the other hand, the same quantum dot excited in above-band excitation will show much higher multi-photon component, shown in Fig. 11.5b. Here the autocorrelation parameter reads 0.282(1).

An autocorrelation measurement is not sufficient to recognize the efficiency of the emitter nor the relation between the efficiency and the multi-photon component of the emission. Nevertheless, there are a number of measurements that one can perform and obtain these numbers including [41, 43–45]. Concerning the efficiency alone,

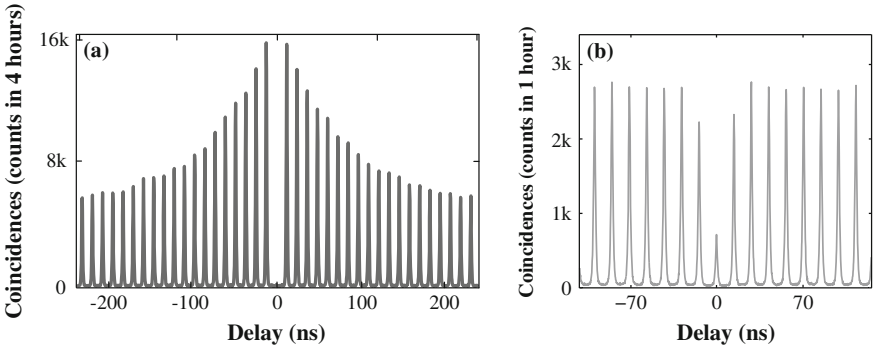

Fig. 11.5 **a** The exciton signal shows excellent suppression of multi-photon events, which can be quantitatively expressed by intensity autocorrelation parameter of 0.0315(2). The plotted data is presented without background subtraction. The decaying peak height observable on both sides of the graph results from the blinking of the quantum dot [42]. **b** The same quantum dot will show far larger probability of multiple excitations when excited above-band

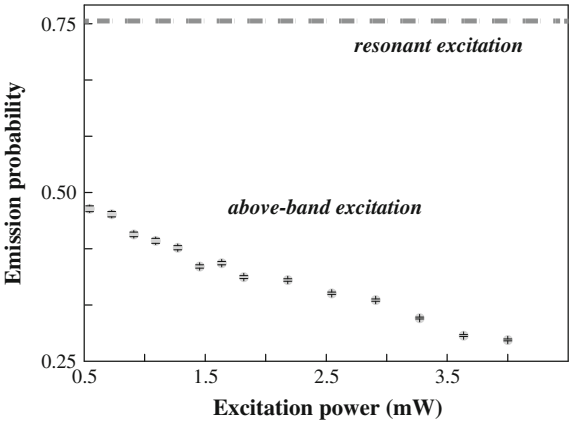

Fig. 11.6 Here, the *dashed line* marks the maximum emission probability of an biexciton-exciton photon pair obtained under two-photon resonant excitation. The *gray circles* show the same probability under above-band excitation. For the latter measurement the excitation power up was gradually increased up to the level where the biexciton saturates (4 mW)

the resonant excitation will always give better numbers, as illustrated in Fig. 11.6. The saturation of the biexciton level in above-band excitation demands large concentration of carriers in the quantum dot surrounding. This implies a large probability that after the biexction photon has been emitted the system never reached the ground state but rather immediately captured another electron-hole pair.

11.3.3 Time-Bin Entanglement

The idea to generate time-bin entanglement of photons emitted by a single quantum emitter can be traced back to a seminal paper by Franson [46]. He suggested that the interference between the probability amplitudes for a photon pair to be emitted by an excited atom at diverse times is a nonlocal effect that violates the Bell inequality. The system described by Franson consists of an atom in an excited state that decays to the ground state via emission of a photon cascade (pair of photons), Fig. 11.7a. The necessary condition given in this proposal is that the atom has a very long-living initial state. Additionally, the intermediate excited state needs to be very short-lived so that the second photon of the cascade is emitted immediately after the first photon. The interference is observed in coincidence events and its detections employs two unbalanced interferometers, one for the each photon of the cascade, Fig. 11.7b. The imbalance of the interferometers is supposed to be longer than the coherence length of the emitted photons otherwise the oscillations in the detected signal come from the beat of the field function.

The first implementations of Franson's scheme were elaborated using spontaneous parametric down-conversion [47, 48]. These experiments used a narrowband continuous wave laser to produce a pair of photons highly correlated in frequency and sent them down a pair of unbalanced interferometers. Here, the role of the long-lived excited state is played by a highly coherent monochromatic laser. These experiments

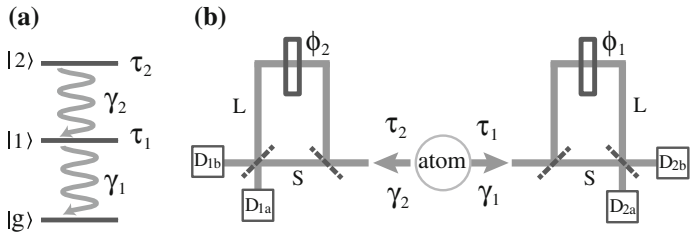

Fig. 11.7 **a** Three-level atomic system with a long lifetime τ_2 for the initial state and a much shorter lifetime τ_1 for the intermediate state. The decay rates are denoted γ_2 and γ_1, respectively. **b** The state-analysis interferometers with the short (S) and long (L) path. In the absence of the interferometers (or interferometer beamsplitters) the coincidence measurement between the D_1 and D_2 detectors would show a very narrow peak of width τ_1. Nevertheless, the uncertainty for the photons to be emitted was initially much longer (τ_2) and therefore the associated wave packet must have had large time and position uncertainty. The detection of one of the photons has as an effect a nonlocal change in the wavefunction describing the other photon. By varying the relative phase between the interferometers ($\phi_2 - \phi_1$) one can observe the visibility contrast and therefore measure the entanglement

were very challenging and suffered from several technological shortcomings such as poor detector resolution. Nevertheless, once these difficulties were overcome, such a type of an experiment showed violation of the Bell inequality [49].

The experiments using narrowband continuous wave lasers were producing photons that were time-energy entangled. In 1999, Brendel et al. [50] introduced a scheme that employs femtosecond-laser pumped parametric down-conversion. Such a scheme is commonly denoted as time-bin entanglement. Here, instead of continuous wave long-coherence laser, one uses a pulsed laser of short coherence. The light derived from such a laser is sent into an unbalanced interferometer. Each laser pulse gives two pulses at the exit of the interferometer, so-called early and late pulse. These are directed onto the system one wants to excite and if the excitation probability is kept low the system will on average be excited by only the early or only the late pulse. The state analysis is performed in a similar manner as proposed by Franson.[5]

Therefore, time-bin entanglement encodes quantum states in superposition of the system's excitation within two distinct time-bins: early and late. The importance of this type of encoding lies in optical-fibre based quantum communication [52, 53], due to the degradation that polarization entanglement can suffer in an optical fibre outside laboratory conditions [54]. The issue behind the degradation of the polarization entanglement in optical fibres is polarization mode dispersion. It is a problem well known in telecommunication technologies that limits the rate of the information transfer. The physical origin of this effect is that even single mode fibres have two well-defined and differentiated polarization modes that in absence

[5] At this point, it becomes obvious that the coherence properties of the pump laser have a very important role in the generation of the entanglement. An intermediate regime of a continuous wave short coherence pump laser was investigated in [51]. They showed that the short coherence of the pump laser limits the visibility contrast to 50 % .

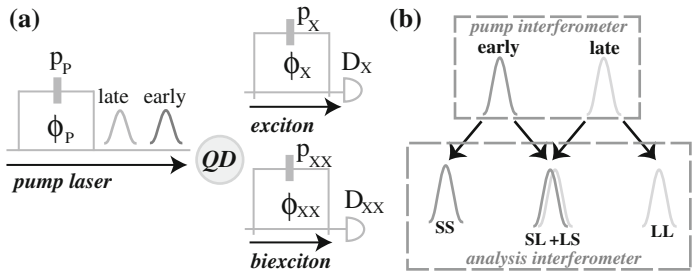

Fig. 11.8 **a** Schematic of time-bin entanglement. The quantum dot (QD) is excited by two consecutive pulses derived from an unbalanced Michelson interferometer shown on the left. The interferometric phase between these pulses is ϕ_P. The state analysis is performed using another two unbalanced interferometers, one for exciton and other for biexciton photons. These two interferometers have their respective phases, ϕ_X and ϕ_{XX}. The photons are detected upon leaving the analysis interferometers using detectors D_X and D_{XX}. The phases of the individual interferometers are controlled using phase plates, p_P, p_X and p_{XX}. **b** A photons pair created by an early pulse but later in analysis travelled the long paths of the analysis interferometers is in its arrival time indistinguishable to a photon pair created in a late pulse that in analysis travelled the short paths

of a controlled environment will couple randomly. In addition to being insensitive to polarization mode dispersion and therefore preferred for a fiber optics long distance communication protocols this type of entanglement can also be employed in quantum computing. Recently, a method was demonstrated to perform linear optical quantum computing using photons entangled in time bin [55].

In its simplest scheme, time-bin entanglement is generated in a very similar manner for both parametric down-conversion [50] and atom-like systems [56] and it demands post-selection in order to be measured. Such a scheme[6] is depicted in Fig. 11.8a. The system is addressed by two excitation pulses, denoted the early and the late pulse. These are derived from an unbalanced interferometer, so-called pump interferometer. The interferometric phase, ϕ_P, between the pulses determines the phase of the entangled state. The analysis of the generated state is performed using two identically-constructed unbalanced interferometers, one for exciton and one for biexciton photons. The entangled state reads

$$|\Phi\rangle = \frac{1}{\sqrt{2}}(|\text{early}\rangle_{XX}|\text{early}\rangle_X + e^{i\phi_P}|\text{late}\rangle_{XX}|\text{late}\rangle_X), \tag{11.8}$$

where ϕ_P is the phase of the pump interferometer and $|\text{early}\rangle$ ($|\text{late}\rangle$) denote photons generated in an early (late) time-bin. The method to write the phase, ϕ_P, onto the system differs between parametric down-conversion and atom-like systems. In particular, quantum dots demand resonant excitation in order to bring the system from the ground to the excited state coherently, while in the process of parametric

[6] A quantum dot system can also give time-energy entangled photon pairs, nevertheless it needs independent control over the lifetimes of the involved energy levels [57].

down-conversion the phase matching process itself ensures that the pump laser and the down-converted fields maintain constant phase relation.

There are two types of factors limiting the degree of time-bin entanglement obtainable from an atom-like system: those associated with excitation and those associated with the intrinsic system coherence. The first type includes the so-called double excitations. In particular, if the entanglement measurement was performed with excitation probability p_1, it will happen in ${p_1}^2$ cases that the system is excited by both the early and the late pulse. These events are observable in time basis[7] being less than unity, and are as well present as incoherent background in both energy bases.[8] The effect of double excitations can be eliminated through use of deterministic schemes for generation of time-bin entanglement [58–60].

The time basis measurements are not affected by the decoherence-induced reduction of the visibility contrast; in contrary the energy bases measurements are. An intuitive picture of how the decoherence affects the time-bin entanglement is the following: the pump interferometer phase, ϕ_P, is transferred onto the quantum dot by means of resonant excitation. Any incoherence in the process of resonant excitation as well as in relation between the ground and the biexciton state will have as a consequence an averaging of the transferred phase, and thus of the phase of the entangled state. This will reduce the visibility contrast as well as decrease the values of entanglement measures and indicators like concurrence and fidelity.

The entanglement analysis involves the two interferometers depicted in Fig. 11.8a (one per qubit) and is a method that includes post selection. The post-selection procedure is schematically plotted in Fig. 11.8b. Namely, the emission time of photons contains the information on which pulse has created the photon pair and the analysis interferometers can partially erase this information. In particular, a photons pair that was created by an early pulse and in analysis travelled the long paths of the interferometers is in its arrival time indistinguishable to a photon pair that was created in a late pulse and in analysis travelled the short paths. If the detectors and the analysis electronics are fast enough to isolate these indistinguishable events the entanglement can be measured.

A very complete method to characterize the entanglement is state tomography [29, 61]. Figure 11.9 shows an example of a reconstructed density matrix. The fidelity of this particular matrix with the maximally entangled state was found to be F = 0.78(3) while the tangle and concurrence are T = 0.31(9) and C = 0.56(7).

In addition, the measurement shown in Fig. 11.9 also gave the visibilities in three orthogonal bases of 92(2) %, 52(3) %, and 57(3) % for E/L, $E + L/E - L$, and $E + iL/E - iL$, respectively. It is worth mentioning that among the measurements that can indicate entanglement the visibility is the simplest and probably the oldest. This particular measurement was forming the central part of the original Franson's proposal [46] and also was the method used in the first measurements of the time-energy entanglement [47, 48]. It is observed in coincidental events. Figure 11.10 shows the diagram of arrival times of the two photons in a time-bin measurement and

[7] early/late(E/L).

[8] $E + L/E - L$ and $E + iL/E - iL$.

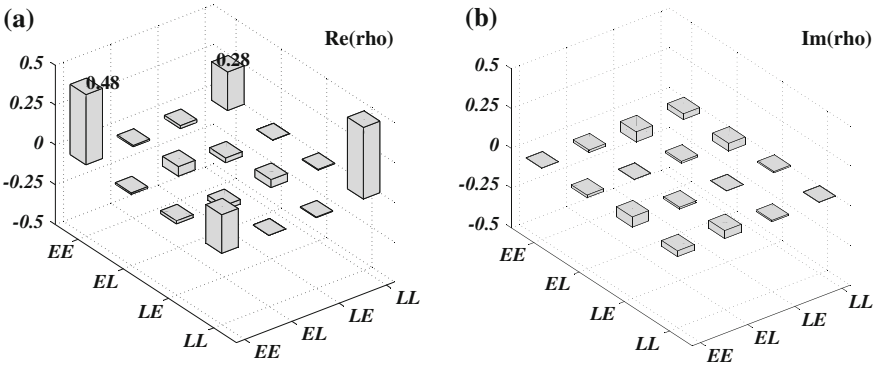

Fig. 11.9 An example of a **a** real and **b** imaginary part of the reconstructed density matrix. Measurements used to obtain this density matrix were performed using 4 ps long excitation pulses while the excitation probability was kept at 6 %

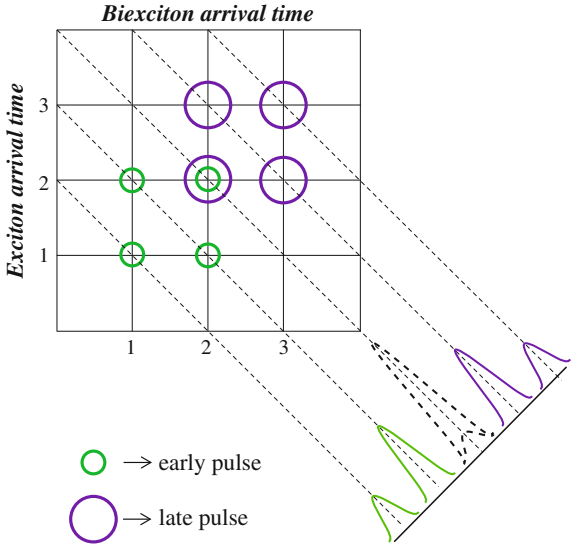

Fig. 11.10 Time-bin entanglement is observed in the coincidence events. The plot depicts the arrival times of the individual photons and how these are forming the coincidence counts. The *green* circles stand for arrival times of the photons produced by an early pulse while the *violet circles* stand for arrival times of the photons produced by a late pulse. Interference of the probability amplitudes is observed at the point of overlap. The diagonal projection shows a coincidence pattern. The existence/absence of the central peak, plotted in *black*, shows the coincidence correlation/anti-correlation

the corresponding coincidence peaks. The central peak comes from the interference of the probability amplitudes. If the system is driven with too high excitation probability it leads to increase in number of events where both the early and the late pulse

have generated an excitation. It is clear from this plot that such events will form a background under the central coincidence peak that reduces the maximum achievable visibility.

11.4 Future Directions

Quantum dots are systems that show great potential. They are compact and integrable in solid state devices. When driven resonantly their atom-like nature allows for high photon generation probability complemented with low probability for multiple excitations. With respect to on-demand generation of photon pairs, the two-photon resonant excitation is a very promising method.

On the other hand, our knowledge on the origin and the nature of decoherence processes in quantum dots is still scarce. The ability to excite the quantum dot resonantly, to coherently manipulate the ground-excited state superposition, and/or to generate time-bin entanglement open up a possibility to use these measurement to further study and characterize the origins of decoherence.

One topic that was not addressed within this chapter is the extraction efficiency. Namely, the extraction efficiency in samples with planar micro-cavities is higher than in the dots without any additional structure but is still limited to about 5 % in best cases. Using etched micro-pillar cavities dramatically increases the collection efficiency. The two-photon resonant excitation can readily be applied to these devices too. We expect the benefits to be multi-fold, ranging from the increased collection efficiency to Purcell enhancement of the emission and therefore a emission of a shorter and less decohered wave-packet. Such an approach would allow for having a photon source capable of fulfilling the high requirements set by quantum information science protocols and schemes.

Acknowledgments I would like to express my gratitude to all my colleagues and collaborators, that over last couple of years, have taken part in the experiments conducted at the University of Innsbruck. Writing of this review was supported by the Austrian Science Fund (V-375). This review in part presents the results of research that was financially supported by Austrian Science Fund (M-1243 and V-375) and University of Innsbruck.

References

1. H.-J. Briegel, W. Dür, J.I. Cirac, P. Zoller, Quantum repeaters: the role of imperfect local operations in quantum communication. Phys. Rev. Lett. **81**, 5932–5935 (1998)
2. L.-M. Duan, M.D. Lukin, J.I. Cirac, P. Zoller, Long-distance quantum communication with atomic ensembles and linear optics. Nature **414**, 413–418 (2001)
3. H.J. Kimble, The quantum internet. Nature **453**, 1023–1030 (2008)
4. C. Simon, W.T.M. Irvine, Robust long-distance entanglement and a loophole-free test with ions and photons. Phys. Rev. Lett. **91**, 110405 (2003)

5. E. Knill, R. Laflamme, G. Milburn, A scheme for eficient quantum computation with linear optics. Nature **409**, 46–52 (2001)
6. D. Bouwmeester et al., Experimental quantum teleportation. Nature **390**, 575 (1997)
7. M. Zukowski, A. Zeilinger, M.A. Horne, A.K. Ekert, "Event-ready-detectors" Bell experiment via entanglement swapping. Phys. Rev. Lett. **71**, 4287 (1993)
8. P. Michler et al., A quantum dot single-photon turnstile device. Science **290**, 2282–2285 (2000)
9. P. Kok et al., Linear optical quantum computing with photonic qubits. Rev. Modern Phys. **79**, 135 (2007)
10. M. Varnava, D. Browne, T. Rudolph, How good must single photon sources and detectors be for efficient linear optical quantum computation? Phys. Rev. Lett. **100**, 060502 (2008)
11. T. Jennewein, M. Barbieri, A. White, Single-photon device requirements for operating linear optics quantum computing outside the post-selection basis. J. Modern Opt. **58**, 276–287 (2011)
12. N. Sangouard et al., Long-distance entanglement distribution with single-photon sources. Phys. Rev. A **76**, 050301 (2007)
13. N. Lütkenhaus, Security against individual attacks for realistic quantum key distribution. Phys. Rev. A **61**, 052304 (2000)
14. O. Benson, C. Santori, M. Pelton, Y. Yamamoto, Regulated and entangled photons from a single quantum dot. Phys. Rev. Lett. **84**, 2513 (2000)
15. R. Stevenson et al., Evolution of entanglement between distinguishable light states. Phys. Rev. Lett. **101**, 170501 (2008)
16. R.Y. Young et al., Improved fidelity of triggered entangled photons from single quantum dots. New J. Phys. **8**, 28 (2006)
17. N. Akopian et al., Entangled photon pairs from semiconductor quantum dots. Phys. Rev. Lett. **96**, 130501 (2006)
18. A. Muller, W. Fang, J. Lawall, G. Solomon, Creating polarization-entangled photon pairs from a semiconductor quantum dot using the optical Stark effect. Phys. Rev. Lett. **103**, 217402 (2009)
19. A. Dousse et al., Ultrabright source of entangled photon pairs. Nature **466**, 217–220 (2010)
20. M. Ghali, K. Ohtani, Y. Ohno, H. Ohno, Generation and control of polarization-entangled photons from GaAs island quantum dots by an electric field. Nat. Commun. **3**, 661 (2012)
21. R.M. Stevenson et al., Magnetic-field-induced reduction of the exciton polarization splitting in InAs quantum dots. Phys. Rev. B **73**, 033306 (2006)
22. R. Trotta, J.S. Wildmann, E. Zallo, O.G. Schmidt, A. Rastelli, Highly entangled photons from hybrid piezoelectric-semiconductor quantum dot devices. Nano Lett. **14**, 3439–3444 (2014)
23. T. Kuroda et al., Symmetric quantum dots as efficient sources of highly entangled photons: Violation of Bell's inequality without spectral and temporal filtering. Phys. Rev. B **88**, 041306 (2013)
24. G. Juska, V. Dimastrodonato, L.O. Mereni, A. Gocalinska, E. Pelucchi, Towards quantum-dot arrays of entangled photon emitters. Nat. Photon. **7**, 527–531 (2013)
25. T. Huber et al., Polarization entangled photons from quantum dots embedded in nanowires. Nano Lett. **14**, 7107–7114 (2014)
26. R. Singh, G. Bester, Nanowire quantum dots as an ideal source of entangled photon pairs. Phys. Rev. Lett. **103**, 063601 (2009)
27. M. Müller, S. Bounouar, K.D. Jons, M. Glassl, P. Michler, On-demand generation of indistinguishable polarization-entangled photon pairs. Nat. Photon. **8**, 224–228 (2014)
28. O. Gühne, G. Tóth, Entanglement detection. Phys. Rep. **474**, 1–75 (2004)
29. D.F.V. James, P.G. Kwiat, W.J. Munro, A.G. White, Measurement of qubits. Phys. Rev. A **64**, 052312 (2001)
30. E. Peter et al., Fast radiative quantum dots: from single to multiple photon emission. Appl. Phys. Lett. **90**, 223118 (2007)
31. H. Jayakumar et al., Deterministic photon pairs and coherent optical control of a single quantum dot. Phys. Rev. Lett. **110**, 135505 (2013)
32. T. Flissikowski, A. Betke, I.A. Akimov, F. Henneberger, Two-photon coherent control of a single quantum dot. Phys. Rev. Lett. **92**, 227401 (2004)

33. S. Stufler et al., Two-photon rabi oscillations in a single $In_xGa_{1-x}As/GaAs$ quantum dot. Phys. Rev. B **73**, 125304 (2006)
34. A.N. Vamivakas, Y. Zhao, C.-Y. Lu, M. Atature, Spin-resolved quantum-dot resonance fluorescence. Nat. Phys. **5**, 19872 (2009)
35. A. Muller et al., Resonance fluorescence from a coherently driven semiconductor quantum dot in a cavity. Phys. Rev. Lett. **99**, 187402 (2007)
36. H. Carmichael, *An Open Systems Approach to Quantum Optics* (Springer, 1993)
37. C. Gardiner, P. Zoller, *Quantum Information with Continuous Variables* (Springer, 2004)
38. C. Santori, D. Fattal, J. Vučkovič, G.S. Solomon, Y. Yamamoto, Indistinguishable photons from a single-photon device. Nature **419**, 594–597 (2002)
39. A.J. Ramsay, A review of the coherent optical control of the exciton and spin states of semiconductor quantum dots. Semicond. Sci. Technol. **25**, 103001 (2010)
40. P. Grangier, G. Roger, A. Aspect, Experimental evidence for a photon anticorrelation effect on a beam splitter: a new light on single-photon interferences. Europhys. Lett. **1**, 173–179 (1986)
41. A. Predojević et al., Efficiency vs. multi-photon contribution test for quantum dots. Opt. Express **22**, 4789 (2014)
42. C. Santori et al., Submicrosecond correlations in photoluminescence from InAs quantum dots. Phys. Rev. B **69**, 205324 (2004)
43. I. Straka et al., Quantum non-Gaussian depth of single-photon states. Phys. Rev. Lett. **113**, 223603 (2014)
44. R. Filip, L. Mišta, Detecting quantum states with a positive Wigner function beyond mixtures of Gaussian states. Phys. Rev. Lett. **106**, 200401 (2011)
45. M. Ježek et al., Experimental test of the quantum non-Gaussian character of a heralded single-photon state. Phys. Rev. Lett. **107**, 213602 (2011)
46. J.D. Franson, Bell inequality for position and time. Phys. Rev. Lett. **62**, 2205–2208 (1989)
47. Z.Y. Ou, X.Y. Zou, L.J. Wang, L. Mandel, Observation of nonlocal interference in separated photon channels. Phys. Rev. Lett. **65**, 321–324 (1990)
48. P.G. Kwiat, W.A. Vareka, C.K. Hong, H. Nathel, R.Y. Chiao, Correlated two-photon interference in a dual-beam Michelson interferometer. Phys. Rev. A **41**, 2910–2913 (1990)
49. P.G. Kwiat, A.M. Steinberg, R.Y. Chiao, High-visibility interference in a Bell-inequality experiment for energy and time. Phys. Rev. A **47**, R2472–R2475 (1993)
50. J. Brendel, N. Gisin, W. Tittel, H. Zbinden, Pulsed energy-time entangled twin-photon source for quantum communication. Phys. Rev. Lett. **82**, 2594–2597 (1999)
51. J. Liang, S.M. Hendrickson, T.B. Pittman, Role of pump coherence in two-photon interferometry. Phys. Rev. A **83**, 033812 (2011)
52. T. Honjo et al., Long-distance distribution of time-bin entangled photon pairs over 100 km using frequency up-conversion detectors. Opt. Express **15**, 13957–64 (2007)
53. J.F. Dynes et al., Efficient entanglement distribution over 200 kilometers. Opt. Express **17**, 11440–11449 (2009)
54. M. Brodsky, E. George, C. Antonelli, M. Shtaif, Loss of polarization entanglement in a fiber-optic system with polarization mode dispersion in one optical path. Opt. Express **36**, 43–45 (2011)
55. P.C. Humphreys et al., Linear optical quantum computing in a single spatial mode. Phys. Rev. Lett. **111**, 150501 (2013)
56. H. Jayakumar et al., Time-bin entangled photons from a quantum dot. Nat. Commun. **5**, 4251 (2014)
57. T. Huber et al., Measurement and modification of biexciton-exciton time correlations. Opt. Express **21**, 9890–9898 (2013)
58. C. Simon, J.-P. Poizat, Creating single time-bin-entangled photon pairs. Phys. Rev. Lett. **94**, 030502 (2005)
59. P.K. Pathak, S. Hughes, Coherent generation of time-bin entangled photon pairs using the biexciton cascade and cavity-assisted piecewise adiabatic passage. Phys. Rev. B **83**, 245301 (2011)

60. P.B.R. Nisbet-Jones, J. Dilley, D. Ljunggren, A. Kuhn, Highly efficient source for indistinguishable single photons of controlled shape. New J. Phys. **13**, 103036 (2013)
61. H. Takesue, Y. Noguchi, Implementation of quantum statetomography for time-bin entangled photon pairs. Opt. Express **17**, 10976–10989 (2009)

Part VI
Distinguishability of Photons

Chapter 12
Generation and Application of Frequency-Uncorrelated Photon Pairs

Tian-Ming Zhao, Xiao-Hui Bao, Bo Zhao and Jian-Wei Pan

Abstract Frequency-uncorrelated photon sources are rather important for quantum information science. They are not only suitable for storage in quantum memories, but also very useful for scalable linear optical quantum computing. In this chapter, we review preparations and applications of frequency-uncorrelated photon pairs. We first introduce the elimination of spectral correlation for the spontaneous parametric down-conversion (SPDC) sources by using the technique of group velocity mismatching. Next we make emphasis on discussing how to eliminate the frequency correlation for narrowband photons created from cavity-enhanced SPDC by pulse engineering. Finally we discuss applications of using the frequency uncorrelation technology to interfere independent photon sources.

12.1 Introduction

Quantum repeaters [1] and quantum networks [2] are developed to realize long distance quantum communication [3] and large scale quantum computation [4]. They are both based on interference between independent sources [5]. In addition, quantum interference plays an important role in quantum teleportation [6] and study of quantum nonlocality.

Generally, in linear optical quantum computation (LOQC) [7] we use beam splitters to implement quantum interference. When two identical photons are superimposed on a beam splitter, the probabilities that both photons are transmitted or both

T.-M. Zhao · X.-H. Bao (✉) · B. Zhao · J.-W. Pan
Hefei National Laboratory for Physical Sciences at Microscale,
Department of Modern Physics, Anhui, China
e-mail: xhbao@ustc.edu.cn

T.-M. Zhao
e-mail: timmizhao@gmail.com

B. Zhao
e-mail: bozhao@ustc.edu.cn

J.-W. Pan
e-mail: pan@ustc.edu.cn

A. Predojević and M.W. Mitchell (eds.), *Engineering the Atom-Photon Interaction*,
Nano-Optics and Nanophotonics, DOI 10.1007/978-3-319-19231-4_12

are reflected interfere with each other and result in two-photon coalescence. Such a two-photon interference effect was first observed by Hong, Ou, and Mandel [8]. From a more fundamental point of view, this interference is due to the bosonic nature of photons [9]. Two photons must have a global wave function that is symmetric under particle exchange. If the photons are identical in all other degrees of freedom, e.g. in frequency and polarization, then their spatial wave-functions must be symmetric, which leads to photon coalescence upon meeting at a beam splitter. In contrast, photons that are antisymmetric in their other degrees of freedom must be spatially anti-symmetric. This spatial anti-symmetry requires that the photons leave by different output ports of the beam splitter. This effect provides a physical basis for both detecting the anti-symmetric Bell state and entanglement of independent photons. This interference effect is efficient only if the two participating photons are in identical pure states. The impurity of the photons will inevitably result in low visibility. So it is essential to guarantee the purity and indistinguishability of the incoming photons.

Single-photon pure state can be expressed as

$$|1\rangle = \int d\omega \psi(\omega) \hat{a}^{+}(\omega)|0\rangle, \tag{12.1}$$

where $\hat{a}^{+}(\omega)$ is the creation operator for photons at angular frequency ω, and $\psi(\omega)$ determines the modal structure of the photon. The corresponding density operator is given by

$$\hat{\rho}_1 = |1\rangle\langle 1| \tag{12.2}$$

Currently single-photon states are created by atoms, quantum dots and other solid state systems. Besides, spontaneous parametric down-conversion (SPDC) [6, 10] is also widely used for conditional preparation of single photons. In SPDC, when a pump photon passes through a nonlinear crystal, with a small probability, it converts into a pair of photons called "signal photon" and "idler photon". We denote the frequencies of the pump, signal, and idler photons as ω_p, ω_s and ω_i, respectively. Because of energy conservation, signal and idler are correlated in frequency and satisfy the condition $\omega_p = \omega_s + \omega_i$. This frequency correlation will hinder the preparation of single photon pure states: because ω_i carries information about ω_s, the broadband detection of an idler photon heralds the presence of a signal photon, with a mixture of different frequencies. When heralded photons from different SPDC sources are interfered, the frequency correlation undermines the indistinguishability between photons involved in interference and reduces the interference visibility. The spectral correlation between photons can make them practically useless for scalable LOQC.

A trivial approach to erase the distinguishability due to the frequency correlation is to use tight spectral filtering to post-select indistinguishable events. However, this reduces the source count rate and make it useless. Fortunately, there are many effective ways to eliminate the frequency correlation between down conversion

photons without loss of photon count rate. Grice et al. [11] proposed that the frequency correlation could be eliminated through proper choice of crystal length and pump bandwidth to satisfy the group velocity mismatching condition between pump, signal and idler. Thereafter many efforts have been made on realizing and modifying group velocity mismatching method [12–14]. Besides, special crystal sequence has been proposed to overcome the limit of wavelength in the previous methods [15]. This crystal sequence is composed of a sequence of nonlinear crystals interspersed with birefringent spacers. By choosing proper thickness of crystals, in principle, the group velocity mismatching can be met at arbitrary wavelength. Another way to break through the wavelength limitation is to generate photon pairs by pulse-pumped cavity enhanced SPDC [16, 17]. Frequency correlation is removed when the pulse length is shorter than the coherence time of down-converted photons. Besides, tunable control of the frequency correlations of entangled photons by employing tilted pulses has been put forward [18, 19]. Recently, flexible control of frequency correlation of biphotons from cold atoms has been demonstrated by manipulating the dispersive property of the cold atomic ensemble, hence, controlling the group velocities [20].

In this chapter, firstly, we introduce how to eliminate the spectral correlation of SPDC photons through group velocity mismatching. Next we make emphasis on discussing how to eliminate the frequency correlation of narrowband photons created from pulse-pumped cavity-enhanced SPDC. Finally, we introduce the applications of frequency uncorrelated photon pairs.

12.2 Single Photon Wavepacket Generation by SPDC

The two-photon state generated by SPDC is described as

$$|\Psi\rangle = |0\rangle + \int d\omega_s d\omega_i f(\omega_s, \omega_i)\hat{a}_s^\dagger(\omega_s)\hat{a}_i^\dagger(\omega_i)|0\rangle, \tag{12.3}$$

where $\hat{a}_s^\dagger(\omega_s)$ and $\hat{a}_i^\dagger(\omega_i)$ are the creation operators for photons at frequencies ω_s and ω_i, respectively. These operators act on the vacuum state to generate a pair of photons. The function $f(\omega_s, \omega_i)$ represents the joint spectral amplitude of two-photon state, which results from the pump field and phase matching functions,

$$f(\omega_s, \omega_i) = N\alpha(\omega_s + \omega_i)\phi(\omega_s, \omega_i)F_s(\omega_s)F_i(\omega_i). \tag{12.4}$$

Here, $\alpha(\omega_s + \omega_i)$ represents the spectral distribution of pump beam, which can be described by Guassian function:

$$\alpha(\omega_s + \omega_i) \propto \exp[-\left(\frac{\omega_s + \omega_i - 2\omega_0}{2\sigma}\right)^2] \tag{12.5}$$

where $\omega_s + \omega_i = \omega_p$, ω_0 is the central frequency for degenerate parametric down conversion, and σ is the spectral linewidth of pump beam and $F_s(\omega_s)$ ($F_i(\omega_i)$) represents the spectral filtering distribution function of signal (idler). Finally, the phase matching function $\phi(\omega_s, \omega_i)$ is given by

$$\phi(\omega_s, \omega_i) = \text{sinc}\kappa \exp[i\kappa] \tag{12.6}$$

$$\kappa \equiv \frac{1}{2} L \Delta k(\omega_s, \omega_i), \tag{12.7}$$

where $\Delta k = k_s(\omega_s) + k_i(\omega_i) - k_p(\omega_p)$ is the wave-vector mismatch. The density operator of such two-photon state can be described as $\hat{\rho} = |\Psi\rangle\langle\Psi|$.

In conditional preparation of single photon via SPDC, each detected idler photon heralds the production of a signal photon. The signal photon state can be described as the reduced density operator

$$\hat{\rho}_s = Tr_i(\hat{\rho} P_i) \tag{12.8}$$

where P_i is the measurement operator acting on idler photon,

$$P_i = \int d\omega |\sigma(\omega)|^2 \hat{a}_i^+(\omega)|0\rangle\langle 0|\hat{a}_i(\omega) \tag{12.9}$$

Here, $\sigma(\omega)$ is the spectral filter transfer function.

According to (12.8) and (12.9), the density operator of signal photon triggered by idler photon is

$$\rho_s = \int d\omega_i \, d\omega_s \, d\omega_s' \, |\sigma(\omega_i)|^2 f(\omega_s, \omega_i) \hat{a}_s^\dagger(\omega_s)|0\rangle\langle 0|\hat{a}_s(\omega_s') f^*(\omega_s', \omega_i) \tag{12.10}$$

This describes a pure state only if it can be written in the form of (12.2).

From (12.10), signal photon is in a pure state under two conditions. One condition is $|\sigma(\omega)| \to \delta(\omega - \Omega)$, but in this way the truly pure states are approached only in the limit of vanishing counts. Another condition is $f(\omega_s, \omega_i) = f(\omega_s) f(\omega_i)$. This is also the condition for eliminating frequency correlation [11–13].

12.3 Group Velocity Mismatching

Group velocity mismatching technology is used for generation of frequency uncorrelated photon pairs. When the group velocity of the signal photon, the idler photon, and the pump photon satisfy a certain condition, the frequency correlation between signal and idler is eliminated. This technology was proposed by Grice et al. [11], and developed both in theory and experiment in the following works. Detailed discussion of the theory of group velocity mismatching was presented by U'ren et al. [12]. Their calculation process is as follows.

First of all, the two-photon state generated by SPDC process can be described by (12.3–12.6).

In order to get the phase mismatch function, they firstly analyse the phase term in $\phi(\omega_s, \omega_i)$ in details. Expressing Taylor expansion up to second order at central frequency ω_0 on (12.6), they get the result as

$$\begin{aligned} L\Delta\tilde{k}(\omega_s, \omega_i) = L\Delta k^0 + \tau_s \Delta\omega_s + \tau_i \Delta\omega_i + \beta_s \Delta\omega_s^2 \\ + \beta_i \Delta\omega_i^2 + \beta_p \Delta\omega_s \Delta\omega_i + O(v^3) \end{aligned} \tag{12.11}$$

where

$$\Delta k^0 = k_s(\omega_s) + k_i(\omega_i) - k_p(\omega_p) \tag{12.12}$$

Equation (12.12) is equal to zero when the phase mismatch is satisfied. And they ignore the higher terms $O(v^3)$ in Taylor expansion. Besides,

$$\begin{aligned} \tau_\mu &= L[k'_\mu(\omega_\mu) - k'_p(\omega_p)] = L(u_\mu^{-1} - u_p^{-1}) \\ \beta_\mu &= \frac{L}{2}[k''_\mu(\omega_\mu) - k''_p(\omega_p)] \\ \beta_p &= -Lk''_p(\omega_p) \end{aligned} \tag{12.13}$$

where $\mu = s, i$.

τ_μ is the temporal walk-off between down converted photon and pump photon. u_μ (u_p) is the group velocity. β_μ (β_p) is the group velocity dispersion. $k'_x(\omega)$ and $k''_x(\omega)$ indicate first and second frequency derivatives of k_x at frequency ω.

Next, in order to analyse the relationship between terms containing ω_s and ω_i in $f(\omega_s, \omega_i)$, it is more convenient to change every term of $f(\omega_s, \omega_i)$ into exponential function. So they introduce a new approximation,

$$\mathrm{Sinc}(x) \approx e^{-\gamma x^2} \quad \text{with} \quad \gamma = 0.193 \tag{12.14}$$

where $\gamma = 0.193$ is chosen not to change the full-width half-maximum(FWHW) value of the function.

Thus the joint spectral amplitude is given as

$$\begin{aligned} f(\omega_s, \omega_i) = M \exp\left[-\frac{(\omega_s + \omega_i - \omega_p)^2}{2\sigma}\right] \\ \times \exp\left[i\beta_t(\Delta\omega_s + \Delta\omega_i)^2\right] \exp\left[-\frac{\gamma}{4}(\tau_s\Delta\omega_s + \tau_i\Delta\omega_i)^2\right] \\ \times \exp\left[i\frac{1}{2}(\tau_s\Delta\omega_s + \tau_i\Delta\omega_i + \beta_s\Delta\omega_s^2 + \beta_i\Delta\omega_i^2 + \beta_p\Delta\omega_s\Delta\omega_i)\right], \end{aligned} \tag{12.15}$$

where M is the normalization constant. β_t is the group velocity dispersion (GVD) term that the pump experiences prior to the crystal. By expanding the exponential terms, we can express the joint spectral amplitude as

$$\begin{aligned} f(\omega_s, \omega_i) \propto & \exp\left[-\left(\frac{1}{2\sigma^2}+\frac{\gamma}{4}\tau_s^2\right)\Delta\omega_s^2\right]\exp\left[i\frac{\tau_s}{2}\Delta\omega_s + i\left(\beta_t+\frac{\beta_s}{2}\Delta\omega_s^2\right)\right] \\ & \times \exp\left[-\left(\frac{1}{2\sigma^2}+\frac{\gamma}{4}\tau_i^2\right)\Delta\omega_i^2\right]\exp\left[i\frac{\tau_i}{2}\Delta\omega_i + i\left(\beta_t+\frac{\beta_i}{2}\Delta\omega_i^2\right)\right] \\ & \times \exp\left[-2\left(\frac{1}{2\sigma^2}+\frac{\gamma}{4}\tau_s\tau_i\right)\Delta\omega_s\Delta\omega_i + i\left(2\beta_t+\frac{\beta_p}{2}\right)\Delta\omega_s\Delta\omega_i\right]. \end{aligned} \tag{12.16}$$

From (12.16), conditions that guarantee a factorizable state are

$$\frac{2}{\sigma^2}+\gamma\tau_s\tau_i = 0 \tag{12.17}$$

and

$$2\beta_t+\frac{\beta_p}{2} = 0 \tag{12.18}$$

Equation (12.17) and (12.18) are the two conditions for frequency uncorrelation. Since condition (12.18) is in the phase term of (12.16), it has no effect on the joint spectral intensity of the two-photon state. But it still has effect on the joint spectral amplitude. β_t is a chirp (quadratic phase) that fulfils (12.18). The quadratic phase that the pump should carry is therefore given by $\beta_t = -\beta_p/4$.

According to (12.13), (12.17) can be written as

$$\frac{2}{\sigma^2}+\gamma L^2(k_s'-k_p')(k_i'-k_p') = 0 \tag{12.19}$$

σ is the bandwidth of the pump, L is the length of the crystal, k_p' is the first frequency derivative of k_p at the frequency of $2\omega_0$, k_μ' ($\mu = s, i$) is the first derivative of k_μ at the frequency of ω_0, and γ is a constant. For specific experimental situations, pairs of values for the pump bandwidth σ and crystal length L may exist such that the condition (12.17) is fulfilled. Note that, for the condition in (12.17) to be fulfilled, one of the following must be true: $k_s' < k_p' < k_i'$ or $k_i' < k_p' < k_s'$. That is to say, the group velocity of the pump must lie between that of the signal and idler.

This condition can be met for several common $\chi^{(2)}$ crystals. In the paper [11] Grice et al. give a table about the group velocity mismatch range for BBO, ADP, KDP, KD*P and LBO. For example, when the wavelengths of signal and idler are in the range $1.169\,\mu\text{m} < \lambda < 1.949\,\mu\text{m}$ photon pairs generated by BBO are frequency uncorrelated. The range for PPKTP given by U'Ren in [12] is $1.207\,\mu\text{m} < \lambda < 2.364\,\mu\text{m}$.

Wavelength ranges described above are more than 1 μm which cannot be detected by single-photon detectors effectively. In addition, in order to meet the condition

(12.17), the linewidth of the pump beam must correspond to the length of the crystal, which makes that the experimental conditions are very limited. In the following, we will discuss an approach to solve the two problems.

Here, we rewrite (12.17) as

$$\frac{2}{\sigma \tau_s} + \gamma \sigma \tau_i = 0. \tag{12.20}$$

If $\tau_s >> \sigma^{-1}$ is in the limit of $L \to \infty$, the condition reduces to the following simpler constraint: $\tau_i = 0$. From this result, we can conclude that spectral decorrelation can also be achieved by employing a long crystal while making one of the temporal walkoff terms vanish [12]. For example, type-II PDC in a 2-cm-long KDP cut at a phase-matching angle of 68° can degenerately generate frequency decorated two-photon at 830 nm.

In the above paragraphs, we introduce the group velocity mismatching approach which is one of the effective methods for frequency uncorrelation, but it is restricted by the parameters of natural crystals. Therefore, such method can be used on limited range of wavelengths. Fortunately, artificial crystals or crystal sequences can break the limitation [12].

As shown in Fig. 12.1, the crystal sequence is composed with two kinds of crystal slice sequences. The sequence of nonlinear crystal is interspersed with birefringent spacers which are used for compensation for the group velocity mismatching.

We assume that the crystal sequence consists of N identical nonlinear crystals and N–1 linear optical spacers. Each crystal has length L, while each spacer has length h. The phase mismatch in each crystal is given by

$$\Delta k = k_p - k_s - k_i \tag{12.21}$$

where k_μ (with $\mu = p, s, i$) denotes the wavenumber for each of the three fields taking into account dispersion in the crystals. The phase mismatch introduced by each of the spacers is equivalently given as

$$\Delta \kappa = \kappa_p - \kappa_s - \kappa_i \tag{12.22}$$

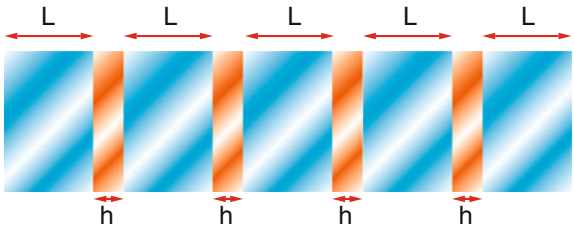

Fig. 12.1 Schematic of the proposed sequence with intermediate birefringent spacers. Each crystal has a length L, while each spacer has a length h

where κ_μ (with $\mu = p, s, i$) represents the wavenumber for each of the three fields taking into account dispersion in the birefringent spacer.

According to U'Ren's calculation, the overall phase matching function can be described as

$$\begin{aligned}\phi_N(\Delta k, \Delta\kappa) &= \sum_{m=0}^{N-1} e^{im(L\Delta k + h\Delta\kappa)} \mathrm{Sinc}\left[\frac{L}{2}\Delta k\right] \\ &= e^{\frac{i(N-1)\Phi}{2}} \frac{\sin\left(\frac{N\Phi}{2}\right)}{\sin\left(\frac{\Phi}{2}\right)} \mathrm{sinc}\left[\frac{L\Delta k}{2}\right] \end{aligned} \tag{12.23}$$

where

$$\Phi = L\Delta k + h\Delta\kappa \tag{12.24}$$

This way the condition of frequency correlation is related to the crystal and spacer materials and their thickness L and h. Theoretically, the group velocity mismatching condition can be satisfied at any wavelength. However, this scheme increases the complexity of crystals' preparation.

12.4 Narrowband Entanglement Sources

The most widely used method for the preparation of entangled states is spontaneous parametric down conversion (SPDC) in nonlinear crystals. However, the linewidth of photons thus produced is very wide, and does not match the linewidths of atoms, quantum dots and NV centers. Therefore, we need to generate narrow linewidth entangled sources. Directly filtering out the narrow linewidth portion will result in a very low count rate. An effective way to generate narrowband photons is to use cavity-enhanced parametric down conversion. The linewidth generated by this method is determined by the linewidth of the optical cavity [16, 17, 21–23]. Simultaneously by putting the nonlinear crystal inside a cavity, the generation probability for the down-converted photons whose frequency matches the cavity mode will be enhanced greatly. In this way, we can get narrowband and bright photon pairs.

As in Sect. 12.2, we have a joint spectral amplitude given by (12.3), but now the filter functions $F_s(\omega_s)$ and $F_i(\omega_i)$ are determined by the cavity. In general, these describe a comb structure; here we assume that additional filters are used to remove the output of all but one spectral mode, with center frequency ω_0, for each of signal and idler. We can then express $F_s(\omega_s)$ and $F_i(\omega_i)$ as

$$\begin{aligned}\mathrm{F}(\omega_s) &= \frac{1}{(\omega_s - \omega_0) + i\frac{\gamma}{2}} \\ \mathrm{F}(\omega_i) &= \frac{1}{(\omega_i - \omega_0) + i\frac{\gamma}{2}} \end{aligned} \tag{12.25}$$

$f(\omega_s, \omega_i)$ contains four functions. In $\alpha(\omega_s + \omega_i)$ and $\phi(\omega_s, \omega_i)$, ω_s and ω_i are coupled while in $F(\omega_s)$ and $F(\omega_i)$, ω_s and ω_i are independent. We neglect the spectral function of the phase matching, whose width is very broad compared to the MHz cavity linewidth. The spectrum response function is centered at ω_0 and decreases rapidly away from ω_0. Therefore, when the bandwidth of $\phi(\omega_s, \omega_i)$ is much larger than the linewidth γ, or in other words, the duration of the pump light is much smaller than the coherence time of the photons, the frequency of the two photons will be mainly determined by the spectrum response function. In this case, the two photon wave function is factorable, and thus the frequency correlation is eliminated, and the purity of the spatiotemporal mode of the photons is unity. In practice, it is more convenient to express the pump light using the pulse length. When $\sigma > \gamma \sim 5$ MHz, the pulse length of the pump light should be shorter than 75 ns.

Because of energy conservation frequencies of signal photon and idler photon satisfy the relation $\omega_s + \omega_i = \omega_p$. Therefore, if the pump is continuous wave, ω_p is a definite value. This means that ω_s and ω_i are tightly correlated. But if we change the continuous pump into pulse beam, when the frequency of the pulse is wider than the linewidth of signal (idler) photons, the corresponding relationship between signal and idler is no longer determined by a definite value. Thus the two-photon are not correlated.

To quantitatively analyze the correlation and the purity of the spatiotemporal mode of the frequency-uncorrelated photons, we perform a three-photon experiment and observe nonclassical interference between an entanglement source and an independent weak coherent light at a single photon level. This kind of three-photon experiment has been used to demonstrate nonclassical interference between independent sources [24].

As illustrated in Fig. 12.2, the experiment is performed by employing a pulse-pumped narrow-band cavity-enhanced SPDC source and a weak coherent light at a single photon level. The weak coherent light is generated from an independent laser. Pulse lengths of the independent laser and the UV pump beam are the same.

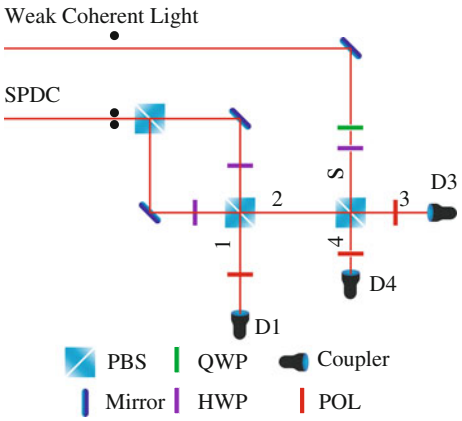

Fig. 12.2 Experimental diagram of three-photon interference. Photon 1 and photon 2 are created by cavity-enhanced SPDC. Photon 2 and weak coherent light interfere on PBS. Photon 1 is detected by D1. Photons output from PBS are detected by D3 and D4

After passing through a cavity with a linewidth of about 5 MHz, the weak coherent light is prepared to have a matching bandwidth with the entangled photon pairs. Photon 1 of the entangled pair is detected, while photon 2 and the weak coherent light are superimposed on a PBS to implement a HOM type interference. We emphasize that no additional frequency filter is applied to the SPDC photons. This is different from previous experiments with conventional SPDC, where additional frequency filters are usually applied to both the weak coherent light and the entangled photons to ensure indistinguishability between them. The initial state can be expressed as

$$|\psi\rangle_{12} \otimes |\phi\rangle_s = (|H\rangle_1|H\rangle_2 + |V\rangle_1|V\rangle_2) \otimes (|H\rangle_s + |V\rangle_s) \tag{12.26}$$

Using polarisers at 45°($|+\rangle$)/-45°($|-\rangle$) in front of detectors we measure three-photon coincidence between D1, D3, and D4 in the states $|-\rangle|+\rangle|+\rangle$ and $|+\rangle|+\rangle|+\rangle$, where $|\pm\rangle \propto |H\rangle \pm |V\rangle$. We denote the number of three-fold coincidence events in these two states as N_{-++} and N_{+++}, respectively. Note that the detection window of photon 1 is larger than photon 1's whole wave packet, and thus the detection of photon 1 is not time resolved and does not contribute temporal filtering. Assuming that the detection is integrated over the whole wave packet, the three-photon interference visibility can be calculated as [25]

$$\begin{aligned} V &= (N_{+++} - N_{-++})/(N_{+++} + N_{-++}) \\ &= \int\int\int d\omega_1 d\omega_2 d\omega_3 \psi_{12}(\omega_1, \omega_2)\psi_{12}^*(\omega_1, \omega_3)\phi_s(\omega_3)\phi_s^*(\omega_2) \end{aligned} \tag{12.27}$$

If the frequency correlation is fully eliminated, $\psi_{12}(\omega_1, \omega_2) = \psi(\omega_1)\psi(\omega_2)$ is factorable. In this case, we will obtain V = 1, if the spectrum of photon 2 matches that of the coherent state, i.e., $\phi_2(\omega) = \phi_s(\omega)$. Therefore, the three photon visibility contains the information how much frequency correlation the entangled photons have, and thus can be used to estimate the correlation.

The visibility can also be expressed in terms of purity

$$V = Tr(\rho_2\rho_s) = [P(\rho_2) + P(\rho_s) - O(\rho_2, \rho_s)]/2 \tag{12.28}$$

where $\rho_2 = Tr_1(|\psi\rangle_{12}\langle\psi|)$ is the reduced density matrix of photon 2, $\rho_s = |\phi\rangle_s\langle\phi|$ is the density matrix of the coherent state, $P(\rho_i) = Tr(\rho_i^2) < 1 (i = 2, s)$ is the purity of photon 2 and the single photon, and $O(\rho_2, \rho_s) = ||\rho_2 - \rho_s||^2 > 0$ is the operational instance between the two photons [26]. In ideal case that the frequency correlation is fully eliminated, $\psi_{12}(\omega_1, \omega_2)$ is factorable and photon 2 is in a pure state with purity of 1. From the three-photon visibility, we can obtain a lower bound of the purity of the spatiotemporal mode of photon 2, by $P(\rho_2) = 2V + O(\rho_2, \rho_s) - P(\rho_s) > 2V - 1$. Therefore a high visibility close to 1 implies a high purity of photon 2. Besides, since $|\phi_s\rangle$ is in a pure state, V is also the fidelity of photon 2 on the single photon state.

In the experiment illustrated in Fig. 12.2, the three photon visibility is mainly suppressed by the background noise due to the second order events in both the weak coherent light and the entangled photons. Therefore, a three-photon coincidence mainly contains two noise terms (1) coincidences contributed by a two-photon event from the weak coherent pulse and a single-photon event in entangled photon mode; (2) coincidences contributed by a double-pair emission from the entangled source. Other background noises, like the dark counts and polarization errors are so small that can be neglected. We measure these two noise counts and subtract the background noises from the raw data to obtain a net visibility. Noise 1, 2 are measured by registering the background three-photon coincidences by blocking photon 2 and the weak coherent light respectively. By subtracting the noise counts, we obtain the net visibility, and thus can estimate the remaining frequency correlation of our narrowband entanglement source and the purity of heralded photon 2. Note that the method of subtracting background noises by blocking one beam has been used to extract the net visibility in previous experiments.

We first performed the experiment with a short pump of 40 ns. The envelopes of the photon 2 and the weak coherent light are shown in Fig. 12.3a. In this case, theoretical analysis suggests that the frequency correlation is eliminated and thus we

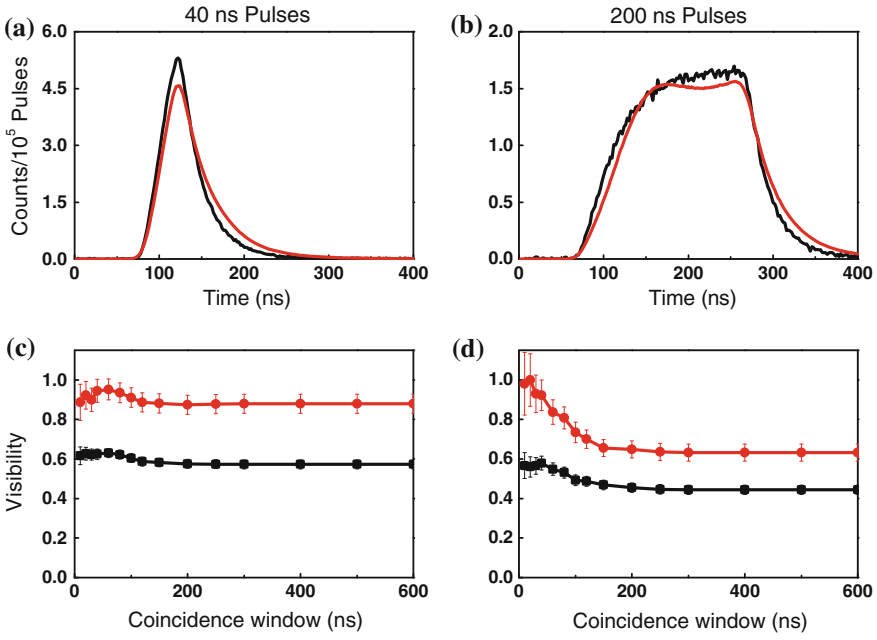

Fig. 12.3 Three-photon interference visibility. **a** The envelopes of photon 2 (*black*) and the weak coherent light (*red*) with a short pump of 40 ns. **b** The envelopes of photon 2 (*black*) and the weak coherent light (*red*) with a pump of 200 ns. **c** Net Visibility (*red*) and raw visibility (*black*) of three-photon interference on +/- basis with pump of 40 ns. **d** Net Visibility (*red*) and raw visibility (*black*) of three-photon interference on $+/-$ basis with pump of 200 ns

expect a high net visibility. The probabilities of detecting an entangled photon and a single photon from the weak coherent light are about 0.0009 and 0.04 respectively. The coincidence window between D1 and D3, D1 and D4, are both 200 ns, which is larger than the wave packet of the pulses. The raw visibility as a function of the coincidence window between D3 and D4 is shown in Fig. 12.3c.

For coincidence window larger than 300 ns, the raw visibilities approach a steady value $V_{raw}^{40\,ns} \approx 0.57$. The raw visibility, being larger than 0.33, is a clear evidence of nonclassical interference between the entangled source and the weak coherent light [27]. By measuring and subtracting the background noises as discussed above, we obtain the net visibility (c), which gives a steady value of $V_{net}^{40\,ns} \approx 0.88$. We can thus obtain a minimum bound of the purity of the spatiotemporal mode of photon 2, i.e., $P(\rho_2) > 2V_{net}^{40\,ns} - 1 = 0.76$. Besides, the net visibility does not change significantly with the coincidence window between D3 and D4, which means that the indistinguishability between photon 2 and the single photon does not change in a time resolved experiment.

For comparison, we perform a similar experiment using a 200 ns pump pulse. The envelopes of the generated pulses are shown in Fig. 12.3b. In this case, theoretical analysis suggests that the frequency correlation is only partially eliminated and thus we expect the net visibility will be smaller than the 40 ns case. The laser power is carefully tuned so that the probability of detecting an entangled photon and a single photon from weak coherent is also about 0.0009 and 0.04 respectively which is the same as the experiment condition for 300 ns pump pulse. The raw visibility is shown in Fig. 12.3d. We achieve a steady raw visibility of $V_{raw}^{200\,ns} \approx 0.45$, which is below the classical limit. We also subtract the background noises and obtain a steady net visibility of $V_{net}^{200\,ns} \approx 0.63$ in Fig. 12.3d. The steady net visibility of 200 ns case is markedly smaller than the 40 ns case. We attribute this to the fact that photon 2 is in a mixed state due to the frequency correlation between the entangled photons. Note that the net visibility of 200 ns case decreases significantly with increasing coincidence window between D3 and D4. This implies that frequency correlation is not eliminated. Photon 2 and the single photon s can be distinguished through a time resolved measurement.

12.5 Applications

In this section, we briefly discuss the applications of frequency uncorrelated photon pairs. Firstly, the frequency uncorrelated light source can be used to produce a pure single-photon state. Secondly, frequency uncorrelation technology is widely used for the interference between independent sources.

In the past few years, many different methods have been put forward to eliminate frequency correlations for the generation of single-photon state. Firstly, Mosley et al. generated heralded single photon pure states from a parametric down-conversion source and eliminate their frequency correlation through controlling the modal structure of the photon pair emission [13]. The measured visibility of 95 % sets a

minimum bound on the mean photon purity. Secondly Evans et al. have presented a bright source of spectrally uncorrelated entangled photons with nearly single-mode emission. The minimum spectral and spatial correlation has been implemented by appropriate pump focusing and careful selection of pump bandwidth, wavelength and phase matching. In this way, they obtain a entanglement visibility of 95 % without any spectral or spatial filtering. Thirdly, in [11], researchers produced single photon by using a microcavity to engineer the density of states of the optical field at the PDC frequencies. The high-finesse cavity mode occupies a spectral interval much narrower than the bandwidth of the pulsed pump laser field, suppressing the spectral correlation, or entanglement, between signal and idler photons. Greater than 99 % pure-state packet production is predicted to be achievable.

On the other hand, recently, several experiments on interference between independent sources have highlighted the advantage of frequency uncorrelation of entangled photon pairs [16, 17].

The result of interference between a photon from SPDC and an independent weak coherent photon has been introduced in the previous paragraphs. In this experiment, the result removes background noise. Next we demonstrate a four-photon experiment in which retains all experimental data. This experiment fully shows the advantage of frequency uncorrelation for interference between independent sources.

In four-photon experiment, firstly, two pairs of narrowband polarization-entangled photons (1, 2) and (3, 4) are each prepared using the cavity-enhanced SPDC. Photon 2 and photon 3 interfere at a PBS. We measure the visibility (Fig. 12.4).

$$\frac{N_{++++} - N_{+++-}}{N_{++++} + N_{+++-}} \tag{12.29}$$

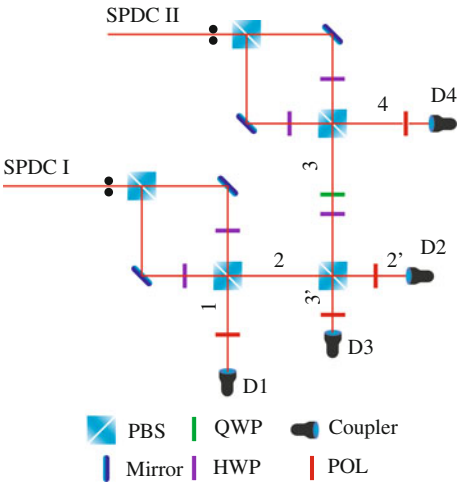

Fig. 12.4 Experimental diagram of four-photon interference. Photon 1 and photon 2 are created by cavity-enhanced SPDCI. Photon 3 and photon 4 are created by cavity-enhanced SPDCII. Photon 2 and photon 3 interfere on PBS. Photon 1 and Photon 4 are detected by D1 and D4. Photons output from PBS are detected by D2 and D3

If the duration of pump pulse is about 300 ns, photon 1, 2 and photon 3, 4 are frequency correlated. When the coincidence window is bigger than coherence time of photons 2, 3 theoretically, we can distinguish them by measurement the detection time of their partner photons 1, 4. As a result, the visibility becomes lower as the coincidence window increases. Vice versa, for frequency uncorrelation photons, like photons from SPDC pumped by 50 ns-long pulses, the visibility is a constant as the coincidence window changes. The measurement results are shown in Fig. 12.5.

In these experiments, the visibilities of three-photon and four-photon interference were measured. As shown in Figs. 12.3 and 12.5, the visibility keeps a constant as the coincidence window is changed for photons without frequency correlation, while, for those photons with frequency correaltion, the visibility steady declines as the coincidence window is increased. This means that we have to sacrifice photon count rate for high visibility when the frequency correlation between photons from SPDC are not eliminated. However, the photon count rate is vitally important for few photon interference in quantum networks.

In short, frequency uncorrelated technology has important applications in generation of single-photon pure state and can be used in any interference experiment in principle. So it is expected that frequency uncorrelation technology can be applied to many fileds of quantum optics and quantum information.

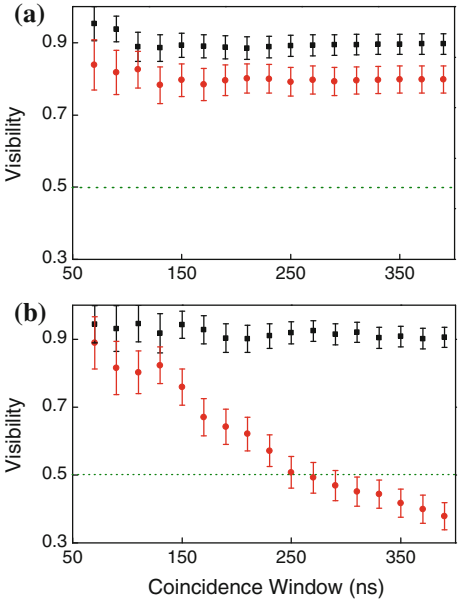

Fig. 12.5 Four-photon interference visibility. Visibility in HV basis (*black*), Visibility in DA basis (*red*), classical line (*dashed line*). **a** 50 ns pump pulse. **b** 300 ns pump pulse

12.6 Conclusions

Frequency uncorrelation technology has been widely used in the generation of single photon pure state wavepacket and in interference between independent sources. In this chapter, we have discussed several methods for eliminating frequency correlations.

One is used the technology of group velocity matching. But this is only effective on specific wavelength. Group velocity mismatching in long crystal can broaden the effective wavelength range. Besides, the group velocity mismatching condition can be fulfilled in any wavelength by using a sequence of crystal and spacers. Then, we introduce how to eliminate the frequency correlation for narrowband photons created from cavity-enhanced SPDC by pulse engineering. At last we discuss the experimental measurement of frequency uncorrelation, including three-photon interference and four-photon interference.

These techniques may provide useful tools for practical implementation of novel quantum-enhanced technologies, such as linear optical quantum computation. Moreover, they are becoming increasingly important for quantum networks and quantum repeaters.

References

1. L.M. Duan, M.D. Lukin, J.I. Cirac, P. Zoller, Long-distance quantum communication with atomic ensembles and linear optics. Nature **414**, 413–418 (2001)
2. H.J. Kimble, The quantum internet. Nature **453**, 1023–1030 (2008)
3. N. Gisin, R. Thew, Quantum communication. Nat. Photon **1**, 165–171 (2007)
4. M. Nielsen, I. Chuang, *Quantum Computation and Quantum Information*, Series on Information and the Natural Sciences (Cambridge University Press, Cambridge, 2000)
5. M. Zukowski, A. Zeilinger, H. Weinfurter, Entangling photons radiated by independent pulsed sourcesa. Ann. N. Y. Acad. Sci. **755**, 91–102 (1995)
6. D. Bouwmeester et al., Experimental quantum teleportation. Nature **390**, 575–579 (1997)
7. E. Knill, R. Laflamme, G.J. Milburn, A scheme for efficient quantum computation with linear optics. Nature **409**, 46–52 (2001)
8. C.K. Hong, Z.Y. Ou, L. Mandel, Measurement of subpicosecond time intervals between two photons by interference. Phys. Rev. Lett. **59**, 2044–2046 (1987)
9. A. Fedrizzi et al., Anti-symmetrization reveals hidden entanglement. N. J. Phys. **11**, 103052 (2009)
10. P.G. Kwiat et al., New high-intensity source of polarization-entangled photon pairs. Phys. Rev. Lett. **75**, 4337–4341 (1995)
11. W.P. Grice, A.B. U'Ren, I.A. Walmsley, Eliminating frequency and space-time correlations in multiphoton states. Phys. Rev. A **64**, 063815 (2001)
12. A.B. U'Ren et al., Generation of pure-state single-photon wavepackets by conditional preparation based on spontaneous parametric downconversion. Laser Phys. **15**, 146 (2004)
13. P.J. Mosley et al., Heralded generation of ultrafast single photons in pure quantum states. Phys. Rev. Lett. **100**, 133601 (2008)
14. P.G. Evans, R.S. Bennink, W.P. Grice, T.S. Humble, J. Schaake, Bright source of spectrally uncorrelated polarization-entangled photons with nearly single-mode emission. Phys. Rev. Lett. **105**, 253601 (2010)

15. M.G. Raymer, J. Noh, K. Banaszek, I.A. Walmsley, Pure-state single-photon wave-packet generation by parametric down-conversion in a distributed microcavity. Phys. Rev. A **72**, 023825 (2005)
16. H. Zhang et al., Preparation and storage of frequency-uncorrelated entangled photons from cavity-enhanced spontaneous parametric downconversion. Nat. Photon **5**, 628–632 (2011)
17. T.-M. Zhao et al., Entangling different-color photons via time-resolved measurement and active feed forward. Phys. Rev. Lett. **112**, 103602 (2014)
18. J.P. Torres, F. Macià, S. Carrasco, L. Torner, Engineering the frequency correlations of entangled two-photon statesby achromatic phase matching. Opt. Lett. **30**, 314–316 (2005)
19. M. Hendrych, M. Micuda, J.P. Torres, Tunable control of the frequency correlations of entangled photons. Opt. Lett. **32**, 2339–2341 (2007)
20. Y.-W. Cho, K.-K. Park, J.-C. Lee, Y.-H. Kim, Engineering frequency-time quantum correlation of narrow-band biphotons from cold atoms. Phys. Rev. Lett. **113**, 063602 (2014)
21. X.-H. Bao et al., Generation of narrow-band polarization-entangled photon pairs for atomic quantum memories. Phys. Rev. Lett. **101**, 190501 (2008)
22. J. Yang et al., Experimental quantum teleportation and multiphoton entanglement via interfering narrowband photon sources. Phys. Rev. A **80**, 042321 (2009)
23. C.-S. Chuu, S.E. Harris, Ultrabright backward-wave biphoton source. Phys. Rev. A **83**, 061803 (2011)
24. J.G. Rarity, P.R. Tapster, Three-particle entanglement from entangled photon pairs and a weak coherent state. Phys. Rev. A **59**, R35–R38 (1999)
25. Z.Y. Ou, J.-K. Rhee, L.J. Wang, Photon bunching and multiphoton interference in parametric down-conversion. Phys. Rev. A **60**, 593–604 (1999)
26. V.P. Belavkin, G.M. D'Ariano, M. Raginsky, Operational distance and fidelity for quantum channels. J. Math. Phys. **46**, 062106 (2005)
27. H.D. Riedmatten, I. Marcikic, W. Tittel, H. Zbinden, N. Gisin, Quantum interference with photon pairs created in spatially separated sources. Phys. Rev. A **67**, 022301 (2003)

Chapter 13
Single Semiconductor Quantum Dots in Microcavities: Bright Sources of Indistinguishable Photons

C. Schneider, P. Gold, C.-Y. Lu, S. Höfling, J.-W. Pan and M. Kamp

Abstract In this chapter we will discuss the technology and experimental techniques to realize quantum dot (QD) single photon sources combining high outcoupling efficiencies and highest degrees of photon indistinguishability. The system, which is based on low density InAs QDs embedded in a quasi planar single sided microcavity with natural photonic traps is an ideal testbed to study quantum light emission from single QDs. We will discuss the influence of the excitation conditions on the purity of the single photon emission, and in particular on the degree of indistinguishability of the emitted photons. While high purity triggered emission of single photons is observed under all tested excitation conditions, single photon interference effects can almost vanish in experiments relying on non-resonant pumping into the quantum dot wetting layer. However, we can observe nearly perfect indistinguishability of single photons in resonance fluorescence excitation conditions, which underlines the superiority of this excitation scheme to create photon wave packets close to the Fourier limit. As a first step towards the realization of solid state quantum networks based on quantum dot single photon sources we test the overlap of photons emitted from remote QDs yielding non-postselected interference visibilities on the order of ($\approx$40 %) for quasi resonant excitation.

13.1 Introduction

The demonstration of single photon emission from a semiconductor quantum dot (QD) [1] triggered 15 years of prospering research devoted towards the application of semiconductor quantum light emitters. In particular the most commonly studied InGaAs/GaAs based QDs can emit highly non-classical light, both under optical and

C. Schneider (✉) · P. Gold · C.-Y. Lu · S. Höfling · J.-W. Pan · M. Kamp
University of Würzburg, Am Hubland, Würzburg, Germany
e-mail: Christian.schneider@physik.uni-wuerzburg.de

C.-Y. Lu · J.-W. Pan
University of Science and Technology of China, Hefei, Anhui 230026, P.R. China

S. Höfling
SUPA, School of Physics and Astronomy, University of St Andrews,
St Andrews KY16 9SS, UK

A. Predojević and M.W. Mitchell (eds.), *Engineering the Atom-Photon Interaction*,
Nano-Optics and Nanophotonics, DOI 10.1007/978-3-319-19231-4_13

electrical excitation [1–4]. However, for many applications beyond simple quantum cryptography schemes, it is vitally important that the emitted single photons are comprising highest degrees of indistinguishability, which means that they have to be identical in all spectral characteristics: Their color, polarization, and furthermore the extension of the wave packet (i.e. their coherence) should be Fourier limited [5, 6]. Such photons are at the heart of applications in quantum communication [7], quantum networks [8] and linear optical quantum computing [9]. Most quantum teleportation schemes strongly rely on photon indistinguishability, and in particular the route towards quantum repeater networks for future long distance quantum communications highly relies on this property [10–12]. First important experiments based on quantum interference and teleportation of photons emitted from single QDs have recently been carried out [13, 14]. In contrast to isolated quantum emitters such as atoms in dilute vapors, QDs are embedded in a solid state environment which imposes limitations on

- the brightness of the source since the photons have to be extracted out of a high refractive index material
- the interference properties of photons emitted from these sources, as coherence and color of the emission can be affected by coupling to the environment of the emitter.

While the source efficiency can be boosted to very high values by embedding quantum emitters in photonic micro- and nanostructures [3, 15–17], increasing the degree of indistinguishability at least partly requires to decouple the emitter from its environment. In particular frequency shifts induced by charges in the QD's vicinity, or effects of phonon induced emitter dephasing strongly and detrimentally affect the interference properties of single QDs. This chapter is structured as follows: In Sect. 13.2 we will briefly address the fundamental mechanisms of two photon interference and its experimental implementation. In Sect. 13.3 we will describe the experimental realization of a bright single photon source as the basis of the following studies. Finally, in Sects. 13.4 and 13.5 we will describe two photon interference experiments carried out on single QDs. We will assess in detail the influence of the excitation scheme on the interference properties of the quantum light emitted from the QD. While carrier refilling effects are identified to strongly detrimentally influence the photon interference in non-resonant excitation schemes, resonance fluorescence conditions can lead to almost perfect interference visibilities of photons. We can furthermore demonstrate significant interference of single photons emitted from separate sources and compare our experimental findings with an analytical model.

13.2 A Pedestrian's Guide to Two Photon Interference

13.2.1 Quantum Dot Single Photon Source

In a very simplified picture, single QDs can be considered as two level systems embedded in a solid state environment: Electrons and holes can be captured and

localized in QDs if the band configuration provides an potential well in the conduction and valence band, and the small size of the QDs leads to strong Coulomb and exchange interactions. As a result, the energetic ground state of a single dot can only be occupied by a single electron-hole pair. This excitonic carrier complex can decay spontaneously and its energy is transferred to a single photon. Since the maximum occupation number of the excited state cannot exceed unity, not more than one photon of the corresponding energy can be emitted at a time interval on the order of the exciton lifetime. The distribution function of the photon stream is hence sub-poissonian (or antibunched), which is usually characterized by the second order correlation function which we write here in terms of the emitted photon intensities and the delay time τ between two detection events: $g^{(2)}(\tau) = \frac{<I(t)I(t+\tau)>}{<I(t)>^2}$. For an ideal single photon source, the value of this function approaches 0 at $\tau = 0$. The antibunched nature of the emission from a single QD makes these quantum emitters highly interesting for quantum cryptography schemes relying on encoding the information of a quantum key into the polarization of a single light particle (such as the famous BB84 protocol [18]). First successful experimental demonstrations of quantum key distribution with QD single photon sources, both under optical [19] and electrical excitation [20] have been realized. However, for more advanced schemes such as the remote entanglement of stationary quantum bits (Qubits), the interference properties of these photons play a dominant role, which we will detail in the following subchapter.

13.2.2 Photon Interference with Quantum Light

The interference properties of single photons and their indistinguishability are very closely related properties. Indistinguishable photons share all relevant properties, such as color, polarization, and extension of the wave-packet in space and time. Directly probing the indistinguishability of single photons is usually carried out in the interference experiment pioneered by Hong et al. [21]. For further details see also the chapters by A. Kuhn and Zhao, Bao, Zhao and Pan). It is manifested as a quantum interference effect when two photons arrive from different sides on a beam splitter: If these photons are indistinguishable and if they overlap in space and time (spatio-temporal overlap) on the beam splitter, quantum interference will force them always to exit through a common output port, which creates a path entangled (N = 2) NOON-state. This is schematically sketched in Fig. 13.1a, d). The fact that the photons leave the beam splitter in bunches with a suppression of the scenarios sketched in Fig. 13.1b, c as a result of destructive quantum interference reflects their bosonic nature, and cannot be explained by classical electrodynamics.

The Hong-Ou-Mandel effect can be experimentally probed by utilizing a configuration of single photon detectors similarly to a Hanbury Brown and Twiss setup which is routinely used to probe the quantum nature of the emitted light [4]. The setup is schematically sketched in Fig. 13.1e. The photons can be emitted from a

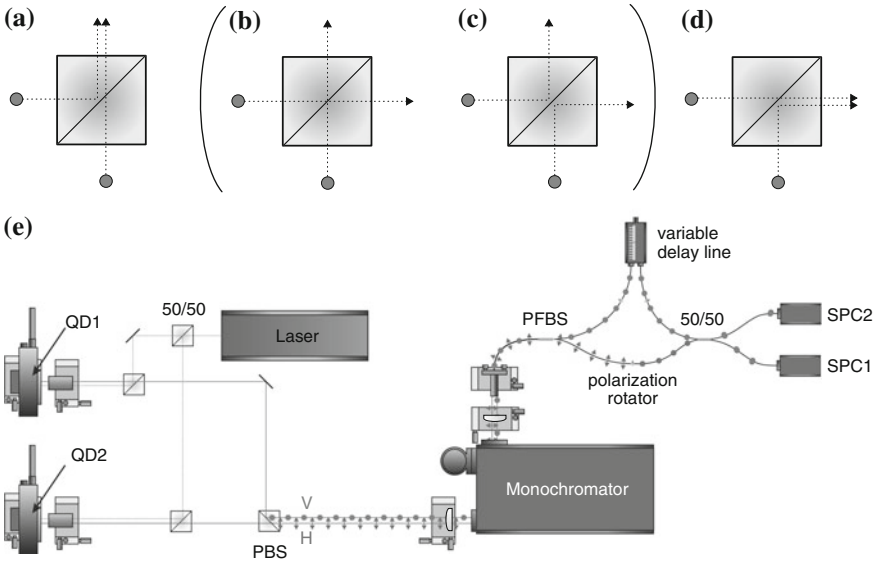

Fig. 13.1 **a**–**d** Possible configurations of two photons entering a beam splitter from different sides. Quantum interference determines the output paths of the photons. If the two input photons were indistinguishable, both photons can only leave the beam splitter in pairs through a common arm (**a** and **d**), rather than separate arms (**b** and **c**). **e** Experimental implementation of the two photon interference experiment: The photons are emitted either from the same source (QD1), or from two separate sources (QD1 and QD2) mounted in different cryostats. In the latter case, the photons are brought together on a polarizing beam splitter (PBS). After spectral filtering, the light is fed into an asymmetric Mach-Zehnder interferometer via a polarizing fiber beam splitter (PFBS), and the two photon interference effect occurs on the last 50/50 beam splitter. Single photon counters (SPCs) are connected to each exit port of the beam splitter to record quantum correlations

single source, or from separate, distant sources mounted in separate cryostats. In the latter case, the photon beams are brought together on a polarizing beam splitter and fed into an unbalanced Mach-Zehnder fiber interferometer after spectral filtering. One arm of the interferometer has a tunable length to adjust the arrival time of the photons on the second beam splitter, where the two photon interference is probed. Single photon detectors are connected to each output port of the beam splitter. The second order photon correlation function is recorded by measuring the time delays between the measurement events of the individual detectors. In case that the photons always take a common exit on the beam splitter, no coincidence detections between both APDs occur, and the second order correlation function approaches 0 at $\tau = 0$. Here, we have to remember that the single photons emitted from our QD source are photon wave packets, which interfere on the beam splitter. Ideally, these wave packets are Fourier-transform limited, with a Lorentzian spectral broadening $\Delta\omega$ being solely determined by the emitter decay time τ_r, and the temporal extension of the wave packet is given by $\tau_c = 2 \times \tau_r$. If additional dephasing channels with a characteristic time τ_{deph}, such as coupling to phonons start to play a role, the coherence

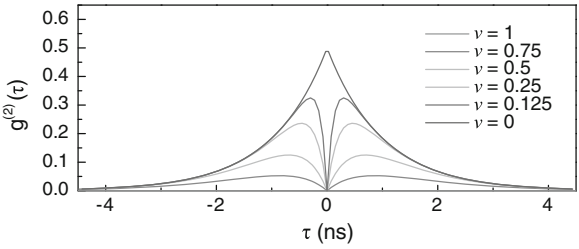

Fig. 13.2 Calculated correlation function $g^{(2)}(\tau)$ of the $\tau = 0$-Peak for the interference of indistinguishable photons with a radiative decay time of $\tau_r = 1\,\text{ns}$ for different visibilities $\nu = \tau_c/2\tau_r$

time τ_c is reduced to $\frac{1}{\tau_c} = \frac{1}{2\tau_r} + \frac{1}{\tau_{deph}}$. For Fourier-transform limited wave packets, the second order correlation function should reach a value of 0 at $\tau = 0$, which converts into a two photon indistinguishability of 100 %. To understand the shape of the second order correlation function around $\tau = 0$ in the presence of dephasing, one has to calculate the overlap integral of two photons incident on the beam splitter. The correlation function of the $\tau = 0$-peak for two photons with identical frequency and a time delay $\delta\tau$ between them is given by [22]

$$g^{(2)}(\tau, \delta\tau) = \frac{1}{4}e^{-\frac{|\tau-\delta\tau|}{\tau_r}} + \frac{1}{4}e^{-\frac{|\tau+\delta\tau|}{\tau_r}} - \frac{1}{2}e^{-\left(\frac{2}{\tau_c}-\frac{1}{\tau_r}\right)|\tau|-\frac{|\tau-\delta\tau|}{2\tau_r}-\frac{|\tau+\delta\tau|}{2\tau_r}}. \qquad (13.1)$$

In (13.1) a homogeneous broadening is assumed by an exponential decay of the coherent amplitude due to dephasing and the existence of (gaussian) spectral jitter is ignored.

The correlation function $g^{(2)}(\tau)$ of the $\tau = 0$-peak for the interference of photons with the same energy and polarization from a pulsed source is shown in Fig. 13.2 for different ratios of $\nu = \tau_c/2\tau_r$. We calculated $g^{(2)}(\tau)$ for a time delay of $\delta\tau = 0$ and a constant radiative decay time of $\tau_r = 1\,\text{ns}$. The variation of ν is achieved by varying the coherence time τ_c between 2 and 0 ns. In the case of Fourier-transform limited photons the visibility is 100 % and the $\tau = 0$-peak disappears completely. For a homogeneous broadening of the emission, represented by a coherence time $\tau_c < 2\tau_r$, the wavepackets do not overlapp perfectly which results in a non-zero contribution to the correlation function around $\tau = 0$. In the limit of very short coherence times $\tau_c \to 0$, the photons leave the beam splitter independently and randomly resulting from the reduced coalescence probability. The outcome of this is a peak in the correlation histogram with a $g^{(2)}(0)$ value of 0.5, which equals the $g^{(2)}(0)$-value for a two photon source $1 - 1/n$ with $n = 2$.

13.3 A Bright Quasi-planar Single Photon Source

The single photon source which is at the heart of this study is based on a low density layer of single In(Ga)As QDs integrated in an asymmetric AlAs/GaAs optical microcavity. The lower distributed Bragg reflector (DBR) consists of 18 AlAs/GaAs

mirrorpairs, providing a reflectivity near unity in the spectral range of the QD emission, which directs the light towards the top surface of the structure. A single layer of ultra low density InAs QDs is vertically centered in a GaAs λ-thick cavity layer, which is covered by 5 AlAs/GaAs distributed Bragg reflector (DBR) segments. The microcavity has a low quality factor (Q-factor) of ≈200. A combination of very low growth rates (<0.01 nm/s), and the partial capping and annealing growth technique [24] allows us to realize sufficiently low QD densities to spectroscopically isolate single QDs in the wavelength range between 900 and 940 nm. It is interesting to note that under such growth conditions, which allow for very long migration lengths of the supplied material, the QDs tend to nucleate at crystal steps, defects or nanoholes [4, 25]. This peculiar nucleation behavior can be directly exploited in QD positioning schemes [25, 26], where nanodefects are intentionally generated on a surface via lithography and etching. In our case, the natural formation of oval crystal defects, which was most likely induced by Gallium droplets during the growth of the bottom DBR similar to observations in [27], serves as such nucleation sites for the QDs in the cavity layer. These defects propagate through the top DBR and are well detectable as nanohills on the surface (Fig. 13.3c) via atomic force microscopy, with a height on the order of 10 nm. Figure 13.3b depicts a CCD image of the sample surface under illumination with white light at a temperature of 4 K. We used a long pass filter (750 nm) to monitor the emission from the QDs in the infrared range. The image is characterized by bright spots which we attribute to the emission of clusters of QDs, whereas no detectably signals occur between these sites.

Comparing the position of bright photoluminescence spots recorded via spatially resolved sample imaging with the nanohill position reveals a coalescence between the position of these hills and the location of QDs in the cavity. Furthermore, the oval

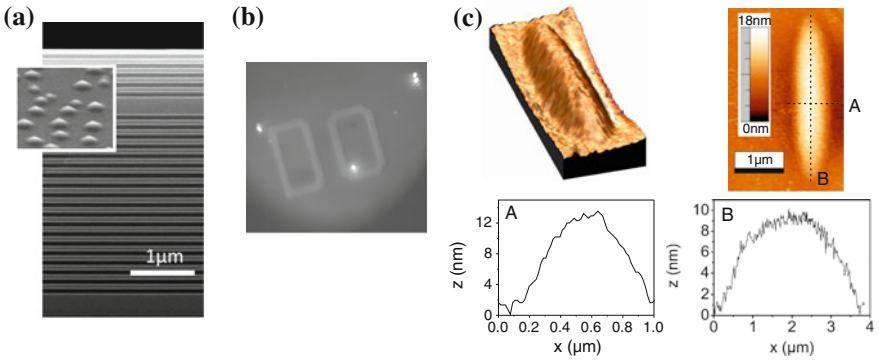

Fig. 13.3 **a** Sample structure and quantum dots: A single layer of In(Ga)As QDs is integrated in a single sided low-Q cavity realized by AlAs/GaAs distributed Bragg reflectors sandwiching a GaAs cavity layer. **b** The very low QD density facilitates the identification of QD emission spots straight forwardly by white light imaging. **c** Nanohills on the sample surface are formed during the growth process acting as natural lenses and significantly improve light outcoupling of the structure. The figure is reproduced from Maier et al. [23]

shape of the hills provides a gentle optical lateral confinement [27] which serves to guide the emitted light out of the semiconductor structure and enhance the photon outcoupling efficiency of the device. For a perfectly two dimensional microcavity structure of our geometry, this efficiency can hardly exceed theoretical values of ≈30 % when the light is collected in the normal direction with a 0.7 NA microscope objective [28]. In contrast, due to the waveguiding effect provided by the nanodefect, this efficiency can be theoretically increased to ≈50 %, as described in [23]. It is worth noting, that more carefully designed shapes of buried Gaussian nanohills are predicted to facilitate strong mode confinement to the sub-micrometer range without strongly reducing cavity Q-factor via lateral scattering losses [29], which makes them very appealing for cavity quantum electrodynamic experiments. In our structure, we could experimentally determine single photon outcoupling efficiencies up to 42 % in a calibrated photoluminescence setup, being in good agreement with the numerical estimations based on realistic sample parameters, and exceeds the theoretical maximum of a perfectly planar two dimensional microcavity (≈30 %) [23]. Most other strategies to achieve bright single photon emission from QDs embedded in a semiconductor matrix are based on the integration in nano- and microphotonic structures, such as pillar microcavities, photonic crystal membranes, nano-waveguides and antennas [30]. In all those approaches, the lithographic definition of the photonic structure creates open surfaces in the close vicinity to the quantum emitter, which can lead to significant dephasing and spectral wondering of the QD emission line. This is partly reflected in emitter line broadening [16, 17], limitations of the QD single photon interference properties [15] and fast spin dephasing [31].

13.4 Emission of Single and Indistinguishable Photons from Single Quantum Dots

13.4.1 Single Photon Emission from Single QDs

In our experiment, we tested three different optical excitation method for single-photon generation from QDs, as sketched in Fig. 13.4. The most conventional method is non-resonant excitation by pump laser with an energy above the band gap (in the barrier or the wetting layer surrounding the QDs, sketched in Fig. 13.4a). These carriers can then be captured by the QD and relax to the ground state via phonon scattering, from where they can decay radiatively. In order to facilitate local generation of excitons in the QD and to reduce possibly detrimental effects from the surrounding, carriers can as well be generated quasi-resonantly in the excited states of the QD (Fig. 13.4b). These states are typically located 20–50 meV on the high-energy side of the exciton ground state in the QD, facilitating spectral filtering of the excitation laser from the collected signal in most cased. The relaxation from the p-shell to the ground state of the QD typically occurs on the ten picoseconds scale [6, 34], which leads to a strong reduction of time jitter in the emission.

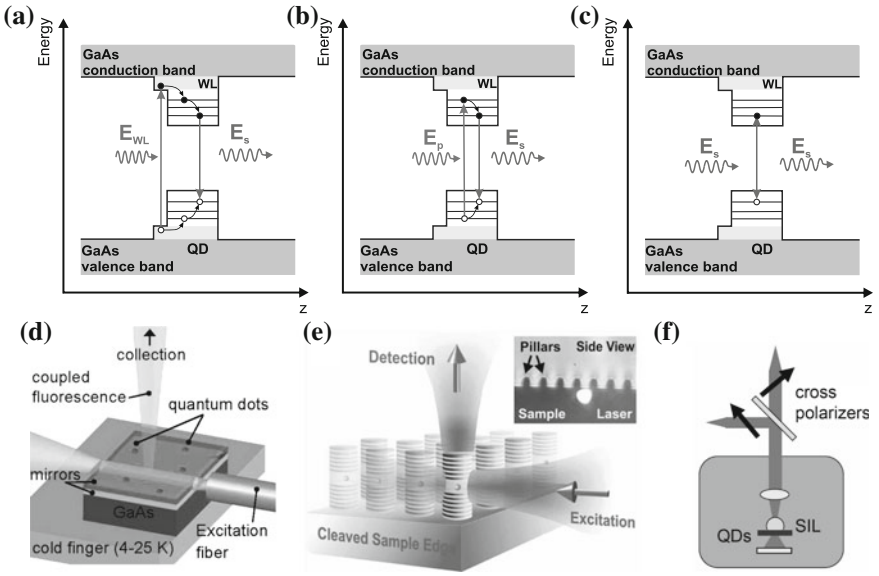

Fig. 13.4 Excitation configurations of a single QD: **a** Non-resonant wetting layer excitation creates carriers in the surrounding of the QD, which relax into the ground state by scattering. **b** Quasi-resonant excitation leads to a direct excitation of the QD without generating a carrier reservoir. **c** Resonance fluorescence selectively excites the QD ground state. For suppression of back scattered laser light in resonance fluorescence, the pathways for excitation and photon collection can be separated in the experimental implementation by an orthogonal arrangement for planar waveguides (**d**) and micropillars (**e**). **f** Sketch for the cross-polarization configuration facilitating resonance fluorescence measurements under normal incidence. **d** and **e** are reproduced from Muller et al. [32] and Ates et al. [33]

The third pump-configuration is strictly resonant excitation (resonance fluorescence), a method widely used in standard atomic physics experiments (Fig. 13.4c). Here, the excitation laser tuned on resonance with the QD transition coherently excites the QD. This excitation condition is by far the hardest to implement, since it requires a careful distinction between QD signal and laser stray light. Spectral filtering of the pump-laser is no longer feasible in strictly resonant excitation conditions, hence other methods have to be applied to isolate the QD emission signal: spatial filtering is one option, when the pump-laser is exciting the QD in the perpendicular direction to the collection beam-path (Fig. 13.4d). This technique was first employed in Bragg waveguides and led to the first successful demonstration of resonance fluorescence from a single QD [32, 35]. Strictly resonant excitation perpendicular to the photon collection direction has also been carried out on single micropillar cavities with sufficiently strong suppression of scattered laser light facilitating two photon interference studies [33]. Another technique is polarization filtering: Here, the excitation laser is linearly polarized, and in case the reflected laser beam preserves this polarization, the QD emission can be detected in the perpendicular polarization basis [36]. In our

confocale microscope setup, the polarization extinction of the pump laser can reach values in excess of 10^7 which allows us to carry out correlation measurements in the resonance fluorescence configuration [37].

Figure 13.5a depicts a photoluminescence spectrum recorded under non-resonant excitation condition. The spectrum is characterized by a pronounced emission feature which is attributed to the neutral exciton emission from a single QD via its spectral properties (such as polarization and power dependency). In the close spectral vicinity we detect a number of other lines, possibly stemming from different charge configuration of the same QD or from neighboring QDs. In the following, we will focus on the characteristics from the brightest transition: The corresponding second order autocorrelation function recorded from this line is shown in Fig. 13.5b, recorded under pulsed excitation with a repetition frequency of 82 MHz. During each excitation pulse, carriers are excited non-resonantly in the wetting layer of the QDs, which is reflected in the distance between the peaks in the correlation histogram. As expected from a single quantum emitter, at $\tau = 0$ the coalescence probability is strongly suppressed and a dip occurs in the histogram. The corresponding $g^{(2)}(\tau = 0)$ value of 0.05 is a clear signature of single photon emission.

However, as a result of the non-resonant excitation, a large number of carriers is generated in the surrounding of the QD during one excitation pulse. If the lifetime of this reservoir exceeds the average recombination time of the QD trion, carriers can re-excite the QD after the first recombination event, which leads to a strong broadening of the peaks in the correlation histogram.

This effect is largely suppressed when the QD is quasi-resonantly excited into an excited state: In Fig. 13.5c we plot the photoluminescence spectrum of a QD which is excited with a laser detuning of 29 meV on the high energy side of the recombination line. Stray-light from the excitation laser is spectrally suppressed by a combination of bandpass filters. Due to the quasi-resonant nature of the excitation, the spectrum is almost background free and a single bright emission line dominates the spectrum over a wide range. More importantly, the effects of strong time jitter and carrier recapturing are suppressed in the corresponding correlation histogram (Fig. 13.5d) and the width of the coincident peaks in the histogram are now determined by the lifetime of the excitonic transition with a characteristic time of 700 ps, which is in good agreement with the time resolved PL trace (inset of Fig. 13.5c). This effective reduction of the measured lifetime (compared to inset of Fig. 13.5a) is again consequence of the absence of carrier recapturing under quasi-resonant excitation. The purity of the source is even improved, as characterized by a value of $g^2(\tau = 0) = 0.023$ which was directly extracted from the raw data without any background correction.

A truly coherent, time-jitter free excitation method made use of an ultrafast (3 ps) pulsed laser with its central frequency resonant with the QD transition. In Fig. 13.5e we plot a spectrum of the QD-emission signal under such resonance flourescence (RF) conditions. The narrow emission line stemming from the driven QD resonance sits on top of a broad, yet dim background from the pump laser (plotted in log-scale). The much broader laser background can be further filtered using a narrow-band etalon, resulting in a signal to background ratio exceeding 300:1 [37]. The QD emission intensity is plotted as a function of the square root of the pump power

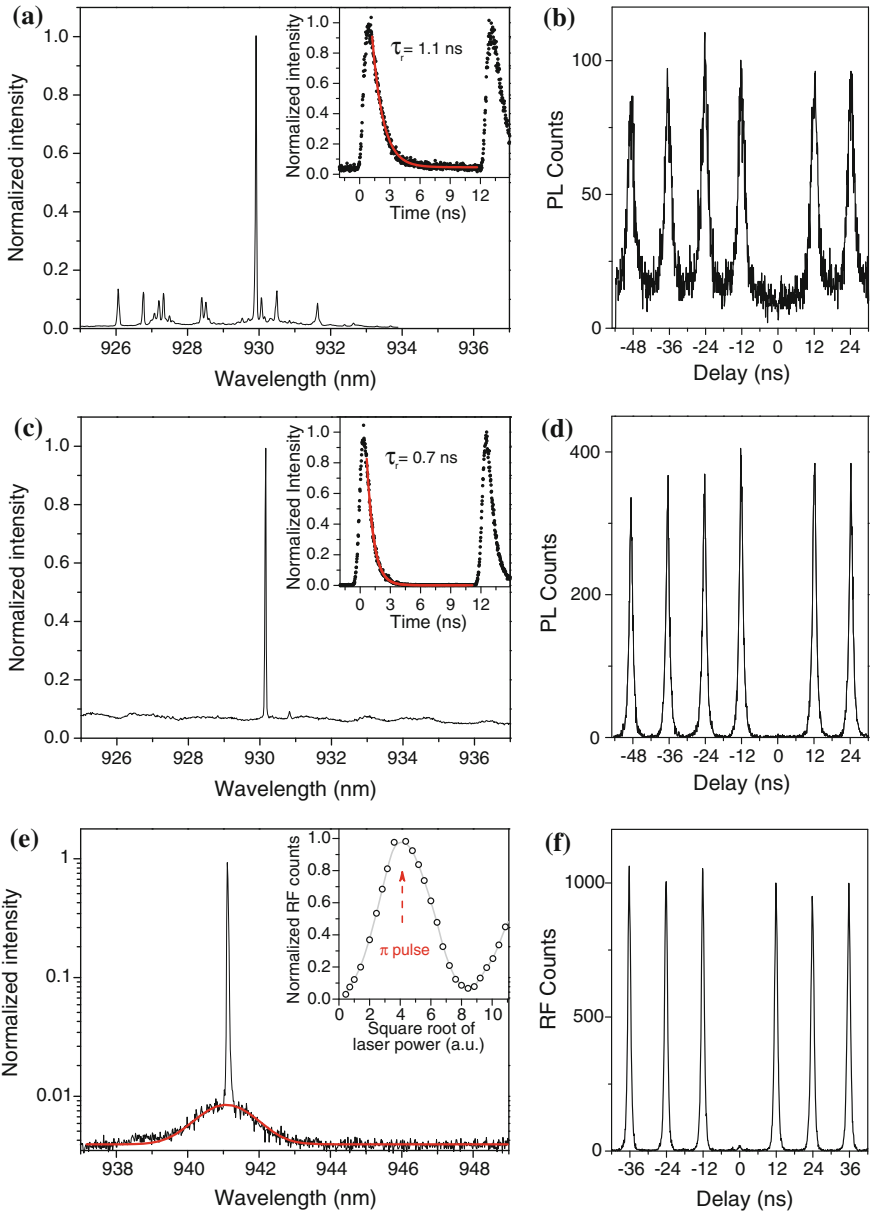

Fig. 13.5 **a** Photoluminescence (*Inset* Time resolved PL) signal of a QD under non-resonant excitation; **c** quasi-resonant excitation; **e** resonance fluorescence. The inset in **e** depicts the power dependency of the emission under pulsed resonance fluorescence, which is characterized by the occurrence of distinct Rabi-oscillations. Corresponding second order correlation histograms: **b** non-resonant pumping, **d** p-shell excitation; **f** resonance fluorescence

of the excitation laser in the inset of Fig. 13.5e: The observed Rabi-oscillations are characteristic for a resonantly driven two-level system and reflect the coherent nature of the excitation process. Single RF photons are deterministically generated at the peak maximum, which corresponds to a π-pulse in the picture of driven Rabi-oscillations. The according second order correlation measurement under these conditions is shown in Fig. 13.5f. The second order autocorrelation function can reach values as low as $g^2(\tau = 0) = 0.003$, pointing out the character of our single QD as a almost perfect single photon source [38].

13.4.2 Two Photon Interference with Single Photons

The combination of high brightness and high purity of the single photon emission allows us to carry out photon interference measurements with the experimental configuration briefly described in Sect. 13.2 and in Chap. 2 by Lanco and Senellart.

First, we study the two-photon interference (TPI) of consecutive photons emitted from a single QD, to scrutinize the dependency of the interference visibility on the excitation condition. Therefore, we adjust the path length difference of the two arms in our Mach-Zehnder interferometer to the laser repetition period of 12.2 ns (see Fig. 13.1d), so that two consecutively excited photons can coincide at the same time on the beam-splitter. Additionally, there is the possibility to change the time delay between the two arms of the interferometer via a variable optical fiber delay.

We first study the TPI of consecutive emitted photons under wetting layer excitation. As we have discussed above, the very long diffusion lengths of our sample lead to a recapturing of charge carriers after a first recombination. This recapturing results in a background in the autocorrelation histogram at $|\tau| > 0$. The corresponding correlation histogram for the TPI of consecutive emitted photons at an interferometer path length difference of $\Delta t \approx 0$ is shown in Fig. 13.6a. Fitting the data with a model based on [22] yields a visibility of only 12 %. This small value is a result of the very large time uncertainty induced by the long emission time induced from the carrier recapturing, which makes a simultaneous collision of two photons on the beam splitter very unlikely.

As a direct comparison, in Fig. 13.6b the second order correlation function for TPI is shown for zero path length difference for a QD under p-shell excitation. Here, the peak at $\tau = 0$ is strongly suppressed below a value of 0.5. The probability for two photons that coincide at the beamsplitter and exit in opposite directions $g^{(2)}_{indist}(\tau = 0)$ is given by the area under the peak at $\tau = 0$ divided by the averaged area of four peaks for $|\tau| > \pm 12.2$ ns. From the raw data we extract values of $g^{(2)}_{indist} = 0.16 < 0.5$, verifying the indistinguishability of the photons generated under quasi resonant pumping. In order to accurately extract the visibility of the two photon interference,

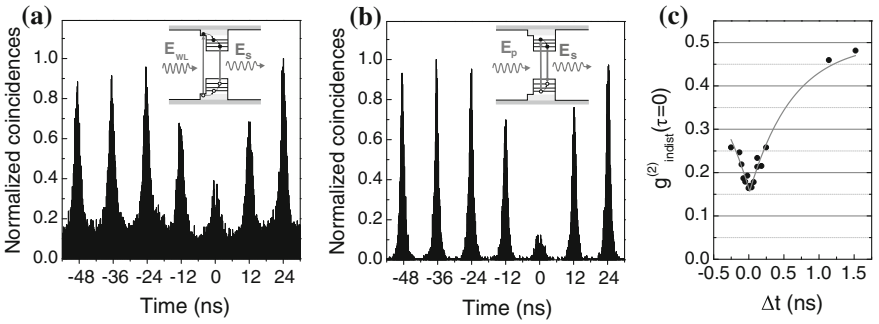

Fig. 13.6 **a** Two photon interference histogram for a QD. The emitter is non-resonantly excited into the wetting layer. **b** TPI under p-shell excitation. **c** The Hong-Ou-Mandel dip evolves when the TPI visibility is plotted against the delay time Δt

we investigate $g^{(2)}_{indist}(\tau = 0)$ in dependence of interferometer path length offset Δt. In this manner, we observe the characteristic Hong-Ou-Mandel dip for $\Delta t = 0$. Via fitting the data with a two sided exponential $g^{(2)}_{indist}(\Delta t) = 0.5[1 - ve^{(-|\Delta t|/\tau_m)}]$ we can extract a non-postselected value of TPI visibility v of 69%. This value is comparable to the values of QDs embedded in micropillar cavities [6, 15], where the Purcell effect is employed to reduce the radiative decay time τ_r and hence improve $\frac{\tau_c}{2\tau_r}$. The visibility under quasi resonant excitation is strongly increased compared to the non-resonant excitation scheme resulting from the direct excitation conditions which lead to a reduced uncertainty in the emission time, a lack of carrier re-capturing processes and reduced charge carriers in the wetting layer. For an ideal spontaneous-emission source, with instantaneous initial excitation and no decoherence, τ_m which characterizes the arrival time of photons on the beam splitter would be equal to the spontaneous emission lifetime of the quantum emitter. From the fit we get values of $\tau_m = 630$ ps which indeed is close to the spontaneous emission lifetime of this QD (see inset Fig. 13.5c).

Ideally, in order to obtain maximum degrees of indistinguishability, Fourier-transform limited sources are required. As we have assessed in Sect. 13.2, the relation between coherence time τ_c and lifetime of the QD emission τ_r, that describes the visibility of TPI is $v_{max} = \frac{\tau_c}{2\tau_r} = 1$. In order to directly assess the coherence time of the QD emission under p-shell excitation, we use a Michelson interferometer, and measure the photon interference signal as a function of the variable time delay (see [5] for details on the method). The fringe contrast in dependence of interferometer path length difference is shown in Fig. 13.7a. The fine structure splitting of the neutral exciton line leads to oscillations in the interference fringe contrast. From a fit (red solid line) to the experimental data with the Fourier transform of two Lorentzians we can extract the coherence times of the fine structure split lines $\tau_{c1} = 330$ ps and $\tau_{c2} = 180$ ps. Compared with the extracted decay time $\tau_r = 670$ ps we can extract a maximum visibility for TPI in this case of 25 %.

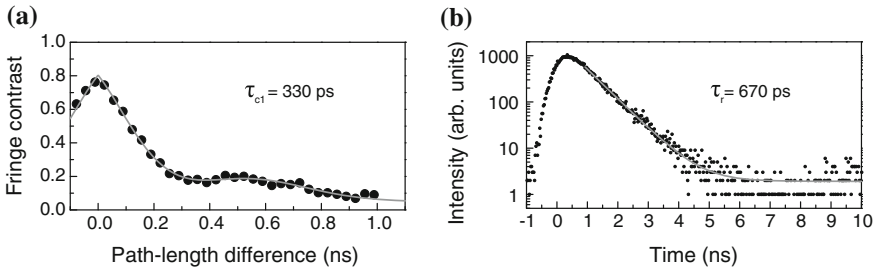

Fig. 13.7 **a** Coherence time and **b** decay time of the QD characterized in Fig. 13.6

This seeming discrepancy to the extracted value of 69 % has been observed before [6] and can be explained by a primary inhomogeneous broadening of the emission lines, for example by charge fluctuations in the vicinity of the QD. These fluctuations can take place on a timescale much longer than the laser repetition frequency, and are hence not affecting the TPI measurement, since only the interference from consecutive photons is measured. On the other hand, in the time averaged Michelson experiment, the interference of photons emitted at much larger time delays contribute, which explains the reduced coherence times. As we will show in the following chapter, however, this argument is no longer true if photons from independent sources are interfered, which asks for the capability to generate photons close to the Fourier limit.

To generate such photons and increase the visibility of the TPI, we study a QD under pulsed resonance fluorescence conditions. In this experiment, each excitation pulse of the pumplaser is split into two pulses with a delay of 2 ns, generating two single photons each 12.5 ns (see Fig. 13.8a). The according correlation histogram from the TPI experiment is depicted in Fig. 13.8b, c. If we combine photons with opposite polarizations on the last beam splitter, we observe the correlation histogram of two perfectly distinguishable photons depicted in Fig. 13.8b, featuring a central peak at $\tau = 0$ with the same magnitude as the neighboring peaks stemming from photons with a time difference of 2 ns. If photons with the same polarization are combined on the beam splitter (Fig. 13.8c) the strong suppression of the central peak indicates the high degree of indistinguishability of the photons generated under these conditions. By evaluating the areas under the coincidence peaks, we can directly extract a raw TPI visibility as high as 91 %, clearly exceeding the value for quasi-resonant excitation. A more recent experiment used adiabatic rapid passage to deterministically and more robustly generate single photons and demonstrated a new record of two-photon interference raw visibility of about 98 % [38]. The strong increase of the TPI for resonance fluorescence clearly underlines the superiority of this excitation scheme, and points towards the possibility to deterministically generate single photons close to the Fourier-limit.

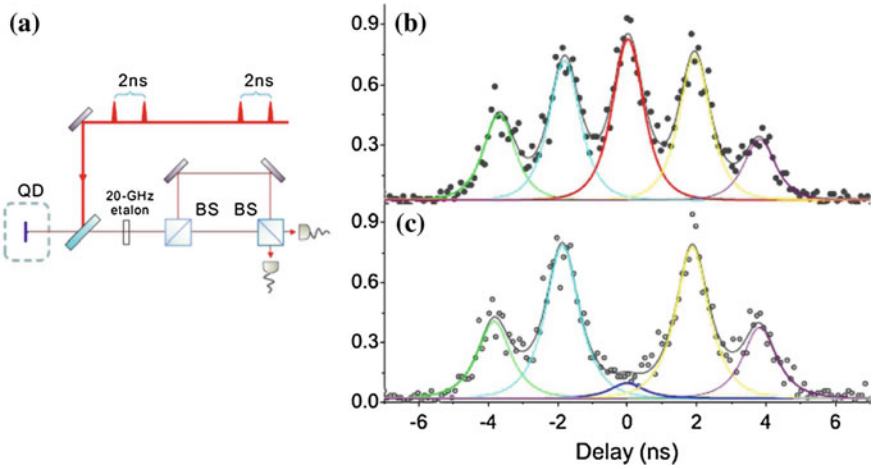

Fig. 13.8 Photon interference spectroscopy in the resonance fluorescence configuration: **a** Sketch of the optical setup: Each pulse of the excitation laser is split into two pulses with a time delay of 2 ns, resulting in a two-fold excitation of the same QD. The fluorescence is fed into a Hong-Ou-Mandel setup, and the RF-photons are recombined on the second beamsplitter. **b** Interference histogram with photons of perpendicular polarizations and **c** photons of the same polarization. The absence of the peak at $\tau = 0$ demonstrates highly indistinguishable photons

13.5 Two Photon Interference from Remote, Single Quantum Dots

The very high TPI visibilities which we have discussed in the previous section puts the observation of pronounced TPI effects from photons emitted from separate sources clearly within reach. Such interference effects have previously been observed under non-resonant exictation conditions [39, 40], or under CW resonant fluorescence excitation resulting in time post selecting [41]. For realistic applications, the non-postselected value of the TPI is however of greater importance, which can only be probed under pulsed excitation conditions. In order to carry out this experiment, we have installed two QD samples in separate cryostats and identified individual QDs with similar emission frequencies and coherence properties as the QD characterized in Fig. 13.6c. Both QDs were excited quasi-resonantly with the same pulsed excitation laser, and the emission was combined on a polarizing beam splitter before it was fed into the Mach-Zehnder interferometer (see Fig. 13.1a). In order to probe the two photon interference from separate QDs, the emitters have to be tuned to spectral resonance. A number of tuning mechanisms are possible, including electric fields [40], strain [39] or magnetic fields [42]. In our experiments, we utilize the sample temperature to spectrally tune the QD energies to resonance. Since the temperature in the cryostats cannot be varied in a wide range without detrimentally affecting the QD emission properties, a pair of QDs was selected with an energy difference as small as 3 μeV. The emission energies could then be equalized by changing the temperature

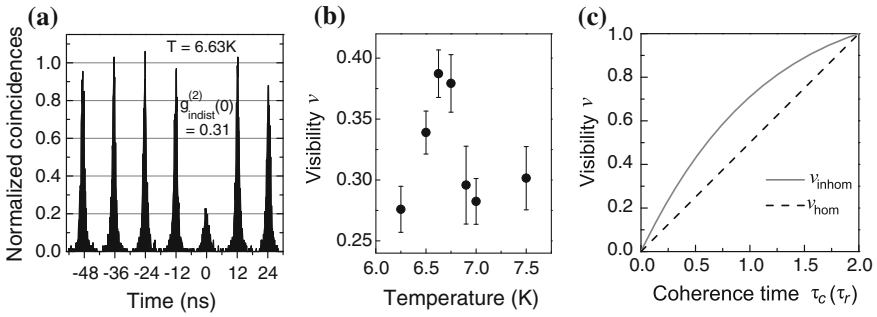

Fig. 13.9 Two photon interference of QDs emitted from separate sources. The QD samples are mounted in separate cryostats with an overall spatial separation of 0.5 m. **a** Interference histogram under spectral resonance. The QDs are tuned into resonance via adjusting the sample temperature. **b** Dependency of the two photon interference visibility on the spectral detuning of the QDs. **c** Theoretical maximum of the indistinguishability as a function of the QD coherence time (in relation to the decay time τ_r), under consideration of homogeneous (*dashed line*) and inhomogeneous (*solid line*) broadening mechanisms

of one sample by only 1.8 K, which should only minorly affect coherence properties of the emission.

The second order correlation function for TPI from separate sources is shown in Fig. 13.9a for QD1 at 5.00 K and QD2 at 6.75 K. We determine the opposite output probability $g^{(2)}_{indist}(\tau = 0)$ from the raw data by the area of the peak at $\tau = 0$ divided by the averaged area of 6 peaks for $|\tau| > 0$. From the data we extract $g^{(2)}_{indist}(\tau = 0) = (0.31 \pm 0.01)$, which verifies that the photons from the two QDs have a nonzero coalescence probability. The according TPI visibility amount to $v = (39 \pm 2)\,\%$, which is the highest value of non-postselected two photon interference from separate QDs observed so far under quasi- or nonresonant excitation conditions. By varying the sample temperature in one cryostat, we can tune the QDs out of resonance, which is directly reflected in a reduced two photon interference visibility, as depiced in Fig. 13.9b.

We will now compare these experimentally observed values with a theory which only takes into account pure dephasing as a decoherence mechanism. As we have described in Sect. 13.2, in the presence of pure dephasing limiting the coherence time $\frac{1}{\tau_c} = \frac{1}{2\tau_r} - \frac{1}{\tau_{deph}}$ the maximum visibility of the TPI is obtained for $v = \frac{\tau_c}{2\tau_r}$. Taking into account the experimentally extracted radiative decay time of 670 ps (Fig. 13.7b) and coherence time of 330 ps (Fig. 13.7a), we can infer a maximum interference visibility of 25 %, which is clearly exceeded in our experiment. For two photons emitted from the same QD, we argued that frequency jitter on a time scale beyond the repetition time of the pulsed excitation laser led to a reduction of the coherence time which was however only weakly affecting the interference visibility from consecutive photons. For photons emitted from independent sources, clearly this argumentation is not valid. In order to take account for the effects of inhomogeneous broadening in the evaluation of the TPI, various frequency components have to be taken into

account. We follow the analysis by Legero et al. (see chapters by A. Kuhn, and Zhao, Bao, Zhao and Pan of this book and [43]) to derive an expression for the visibility of TPI in the presence of inhomogeneous broadening represented by a Gaussian frequency distribution. We assume that the two photons which interfere at the beam splitter originate from independent ensembles of Fourier transform limited photons. The Fourier limited single-photon wave packets for QD1 and QD2 are one sided exponential functions:

$$\xi_1(t) = \begin{cases} \sqrt[4]{\frac{1}{\pi\tau_r}} e^{-\frac{t-\frac{\delta\tau}{2}}{2\tau_r} - i\left(\omega - \frac{\Delta}{2}\right)t} & \text{if } t - \frac{\delta\tau}{2} > 0 \\ 0 & \text{otherwise} \end{cases} \tag{13.2}$$

and

$$\xi_2(t) = \begin{cases} \sqrt[4]{\frac{1}{\pi\tau_r}} e^{-\frac{t+\frac{\delta\tau}{2}}{2\tau_r} - i\left(\omega + \frac{\Delta}{2}\right)t} & \text{if } t + \frac{\delta\tau}{2} > 0 \\ 0 & \text{otherwise} \end{cases}, \tag{13.3}$$

where $\delta\tau$ is the time delay and Δ the frequency difference between them. An inhomogeneous broadening of the emission lines can be considered by a Gaussian frequency distribution $f(\omega)$ with σ^2 being the variance:

$$f_{i=1,2}(\omega_i) = \frac{1}{\sqrt{\pi}\, 2\sigma_i} e^{-\frac{(\omega_{0i} - \omega_i)^2}{2\sigma_i^2}}. \tag{13.4}$$

With $\omega_1 = \omega$ and $\omega_2 = \omega + \Delta$ we get the frequency distribution as a function of the frequency difference Δ

$$f(\Delta) = \int \mathrm{d}\omega\, f_1(\omega) f_2(\omega,\ \Delta) = \frac{1}{\sqrt{\pi}\, 2\sigma_g} e^{-\frac{(\Delta - \Delta_0)^2}{4\sigma_g^2}}, \tag{13.5}$$

with $\sigma_g = \sqrt{\sigma_1^2 + \sigma_2^2}$ and $\Delta_0 = \omega_{02} - \omega_{01}$. The correlation function is then given by

$$G^{(2)}_{\text{inhom}}(t_0,\ t_0 + \tau) = \int \mathrm{d}\Delta\, f(\Delta)\, \mathrm{tr}\left(\hat{\rho}(\xi_1, \xi_2)\, \hat{A}(t_0,\ t_0 + \tau)\right), \tag{13.6}$$

where $\mathrm{tr}\left(\hat{\rho}(\xi_1, \xi_2)\, \hat{A}(t_0,\ t_0 + \tau)\right)$ is the correlation function for two Fourier transform limited photons with the same polarization:

$$G^2_{\text{TL}}(t_0, t_0 + \tau) = \frac{|\xi_1(t_0)\xi_2(t_0 + \tau) - \xi_2(t_0)\xi_1(t_0 + \tau)|^2}{4} \tag{13.7}$$

Finally, the probability for detecting a photon at time $t_0 + \tau$ in one output of the beam splitter while a photon is detected at time t_0 in the other one for inhomogeneous broadened ensembles of photons is given by

$$\begin{aligned} P_{\text{inhom}} &= \int_{-\infty}^{\infty} \mathrm{d}t_0 \, G^{(2)}_{\text{inhom}}(t_0,\, t_0 + \tau) \\ &= \frac{1}{8\tau_r} \left(e^{-\frac{|\delta\tau - \tau|}{\tau_r}} + e^{-\frac{|\delta\tau + \tau|}{\tau_r}} - 2\cos(\Delta_0\,\tau)\, e^{-\frac{|\delta\tau| + |\tau|}{\tau_r}}\, e^{-\sigma_g^2 \tau^2} \right) \end{aligned} \tag{13.8}$$

From this expression, we yield an expression for the two photon interference visibility for $\delta\tau = 0$ and $\Delta_0 = 0$, only depending on the radiative decay time τ_r and the geometric average of the broadening of the two photon ensembles $\sigma_g = \sqrt{\sigma_1^2 + \sigma_2^2}$:

$$\nu_{\text{inhom}} = 1 - \frac{1}{\tau_r \sigma_g} \left(2\tau_r \sigma_g - e^{\frac{1}{4\tau_r^2 \sigma_g^2}} \sqrt{\pi}\,\text{erfc}\left(\frac{1}{2\tau_r \sigma_g} \right) \right) \tag{13.9}$$

In Fig. 13.9c we plot the maximum TPI of such inhomogeneously broadened wave packets as a function of the coherence time (in multiples of the lifetime τ_r), to visualize the strong influence of the broadening's origin on the maximum interference visibilty. From this analysis, we can estimate a maximum visibility of $\nu_{inhom} = (36.4 \pm 1.5)\%$ which is in good agreement with the experiment. This underlines the importance of effects as spectral wandering, time jitter and other inhomogeneous broadening channels in particular for photon interference experiments from independent sources. It is worth noting, that major improvements have recently been accomplished by utilizing resonance fluorescence conditions in such an experiment. Due to the suppression of inhomogeneous broadening effects under strict resonant excitation, two photon interference visibilities beyond 80 % [14, 44] were obtained.

13.5.1 Conclusion

Single semiconductor quantum dots have been established as compact single photon sources on a solid state platform. Towards the implementation of these quantum emitters as sources of highly indistinguishable photons, which is key to realize quantum teleportation schemes and highly desired quantum repeaters, the degree of indistinguishability of the photon emission is a key parameter. As we have reviewed in this chapter, besides utilizing the effects of cavity quantum electrodynamics to modify the radiative decay time of the photon emission, the appropriate excitation scheme plays a crucial role to realize high degrees of indistinguishabilities. In particular resonance fluorescence conditions can be considered as a reliable technique

to generate single photons near unity indistinguishability. We highly anticipate that a combination of such sophisticated pumping schemes and the exploitation of light matter coupling effects can lead to even further simultaneous improvements of the photon coupling efficiencies and degrees of indistinguishability, which makes single QDs an truly appealing alternative to cold atoms and ions towards the realization of quantum repeaters.

Acknowledgments The authors acknowledge the great support of the following persons throughout the last years: S. Maier, A. Thoma, Y. He, Y.-M. He, N. Gregersen, J. Mork, J. Schary, M. Lermer, M. Wagenbrenner, L. Worschech, S. Reitzenstein and A. Forchel. We acknowledge financial support by the BMBF (Projects QuaHLRep and Q.com-H) as well as the state of Bavaria.

References

1. P. Michler et al., A quantum dot single-photon turnstile device. Science **290**, 228 (2000)
2. Z.L. Yuan et al., Electrically driven single-photon source. Science **295**, 102–105 (2002)
3. T. Heindel et al., Electrically driven quantum dot-micropillar single photon source with 34% overall efficiency. Appl. Phys. Lett. **96**, 011107 (2010)
4. P. Michler, *Single Quantum Dots* (Springer, Heidelberg, 2003)
5. P. Michler, *Single Semiconductor Quantum Dots* (Springer, Heidelberg, 2009)
6. C. Santori, D. Fattal, J. Vuckovic, G.S. Solomon, Y. Yamamoto, Indistinguishable photons from a single-photon device. Nature **419**, 594–597 (2002)
7. J.W. Pan et al., Multiphoton entanglement and interferometry. Rev. Mod. Phys. **84**, 777 (2012)
8. P. Kok et al., Linear optical quantum computing with photonic qubits. Rev. Mod. Phys. **79**, 135–174 (2007)
9. J.L. O'Brien, Optical quantum computing. Science **318**, 1567–1570 (2007)
10. H.J. Briegel, W. Dur, J.I. Cirac, P. Zoller, Quantum repeaters: the role of imperfect local operations in quantum communication. Phys. Rev. Lett. **81**, 5932–5935 (1998)
11. J. Hofmann et al., Heralded entanglement between widely separated atoms. Science **337**, 72–75 (2012)
12. J.I. Cirac, P. Zoller, H.J. Kimble, H. Mabuchi, Quantum state transfer and entanglement distribution among distant nodes in a quantum network. Phys. Rev. Lett. **78**, 3221–3224 (1997)
13. J. Nilsson et al., Quantum teleportation using a light-emitting diode. Nat. Photonics **7**, 311–315 (2013)
14. W.B. Gao et al., Quantum teleportation from a propagating photon to a solid-state spin qubit. Nat. Commun. **4**, 2744 (2013)
15. O. Gazzano et al., Bright solid-state sources of indistinguishable single photons. Nat. Commun. **4**, 1425 (2013)
16. J. Claudon et al., A highly efficient single-photon source based on a quantum dot in a photonic nanowire. Nat. Photonics **4**, 174–177 (2010)
17. M.E. Reimer et al., Bright single-photon sources in bottom-up tailored nanowires. Nat. Commun. **3**, 737 (2012)
18. C. Bennett, G. Brassard, Quantum cryptography: public key distribution and coin tossing. Proc. IEEE Int. Conf. Comput. Syst. Signal Process. **175**, 8 (1984)
19. E. Waks et al., Secure communication: quantum cryptography with a photon turnstile. Nature **420**, 762–762 (2002)
20. T. Heindel et al., Quantum key distribution using quantum dot single-photon emitting diodes in the red and near infrared spectral range. New J. Phys. **14**, 083001 (2012)
21. C.K. Hong, Z.Y. Ou, L. Mandel, Measurement of subpicosecond time intervals between 2 photons by interference. Phys. Rev. Lett. **59**, 2044–2046 (1987)

22. J. Bylander, I. Robert-Philip, I. Abram, Interference and correlation of two independent photons. Eur. Phys. J. D **22**, 295–301 (2003)
23. S. Maier et al., Bright single photon source based on self-aligned quantum dot-cavity systems. Opt. Sxpress **22**, 8136–8142 (2014)
24. J.M. Garcia et al., Intermixing and shape changes during the formation of InAs self-assembled quantum dots. Appl. Phys. Lett. **71**, 2014–2016 (1997)
25. O. Schmidt, *Lateral Alignment of Epitaxial Quantum Dots* (Springer, Berlin, 2009)
26. C. Schneider et al., Single site-controlled in(ga)as/gaas quantum dots: growth, properties and device integration. Nanotechnology **20**, 434012 (2009)
27. J.M. Zajac, W. Langbein, Structure and zero-dimensional polariton spectrum of natural defects in GaAs/AlAs microcavities. Phys. Rev. B **86**, 195401 (2012)
28. P. Royo, R.P. Stanley, M. Ilegems, Planar dielectric microcavity light-emitting diodes: analytical analysis of the extraction efficiency. J. Appl. Phys. **90**, 283–293 (2001)
29. F. Ding, T. Stoeferle, L.J. Mai, A. Knoll, R.F. Mahrt, Vertical microcavities with high q and strong lateral mode confinement. Phys. Rev. B **87**, 161116 (2013)
30. W.L. Barnes et al., Solid-state single photon sources: light collection strategies. Eur. Phys. J. D **18**, 197–210 (2002)
31. D. Press et al., Ultrafast optical spin echo in a single quantum dot. Nat. Photonics **4**, 367–370 (2010)
32. A. Muller et al., Resonance fluorescence from a coherently driven semiconductor quantum dot in a cavity. Phys. Rev. Lett. **99**, 187402 (2007)
33. S. Ates et al., Post-selected indistinguishable photons from the resonance fluorescence of a single quantum dot in a microcavity. Phys. Rev. Lett. **103**, 167402 (2009)
34. E.B. Flagg, S.V. Polyakov, T. Thomay, G.S. Solomon, Dynamics of nonclassical light from a single solid-state quantum emitter. Phys. Rev. Lett. **109**, 163601 (2012)
35. E. Flagg et al., Resonantly driven coherent oscillations in a solid-state quantum emitter. Nat. Phys. **5**, 203–207 (2009)
36. A.N. Vamivakas, Y. Zhao, C.-Y. Lu, M. Atatüre, Spin-resolved quantum-dot resonance fluorescence. Nat. Phys. **5**, 198–202 (2009)
37. Y.M. He et al., On-demand semiconductor single-photon source with near-unity indistinguishability. Nat. Nanotechnol. **8**, 213–217 (2013)
38. Y.-J. Wei et al., Deterministic and robust generation of single photons on a chip with 99.5% indistinguishability using rapid adiabatic passage (2014). arXiv preprint arXiv:1405.1991
39. E.B. Flagg et al., Interference of single photons from two separate semiconductor quantum dots. Phys. Rev. Lett. **104**, 137401 (2010)
40. R.B. Patel et al., Two-photon interference of the emission from electrically tunable remote quantum dots. Nat. Photonics **4**, 632–635 (2010)
41. K. Konthasinghe et al., Field-field and photon-photon correlations of light scattered by two remote two-level inas quantum dots on the same substrate. Phys. Rev. Lett. **109**, 237403 (2012)
42. S. Reitzenstein et al., Control of the strong light-matter interaction between an elongated $In_{0.3}Ga_{0.7}As$ quantum dot and a micropillar cavity using external magnetic fields. Phys. Rev. Lett. **103**, 127401 (2009)
43. T. Legero, T. Wilk, A. Kuhn, G. Rempe, Characterization of single photons using two-photon interference. Adv. At. Mol. Opt. Phys. **53**, 254 (2006)
44. Y. He et al., Indistinguishable tunable single photons emitted by spin-flip raman transitions in InGaAs quantum dots. Phys. Rev. Lett. **111**, 237403 (2013)

Part VII
Beyond Photons

Chapter 14
Towards Quantum Repeaters with Solid-State Qubits: Spin-Photon Entanglement Generation Using Self-assembled Quantum Dots

Peter L. McMahon and Kristiaan De Greve

Abstract In this chapter we review the use of spins in optically-active InAs quantum dots as the key physical building block for constructing a quantum repeater, with a particular focus on recent results demonstrating entanglement between a quantum memory (electron spin qubit) and a flying qubit (polarization- or frequency-encoded photonic qubit). This is a first step towards demonstrating entanglement between distant quantum memories (realized with quantum dots), which in turn is a milestone in the roadmap for building a functional quantum repeater. We also place this experimental work in context by providing an overview of quantum repeaters, their potential uses, and the challenges in implementing them.

14.1 Introduction

Self-assembled InAs quantum dots[1] can trap a single electron; when the quantum dot is in an external magnetic field, a trapped electron's spin states can be used to encode a quantum bit (qubit). Over the past decade, a series of studies [4] have shown that such a qubit can be optically initialized [6, 7], controlled [8, 9] and measured [8, 10, 11]. Measurements of the coherence time of such a qubit have shown that the time required to perform an arbitrary single qubit operation ($\sim$50 ps [8]) on the qubit is roughly five orders of magnitude shorter than the spin echo T_2 time

[1]This chapter focuses exclusively on optically-active self-assembled quantum dots, which can trap single charges (electrons or holes), as well as neutral and charged excitons. References [1–4] provide detailed reviews of how these quantum dots are formed, how they provide a photonic interface, and how they can store spin qubits. This chapter does not review any of the work in the electrostatically-defined quantum dot [5] community.

P.L. McMahon (✉)
E.L. Ginzton Laboratory and Department of Applied Physics,
Stanford University, Stanford, CA 94305, USA
e-mail: pmcmahon@stanford.edu

K. De Greve
Department of Physics, Harvard University, Cambridge, MA 02138, USA
e-mail: kdegreve@physics.harvard.edu

A. Predojević and M.W. Mitchell (eds.), *Engineering the Atom-Photon Interaction*,
Nano-Optics and Nanophotonics, DOI 10.1007/978-3-319-19231-4_14

($\sim$3 μs [12, 13]). In light of this, electron spins in quantum dots[2] are considered appealing candidates as quantum memories, and will be even more so if dynamical decoupling techniques [19, 20] can be used to further extend the coherence time. Long-distance quantum cryptography will likely require the development of quantum repeaters, as will other applications of remote entangled states. Charged quantum dots are one of several candidate technologies for building quantum repeaters, and are interesting as such because they provide both a good stationary qubit (to be used as a memory), and a fast optical interface. One of the very first steps towards building a quantum repeater using quantum dots is to show that one can generate a photonic qubit that is entangled with a spin (memory) qubit.

In this chapter, we review how quantum dots might be used to ultimately build a quantum repeater, and describe recent experiments that have demonstrated the generation of entanglement between a single photon and a quantum dot. In particular, we will review experiments that have generated and verified entanglement between the polarization or frequency state of a photon emitted by a single quantum dot, and the spin state of the electron in that quantum dot [21–23]. We also review how tomography can be performed on a spin-photon qubit pair, and describe the result in [24], which showed that quantum dots can produce spin-photon entanglement with fidelity in excess of 90 %. We provide a summary of spin-photon entanglement generation results in many different physical systems. We also address briefly some questions surrounding what work needs to happen to proceed from the present state of affairs to a functioning quantum-dot-based quantum repeater.

14.2 Quantum Repeaters

Before we discuss how optically-active quantum dots may be suitable building blocks for constructing a quantum repeater, we would like to provide a general overview of quantum repeaters. We attempt to provide answers to the following questions:

- What are quantum repeaters, and why is there substantial interest in building them?
- What are the technological requirements for building useful quantum repeaters?

[2]Incidentally, holes can also be trapped in quantum dots, and the spin of the hole can also be used as a qubit. Analogous demonstrations to those performed with electron spins have been done with hole spins, including: initialization [14–16], complete control [16, 17], optical readout [16, 17], T_2^* measurement [16–18], and T_2 (spin echo) measurement [16]. Hole spin qubits in InAs QDs have an advantage over electron spin qubits in InAs QDs: they have a much-reduced hyperfine interaction with the nuclear spin ensemble in the QD, and this results in hole spin qubits exhibiting non-hysteretic behaviour, whereas electron spin qubits suffer from a pronounced hysteresis [16]. In other words, control of electron spin qubits in this material system depends on the history of previous operations performed on it, whereas control of hole spin qubits does not require knowledge of the history; this is a significant difference when long sequences of operations are to be used.

14.2.1 Motivation for Quantum Repeaters

The main high-level motivation for research in quantum communication is the development of practical long-distance quantum cryptography. As we will explain, quantum repeaters are central to quantum communication research. Quantum cryptography can be implemented in two different ways (non-entanglement-based and entanglement-based), only one of which involves quantum networks and quantum repeaters. However, we begin with a lower-level motivation (a physics-based, rather than application-based motivation) for quantum repeaters, and provide a summary of several important protocols and proposals that are relevant to their design.

14.2.1.1 Physical Motivation for Quantum Repeaters

A simple description of the purpose of quantum repeaters is that they enable the generation and/or distribution of entangled qubit pairs over long distances; without quantum repeaters, it may be impossible to generate entangled qubit pairs at high rates over distances much greater than several hundreds of kilometers. Throughout this chapter, we will use the term quantum memories to refer to stationary qubits[3] at the network endpoints and in the quantum repeater stations. A key part of entanglement distribution protocols is how photons (generically referred to as flying qubits, and more precisely as photonic qubits) can be used to mediate the entanglement of distant quantum memories.

One of the fundamental intuitions behind the need for quantum repeaters in quantum communication is the same as the motivation for classical repeaters in classical communication: photon loss in optical fibres (or in free-space) reduces the power of the signal being transmitted [25], and without regeneration of the signal, low-error-rate, high-bandwidth communication becomes impossible. Since it is impossible to clone a single quantum mechanical state [26, 27], quantum repeaters need to use a different method than classical repeaters to transmit quantum information from one node to the next. This is one of the essential goals of entanglement swapping in quantum repeaters. Entanglement swapping in a repeater network allows an entangled qubit pair to be generated at the endpoints of the network, by linking together qubits that are initially just entangled with those at neighboring nodes. With this resource in place, teleportation [28] can be used to transmit an arbitrary qubit from one end of the network to the other.[4]

Repeaters in classical communication serve another important purpose besides just amplifying the transmitted signal: they perform error correction by recreating high-quality representations of bits from low-quality representations, since

[3]Typically implemented using matter, as opposed to light. We focus on the use of spin qubits stored in quantum dots as quantum memories.

[4]We note this use of teleportation for the sake of completing the analogy with a classical repeater network, which is used to transmit classical bits from one end of the network to the other. Quantum key distribution, i.e., quantum cryptography, typically does not make use of teleportation.

distortions caused by transmission through the optical fibre ultimately lead to bit-discrimination errors if left unchecked [29]. This purpose of classical repeaters suggests an equivalent function for quantum repeaters in quantum networks: quantum repeaters should correct decoherence in the entangled qubits before the decoherence becomes so severe that it is uncorrectable. The analogy between the error correction task of classical repeaters and quantum repeaters is, however, imperfect, for the following reason. Classical repeaters, for which the primary source of errors that need correcting are those caused by distortions to the signals (electrical or photonic) propagating between repeater sites, can be assumed to have perfect memories and completely error-free local operations on those memories. However, in a quantum network, quantum repeaters not only need to ameliorate the channel-induced decoherence to the flying qubits,[5] but also the loss in fidelity of the final stationary entangled qubits (quantum memories), which occurs for a myriad of reasons that are unrelated to the channel-induced decoherence of the photonic qubits. One of the dominant reasons is simply the natural decoherence of the physical stationary qubits, characterized by their T_2 time. Furthermore, the local quantum operations in each repeater are imperfect, and will cause reductions in fidelity when they are applied. This chapter has a focus on the interface between the stationary qubits and the flying qubits, and as we will see, the fundamental task of generating spin-photon entangled states occurs with remarkably low fidelity in most physical systems. Quantum repeaters need to compensate for all these mechanisms that result in reduced fidelity of the entangled qubit pairs.

One interesting approach to this problem is to use entanglement purification [30, 31]: this is a technique by which two lower-fidelity entangled qubit pairs can be combined (using only local operations) to produce one higher-fidelity entangled qubit pair. The initial proposals [32, 33] for quantum repeaters analyzed this approach to combating errors. However, this is not the only possibility: a large body of work on error correction for quantum computers has been developed, and much of this work is potentially relevant to quantum repeaters.[6] Several contemporary quantum repeater proposals, such as [35], explicitly call for quantum error correcting codes [36, 37] to be used as the mechanism for combating errors in quantum networks, instead of entanglement purification. Hybrid approaches, in which both quantum error correction and entanglement purification are used, have also been proposed [38].

[5] An example of channel-induced decoherence is that caused by uncontrolled birefringence in an optical fibre, when transmitting a polarization-encoded photonic qubit ($|\psi\rangle = \alpha\,|\mathrm{H}\rangle + \beta\,|\mathrm{V}\rangle$): this leads to random qubit rotations (leading to a loss of state fidelity), and polarization mode dispersion (which in turn results in the overlapping of different qubits' temporal wavepackets, and consequently a reduction in entanglement).

[6] Bennett et al. [34] showed that entanglement purification is deeply connected to quantum error correction; in particular, they showed that entanglement purification with a classical communication channel is equivalent to quantum error correction, so it is not surprising that quantum repeater protocols can in principle make use of either entanglement purification or quantum error correction protocols to distribute high-fidelity states in the presence of noise.

Table 14.1 A summary of the analogues between classical communication repeaters and quantum repeaters

Problem	Classical repeater solution	Quantum repeater solution
Channel-induced loss	Signal amplification (via regeneration)	Entanglement swapping
Channel-induced distortion	Signal regeneration	Entanglement purification/quantum error correction

The connections between the functionality of classical communication repeaters and quantum repeaters are summarized in Table 14.1.

14.2.1.2 Quantum Key Distribution and Quantum Cryptography

Over the past two decades, nearly all experimental work on implementing quantum cryptography has focused on schemes derived from one of two sources: the original BB84 protocol [39] (which does not involve entanglement) and the Ekert91 protocol [40, 41] (which does rely on entanglement). The fundamental ideas behind quantum cryptography have been well-explained in many previous review articles and books; we do not repeat them here, but recommend instead [42] and [43] as starting points for readers unfamiliar with the BB84 and Ekert91[7] protocols.

Bennett et al. showed [41] that the Ekert91 protocol is in some sense equivalent to the BB84 protocol. One might naïvely conclude that BB84 is a superior choice for practical implementation, since it calls for only a single source of unentangled flying qubits, whereas Ekert91 requires the generation of high-fidelity entangled qubit pairs. However, there is a crucial difference between BB84-based schemes and Ekert91-based schemes that we would like to emphasize here: BB84-based QKD can be achieved over long distances using classical relays that need physical security, whereas Ekert91-based QKD can be achieved over long distances using quantum repeaters that need not be secure. Given that repeaters in a fibre-based network will likely need to be placed somewhere between every 10 km and every 300 km, the advantage of not needing trusted, armed guards at every repeater station in order to ensure the integrity of the system is highly non-trivial.

Satellite-based schemes [44] largely avoid the need for repeaters, but have their own disadvantages (for example, the ease with which an attacker could perform a denial-of-service attack by simply blocking the free-space path, or by destroying the satellite). Nevertheless, practical satellite-based Ekert91 may well be implemented before fibre-and-quantum-repeater-based Ekert91, due to the extreme difficulty in implementing a practically-relevant quantum repeater. To the extent that satellite-based QKD schemes do use repeaters (for example, for dealing with the lack of a

[7] We generally refer to the version of the Ekert91 protocol described by Bennett et al. [41].

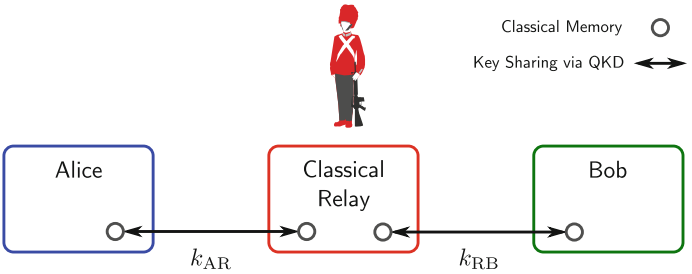

Fig. 14.1 Quantum Key Distribution using a Classical Relay. If a key k_{AR} is shared between Alice and a relay, and another key k_{RB} is shared between the relay and Bob, then a secure message can be sent from Alice to Bob, assuming that the relay site is secured. Classical relays are much simpler to build than quantum repeaters, since they only need classical memories. All relays must however be secured, otherwise the privacy of the communications between Alice and Bob cannot be guaranteed

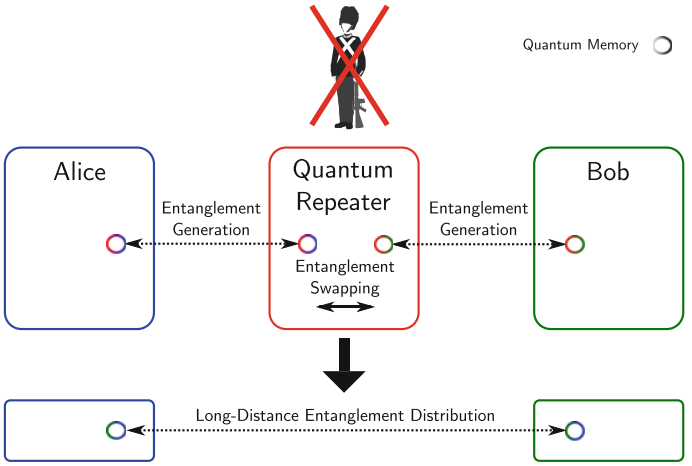

Fig. 14.2 Entanglement Distribution using a Quantum Repeater. Quantum key distribution without the need for secured relays is made possible by the use of a quantum repeater network, which can distribute entanglement between the endpoints (Alice and Bob), and an entanglement-based QKD protocol (Ekert91, or derivatives thereof). If an eavesdropper disturbs even one of the quantum repeater stations or links, and attempts to gain information about the key being distributed, this disturbance will be detectable (unlike with the classical relay scheme)

direct free-space path from one side of the earth to the other), our descriptions of classical relays and quantum repeaters, and the potential role of QDs in building these quantum communication technologies, remain relevant (Figs. 14.1 and 14.2).

14.2.1.3 Long-Distance Quantum Key Distribution with Classical Relays

Scarani et al. [45] provide a comprehensive review of the derivatives of the original BB84 protocol that have been developed over the past 20 years as a result of the challenges in making single-photon sources and in transmitting polarization-encoded qubits over substantial distances without decoherence. In Sect. VIII.A.5 of [45], they provide a very brief summary of the use of classical relays to extend the distances over which quantum key distribution can work.

The idea of a classical relay for QKD is very simple. Suppose we have distant stations for Alice (A), Bob (B), and a relay (R). We begin by having A and R share a secret key k_{AR} (using, for example, BB84), and having R and B share a (different) secret key k_{RB}. There are now two main options—Option 1, as described in [45, 46]: if Alice wants to send a secure message to Bob, she can encrypt the message using the key k_{AR}, the relay can decrypt the message (using the key k_{AR}), then re-encrypt the message using key k_{RB}, and send the encrypted message to Bob, who can decrypt the message. In this option, the QKD relay stores both keys and is involved in transmitting the actual message. Option 2, as described in [46–48] and implemented in the Vienna QKD network [48]: alternatively the relay can use the key k_{RB} to encrypt a message consisting of the key k_{AR} (which is the key Alice holds), and send this message to Bob, who can decrypt it using the key k_{RB}. Bob thus ends up with the key k_{AR}, and so a secret key (k_{AR}) has been distributed between Alice and Bob, via the relay. Alice and Bob can then communicate using this key over whatever classical channel they like. In this option, the QKD relay is only ever used to transfer keys.

As we have noted, the classical relay strategy given here does not depend on the method used to share the private keys between stations A and R, and between stations R and B.

14.2.1.4 Long-Distance Quantum Key Distribution Using Ekert91 and Quantum Repeaters

A quantum repeater is a device that allows for the distribution of entangled qubits over distances that are beyond the limits imposed by loss and decoherence when considering sending qubits directly from one node (Alice) to another node (Bob). The fundamental advantage that quantum repeaters have over classical relays for extending the range over which QKD is possible is, as we have mentioned, that the quantum repeater nodes need not be physically secure.

The Ekert91 protocol [40–42] for QKD between two nodes (Alice and Bob) calls for the generation of an entangled qubit pair where one of the qubits is sent to Alice, and the other is sent to Bob. If we place a repeater (R) between these nodes, the distance between Alice and Bob can be extended. First we need Alice and the Repeater to share an entangled qubit pair, and for Bob and the Repeater to share another entangled qubit pair. Now, at the Repeater node, we perform a measurement of the two qubits in the Bell state basis; the outcome heralds the creation of an

entangled Bell qubit pair between the qubits held by Alice and Bob. This procedure is called entanglement swapping, since the qubits that were at Alice and at Bob, which were originally not entangled, become entangled as a result of the local measurement operations that are performed at the Repeater. This is one of the two fundamental operations of a quantum repeater, and was described in 1993 by Bennett et al. [28] and by Żukowski et al. [49].

A rudimentary repeater using only entanglement swapping may make long-distance entanglement distribution over fibre practical, assuming that the Bell pair generation at Alice and Bob (and at the repeaters, when more than one repeater is used) is perfect, that the quantum memories are perfect, and that the local operations at the repeaters are perfect. Entanglement purification [30, 31, 50] allows some of these assumptions to be relaxed. As we have mentioned already, entanglement purification refers to a class of procedures that each use a set of lower-fidelity entangled qubit pairs to produce a smaller number of higher-fidelity entangled qubit pairs, provided that the fidelity of the initial qubit pairs is above a certain threshold. Entanglement purification provides a clever solution to deal with the imperfections of a real system, since the effect of all imperfections is just the degradation of the fidelity of the entangled qubit pairs. Some of the early quantum repeater proposals [32, 33] analyzed how one may perform long-distance entanglement distribution using quantum repeaters (incorporating both entanglement swapping and entanglement purification) that have faulty local operations, and found that error rates of $\sim$1 % for local one- two-qubit gates and measurement may be tolerated (i.e., the system may still be able to distribute high-fidelity entangled pairs, even when the local operations in the repeaters are imperfect).

Unfortunately achieving the assumed fidelities and operation error probabilities in experimental systems is very challenging. Furthermore, it is unreasonable to assume that physical stationary qubits will be arbitrarily long-lived, and in the case of spins in quantum dots, it is unlikely that T_2 times beyond several milliseconds will be achievable [13, 51], even with substantial materials and device engineering effort. Fortunately it is in principle possible to make an arbitrarily long-lived logical quantum memory by using quantum error correction [37], provided enough physical qubits are available, and sufficiently high-fidelity local operations can be performed on them. Building quantum repeaters using a fault-tolerant error correcting scheme also allows for the construction of logical local operations with fidelities that are much higher than the fidelities of the native operations on physical qubits.

More recent theoretical work on quantum repeaters has also considered how to perform the task of entanglement purification (which is effectively that of correcting errors in the distributed Bell pairs) using other methods based on fault-tolerant quantum error correction, such as Calderbank-Shor-Steane codes [38], the surface code [35], and topologically-protected cluster states [52]. These approaches may also have advantages over entanglement-purification-based quantum repeaters [32, 33] in the reduced classical communication required for operation, which is predicted to have dramatic effects on performance [35, 38].

The high-level architectural studies of quantum repeaters are currently far-removed from practical experimental realities, and we will not go into further detail

about them in this chapter. However, one important overall point for us to emphasize is that these state-of-the-art proposals for quantum repeaters essentially call for the implementation of quantum repeaters as small[8] fault-tolerant quantum computers that are also equipped with photonic interfaces. The task of constructing practical quantum repeaters thus appears to be at least as difficult, if not more difficult than, building a practical fault-tolerant gate-model quantum computer.

14.2.2 Design of Quantum Repeaters

14.2.2.1 Heralded Entanglement Generation

As we have explained in the previous section (Sect. 14.2.1.4), quantum repeaters need to incorporate quantum memory. One approach is to directly store photonic qubits, for example using a cavity. The alternative, which we focus on, is to introduce quantum memories based on matter, and an interface between these quantum memories and photons (both for incoming and outgoing photons).

In 2001, Duan et al. [53] introduced a protocol (known as the "DLCZ" scheme) for entangling two remote atomic-ensemble-based quantum memories, using photons, and in such a way that successful entanglement is heralded. The DLCZ protocol is a member of a class of heralded protocols that can be used to entangle distant quantum memories provided that it is possible to generate an entangled state between each quantum memory and a photonic qubit.

Another protocol from this class is the Simon-Irvine protocol [54]. The treatment of it that we give here follows closely the formulation given by Moehring et al. [55]. Assume that we have two remote quantum memories, Alice (A) and Bob (B), and each memory can be described as a single qubit: Alice has memory basis states $\{|\uparrow\rangle_A, |\downarrow\rangle_A\}$, and Bob has memory basis states $\{|\uparrow\rangle_B, |\downarrow\rangle_B\}$. Let's suppose that each memory can be entangled with a polarization-encoded photonic qubit, i.e., each quantum memory has associated with it a single photon whose polarization state we use to represent a qubit. We will label the basis states of the photonic qubit for Alice as $\{|H\rangle_A, |V\rangle_A\}$, and for Bob as $\{|H\rangle_B, |V\rangle_B\}$.

Suppose that both Alice and Bob can, through some as-yet-undescribed method, produce the following spin-photon entangled states:

$$|\psi\rangle_A = \frac{1}{\sqrt{2}}(|\uparrow\rangle_A \otimes |H\rangle_A - |\downarrow\rangle_A \otimes |V\rangle_A) \tag{14.1}$$

$$|\psi\rangle_B = \frac{1}{\sqrt{2}}(|\uparrow\rangle_B \otimes |H\rangle_B - |\downarrow\rangle_B \otimes |V\rangle_B) \tag{14.2}$$

[8] Fowler et al. [35] predict that their scheme will be able to distribute entangled pairs from one side of the earth to the other at a MHz rate if the endpoints are connected by $\sim 10^4$ repeaters, each containing $\sim 10^3$ physical qubits, provided that initial entangled pair fidelities are $\gtrsim 0.96$, and quantum gates that can operate on nanosecond timescales are available.

In this case, Alice has a quantum memory and a photon that is entangled with it, and similarly Bob has a quantum memory, and a photon that is entangled with it. The key idea of the protocol is that we can perform a simple operation that will perform entanglement swapping on the photons from Alice and Bob, such that when the entanglement swapping operation has been completed, the two quantum memories of Alice and Bob will be entangled, even though they never directly interacted with each other.

Figure 14.3 illustrates the Moehring et al. variant of the Simon-Irvine scheme. The photon from Alice and the photon from Bob are mixed on a non-polarizing 50/50 beamsplitter, and each output port of the beamsplitter is monitored by a single-photon detector (which produces a click if a photon is present in the mode, and otherwise does not). The state of the system before the beamsplitter is:

$$|\psi\rangle_{\text{system}} = |\psi\rangle_{\text{A}} \otimes |\psi\rangle_{\text{B}} \tag{14.3}$$

$$= \frac{1}{2}\left[(|\uparrow\rangle_{\text{A}}|\text{H}\rangle_{\text{A}} - |\downarrow\rangle_{\text{A}}|\text{V}\rangle_{\text{A}}) \otimes (|\uparrow\rangle_{\text{B}}|\text{H}\rangle_{\text{B}} - |\downarrow\rangle_{\text{B}}|\text{V}\rangle_{\text{B}})\right] \tag{14.4}$$

$$= \frac{1}{2}\Big[|\Phi^{+}\rangle_{\text{memories}}|\Phi^{+}\rangle_{\text{photons}} + |\Phi^{-}\rangle_{\text{memories}}|\Phi^{-}\rangle_{\text{photons}} - |\Psi^{+}\rangle_{\text{memories}}|\Psi^{+}\rangle_{\text{photons}} - |\Psi^{-}\rangle_{\text{memories}}|\Psi^{-}\rangle_{\text{photons}}\Big] \tag{14.5}$$

As given by Moehring et al. [55], this rewriting of the system state in terms of states of the memories and of the photons allows us to easily interpret the outcomes of such a setup. Here $|\Phi^{\pm}\rangle_{\text{memories}} = \frac{1}{\sqrt{2}}(|\uparrow\rangle_{\text{A}}|\uparrow\rangle_{\text{B}} \pm |\downarrow\rangle_{\text{A}}|\downarrow\rangle_{\text{B}})$, and $|\Psi^{\pm}\rangle_{\text{memories}} = \frac{1}{\sqrt{2}}(|\uparrow\rangle_{\text{A}}|\downarrow\rangle_{\text{B}} \pm |\downarrow\rangle_{\text{A}}|\uparrow\rangle_{\text{B}})$. Identical photons impinging on a beamsplitter give rise to the Hong-Ou-Mandel effect [56]: they will bunch into the same output port. For photons that are indistinguishable in all but their polarization,

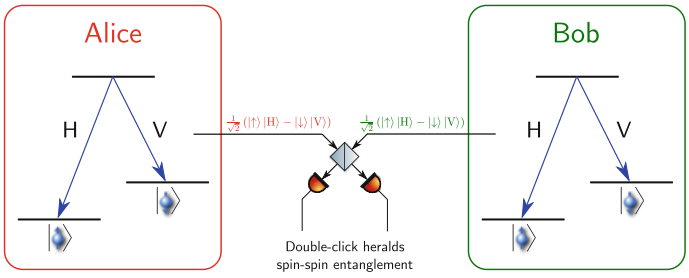

Fig. 14.3 Protocol for Entangling Remote Quantum Memories. A quantum memory (represented here by a single spin) located with Alice can be entangled with a quantum memory located with Bob if both quantum memories can emit photons that are entangled with their respective spins. The photons from Alice and Bob are interfered on a beam splitter, which has detectors on both output ports. If both detectors detect a photon, then entanglement between Alice's and Bob's memories has been generated. In particular, the following maximally-entangled state of Alice's and Bob's memories is heralded: $|\Psi^{-}\rangle_{\text{memories}} = \frac{1}{\sqrt{2}}(|\uparrow\rangle_{\text{A}}|\downarrow\rangle_{\text{B}} - |\downarrow\rangle_{\text{A}}|\uparrow\rangle_{\text{B}})$

the net effect gives rise to a situation where only a fully antisymmetric two-photon state[9] impinging on the beamsplitter in this experimental setup (Fig. 14.3) can result in both detectors clicking at the same time. Any symmetric two-photon input state leads to photon bunching, where both photons exit out of a single port, resulting in (at most) only one of the detectors clicking in the relevant time window. Of the four two-photon states $\left|\Phi^{\pm}\right\rangle_{\text{photons}}$, $\left|\Psi^{\pm}\right\rangle_{\text{photons}}$, only $\left|\Psi^{-}\right\rangle_{\text{photons}} = \frac{1}{\sqrt{2}}\left(|\mathrm{H}\rangle_{\mathrm{A}}|\mathrm{V}\rangle_{\mathrm{B}} - |\mathrm{V}\rangle_{\mathrm{A}}|\mathrm{H}\rangle_{\mathrm{B}}\right)$ is antisymmetric. Therefore if both single-photon detectors after the beamsplitter click, we have measured the photonic part of the system state to be $\left|\Psi^{-}\right\rangle_{\text{photons}}$, and therefore the memories are projected to be in the state $\left|\Psi^{-}\right\rangle_{\text{memories}}$. Therefore a double-click event heralds the generation of entanglement between the quantum memories at Alice and Bob's nodes.[10]

Heralding and Experimental Errors

The use of the double-click event to herald success is very important. However, so long as detector dark counts are sufficiently low, there can be a high probability that if both detectors click that this was because the photonic state really was $\left|\Psi^{-}\right\rangle_{\text{photons}}$, so the memories are in the entangled state $\left|\Psi^{-}\right\rangle_{\text{memories}}$.

Besides imperfections in the detectors (leading to dark counts), there is another way in which this protocol can falsely indicate that $\left|\Psi^{-}\right\rangle_{\text{memories}}$ has been generated, when in fact it has not. If the quantum memories produce, with non-zero probability, more than one photon within the time window being considered for detector clicks, then the experimentalist may measure two clicks, but have the memories not actually be in the state $\left|\Psi^{-}\right\rangle_{\text{memories}}$, i.e., the heralded state will not be the target state. This is undesirable. Therefore the second-order correlation function, $g^{(2)}(\tau)$, and in particular, the value $g^{(2)}(\tau = 0)$, is an important parameter for determining the suitability of a quantum-memory–photon interface for use in a quantum repeater. Ideally $g^{(2)}(0) = 0$, and the larger it is, the greater will be the percentage of heralding events that incorrectly indicate that the target entangled state has been generated.

Impact of Photon Loss on the Effectiveness of Heralded Entanglement Distribution

Protocols that rely on a double-click event to herald the generation of entanglement are sensitive to loss. For an attempt at the heralded generation of entanglement between quantum memories to succeed, a photon from Alice must arrive at a detector (and be detected by it), and a photon from Bob must arrive and be detected. Therefore the probabilities p_{A}, p_{B} of photons from Alice and Bob being detected determine the probability p_{success} of successful heralded entanglement generation between Alice and Bob as $p_{\text{success}} = p_{\mathrm{A}} p_{\mathrm{B}}$. We have mentioned several ways in which photon loss

[9] More precisely, the quantum state describing the polarization degree of freedom of each photon should be antisymmetric.

[10] If the single-photon detectors are replaced with number-resolving detectors, then all four memory Bell states can be heralded. If four single-photon detectors (and two polarizers) are available, then both $\left|\Psi^{+}\right\rangle_{\text{memories}}$ and $\left|\Psi^{-}\right\rangle_{\text{memories}}$ can be heralded.

may occur, but here let's assume that we have the nearly ideal scenario that the only loss is due to absorption in an optical fibre. We now briefly analyze how this photon loss affects the system performance as a function of distance between Alice and Bob.

One of the lowest-loss optical fibres currently available has an attenuation of $\alpha \approx 0.17$ dB/km [57], when transmitting photons with wavelength $\sim$1550 nm.[11] Let's suppose that Alice and Bob's memories can emit photons entangled with them at a rate of $R_0 = 1$ MHz (in general, the rate R_0 cannot be faster than the inverse of the lifetime of the optically excited state in the quantum memory. With perfect photon collection and perfect detectors, the entangled memory generation rate would be $R = 1$ MHz, in the absence of photon loss. Now let's consider the impact of photon loss in the fibre. Let's suppose that Alice and Bob are a distance $2L$ apart, that the beamsplitter and detectors are located at the midpoint of Alice and Bob, and thus that both memories emit photons into fibres of length L. The photon loss in the fibre results in a reduction of photon transmission probabilities: $p_A = p_B = 10^{\frac{-L\alpha}{10}}$. Thus the entanglement generation rate R is $R = R_0 p_A p_B = R_0 p_{\text{success}} = R_0 \left(10^{\frac{-L\alpha}{10}}\right)^2$. For $L = 10$ km, the loss in each fibre is 1.7 dB, so $p_A = p_B \approx 0.68$, thus $p_{\text{success}} \approx 0.46$, so the entanglement rate R drops to $R \approx 460$ kHz. If $L = 100$ km, then $p_{\text{success}} \approx 4.0 \times 10^{-4}$, so $R \approx 400$ Hz. If $L = 200$ km, then $R \approx 0.1585$ Hz. And if $L = 300$ km, then $R \approx 6.3 \times 10^{-5}$ Hz; note that this implies the successful generation of an entangled pair only once every $\frac{1}{R} \approx 4.4$ hr.[12] It is clear from this simple calculation why quantum repeaters are necessary to generate entanglement over fibre for distances of $\gg 100$ km. When one considers the other losses in the system, estimates for the distances over which entanglement distribution can be performed through fibre without quantum repeaters are even smaller.

The Importance of Heralding for Entanglement Distribution in a Quantum Network

Heralding is important, for at least two reasons: (1) non-heralded entanglement protocols result in a mixed state $\rho = q\,|\Psi\rangle\langle\Psi| + \sum_i r_i\,|\phi\rangle_i\langle\phi|_i$, where $|\Psi\rangle$ is the desired (target) entangled state (for example, one of the Bell states), $|\phi\rangle_i$ are other states, and r_i are the probabilities[13] of the system ending in one of these states.

[11] What we outline in this section is a best-case scenario for the loss, since we assume that the photons are in the lowest loss band (covering approximately the range 1525–1575 nm [57]). Note that the vast majority of current quantum technology experiments occur with systems that emit photons at wavelengths that experience dramatically higher attenuation. For example, the attenuation coefficient for 850 nm photons is typically $\alpha \sim 3.5$ dB/km. See Table 14.2 for a few examples. This strongly motivates work to either engineer quantum systems that natively emit $\sim$1550 nm photons, or to build nonlinear optical systems [21, 58, 59] that can convert light at high-loss wavelengths to wavelengths that have low loss in fibres.

[12] We would like a high rate of entangled-pair generation in general (for example, to facilitate a high generation rate of distributed keys in QKD applications), so naturally we seek to maximize the success probability p_{success}. However, there is also a crucial limit to how low the heralded success rate can be before the entanglement distribution stops working at all: the rate of coincident arrivals of photons at the detectors needs to be higher than the dark count rate of the detectors (in the appropriate time windows).

[13] The r_i should satisfy the relation $\sum_i r_i = (1 - q)$.

The state ρ will not violate Bell's inequality, and will generally fail to serve as a useful quantum information resource, if the success probability q is not sufficiently high (as opposed to a heralded scheme, where q can be arbitrarily low, and you can still measure Bell inequality violations provided that you rerun the experiment of generating and measuring the state sufficiently many times that you do actually obtain a set of successfully heralded states). In unheralded schemes, reductions in q directly reduce the fidelity of the output state.[14] (2) As we explained in Sect. 14.2.1.4, quantum repeaters only confer an advantage if they have quantum memories, since the memory allows for one link to stop trying to generate entanglement after it succeeds. However, if there is no heralding mechanism, there is no way to know when to tell a particular link to stop trying to generate entanglement because it has succeeded!

We can consider the impact on the performance of a quantum network where entanglement generation between nodes is performed with heralding or without heralding in the following way. Suppose we have a network with N nodes (Alice, Bob, and $N-2$ repeater nodes), and that the entanglement generation between adjacent nodes succeeds, on each attempt, with probability p_{success}, and assume that attempts can be made at a rate R_0. With a heralded entanglement generation protocol, the overall rate of entanglement generation between Alice and Bob will scale roughly as[15] $R_0 p_{\text{success}}/\log(N)$, where we note that there is only a very weak (inverse logarithmic) dependence on the number of nodes. However, if the entanglement generation protocol is unheralded, then the rate is dramatically reduced: it will scale as $R_0 p_{\text{success}}^N$. Note that for even very small numbers of repeaters (e.g., 10), the rate will become unusably small for realistic single-hop success probabilities ($p_{\text{success}} \ll 1$).

14.2.2.2 Constraints on Entanglement Distribution and on Quantum Repeater Design from Finite Quantum Memory Coherence Time

In this section, we briefly outline how the coherence times of the quantum memories used impact both simple entanglement distribution experiments, and the design of quantum repeaters for more advanced experiments that incorporate entanglement swapping and purification and/or quantum error correction.

---

[14] If all the other states $|\phi\rangle_i$ are not very "different" from the target state $|\Psi\rangle$, i.e., $\langle\Psi|\phi\rangle_i \sim 1$, then the reduction in fidelity from measuring the mixed state ρ, as opposed to the heralded ensemble of target states, will not be severe. However, in many situations, there will be some states $|\phi\rangle_i$ that are nearly orthogonal to $|\Psi\rangle$, and have high probabilities r_i of being generated, and this will dramatically decrease the measured fidelity.

[15] To illustrate our point, we assume here a simple entanglement-swapping-based approach to distributing entanglement, in which the adjacent nodes each attempt to become entangled with their immediate neighbours (stopping once they have succeeded), and where the protocol is reset once every pair of adjacent nodes shares an entangled qubit pair. This yields an unbroken chain of entanglement that can be converted, via entanglement swapping, to an entangled qubit pair being shared between Alice and Bob. Once an entangled qubit pair is shared between Alice and Bob, we assume it is used, and protocol begins all over again.

Constraints on Simple Entanglement Distribution from Finite Quantum Memory Coherence Time

The current state-of-the-art in experimental demonstrations of entanglement distribution between quantum memories is the generation of entangled states between two quantum memories that are spatially separated by several meters, either through free-space photon propagation, or through optical fibre. This has been achieved with quantum memories implemented in a variety of physical systems, including single $^{171}Yb^{+}$ ions [55], single ^{87}Rb atoms [60, 61], ensembles of Cs atoms [62], and with NV centers in diamond [63]. Entanglement between spins in distant quantum dots has not yet been demonstrated.

Before quantum repeaters using error correction (such as in [35, 38, 52]) become practical, prototype repeaters using no error correction are likely to be tested. In these demonstrations, the coherence time of the quantum memory qubits is a crucial parameter. In the case of qubits formed from spins in quantum dots, $T_2 \gg T_1$, so the T_2 time provides the limit on how long the spin can store a qubit.[16]

Suppose that for the purposes of demonstrating quantum repeater functionality with just two end nodes (Alice and Bob) and a single repeater (endowed only with two quantum memories, and entanglement swapping capability), one uses the following simple protocol. The protocol repeatedly attempts to form entanglement between Alice and the Repeater, and between the Repeater and Bob, and pauses entanglement generation over one of those hops when entanglement is successfully generated over it. In this protocol, the T_2 times of the memories at Alice, Bob, and the Repeater should be larger than the time required for the photons to propagate to the midpoint heralding apparatus, in addition to the time required to classically communicate that entanglement generation between Alice and the Repeater (for example) was successful (this will be at least the time required for light to travel half the distance between Alice and the Repeater).[17] Thus we obtain the limit $T_2 > (\frac{L}{2c} + \frac{L}{2c}) = \frac{L}{c}$. The T_2 times should also be longer than the time required to perform the entanglement swapping operation on the quantum memories in the repeater, i.e., T_2 should be longer than the one-qubit-gate, two-qubit-gate, and measurement times. For any long distance L, the limit from the photon propagation time ($T_2 > \frac{L}{c}$) will be the more stringent one, but for prototype demonstrations (e.g., $L = 10\,\text{m}$), the limit from the local operation times may be more relevant. However, the use of memory is not particularly helpful in improving the rate of generation of entanglement between Alice and Bob if the memories cannot store the qubits for substantially longer than it takes to attempt generating entanglement over a single hop (e.g., between the

[16] Since the longitudinal relaxation time T_1 adheres to the relation $2T_1 > T_2$ (under the assumption that the noise is isotropic with respect to the different qubit axes; this is a good assumption in most systems for physically-relevant noise sources), the T_1 time is generally not the limiting timescale. T_2, the coherence time (or transverse relaxation time), is generally what defines the useful lifetime of a qubit.

[17] Jones et al. [64] introduced a scheme whereby the heralding is performed at the repeater sites (as opposed to at locations midway between the repeaters), and failed attempts can be reattempted without waiting for a delayed classical signal. Even in this protocol though, when a node measures a heralding success, it still has to wait for a classical signal from the adjacent node.

Repeater and Bob). To demonstrate a substantial benefit from the use of the repeater in distributing entanglement between Alice and Bob, it is necessary for T_2 to be at least on the order of the average time it takes for heralded generation of entanglement over a single hop to succeed.[18] Note that meeting this criteria with current technology is not trivial: even for very short distances (on the order of meters), the T_2 time will likely need to be seconds.[19] If one wants to add additional repeaters in such a demonstration experiment, then the T_2 time needs to be increased accordingly.

Constraints on Quantum Repeater Design from Finite Quantum Memory Coherence Time

There are many possible designs for a fault-tolerant quantum repeater, and we don't aim to provide comprehensive coverage of them in this chapter. However, given the rather dire predictions in the previous section for what quantum memory coherence times are necessary in order to gain an advantage from using quantum repeaters, we would like to now provide a very brief summary of how the required physical qubit T_2 time may be dramatically reduced to values that are more conceivable for quantum dot spin qubits.

For a long-distance quantum network with many hops, without the use of error correction, the physical qubit T_2 time may need to be many hundreds, or possibly even thousands, of seconds, in order for the network to sustain a reasonable rate of high-fidelity entanglement generation. Almost no physical qubit implementations offer such T_2 times, and certainly not quantum dot spin qubits, which seem unlikely to surpass 10–100 ms [13, 51].

As we have mentioned before, the general plan in the quantum repeater community for alleviating this problem is to not use physical qubits directly as quantum memories, but rather to implement some form of quantum error correction scheme, in which many physical qubits encode a single logical qubit. Then, so long as local gate operations are sufficiently fast and of sufficiently high fidelity, a logical qubit can be constructed to have an arbitrarily long coherence time (where the ratio of physical qubits required to implement a single logical qubit increases as the desired coherence time increases). For example, the surface code may be able to suitably protect qubits that have $T_2 \sim 100\,\mu\text{s}$, provided that nearest-neighbour single-qubit gates, two-qubit gates, and measurement, are available on nanosecond timescales, and with an encoding where $\sim$1000 physical qubits are used to encode a single logical qubit (quantum memory) [35, 65].

The prospect of, for each repeater, essentially implementing a fault-tolerant universal quantum computer with thousands of physical qubits, is daunting. There is much work underway to try to find repeater designs that may be more realistically

[18] If the time taken to make a single attempt at generating entanglement over a single hop, set by the distance between the nodes, is T_{rep}, and the probability of success is p_{success}, then we want $T_2 \gtrsim T_{\text{rep}}/p_{\text{success}}$.

[19] The repetition time T_{rep} will be determined by how quickly the heralding signal can be processed by a classical feedback circuit. Let's assume $T_{\text{rep}} \sim 1\,\mu\text{s}$. Over short distances, p_{success} will be dominated by losses other than those from absorption in the fibre; e.g., coupling losses. A reasonable value to assume for quantum dots is $p_{\text{success}} \sim 10^{-6}$. Thus $T_2 > T_{\text{rep}}/p_{\text{success}} \sim 1\,\text{s}$.

implemented in the near- to medium-term, but currently all proposals require either error rates, or scalability, or both, that are far out of reach of current technology. For a review of many of the leading contemporary proposals, we recommend [66].

14.3 Quantum Dots as Building Blocks for Quantum Repeaters

We have until now described in a fairly abstract way the necessary features and functions of a quantum repeater. There are many physical systems that are currently being considered as candidates for implementing quantum repeaters.

Charged quantum dots are an interesting candidate physical system for building a high-bandwidth quantum network; one aspect of their appeal is that quantum dot development can leverage progress in commercial semiconductor technology. Schneider et al. [67], Maier et al. [68], and others have succeeded in growing regular 2D arrays of single InAs quantum dots. Jones et al. [65] discussed the prospects for designing a large-scale quantum computer that can integrate $>10^8$ quantum dots (each one implementing a single physical qubit) on a single $\sim$4 cm^2 chip; one can imagine a very similar design being relevant for a quantum repeater node, except that an additional outcoupling of each photonic interface quantum dot to fibre would need to be implemented. Unfortunately the goal of realizing a 10^8-physical-qubit quantum computer using quantum dots is still sufficiently divorced from experimental reality that it's not even possible to predict with any certainty when or if it will be possible to realize such a machine. However, if a many-physical-qubit machine can be realized, it is possible that a high-bandwidth repeater system could be implemented despite the large overhead imposed by the use of an error correction code such as the surface code.

Besides the requirement for many physical qubits if one implements a quantum repeater using a large-overhead error correcting code, there is another advantage to having repeater nodes with many quantum memories and photonic interfaces per node: it should be possible to attempt to generate entanglement between memories in adjacent nodes via many channels simultaneously, and this will allow for proportionately higher rates of entanglement generation than if only a few parallel channels (or just a single channel) are used.

Arguably the major fundamental disadvantage of using quantum dots to implement a quantum repeater is the need for the semiconductor sample to be cooled to liquid helium temperatures. At temperatures significantly above 10 K, the optical properties of quantum dots degrade dramatically. Many quantum dot spin qubit experiments also currently use superconducting magnets (which are kept at $T \lesssim 4.2$ K), although it is conceivable that lower magnetic fields (achievable using

non-superconducting magnets) may be sufficient.[20] The use of cryogenic equipment at every repeater station is in principle feasible. However, given the cost of such equipment, there is a strong motivation to find physical systems that offer the advantages of quantum dots, but with the possibility of room-temperature ($T \sim 300\,\mathrm{K}$) operation.

One common standard for coarsely evaluating a candidate physical realization of qubits for implementing a quantum repeater is the set of "Five (Plus Two)" DiVincenzo criteria [71]. The first five DiVincenzo criteria were initially intended for helping to evaluate the suitability of physical qubits for implementing quantum computers. However, as we have covered, most designs for fault-tolerant quantum repeaters call for the creation of machines that are very similar to general-purpose quantum computers, so the DiVincenzo criteria are also relevant when evaluating technology for repeaters.

We have grouped our discussion into two subsections: one relating to the quantum memory requirements for a repeater, and one relating to the photonic interface between the quantum memory (stationary) qubits and the photonic (flying) qubits.

14.3.1 Quantum Dots as Quantum Memories

To evaluate the potential for quantum dot spin qubits to be used as quantum memories in a quantum repeater, one can evaluate them against the first five DiVincenzo criteria. The DiVincenzo criteria are, however, only a rough guide, and to accurately assess whether a technology may be used to produce a working repeater or not, one needs to consider a detailed repeater design, including the specifics of the error correction scheme to be used. Work towards this goal has been done by Jones et al. [65] for a quantum computer based on optically controlled quantum dot qubits, but a detailed design for a quantum-dot-based quantum repeater is not yet available. However, from [65], we have a basic idea of the performance required from quantum dot qubits in order to produce a functioning fault-tolerant machine, and at this stage more experimental progress is needed (to provide precise numbers about achievable operation fidelities and times) before a more specific design will be needed to provide a roadmap for further experiments.

Before we start to consider the details of how a fault-tolerant quantum repeater may be constructed using quantum dots, let us first review how quantum dots may meet the DiVincenzo criteria for quantum memories.

---

[20] The main reason that large magnetic fields (up to $B \sim 6\,\mathrm{T}$) are currently used is to ensure high-fidelity initialization and readout, when these two operations are performed using optical pumping [4]. However, if high-fidelity, single-shot, quantum nondemolition readout is realized (which is currently thought to be required for any gate-model large-scale quantum computing system [65]), then it is quite plausible that only small magnetic fields ($B \ll 1\,\mathrm{T}$) may be required, since there exist proposals for single-shot readout of spins in quantum dots that do not require large magnetic fields [69, 70].

14.3.1.1 DiVincenzo Criterion 1: "A Scalable Physical System with Well-Characterized Qubits"

This criterion imposes two main requirements: that the system being proposed to implement a qubit can be well-described as a quantum two-level system (and therefore that the system has a negligible probability of being found in states besides $|0\rangle$ and $|1\rangle$), and that this system is scalable.

A single quantum dot can trap a single conduction band electron, or a single valence-band (heavy) hole. This can be done deterministically, by embedding a layer of quantum dots in a diode structure—this is likely the configuration that will be used in a large-scale system. However, many current experiments use stochastic charging of the quantum dots, by placing a layer of n-type or p-type dopant near the quantum dot layer.

Regardless of the engineering method used to charge the quantum dots in a sample, the key idea is that a single quantum dot can stably trap a single charge (electron or hole), and the spin state of this charge (which we denote as $|\uparrow\rangle$ and $|\downarrow\rangle$ in the case of an electron[21]) will serve as the qubit, i.e., $|\psi\rangle = \alpha\,|\uparrow\rangle + \beta\,|\downarrow\rangle$. We can define the traditional quantum information "computational basis" in terms of these eigenstates ($|0\rangle \triangleq |\uparrow\rangle$, and $|1\rangle \triangleq |\downarrow\rangle$), which gives us a single qubit with the notation used in the quantum information literature: $|\psi\rangle = \alpha\,|0\rangle + \beta\,|1\rangle$.

In the case of the electron, which is a spin-$\frac{1}{2}$ particle, there are only two spin eigenstates, so an isolated spin seems to easily meet the requirement that the system we choose should have a low probability of being found in a state besides $|\uparrow\rangle$ or $|\downarrow\rangle$. A magnetic field is typically used to split the spin eigenstates in energy.

14.3.1.2 DiVincenzo Criterion 2: "The Ability to Initialize the State of the Qubits to a Simple Fiducial State"

In quantum computation, the ability to initialize qubits is crucial for implementing any algorithm, since (in the gate model) algorithms begin by assuming that qubits are in some particular initial state (for example, each qubit being in the state $|0\rangle$). Repeaters have a similar requirement, although depending on the specifics of the physical protocol used to interface the quantum memory with photonic qubits, the initial state might not necessarily be one of the computational basis states ($|0\rangle$ and $|1\rangle$), nor a superposition of them, but some third state.

For the proposals we discuss in this chapter concerning quantum memories made from spins in optically-active quantum dots, it is sufficient to be able to initialize each qubit in the quantum memory to one of the computational basis states, e.g., $|0\rangle$.

The primary method that is used to perform spin initialization of optically-active quantum dots is optical pumping. This is a technique borrowed from atomic physics [72], and was demonstrated for spins in quantum dots in the so-called Voigt geometry by Xu et al. in 2007 [7]. The Voigt geometry is the name given to the experimental

[21] We use $|\Uparrow\rangle$ and $|\Downarrow\rangle$ to refer to the pseudospin eigenstates of a hole.

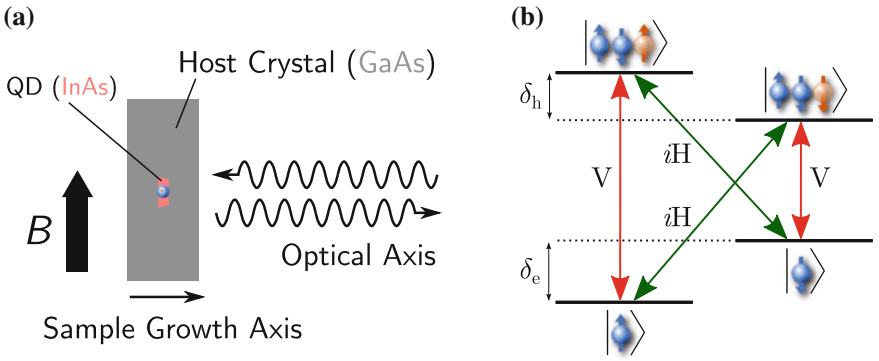

Fig. 14.4 **a** Voigt Geometry. The Voigt geometry denotes an experimental setup in which a magnetic field is applied perpendicular to the growth axis of the sample. The optical axis (the axis along which excitation light that impinges on the sample propagates, and the axis along which emitted or reflected light that is collected by a lens propagates) is parallel to the growth axis. Self-assembled InAs quantum dots in a GaAs host crystal are significantly shorter in the growth axis than in either of the in-plane axes. A QD typically has a height (dimension in the growth axis) in the range 1.5–4 nm, and a diameter (base length) in the range 20–40 nm. **b** Level Diagram and Optical Selection Rules of a Quantum Dot in a Magnetic Field in the Voigt Geometry. When a charged quantum dot is placed in a magnetic field, the electron spin states are split in energy; this Zeeman splitting is denoted in this figure as $\hbar\delta_e$. The two lowest-energy optical excited states are shown, and also have a Zeeman splitting (due to the interaction of the hole with the magnetic field). Both trion states can decay to either electron spin ground state, with approximately equal probability (oscillator strength). Note that the transitions $|\uparrow\rangle \leftrightarrow |\uparrow\downarrow\Uparrow\rangle$ and $|\downarrow\rangle \leftrightarrow |\uparrow\downarrow\Downarrow\rangle$ have vertical-polarization selection rules, and the transitions $|\uparrow\rangle \leftrightarrow |\uparrow\downarrow\Downarrow\rangle$ and $|\downarrow\rangle \leftrightarrow |\uparrow\downarrow\Uparrow\rangle$ have horizontal-polarization selection rules, but with a 90° phase shift

configuration when the magnetic field is aligned perpendicular to the optical axis and crystal growth axis, as shown in Fig. 14.4a. This is the geometry in which spin-photon entanglement has been achieved, so it is the geometry we focus on in this review.

In the Voigt geometry, the first optically excited states of a charged quantum dot are the trion states. Suppose that a quantum dot contains a single electron. If this quantum dot absorbs a photon, it will then contain an electron-hole pair, and the conduction-band electron that was already in the QD, i.e., a trion (as we explained in Sect. 14.3.1.1).

The relevant energy level diagram and optical selection rules for the system in the Voigt geometry are shown in Fig. 14.4b. A feature of this diagram that is relevant to optical pumping, as well as spin rotation and spin-photon entanglement, is that the optically-excited states form two Λ systems with the ground spin states. The fact that the two trion states have allowed optical transitions to both spin ground states is crucial.

Optical pumping allows the spin to be initialized into one of the two spin ground states on a few nanosecond timescale by applying a narrowband CW laser resonantly on any one of the four optical transitions.

We will discuss briefly in Sect. 14.3.1.5 how optical pumping can also be used to perform spin measurement. There are alternatives to spin pumping for initialization, and the one most likely to be used in a large-scale, fault-tolerant system is some form of single-shot, quantum non-demolition (QND) measurement: if one can perform an ideal von Neumann projective measurement on a qubit, then after the measurement the qubit will be in the state $|0\rangle$ or $|1\rangle$, and based on the measurement result one can perform a NOT gate to flip the spin if needed, and in that way initialize the spin to $|0\rangle$ (or $|1\rangle$, if desired).

14.3.1.3 DiVincenzo Criterion 3: "Long Relevant Decoherence Times, Much Longer than the Gate Operation Time"

Spin-based qubits have been considered in many physical systems, since spin is an especially attractive degree of freedom to use for storing quantum information. Not only do spin-$\frac{1}{2}$ particles by definition have only two spin levels (which helps in avoiding the problem of keeping whatever subsystem is being used as a qubit from accidentally exiting into third, fourth, etc., levels), but spin tends to not couple as strongly to uncontrolled degrees of freedom. For example, one could imagine defining a qubit's two states as being two different spatial wavefunctions of an electron. This has the significant disadvantage that not only does one then need to find a way to avoid exiting from the two-state manifold, but also that the wavefunction degree of freedom is significantly affected by Coulomb interactions with nearby charges (i.e., charge noise) [73]. The relative insensitivity of the spin degree of freedom to many sources of noise leads to spin qubits having relatively long coherence times, not only in quantum dots, but in other physical systems too.

In the case of electron spin qubits in self-assembled, optically-active InAs quantum dots formed in GaAs, the T_2 coherence time is typically in the range 1–3 μs; this has been measured for a single quantum dot using a spin echo [74] sequence. Hole spin qubits have also been created and their coherence time directly measured using a spin echo sequence; De Greve et al. measured $T_2 \approx 1.1\ \mu$s [16] for one such qubit. As the third DiVincenzo criterion says, these T_2 values need to be compared to the gate operation times in order to evaluate their suitability.[22]

[22] Comparing the T_2 time to the gate operation times is overly simplistic. In prototype demonstrations of quantum repeaters where the quantum memories are not protected by quantum error correcting codes, then, as we have explained previously, the T_2 times need to also be compared to the relevant photon propagation times, with some consideration of entanglement generation heralding success probability. In the case where fault-tolerant quantum-error-corrected memories are to be built, the code and implementation details may call for T_2 times much longer than the gate times, but certainly the gate times provide a lower-bound on the requisite T_2 times.

The existence of optical transitions in the quantum dots is useful for several reasons. The main focus of this book, and of this chapter, is on the interface between photonic qubits and stationary (memory) qubits, and the optical transitions naturally facilitate direct conversion between these two forms of qubits in the quantum dot system. Another advantage has to do with scaling: if we can perform all the operations on our stationary qubits using radiation at optical frequencies, there may be no need for complicated wiring on-chip in order to deliver initialization, control and measurement pulses to specific quantum dots. As [65] discusses in some detail, a full quantum processor could potentially be made from a sample that contains no wiring between any of the quantum dots in a large 2D array, where all addressing is performed by beam-steering using micromirrors. The use of optical radiation allows neighbouring qubits to be individually addressed despite being very densely packed; a spacing of 1 μm should be sufficient to allow diffraction-limited spots to focus on individual quantum dots with negligible undesired impact on neighbouring qubits. The benefit of optical transitions most relevant to the third DiVincenzo criterion is, however, that gates implemented using optical pulses can be significantly faster than gates implemented using microwave frequency pulses that manipulate the spin ground states directly [75].

14.3.1.4 DiVincenzo Criterion 4: "A 'universal' Set of Quantum Gates"

Universal control over a single quantum dot spin qubit has already been demonstrated, both for an electron spin qubit [8], and for a hole spin qubit [16]. In both cases, a single rotation about the optical axis can be implemented on a timescale of approximately 2–4 ps, and a single rotation about the magnetic field (orthogonal) axis is realized by Larmor precession on a timescale of up to 50 ps (depending on the magnitude of the external magnetic field used, and on the spin g-factor). A single qubit can be set to an arbitrary position on the Bloch sphere in well under 100 ps. The single qubit gate time is thus four orders of magnitude shorter than the T_2 coherence time.[23] In other words, $\sim 10^4$ single qubit operations could be performed on a qubit before it decoheres, provided that a suitable spin echo scheme is used, and under the assumption that the fidelities of the single qubit operations are sufficiently high.[24,25]

[23] While the single qubit gate time clearly passes the DiVincenzo criterion that it should be much shorter than the T_2 time, it is necessary to develop and evaluate a full quantum computer design to be able to properly assess whether the timescales are truly compatible. We focus more on near-term experiments in this chapter, but for a discussion of the requirements in a fault-tolerant quantum computer based on quantum dots, see [65].

[24] Currently the fidelities of the single qubit gates limit the number of operations that can be applied to $\ll 100$; in practice, several orders of magnitude improvement in the gate infidelities would be needed to allow a sequence of 10^4 operations to be usefully applied to a qubit.

[25] Thus far we have avoided mentioning the dephasing time T_2^*. However, it is not irrelevant, even when spin echo pulses are used: the single-qubit gate fidelities are closely related to this parameter (T_2^*). The dephasing time reflects the (time-averaged) uncertainty about the Larmor precession frequency, and this uncertainty results in errors in single-qubit gates. For example, for rotations

For all experiments that have been performed so far, and all those likely to be performed in the near future, the time required to perform single qubit operations does not considerably affect the fidelity of the output state, so long as a spin echo refocussing pulse is used. The dephasing time T_2^*, which is the relevant decoherence timescale when a spin echo pulse is not used, is approximately 1 ns for electron spins [13]. The T_2^* time is thus only roughly an order of magnitude larger than the single-qubit gate time.

Although the T_2 time is sufficiently long that the finiteness of the time taken to perform single qubit gates is generally not a dominant cause of error (infidelity), the T_2 time is nevertheless an important experimental parameter in current experiments exploring spin-photon and spin-spin entanglement with quantum dots. As we have mentioned earlier in this chapter, in even the simplest entanglement distribution experiments, the coherence time of the memory needs to be long compared to the time taken for photons to propagate. For example, if one intends to entangle two remote spins in quantum dots using the Simon-Irvine scheme, the two cryostats should be connected by a fibre length that is substantially less than $L_{\max} = T_2 \frac{c}{2 \cdot n_{\text{core}}}$, which for $T_2 \approx 3$ μs, yields $L_{\max} \approx 555$ m. This is a perfectly reasonable value for the purposes of laboratory proof-of-principle demonstrations, but clearly an extension to the intrinsic coherence time, or the development of an error-protected quantum memory, will be necessary to perform long-distance experiments.

Single qubit gates alone are not universal for computation, so the second part of this DiVincenzo criterion calls for the demonstration of a scalable two-qubit (entangling) gate, for example, a CNOT gate. There are several proposals for how to implement such a gate for quantum dot spin qubits [76–80], but there have been no experimental demonstrations thus far. Kim et al. [81] showed that one can perform a two-qubit gate that is mediated by an always-on exchange interaction between two adjacent quantum dots in a quantum dot molecule structure, but unfortunately this approach is not scalable beyond a few qubits. One of the major outstanding experimental challenges for optically-active quantum dot spin qubits is the demonstration of a scalable, fast, high-fidelity two-qubit gate.

(Footnote 25 continued)
(nominally) about the optical axis (induced by picosecond optical pulses), the dephasing processes result in a random, off-axis component on top of the optical-axis rotation, i.e., a random deviation from the ideal behaviour of the gate. This error mechanism can be mitigated if carefully-designed spin-echo-related schemes are used; these methods call for the concatenation of pulses in order to make so-called decoherence-protected gates, but have yet to be realized for quantum dot spin qubits. For the conventional single-qubit gate operations described above, the ratio between the gate operation time and the dephasing time ($T_2^* \approx 1$ ns [13]) results in single-qubit gate fidelities that are theoretically limited (by this effect) to $\sim 99.6\,\%$ (optical-axis gate) and $\sim 95\,\%$ (Larmor gate); these limits are slightly higher than what has been measured experimentally [16].

14.3.1.5 DiVincenzo Criterion 5: "A Qubit-Specific Measurement Capability"

As a method for qubit initialization, optical pumping performs well. However, this method is also used to perform qubit readout in most[26] optical quantum dot spin qubit experiments [4]. The basic principle of this type of readout is that during optical pumping, the quantum dot will emit a single photon on the branch of the Λ system that is not being pumped (e.g., $|\uparrow\downarrow\Downarrow\rangle \rightarrow |\uparrow\rangle$) if and only if the spin was in one particular state ($|\downarrow\rangle$), but the quantum dot will emit no photons along that branch if the spin was in the other state ($|\uparrow\rangle$). There are two major disadvantages to this optical pumping procedure regarding its use for readout. The most important disadvantage, from the perspective of current experiments, is that per experimental run,[27] at most a single photon will be emitted indicating the spin is in a particular state. Since the overall collection and detection efficiency is small (typically less than 0.1 %), it is necessary to re-run a particular experiment many times in order to obtain a reasonable signal-to-noise ratio. In the sense that it is necessary to repeat the experiment multiple times to obtain an average measurement outcome, this type of readout does not implement a "single-shot" measurement, and, for example, cannot be used to detect quantum jumps (or other phenomena associated with single quantum trajectories).

The second disadvantage of the spin readout based on optical pumping fluorescence is that regardless of the measurement outcome, the qubit ends up in one particular state (for example, $|\uparrow\rangle$). In this sense the method does not perform a "quantum non-demolition" (QND) measurement, which we use here to mean just that the measurement does not act as a textbook von Neumann projective measurement.

14.3.2 Quantum Dots as Photon Sources

The suitability of quantum dot spins as quantum memories can be evaluated against the first five DiVincenzo criteria. To evaluate their use as building blocks for a quantum repeater, we need to consider the final two DiVincenzo criteria. We will first consider DiVincenzo Criterion 7: "The ability to faithfully transmit flying qubits between specified locations". One can imagine using electrons, or some other matter particles, as flying qubits, but this seems exceptionally difficult for even moderate macroscopic distances (i.e., on the order of meters). Therefore nearly all proposals for flying qubits consider optical-frequency photons, either in free-space or in optical fibre: these photons can encode quantum information in degrees of freedom that are

[26] For example, the recent demonstrations of spin-photon entanglement from three different groups all used this method [21–24].

[27] A single run may be a sequence of events such as: (1) Initialize the spin, (2) Perform one or more rotation gates on the spin, (3) Measure the spin.

very robust against decoherence, and they can be transmitted over relatively long distances with relatively low loss.

The use of quantum dots as photon sources doesn't directly address either DiVincenzo Criteria 6 or 7, but is related to both, and is an important area of research in the quantum dot community, both for its relevance to quantum repeaters, and other aspects of quantum-optics-based quantum information technology.

As is reviewed in chapter by Schneider, Gold, Lu, Höfling, Pan and Kamp in this book, quantum dots have been shown to be outstanding single-photon sources, i.e., they can produce single photons on demand (with either electrical or optical triggering). Considerable effort has been expended over the past 15 years in making quantum-dot-based single-photon sources that have very low $g^{(2)}(0)$ values, and good indistinguishability. Both of these are important parameters for quantum repeaters. It is easy to see why a non-zero $g^{(2)}(0)$ value negatively affects the entanglement generation protocol we have described: if either of two quantum dots that are to be entangled have non-zero $g^{(2)}(0)$, then it is possible that the detectors measure a double-click event (which should herald entanglement between the two quantum dots) even though no photon arrived at the detectors from one of the quantum dots. Therefore some of the heralded events will not actually correspond to cases where the quantum dots are in the target entangled state, and this will result in an overall reduction in the fidelity of the entangled state. Imperfect indistinguishability of photons also results in a reduction in state fidelity, and in reduced efficiency of entanglement generation.

The inhomogeneity of quantum dots (different quantum dots tend to have different optical emission wavelengths, and different linewidths) is a major drawback; photon indistinguishability is a prerequisite for interference, and the protocols we have discussed (e.g., Simon-Irvine) rely centrally on Hong-Ou-Mandel-style interference. There have been demonstrations of interference between photons emitted from different, remote quantum dots [82–84], but certainly for large-scale use, the lack of homogeneity is an outstanding problem. One main approach to solving this problem is to tackle it directly through improvements in sample growth and fabrication; however, it may also be possible to use frequency conversion [21, 58, 59] to help achieve interference of photons emitted from quantum dots at disparate wavelengths [85].

14.3.3 Entanglement Between a Spin in a Quantum Dot and an Emitted Photon

In the previous subsection we have summarized how research on quantum dots as single photon and entangled photon pair sources may bear on the use of quantum dots in quantum repeater networks. A physical system that can act as a good single-photon source has some promising attributes that may also allow it to perform as a good spin-photon interface, but we have not yet described the other necessary conditions.

The final DiVincenzo criterion for us to consider is Number 6: "The ability to interconvert stationary and flying qubits". As we have described earlier, one popular technique to generate entanglement between stationary qubits mediated by flying qubits is to use the Simon-Irvine protocol, or a variant thereof. This protocol requires the generation of pairs of stationary and flying qubits that are entangled. The sixth DiVincenzo criterion suggests a requirement more along the lines of converting a stationary qubit into a flying qubit, and then converting that flying qubit into a stationary qubit at a different location, but the literal interpretation of this as necessarily being a direct physical process is overly restrictive: so long as you can distribute entanglement over long distances using flying qubits, you can transfer quantum information using quantum teleportation.

The Simon-Irvine protocol is an elegant way to distribute entanglement, and is very well-suited to quantum dots, since charged quantum dots provide a direct mechanism for generating entanglement between a stationary qubit and a flying qubit [86]. Consider the energy level diagram describing the relevant spin ground states, the first optically-excited states (trions), and the relevant optical selection rules for a charged quantum dot, in a Voigt-geometry magnetic field. Figure 14.5 shows the four-level diagram, and the optical selection rules for the allowed transitions from the trion state $|\uparrow\downarrow\Downarrow\rangle$. We denote as $\hbar\omega$ the energy of the $|\uparrow\downarrow\Downarrow\rangle \leftrightarrow |\downarrow\rangle$ optical transition. If the system begins in the trion state $|\uparrow\downarrow\Downarrow\rangle$, then once this state decays (which takes on average approximately 1 ns if the quantum dot emission is not enhanced by an optical cavity), the following spin-photon entangled state is produced:

$$|\psi\rangle = \frac{1}{\sqrt{2}} \left(|\uparrow\rangle \, |i\mathrm{H}, \hbar(\omega + \delta_\mathrm{e})\rangle + |\downarrow\rangle \, |\mathrm{V}, \hbar\omega\rangle \right). \tag{14.6}$$

This state is hyperentangled, in the sense that the spin qubit is entangled with two different properties of the emitted photon: both its polarization and its energy. Entanglement between the spin and the photon polarization, and between the spin and the photon energy, have both been experimentally verified.

14.3.3.1 Demonstrations of Spin-Photon Entanglement with Quantum Dots

We have provided some intuition for how a single charged quantum dot in a Voigt-geometry magnetic field can be used to generate a two-qubit entangled state, consisting of spin (stationary qubit) and a photon (flying qubit), in the state $|\psi\rangle = \frac{1}{\sqrt{2}} \left(|\uparrow\rangle \, |i\mathrm{H}, \hbar(\omega + \delta_\mathrm{e})\rangle + |\downarrow\rangle \, |\mathrm{V}, \hbar\omega\rangle \right)$.

Thus far three groups have provided evidence of spin-photon entanglement generation using charged quantum dots. The first two experiments, published jointly in 2012, showed evidence for entanglement between spin and photon polarization, and between spin and photon energy respectively [21, 22]. A report from Schaibley et al. [23] also showed evidence of entanglement between a quantum dot spin, and photon polarization. All three of these reports produced bounds on the state

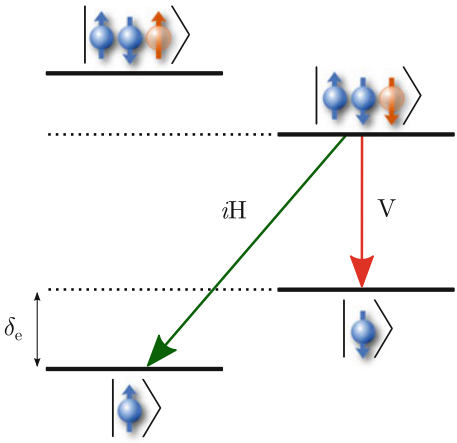

Fig. 14.5 Spin-Photon Entanglement Generation from a Charged Quantum Dot in a Voigt-geometry External Magnetic Field. When the trion state $|\uparrow\downarrow\Downarrow\rangle$ decays via spontaneous emission, it does so with with an equal amplitude of decaying to the state $|\uparrow\rangle$ or the state $|\downarrow\rangle$. However, the polarization selection rules for the $|\uparrow\downarrow\Downarrow\rangle \rightarrow |\uparrow\rangle$ and the $|\uparrow\downarrow\Downarrow\rangle \rightarrow |\downarrow\rangle$ decays are different. Furthermore, the $|\uparrow\rangle$ and $|\downarrow\rangle$ states are not energy-degenerate: they are split by a Zeeman energy $\hbar\delta_e$. Therefore the decay of the trion state results in the generation of an entangled state, where there is hyperentanglement between the electron ground spin states and two properties of the emitted single photon: its energy, and its polarization. The state produced can be written as $|\psi\rangle = \frac{1}{\sqrt{2}}(|\uparrow\rangle\,|i\mathrm{H}, \hbar(\omega+\delta_e)\rangle + |\downarrow\rangle\,|\mathrm{V}, \hbar\omega\rangle)$, where $\hbar\omega$ is the energy of the $|\uparrow\downarrow\Downarrow\rangle \leftrightarrow |\downarrow\rangle$ optical transition

fidelity by calculating the conditional probabilities for measurements in two orthogonal bases. In a follow-up [24] to their first paper [21], De Greve et al. showed results from a full tomographic reconstruction of the density matrix, yielding strong experimental proof that the entangled state produced by a charged quantum dot is $|\psi\rangle = \frac{1}{\sqrt{2}}(|\uparrow\rangle\,|i\mathrm{H}, \hbar(\omega+\delta_e)\rangle + |\downarrow\rangle\,|\mathrm{V}, \hbar\omega\rangle)$. All the experiments we have mentioned so far in this section [21–24] work in quite similar ways. We will focus in particular on the experiments by De Greve et al. [21, 24], but the basic concept of how the entanglement generation and verification is performed shares many common aspects with the other works.

The high-level procedure that is carried out is as follows:

1. The quantum dot is prepared in the state $|\downarrow\rangle$ by a combination of optical pumping and, depending on the particular experiment, a π rotation operation (that flips the spin from $|\uparrow\rangle$ to $|\downarrow\rangle$).
2. A pulse that drives the $|\downarrow\rangle \leftrightarrow |\uparrow\downarrow\Downarrow\rangle$ transition is applied, with the goal of setting the quantum dot to be in the state $|\uparrow\downarrow\Downarrow\rangle$.
3. The state $|\uparrow\downarrow\Downarrow\rangle$ spontaneously decays and emits a photon, which results in the creation of the spin-photon entangled state $|\psi\rangle = \frac{1}{\sqrt{2}}(|\uparrow\rangle\,|i\mathrm{H}, \hbar(\omega+\delta_e)\rangle + |\downarrow\rangle\,|\mathrm{V}, \hbar\omega\rangle)$.
4. Now that the entangled state has been produced, we seek to measure it. First we measure the state of the photon. In the case of polarization, this is done by using

a polarizer and a single-photon detector: if a photon is detected, the photon must have been of the polarization that the polarizer transmits.

5. Next we measure the state of the spin. This is done by performing an optional spin rotation (depending on which basis we want to measure the spin in), and then optical pumping again. A different single-photon detector is used to record if a photon is emitted. The detection or non-detection of a photon by this detector provides the spin measurement result.

This describes just a single run of an experiment; for a single choice of measurement bases for the spin and the photon, this is repeated many times. The correlation between photon detections at the two different detectors during the same run of the experiment allows us to determine the conditional probability between a photon polarization measurement outcome and a spin measurement outcome. This whole procedure is then repeated for several different measurement bases, so that at least eight conditional probabilities for different orthogonal measurement outcomes can be determined.

Figure 14.6 shows the conditional probabilities obtained by De Greve et al. [21]. These conditional probabilities are given as the probability of a spin measurement outcome, given a photon polarization measurement outcome. For example, from the first panel, we can read that $\Pr\left[\text{spin} = \uparrow | \text{photon} = \text{H}\right] \approx 1, \Pr\left[\text{spin} = \downarrow | \text{photon} = \text{H}\right] \approx 0$, $\Pr\left[\text{spin} = \uparrow | \text{photon} = \text{V}\right] \approx 0$, and $\Pr\left[\text{spin} = \downarrow | \text{photon} = \text{V}\right] \approx 0.85$. These conditional probabilities are sometimes referred to as "classical correlations", because a classical two-particle state that has no entanglement could conceivably be constructed that would also yield such strong correlations. However, when these probabilities are considered in combination with the results shown in the right panel of Fig. 14.6, they are unambiguously reflective of a two-qubit state that is entangled. The conditional probabilities in the orthogonal basis also show strong correlations; for example, $\Pr\left[\text{spin} = \leftarrow \middle| \text{photon} = \sigma^+\right] \approx 1$. These measured conditional probabilities are strikingly similar to those we would expect if there were no measurement errors, and the state we produced was $|\psi\rangle = \frac{1}{\sqrt{2}} \left(|\uparrow\rangle\, |i\text{H}, \hbar(\omega + \delta_\text{e})\rangle + |\downarrow\rangle\, |\text{V}, \hbar\omega\rangle\right)$.

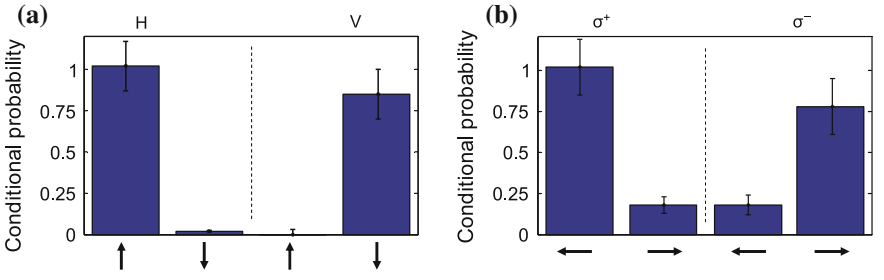

Fig. 14.6 Derived and reprinted with permission from De Greve et al. [21]. The *left panel* **a** shows the conditional probabilities when measurements were performed in the $\{|\uparrow\rangle, |\downarrow\rangle\}$ basis for the spin, and in the $\{|\text{H}\rangle, |\text{V}\rangle\}$ basis for the photon. The *right panel* **b** shows the conditional probabilities when measurements were performed in the $\{|\rightarrow\rangle, |\leftarrow\rangle\}$ basis for the spin, and in the $\left\{\left|\sigma^+\right\rangle, \left|\sigma^-\right\rangle\right\}$ basis for the photon

This is easy to see if we rewrite the state $|\psi\rangle$ using the $\{|\rightarrow\rangle, |\leftarrow\rangle\}$ basis for the spin, and the $\left\{\left|\sigma^+\right\rangle, \left|\sigma^-\right\rangle\right\}$ basis for the photon:

$$|\psi\rangle = \frac{1}{\sqrt{2}}\left(|\uparrow\rangle |iH\rangle + |\downarrow\rangle |V\rangle\right) \tag{14.7}$$

$$= \frac{1}{\sqrt{2}}\left(i\,|\uparrow\rangle |H\rangle + |\downarrow\rangle |V\rangle\right) \tag{14.8}$$

$$= \frac{i}{\sqrt{2}}\left(|\rightarrow\rangle \left|\sigma^-\right\rangle + |\leftarrow\rangle \left|\sigma^+\right\rangle\right) \tag{14.9}$$

Here we have neglected the energy information, since in De Greve et al. [21, 24] (and in the work by Schaibley et al. [23]), the energy information is not measured.[28] A similar rewriting procedure is used for frequency/energy photonic qubits instead of polarization qubits in Gao et al. [22].

Equation 14.9 indicates that we should expect the conditional probabilities in the orthogonal bases to be $\Pr\left[\text{spin} = \rightarrow \middle| \text{photon} = \sigma^-\right] = 1$, $\Pr\left[\text{spin} = \leftarrow \middle| \text{photon} = \sigma^-\right] = 0$, $\Pr\left[\text{spin} = \rightarrow \middle| \text{photon} = \sigma^+\right] = 0$, and $\Pr\left[\text{spin} = \leftarrow \middle| \text{photon} = \sigma^+\right] = 1$.

An important subtlety in these experiments [21, 23, 24] arises from the fact that as soon as the photonic qubit is measured in the $\left\{\left|\sigma^+\right\rangle, \left|\sigma^-\right\rangle\right\}$ basis, the spin state collapses to either $|\rightarrow\rangle$ or $|\leftarrow\rangle$ (depending on the photon polarization measurement outcome), and due to the presence of an external magnetic field, the spin will undergo Larmor precession. For example, if the spin state is collapsed to $|\rightarrow\rangle$, after half a Larmor period, it will have evolved to become $|\leftarrow\rangle$. This Larmor precession is a convenient feature, since when it is combined with optical rotation pulses, it allows for the measurement of the spin in bases other than $\{|\uparrow\rangle, |\downarrow\rangle\}$. However, it also has a detrimental effect: these experiments are performed on time ensembles, where the same quantum dot is observed many times, and in each run of the experiment, the spontaneous decay of the $|\uparrow\downarrow\Downarrow\rangle$ state can occur at a different time (roughly within the lifetime of that trion state, which was approximately 600 ps in [21, 24]). The timing resolution of the detection used to measure the photonic qubit is thus crucial; if the timing resolution is not much faster than the Larmor period, the experimeter will bin together runs of the experiment where the trion decays occurred at substantially different times,[29] and the spin measurements in the $\{|\rightarrow\rangle, |\leftarrow\rangle\}$ basis will consequently yield greatly reduced correlations. This is explained in detail in the supplementary information of [21]. The solution used in the experiments reported in [21, 24] was to develop an ultrafast (sub-10-ps) optical gate, using frequency downconversion, which resulted in an effective timing resolution of photon

[28] In [21, 24], due to the sub-10-ps timing resolution achieved using pulsed downconversion, energy information that can distinguish between the two photons is unobtainable even in principle. Explicit "erasure" of the energy information is crucial; simply not measuring would lead to tracing over all possible outcomes, resulting in a reduction of the observed state fidelity.

[29] The "time" here means the time delay between a synchronization pulse that occurs at the start of every run of the experiment, and of the photon emission by the quantum dot, as opposed to the absolute time.

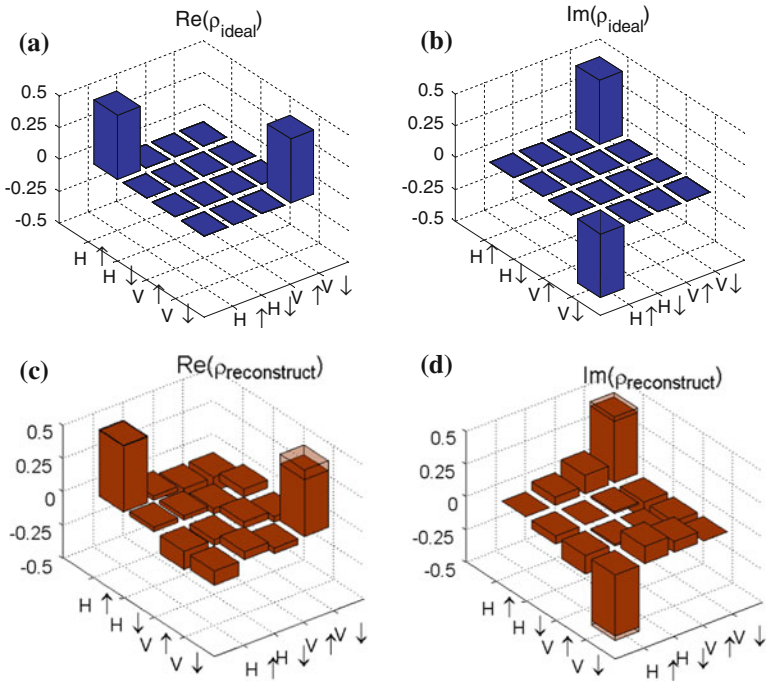

Fig. 14.7 Entangled Spin-Photon State Density Matrices. Reprinted with permission from De Greve et al. [24]. **a** The real and **b** imaginary parts of the ideal density matrix ρ_{ideal}. **c** The real and **d** imaginary parts of the density matrix reconstructed using the direct procedure, $\rho_{\text{reconstruct}}$. The shaded regions depict the ideal density matrix

detection of approximately 8 ps. This compared to a Larmor period of approximately 57 ps. This technique provided the added benefit that the frequency conversion that was performed had a target wavelength of approximately 1560 nm, which is in the low-loss band used for telecommunications in optical fibres.

The ideal density matrix is $\rho_{\text{ideal}} = |\psi\rangle\langle\psi|$, where $|\psi\rangle$ is given in (14.8). A two-qubit (4×4) density matrix has 16 complex entries, but since it is constrained to be Hermitian, it can be specified by just 16 real numbers.[30] As is described in detail in the supplementary information of [24], De Greve et al. performed measurements to obtain 16 conditional probabilities in a combination of three different orthogonal bases for the spin and the photon polarization. The reconstructed density matrix can be computed using the formula $\rho_{\text{reconstruct}} = \frac{1}{4}\sum_{i,j} r_{i,j}\sigma_i \otimes \sigma_j$, where the $r_{i,j}$ are related to the measurement results ($r_{i,j} \triangleq \text{Tr}\left[\rho\sigma_i \otimes \sigma_j\right]$) [42]. The ideal and reconstructed density matrices are depicted in Fig. 14.7, in the $\{|\text{H}\rangle, |\text{V}\rangle\} \otimes \{|\uparrow\rangle, |\downarrow\rangle\}$ basis.

[30] Since a density matrix should also have a trace of one, a two-qubit density matrix should only need 15 real numbers to be specified, although typically in quantum state tomography 16 numbers are used, since the reconstruction procedure is more convenient in this case.

This direct reconstruction of the density matrix is simple, but has a flaw: due to imperfections in the measurements (for example, detector dark counts), the reconstructed density matrix may be non-physical: it may not have a trace of one, and moreover, it may not be positive semi-definite. The trace can be forced to be one by normalizing the reconstructed density matrix, but there is no simple method to force the matrix to be positive semi-definite after it has already been reconstructed using the direct method.

One can see an example of the kind of measurement error that results in a non-physical result in Fig. 14.6: note that the conditional probability $\Pr[\text{spin} = \uparrow | \text{photon} = \text{H}]$ is measured as being slightly greater than 1. This isn't physically possible, since the probability of measuring the spin to be in state $|\uparrow\rangle$ is at most 1.

One solution to this problem that is commonly used in quantum state tomography is to perform a reconstruction of the density matrix that is constrained to produce the positive-semi-definite, trace-one density matrix that is most consistent the measurement results. This can be done using a maximum likelihood estimation (MLE) procedure, as described by James et al. [87], and in the supplementary information of De Greve et al. [24]. The MLE procedure produces a density matrix that we denote as ρ_{MLE}.

Since the procedure used to obtain ρ_{MLE} is an iterative numerical optimization, it is not possible to use standard propagation of error methodology to determine the uncertainty in, for example, the fidelity F of the state ($F \triangleq \langle \psi_{\text{ideal}} | \rho_{\text{MLE}} | \psi_{\text{ideal}} \rangle$). However, by resampling [24, 88] the original photon counting data, it is possible to generate a distribution of reconstructed density matrices, and hence a distribution of metrics on those matrices. Figure 14.8 shows both the density matrix reconstructed using the MLE procedure on the original data.

The mean fidelity of the spin-photon entangled state produced by De Greve et al. in [24] was $F = 92.1\,\%$, with a single-standard-deviation uncertainty of $\pm 3.2\,\%$. If two spatially-separated quantum dots are used to produce spin-photon entangled

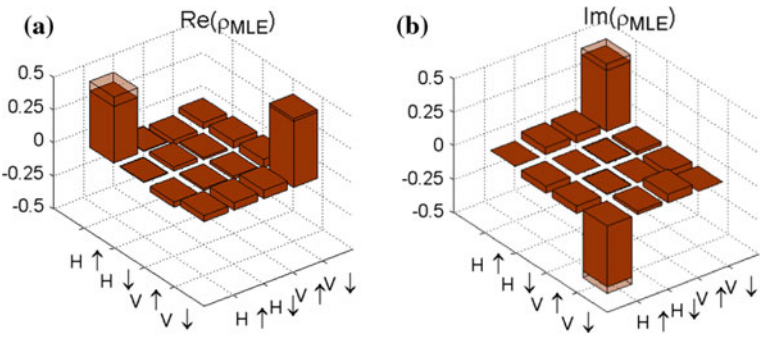

Fig. 14.8 Maximum-Likelihood-Estimation-based Density Matrix Reconstruction and Uncertainty Analysis. Reprinted with permission from De Greve et al. [24]. **a** The real and **b** imaginary parts of the density matrix reconstructed using the MLE procedure, ρ_{MLE}. The shaded regions depict the ideal density matrix

Table 14.2 Spin-photon entanglement results

Physical system	Photon emission wavelength	Spontaneous emission time	Entangled state fidelity	Institution	Reference
Trapped ion ($^{111}Cd^{+}$)	214.5 nm	3 ns	$\geq 87\,\%$	U. Maryland[a]	[89]
Neutral atom (^{87}Rb)	780 nm	26 ns[b]	$87 \pm 1\,\%$	LMU München	[90]
Neutral atom (^{87}Rb)	780 nm	26 ns[c]	$> 86.0(4)\,\%$	MPI Garching	[91]
NV centre	637 nm	11 ns	$\geq 70 \pm 7\,\%$	Harvard U.	[92]
Trapped ion ($^{40}Ca^{+}$)	854 nm	14 ns	$97.4 \pm 0.2\,\%$	U. Innsbruck	[93]
Quantum dot (InAs)	910 nm $\rightarrow$ 1560 nm[d]	0.6 ns	$\geq 80 \pm 8.5\,\%$	Stanford U.	[21]
Quantum dot (InGaAs)	967 nm	$\approx$ 1 ns	$\geq 68 \pm 5\,\%$	ETH Zürich	[22]
Quantum dot (InAs)	950 nm	$\approx$ 1 ns	$\geq 59 \pm 4\,\%$	U. Michigan	[23]
Quantum dot (InAs)	910 nm $\rightarrow$ 1560 nm[d]	0.6 ns	$92.1 \pm 3.2\,\%$	Stanford U.	[24]

[a]The group of Monroe was based at the University of Michigan at the time [89] was published, but has since moved to the University of Maryland.
[b][60] (also from the group of Weinfurter at LMU) shows time-resolved measurements of $^{87}Rb\ 5^2P_{3/2} \rightarrow 5^2S_{1/2}$ decay that are consistent with the value of 26 ns given in [94].
[c][91] gives the atomic dipole decay rate as $2\pi \cdot 3$ MHz (HWHM). This is $2\pi \cdot 6$ MHz (FWHM), and corresponds to a $\approx$ 26 ns lifetime, as per [94].
[d]The quantum dot emitted photons at 910 nm, but these photons were converted to the telecommunications wavelength, 1560 nm.
A summary of spin-photon entanglement generation experiment results in different single-particle physical systems, given in chronological order

qubits each with fidelity greater than $1/\sqrt{2} \approx 0.71$, and we assume perfect photon interference, then a spin-spin entangled state can certainly be produced (via a suitable heralded entanglement generation protocol) that will have a fidelity greater than 0.5. Therefore a spin-photon state fidelity of 0.92 is certainly sufficient for a demonstration of spin-spin entanglement with quantum dots.

Table 14.2 compares this spin-photon state fidelity to that of fidelities obtained in other spin-photon entanglement experiments. This table also highlights the feature that quantum dots have optically excited states with relatively short lifetimes ($\sim$600 pswhen the quantum dot is embedded in low-Q planar microcavity); this affects the rate at which spin-photon entangled states can be generated.

14.4 Conclusion

We have explained how quantum dots might be used as the building blocks for a quantum repeater, but there is still much work to be done before a useful quantum repeater may be built from quantum dots, or indeed before such a repeater can even be designed in detail.

In the short term, one of the major outstanding experimental goals is the demonstration of spin-spin entanglement using quantum dots, i.e., the entanglement of spins in two different quantum dots that are spatially separated by a macroscopic distance. Spin-spin entanglement has been achieved using atomic ensembles [62, 95], trapped ion qubits [55], single atom qubits [60, 61], and NV center qubits [63], so the spin-spin generation protocols are well-tested, but a demonstration of spin-spin entanglement with quantum dots is nevertheless seen as an important milestone for the quantum dot spin qubit community.

The spin readout mechanism that was used in all the recent quantum dot spin-photon entanglement experiments we have highlighted [21–24] yields only a single photon (at most) per experimental run, and so can only be used as a multi-shot readout by averaging over many experimental runs (since photon collection and detection efficiency is not unity). Demonstration of a single-shot readout mechanism that can be integrated with the other important operations for a quantum repeater memory qubit is an important goal. This would make a spin-spin demonstration easier (since then only two-photon coincidences would need to be observed, rather than four-photon coincidences), and is also a key requirement for implementation of the surface code [65].

The lack of a scalable two-qubit gate is arguably the biggest challenge that the community needs to overcome. Two-qubit operations on memory qubits are ubiquitous in all the large-scale quantum repeater proposals we have discussed, and at the very least will be needed to perform error correction. There have as-yet been no demonstrations in any physical system of quantum error correction that allow a memory qubit to stay coherent for an arbitrarily long time, or even for a time much longer than the native T_2 time. However, with quantum dot spin qubits, this is especially important even for early demonstrations, since InAs quantum dot spin qubits

have rather short T_2 times, which limit the communication distance. Demonstrating a QEC-enabled extension of a logical qubit coherence time in quantum dots is a major goal, but one that can only be tackled after a scalable two-qubit gate has been developed.

The high-level designs for large-scale quantum devices using quantum dots call for the use of arrays of site-controlled quantum dots, but here too there is much work to be done: developing methods to produce such arrays with a high yield of quantum dots that have good, homogeneous optical properties is a major challenge. In the near term, spin results that have been achieved using randomly-located quantum dots should be replicated using site-controlled quantum dots, to aid in the development of site-controlled QD arrays that are suitable for spin qubits.

The challenges in constructing a high-fidelity, high-bandwidth (measured in "entangled qubit pairs per second") quantum network are daunting. For approaches using neutral atoms or ions to succeed, researchers need to overcome significant barriers to scaling. Meanwhile solid-state approaches have struggled to achieve the required operation fidelities for fault-tolerant operation, in some cases suffer from insufficiently-long coherence times, and in many cases don't yet have a scalable two-qubit gate operation, among other imperfections. Gisin and Thew, in 2007 [96], wrote:

> The development of a fully operational quantum repeater and a realistic quantum-network architecture are grand challenges for quantum communication. Despite some claims, nothing like this has been demonstrated so far and one should not expect any real-world demonstration for another five to ten years.

Seven years later, much the same can still be said. Several months after Gisin and Thew's review was published, results showing entanglement between distant quantum memories using the DLCZ protocol for atomic ensembles [95] and the Simon-Irvine protocol for single trapped ions [55] were reported. As we have already mentioned, many other experiments generating entanglement between a quantum memory and a photon, or between quantum memories, have subsequently been performed [21–24, 60, 61, 63, 92, 93]. However, even the demonstration of just a single round of entanglement purification between distant quantum memories has not yet been completed, in any physical system. Similarly, there have been no demonstrations of entanglement swapping to connect two distant quantum memories via an intermediate quantum memory. Entanglement generation between two quantum memories is now well-established in both atomic and in some solid-state systems, but the goal of implementing both entanglement swapping and entanglement purification between remote quantum memories to demonstrate a proof-of-concept quantum repeater is still a distant hope rather than a soon-to-be-completed milestone.

Building a quantum repeater is evidently a grand challenge, and one that seems unlikely to be met for many years to come. Besides the challenges for how to make a quantum repeater, there is also a challenge to find uses for a quantum repeater. The canonical application at present is long-distance quantum key distribution. However, private key distribution can currently be performed with very high bandwidth using classical means, and the cost-benefit analysis for quantum repeaters for this

application is not necessarily favourable.[31] Tests of the Bell inequality over ever-longer distances are an interesting fundamental application of the distributed entanglement that quantum repeaters would provide. Teleportation [28] is also an interesting fundamental application of distributed entanglement, and may also play a role in the construction of distributed quantum computers [99]. Gottesman et al. [100] have proposed an optical interferometer design that could overcome current optical telescope resolution limits if a quantum repeater is realized, and Kómár et al. [101] have proposed a global atomic clock network design that fundamentally uses remote entangled states. Both these proposals are recent, so there is some hope that more uses of distributed entanglement may yet be uncovered.

Acknowledgments We would like to acknowledge our coauthors of those papers covered in this chapter that we were involved in (namely [13, 21, 24]), with whom we had many valuable discussions. We would like to thank especially Yoshihisa Yamamoto (who supervised these works), Thaddeus Ladd, Christian Schneider and Cody Jones for numerous conversations about the place and use of quantum dots in quantum communication technology. We would also like to thank Ana Predojević for her thorough editing of this chapter, including many helpful suggestions, and Jelena Vučković for her careful reading of a draft of this chapter. PLM acknowledges support from the Cabinet Office, Government of Japan, and the Japan Society for the Promotion of Science (JSPS) through the Funding Program for World-Leading Innovative R&D on Science and Technology (FIRST Program). KDG acknowledges support from a Harvard Quantum Optics Fellowship.

References

1. S. Kiravittaya, A. Rastelli, O.G. Schmidt, Advanced quantum dot configurations. Rep. Prog. Phys. **72**, 046502 (2009)
2. S. Buckley, K. Rivoire, J. Vučković, Engineered quantum dot single-photon sources. Rep. Prog. Phys. **75**, 126503 (2012)
3. R.J. Warburton, Single spins in self-assembled quantum dots. Nat. Mater. **12**, 483–493 (2013)
4. K. De Greve, D. Press, P.L. McMahon, Y. Yamamoto, Ultrafast optical control of individual quantum dot spin qubits. Rep. Prog. Phys. **76**, 092501 (2013)
5. R. Hanson, L.P. Kouwenhoven, J.R. Petta, S. Tarucha, L.M.K. Vandersypen, Spins in few-electron quantum dots. Rev. Mod. Phys. **79**, 1217–1265 (2007)
6. M. Atatüre et al., Quantum-dot spin-state preparation with near-unity fidelity. Science **312**, 551–553 (2006)

[31] A briefcase packed with hard drives or tapes can easily store over 100 TB of private keys, and can be transported to the opposite side of the world via a trusted courier in an airplane in approximately 24 hours. This yields a key distribution rate of approximately 10 Gbits/s. This can be compared to an achievable rate of Mbits/s using 10^4 quantum repeater stations, which was calculated by Fowler et al. [97]. A hybrid approach has been suggested by Devitt et al. [98]: if quantum memories can be made to have coherence times on the order of weeks, then Devitt et al. propose literally shipping the quantum memories from Alice to Bob. This avoids the need for long-distance fibre communication. The only use of optics in such an implementation of long-distance entanglement distribution would likely be the initial generation of the entanglement over a distance of a few meters. The coverage in this chapter of entanglement generation and construction of quantum memories, both in the abstract and for the particular case of quantum dots, is still relevant for such a physical-transport-based entanglement distribution scheme.

7. X. Xu et al., Fast spin state initialization in a singly charged InAs-GaAs quantum dot by optical cooling. Phy. Rev. Lett. **99**, 097401 (2007)
8. D. Press, T.D. Ladd, B. Zhang, Y. Yamamoto, Complete quantum control of a single quantum dot spin using ultrafast optical pulses. Nature **456**, 218–221 (2008)
9. J. Berezovsky, M.H. Mikkelsen, N.G. Stoltz, L.A. Coldren, D.D. Awschalom, Picosecond coherent optical manipulation of a single electron spin in a quantum dot. Science **320**, 349–352 (2008)
10. J. Berezovsky et al., Nondestructive optical measurements of a single electron spin in a quantum dot. Science **314**, 1916–1920 (2006)
11. M. Atatüre, J. Dreiser, A. Badolato, A. Imamoglu, Observation of faraday rotation from a single confined spin. Nat. Phys. **3**, 101–106 (2007)
12. A. Greilich et al., Mode locking of electron spin coherences in singly charged quantum dots. Science **313**, 341–345 (2006)
13. D. Press et al., Ultrafast optical spin echo in a single quantum dot. Nat. Photonics **4**, 367–370 (2010)
14. B.D. Gerardot et al., Optical pumping of a single hole spin in a quantum dot. Nature **451**, 441–444 (2008)
15. A.J. Ramsay et al., Fast optical preparation, control, and readout of a single quantum dot spin. Phys. Rev. Lett. **100**, 197401 (2008)
16. K. De Greve et al., Ultrafast coherent control and suppressed nuclear feedback of a single quantum dot hole qubit. Nat. Phys. **7**, 872–878 (2011)
17. A. Greilich, S.G. Carter, D. Kim, A.S. Bracker, D. Gammon, Optical control of one and two hole spins in interacting quantum dots. Nat. Photonics **5**, 702–708 (2011)
18. D. Brunner et al., A coherent single-hole spin in a semiconductor. Science **325**, 70–72 (2009)
19. L. Viola, E. Knill, S. Lloyd, Dynamical decoupling of open quantum systems. Phys. Rev. Lett. **82**, 2417–2421 (1999)
20. K. Khodjasteh, D.A. Lidar, Fault-tolerant quantum dynamical decoupling. Phys. Rev. Lett. **95**, 180501 (2005)
21. K. De Greve et al., Quantum-dot spin-photon entanglement via frequency downconversion to telecom wavelength. Nature **491**, 421–425 (2012)
22. W.B. Gao, P. Fallahi, E. Togan, J. Miguel-Sanchez, A. Imamoglu, Observation of entanglement between a quantum dot spin and a single photon. Nature **491**, 426–430 (2012)
23. J.R. Schaibley et al., Demonstration of quantum entanglement between a single electron spin confined to an InAs quantum dot and a photon. Phys. Rev. Lett. **110**, 167401 (2013)
24. K. De Greve et al., Complete tomography of a high-fidelity solid-state entangled spin–photon qubit pair. Nat. Commun. **4**, 2228 (2013)
25. G. Keiser, in *Optical Fiber Communications*, Wiley Encyclopedia of Telecommunications (Wiley, Hoboken, 2003)
26. W.K. Wootters, W.H. Zurek, A single quantum cannot be cloned. Nature **299**, 802–803 (1982)
27. D. Dieks, Communication by EPR devices. Phys. Lett. A **92**, 271–272 (1982)
28. C.H. Bennett et al., Teleporting an unknown quantum state via dual classical and einstein-podolsky-rosen channels. Phys. Rev. Lett. **70**, 1895–1899 (1993)
29. G. Morthier, J.D. Merlier, in *Optical Signal Regeneration*, ed. by Wiley Encyclopedia of Telecommunications (Wiley, Hoboken, 2003)
30. C.H. Bennett et al., Purification of noisy entanglement and faithful teleportation via noisy channels. Phys. Rev. Lett. **76**, 722–725 (1996)
31. C.H. Bennett, H.J. Bernstein, S. Popescu, B. Schumacher, Concentrating partial entanglement by local operations. Phys. Rev. A **53**, 2046–2052 (1996)
32. H.-J. Briegel, W. Dür, J.I. Cirac, P. Zoller, Quantum repeaters: the role of imperfect local operations in quantum communication. Phys. Rev. Lett. **81**, 5932–5935 (1998)
33. W. Dür, H.-J. Briegel, J.I. Cirac, P. Zoller, Quantum repeaters based on entanglement purification. Phys. Rev. A **59**, 169–181 (1999)
34. C.H. Bennett, D.P. DiVincenzo, J.A. Smolin, W.K. Wootters, Mixed-state entanglement and quantum error correction. Phys. Rev. A **54**, 3824–3851 (1996)

35. A.G. Fowler et al., Surface code quantum communication. Phys. Rev. Lett. **104**, 180503 (2010)
36. S.J. Devitt, W.J. Munro, K. Nemoto, Quantum error correction for beginners. Rep. Prog. Phys. **76**, 076001 (2013)
37. D.A. Lidar, T.A. Brun (eds.), *Quantum Error Correction* (Cambridge University Press, Cambridge, 2013)
38. L. Jiang et al., Quantum repeater with encoding. Phys. Rev. A **79**, 032325 (2009)
39. C.H. Bennett, G. Brassard, Quantum cryptography: public key distribution and coin tossing, in *Proceedings of the IEEE International Conference on Computers, Systems and Signal Processing* (1984), pp. 175–179
40. A.K. Ekert, Quantum cryptography based on bell's theorem. Phys. Rev. Lett. **67**, 661–663 (1991)
41. C.H. Bennett, G. Brassard, N.D. Mermin, Quantum cryptography without bell's theorem. Phys. Rev. Lett. **68**, 557–559 (1992)
42. M.A. Nielsen, I.L. Chuang, *Quantum Computation and Quantum Information*, 10th anniversary edition. (Cambridge University Press, Cambridge, 2011)
43. N. Gisin, G. Ribordy, W. Tittel, H. Zbinden, Quantum cryptography. Rev. Mod. Phys. **74**, 145–195 (2002)
44. M. Aspelmeyer, T. Jennewein, M. Pfennigbauer, W. Leeb, A. Zeilinger, Long-distance quantum communication with entangled photons using satellites. IEEE J. Sel. Top. Quantum Electron. **9**, 1541–1551 (2003)
45. V. Scarani et al., The security of practical quantum key distribution. Rev. Mod. Phys. **81**, 1301–1350 (2009)
46. C. Elliott, Building the quantum network. New J. Phys. **4**, 46 (2002)
47. M. Dianati, R. Alleaume, Architecture of the secoqc quantum key distribution network, in *First International Conference on Quantum, Nano, and Micro Technologies, 2007. ICQNM '07* (2007), pp. 13–13
48. M. Peev et al., The SECOQC quantum key distribution network in vienna. New J. Phys. **11**, 075001 (2009)
49. M. Żukowski, A. Zeilinger, M.A. Horne, A.K. Ekert, "Event-ready-detectors" bell experiment via entanglement swapping. Phys. Rev. Lett. **71**, 4287–4290 (1993)
50. D. Deutsch et al., Quantum privacy amplification and the security of quantum cryptography over noisy channels. Phys. Rev. Lett. **77**, 2818–2821 (1996)
51. M. Kroutvar et al., Optically programmable electron spin memory using semiconductor quantum dots. Nature **432**, 81–84 (2004)
52. Y. Li, S.D. Barrett, T.M. Stace, S.C. Benjamin, Long range failure-tolerant entanglement distribution. New J. Phys. **15**, 023012 (2013)
53. L.-M. Duan, M.D. Lukin, J.I. Cirac, P. Zoller, Long-distance quantum communication with atomic ensembles and linear optics. Nature **414**, 413–418 (2001)
54. C. Simon, W. Irvine, Robust long-distance entanglement and a loophole-free bell test with ions and photons. Phys. Rev. Lett. **91**, 110405 (2003)
55. D.L. Moehring et al., Entanglement of single-atom quantum bits at a distance. Nature **449**, 68–71 (2007)
56. C.K. Hong, Z.Y. Ou, L. Mandel, Measurement of subpicosecond time intervals between two photons by interference. Phys. Rev. Lett. **59**, 2044–2046 (1987)
57. Corning. PI1470: Corning SMF-28 ULL optical fiber product information (2014)
58. S. Zaske et al., Visible-to-telecom quantum frequency conversion of light from a single quantum emitter. Phys. Rev. Lett. **109**, 147404 (2012)
59. J.S. Pelc et al., Downconversion quantum interface for a single quantum dot spin and 1550-nm single-photon channel. Opt. Express **20**, 27510–27519 (2012)
60. J. Hofmann et al., Heralded entanglement between widely separated atoms. Science **337**, 72–75 (2012)
61. S. Ritter et al., An elementary quantum network of single atoms in optical cavities. Nature **484**, 195–200 (2012)

62. C.W. Chou et al., Measurement-induced entanglement for excitation stored in remote atomic ensembles. Nature **438**, 828–832 (2005)
63. H. Bernien et al., Heralded entanglement between solid-state qubits separated by three metres. Nature **497**, 86–90 (2013)
64. C. Jones, K. De Greve, Y. Yamamoto, A high-speed optical link to entangle quantum dots. arXiv:1310.4609 (2013)
65. N.C. Jones et al., Layered architecture for quantum computing. Phys. Rev. X **2**, 031007 (2012)
66. R. Van Meter, *Quantum Networking*, 1st edn. (Wiley-ISTE, Hoboken, 2014)
67. C. Schneider et al., Lithographic alignment to site-controlled quantum dots for device integration. Appl. Phys. Lett. **92**, 183101 (2008)
68. S. Maier et al., Site-controlled InAs/GaAs quantum dots emitting at telecommunication wavelength. Semiconduct. Sci. Technol. **29**, 052001 (2014)
69. S. Puri, P.L. McMahon, Y. Yamamoto, Single-shot quantum nondemolition measurement of a quantum-dot electron spin using cavity exciton-polaritons. Phys. Rev. B **90**, 155421 (2014)
70. S. Puri, P.L. McMahon, Y. Yamamoto, Optical manipulation of quantum dot electron spin qubits using microcavity quantum well exciton-polaritons. arXiv:1408.5160 (2014)
71. D.P. DiVincenzo, The physical implementation of quantum computation. Fortschr. Phys. **48**, 771–783 (2000)
72. W. Happer, Optical pumping. Rev. Mod. Phys. **44**, 169–249 (1972)
73. D. Loss, D.P. DiVincenzo, Quantum computation with quantum dots. Phys. Rev. A **57**, 120–126 (1998)
74. E.L. Hahn, Spin echoes. Phys. Rev. **80**, 580–594 (1950)
75. K. De Greve, *Towards Solid-State Quantum Repeaters: Ultrafast, Coherent Optical Control and Spin-Photon Entanglement in Charged InAs Quantum Dots*, 1st edn. (Springer, New York, 2013)
76. A. Imamoglu et al., Quantum information processing using quantum dot spins and cavity QED. Phys. Rev. Lett. **83**, 4204–4207 (1999)
77. C. Piermarocchi, P. Chen, L.J. Sham, D.G. Steel, Optical RKKY interaction between charged semiconductor quantum dots. Phys. Rev. Lett. **89**, 167402 (2002)
78. G.F. Quinteiro, J. Fernández-Rossier, C. Piermarocchi, Long-range spin-qubit interaction mediated by microcavity polaritons. Phys. Rev. Lett. **97**, 097401 (2006)
79. T.D. Ladd, Y. Yamamoto, Simple quantum logic gate with quantum dot cavity QED systems. Phys. Rev. B **84**, 235307 (2011)
80. S. Puri, N.Y. Kim, Y. Yamamoto, Two-qubit geometric phase gate for quantum dot spins using cavity polariton resonance. Phys. Rev. B **85**, 241403 (2012)
81. D. Kim, S.G. Carter, A. Greilich, A.S. Bracker, D. Gammon, Ultrafast optical control of entanglement between two quantum-dot spins. Nat. Phys. **7**, 223–229 (2011)
82. R.B. Patel et al., Two-photon interference of the emission from electrically tunable remote quantum dots. Nat. Photonics **4**, 632–635 (2010)
83. W.B. Gao et al, Quantum teleportation from a propagating photon to a solid-state spin qubit. Nat. Commun. **4**, 2744 (2013)
84. P. Gold et al., Two-photon interference from remote quantum dots with inhomogeneously broadened linewidths. Phys. Rev. B **89**, 035313 (2014)
85. S. Ates et al., Two-photon interference using background-free quantum frequency conversion of single photons emitted by an InAs quantum dot. Phys. Rev. Lett. **109**, 147405 (2012)
86. S.E. Economou, R.-B. Liu, L.J. Sham, D.G. Steel, Unified theory of consequences of spontaneous emission in a λ system. Phys. Rev. B **71**, 195327 (2005)
87. D.F.V. James, P.G. Kwiat, W.J. Munro, A.G. White, Measurement of qubits. Phys. Rev. A **64**, 052312 (2001)
88. B. Efron, R.J. Tibshirani, *An Introduction to the Bootstrap*, 1st edn. (Chapman and Hall/CRC, New York, 1993)
89. B.B. Blinov, D.L. Moehring, L.-M. Duan, C. Monroe, Observation of entanglement between a single trapped atom and a single photon. Nature **428**, 153–157 (2004)

90. J. Volz et al., Observation of entanglement of a single photon with a trapped atom. Phys. Rev. Lett. **96**, 030404 (2006)
91. T. Wilk, S.C. Webster, A. Kuhn, G. Rempe, Single-atom single-photon quantum interface. Science **317**, 488–490 (2007)
92. E. Togan et al., Quantum entanglement between an optical photon and a solid-state spin qubit. Nature **466**, 730–734 (2010)
93. A. Stute et al., Tunable ion-photon entanglement in an optical cavity. Nature **485**, 482–485 (2012)
94. U. Volz, H. Schmoranzer, Precision lifetime measurements on alkali atoms and on helium by beam–gas–laser spectroscopy. Phys. Scr. **1996**, 48 (1996)
95. C.-W. Chou et al., Functional quantum nodes for entanglement distribution over scalable quantum networks. Science **316**, 1316–1320 (2007)
96. N. Gisin, R. Thew, Quantum communication. Nat. Photonics **1**, 165–171 (2007)
97. A.G. Fowler, M. Mariantoni, J.M. Martinis, A.N. Cleland, Surface codes: towards practical large-scale quantum computation. Phys. Rev. A **86**, 032324 (2012)
98. S.J. Devitt, A.D. Greentree, A.M. Stephens, R. Van Meter, High-speed quantum networking by ship. arXiv:1410.3224 (2014)
99. R. Doyle Van Meter, III, Architecture of a quantum multicomputer optimized for Shor's factoring algorithm. arXiv:quant-ph/0607065 (2006)
100. D. Gottesman, T. Jennewein, S. Croke, Longer-baseline telescopes using quantum repeaters. Phys. Rev. Lett. **109**, 070503 (2012)
101. P. Kómár et al., A quantum network of clocks. Nat. Phys. **10**, 582–587 (2014)

Index

A
Above-band excitation, 307
Adiabatic coupling, 9
AFC spin-wave memory, 248
Atom-cavity coupling, 9
Atomic frequency comb, 245, 246, 251, 261, 263–265
Atomic frequency filters, 185
Atom-mirror cavity, 108
Atom-photon entanglement, 3
Atom-resonant photons, 184, 203, 204
Autocorrelation, 314

B
Backward-wave, 149, 150, 155–157
Bad-cavity regime, 10
Bell's inequality, 278
Biexciton binding energy, 308
Biphoton, 145, 146, 150, 152, 153, 155–171, 173, 179
Biphoton wave-function, 186, 196

C
Cauchy-Schwarz inequality, 264
Cavity, 3
Cavity-enhanced SPDC, 185, 208
Cavity-enhanced spontaneous emission, 9
Cavity quantum electrodynamics (cavity-QED), 4, 5, 39
CESPDC, 184–186, 190, 191, 193, 196, 198, 199, 202, 203, 205, 209
Characterization photon pair sources, 253
Clauser-Horne-Shimony-Holt inequality, 261, 262
Cluster spacing, 146–148, 156
Coherence, 21, 313
Concurrence, 262, 263
Controlled reversible inhomogeneous broadening, 245, 246, 248–250
Cooperativity, 33
Coupling efficiency, 78

D
Dark state, 8
Density matrix, 20
Dephasing, 23
Deterministic sources of single photons, 303
Dipole, 76
Double-pass pumping, 147, 148
Dressed-state, 8
Dynamical decoupling, 244, 267

E
Electric field, 280
Electromagnetically induced transparency (EIT), 101, 107, 146, 157, 158, 160, 162, 164, 169–171, 174–176, 179
Energy-time entanglement, 250, 260
Entangled photon pairs, 278, 303
Entanglement, 3, 18, 111
Entanglement generation rate, 111
Entanglement purification, 368
Entanglement swapping, 367
Equivalent-noise bandwidth, 189
Extinction, 101
Extraction efficiency, 48

A. Predojević and M.W. Mitchell (eds.), *Engineering the Atom-Photon Interaction*, Nano-Optics and Nanophotonics, DOI 10.1007/978-3-319-19231-4

F
Faraday anomalous dispersion optical filter (FADOF), 186–190, 192–194, 202
Faraday rotation, 187, 188, 198, 204–208
Fidelity, 112
Fine structure splitting, 278
Flying qubits, 367
Free space, 78
Free space coupling, 100
Frequency correlation, 328
Frequency uncorrelated photon pairs, 338

G
Gradient echo memory, 245, 246, 248–250
Group delay, 160, 162, 163, 169–171, 174
Group velocity mismatching, 329

H
Hanbury-Brown and Twiss (HBT), 15
Heralded, 111
Heralded photons, 328
Heralded single photons, 250, 263
High numerical aperture optics, 100
High-purity, 218, 219, 229
Homodyne, 219, 224–227, 229, 233, 238
HOM type interference, 336
Hong-Ou-Mandel (HOM), 21

I
Impedance-matched cavity, 249
Impedance matching, 28
Indistinguishable photons, 183, 184, 345
Induced dichroism atomic filter, 202, 209
Input-output coupling, 29
Input-output formalism, 102
In-situ lithography, 43
Interference, 112
Interference between independent sources, 327

J
Jaynes-Cummings model, 5

L
Lamb-Dicke regime, 109
Laser scattering, 307
Level dephasing, 309
Linear optics quantum computing (LOQC), 21
Local-oscillator photons, 26

M
Master equation, 24, 30
Matter-light interaction, 126
Memory efficiency, 33
Microcavity, 347
Micro-cavity quantum dot, 309
Mixing angles, 8
Multi-photon component, 315

N
Narrow linewidth entangled sources, 334
NooN state, 184, 197, 198, 200, 201, 204–209

O
Optical pumping, 382

P
Parabolic mirror, 78
Periodically-poled potassium titanyl phosphate (PPKTP), 186, 187, 198, 199
Phase matching, 146, 150, 155–157, 171
Phase shift, 102
Photon-atom coupling, 82
Photon cascade, 305
Photonic qubits, 367
Photon indistinguishability, 52
Photon pairs, 126
Photon shaping, 23
Photon statistics, 14
Piezoelectric-induced strains, 279
Polarization-entangled, 280
Polarization entangled photon pairs, 130, 305
Polarization entanglement, 20, 131
Precursor, 164, 170, 174, 175
Purcell effect, 9
Purcell factor, 10, 39
Pure, 218, 225, 227, 238
Purity, 224, 227

Q
Quantum dot, 303
Quantum electrodynamic (QED), 110
Quantum gate, 21
Quantum-homodyne, 22
Quantum information processing, 126
Quantum interfaces, 3
Quantum light, 343

Quantum light source, 251, 252, 255, 257, 268
Quantum light storage, 243, 249, 250, 259, 260, 263, 267
Quantum memory, 28, 218, 219, 221, 222, 229, 230, 242, 243, 245, 246, 251, 252, 255, 256, 259, 261, 367
Quantum-network, 21, 126

R
Rabi oscillation, 160–162, 171, 308
Raman process, 114
Ramsey interference, 308
Rare-earth doped crystals, 242, 243
Recoil, 115
Resonant excitation, 343

S
Second order cross-correlation function, 254
Semiconductor quantum dots, 277
Signal photons, 27
Single photons, 3, 126, 278
Single photon absorption, 126, 133
Single photon counter, 129
Single photon detector, 129
Single photon source, 127, 343–345
Single-photon entanglement, 262
Single trapped ion, 100
Spectral brightness, 252, 256, 259
Spectral purity, 186, 187, 191, 192, 197, 203, 204, 208, 209
Spin echo, 245, 267, 313
Spontaneous four-wave mixing (SFWM), 145, 146, 150, 157–159, 165, 168–173, 179
Spontaneous parametric down-conversion, 130, 328
Stark-effect, 279
Stark tuning, 56
State mapping, 28
Stimulated Raman scattering by adiabatic passage (STIRAP), 13
Strain, 280
Strong coupling, 10
Sub-Poissonian, 14
Sub-Poissonian distribution, 304
Success probability, 113

T
Teleportation, 21
Time-bin encoding, 25
Time-bin entanglement, 316
Trion, 383
Triple-peak photons, 26
Two-photon interference, 14
Two-photon resonant excitation, 307

V
Vacuum mode density, 110
Vacuum-Rabi oscillation, 10
Vacuum stimulated Raman scattering by adiabatic passage (V-STIRAP), 13

W
Wigner function, 218, 219, 226–230